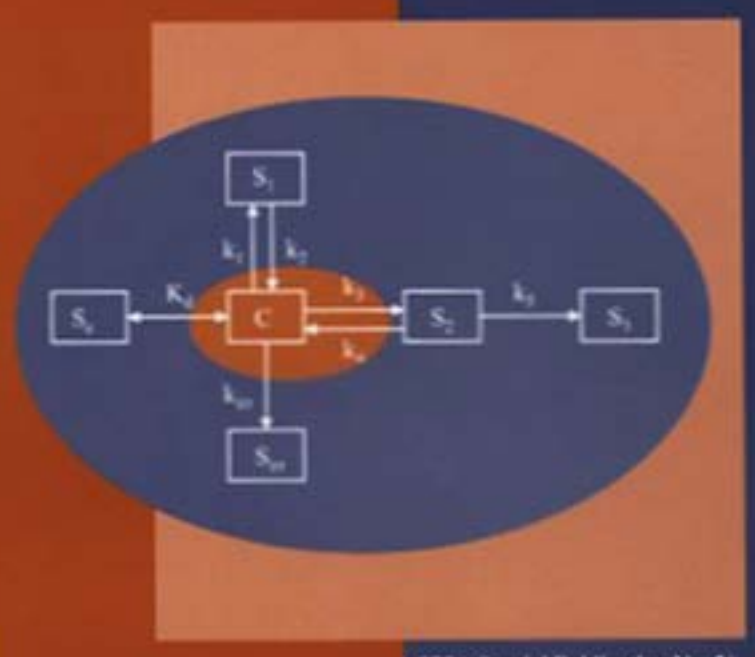
### Dear Reader!

The publication of this document does not pursue for itself any commercial benefit. But such documents promote the most rapid professional and spiritual growth of readers and are advertising of paper editions of such documents.

You can download (copy) this file for educational purposes only. PLEASE NOTE that ANY COMMERCIAL USE of this file IS STRICTLY FORBIDDEN You should delete it immediately after your reading is completed. Under international legislation you are responsible for prorer use of this file. All copywrite reserved by owner.

### Physical and Chemical Processes of Water and Solute Transport/Retention in Soil



SSSA Special Publication No. 56

# Physical and Chemical Processes of Water and Solute Transport/Retention in Soils

Proceedings of a symposium sponsored by Divisions S-1 and S-2 of the Soil Science Society of America in Baltimore, MD, 18 to 22 October 1998

*Editors* H. M. Selim and D. L. Sparks

Editorial Committee H. M. Selim

D. L. Sparks

H. D. Scott

Organizing Committee

H. M. Selim

D. L. Sparks

H. D. Scott

M. A. Tabatabai

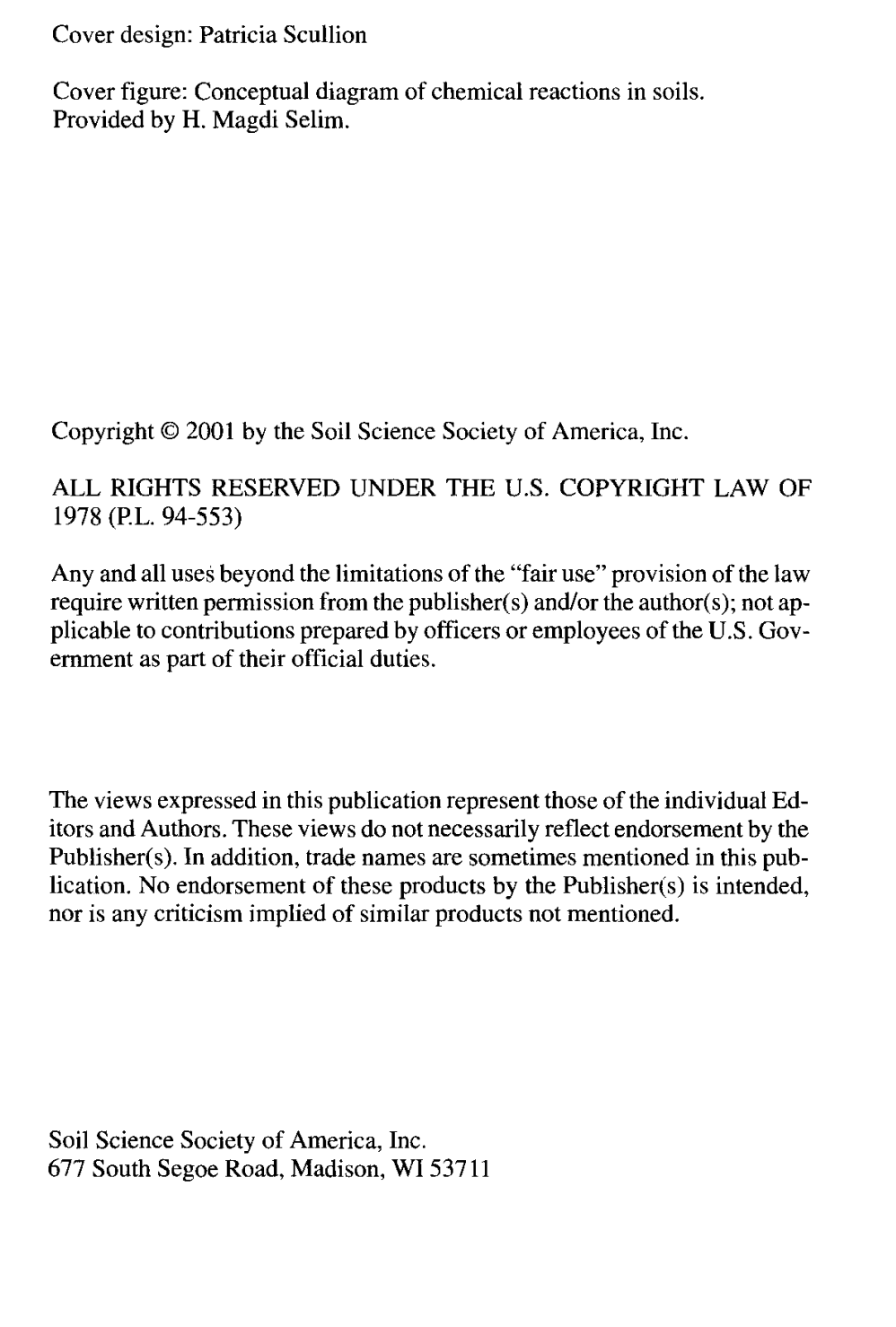
M. B. Kirkham

Editor-in-Chief SSSA Warren A. Dick

Managing Editor
J. M. Bartels

SSSA Special Publication Number 56

Soil Science Society of America, Inc. Madison, Wisconsin 2001



Library of Congress Catalog Card Number: 00 136276

### **CONTENTS**

	rward	vii :
	eface	ix xi
	nversion Factors for SI and non-SI units	xiii
1	Adsorption and Capillary Processes in Variably Saturated Porous Media—Pore Scale Hydrostatic and Hydrodynamic Considerations Dani Or and Markus Tuller	1
2	Transport of Water and Solutes in Soils as in Fractal Porous Media Yakov Pachepsky, David A. Benson, and Dennis J. Timlin	51
3	Models Relating Solute Dispersion to Pore Space Geometry in Saturated Media: A Review  Ed Perfect and Michael C. Sukop	77
4	Testing Kinematic Wave Solutions for Flow in Macroporous Soils Against a Lattice-Gas Simulation Liliana Di Pietro and Peter F. Germann	147
5	Tracer Transport in a Soil Column for Sine Wave Loading Donald Dean Adrian, Akram N. Alshawabkeh, and Senda Ozkan	169
6	Modeling Nonlinear Kinetic Behavior of Copper Adsorption-Desorption in Soil H. M. Selim and Liwang Ma	189
7	Application of Spectroscopic Methods to Sorption Model Parameter Estimation Lynn E. Katz and Eric J. Boyle-Wight	213
8	Molecular Dynamics Simulations of Adsorption Processes at the Clay Mineral/Aqueous Solution Interface David M. Miller, Brian J. Teppen, Ching-Hsing Yu, and Lothar Schäfer	257

#### **FOREWORD**

The transport and retention of water, nutrients, and inorganic and organic contaminants in the environment is greatly affected by physical and chemical processes and reactions in porous media such as soils. To definitively and comprehensively understand and model these processes/reactions, it is important that multiple scales—ranging from the landscape to the molecular—be investigated. Over the past decade numerous developments at multiple scales, have occurred in the soil, physical, and environmental sciences. These developments, which are discussed in this book, include: employment of fractal and spatial heterogeneity analyses in describing transport phenomena; development of sophisticated molecular models; use of in situ spectroscopic and microscopic techniques to elucidate reaction mechanisms and models in soils; and, inclusion of time-dependent phenomena in predicting solute transport/retention in soils. This important publication presents the state-of-the-art on physicochemical processes of water/solute transport/retention. It brings together a rich combination of soil and environmental scientists and engineers. This publication will be most useful to scientists, professionals, and students who are interested in aqueous and terrestrial ecosystems.

DONALD L. SPARKS, *President* Soil Science Society of America

#### **PREFACE**

The subject of water and solute transport in porous media is one of the most fascinating areas of science. Tremendous advances have been recently made in understanding the soil physical/chemical processes of water and solute transport/retention in soils. Recent emphasis includes water retention based on pore-scale modeling, flow in multiregions/multidomains, scaling and heterogeneity, prefractal networks, percolation models, numerical simulations, and cellular automata. Advances in experimental methods include confirmation and measurement of adsorption phenomena at the clay mineral/aqueous solution interface, surface complexation modeling based on molecular spectroscopy and microscopy, and precipitation/dissolution. Interest in these topics led to the organization of a symposium on "Physical and chemical processes of water and solute transport/retention in soils" held in two sessions at the 1998 Soil Science Society of America Annual Meeting in Baltimore, Maryland, 18 to 22 Oct. 1998. This symposium was organized by Divisions S-1 and S-2.

This book contains eight chapters that represent the state of knowledge on physical and chemical processes of water and solutes in soils. Moreover, this book provides a review of recent knowledge of modeling the heterogeneous soil system. In Chapter 1, a review on recent progress in modeling liquid retention and interfacial configurations in variably saturated porous media is presented. Pore scale hydrodynamic modeling approaches for prediction of hydraulic conductivity of unsaturated porous media are discussed. In Chapter 2, the focus is on the transport of water and solutes in soils as a fractal porous media. Chapter 3 provides a review of models relating solute dispersion to pore space geometry in saturated media and a discussion of emerging areas of prefractal networks, percolation models, numerical simulations, cellular automata, and physical micro-models. Chapter 4 focuses on lattice-gas models for simulation of preferential infiltration in fractured media. In Chapter 5, a solution for the convection-dispersion equation is presented for a tracer solute subject to a periodic loading function. The focus of Chapter 6 is on nonlinear-kinetic behavior of solute retention mechanisms in soils. Limitations of nonlinear and kinetic multireaction and second-order models are also presented. In Chapter 7, parameter estimation of surface complexation models based on molecular spectroscopy and microscopy (XAS and EXFS) are discussed. The scope of Chapter 8 is on molecular dynamics simulation techniques to study adsorption phenomena at the clay mineral/aqueous solution interface.

We wish to extend our deep appreciation to the authors for their contributions. The editors also wish to thank the anonymous reviewers and the SSSA headquarters staff for their efforts on this special publication.

H. MAGDI SELIM, *co-editor* Louisiana State University, Baton Rouge, Louisiana

DONALD L. SPARKS, co-editor University of Delaware, Newark, Delaware

#### **CONTRIBUTORS**

Donald Dean Adrian Rubicon Professor of Civil and Environmental Engineering,

Louisiana State University, Baton Rouge, LA 70803-6405

Akram N. Alshawabkeh Assistant Professor, Department of Civil and Environmental En-

gineering, 420 Snell Engineering, Northeastern University,

Boston, MA 02115

David A. Benson Assistant Professor, Desert Research Institute, 2215 Raggio Park-

way, Reno, NV 89512

Eric J. Boyle-Wight Department of Civil and Environmental Engineering, The Uni-

versity of Maine, Orono, ME 04469-5706

Liliana Di Pietro Researcher, Institut National de la Recherche Agronomique, Unité

de Science du Sol, Domaine St. Paul, Site Agroparc, , 84914 Avi-

gnon Cedex 9, France

**Peter F. Germann** Professor of Soil Science, Department of Geography, University

of Bern, Hallerstrasse 12, CH 3012 Bern, Switzerland

**Lynn E. Katz** Department of Civil Engineering, The University of Texas,

Austin, TX 78712

Liwang Ma Soil Scientist, USDA-ARS, Great Plains Systems Research, P.O.

Box E, Fort Collins, CO 80522

David M. Miller Associate Professor, Department of Crop, Soil, and Environ-

mental Sciences, PTSC 115, University of Arkansas, Fayetteville,

AR 72701

**Dani Or** Assistant Professor of Soil Physics, Department of Plants, Soils,

and Biometeorology, Utah State University, 4820 Old Main Hill,

Logan, UT 84322-4820

Senda Ozkan Research Assistant, Department of Civil and Environmental En-

gineering, Louisiana State University, Baton Rouge, LA 70803-

6405

Yakov Pachepsky Senior Research Scholar, Duke University Phytotron; present ad-

dress and title is Research Physical Scientist, USDA-ARS Hydrology and Remote Sensing Laboratory, Bldg. 007, Rm. 104,

10300 Baltimore Ave., Beltsville, MD 20705

E. Perfect Assistant Professor, Department of Agronomy, University of

Kentucky, Lexington, KY 40546-0091

Lothar Schäfer Edgar Wertheim Professor, Chemistry Department, University of

Arkansas, Fayetteville, AR 72701

H. M. Selim Professor of Soil Physics, Agronomy Department, Louisiana

State University, Baton Rouge, LA 70803-2110

Michael C. Sukop Department of Agronomy, University of Kentucky, Lexington,

KY 40546-0091

Brian J. Teppen Assistant Professor, Department of Crop and Soil Sciences, Michi-

gan State University, East Lansing, MI 48824-0270

xii **CONTRIBUTORS** 

**Dennis Timlin** 

Soil Scientist, USDA-ARS Remote Sensing and Modeling Laboratory, Bldg. 007, Rm. 116 BARC-WEST, 10300 Baltimore

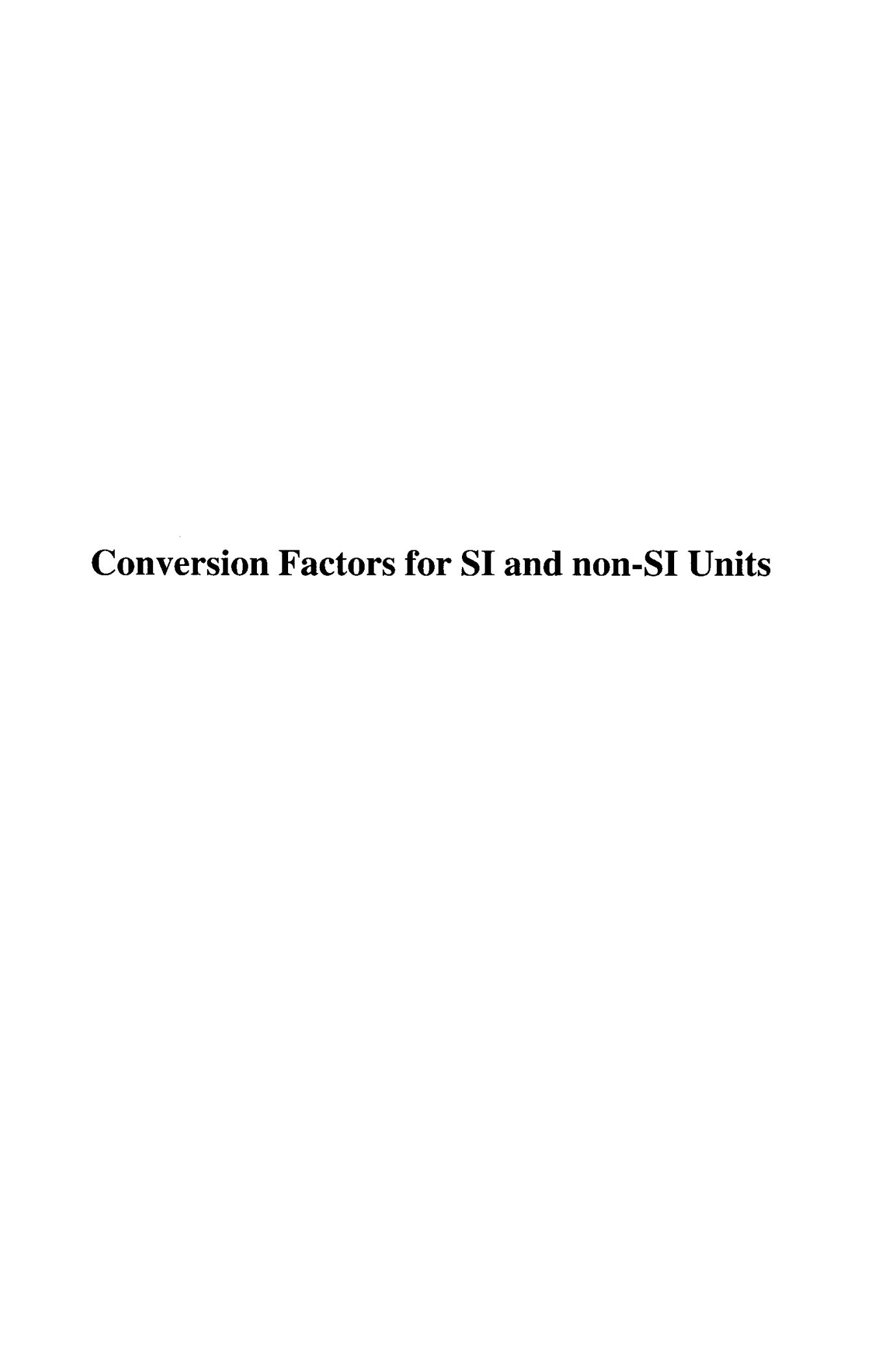
Ave., Beltsville, MD 20705

**Markus Tuller** 

Research Associate, Department of Plants, Soils, and Biometeorology, Utah State University, 4820 Old Main Hill, Logan, UT

84322-4820

Postdoctoral Associate, Chemistry Department, University of Arkansas, Fayetteville, AR 72701 Ching-Hsing Yu



## **Conversion Factors for SI and non-SI Units**

To convert Column 1 into Column 2, multiply by	Column 1 SI Unit	Column 2 non-SI Units	To convert Column 2 into Column 1, multiply by
-		Length	<del>-</del>
0.621	kilometer, km (10 <sup>3</sup> m)	mile, mi	1.609
1.094	meter, m	yard, yd	0.914
3.28	meter, m	foot, ft	0.304
1.0	micrometer, $\mu$ m (10 <sup>-6</sup> m)	micron, μ	1.0
$3.94 \times 10^{-2}$	millimeter, mm (10 <sup>-3</sup> m)	inch, in	25.4
10	nanometer, nm $(10^{-9} \text{ m})$	Angstrom, Å	0.1
		Area	
2.47	hectare, ha	acre	0.405
247	square kilometer, km <sup>2</sup> (10 <sup>3</sup> m) <sup>2</sup>	acre	$4.05 \times 10^{-3}$
0.386	square kilometer, $km^2 (10^3 \text{ m})^2$	square mile, mi <sup>2</sup>	2.590
$2.47 \times 10^{-4}$	square meter, m <sup>2</sup>	acre	$4.05 \times 10^{3}$
10.76	square meter, m <sup>2</sup>	square foot, ft <sup>2</sup>	$9.29 \times 10^{-2}$
$1.55\times10^{-3}$	square millimeter, mm <sup>2</sup> $(10^{-3} \text{ m})^2$	square inch, in <sup>2</sup>	645
		Volume	
$9.73 \times 10^{-3}$	cubic meter, m <sup>3</sup>	acre-inch	102.8
35.3	cubic meter, m <sup>3</sup>	cubic foot, ft <sup>3</sup>	$2.83 \times 10^{-2}$
$6.10 \times 10^4$	cubic meter, m <sup>3</sup>	cubic inch, in <sup>3</sup>	$1.64 \times 10^{-5}$
$2.84 \times 10^{-2}$	liter, $L(10^{-3} \text{ m}^3)$	bushel, bu	35.24
1.057	liter, $L(10^{-3} \text{ m}^3)$	quart (liquid), qt	0.946
$3.53 \times 10^{-2}$	liter, $L(10^{-3} \text{ m}^3)$	cubic foot, ft <sup>3</sup>	28.3
0.265	liter, L $(10^{-3} \text{ m}^3)$	gallon	3.78
33.78	liter, L $(10^{-3} \text{ m}^3)$	ounce (fluid), oz	$2.96 \times 10^{-2}$
2.11	liter, L $(10^{-3} \text{ m}^3)$	pint (fluid), pt	0.473

$2.20 \times 10^{-3}$ $3.52 \times 10^{-2}$ 2.205 0.01 $1.10 \times 10^{-3}$ 1.102 1.102	gram, g (10 <sup>-3</sup> kg) gram, g (10 <sup>-3</sup> kg) kilogram, kg kilogram, kg kilogram, kg megagram, Mg (tonne) tonne, t	pound, lb ounce (avdp), oz pound, lb quintal (metric), q ton (2000 lb), ton ton (U.S.), ton ton (U.S.), ton	454 28.4 0.454 100 907 0.907
1.102			0.507
	Yield	and Rate	
$0.893$ $7.77 \times 10^{-2}$ $1.49 \times 10^{-2}$ $1.59 \times 10^{-2}$ $1.86 \times 10^{-2}$ $0.107$ $893$ $893$ $0.446$ $2.24$	kilogram per hectare, kg ha <sup>-1</sup> kilogram per cubic meter, kg m <sup>-3</sup> kilogram per hectare, kg ha <sup>-1</sup> kilogram per hectare, kg ha <sup>-1</sup> kilogram per hectare, kg ha <sup>-1</sup> liter per hectare, L ha <sup>-1</sup> tonne per hectare, t ha <sup>-1</sup> megagram per hectare, Mg ha <sup>-1</sup> megagram per hectare, Mg ha <sup>-1</sup> meter per second, m s <sup>-1</sup>	pound per acre, lb acre <sup>-1</sup> pound per bushel, lb bu <sup>-1</sup> bushel per acre, 60 lb bushel per acre, 56 lb bushel per acre, 48 lb gallon per acre pound per acre, lb acre <sup>-1</sup> pound per acre, lb acre <sup>-1</sup> ton (2000 lb) per acre, ton acre <sup>-1</sup> mile per hour	1.12 12.87 67.19 62.71 53.75 9.35 1.12 × $10^{-3}$ 1.12 × $10^{-3}$ 2.24 0.447
	Specia	fic Surface	
10 1000	square meter per kilogram, m <sup>2</sup> kg <sup>-1</sup> square meter per kilogram, m <sup>2</sup> kg <sup>-1</sup>	square centimeter per gram, cm <sup>2</sup> g <sup>-1</sup> square millimeter per gram, mm <sup>2</sup> g <sup>-1</sup>	0.1 0.001
	Pi	ressure	
9.90 10 1.00 $2.09 \times 10^{-2}$ $1.45 \times 10^{-4}$	megapascal, MPa (10 <sup>6</sup> Pa) megapascal, MPa (10 <sup>6</sup> Pa) megagram, per cubic meter, Mg m <sup>-3</sup> pascal, Pa pascal, Pa	atmosphere bar gram per cubic centimeter, g cm <sup>-3</sup> pound per square foot, lb ft <sup>-2</sup> pound per square inch, lb in <sup>-2</sup>	$0.101$ $0.1$ $1.00$ $47.9$ $6.90 \times 10^{3}$

Mass

(continued on next page)

## **Conversion Factors for SI and non-SI Units**

convert Column 1 into Column 2, multiply by	Column 1 SI Unit	Column 2 non-SI Units	To convert Column 2 into Column 1, multiply by
	Ter	nperature	
1.00 (K - 273)	kelvin, K	Celsius, °C	1.00 (°C + 273)
$(9/5  ^{\circ}\text{C}) + 32$	Celsius, °C	Fahrenheit, °F	5/9 (°F – 32)
	Energy, Wor	k, Quantity of Heat	
$9.52 \times 10^{-4}$	joule, J	British thermal unit, Btu	$1.05 \times 10^{3}$
0.239	joule, J	calorie, cal	4.19
$10^{7}$	joule, J	erg	$10^{-7}$
0.735	joule, J	foot-pound	1.36
$2.387 \times 10^{-5}$	joule per square meter, J m <sup>-2</sup>	calorie per square centimeter (langley)	$4.19 \times 10^4$
10 <sup>5</sup>	newton, N	dyne	$10^{-5}$
$1.43 \times 10^{-3}$	watt per square meter, W m <sup>-2</sup>	calorie per square centimeter minute (irradiance), cal cm <sup>-2</sup> min <sup>-1</sup>	698
	Transpiration	and Photosynthesis	
$3.60 \times 10^{-2}$	milligram per square meter second, $mg m^{-2} s^{-1}$	gram per square decimeter hour, $g dm^{-2} h^{-1}$	27.8
$5.56 \times 10^{-3}$	milligram (H <sub>2</sub> O) per square meter second, mg m <sup>-2</sup> s <sup>-1</sup>	micromole (H <sub>2</sub> O) per square centi- meter second, $\mu$ mol cm <sup>-2</sup> s <sup>-1</sup>	180
10-4	milligram per square meter second, mg m <sup>-2</sup> s <sup>-1</sup>	milligram per square centimeter second, mg cm <sup>-2</sup> s <sup>-1</sup>	$10^4$
35.97	milligram per square meter second, mg m <sup>-2</sup> s <sup>-1</sup>	milligram per square decimeter hour, $mg dm^{-2} h^{-1}$	$2.78 \times 10^{-2}$
	Pla	ane Angle	
57.3	radian, rad	degrees (angle), °	$1.75 \times 10^{-2}$

Electrical Co	onductivity.	Electricity.	and Magnetism
---------------	--------------	--------------	---------------

		· · · · · · · · · · · · · · · · · · ·	
10	siemen per meter, S m <sup>-1</sup>	millimho per centimeter, mmho cm <sup>-1</sup>	0.1
104	tesla, T	gauss, G	10 <sup>-4</sup>
	Water	Measurement	
$9.73 \times 10^{-3}$	cubic meter, m <sup>3</sup>	acre-inch, acre-in	102.8
$9.81 \times 10^{-3}$	cubic meter per hour, m <sup>3</sup> h <sup>-1</sup>	cubic foot per second, ft <sup>3</sup> s <sup>-1</sup>	101.9
4.40	cubic meter per hour, m <sup>3</sup> h <sup>-</sup> 1	U.S. gallon per minute, gal min <sup>-1</sup>	0.227
8.11	hectare meter, ha m	acre-foot, acre-ft	0.123
97.28	hectare meter, ha m	acre-inch, acre-in	$1.03 \times 10^{-2}$
$8.1 \times 10^{-2}$	hectare centimeter, ha cm	acre-foot, acre-ft	12.33
	Con	centrations	
1	centimole per kilogram, cmol kg <sup>-1</sup>	milliequivalent per 100 grams, meq $100 \text{ g}^{-1}$	1
0.1	gram per kilogram, g kg <sup>-1</sup>	percent, %	10
1	milligram per kilogram, mg kg <sup>-1</sup>	parts per million, ppm	1
	Rac	dioactivity	
$2.7 \times 10^{-11}$	becquerel, Bq	curie, Ci	$3.7 \times 10^{10}$
$2.7 \times 10^{-2}$	becquerel per kilogram, Bq kg <sup>-1</sup>	picocurie per gram, pCi g <sup>-1</sup>	37
100	gray, Gy (absorbed dose)	rad, rd	0.01
100			0.01
	Plant Nut	rient Conversion	
	Elemental	Oxide	
2.29	P	$P_2O_5$	0.437
1.20	K	$K_2O$	0.830
1.39	Ca	CaO	0.715
1.66	Mg	MgO	0.602

# 1

# Adsorption and Capillary Processes in Variably Saturated Porous Media—Pore Scale Hydrostatic and Hydrodynamic Considerations

#### Dani Or and Markus Tuller

Utah State University Logan, Utah

Common conceptual models for liquid distribution and transport in variably saturated porous media often rely on oversimplified representation of media pore space geometry as a bundle of cylindrical capillaries, and on incomplete thermodynamic account of pore scale processes. For example, liquid adsorption due to surface forces and flow in thin films are often ignored. In this study we provide a review of recent progress in modeling liquid retention and interfacial configurations in variably saturated porous media and application of pore scale hydrodynamic considerations for prediction of hydraulic conductivity of unsaturated porous media.

We propose a new framework for improved modeling of liquid behavior in porous media based on two complementary elements: (i) a unitary approach for considering the individual contributions of adsorptive and capillary forces to the matric potential; and (ii) a more realistic model for media pore space comprising an angular pore connected to slit-shaped spaces with internal surface area. The augmented Young Laplace (AYL) equation provides the necessary representation for combining adsorptive and capillary processes. Pore scale liquid-vapor configuration, saturation, and liquid-vapor interfacial area are calculated for different potentials and pore dimensions.

The pore-scale model provides the basis for development of a statistical framework for upscaling from a single pore to a sample of variably saturated porous medium. The statistical distribution of pore sizes is modeled as a gamma distribution with the expected values of liquid configuration in pore space calculated from geometrical and chemical potential considerations within the statistical framework. Model predictions compare favorably with measured retention data, yielding similarly close fits to data as the widely used van Genuchten parametric model. Liquid-vapor interfacial area as a function of chemical potential is readily calculated from estimated retention parameters. Comparisons of calculated inter-

facial area for sand with measurements obtained with surface-active tracers show reasonable agreement. Results indicate that interfaces associated with films dominate contributions of capillary menisci to the total liquid-vapor interfacial area, often by several orders of magnitude.

The detailed picture of liquid vapor interfaces under hydrostatic conditions provides a basis for introducing hydrodynamic considerations. The underlying assumption is that the liquid configurations and interfaces remain relatively unchanged under slow laminar flow conditions. Furthermore, network effects are ignored, and only flow into the liquid cross-section is considered. These simplifying assumptions facilitate derivation of closed form expressions for pore scale flow processes under saturated and partially saturated conditions. The pore scale solutions serve as building blocks for modeling the unsaturated hydraulic conductivity representing flow in a porous medium sample. Insights gained from the preliminary studies reviewed in this work were instrumental in developing models for flow in unsaturated fractured porous media with emphasis on flow on rough surfaces.

#### INTRODUCTION

Conventional models for liquid distribution, flow and transport in variably saturated porous media are often based on representation of pore space geometry as a "bundle of cylindrical capillaries" (BCC) (Childs, 1940; Milington & Quirk, 1961; Mualem, 1976a; Hassanizadeh & Gray, 1993). Implicit in the BCC model is the assumption that certain pore sizes are completely liquid-filled, whereas larger pores are completely empty at a given saturation level. No provision is made for adsorption processes nor for dual-occupancy of wetting and nonwetting phases within the same pores. Moreover, the practical interpretation of liquid retention measurements (e.g., soil water characteristic curves) for determination of media pore size distribution relies solely on cylindrical-capillarity, ignoring the role of surface area and adsorbed liquid films (Childs, 1940). The lack of consideration of surface forces, the "empty-full" approach precluding dual-occupancy of pores, and the unrealistic (surface less) cylindrical geometry were identified in reviews by Celia et al. (1995) and Nitao and Bear (1996) as a primary hindrance to future progress in modeling flow and transport processes in variably saturated porous media. Sophisticated pore network models employ concepts of invasion percolation in angular pore systems for modeling wetting and non-wetting phase drainage and imbibition driven by capillary processes (Blunt & Scher, 1995; Lenormand et al., 1983). Berkowitz and Ewing (1998) provide a comprehensive review of percolation theory and various pore network models. Flow in corners and crevices of angular pores (Blunt & Scher, 1995), and in thin liquid films (Li & Wardlaw, 1986a; Lenormand, 1990) were identified as important flow regimes in partially saturated porous media. However, these flow regimes were not previously integrated into a complete thermodynamic pore-scale theory that considers adsorptive surface forces towards development of self-consistent constitutive hydraulic relationships at the sample scale.

Tuller et al. (1999) proposed an alternative framework for modeling liquid behavior in variably saturated porous media. This framework included two complementary elements: (i) a unitary approach for explicit consideration of the individual contributions of adsorptive and capillary forces to matric (chemical) potential (Philip, 1977a); and (ii) its implementation within a new pore space geometry (unit cell) comprising an angular central pore for capillary processes attached to slit-shaped spaces with surface area for adsorptive processes. Interface science formalism and the concept of the disjoining pressure (Derjaguin et al., 1987) provided the physicochemical basis for incorporation of adsorption phenomena into the augmented Young-Laplace (AYL) equation (Derjaguin, 1957; Philip, 1977a; Novy et al., 1989; Blunt et al., 1995). Simplifications of the rigorous AYL equation have been instrumental in the development of practical closed-form expressions for both saturation and interfacial area as a function of chemical potential at the pore scale.

In a subsequent study, Or and Tuller (1999) have used the pore-scale model to develop a statistical framework for upscaling from pore to a sample of variably saturated porous medium. The statistical distribution of pore sizes was modeled as a gamma distribution with the expected values of liquid configuration in pore space calculated from geometrical and chemical potential considerations within the statistical framework. One of the advantages of Or and Tuller (1999) framework is the use of measurable media properties to estimate upscaling parameters. This is accomplished by matching predicted and measured retention data subject to measured porosity and surface area constraints.

The objective of this work is to provide a review of recent progress in poreand sample-scale liquid retention and liquid-vapor interfacial area modeling. These new modeling approaches for liquid configuration in porous media provide explicit calculations of liquid-vapor interfacial area an important variable for multiphase flow, gas exchange, and microbial habitat studies. Information about liquid configuration also provides a reasonable starting point for pore scale hydrodynamic considerations leading to prediction of hydraulic conductivity of unsaturated porous media.

The review is organized as follows: first, we discuss aspects of the unitary approach for combining adsorptive and capillary contributions, and present the new pore scale model of Tuller et al. (1999). The upscaling scheme of Or and Tuller (1999) for representing sample scale retention properties will be presented, followed by illustrative examples with measured characteristic data and a discussion of critical soil parameters. The role of liquid-vapor interfacial area will be highlighted by comparisons of model predictions with limited measurements. Finally, we introduce hydrodynamic considerations of unsaturated flow in films and corners leading to prediction of hydraulic conductivity of rough rock surfaces and unsaturated porous media.

#### HYDROSTATIC CONSIDERATIONS

#### **Unitary Approach to Adsorption and Capillary Condensation**

The pioneering work of Edlefsen and Anderson (1943) on mechanisms of water distribution on soil particles provided the qualitative basis for Philip's (1977a)

development of a quantitative unitary approach to capillary condensation and adsorption in porous media. The liquid-vapor interface is considered as a surface of constant partial specific Gibbs free energy [or chemical potential  $\mu$  (Nitao & Bear, 1996)] made up of an adsorptive component (A) and a capillary component (C):

$$\mu = A(h) + C(\kappa) \tag{1}$$

with  $\kappa$  as the mean curvature of the liquid-vapor interface, and h as the distance from the solid to the liquid-vapor interface, taken normal to the solid surface (thickness of the adsorbed film). Philip (1977a) has used an empirical expression for the adsorptive component, assuming it is dependent on film thickness only:

$$A(h) = -v R'T/h$$
 [2]

where v is a positive constant ( $10^{-10}$  m), R' is the gas constant per unit mass of the vapor (J K<sup>-1</sup> kg<sup>-1</sup>) and T is temperature (K). The capillary component C is given by the Young-Laplace equation:

$$C(\kappa) = -2\sigma\kappa/\rho$$
 [3]

where  $\kappa$  is positive for an interface concave outward from the liquid,  $\sigma$  is the surface tension at the interface and  $\rho$  is the density of the liquid. Philip's unitary approach was preceded by Derjaguin (1957) and others (Vershinin et al., 1966) who modified the Young-Laplace equation by adding an adsorptive term, resulting in an equation identical to Eq. [1] known as the augmented Young-Laplace (AYL) equation (Novy et al., 1989; Blunt et al., 1995).

Philip's (1977a,b; 1978) work is further extended in this study by: (i) establishing a linkage with modern interface science concepts (Derjaguin et al, 1987; Iwamatsu & Horii, 1996); and (ii) applying the updated theory to an entire pore space model rather than to individual geometrical features (e.g., corners, wedges, etc.). An important component in the updated unitary approach is the application of more general and versatile adsorption terms based on Derjaguin's disjoining pressure concept. Such refinements are important at very low water contents when films on adjacent surfaces are completely separated by a vapor phase. They also allow for direct incorporation of various surface electrochemical properties that, in turn, affect flow in thin liquid films and give rise to various viscoelectric effects.

#### The Disjoining Pressure and Liquid Films

In their monograph *Surface Forces*, Derjaguin et al. (1987) provide an indepth review of the behavior of thin liquid films adsorbed on solid surfaces. In the core of modern interface science theory is the notion that surface forces modify the intensive properties of interfacial regions relative to their bulk phase values. Derjaguin et al. (1987) distinguished between two types of surface forces. The first kind includes long-range (>500Å) electrostatic forces (e.g., diffuse double layer, DDL), and short-range (<100Å) van der Waals and hydration forces, responsible for molecular interactions and structural changes in water molecules near the solid surface.

The combined effect of interfacial interactions results in a difference in chemical potentials between the liquid in the adsorbed film and the bulk phase. This difference in chemical potentials may be expressed as an equivalent interfacial force per unit area of the interface, termed by Derjaguin et al. (1987) as the disjoining pressure ( $\Pi$ ). The disjoining pressure is a function of the film thickness (h), and it can also be viewed as the difference between a normal component of film pressure,  $P_N$  (in equilibrium with the gaseous phase  $P_N = P_G$ ), and the pressure in the bulk liquid phase,  $P_L$ .

$$\Pi(h) = P_N(h) - P_L = P_G - P_L$$
 [4]

The disjoining pressure is related to more conventional thermodynamic quantities such as Gibbs free energy (Adamson, 1990; Nitao & Bear, 1996). Gibbs free energy (G) per unit area of the interface may be defined on the basis of  $\Pi(h)$  isotherm for constant pressure  $P_L$ , temperature T, chemical  $\mu$  and electric potentials of the liquid-gaseous ( $\psi_g$ ) and the liquid-solid ( $\psi_s$ ) interfaces as (Derjaguin et al., 1987):

$$G(h) = -\int_{\infty}^{h} \Pi(h)dh$$
 [5]

The value of G(h) is equal to the work of thinning the film in a reversible, isobaric, and isothermal process from infinity to a finite thickness h, with  $\Pi(h) = -(\partial G/\partial h)_{T,P_L,\mu,\psi g,\psi s}$ . Derjaguin et al. (1987) point out that the choice of  $\Pi(h)$  as the basic thermodynamic property is not a mere change of notation, but  $\Pi(h)$  has advantages in cases where Gibbs thermodynamic theory is not well defined, such as, when interfacial zones overlap to the extent that the film does not retain the intensive properties of the bulk phase. The use of the disjoining pressure is advantageous from an experimental point of view because of the relative ease to account for different contributions (e.g., electrostatic effects).

The disjoining pressure is a sum of several components (just as with soil water potential). The major components of the  $\Pi(h)$ -isotherm in porous media are molecular,  $\Pi_{\rm m}(h)$ ; electrostatic,  $\Pi_{\rm e}(h)$ ; structural,  $\Pi_{\rm s}(h)$ ; and adsorptive  $\Pi_{\rm a}(h)$ :

$$\Pi(h) = \Pi_{\rm m}(h) + \Pi_{\rm e}(h) + \Pi_{\rm s}(h) + \Pi_{\rm a}(h).$$
 [6]

- $\Pi_{\rm m}(h)$ —The component originates from van der Waals molecular interaction between macro-objects (e.g., parallel clay plates). Various expressions with  $\Pi_{\rm m}(h)$  often proportional to  $h^{-3}$  were derived by Paunov et al. (1996) and Iwamatsu and Horii (1996).
- $\Pi_{\rm e}(h)$  The electrostatic component of the disjoining pressure is calculated from the solution of the Poisson-Boltzmann equation for the DDL with appropriate boundary conditions. Approximate solutions are adequate for many applications and are available in the literature (e.g., Paunov et al., 1996; Derjaguin et al., 1987) often with  $\Pi_{\rm e}(h) \propto h^{-2}$ .
- $\Pi_s(h)$  Some controversy exists regarding the origin of this structural component; some attribute it to changes in the structure (density) of water adjacent to solid surfaces and deformation of hydrated shells, while others attribute this force to the presence of a layer with a lower dielectric constant near

the surface (Paunov et al., 1996). Regardless of its exact origin, this component is responsible for the so-called hydration repulsion that stabilizes dispersion and prevents coagulation of some colloidal particles, even at high electrolyte concentrations (Mitlin & Sharma, 1993),  $\Pi_s(h) \propto h^{-1}$  (Novy et al., 1989).

 $\Pi_a(h)$ — This adsorptive component of the disjoining pressure results from nonuniform concentrations in the film due to unequal interaction energies of solute and solvent with interfaces in nonionic solutions. (This is different than the nonuniform distribution of charged ions.) This component of the disjoining pressure is likely to become very important for interactions between nonpolar molecules (e.g., nonaqueous phase liquids) that give rise to repulsive forces in the liquid film [see discussion by Derjaguin et al. (1987, p. 171)].

#### Film Adsorption on Flat Surfaces and in Slit-Shaped Pores

Several physically based expressions relating the thickness of adsorbed films to surface and liquid properties, geometry, and chemical potential have been developed (Iwamatsu & Horii, 1996). The simplest case considered here is that of a liquid film adsorbed on a planar surface (Fig. 1–1a) because of interfacial interactions induced by long-range molecular (van der Waals) forces only. The relationships between the disjoining pressure  $\Pi(h)$  and film thickness h for the planar film are given by (Derjaguin, et al., 1987; Iwamatsu & Horii, 1996):

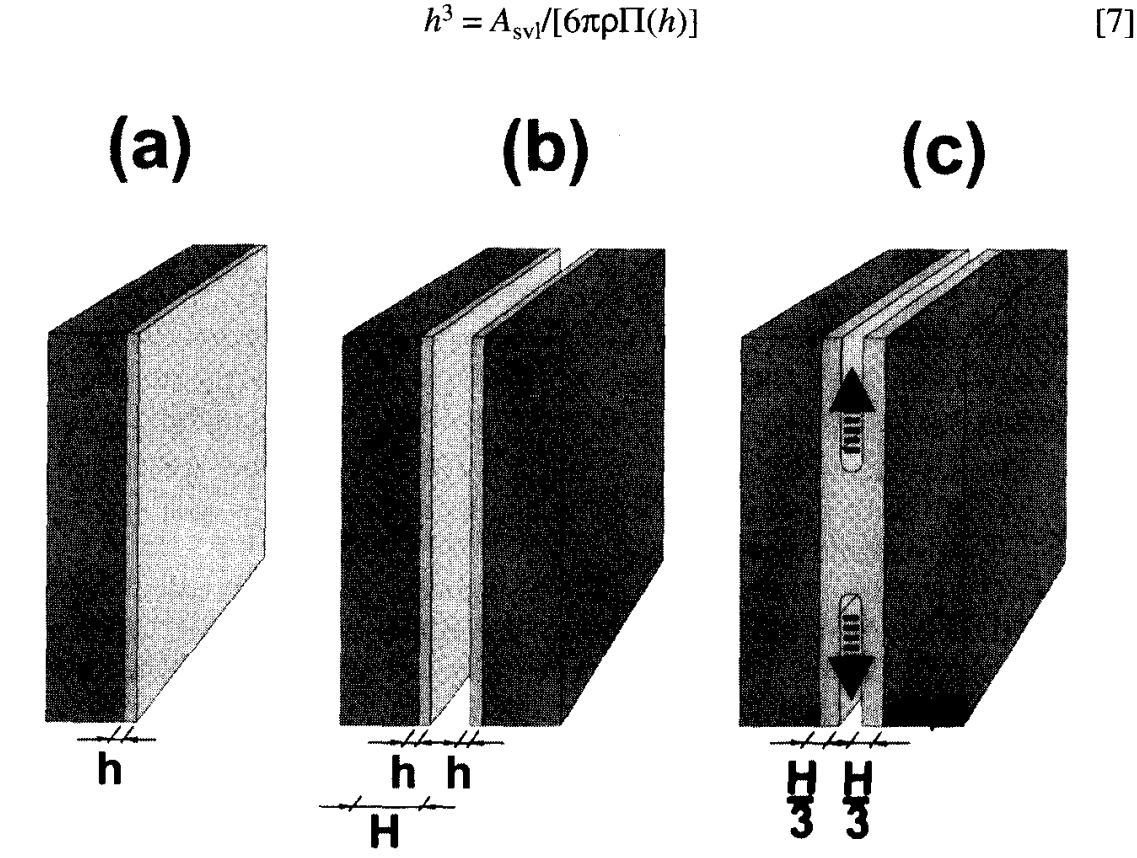


Fig. 1–1. Adsorption on planar surfaces and between parallel plates (slit shaped spaces): (a) single surface, (b) parallel plates, and (c) forming of a liquid neck at slit snappoff.

where h is film thickness,  $A_{\rm svl}$  is the Hamaker constant for solid-vapor interactions through the intervening liquid [for condensation  $A_{\rm svl} < 0$  (Iwamatsu & Horii, 1996)], and  $\rho$  is the density of the liquid. Considering adsorption only (no capillary interactions) we may equate the disjoining pressure with the relative vapor pressure through the Kelvin equation (Adamson, 1990):

$$\Pi(h) = (RT/V_{\rm m}) \ln(p/p_{\rm sat})$$
 [8]

where R is the gas constant (J K<sup>-1</sup> mol<sup>-1</sup>), T is the temperature (K),  $V_{\rm m}$  is the molar volume of liquid (m<sup>3</sup> mol<sup>-1</sup>), and  $p/p_{\rm sat}$  is the relative vapor pressure. Because no other interactions are considered,  $\Pi(h)$  equals the chemical potential  $\mu$  (when expressed as J kg<sup>-1</sup>, it should be multiplied by liquid density).

A situation of considerable practical importance is that of adsorption on two planar solid surfaces forming a narrow slit-shaped pore (Fig. 1–1b). The resulting expressions are somewhat more complicated due to the mutual interactions between the two plates. In this case, polymolecular adsorption of films is not dependent on surface properties only, but also on the overlapping force fields emanating from the facing solid surfaces. For a similar vapor pressure, film thickness in narrow slits is larger than on a single planar surface. Derjaguin and Churaev (1976), and, more recently, Iwamatsu and Horii (1996) provide an expression for the relationships between slit spacing H, equilibrium film thickness h, and the disjoining pressure  $\Pi(H,h)$ :

$$\Pi(H,h) = (RT/V_{\rm m}) \ln(p/p_{\rm sat})$$

$$= A_{\rm svl}/(6\pi h^3) - A_{\rm Hv}/[6\pi (H-2h)^3] + A_{\rm svl}/[6\pi (H-h)^3]$$
[9]

where  $A_{svl}$  is the Hamaker constant for solid-vapor interactions through the intervening liquid and  $A_{llv}$  is the Hamaker constant for liquid-liquid interactions through the intervening vapor.

The mutual attraction through the slit gap affects liquid film stability, and at a certain critical vapor pressure (or film thickness) the two films form a liquid bridge (Fig. 1–1c) followed by a spontaneous filling up of the slit (assuming the film is in contact with the bulk liquid phase). The liquid-vapor interface moves to the plate boundaries. This phase transition from dilute vapor to a dense liquid is known as capillary condensation and was observed experimentally with the surface force apparatus by Christenson (1994) and Curry and Christenson (1996). Extensive theories for this phenomenon and its critical points are provided by Derjaguin and Churaev (1976), Evans et al. (1986), Forcada (1993), and Iwamatsu and Horii (1996). In general, slit-shaped pores fill up at a film thickness of about H/3, or when  $\partial I I(H,h)/\partial h = 0$ , such that

$$h_c = H/[2 + (-2A_{IIV}/A_{SVI})^{1/4}] \cong H/3$$
 [10]

In summary, interfacial processes lead to relatively simple algebraic expressions for adsorption of fiquid films on solid surfaces. In these examples, we have considered the simple case of long range molecular interfacial forces only. The spe-

cific properties of surfaces and liquids are embodied in the values of the Hamaker constant for the various interactions. Many textbooks refer to these processes as "macroscopic" (Adamson, 1990). This is true from a molecular point of view; however, for hydrological applications, these are certainly microscopic adsorption processes taking place at the pore scale.

#### Capillarity and Pore Shape

Inspection of thin sections or micrographs of rocks and soils (e.g., Fig. 1–2a,b) reveal that natural pore spaces do not resemble cylindrical capillaries. Because many types of porous media are formed by aggregation of primary particles and various mineral surfaces, the resulting pore space is more realistically described by angular or slit-shaped pore cross sections rather than by cylindrical capillaries (Li & Wardlaw, 1986b; Mason & Morrow, 1991). Additionally, when angular pores are drained, a fraction of the wetting phase remains in the pore corners (Fig. 1–2c). This aspect of "dual occupancy" of the invaded portion of the tube (Lenormand et al., 1983; Blunt & Scher, 1995; Morrow & Xie, 1999), not possible in cylindrical tubes, represents more realistically liquid configurations and mechanisms for maintaining hydraulic continuity in porous media (Dullien et al., 1986). Liquid-filled

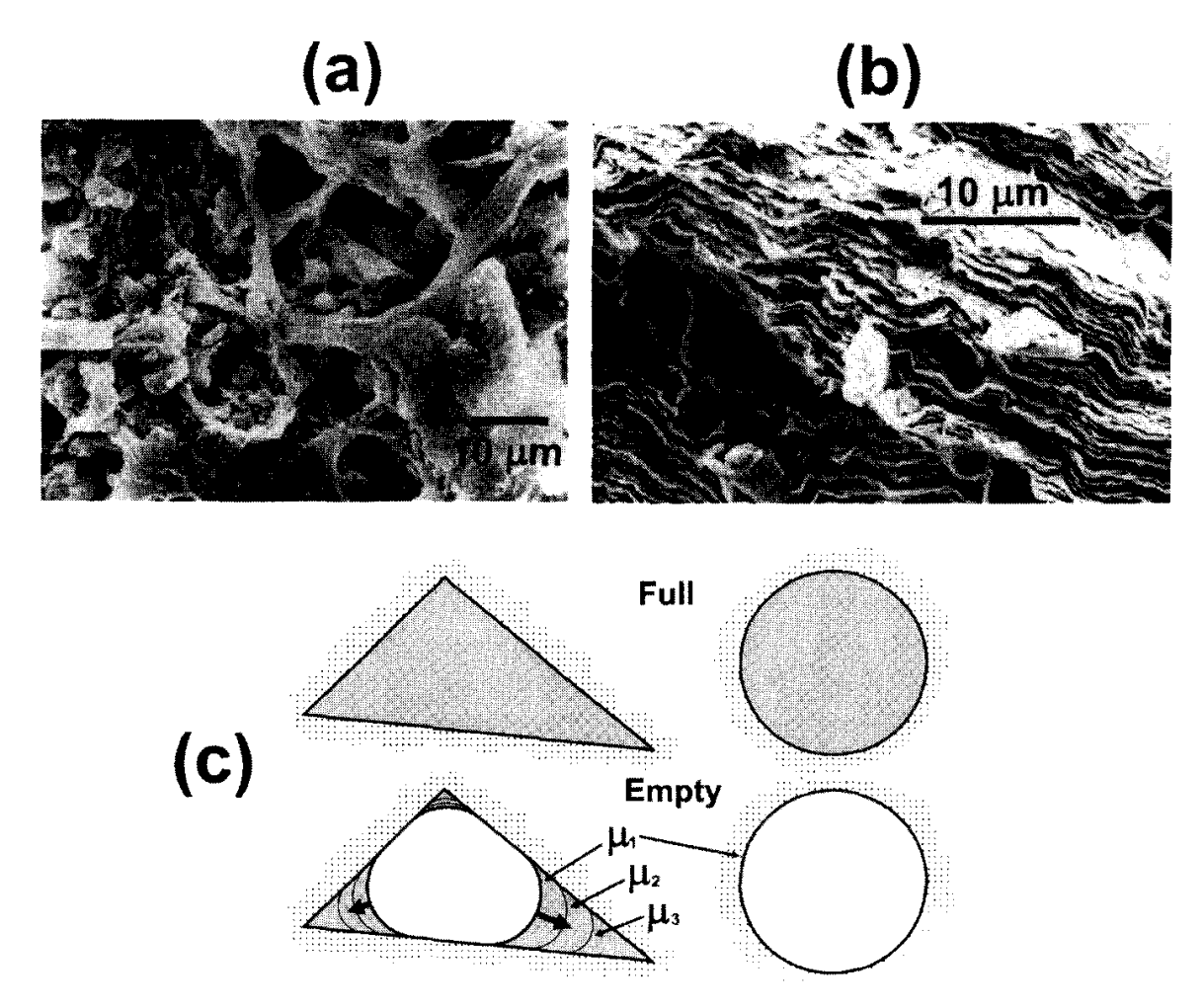


Fig. 1–2. Angular pore spaces in natural porous media: (a) scanning electron micrograph (SEM) of a soil composed of fine-sand, silt, and clay (Blank & Fosberg, 1989), (b) SEM of calcium saturated montmorillonite, (c) liquid retention in triangular and cylindrical pores.

corners and crevices play an important role in displacement rates of oil (Blunt et al., 1995) and in other transport processes in partially saturated porous media. Finally, in contrast to the "empty-full" states of cylindrical pores, angular pores are filled or drained gradually (according to changes in potential); hence, for practical media pore space characterization, a single angular pore may be used to represent a range of cylindrical tubes.

Studies by Mason and Morrow (1991; 1984) and others (Li & Wardlaw, 1986b; Lenormand et al., 1983) on capillary behavior of liquids in angular tubes provide a basis for developing relationships between liquid retention and pore angularity. We have been able to simplify Mason and Morrow's (1991) expressions for liquid retention in triangular pores and expand the result to other polygonal pore shapes and angularity.

The water-filled cross-sectional area  $A_{\rm W}$  for all regular and irregular triangles (Fig. 1–3), and for all regular higher-order polygons is given by the following expression:

$$A_{\mathbf{w}} = r^2 F_{\mathbf{n}} \tag{11}$$

where  $F_n$  is a shape or angularity factor dependent on angularity of the pore cross-section only (Table 1–1), and r is the radius of curvature of the liquid-vapor interface dependent on chemical potential ( $\mu$ ) or capillary pressure ( $p_c$ ) according to the Young-Laplace equation,

$$\mu = -\sigma/(r\rho)$$
 or  $p_c = -\sigma/r$  [12]

where  $\sigma$  is the surface tension of the liquid, and  $\rho$  is the density of the liquid. For detailed derivations interested readers are referred to Tuller et al. (1999). Note that in this discussion we consider capillary behavior only, ignoring adsorbed liquid films. The point of "snap-off" during imbibition, where the liquid spontaneously fills up the entire pore, occurs when the separate liquid-vapor interfaces touch to

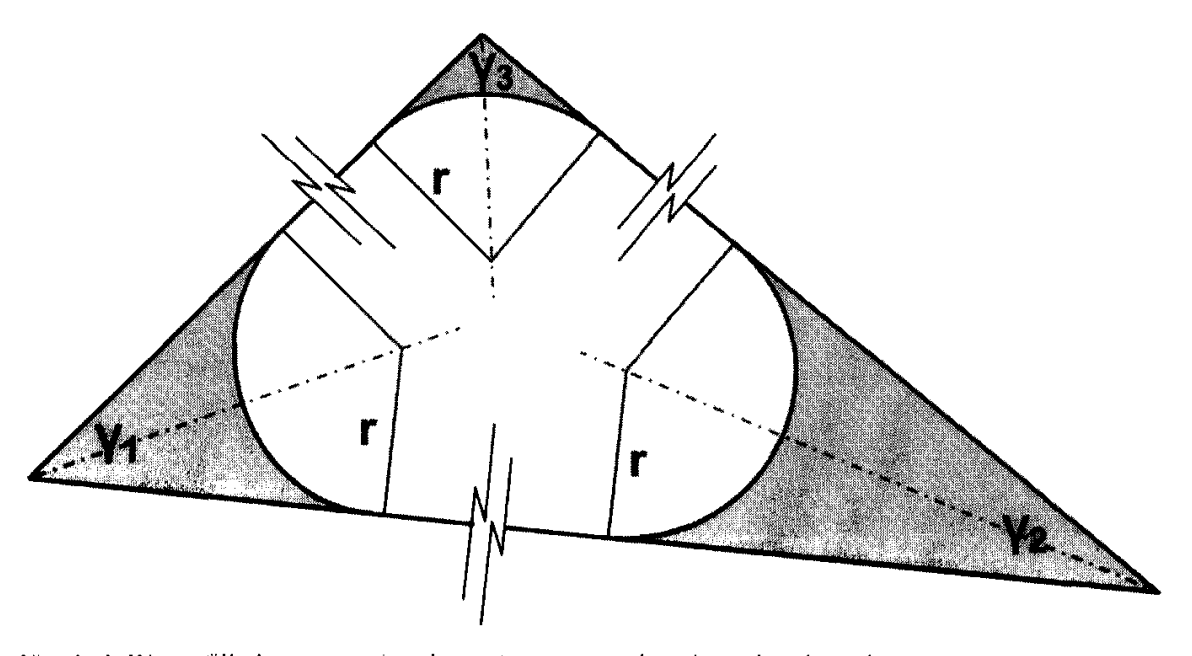


Fig. 1-3. Water filled cross sectional area for an irregular triangular shaped pore.

Table 1-1. Angularity factor, area factor, and drainage radius of curvature coefficient Cn<sup>†</sup> (used to determine maximum pore length L<sub>1</sub> for completely full unit cells) for different regular polygon-shaped central pores.

Corners	Angle	Angularity factor $F_n$	Area factor A <sub>n</sub>	Coefficient $C_n$ defining drainage curvature	Pore shapes
n	γ	$F_{\rm n} = \sum_{i=1}^{n} \left( \frac{1}{\tan{(\gamma_i/2)}} - \frac{\pi(180 - \gamma_i)}{360} \right)$	$A_{n} = \frac{n}{4} \cot \left(\frac{\pi}{n}\right)$	$C_{\rm n} = \frac{2}{n} \left[ F_{\rm n} + \pi + \sqrt{\pi (F_{\rm n} + \pi)} \right]$	
3	60	$3\sqrt{3}-\pi$	$\frac{\sqrt{3}}{4}$	$\frac{2(3+4\sqrt{3}\sqrt{\pi})}{\sqrt{3}}$	
4	90	$4-\pi$	1	$2 + \sqrt{\pi}$	
12	150	$\frac{12}{2+\sqrt{3}}-\pi$	$3(2+\sqrt{3})$	$\frac{6 + \sqrt{3}\sqrt{(2 + \sqrt{3})}\pi}{3(2 + \sqrt{3})}$	

The radius of curvature for imbibition,  $r_{\text{imb}}$ , is related to  $r_{\text{d}}$  by:  $r_{\text{imb}} = r_{\text{d}} \left[ 1 + \sqrt{\pi/(F_{\text{n}} + \pi)} \right]$ .

form a circle. This radius is simply the radius of the inscribed circle in the pore cross section given by:

$$r_{\text{imb}} = 2A/P = P/[2F_{\text{n}} + \pi)]$$
 [13]

where P is the perimeter of the pore cross section. For drainage, at a certain potential (or capillary pressure) a liquid-vapor meniscus invades the tube and liquid is displaced from the center leaving liquid in the corners (Mason & Morrow, 1991). The radius of curvature at this point,  $r_{\rm d}$ , is given as (Tuller et al., 1999):

$$r_{\rm d} = P/\{2[F_{\rm n} + \pi + \sqrt{\pi(F_{\rm n} + \pi)}]\}$$
 [14]

We point out the existence of an additional potential snap-off mechanism due to piston-like advance of an invading meniscus [termed by Mason & Morrow (1991) as the main terminal meniscus MTM] in direction perpendicular to the cross-sectional plane of the unit cell. This snap-off mechanism is only important for very high flow rates and when the liquid front is very well connected (Blunt & Scher, 1995).

An illustrative example of the effects of pore shape (and angularity) on imbibition and drainage processes is depicted in Fig. 1–4, showing marked differences between cylindrical and angular pores (all pore cross sectional areas are equal). Liquid displacement in cylindrical tubes during drainage is pistonlike, leaving no liquid in the cross-section after the drainage threshold. Angular pores, however, show that liquid is displaced from the central region first (at a radius of curvature given by Eq. [14]), leaving some liquid in the corners. Subsequent decrease in chemical potential results in decreasing amounts of liquid in the corners ("lower" chemical potential or capillary pressure indicates more negative values much like the terminology for the subzero temperature scale). The threshold chemical potential for different pore shapes with the same cross-sectional area increases (becomes less negative) with increasing angularity factor  $F_n$ . The same holds for the amount of liquid held in the corners.

The conditions during imbibition are slightly different. The liquid-vapor interfaces in corners of angular pores grow with increasing chemical potential to the point of "snap-off" (Eq. [13]) when the pore completely fills up with liquid. Prior to pore saturation, the liquid vapor curvature adjusts itself to its corresponding value for drainage (with a lower chemical potential). Again, the threshold chemical potential for "snap-off" increases with angularity  $F_n$ , and the amount of liquid held in the corners at a given chemical potential is directly proportional to angularity. Highly angular pore shapes, such as triangular pores, retain more liquid at the same potential than squares or hexagons. In cylindrical tubes, no liquid is held prior to "snap-off" which subsequently fills up spontaneously (the "empty-full" behavior).

#### A New Model for Pore Space Geometry

The discussions in the preceding sections illustrate several shortcomings of cylindrical capillaries representation (BCC model), hence the need for a more realistic representation of pore space geometry. Some studies have used angular pore systems for observation and modeling of capillary phenomena in porous

media (Lenormand, 1990; Ioannidis & Chatzis, 1993; Dong & Chatzis, 1995; Blunt & Scher, 1995). The new pore geometry proposed by Tuller et al. (1999) is capable of accommodating adsorptive processes in an internal surface area in addition to capillarity. The proposed elementary unit cell is comprised of a square-shaped (relatively large) pore for capillary processes connected to slit-shaped spaces representing internal surface area (Fig. 1–5a). Though the choice of a square-shaped pore is arbitrary (representing an intermediate angularity between triangular and cylindrical pores), it does not affect the generality of the derivations that are easily extendable to triangular or other higher order polygons.

Additional geometrical features, such as surface roughness, may be superimposed on all surfaces, and their effects on adsorption and capillarity may be calculated by means of Philip's (1978) solutions for surfaces with conical pits [see also

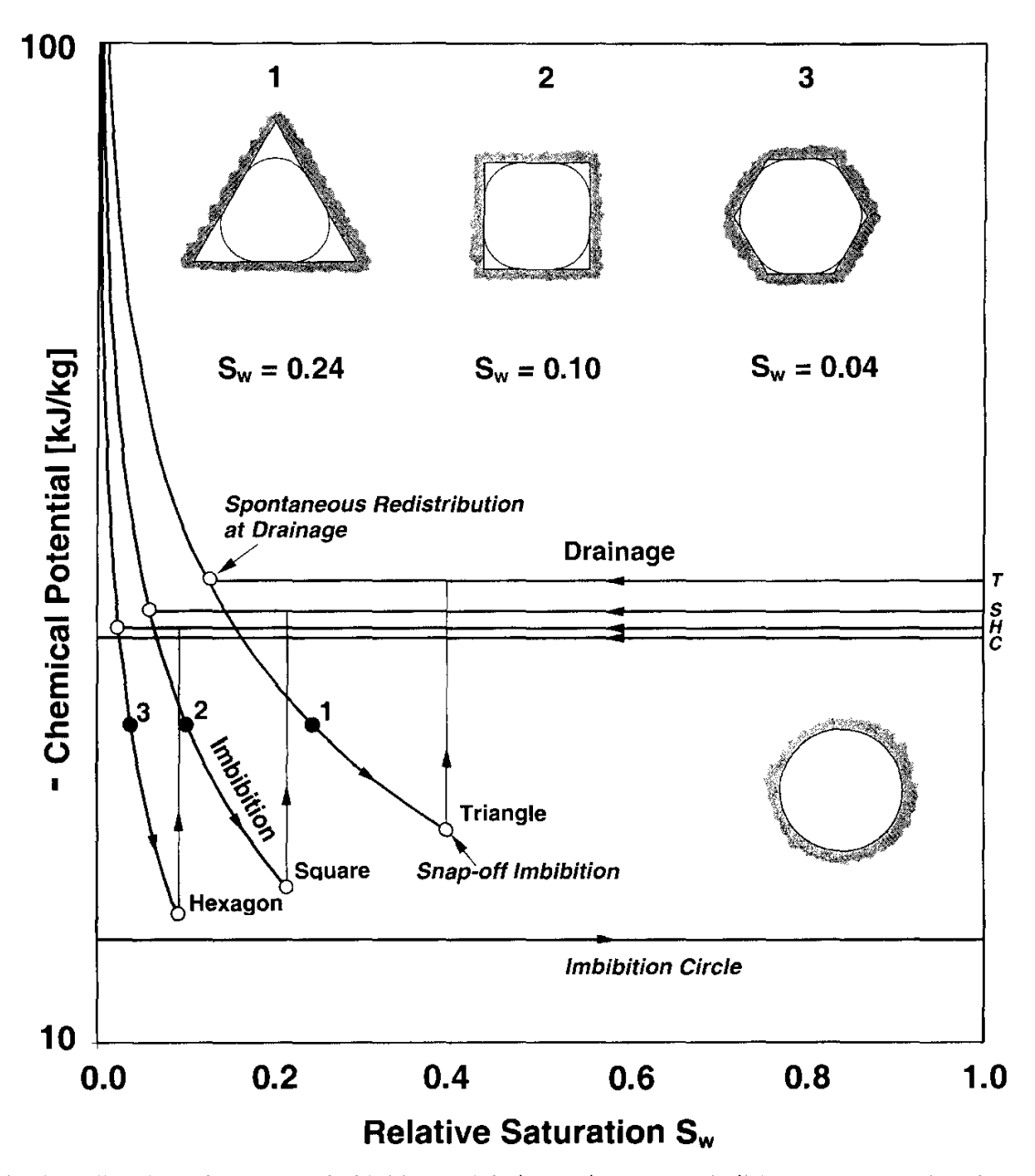


Fig. 1–4. Capillary phenomena (imbibition and drainage) in pores with different cross-section shapes but identical pore cross-sectional area.

Novy et al.(1989)], or more recently by solutions of Or and Tuller (2000). Different soil textural and structural classes may be represented by adjusting pore width (L) and the proportions of exposed surfaces (determined by the slit-width  $\alpha L$  and the slit-length  $\beta L$ ), or even modifying the pore shape and angularity according to scanning electron micrographs. For example, to study liquid adsorption and capillary behavior in clayey soils, a unit cell with a small pore size (e.g.,  $L = 10^{-5}$  m) coupled with a relatively large exposed surface area (e.g.,  $\alpha L = 2 \times 10^{-9}$  m;  $\beta L = 5 \times 10^{-3}$  m) may be considered. For a sandy soil, however, the pore size is likely to be relatively large, whereas, the surface area is small. Finally, the proposed unit cell may serve as a building block for three-dimensional pore networks (Fig. 1–5b).

The modified unitary approach of Philip (1977a), supplemented by adsorption terms presented by Iwamatsu and Horii (1996), provides a means of calculating equilibrium liquid-vapor interfaces for various chemical potentials during drainage and imbibition. Four major steps are discerned during the transition from adsorption to capillary-dominated imbibition (Fig. 1–6). At low matric potentials,

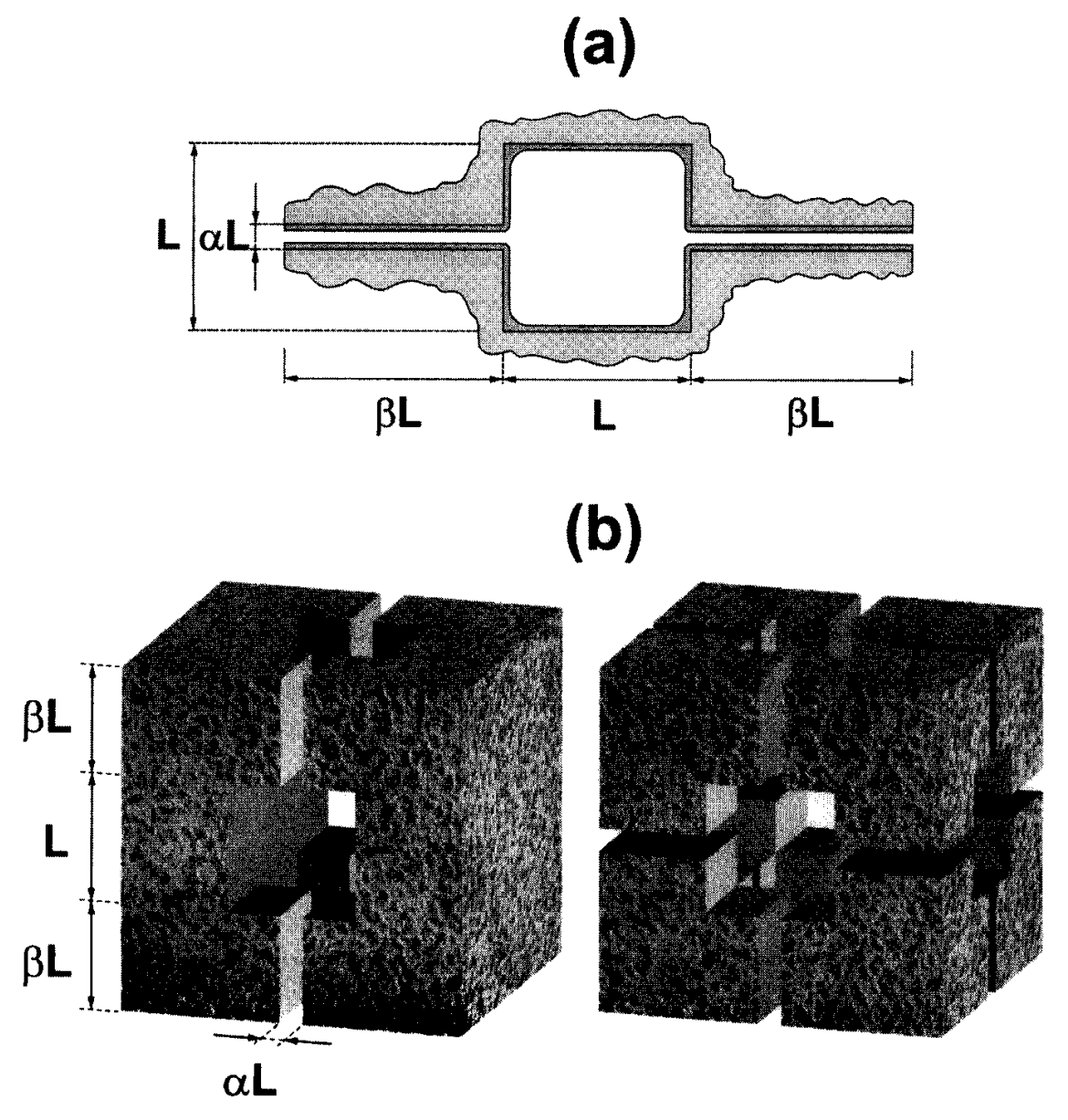


Fig. 1–5. (a) The new pore geometry model, (b) extension of the new pore geometry to simple three-dimensional pore networks with different connectivity and isotropy.

thin liquid films coat pore and slit walls. Some liquid is held behind liquid-vapor interfaces formed at the corners and contributes to capillary forces (Fig. 1–6a). With increasing matric potentials, liquid films thicken to a point where the slits spontaneously fill up with liquid (capillary condensation, Fig. 1–6b). A further increase in matric potential results in a further increase in film thickness within the pore, and a reduction in the radius of curvature of liquid-vapor interfaces until they contact and form an inscribed circle (Fig. 1–6c). Subsequently, (Fig. 1–6d), the pore spontaneously fills up ("snap-off") to a complete saturation (Mason & Morrow, 1991).

# The Unitary Approach (Augmented Young-Laplace Equation) in the New Pore Geometry

The AYL equation that forms the basis for Philip's (1977a) approach was modified by adsorption terms proposed by Derjaguin et al. (1987) and Iwamatsu and Horii (1996):

$$\mu = A_{\text{svl}}/(6\pi\rho h^3) - 2\sigma\kappa/\rho$$
 [15]

This form of the AYL equation was used by Philip (1977a) to develop solutions for liquid-vapor configurations between parallel plates, in wedge-shaped pores, corners, and for spaces between circular cylinders, circular tubes, and contacting spheres. Liquid configuration for a given potential was calculated for different geometrical features that make up a cross-section of the proposed pore space model. Liquid behavior in the slit-shaped spaces of the new pore geometry model was cal-

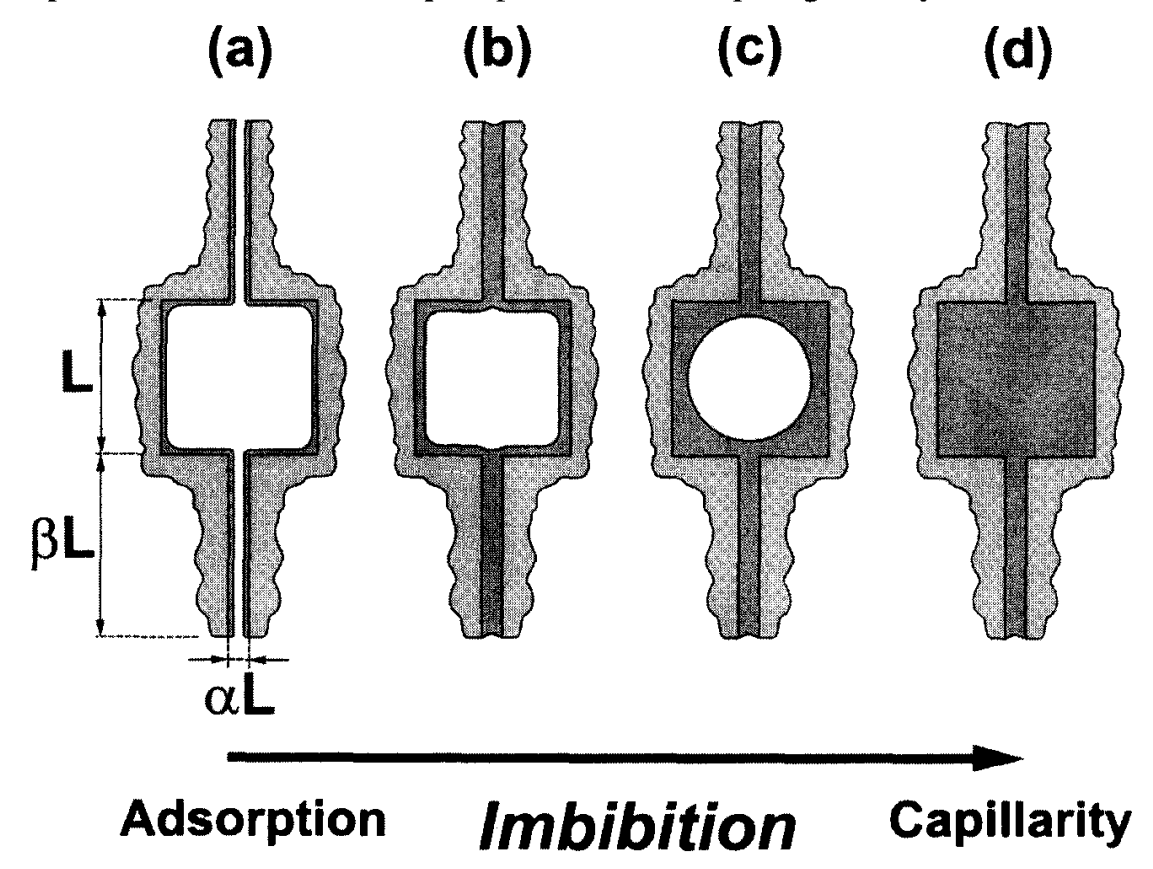


Fig. 1–6. A sketch illustrating liquid-vapor interfacial configurations during transition from adsorption to capillary-dominated imbibition in the proposed unit cell: (a) liquid films adsorbed on pore and slit walls and liquid held in corners due to capillary forces at low matric potentials, (b) spontaneous slit fill up (capillary condensation), (c) pore snap-off, and (d) full unit cell.

culated by means of Eq. [7] and [9]. (Philip's approach does not account for separated liquid films in a slit.) The appropriate boundary conditions were applied to solve for the liquid-vapor interface for each geometrical feature (e.g., a specified film thickness at the boundaries). These solutions were then combined to provide a complete liquid configuration picture for the entire pore cross-section. For detailed derivations of the complex AYL-equation, interested readers are referred to Tuller et al. (1999) and Philip (1977a). All calculations were limited to the two-dimensional space representing a pore cross-section (i.e., pore connectivity and other network effects were neglected). Finally, we assumed continuity of all phases (wetting and nonwetting) to facilitate spontaneous liquid "snap-off" and avoid air entrapment.

# **Application of the Simplified Augmented Young-Laplace Equation in the New Pore Geometry**

The complex calculations of liquid-vapor interfaces in the assumed pore geometry based on the AYL equation (Eq. [15]) are considerably simplified by using a superposition of adsorptive and capillary calculations for the interfaces. In the simplified approach we determine the liquid-vapor radius of curvature in the corners using the classical Young-Laplace equation  $r = -\sigma/(\rho\mu)$  considering capillary forces only. The curved interface is then shifted by a constant film thickness that is independently calculated for the same potential using Eq. [7]. Liquid vapor interfaces are then assembled to obtain a complete picture for the proposed unit cell leading to simple shifted Young Laplace (SYL)-based expressions. The conditions for the onset of spontaneous filling of slits (termed slit snap-off) occur when the separate films reach a critical thickness  $h_c$  (Eq. [10]). The spontaneous filling of the central pore at imbibition occurs when an inscribed circle  $(r_{imb} = L/2)$  is formed (i.e., the curved liquid-vapor interfaces from the corners merge at L/2). The large dimensional disparity between slit spacing ( $\alpha L$ ) and pore size (L), ensures that slit snap-off precedes pore snap-off during an imbibition cycle, and follows pore snapoff for drainage conditions.

The spontaneous snap-off processes require two scenarios to be considered—prior to and after slit filling—for calculation of pore saturation and liquid-vapor interfacial area. Following pore snap-off the pore is completely saturated and the liquid-vapor interface is zero. Expressions for calculating saturation,  $S_W(\mu)$ , defined as liquid area per pore cross-sectional area (these are translated to their respective volumes for three-dimensional pores) for all regular polygon-shaped central pores are given as:

(i) before slits fill ( $\mu < \mu_C$ )

$$S_{w}(\mu) = \frac{Lh(\mu)(n - 2\alpha + 4\beta) - nh(\mu)^{2} + r(\mu)^{2}F_{n}}{2\alpha\beta L^{2} + A_{n}L^{2}}$$
[16]

(ii) after slits fill ( $\mu \ge \mu_C$ )

$$S_{w}(\mu) = \frac{2\alpha\beta L^{2} + nh(\mu)[L - h(\mu)] + r(\mu)^{2}F_{n}}{2\alpha\beta L^{2} + A_{n}L^{2}}$$
[17]

where  $h(\mu)$  is film thickness,  $r(\mu)$  is the radius of liquid-vapor meniscus curvature,  $F_n$  is the angularity factor for the central pore (Tuller et al., 1999), and  $A_n$  is the area factor of the central pore. The film thickness  $h(\mu)$  and the radius of interface curvature  $r(\mu)$  are derived by rearranging Eq. [7] and Eq. [12]:

$$h(\mu) = \sqrt[3]{A_{\text{svl}}/(6\pi\rho\mu)}$$
 [18a]

$$r(\mu) = -\sigma/(\rho\mu)$$
 [18b]

Angularity and area factors for several regular polygon-shaped central pores are listed in Table 1–1.

#### Pore Scale Liquid-Vapor Interfacial Area

The liquid-vapor interfacial area relative to the entire pore cross-section is calculated as:

(i) before slits fill ( $\mu < \mu_C$ )

$$A_{\rm lv}(\mu) = \frac{4\beta L + nL - 2F_{\rm n} r(\mu)}{2\alpha\beta L^2 + A_{\rm n} L^2}$$
[19]

(ii) after slits fill  $(\mu \ge \mu_C)$ 

$$A_{\text{lv}}(\mu) = \frac{nL - 2F_{\text{n}} r(\mu)}{2\alpha\beta L^2 + A_{\text{n}} L^2}$$
 [20]

with n as the number of corners of the central pore, and  $F_n$  and  $A_n$  the previously defined pore shape factors.

#### **Upscaling Considerations From Pore- to Sample Scale**

#### Statistical Representation of Unit Cell Dimensions

The representation of liquid behavior in a variably saturated sample (~0.001 m³) of porous medium invariably involves consideration of a range of pore sizes. An approach that has been successful with similar conceptual models is to adopt a statistical framework whereby pore sizes (or other geometrical attributes) are represented by a statistical probability distribution. The statistical approach has been instrumental in representing the distribution for the pore radii in the bundle of cylindrical capillaries model as illustrated in the studies of Laroussi and de Backer (1979) or more recently by Kosugi (1994, 1996) who assumed log-normal distribution of pore radii. In the proposed upscaling scheme outlined in this study we represent the statistical distribution of central pore length (*L*) by a gamma distribution (Rice, 1995). The gamma distribution resembles the commonly used lognormal distribution with its positive skewness, and also facilitates derivation of closed-form expressions for liquid retention and interfacial area. Several other probability laws,

including the incomplete gamma distribution (Brutsaert, 1966) or the Weibull distribution (Assouline et al., 1998) may also be considered in future studies.

The gamma density function for the central pore length, f(L), is dependent on two parameters,  $\xi$  and  $\omega$ :

$$f(L) = [L^{\xi}/(\xi!\omega^{\xi+1})] \exp(-L/\omega) \qquad L \ge 0$$
 [21]

The parameter  $\xi$  is limited to integer values. Calculations involving expectations of f(L) are greatly simplified by the choice of  $\xi = 2$  that provides a balance between flexibility and tractability ( $\xi = 2$  was used in this study). The moment-generating function of the gamma distribution (Rice, 1995) is used to obtain expressions for the mean m(L) and variance v(L) of L given as:

$$m(L) = \omega(\xi + 1)$$
 [22a]

$$v(L) = \omega^2(\xi + 1)$$
 [22b]

We also limit the range of admissible L values for the assumed gamma distribution to values between  $L_{\min}$  and  $L_{\max}$ , representing the smallest and largest central pore lengths, respectively. The relationships between slit length and central pore length distribution is expressed as  $\beta(L_{\max}-L)$ . Such inverse relationships facilitate the representation of clayey soils by unit cells with relatively small central pores and large slits (on average), whereas sandy soils would be represented by larger central pores attached to shorter slits (i.e., less internal surface area). The relationships between pore length distribution and slit spacing is expressed as  $\alpha L$ . Constraints on the values of  $\alpha$ ,  $\beta$ , and f(L) are imposed based on measurable medium properties such as porosity, specific surface area, and measured liquid retention/characteristic curves (as will be outlined in "Parameter Estimation and Physical Constraints").

A conceptual sketch of the proposed upscaling scheme is depicted in Fig. 1–7. A population of gamma-distributed square pores (Fig. 1–7a) is represented for illustrative purposes by 6 bins ( $L_1$ – $L_6$ ). The fixed ratio between central pore length L and slit spacing  $\alpha L$  results in an adjoint gamma distribution of slit spacing as depicted in Fig. 1–7a. The physical model predicts the shapes of liquid-vapor interfaces for each pore size and chemical potential  $\mu$ , leading to different stages of pore filling according to chemical potential and pore geometry (Fig. 1–7b). The fraction of pores at each of the several filling stages is determined from the statistical distribution of pore length, f(L), and is expressed as the expected value of a certain range of pore spaces to be completely or partially liquid filled. The total sample scale saturation is calculated as the weighted sum of different pore filling stages. The resulting characteristic curve is illustrated in Fig. 1–7c for three values of chemical potential. Details of these calculations are discussed in the following section.

#### **Sample Scale Saturation (Drainage Branch)**

The upscaling scheme was applied to the pore scale model based on the SYL formulation, leading to the development of closed-form expressions for sample scale

saturation as a function of chemical potential. General closed-form expressions were derived for all regular polygon-shaped pores. The calculations are illustrated for the drainage branch of a characteristic curve, though the results may be readily extended to the imbibition branch. The sample scale saturation as a function of chemical potential is expressed as the sum of five terms related to the expected values of five distinct unit cell filling stages:

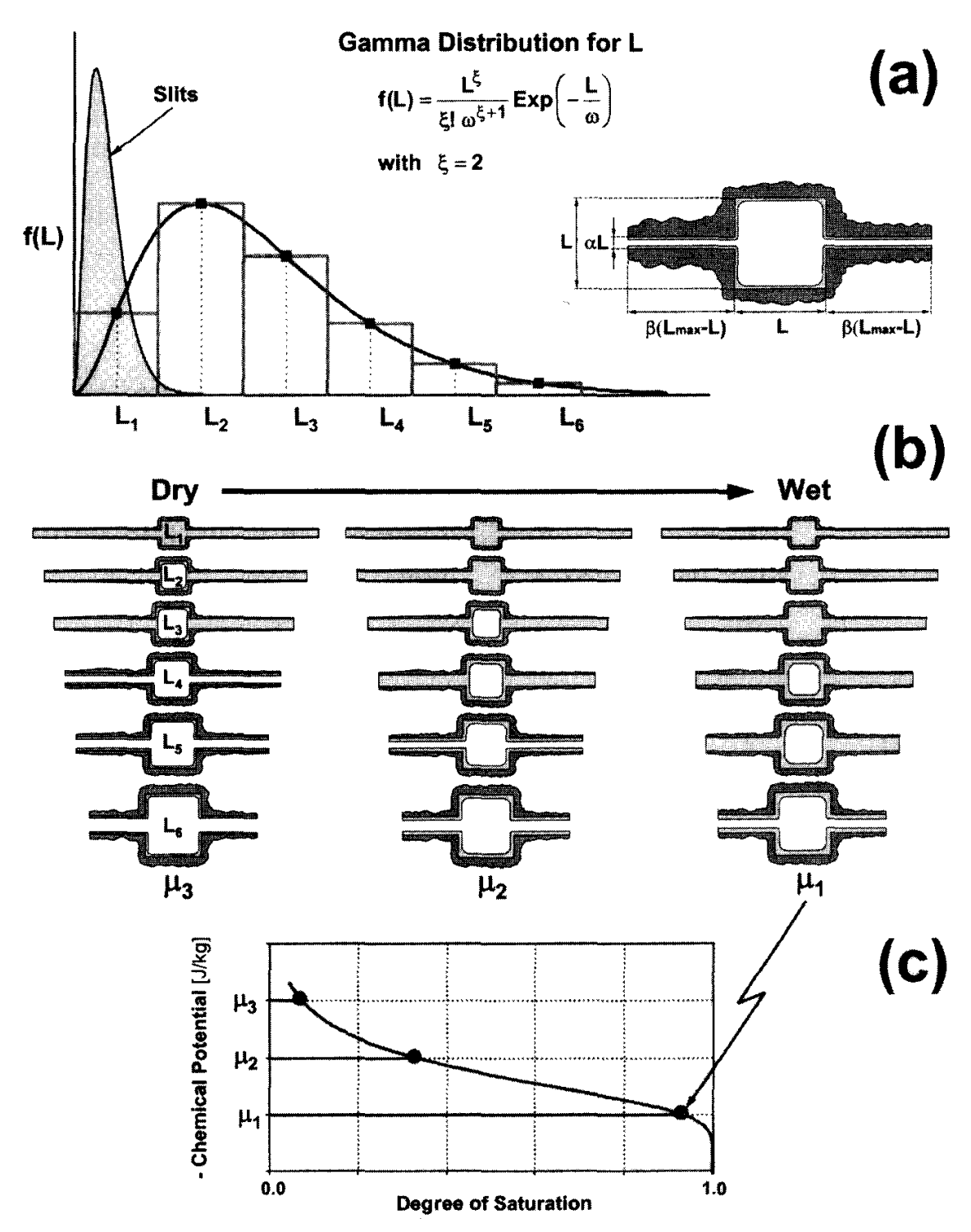


Fig. 1–7. A definition sketch for the proposed upscaling scheme depicting: (a) gamma distribution of central pore lengths with  $\xi = 2$ , and hypothetical six bins (note the inverse relationships between  $\beta$  and L); (b) three different filling stages in the population of unit cells (represented by L<sub>1</sub> L<sub>0</sub>) defined at three chemical potential values  $\mu_3$  to  $\mu_1$  (dry-wet); and (c) the resulting hypothetical characteristic curve.

$$Sw(\mu) = S_{w1}(\mu) + S_{w2}(\mu) + S_{w3}(\mu) + S_{w4}(\mu) + S_{w5}(\mu)$$
 [23]

with:

$$S_{w1}(\mu) = \int_{L_{min}}^{L_1(\mu)} f(L)dL = \int_{L_{min}}^{L_1(\mu)} (L^2/2\omega^3) \cdot \text{Exp}(-L/\omega)dL$$
 [23a]

$$S_{w2}(\mu) = \int_{L_1(\mu)}^{L_{max}} \frac{r(\mu)^2 F_n}{2\alpha\beta L(L_{max} - L) + A_n L^2} \bullet f(L) dL$$
 [23b]

$$S_{w3}(\mu) = \int_{L_1(\mu)}^{L_2(\mu)} \frac{2\alpha\beta L(L_{max} - L)}{2\alpha\beta L(L_{max} - L) + A_n L^2} \cdot f(L)dL$$
 [23c]

$$S_{w4}(\mu) = \int_{L_1(\mu)}^{L_2(\mu)} \frac{nLh(\mu)}{2\alpha\beta L(L_{max} - L) + A_n L^2} \bullet f(L)dL$$
 [23d]

$$S_{w5}(\mu) = \int_{L_2(\mu)}^{L_{max}} \frac{h(\mu) \{4\beta (L_{max} - L) + n[L - h(\mu)]\}}{2\alpha\beta L(L_{max} - L) + A_n L^2} \bullet f(L)dL$$
 [23e]

The term  $S_{\rm w1}$  (Eq. [23a]) is the expected value of completely filled pores. Because saturation for completely filled pores equals one, the expected value operation amounts to integration of the gamma distribution between the smallest central pore dimension  $L_{\rm min}$  (the lower limit of integration depicted in Fig. 1–8), and a certain pore size denoted by  $L_1$ . The upper limit  $L_1$  is determined from the radius of curvature at the onset of drainage in the central pore,  $r_{\rm d}$  (Mason & Morrow, 1991; Tuller et al., 1999). It is often referred to as the radius of curvature at "air-entry", and is given by:

$$r_{\rm d} = L/C_{\rm p} \tag{24}$$

The particular value  $L = L_1$  is obtained by the substitution  $r_d = -\sigma/(\rho\mu)$  (the standard Young-Laplace equation) using the proper value of the coefficient  $C_n$  that defines drainage curvature for different shaped central pores (as listed in Table 1–1) to yield for a given potential:

$$L_1(\mu) = [-\sigma/(\rho\mu)] C_n$$
 [25]

The limit of integration  $(L_1)$  indicates that all unit cells with pore lengths L smaller than  $L_1$  will remain completely full at the given potential  $\mu$ .

The second and third terms ( $S_{w2}$  and  $S_{w3}$ ) describe the fraction of unit cells having partially liquid-filled central pores (Fig. 1–8) The term  $S_{w2}$  is used for calculating the expected value of liquid retention in the central pores due to capillarity only (disregarding the adsorptive part). The calculation of  $S_{w2}$  is taken for all

partially filled central pores between  $L_1$  and largest pore length  $L_{\rm max}$ , the pore size range for capillary processes at a given chemical potential  $\mu$ .  $S_{\rm w3}$  describes the contribution to the sample scale saturation due to liquid retained in full slits (not considered by  $S_{\rm w1}$ ). It is implicitly assumed that slits remain full for all slit spacing smaller than  $\alpha L_2$  which defines slit spacing for the onset of spontaneous slit snapoff at the chemical potential  $\mu$ . Spontaneous slit filling occurs when film thickness  $h(\mu)$  is approximately one-third of the slit-spacing  $\alpha L$ :

$$h(\mu) = \alpha L/3 \tag{26}$$

Rearranging Eq. [26] and substituting Eq. [18a] for  $h(\mu)$  yields the required upper limit of integration  $L_2$ :

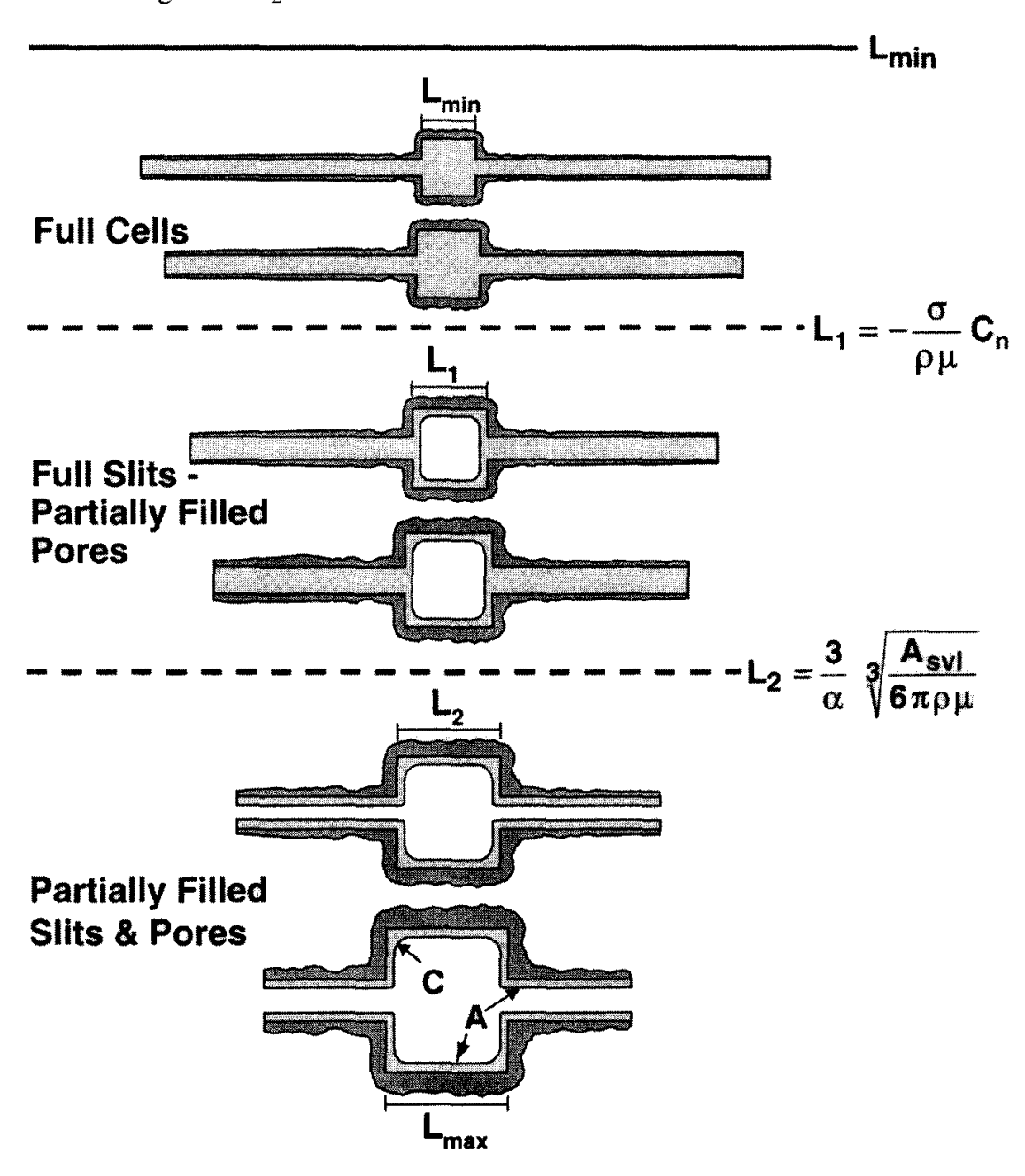


Fig. 1–8. Limiting pore size values used for determining the expected pore filling stage at different potentials. These limits are expressed in terms of pore length L and vary with the chemical potential (see text for details).

$$L_2(\mu) = (3/\alpha)^3 \sqrt{A_{\text{svl}}/(6\pi\rho\mu)}$$
 [27]

Although it is unclear whether slit snap-off during drainage occurs at the same chemical potential as for imbibition, we have adopted a similar expression for simplicity. In any case, we expect effects of slits emptying at lower chemical potentials to have a minor influence on the upscaling scheme due to the presence of a distribution of slit spacing in a sample.

The fourth term  $S_{\rm w4}$  represents a minor correction due to the presence of liquid film between corners within the central pore. Because this term applies between the relatively narrow limits  $L_1$  to  $L_2$ , it may be safely neglected for all practical calculations but is presented here for completeness. The last term  $S_{\rm w5}$  calculates the contribution (in terms of its expected value) of adsorbed liquid films lining partially filled slits and central pores as induced by adsorptive forces only. The limits of integration are defined between  $L_2$ , the onset of slit snap-off or emptying of slits during drainage, and  $L_{\rm max}$ . Figure 1–8 is a definition sketch for the limits of integration as related to different pore filling stages. Detailed closed-form solutions for the integrals are given in Tuller and Or (2001).

#### Sample Scale Liquid-Vapor Interfacial Area

Closed-form expressions for liquid-vapor interfacial area are derived in a similar fashion as for liquid saturation. A general expression is given as the sum of two terms subjected to identical limits of integration as depicted in Fig. 1–8:

$$A_{1v}(\mu) = A_{1v1}(\mu) + A_{1v2}(\mu)$$
 [28]

with:

$$A_{\text{lv1}}(\mu) = \int_{L_1(\mu)}^{L_2(\mu)} \frac{nL - 2F_n \, r(\mu)}{2\alpha\beta L(L_{\text{max}} - L) + A_n \, L^2} \, \bullet f(L) dL$$
 [28a]

$$A_{\text{lv2}}(\mu) = \int_{L_1(\mu)}^{L_{\text{max}}} \frac{4\beta(L_{\text{max}} - L) + nL - 2F_n r(\mu)}{2\alpha\beta L(L_{\text{max}} - L) + A_n L^2} \bullet f(L)dL$$
 [28b]

The first term describes the interfacial area per pore volume following pore emptying (while slits are still liquid filled). Liquid-vapor interfaces are composed of the curved interfaces in the corners (capillary contribution) and film interfaces in the flat areas between corners (adsorptive contribution). The second term is for the expected value of liquid-vapor interfacial area following the formation of liquid-vapor interface in the slits following slit snap-off. These include interfaces in the central pore and flat film interfaces in the slits. Detailed solutions for the integrations are given in Tuller and Or (2001).

#### Parameter Estimation and Physical Constraints

Relationships Between Slit Space Scaling Parameters  $\alpha$  and  $\beta$ . The dimensionless scaling parameter  $\alpha$  is determined from the adjoint Gamma distrib-

uted slit-spacing  $\alpha L$ . The extent of overlap between central pore length (L) distribution and its adjoint distribution for slit spacing  $(\alpha L)$  (Fig. 1–7a) plays an important role in realistic representation of media pore space. The largest slit aperture (or the leading edge of slit-spacing distribution) is determined by a distribution overlap parameter  $\lambda$  (a fitting parameter) that relates slit spacing ratio  $(\alpha)$  to largest  $(L_{\text{max}})$  and mean m(L) pore lengths according to:

$$\alpha = m(L)/(L_{\text{max}} \lambda)$$
 [29]

According to these relationships, increasing the parameter  $\lambda$  results in a decrease in overlap and smaller slit spacing. The dimensionless slit length parameter  $\beta$  is a fitting parameter and highly dependent on measured media specific surface area.

**Specific Surface Area Constraint.** An important requirement for model parameter estimation is that calculated sample scale specific surface area should be within 90% of independently measured surface area. A 90% limit was chosen based on the relatively large uncertainty in most standard methods for surface area measurements [e.g., EGME method (Carter et al., 1986)]. The sample scale expected value of specific surface area  $SA_e$  is calculated according to:

$$SAe = \int_{L_{\min}}^{L_{\max}} \left( \frac{4\beta(L_{\max} - L) + nL}{2\alpha\beta L(L_{\max} - L) + A_n L^2} \phi \right) \cdot f(L)dL$$
 [30]

with  $\phi$  as the porosity of the porous medium. The dominant fitting parameter in this expression is the slit length scaling parameter  $\beta$ . The derivation and a closed form solution for the SA integral in Eq. [30] are given in Tuller and Or (2001).

Chemical Potential at Air Entry Value and Maximum Pore Length Value. The chemical potential at the onset of drainage  $\mu_d$  (air entry value) is often attributed to the largest size present in the porous medium, which we denote as  $L_{\text{max}}$ . Eq. [25] is used to obtain the appropriate pore dimension  $L_1(\mu_d)$ . A small correction is introduced by calculating film thickness  $h(\mu_d)$  lining the pore walls according to Eq. [18a]. The resulting maximum pore size is given as:

$$L_{\text{max}} = L_1(\mu_{\text{d}}) + 2h(\mu_{\text{d}})$$
 [31]

The minimum pore length  $(L_{\min})$  was set to an arbitrary value of  $10^{-9}$  m in this study. These two pore sizes define the limits of the gamma distribution.  $L_{\max}$  (or the potential  $\mu_d$  at the onset of drainage) is estimated as one of the fitting parameters.

Estimation of the Effective Hamaker Constant for Solid-Vapor Interactions for Different Soils. The Hamaker constant represents interactions between macro-objects such as mineral surfaces and liquid due to short-range (<100Å) van der Waals forces (Ackler et al., 1996; Bergström, 1997). The presence of van der Waals surfacial interactions in most liquid adsorption processes in natural porous media renders the proper estimation of the Hamaker constant an important task. The Hamaker constant for liquid-liquid interactions through the intervening vapor is a

well-known quantity ( $A_{\text{llv}} = 3.7 \times 10^{-20} \text{J}$ ) (Iwamatsu & Horii, 1996). On the other hand, estimates of the Hamaker constant  $A_{\text{svl}}$  for solid-vapor interactions through the intervening liquid rely solely on data measured on pure mica and quartz surfaces (Iwamatsu & Horri, 1996; Beaglehole et al., 1991; Cury & Christenson, 1996; Ackler et al., 1996).

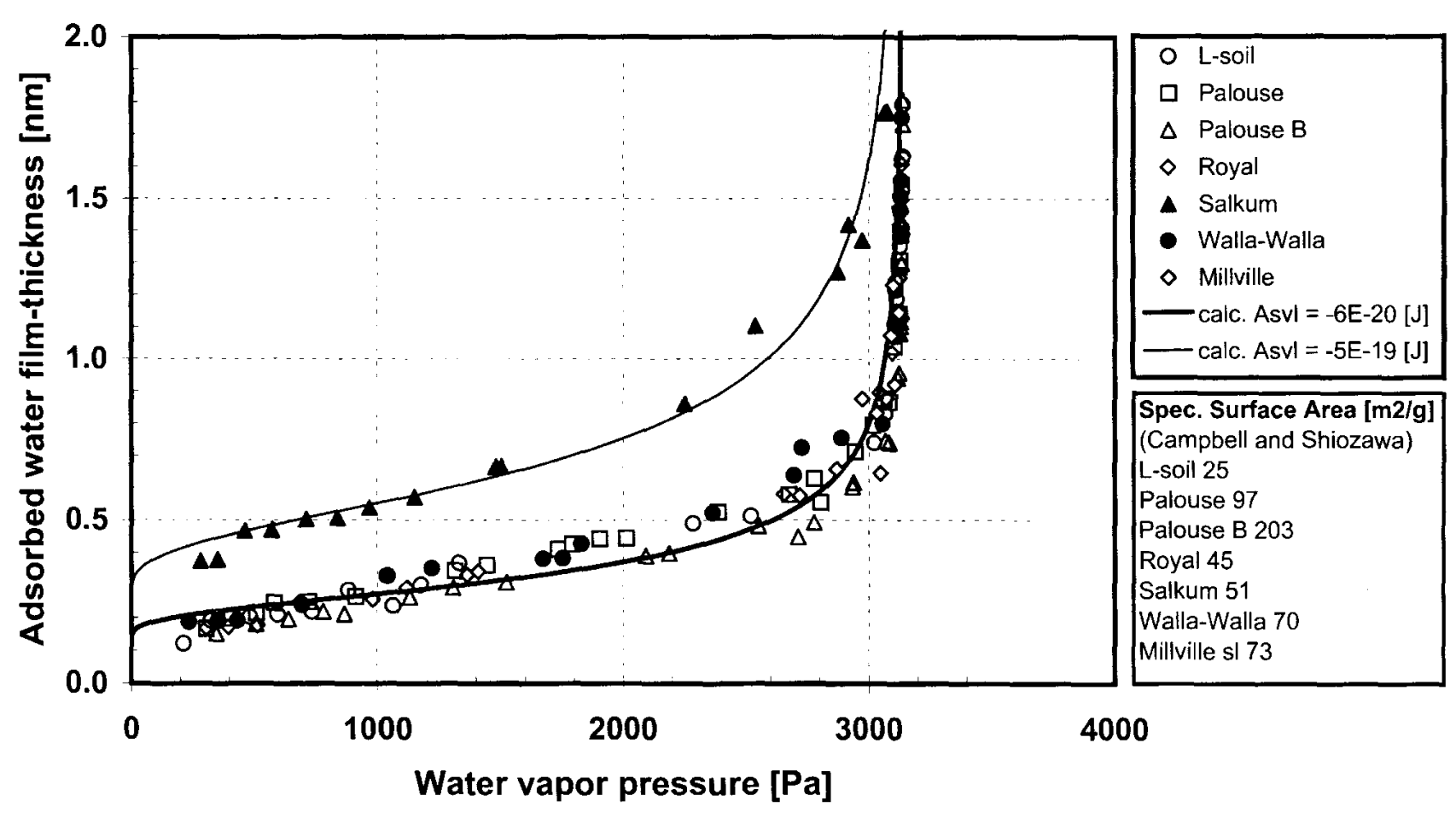
We propose a potential methodology to estimate an "effective" Hamaker constant for soils using the single film adsorption equation (Eq. [18a]) fitted to data obtained from the dry end of the measured characteristic curve (presumably reflecting conditions where adsorption dominates). The "dry end" volumetric water content divided by the measured specific surface area provides an estimate of adsorbed liquid film thickness as a function of chemical potential. The procedure for Hamaker constant estimation is illustrated in Fig. 1–9 using water retention data for the soils under study (Table 1-2). The results reveal that adsorption in soils with mixed clay mineralogy may be described by a single Hamaker constant value of  $A_{\rm syl} = -6.0 \times 10^{-20} \, \rm J$ . The fitted Hamaker constant for the kaolinite-dominated Salkum soil was about one order of magnitude larger or  $A_{\text{syl}} = -5.0 \text{ x } 10^{-19} \text{ J}$ . Such effects of clay mineralogy on liquid adsorption behavior are predicted by interface science theory (Derjaguin et al., 1987). However, the adsorption picture becomes somewhat more complex as it requires invoking electrostatic effects due to the diffuse double layer (DDL). Expressions for the more general case (including DDL effects) were developed by Derjaguin and Churaev (1976). For the sake of simplicity, we retain van der Waals molecular interactions only, and designate the estimated parameter an "effective" Hamaker constant reflecting bulk adsorption response, which is likely to involve other mechanisms and more complex geometry than planar surfaces.

# ILLUSTRATIVE EXAMPLES—LIQUID SATURATION AND CONFIGURATION

# **Liquid Saturation**

We proceed with illustrative examples for application of the proposed upscaling scheme to seven soil types with properties listed in Table 1–2. The closed-form solution for degree of saturation (Eq. [23]) was fitted to measured data by optimizing parameters  $\beta$ ,  $\omega$ ,  $\lambda$ , and the chemical potential  $\mu_d$  at air entry point (that defines  $L_{max}$ ). Note that the Hamaker constant was estimated beforehand, as described in "Estimation of the Effective Hamaker Constant for Solid-Vapor Interactions for Different Soils" above. The estimated parameters were then used to calculate the liquid-vapor interfacial area for each soil (Eq. [28]). We used square shaped central pores for all soil types except the artificial sand mixture, where triangular pores were applied to emphasize capillary processes over adsorption in sand. However, the closed-form solutions for retention and interfacial area were derived to accommodate any regular polygon-shaped central pore. Constants for various shapes are described in Table 1–1. The values of primary physical constants employed in the calculations and their units are shown in Table 1–3.

The van Genuchten (VG) parametric model (van Genuchten, 1980) was also fitted to the measured characteristic curves; recall that the VG model and its para-



Estimation of "effective" Hamaker constant from water adsorption behavior in soils under study using Eq. [18a]. The top (fine) curve with  $A_{svl} = -5 \times 10^{-19}$  (J) was fitted to the kaolinite-dominated Salkum soil, and the bottom (bold) curve with  $A_{svl} = -6 \times 10^{-20}$  (J) was fitted to adsorption data from all other soils in this study which have mixed montmorillonite-kaolinite clay mineralogy).

Soil series	Sand	Silt	Clay	Clay type	SA§ (m <sup>2</sup> g <sup>-1</sup> )	Porosity
Sand†	1.000	0.000	0.000	NA	0.01	0.35
L-soil‡	0.888	0.061	0.051	Mixed	25	0.45
Royal‡	0.536	0.319	0.145	Mixed	45	$0.48\P$
Salkum‡	0.190	0.585	0.225	Kaolinitic	51	0.58¶
Walla Walla‡	0.228	0.633	0.139	Mixed	70	$0.52\P$
Millville	0.330	0.490	0.180	Mixed	73	0.47
Palouse‡	0.113	0.682	0.205	Mixed	97	0.55¶
PalouseB‡	0.093	0.439	0.468	Mixed	203	$0.59\hat{\P}$

Table 1–2. Measured soil properties.

meters ( $\alpha_{VG}$  and  $n_{VG}$ ) are entirely empirical. We use the results for Millville silt loam (Or & Tuller, 1999) depicted in Fig. 1–10 to illustrate in some detail the primary features of the proposed scheme. The calculated water characteristic curve (Fig. 1–10a) fits measured data as well as the VG model (the two curves are indistinguishable). An important feature of the new model is the ability to separate the individual contributions of adsorptive and capillary forces to the resulting liquid retention curve. The adsorption curve (A) is represented by the terms  $S_{w4}$  and  $S_{w5}$  in Eq. [23]. The liquid retained in completely filled pores and slits ( $S_{w1} + S_{w3}$ ), and the liquid retained due to capillary forces in the corners of partially filled pores ( $S_{w2}$ ) are added to obtain the capillary curve (C). The point of crossover separates the retention curve into capillary- and adsorption-dominated portions. The contributions illustrated in Fig. 1–10a should be considered as follows: for a given chemical potential  $\mu$ , the corresponding saturation value (thick line denoted as "New Model") is made up of adsorptive (A) plus capillary (C) components.

# **Liquid-Vapor Interfacial Area**

Liquid-vapor interfacial area per pore volume (Eq. [28]) was calculated as a function of chemical potential (Fig. 1–10b) using the parameters estimated from the retention curve. The resulting liquid-vapor interfacial values were then multiplied by the medium porosity to yield interfacial area per bulk sample volume as depicted in Fig.1–10b. The interfacial area  $A_{lv} = 0$  for  $\mu > \mu_d$  (or until the largest pore is invaded by air/vapor). At the dry end of the  $A_{lv}$  curve the interfacial area

Table 1–3. Physical constants and dimensions used in the illustrative example calculations.

Property	Symbol		Unit
Hamaker Constant (liquid-liquid through vapor)	$A_{ m llv}$	$3.7 \times 10^{-20}$	[J]
Hamaker Constant (solid-vapor through liquid) mixed†	$A_{ m svl}$	$-6.0 \times 10^{-20}$	[J]
Hamaker Constant (solid-vapor through liquid) kaolinitie†	$A_{ m svl}$	$-5.0 \times 10^{-19}$	[J]
Surface tension of water	σ	0.0715	$[N m^{-1}]$
Density of water	ρ	1000	$[kg m^{-3}]$

<sup>1</sup> See "Estimation of the Effective Hamaker Constant A<sub>set</sub> for Different Soils".

<sup>†</sup> From Kim et al., 1997.

<sup>‡</sup> From Campbell and Shiozawa, 1992.

<sup>§</sup> Determined with the ethylene glycol monoethyl ether (EGME) method (Carter et al., 1986).

<sup>¶</sup> Estimated by assuming a particle density of 2650 kg m<sup>-3</sup> and matching the gravimetric water content in Campbell and Shiozawa, 1992.

approaches a constant value equal to the estimated specific surface area of the medium,  $SA_{\rm e}$  (Eq. [30]). The asymptotic behavior and the attainment of a nearly constant value occurs when only a few molecular layers of liquid are adsorbed on the solid surface.

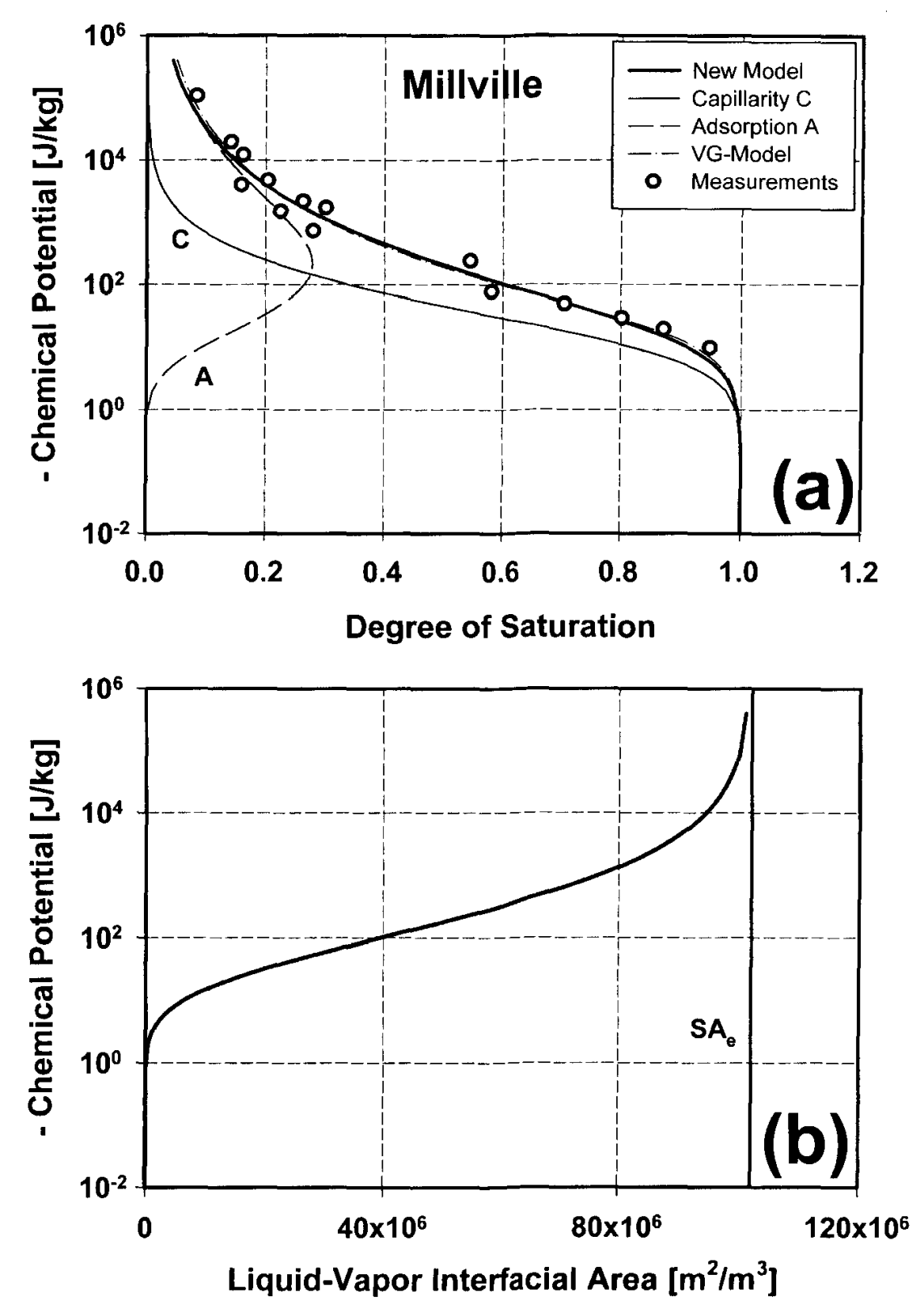


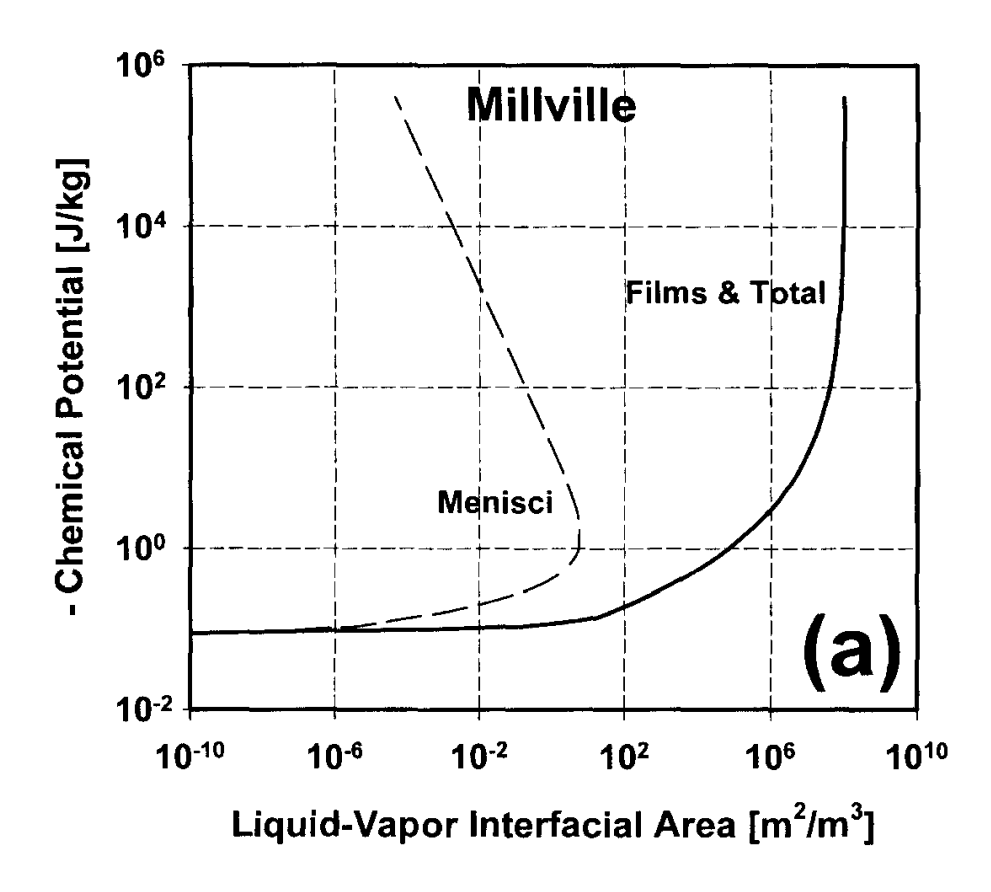
Fig. 1–10. (a) Measured and fitted water retention curves, and (b) calculated liquid vapor interfacial area for Millville silt loam soil.

Knowledge of detailed liquid-vapor configurations enables separation of capillary and adsorptive contributions to the interfacial area as shown in Fig. 1–11a (note the log-log scale). We denote liquid-vapor interfacial areas associated with menisci (curved interfaces at pore corners) as capillary contributions, and those associated with films as adsorptive contributions. The results in Fig. 1–11a illustrate the dominant contribution of liquid films to the total liquid-vapor interfacial area of a partially saturated porous medium (Millville silt loam). Note that the "flat" region in Fig. 1–11a (changes in SA with no change in  $\mu$ ) reflects pore snap-off processes.

Even for very coarse sand such as used by Kim et al (1997), the contribution to liquid-vapor interfacial area by films (F) dominates the contribution by menisci (M) as evident from the results in Fig. 1–11b (calculated for triangular-shaped pores to accentuate capillary effects). The comparisons shown in Fig. 1–11b between liquid-vapor interfacial area measurements by Kim et al. (1997) and Karkare and Fort (1996), and model calculations (expressed as SA per bulk sample volume) are based on retention and media parameters given in Tables 1-2 and 1-4. The measurements of Karkare and Fort (1996) were obtained in sand with a similar particle size range as used by Kim et al. (1997). For the reported sand specific surface area of 10 m<sup>2</sup> kg<sup>-1</sup> (based on calculation for smooth spherical particles) (Kim et al., 1997), model predictions slightly underestimate measured  $A_{lv}$ . However, surface area estimates assuming smooth spherical particles were shown by Borkovec et al. (1993) to produce significantly lower estimates than measured specific surface area (due to the contribution of particle surface roughness). Figure 5 in Borkovec et al. (1993) shows differences in excess of two orders of magnitude between measured SA (obtained by various methods) and SA estimated from geometrical calculations for similar particle sizes as used by Kim et al. (1997). An increase in the value of sand specific surface area to 50 m<sup>2</sup> kg<sup>-1</sup> (dash-dotted line) yields a great improvement in matching model predictions with measurements.

The primary reason for the minor capillary contribution to liquid-vapor interfacial area even in a medium with relatively large (triangular-shaped) pores and small surface area lies in the control exerted by the chemical potential on liquid-vapor menisci. For a given potential, meniscus curvature is constant throughout the porous medium irrespective of pore size. This means that after pore snap-off the capillary contribution to liquid-vapor interfacial area from small and large pores is equal if their shapes (polygon and angularity) are similar.

The shape of the capillary portion of the liquid-vapor interfacial area for sand (Fig. 1–11b) resembles simulation results of Reeves and Celia (1996) of interfacial areas in pore networks due to capillarity only. The discussion illustrates potential limitations in using cylindrical pore network models (Reeves & Celia, 1996) especially for studies of volatile liquids and surfactants, and other multiphase transport processes where interfacial areas play a crucial role (Kim et al., 1997; Karkare & Fort, 1996). Furthermore, the overwhelming role of adsorbed liquid films casts doubts on several proposed constitutive relationships between capillary pressure (saturation) and interfacial area (Skopp, 1985; Hassanizadeh & Gray, 1993) most of which were based on assumed cylindrical capillary geometry in the absence of adsorption.



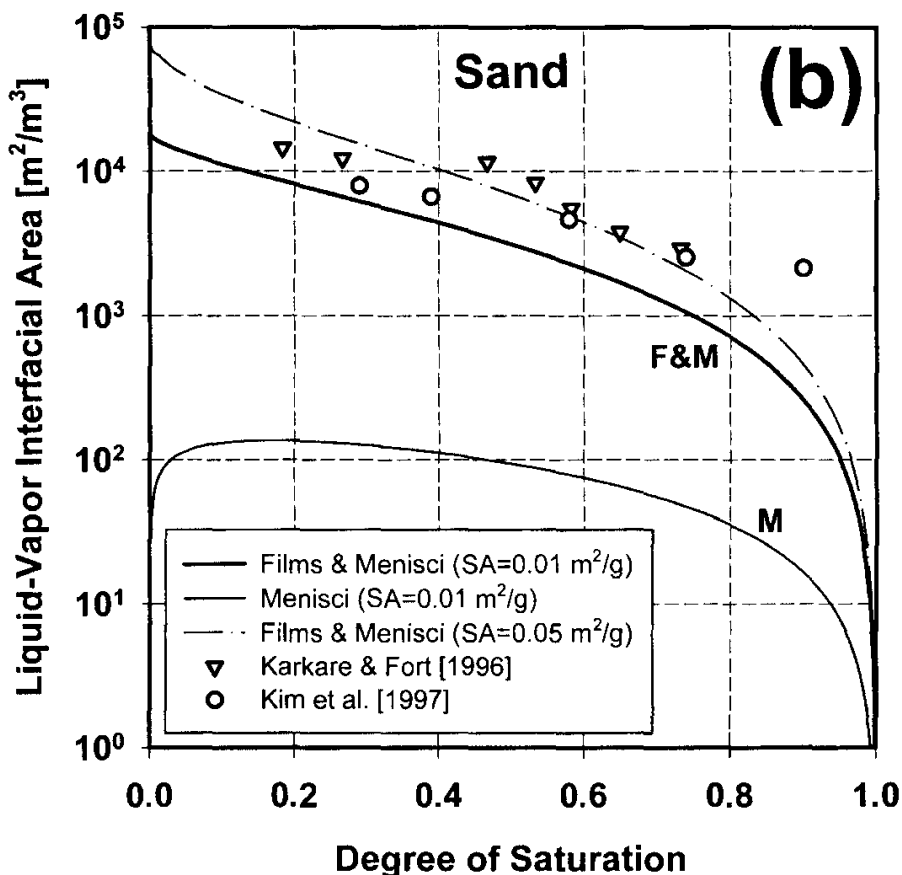


Fig. 1–11. (a) Calculated capillary (menisci) and adsorptive (film) contributions to liquid-vapor interfacial area as a function of chemical potential for Millville silt loam soil, (b) comparison of model calculated capillary and adsorptive contributions to liquid-vapor interfacial area as a function of saturation in an artificial sand mixture and measurements obtained by Kim et al. (1997), and Karkare and Fort (1996).

Table 1-4: Fitted parameters for the proposed model and the VG-model

Proposed Model							VG-Model			
Soil Series	β‡	α	ω‡	λ‡	$\mu_d$ ‡	$L_{\max}$	$SA_{\rm e}$	SA ratio§	$\alpha_{ m VG}$ ‡	n <sub>VG</sub> ‡
					J kg <sup>-1</sup>	m	$m^2 kg^{-1}$	%	$(J kg^{-1})^{-1}$	
Sand (Kim et al., 1997)†	0.275	6.73E-05	0.000 650	1 900	-0.003 0	0.015 26	10	99.4	3.300	6.199
L-Soil (Campbell & Shiozawa, 1992)	18 500	5.71E-05	0.000 220	2 100	-0.0050	0.005 50	22 517	90.1	2.917	1.338
Royal (Campbell & Shiozawa, 1992)	50 000	5.11E-05	0.000 170	2 180	-0.0062	0.004 44	40 491	90.0	0.127	1.465
Salkum (Campbell & Shiozawa, 1992)	65 000	6.06E-05	0.000 170	2 200	-0.0072	0.003 82	50 918	99.8	0.100	1.297
Walla Walla (Campbell & Shiozawa, 1992)	100 000	4.52E-05	0.000 130	2 350	-0.0075	0.003 67	68 106	97.3	0.189	1.305
Millville (Or & Tuller, 1999)	250 000	4.30E-05	0.000 107	2 750	-0.0102	0.002 71	72 848	99.8	0.050	1.303
Palouse (Campbell & Shiozawa, 1992)	300 000	4.47E-05	0.000 105	3 200	-0.012 5	0.002 20	96 735	99.7	0.190	1.274
PalouseB (Campbell & Shiozawa, 1992)	2 500 000	3.34E-05	0.000 090	5 000	-0.017 0	0.001 62	182 604	90.0	0.168	1.216

Calculated for a triangular-shaped central pore.
 Fitted parameters.
 Ratio between model calculated and measured specific surface area.

A summary of parameters estimated and calculated for all soils is given in Table 1–4, showing a clear trend with values of  $\omega$ , and  $L_{\text{max}}$  increasing with coarsening of the soil texture, and the value of  $\beta$  increasing with increase in surface area, as it should. The decrease in  $\lambda$  with coarsening texture emphasizes the increasing contribution of the central pores (small  $\lambda$  yields extended overlap of the Gamma distributions).

### HYDRODYNAMIC CONSIDERATIONS

Motivated by the detailed picture of liquid vapor interfaces under hydrostatic equilibrium we proceed with the introduction of hydrodynamic considerations. The underlying assumption is that these liquid configurations and interfaces remain relatively stable under slow laminar flow conditions. Furthermore, network effects are ignored and only flow into the liquid cross-section is considered—similar to derivations used in the BCC model (Milington & Quirk, 1961; Mualem, 1976a). Considering these simplifying assumptions, we develop in the following sections a model for pore scale hydrodynamic processes starting with flow in individual geometrical features of a unit cell and scaling up to represent the hydraulic conductivity of unsaturated sample [using a statistical scaling procedure similar to the one presented in "Upscaling Considerations from Pore-to Sample Scale (Or and Tuller, 1999)"]. Potential applications of the proposed modeling approach for estimation of unsaturated hydraulic conductivity of rough fracture surfaces and fractured porous media are presented.

## Flow Phenomena in Angular Pore Space

A cross-section of a unit cell with triangular- or square-shaped central pore is considered. We distinguish between three flow regimes: (i) flow in ducts and between parallel plates for completely filled slits and central pores, (ii) flow in thin liquid films adsorbed on the flat parts of the unit cell after slit or pore snap-off, and (iii) flow in the corners of the central pore after pore snap-off. The onset and contribution of each flow regime is dependent on the filling stage of the unit cell as determined by chemical potential. Solutions of the Navier-Stokes equation for different geometry and boundary conditions are used to obtain the average velocities in films, corners, ducts, and parallel plates. We then use analogy with Darcy's law to obtain the proportionality coefficient between flux and hydraulic gradient that represents the average hydraulic conductivity for laminar flow regimes under consideration. In some cases we consider modified liquid viscosity in vicinity of solid surfaces for thin liquid film flow calculations. The unsaturated hydraulic conductivity for the entire cross-section of the unit cell is derived by averaging film and corner conductivities over the associated liquid-occupied areas and dividing by the entire crosssectional unit cell area (pore and solid shell). Using the equilibrium liquid-vapor interface the saturated hydraulic conductivity for a unit cell is calculated by assembling solutions for the full duct (main pore) and parallel plate (slits), representing the cell elements. Relative hydraulic conductivity as a function of  $\mu$  is calculated as the quotient of unsaturated and saturated conductivities.

#### Flow in Ducts and Between Parallel Plates

Spurk (1997) derived closed-form solutions for the average flow velocity  $\overline{v}$  between parallel plates and in full ducts. For laminar flow between parallel plates relationships between viscosity, geometry, pressure gradient and mean flow velocity are given as:

$$\bar{v} = [(\alpha L)^2/(12\eta_0)] (-dP/dz)$$
 [32]

where  $\eta_0$  is the viscosity of bulk liquid,  $\alpha L$  is the spacing between the plates (i.e., slit spacing), and -dP/dz is the pressure gradient in flow direction z.

In this study we consider flow through ducts with triangular, square-shaped, and higher order polygonal cross-sections. For simplicity we employ the circular duct solution to approximate average velocities in higher order polygons (n > 4).

The average velocity in a full rectangular duct (of dimensions  $L_1 \times L_2$  with  $L_1 > L_2$ ) is given by:

$$\overline{v} = [L_2^2 B_s/(4 \eta_0)] (-dP/dz)$$
 [33]

with

$$BS = \frac{1}{3} - \frac{L_2}{L_1} \frac{64}{\pi^5} \sum_{n=1}^{\infty} \frac{\tanh \{(L_1/L_2)[\pi(2n-1)/2]\}}{(2n-1)^5}$$

For a square-shaped duct the solution simplifies as  $L_2/L_1 = 1$ . The solution for an equilateral triangular duct is given as (Spurk, 1997):

$$\overline{v} = [L^2/(80 \,\eta_0)] \,(-dP/dz)$$
 [34]

The circular duct solution related to a polygon with the same cross-sectional area is given as (Spurk, 1997):

$$\overline{v} = [L^2 A_n / (8 \eta_0 \pi)] (-dP/dz)$$
 [35]

where L is the side-length of the polygon, and  $A_n$  is the area factor defined in Table 1–1 [for comprehensive derivations see Tuller and Or (2001)].

### Flow in Thin Films

The flow velocity profile normal to film cross-section is obtained from a solution of the following Navier-Stokes equation (Spurk, 1997):

$$(-dP/dz) = \eta_0 (d^2v/dy^2)$$
 [36]

where y is the distance taken normal to the solid surface. Double integration of Eq. [36] yields the velocity profile normal to the solid surface:

$$v(y) = [(y^2 - 2hy)/(2\eta_0)] (-dP/dz)$$
 [37]

with h as the thickness of the liquid film. The velocity profile (Eq. [37]) may be integrated again (between zero and film thickness) and divided by film thickness h to yield an average liquid velocity for a given chemical potential:

$$\overline{v} = [h(\mu)^2/(3\eta_0)] (-dP/dz)$$
 [38]

This expression relates the film thickness h (Eq. [18a]) as a function of the chemical potential  $\mu$  and the mean velocity, and is valid only when the liquid viscosity is constant throughout the film. Experimental and theoretical evidence shows a presence of a thin layer with modified viscosity close to the solid surface. Liquid viscosity is elevated relative to bulk liquid due to short- and long-range interfacial forces (Low, 1976, 1979; Derjaguin et al., 1987; McBride & Baveye, 1995). Expressions derived by Low (1979) for viscosity profiles of water altered by interfacial forces were recently modified by Or and Wraith (1999) to represent viscosity  $\eta$  in terms of distance from the solid surface:

$$\eta(y, T) = \eta_0 \exp[a^*/(yT)]$$
 [Pa s] [39]

where y is the distance from the solid surface (Å), T is temperature (K), and  $a^* = 1621$  (Å K) is a constant modified from Low (1976). Substituting Eq. [39] into Eq. [36] and carrying out the integrations yields an expression for average velocity considering effects of modified liquid viscosity near solid surfaces (Or & Tuller, 1999):

$$\overline{v} = \{A(\mu)/[12 \, \eta_0 \, h(\mu)]\} \, (-dP/dz)$$
 [40]

With the function  $A(\mu)$  for a given film thickness  $h(\mu)$ :

$$A(\mu) = [4h(\mu)^3 - 5ah(\mu)^2 - a^2h(\mu)] \exp[-a/h(\mu)] - [6a^2h(\mu) + a^3] Ei [-a/h(\mu)]$$

where  $E_i[x] = \int_{-\infty}^{x} (e^t/t) dt$  is the exponential integral (Abramowitz & Stegun, 1964), and a for room temperature (293 K) is defined as  $a = (a^*/293) \cdot 10^{-10} = 5.53 \cdot 10^{-10}$  m.

The resulting average velocities for constant (Eq. [38]) and variable viscosity (Eq. [40]) become indistinguishable for liquid films thicker than about 10 nm. We therefore use the simpler expression in Eq. [38] for films thicker than 10 nm, and the more complex Eq. [40] for flow in very thin films.

# Liquid Flow in Corners Bounded by a Liquid-Vapor Interface

Ransohoff and Radke [1988] derived mathematical expressions for average liquid velocity in corners bounded by liquid-vapor interfaces. They used a detailed numerical scheme to solve the Navier-Stokes equations for the assumed geometry and boundary conditions. Their results were reduced to the general form:

$$\overline{v} = [r(\mu)2/(\varepsilon \eta_0)] (-dP/dz)$$
 [41]

where  $\varepsilon$  is a dimensionless flow resistance parameter dependent on the corner angle  $\gamma$  (Ransohoff & Radke, 1988). The tabulated values of Ransohoff and Radke

(1988) for for different corner angles and for zero surface shear stress (i.e., liquid-vapor interface) were fitted with the following parametric expression (Fig.1–12):

$$\varepsilon(\gamma) = \exp[(b + d\gamma)/(1 + c\gamma)]$$
 [42]

with b = 2.124, c = -0.00415, and d = 0.00783 ( $r^2 = 0.995$ ) for  $\gamma$  values in the range of  $10^{\circ} < \gamma < 150^{\circ}$  (Fig.1–12).

# Average Hydraulic Conductivity for Flow in Parallel Plates, Ducts, Films, and Corners

We use the analogy between the average flow velocities calculated for pore-scale flow regimes from the Navier-Stokes solutions (Eq. [32], [33], [34], [35], [38], [40], and [41]) and Darcy's law representation of the liquid flux to obtain the per-meabilities of parallel plates, ducts, films, and corners. The analogy of pore-scale flow processes with Darcy's law was instrumental to compute unsaturated hydraulic conductivity in studies by Childs and Collis-George (1950), Burdine (1953), Gardner (1958), Mualem (1976a), and many others. Darcy's law is given as:

$$\overline{v} = Q/A = [K/(\rho g)] (-dP/dz)$$
 [43]

where Q is the volumetric discharge rate, A is the cross-sectional area occupied by the liquid, K is the hydraulic conductivity, and g is the acceleration of gravity. Assuming a unit pressure gradient, rearranging Eq. [43], and inserting the solution in

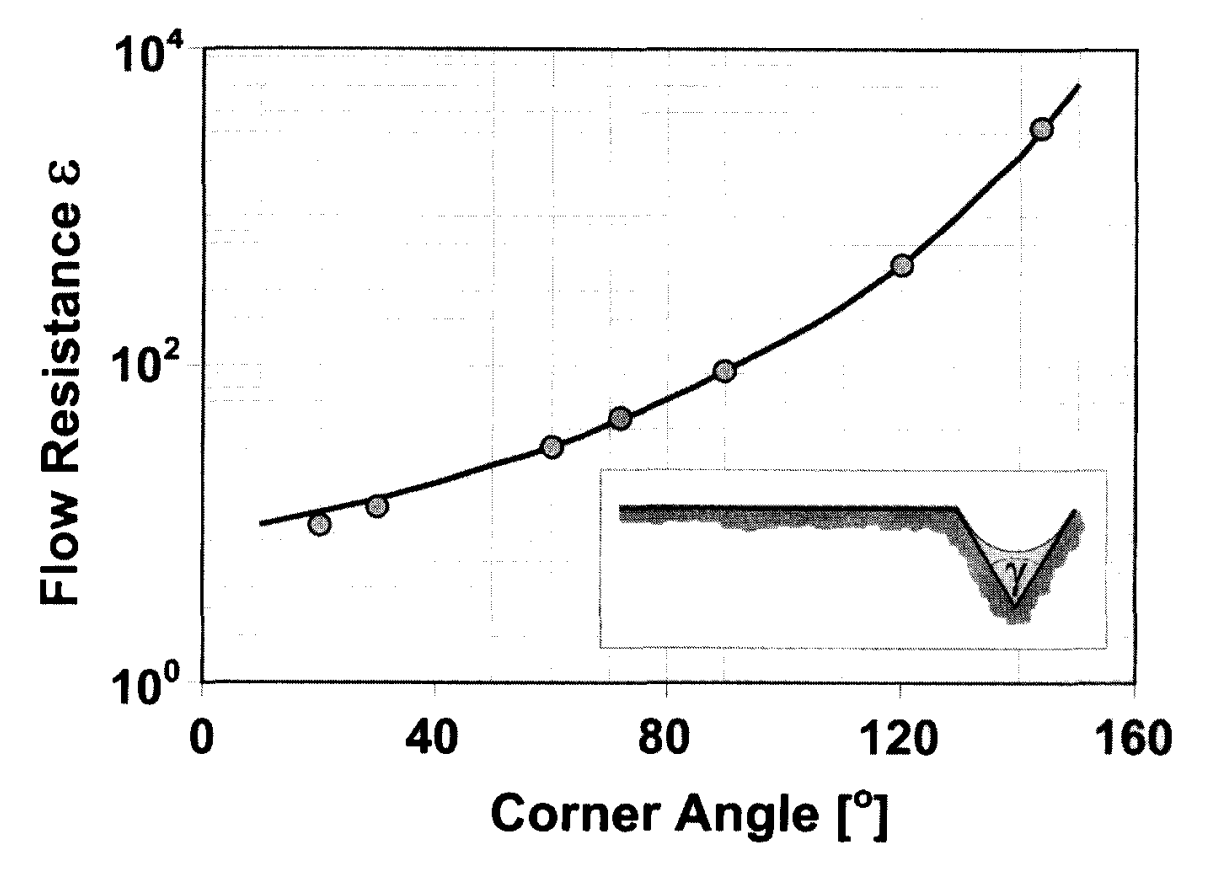


Fig. 1–12. Nondimensional corner resistance to flow as a function of corner (pit) angle γ (calculated from tabulated values of Ransohoff & Radke, 1988).

Eq. [32], [33], [34], [35], [38], [40], and [41], yield the following expressions for *K*:

Parallel plates (slits) 
$$KS = K_s L^2 = [\rho g \alpha^2 / (12 \eta_0)] L^2$$
 [44]

Triangular duct 
$$KD_{\rm T} = Kd_{\rm T} L^2 = [\rho g/(80 \, \eta_0)] L^2$$
 [45]

Square-shaped duct 
$$KD_S = Kd_S L^2 = [\rho g B_s/(4 \eta_0)] L^2$$
 [46]

Circular duct 
$$KD_{\rm C} = Kd_{\rm C} L^2 = [\rho g A_{\rm p}/(8 \pi \eta_0)] L^2$$
 [47]

Thick film 
$$(h \ge 10 \text{ nm})$$
  $KF(\mu) = (\rho g/\eta_0) [h(\mu)^2/3]$  [48]

Thin film 
$$(h < 10 \text{ nm})$$
  $KF(\mu) = (\rho g/\eta_0) [A(\mu)/(12h(\mu))]$  [49]

Corner 
$$KC(\mu) = (\rho g/\eta_0) [r(\mu)^2/\epsilon]$$
 [50]

The thickness of the adsorbed film  $h(\mu)$  and the radius of interface curvature  $r(\mu)$  are calculated according to Eq. [18a], and [18b].

### Saturated and Unsaturated Hydraulic Conductivity for a Unit Cell

Saturated and unsaturated hydraulic conductivities for the entire unit cell is calculated by weighting the conductivities of single elements discussed above over the liquid occupied cross-sectional areas and dividing by the total cross-sectional cell area (pore plus solid shell). The total cross-sectional area  $A_T$  is simply calculated by dividing the pore cross-sectional area (see Fig. 1–5a) by the porosity  $\phi$  of the porous medium:

$$A_{\rm T} = [(2\alpha\beta + A_{\rm n})L^2]/\phi$$
 [51]

where  $A_n$  is the area factor of the central pore, listed in Table 1–1.

To calculate unsaturated hydraulic conductivity  $K(\mu)$  we have to take into consideration the spontaneous filling (snap-off) of the slit and the central pore for imbibition and the spontaneous redistribution of liquid for drainage. These aspects are extensively discussed in "Film Adsorption on Flat Surfaces and in Slit-Shaped Pores" and "Capillarity and Pore Shape". The unsaturated conductivity before slit filling is given as:

$$K(\mu) = \frac{h(\mu) \left[ 4\beta L + n \left( L - \frac{2r(\mu)}{\tan(\gamma/2)} \right) \right] KF(\mu) + r(\mu)^2 F_n KC(\mu)}{A_T}$$
[52]

with  $KF(\mu)$  and  $KC(\mu)$  as the hydraulic conductivities for films and corners (Eq. [48], [49], and [50]). Note that the thin film solution (Eq. [49]) is employed for films thinner 10 nm. Detailed derivations of liquid occupied cross-sectional areas are given in Tuller and Or (2001). The unsaturated conductivity after slit filling is given as:

$$K(\mu) = \frac{2\alpha\beta L^2 KS + h(\mu)n\left(L - \frac{2r(\mu)}{\tan(\gamma/2)}\right)KF(\mu) + r(\mu)^2 F_n KC(\mu)}{A_T}$$
 [53]

The saturated hydraulic conductivity after main pore snap-off, when the entire cross-section is occupied by liquid, is given as:

$$K_{\text{sat}} = (2\alpha\beta L^2 KS + A_n L^2 KD)/A_T$$
 [54]

where KS and KD are the parallel plate and duct hydraulic conductivities defined in "Average Hydraulic Conductivity for Flow in Parallel Plates, Ducts, Films, and Corners". Relative hydraulic conductivity is obtained by dividing Eq. [52], [53], and [54] by the saturated conductivity (Eq. [54]).

# **Upscaling From Pore- to Sample Scale Hydraulic Conductivity**

The same upscaling scheme as presented in "Upscaling Considerations from Pore- to Sample Scale (Or and Tuller, 1999)", using a gamma distribution for the central pore dimension L, was applied to obtain saturated and unsaturated hydraulic conductivities for a sample of porous medium. To obtain closed form expressions for the expected value of sample-scale hydraulic conductivity we set the distribution parameter  $\xi = 2$ . Inverse relationship between slit length and central pore length (see discussion in "Statistical Representation of Unit Cell Dimensions") is facilitated by expressing the slit length as  $\beta(L_{\text{max}}-L)$ . The general closed-form expression for sample-scale hydraulic conductivity is expressed as the sum of five terms related to five distinct cell filling stages as determined by chemical potential and geometry (snap-off mechanisms):

$$K(\mu) = K_1(\mu) + K_2(\mu) + K_3(\mu) + K_4(\mu) + K_5(\mu)$$
 [55]

The separation into five terms was necessary to distinguish between flow contributed by films and by corners and full ducts. The integrals for the five terms may be expressed in a general form

$$K_{i}(\mu) = \int_{L_{I}}^{L_{U}} \frac{AL^{4} + BL^{3} + CL + D}{EL^{2} + FL} f(L)dL$$
 [56]

where f(L) is the gamma density function with  $\xi = 2$  (Eq. [21]),  $L_L$  and  $L_U$  are the lower and upper integration limits, and A, B, C, D, E, and F are constants and variables listed in Table 1–5. For a detailed analytical solution of this general integral we refer to Tuller and Or (2001). Note that in Tuller and Or (2001) Eq. [56] was extended to allow calculation of liquid saturation, liquid-vapor interfacial area, medium specific surface area, and saturated and unsaturated hydraulic conductivity with a single general equation.

The first term  $K_1(\mu)$  is the expected value of unsaturated hydraulic conductivity for completely filled central pores integrated between the minimum pore di-

Table 1–5. Integration limits, constants, and variables used in the hydraulic conductivity calculations (Eq. [56]).

Conductivity term (Integration limits†)	$A\ddagger$	$B\ddagger$	<i>C</i> ‡	D‡	E	F
$K_{\text{sat}}(L_{\min}, L_{\max})$	$(A_n K_d - 2 \alpha \beta K_s) \phi$	$2 \alpha \beta L_{\text{max}} K_{\text{s}} \phi$	0	0	$A_{\rm n}-2\alpha\beta$	2 α β L <sub>max</sub>
$K(\mu)_1 (L_{\min}, L_1)$	$A_{\mathrm{n}} K_{\mathrm{d}} \Phi$	0	0	0	$A_n - 2 \alpha \beta$	$2 \alpha \beta L_{\text{max}}$
$K(\mu)_2 (L_{\min}, L_2)$	$-2 \alpha \beta K_s \phi$	$2 \alpha \beta L_{\text{max}} K_{\text{s}} \phi$	0	0	$A_n - 2 \alpha \beta$	$2 \alpha \beta L_{\text{max}}$
$K(\mu)_3 (L_2, L_{\text{max}})$	0	0	$-4 \beta h(\mu) KF(\mu) \phi$	$4 \beta L_{max} h(\mu) KF(\mu) \phi$	$A_n - 2 \alpha \beta$	$2 \alpha \beta L_{\text{max}}$
$K(\mu)_4 (L_1, L_{\text{max}})$	0	0	$n h(\mu)KF(\mu) \phi$	$-nh(\mu) [2r(\mu)/\tan(\gamma/2)] KF(\mu) \phi$	$A_n - 2 \alpha \beta$	2 α β $L_{max}$
$K(\mu)_{5}(L_{1},L_{\max})$	0	0	0	$r(\mu)^2 F_n KC(\mu) \phi$	$A_n - 2 \alpha \beta$	$2 \alpha \beta L_{\text{max}}$

 $<sup>\</sup>frac{1}{L_{\text{max}}} = 10^{-9} \text{ m}; L_{\text{max}}, L_1, \text{ and } L_2 \text{ are given in Eq. [31], [25], and [27].}$   $\frac{1}{L_{\text{max}}} = 10^{-9} \text{ m}; L_{\text{max}}, L_1, \text{ and } L_2 \text{ are given in Eq. [31], [25], and [27].}$ 

mension  $L_{\min}$  and the upper limit  $L_1$ , which is determined from the radius of curvature at the onset of drainage in the central pore (Eq. [24]). The second term describes the fraction of unit cells having full slits with integration limits  $L_{\min}$  and  $L_2$ . The upper limit  $L_2$  (Eq. [27]) is determined from the chemical potential at slit snapoff [see discussion in "Sample Scale Saturation (Drainage Branch)"]. Flow in films adsorbed on slit walls is accounted for in  $K_3(\mu)$  with the integration limits  $L_2$  and the maximum pore dimension  $L_{\max}$  associated with the air entry value  $\mu_d$  (Eq. [31]). The fourth term represents the contribution of films aligning the flat parts of the central pore (between the curved corner menisci). The limits of integration are defined between  $L_1$  and  $L_{\max}$ . Finally  $K_5(\mu)$  calculates the contribution of corner flow within the central pore from pore snap-off  $(L_1)$  to  $L_{\max}$ . An illustration about the relation of integration limits and pore filling stages is depicted in Fig. 1–8. The contribution of film flow to the overall unsaturated hydraulic conductivity is represented by the sum of terms  $K_2(\mu)$ ,  $K_3(\mu)$ , and  $K_4(\mu)$ .

The expected value of sample-scale saturated hydraulic conductivity  $K_{\rm sat}$  is obtained by integrating Eq. [56] with variables and constants listed in Table 1–5 between  $L_{\rm min}$  and  $L_{\rm max}$  (full saturation). The relative hydraulic conductivity is simply the quotient of  $K(\mu)$  and  $K_{\rm sat}$ .

# Illustrative Examples for Pore and Sample-Scale Unsaturated Hydraulic Conductivity

The application of the proposed hydraulic conductivity model is demonstrated for three soils with physical properties and measured retention and conductivity data reported by Brooks and Corey (1964) and Mualem (1976b). Saturation curves are obtained by fitting the pore scale (Eq. [16] and [17]) or sample scale expressions (Eq. [23]) for saturation to measured retention data [see discussions in "Applications of Simplified Augmented Young-Laplace Equation in the New Pore Geometry", "Sample Scale Saturation (Drainage Branch)", and "Liquid Saturation"]. The resulting fitting parameters L,  $\alpha$ , and  $\beta$  (single cell) and the scaling parameters  $\omega$ ,  $\lambda$ ,  $\mu_d$ , and  $\beta$  (upscaled model) are then employed to predict saturated and unsaturated hydraulic conductivities at the pore (Eq. [52], [53], and [54]) and sample scale (Eq. [55]). The resulting  $K(\mu)$  curves are compared with measured data and the van Genuchten (1980) parametric model for unsaturated hydraulic conductivity.

The physical constants used in the calculations are listed in Table 1–3. Measured properties, VG-model parameters, and calculated  $K_{\rm sat}$  values of the soils under investigation are listed in Table 1–6. Additional examples over a wide range of soil textural classes are discussed in Tuller and Or (2001).

# Pore-Scale Unsaturated Hydraulic Conductivity

Closed-form expressions for pore-scale saturation (Eq.[16] and [17]) for a unit cell with triangular central pore were fitted to measured saturation data of Hygiene Sandstone (Brooks & Corey, 1964). A triangular central pore was selected to emphasize capillary contributions expected for sand pore space. An elementary unit cell with dimensions L = 0.033 mm,  $\alpha = 0.0012$ ,  $\beta = 0.0001$  was found to yield best fit to the measured data as depicted in Fig.1—13a. The resulting saturation curve is

Table 1–6. Measured properties and best fit parameters for the proposed and the VG-Mualem model for the investigated soils.

Soil	Gilat loam‡	Touchet silt loam§	Hygiene sandstone§
	Measurem	ents	
$K_{\rm sat}$ , m d <sup>-1</sup>	0.17	3.03	1.08
$K_{\rm sat}$ , m d <sup>-1</sup> $SA^{\dagger}$ , m <sup>2</sup> g <sup>-1</sup>	58	46	8
	New moo	del	,
β	250 000	10	Cell dimensions
ω	0.000 026	0.000 007	L = 0.033  mm
λ	600	350	$\alpha = 0.001 \ 2$
$\mu_d$ , J kg <sup>-1</sup>	-0.98	-2.94	$\beta = 0.000 \ 1$
Predicted $K_{\text{sat}}$ , m d <sup>-1</sup>	0.054	2.33	1.59
Predicted $SA_e$ , m <sup>-2</sup> g <sup>-1</sup>	40	31	NA
	Van Genuchten-Mu	ıalem model	
$\alpha_{VG} (J \ kg^{-1})^{-1}$	0.233	0.051	0.081
$n_{ m VG}$	1.67	7.09	10.40

<sup>†</sup> Estimated from soil texture.

similar to curves obtained with the Brooks and Corey (1964) model, in which the pore is completely saturated for potentials from zero to the air entry value. The cell dimensions obtained from the saturation curve were then used for saturated and unsaturated hydraulic conductivity calculations (Eq.[52], [53], and [54]). The resulting relative conductivity curve in Fig.1–13b clearly shows that soils with a narrow pore-size distribution (e.g., sand) may be represented by a single unit cell. This offers a simple and powerful tool for prediction of unsaturated hydraulic conductivity from measured retention data.

# Sample-Scale Unsaturated Hydraulic Conductivity

The primary features of the unsaturated hydraulic conductivity upscaling scheme are demonstrated for Gilat Loam (Mualem, 1976b; Bresler et al., 1971). We use a solver tool available in most spreadsheet software to fit Eq. [23a–e] to measured saturation, applying an objective function (Or & Tuller, 1999) and constraints discussed in "Parameter Estimation and Physical Constraints", to receive a set of best fit parameters  $\beta$ ,  $\omega$ ,  $\lambda$ , and  $\mu_d$ . Figure 1–14a reveals that the surface area constraint (see discussion in "Specific Surface Area Constraint") and the rigid shape of the gamma distribution ( $\xi$  = 2) resulted in an unsatisfactory match at the intermediate saturation range, but was in good agreement with measurements at the wet and the dry end of the saturation curve. The VG-model was unable to match the measured endpoints, but it was in good agreement with measurements at a saturation range from 0.4 to 0.75. The dotted lines show the contributions of liquid retained due to capillary and adsorptive forces ("Liquid Saturation").

The predicted relative hydraulic conductivity curve (Fig.1–14b) shows excellent agreement with measured data. The dash-dotted line represents the contribution of film flow to the overall hydraulic conductivity. Figure 1–14b also illustrates the important role of film flow, whose contribution begins to dominate the

<sup>‡</sup> Source is Mualem (1976b).

<sup>§</sup> Source is Brooks and Corey (1964).

contribution of corners and full ducts at relatively high chemical potentials in the range of  $-70 \,\mathrm{J\,kg^{-1}}$ . Such film contributions are often discounted in pore scale models (e.g., Ransohoff & Radke, 1988; Dullien et al., 1986). Another interesting feature of the proposed model is ability to reproduce the s-shaped  $K(\mu)$  curve (on a

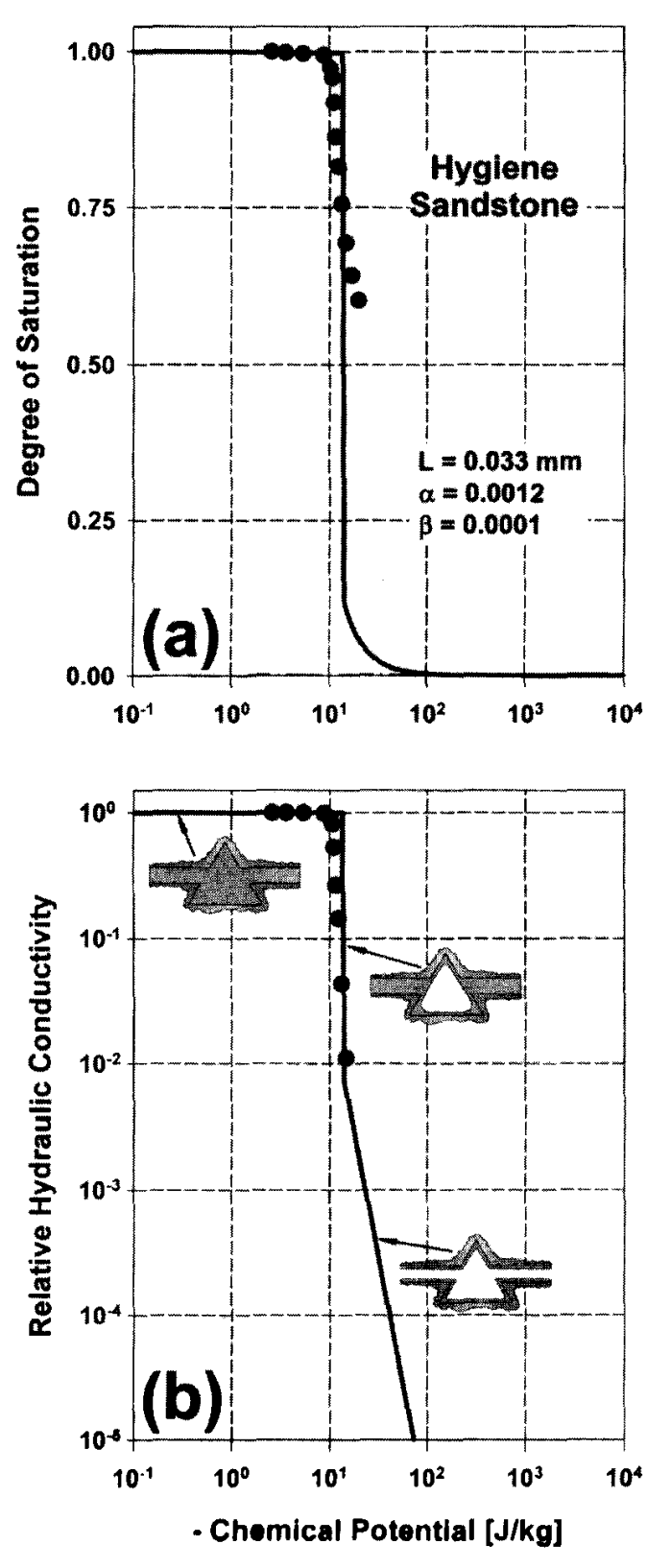


Fig. 1–13. (a) Calculated liquid saturation for Hygiene Sandstone using a single cell with triangular central pore, and (b) predicted relative hydraulic conductivity.

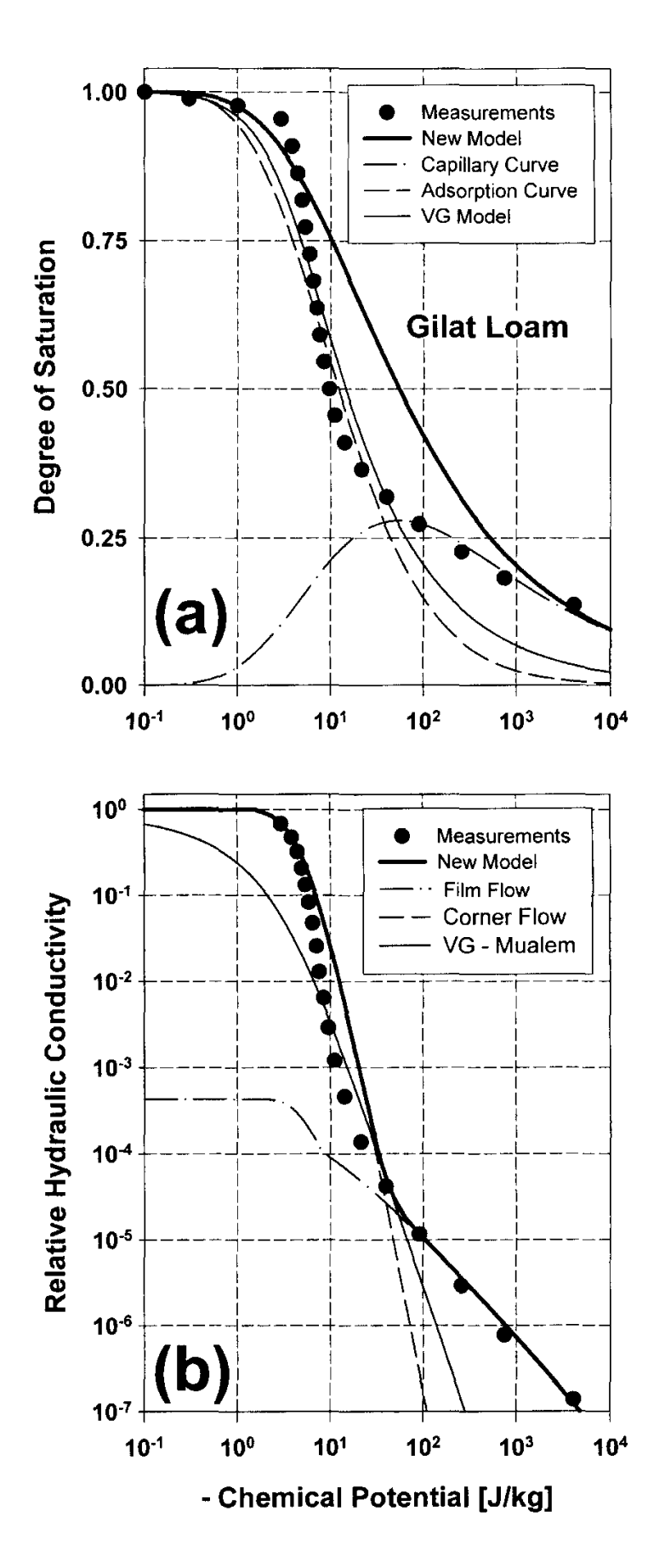


Fig. 1–14. (a) Calculated sample-scale liquid saturation for Gilat Loam, (b) predicted relative hydraulic conductivity (dash-dotted and dashed lines indicate the individual contributions of film and corner flow).

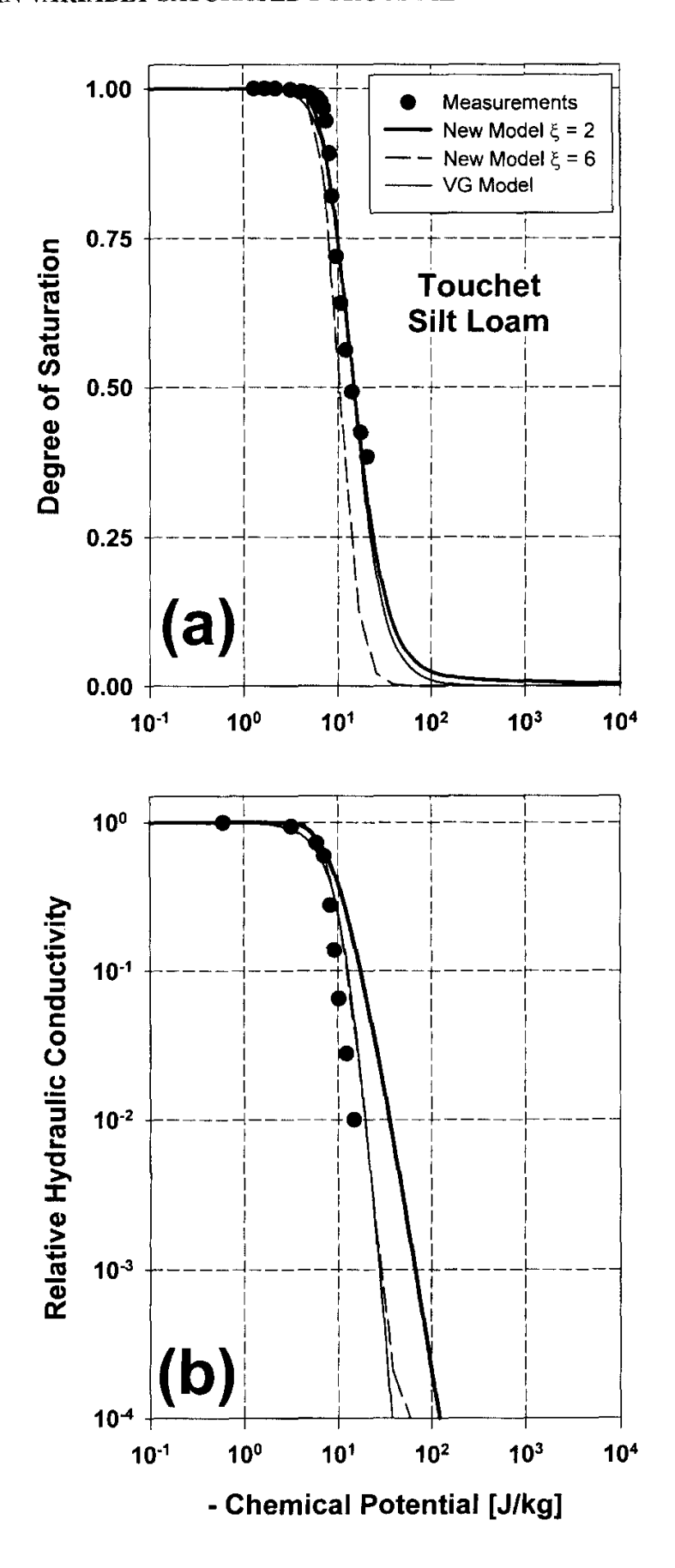


Fig. 1–15. (a) Calculated sample-scale liquid saturation for Touchet Silt Loam (van Genuchten, 1980; comparison between analytical and numerical solutions), (b) comparison of predicted relative hydraulic conductivity curves obtained from analytical and numerical solutions of the new model and the VG-Mualem model.

log-log scale) as evidenced by measurements. Empirical models [e.g., Van Genuchten (1980)] usually are unable to capture the film flow contribution which alters the slope of  $K(\mu)$  significantly; instead they exhibit a monotonous decrease in  $K(\mu)$  for potentials lower than the air entry value.

In an attempt to derive closed-form expressions for unsaturated hydraulic conductivity, we were forced to fix the shape of the gamma distribution by using a constant distribution parameter  $\xi = 2$ . This led to a reduced flexibility, especially for soils with narrow pore size distribution. In Fig. 1–15 we show improved predictions of  $K(\mu)$  when the distribution parameter  $\xi$  is left as a free parameter (using a numerical scheme for the upscaling). The dashed line in Fig. 1–15b represents the numerically evaluated relative saturation curve ( $\xi = 6$ ) that is almost indistinguishable from the VG-Mualem model. A summary of resulting parameters is listed in Table 1–6.

# Other Potential Applications—Unsaturated Flow on Rough Fracture Surfaces

The approach for unsaturated conductivity outlined in previous sections was extended to modeling the unsaturated hydraulic conductivity of rough fracture surfaces (Or & Tuller, 2000). Flow on rough fracture surfaces is an essential component required for deriving constitutive relationships for flow in unsaturated fractured porous media (Or & Tuller, 2001). The detailed derivations are obtained by consideration of a dual porosity model (matrix – fracture) and the proportional contributions to flow from these different pore spaces.

Considering a cross-sectional segment (unit element) of an unsaturated fracture with a wide aperture (Fig. 1–16), the unsaturated conductivity as a function of chemical potential is modeled following principles of the unitary approach as outlined in previous sections. The fracture aperture is assumed to be sufficiently wide to preclude fracture snap-off (spontaneous filling of the gap) at all flow rates and chemical potentials under consideration. The extension of the analysis to fully saturated fractures is simple for a known aperture size (or a distribution of aperture sizes). Each fracture element contains a pit representing either surface roughness due to unconnected pits, or a connected groove on the fracture surface. Individual pit geometry is defined by the pit's depth L and its angle  $\gamma$ . Pit density per unit fracture surface is determined by a nondimensional parameter  $\beta$  that relates pit spacing to its depth (L).

We consider the individual contributions of film and groove (corner) flow to the total flow on the fracture surface, thereby enabling separation and identification of flow regimes for different scenarios (fracture surface properties and chemical potentials). If most of the pits are isolated, we expect the flow to be dominated by liquid film flow. In the presence of an appreciable amount of continuous grooves, most of the flow is expected to be in the form of "corner" flow (Ransohoff & Radke, 1988; Dullien et al., 1986). Under realistic conditions, flow in unsaturated fractures is likely to be a result of these two processes. Analytical solutions for liquid retention and unsaturated hydraulic conductivity on rough surfaces are derived in Or and Tuller (2000) for a single fracture element, and for a population of elements with a statistical distribution of their pit depth. An illustrative example for average conductivity and the individual contributions of film and corner flow for a single frac-

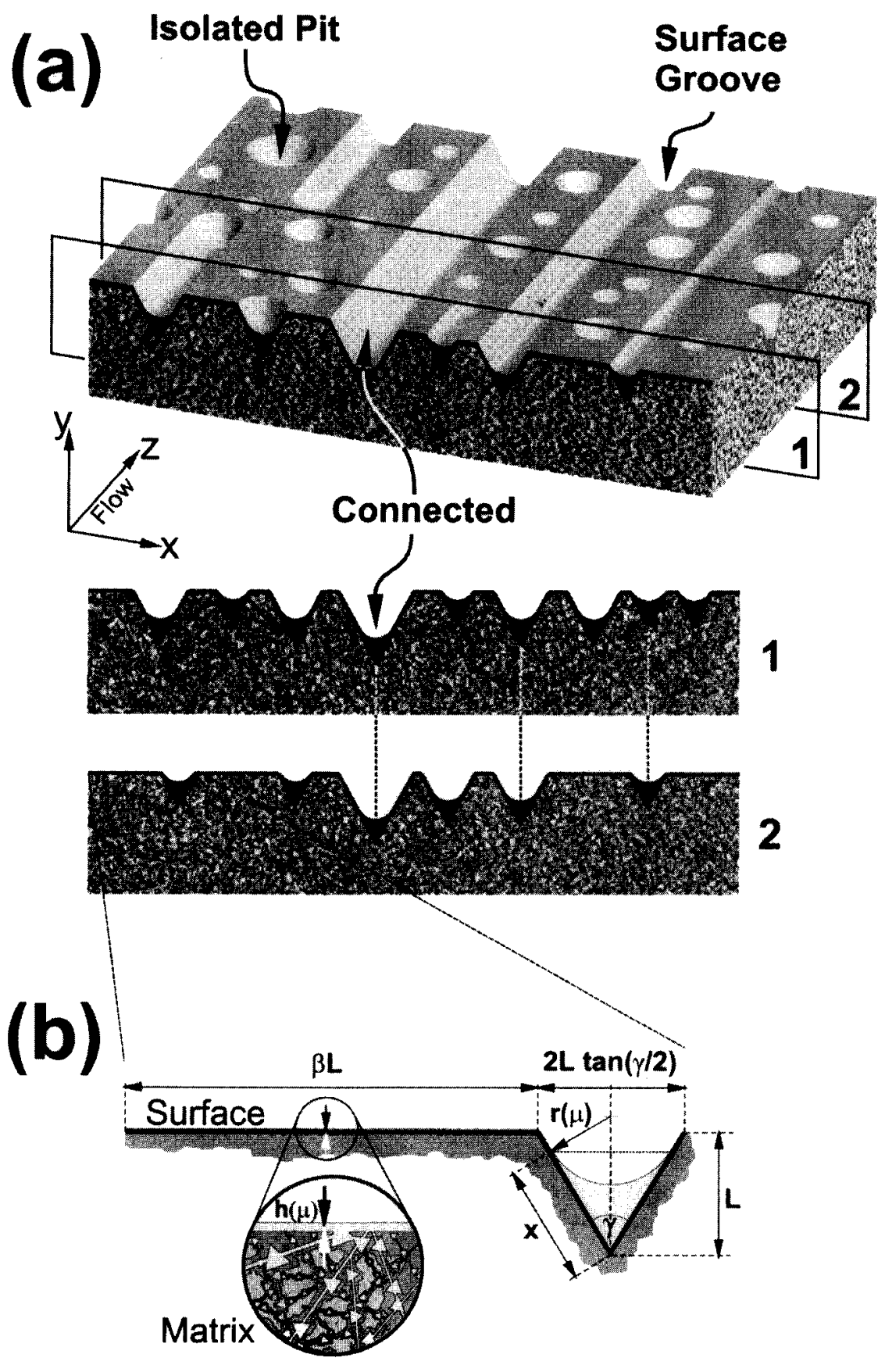
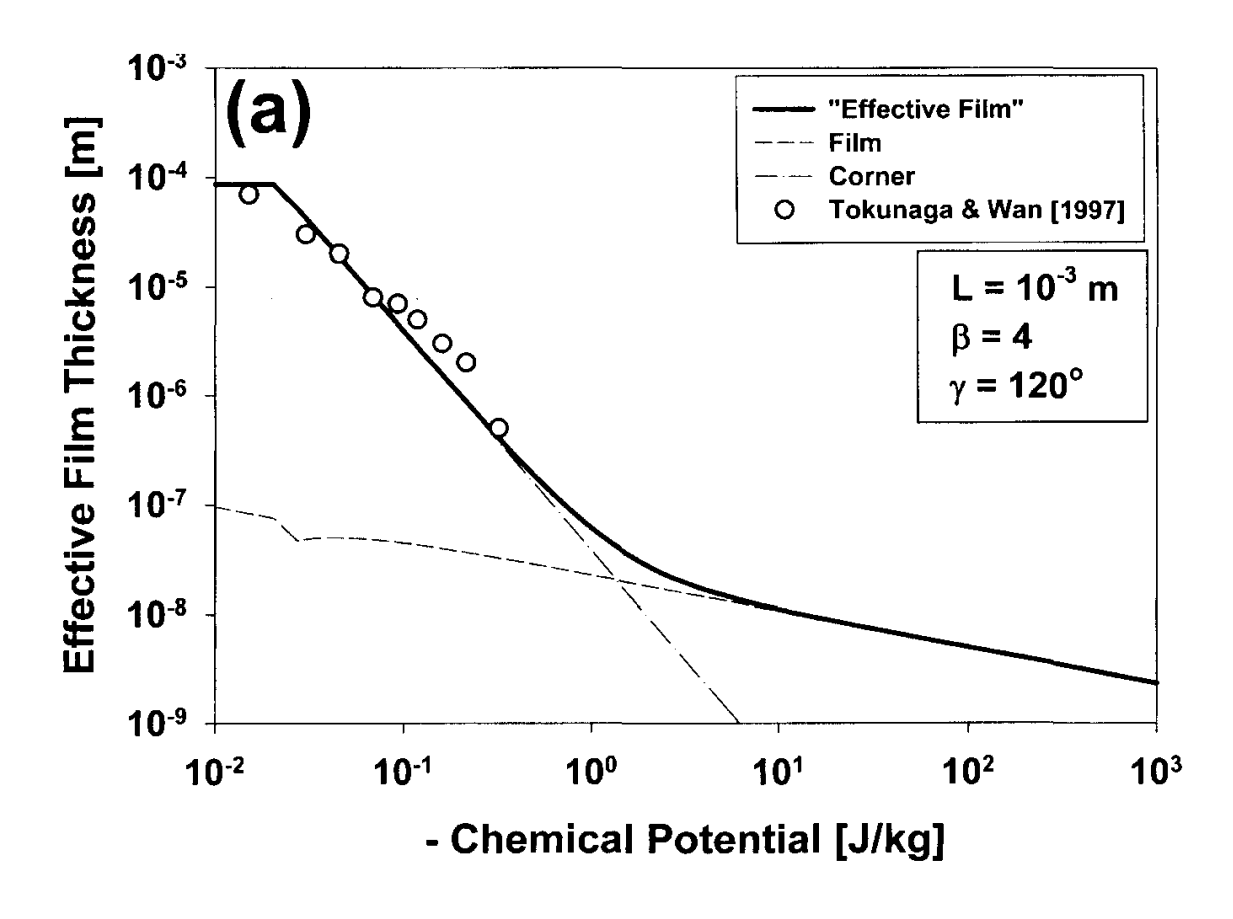


Fig. 1–16. (a) Conceptual picture of a rough fracture surface with (b) a definition sketch for a unit element representing an unsaturated fracture surface with a single pit of depth L and angle  $\gamma$ . Liquid-vapor interfaces are functions of the chemical potential  $\mu$  that determines the radius of curvature in the pit  $r(\mu)$ , and film thickness  $h(\mu)$ . The inset represents the partially saturated porous rock forming the fracture, water in the rock pore space is in equilibrium with water on fracture surface.



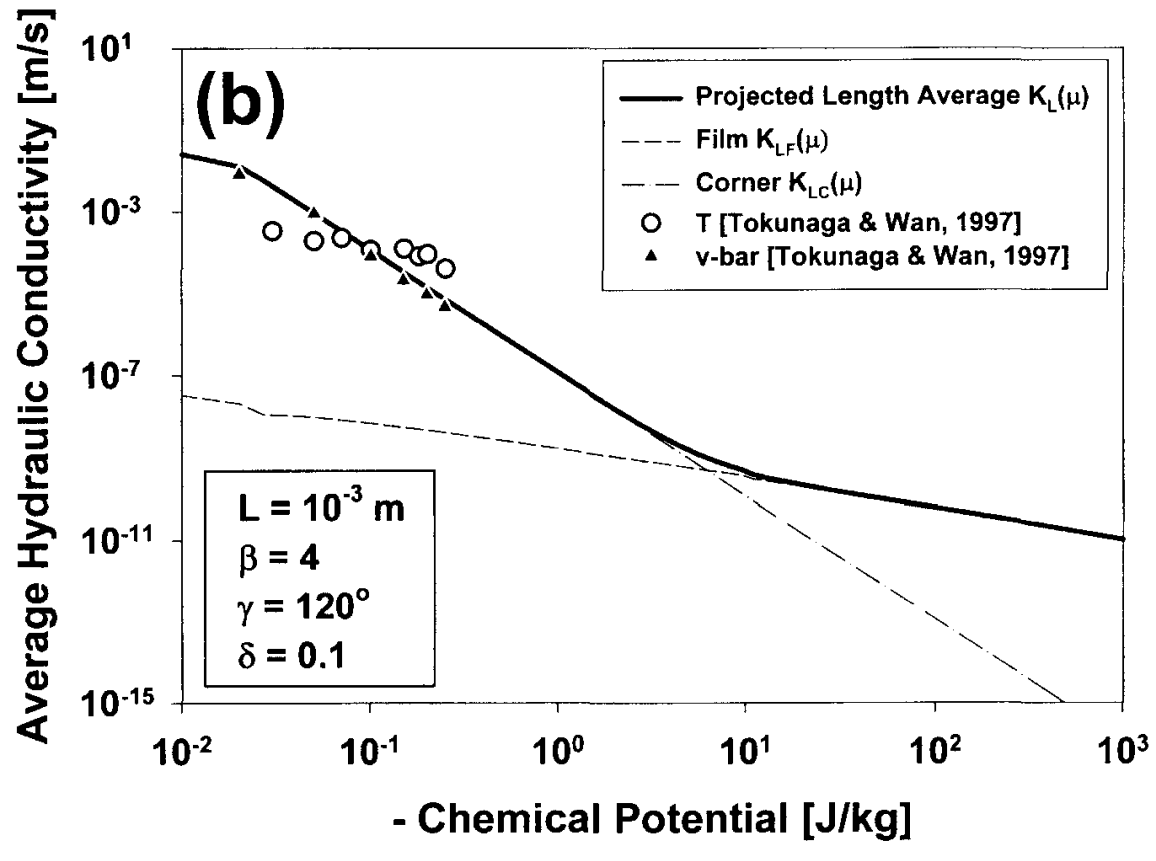


Fig. 1–17. Evaluation of Tokunaga and Wan's (1997) experimental results with unsaturated hydraulic conductivity expressions for single element weighed by  $\delta = 0.1$ .

ture element is depicted in Fig.1–17. Measurements by Tokunaga and Wan (1997) are represented as symbols.

The results for flow on a single fracture surface are incorporated in the derivation of hydraulic properties of unsaturated fractured rock mass. Liquid retention and hydraulic conductivity in partially saturated fractured porous media are modeled in angular pores and slit-shaped spaces representing rock matrix and fractures, respectively. A bimodal distribution of pore sizes and apertures accounts for the two disparate pore scales and porosity. These considerations provide a framework for derivation of retention and hydraulic conductivity functions for fractured porous media (Or & Tuller, 2001).

### **SUMMARY AND CONCLUSIONS**

The focus of this review was a new physically based framework for modeling liquid retention and liquid-vapor interfacial area in partially saturated porous media developed by Tuller et al. (1999). The primary elements of the new framework are: (i) the explicit consideration of individual contributions of capillary and adsorptive forces to the matric potential; and (ii) a new model for media pore space geometry that includes internal surface area and angular rather than cylindrical pore space. The augmented Young-Laplace (AYL) equation combines the classical capillary component with an adsorptive term based on liquid-solid interfacial processes into a unitary representation (Philip, 1977a). The disjoining pressure is the basic thermodynamic property used to express interfacial interactions, using results from the pioneering work of Derjaguin et al. (1987). These developments were applied to newly proposed pore space geometry (elementary unit cell) comprising of an angular central pore (for capillary processes) connected to slit-shaped spaces with internal surface area (for adsorption processes). A key development for practical use was the simplification of the complex AYL-equation by superposition of adsorptive and capillary interfaces. The results of the simplified solution, termed shifted Young-Laplace equation (SYL), were indistinguishable from those obtained by detailed solution of the AYL equation. New expressions for capillary behavior in angular pore spaces further assisted in the development of extremely simple expressions ("Capillarity and Pore Shape") for calculation of saturation and liquid-vapor interfacial area at the pore scale.

The proposed pore scale model served as the basis for development of a statistical framework for upscaling to a variably saturated sample of a porous medium (Or & Tuller, 1999), where the distribution of cross sectional pore lengths is modeled with the gamma distribution. The model calculates the expected values of various liquid configurations in pore space using geometrical and chemical potential considerations of liquid behavior within the assumed statistical framework. Model predictions using optimally estimated parameters compare favorably with water retention measurements. Among the advantages of the proposed physically based retention model is the ability to separate capillary and adsorptive contributions, thereby enhancing the explanatory power of the model. Furthermore, liquid-vapor interfacial area as a function of chemical potential (or saturation) is readily calculated using the same parameters used for retention calculations. Both calculations

(saturation and interfacial area) are made possible by detailed knowledge of liquid-vapor configuration for the entire pore size population. Model calculations reveal a dominant role of liquid films in determining liquid-vapor interfacial area.

Hydrodynamic considerations were introduced with the underlying assumption that equilibrium liquid-vapor interfaces remain relatively constant under slow laminar flow conditions. Considering cross-sectional flow only (no network effects), unsaturated conductivity was calculated by combining the individual contributions of flow in adsorbed liquid films and in corners of the considered pore (cell) cross sections (Tuller & Or, 2001). The average liquid velocity for a unit pressure gradient in films was obtained by solving the Navier-Stokes equation for plane flow and including effects of modified liquid viscosity in the vicinity of solid surfaces. The analysis and expressions derived by Ransohoff and Radke (1998) were used to calculate liquid flow in corners bounded by liquid-vapor interface. The unsaturated hydraulic conductivity for the entire cell cross-section was obtained by averaging over the liquid occupied areas. The pore-scale model was scaled to represent a sample of porous medium, applying a similar scheme as introduced for liquid saturation. Scaling parameters derived from the retention model were applied to calculate sample-scale unsaturated hydraulic conductivity. Sample calculations for different soils clearly reveal the dominant role of film flow at lower chemical potentials, a phenomenon often neglected in similar studies.

The potential to extend the proposed approach to model hydraulic conductivity on rough fracture surfaces (Or & Tuller, 2000), and to model the combined matrix and fracture flow in fractured porous media (Or & Tuller, 2001) is illustrated in examples.

The primary contributions of the new approaches reviewed are summarized:

- 1. A physically based unitary approach for adsorptive and capillary contributions to the matric potential—including the incorporation of disjoining pressure representation of interfacial forces was introduced.
- 2. A new pore geometry model was proposed for a more realistic representation of pore space of natural porous media using angular pore geometry and slit-shaped spaces for surface area considerations.
- 3. Simple expressions for capillary phenomena in angular pores based on angularity shape factor  $F_n$  and curvature only, were developed.
- 4. Liquid-vapor interfacial area was determined for improved understanding of microbiological and related processes in unsaturated porous media.
- 5. The pore scale model and the associated unitary approach were upscaled to represent a sample of partially saturated porous medium.
- 6. Direct links between soil physical properties and liquid-solid interactions were established.
- 7. The dominant role of liquid films in creating liquid-vapor interfacial areas was elucidated (pending experimental confirmation).
- 8. The introduction of hydrodynamic considerations led to direct calculations of unsaturated hydraulic conductivity at the pore and sample scale and provide the basis for incorporating fundamental aspects of reactive solute transport.

### ACKNOWLEDGMENTS

The authors gratefully acknowledge the partial support of NSF under grant EAR-9805409 and the partial support of the Utah Agricultural Experimental Station, Utah State University, Logan, Utah. Approved as UAES journal paper no.7218.

### **APPENDIX**

```
\alpha = Dimensionless parameter relating slit spacing to the central pore dimension
```

 $\beta$  = Dimensionless parameter relating slit length to the central pore dimension

 $\varepsilon$  = Dimensionless flow resistance parameter

 $\eta_0$  = Viscosity of bulk liquid (kg m<sup>-1</sup> s<sup>-1</sup>)

 $\kappa$  = Mean curvature of the liquid vapor interface (Philip, 1977a)

 $\lambda$  = Slit spacing distribution overlap parameter

 $\mu$  = Chemical potential (J kg<sup>-1</sup>)

 $\mu_d$  = Critical chemical potential for the onset of drainage (J kg<sup>-1</sup>)

v = Positive constant used by Philip (1977a) (m)

 $\xi$  = Gamma distribution parameter

 $\Pi$  = Disjoining pressure (N m<sup>-2</sup>)

 $\rho$  = Density of the liquid (kg m<sup>-3</sup>)

 $\sigma$  = Surface tension at the liquid-vapor interface (N m<sup>-1</sup>)

 $\phi$  = Porosity of the porous medium

 $\omega$  = Gamma distribution parameter

 $\gamma$  = Corner/pit angle

 $A_n$  = Pore area factor

 $A_{\text{llv}}$  = Hamaker constant for liquid-liquid interactions through intervening vapor (J)

 $A_{1v}$  = Liquid-vapor interfacial area (m<sup>2</sup>)

 $A_{\text{svl}}$  = Hamaker constant for solid vapor interactions through intervening liquid (J)

 $A_{\rm w}$  = Liquid occupied area (m<sup>2</sup>)

a =Constant for modified liquid viscosity in vicinity of solid surfaces

 $C_{\rm n}$  = Coefficient for the limits of integration

 $F_{\rm n}$  = Angularity factor

 $G = \text{Gibbs free energy } (\text{J m}^{-2})$ 

H = Slit spacing (m)

h = Film thickness (m)

 $h_c$  = Critical film thickness for spontaneous slit snap off (m)

 $K_{\text{sat}}$  = Saturated hydraulic conductivity (m s<sup>-1</sup>)

 $K(\mu)$  = Unsaturated hydraulic conductivity (m s<sup>-1</sup>)

L = Dimension of the central pore (m)

 $L_{\text{max}}$  = Maximal dimension of the central pore (m)

 $L_{\min}$  = Minimal dimension of the central pore (m)

m = Mean of the gamma distribution

n = Number of corners of the central pore

P = Pore perimeter (m)

p = Vapor pressure (Pa)

 $p_c$  = Capillary pressure (Pa)

 $p_{\text{saf}}$  = Vapor pressure at saturation (Pa)

 $R = \text{Gas constant } (J K^{-1} \text{ mol}^{-1})$ 

R' = Gas constant per unit mass of vapor (J K<sup>-1</sup> kg<sup>-1</sup>)

r = Radius of interface curvature (m)

 $r_{\rm d}$  = Radius of interface curvature for spontaneous liquid distribution at drainage (m)

 $r_{\rm imb}$  = Radius of interface curvature for pore snap-off at imbibition (m)

SA = Specific surface area (m<sup>2</sup> kg<sup>-1</sup>)

 $S_{\rm w}$  = Liquid saturation

T = Temperature (K)

 $V_{\rm m}$  = Molar volume of the liquid (m<sup>3</sup> mol<sup>-1</sup>)

v = Variance of the gamma distribution

 $\overline{v}$  = Average liquid velocity (m s<sup>-1</sup>)

#### REFERENCES

- Abramowitz, M., and I.E. Stegun. (ed.). 1964. Handbook of mathematical functions with formulas, graphs, and mathematical tables. Natl. Bur. Stand. Appl. Math. Ser. 55. U.S. Dep. Commerce, Washington, DC.
- Ackler, H.D., R.H. French, and Y-T Chiang. 1996. Comparisons of Hamaker constants for ceramic systems with intervening vacuum or water: From force laws and physical properties. J. Colloid Interface Sci. 179:460–469.
- Adamson, A.W. 1990. Physical chemistry of surfaces. 5th ed. John Wiley & Sons, Inc., New York.
- Assouline S., D. Tessier, and A. Bruand. 1998. A conceptual model of the soil water retention curve. Water Resour. Res. 34:223–231.
- Beaglehole, D., E.Z. Radlinska, B.W. Ninham, and H.K. Christenson. 1991. Inadequacy of Lifshitz theory for thin liquid films. Phys. Rev. Lett. 66:2084–2087.
- Bergström, L. 1997. Hamaker constants of inorganic materials. Adv. Colloid Interface Sci. 70:125-169.
- Berkowitz, B., and R.P. Ewing. 1998. Percolation theory and network modeling applications in soil physics. Surv. Geophys. 19:23–72.
- Blank, R.R., and M.A. Fosberg. 1989. Cultivated and adjacent virgin soils in northcentral South Dakota. Chemical and physical comparisons. Soil Sci. Soc. Am. J. 53:1484–1490.
- Blunt, M., and H. Scher. 1995. Pore-level modeling of wetting. Phys. Rev. (E) 52:6387–6403.
- Blunt, M., D. Zhou, and D. Fenwick. 1995. Three-phase flow and gravity drainage in porous media. Transp. Porous Media 20:77–103.
- Borkovec, M., Q. Wu, G. Degovics, P. Laggner, and H. Sticher. 1993. Surface area and size distributions of soil particles. Colloids Surf. A 73:65–76.
- Bresler, E., J. Heller, N. Diner, I. Ben-Asher, A. Brandt, and D. Goldberg. 1971. Infiltration from a trickle source: II. Experimental data and theoretical predictions. Soil Sci. Soc. Am. Proc. 35:683–689.
- Brooks, R.H., and A.T. Corey. 1964. Hydraulic properties of porous media. Hydrol. Pap. no.3. Colorado State Univ., Fort Collins, CO.
- Brutsaert, W. 1966. Probability laws for pore-size distributions. Soil Sci. 101:85–92.
- Burdine, N.T. 1953. Relative permeability calculation size distribution data. Pet. Trans. Am. Inst. Min. Metal. Pet. Eng. 198:71–78.
- Campbell, G.S., and S. Shiozawa. 1992. Prediction of hydraulic properties of soils using particle-size distribution and bulk density data. *In M.Th.* van Genuchten et al. (ed.) Proc. Int. Workshop on Indirect Methods Estimat. Hydraul. Propert. Unsaturat. Soils. Univ. California, Riverside.
- Carter, D.L., M.M. Mortland, and W.D. Kemper. 1986. Specific surface. p. 413–423. *In A. Klute* (ed.) Methods of soil analysis. Part 1. 2nd ed. Agron. Monogr. 9. ASA and SSSA, Madison, WI.
- Celia, M.A., P.C. Reeves, and L.A. Ferrand. 1995. Pore scale models for multiphase flow in porous media. Rev. Geophys. Suppl. 33:1049–1057.
- Childs, E.C. 1940. The use of soil moisture characteristics in soil studies. Soil Sci. 50:239–252.
- Childs, E.C., and G.N. Collis-George. 1950. The permeability of porous materials. Proc. R. Soc. London (A) 201:392–405.
- Christenson, H.K. 1994. Capillary condensation due to van der Waals attraction in wet slits. Phys. Rev. Lett. 73:1821–1824.
- Curry, J.E., and H.K. Christenson. 1996. Adsorption, wetting, and capillary condensation of nonpolar fluids in mica slits. Langmuir 12:5729–5735.
- Derjaguin, B.V. 1957. Correct form of the equation of capillary condensation in porous bodies in application to the separation of adsorption and capillary condensation in slits and porous bodies of known structure and determination of their structure by adsorption and sorption isotherms.

- p. 153–159. *In* J.H. Schulman (ed.) *In* Solid-gas interface. Proc. 2nd Int. Congr. Surf. Activity. Vol. 2. Butterworths Sci. Publ., London.
- Derjaguin, B.V., and N.V. Churaev. 1976. Polymolecular adsorption and capillary condensation in narrow slit pores. J. Colloid Interface Sci. 54(2):157–175.
- Derjaguin, B.V., N.V. Churaev, and V.M. Muller. 1987. Surface forces. Plenum Publ. Corp., Consult. Bur., New York.
- Dong, M., and I. Chatzis. 1995. The imbibition and flow of a wetting liquid along the corners of a square capillary tube. J. Colloid Interface Sci. 172:278–288.
- Dullien, F.A.L., F.S.Y. Lai, and I.F. Macdonald. 1986. Hydraulic continuity of residual wetting phase in porous media. J. Colloid Interface Sci. 109(1):201–218.
- Edlefsen, N.E., and A.B.C. Anderson. 1943. Thermodynamics of soil moisture. Hilgardia 15:31–298.
- Evans, R., U.M.B. Marconi, and P. Tarazona. 1986. Fluids in narrow pores: Adsorption, capillary condensation, and critical points. J. Chem. Phys. 84:2376–2399.
- Forcada, M.L. 1993. Instability in a system of two interacting liquid films: Formation of liquid bridges between solid surfaces. J. Chem. Phys. 98(1):638–643.
- Gardner, W.R. 1958. Some steady state solutions of the unsaturated moisture flow equation with application to evaporation from a water table. Soil Sci. 85:228–232.
- Hassanizadeh, S.M., and W.G. Gray. 1993. Thermodynamic basis of capillary pressure in porous media. Water Resour. Res. 29:3389–3405.
- Ioannidis, M.A., and I. Chatzis. 1993. A mixed-percolation model of capillary hysteresis and entrapment in mercury porosimetry. J. Colloid Interface Sci. 161:278–291.
- Iwamatsu, M., and K. Horii. 1996. Capillary condensation and adhesion of two wetter surfaces. J. Colloid Interface Sci. 182:400–406.
- Karkare, M.V., and T. Fort. 1996. Determination of the air-water interfacial area in wet "unsaturated" porous media. Langmuir 12(8):2041–2044.
- Kim, H., P.S.C. Rao, and M.D. Annable. 1997. Determination of effective air-water interfacial area in partially saturated porous media using surfactant adsorption. Water Resour. Res. 32:2705–2711.
- Kosugi, K. 1994. Three-parameter lognormal distribution model for soil water retention. Water Resour. Res. 30:891–901.
- Kosugi, K. 1996. Lognormal distribution model for unsaturated soil hydraulic properties. Water Resour. Res. 32:2697–2703.
- Laroussi, C., and L.W. De Backer. 1979. Relations between properties of glass beads media and their main  $\psi\theta$ ) hysteresis loops. Soil Sci. Soc. Am. J. 43:646–650.
- Lenormand, R., C. Zarcone, and A. Sarr. 1983. Mechanisms of the displacement of one fluid by another in a network of capillary ducts. J. Fluid Mech. 135:337–353.
- Lenormand, R. 1990. Liquids in porous media. J. Phys. Condens. Matt. 2:SA79–SA88.
- Li, Y., and N.C. Wardlaw. 1986a. The influence of wettability and critical pore-throat size ratio on snap-off. J. Colloid Interface Sci. 109:461–472.
- Li, Y., and N.C. Wardlaw. 1986b. Mechanisms of nonwetting phase trapping during imbibition at slow rates. J. Colloid Interface Sci. 109:473–486.
- Low, P.F. 1976. Viscosity of interlayer water in montmorillonite. Soil Sci. Soc. Am. J. 40:500-505.
- Low, P.F. 1979. Nature and properties of water in montmorillonite-water systems. Soil Sci. Soc. Am. J. 43:651–658.
- Mason, G., and N.R. Morrow. 1984. Meniscus curvatures in capillaries of uniform cross-section. J. Chem. Soc. Faraday Trans. (I) 80:2375–2393.
- Mason, G., and N.R. Morrow. 1991. Capillary behavior of a perfectly wetting liquid in irregular triangular tubes. J. Colloid Interface Sci. 141:262–274.
- McBride, M.B., and P. Baveye. 1995. Mobility of anion spin probes in hectorite gels: Viscosity of surficial water. Soil Sci. Soc. Am. J. 59:388–394.
- Milington, R.J., and J.P. Quirk. 1961. Permeability of porous media. Nature (London) 183:387–388.
- Mitlin, V.S., and M.M. Sharma. 1993. A local gradient theory for structural forces in thin fluid films. J. Colloid Interface Sci. 157:447–464.
- Morrow, N.R., and X. Xie. 1999. Surface energy and imbibition into triangular pores. p. 109–120. *In* M.Th. van Genuchten et al. (ed.) Proc. Int. Workshop Characterizat. Measurement of the Hydraul. Prop. of Unsaturat. Porous Media, Riverside, CA. 22–24 Oct. 1997. Univ. California, Riverside.
- Mualem, Y. 1976a. A new model for predicting the hydraulic conductivity of unsaturated porous media. Water Resour. Res. 12:513–522.
- Mualem, Y. 1976b. A catalogue of the hydraulic properties of unsaturated soils. Res. Proj. Rep. no. 442. Technion, Israel Inst. Technol., Haifa.

Novy, R.A., P.G. Toledo, H.T. Davis, and L.E. Scriven. 1989. Capillary dispersion in porous media at low wetting phase saturations. Chem. Eng. Sci. 44:1785–1797.

- Nitao, J.J., and J. Bear. 1996. Potentials and their role in transport in porous media. Water Resour. Res. 32:225–250.
- Or, D., and M. Tuller. 1999. Liquid retention and interfacial area in variably saturated porous media: Upscaling from single-pore to sample-scale model. Water Resour. Res. 35:3591–3606.
- Or, D., and M. Tuller. 2000. Flow in unsaturated fractured porous media: Hydraulic conductivity of rough surfaces. Water Resour. Res. 35:1165–1177.
- Or, D., and M. Tuller. 2001. Hydraulic conductivity model for unsaturated fractured porous media. Water Resour. Res. (In press.)
- Or, D., and J.M. Wraith. 1999. Temperature effects on soil bulk dielectric permittivity measured by time domain reflectometry: A physical model. Water Resour. Res. 35:371.
- Paunov, V.N., R.I. Dimova, P.A. Kralchevsky, G. Broze, and A. Mehreteab. 1996. The hydration repulsion between charged surfaces as an interplay of volume exclusion and dielectric saturation effects. J. Colloid Interface Sci. 182:239–248.
- Philip, J.R. 1977a. Unitary approach to capillary condensation and adsorption. J. Chem. Phys. 66:5069–5075.
- Philip, J.R. 1977b. Adsorption and geometry: The boundary layer approximation. J. Chem. Phys. 67:1732–1741.
- Philip, J.R. 1978. Adsorption and capillary condensation on rough surfaces. J. Phys. Chem. 82:1379–1385.
- Ransohoff, T.C., and C.J. Radke. 1988. Laminar flow of a wetting liquid along the corners of a predominantly gas-occupied noncircular pore. J. Colloid Interface Sci. 121:392–401.
- Reeves, P.C., and M.A. Celia. 1996. A functional relationships between capillary pressure, saturation, and interfacial area as revealed by a pore-scale network model. Water Resour. Res. 32:2345–2358.
- Rice, J.A. 1995, Mathematical statistics and data analysis. 2nd ed. Duxbury Press, Belmont, CA.
- Skopp, J. 1985. Oxygen uptake and transport in soils: Analysis of the air-water interfacial area. Soil Sci. Soc. Am. J. 49:1327–1331.
- Spurk, J.H. 1997. Fluid mechanics. Springer-Verlag, Berlin, Heidelberg.
- Tokunaga, T.K., and J. Wan. 1997. Water film flow along fracture surfaces of porous rock. Water Resour. Res. 33:1287–1295.
- Tuller, M., D. Or, and L.M. Dudley. 1999. Adsorption and capillary condensation in porous media: Liquid retention and interfacial configurations in angular pores. Water Resour. Res. 35:1949–1964.
- Tuller, M., and D. Or. 2001. Hydraulic conductivity of variably saturated porous media: Film and corner flow in angular pore space. Water Resour. Res. (In press.)
- van Genuchten, M.Th. 1980. A closed-form equation for predicting the hydraulic conductivity of unsaturated soils. Soil Sci. Soc. Am. J. 44:892–898.
- Vershinin, P.V., M.K. Mel'nikova, B.N. Michurin, B.S. Moshkov, N.P. Poyasov, and A.F. Chudnovskii. 1966. Water properties of soil and their physical nature. p. 505–561. *In A.F. Joffe and I.B. Revut* (ed.) Fundamentals of agrophysics. USDA, NSF, and Israel Program for Sci. Translat., Washington, DC.

# Transport of Water and Solutes in Soils as in Fractal Porous Media

### Yakov Pachepsky and Dennis Timlin

USDA-ARS Remote Sensing and Modeling Laboratory Beltsville, Maryland

David A. Benson

Desert Research Institute Reno, Nevada

Fractal models have been useful in quantifying inherent soil variability and structural hierarchy. Diffusion of solutes in a fractal pore network does not obey Fick's law; anomalous, or non-Fickian diffusion, takes place instead. We explore (i) the extent to which solute dispersion and horizontal water movement exhibit anomalous behavior; and (ii) the application of some simple fractal-based modeling approaches that accommodate the anomalous transport phenomena. The literature presents solid experimental evidence of non-Fickian solute dispersion in unsaturated soils. The dispersivity  $D_s$  in the advective-dispersive equation (ADE) has a power-law dependence  $D_s \propto L_s^{\gamma}$  on the mean solute transport distance  $L_s$ . The exponent  $\gamma$  varied between 0.3 and 1.7 in different data sets. Water transport in horizontal columns in some published data sets does not obey Boltzmann scaling that should occur if the water diffusivity in Richards' equation were scale-independent. The diffusivity  $D_{\rm w}$  in the Richards' equation has a power-law dependence on the mean distance of horizontal water transport  $(L_w)$  in form  $D_w \propto L_w^{-\beta}$ . The exponent  $\beta$  varies between 0.04 and 0.91 in published data. Soil heterogeneity gives rise to scale-dependence of transport parameters. When solute movements are spatially fractal, they can be described by the fractional advective-dispersive equation (FADE). We applied the FADE to two sets of solute breakthrough curves, and found an improvement in accuracy compared with ADE. In the FADE, the scale effects are reflected by the order of the fractional derivative, and the transport coefficient is not scale-dependent. The heavy tails of the breakthrough curves were well modeled by the FADE. The Richards equation with fractional time derivative has shown promise in simulating the horizontal water transport in soil. The anomalous transport of solutes can be an important phenomenon to consider in estimations of the fate of agricultural chemicals.

52 PACHEPSKY ET AL.

### INTRODUCTION

Structural hierarchy and heterogeneity are intrinsic soil properties that have profound effects on soil functioning in natural and man-made ecosystems. Quantifying soil structural hierarchy and its effects on soil processes is both an imperative and a challenge for soil physicists. Continual advances in this field benchmark soil science history. One of the advances was the introduction of the scaling concept, which showed simple and consistent ways of quantifying inherent soil variability and structural hierarchy (Nielsen et al., 1998).

### **Fractal Scaling in Soils**

Fractal models have been useful in describing the scaling properties of soil. This type of scaling was introduced in soil studies by Burrough 15 yr ago (Burrough, 1983a,b). It gained popularity after Tyler and Wheatcraft's (1989) work on scaling of soil water retention and Rieu and Sposito's (1991) work on developing a unified approach to scaling fragmentation, soil water retention, and bulk density in soils. Fractal geometry was developed to describe the hierarchy of purely mathematical objects but had immediate applications to objects in the real world (Mandelbrot, 1983). Natural objects often have similar features at different scales. Measures of these features, e.g., total number, total length, total mass, average roughness, total surface area, etc., are dependent on the scale on which the features are observed. Fractal geometry assumes that this dependence is the same over a range of scales, i.e., it is scale-invariant within this scale range.

Several soil properties have been shown to obey fractal scaling. Soil particle collections (textures) exhibit fractal scaling laws (Bartoli et al., 1991; Tyler & Wheatcraft, 1992; Niemeyer & Ahl, 1991; Wu et al., 1993; Kozak et al., 1996; Barak et al., 1996; Groute et al., 1998, Martin & Taguas, 1998). Fractal scaling has also been demonstrated for collections of soil aggregates (Young & Crawford, 1991; Perfect & Kay, 1991; Eghball et al., 1993a; Rasiah et al., 1996; Logsdon et al., 1996; Anderson et al., 1996). Variations in soil strength can be explained using fractal scaling (Folorunso et al., 1994: Pan & Lu, 1994). Soil surface roughness may be scaledependent according to fractal law (Huang & Bradford, 1992; Eltz & Norton, 1997; Pardini & Gallart, 1998). Pore surfaces exhibit fractal scaling when probed with various methods (Avnir et al., 1985; Sokolowska, 1989; Pachepsky et al., 1995a; Pachepsky et al., 1996a) and the same was found for soil colloidal constituents (Senesi et al., 1996; van Damme, 1998). Branching patterns of plant roots and mycelium also follow fractal scaling (Fitter & Strickland, 1992; Crawford et al., 1993; Eghball et al., 1993b; Spek & van Noordwijk, 1994; Donnelly & Boddy, 1997). Fractal scaling of soil properties was summarized in several recent topical reviews and collections of papers (Perfect & Kay, 1995; Baveye et al., 1998, p. 1–377, Anderson et al., 1998; Giménez et al., 1998; Pachepsky et al., 1999).

Soil pore arrangement, characterized with various methods, has been described with models assuming solid particles obey fractal scaling. This type of scaling was found from water retention data (Bird et al., 1996; Comegna et al., 1998; Kravchenko & Zhang, 1998; Perfect, 1999) and from thin section data (Crawford et al., 1995, Oleshko, 1998). Assumption of fractal pore surface produced good

agreement with data from mercury porosimetry (Bartoli et al., 1991; Pachepsky et al., 1995a), from thin sections (Pachepsky et al., 1996a) and hydraulic conductivity at low water contents (Toledo et al., 1990). Other authors assumed the pore space itself to be fractal and found a reasonable agreement with water retention data (Rawls & Brakensiek, 1995; Pachepsky et al., 1995b; Perrier et al., 1996). Computer tomography images presented fractal pore space structures (Zeng et al., 1996, Rasiah et al., 1998). Macropore and crack sizes have been known to scale according to fractal laws (Brakensiek et al., 1992; Peyton et al., 1994; Preston et al., 1997). Recently, Hatano and Booltink (1998) showed that pathways of solutes in soils as revealed by dye application data were fractal. On a smaller scale, Anderson et al. (1996) simulated the movement of solute particles in pore space digitized from soil thin sections. The pathways of the simulated particles followed a fractal model. Saturated and unsaturated hydraulic conductivities were correctly predicted with models having fractal scaling of pore or solid space as the underlying assumption (Rawls et al., 1993; Shepard, 1993; Crawford, 1994; Fuentes et al., 1996; Rawls & Brakensiek, 1995; Giménez et al., 1997). Recent advances in scaling soil porosity were reviewed by Giménez et al. (1998).

### **Diffusion and Dispersion in Fractal Porous Media**

It has long been known that, when the network of pores is fractal, diffusion by molecular movement in this network differs from the transport in media with properties independent of scale. In particular, diffusion of solutes in a fractal pore network does not obey Fick's law, and anomalous, or non-Fickian diffusion takes place instead (Gefen at al., 1983). When Fick's second law

$$\partial c/\partial t = D \left( \partial^2 c/\partial x^2 \right)$$

is valid, the dependence of concentration on time t and distance x from the source of a solute can be expressed as a function of a single Boltzmann variable  $\lambda$ 

$$\lambda = x/t^{1/2} \tag{1}$$

With anomalous diffusion, the dependence of concentration on time and distance can also be expressed as a function of a single variable  $\zeta$ 

$$\zeta = x/t^n \tag{2}$$

where the exponent n can be both greater than and less than 0.5, depending on the fractal properties of the pore network where the transport occurs (Orbach, 1986). When n > 0.5, the diffusional spreading increases with time faster than Fick's law predicts. If one tries to calculate a diffusion coefficient for Fick's law based on data from different stages of anomalous diffusion with n > 0.5, an increase in the diffusion coefficient will be found as the anomalous diffusion progresses. On the contrary, diffusional spreading that grows slower than Fick's law predicts, may obey the Eq. [2] with n < 0.5. In this case, Fick's diffusion coefficient will decrease with time or distance of spreading.

54 PACHEPSKY ET AL.

Adler (1996) summarized results of theoretical studies of the Taylor dispersion in fractal porous media and numerical experiments with Taylor dispersion of particles in computer-generated porous space. He showed that the anomalous dispersion occurs when the material is fractal over all considered scales. Fickean dispersion was found when the material was homogeneous at the large scale, but contained a fractal microstructure.

To our knowledge, anomalous molecular diffusion has not been observed in soils and porous geologic materials. However, the dispersion of solutes, i.e., diffusion-like deviation of the solute transport from uniform piston flow, has long known to be an increasing function of the distance the solute traveled. Neuman (1990, 1995) summarized results of numerous studies of solute dispersion in saturated geologic materials and found that the solute dispersivity increased with the scale as approximately  $L^{1.5}$  where L is the mean transport scale. Wheatcraft and Tyler (1988) attributed the scale-dependent dispersivities in aquifers to the fractal geometry of the particle paths. Pachepsky et al. (1995a) suggested that the development of hyperdispersive or non-Fickian solute movement in soils can be expected because of the fractal nature of soil pore surfaces. In experiments with soil columns and in field observations, several authors observed an increase in the solute dispersivity as the sampling depth, i.e., mean transport scale, increased (Jaynes et al., 1988; Butters & Jury, 1989; Khan & Jury, 1990; Hamlen & Kachanoski, 1992; Jaynes & Rice, 1993; Porro et al., 1993; Snow et al., 1994; Zhang et al., 1994; Toride et al., 1995; Elsworth et al., 1996).

Transport of water alone in unsaturated soil is more complex than solute diffusion in water saturated media, because the soil water diffusivity depends on soil water content. Soil water transport similar to anomalous diffusion has been observed in horizontal soil columns. Ferguson and Gardner (1963) suggested that the soil water diffusivity may be a function of distance or some other variable as well as water content. Rawlins and Gardner (1963) found that soil water diffusivity should be considered a function either of time or of distance. Guerrini and Swartzendruber (1992) demonstrated that the diffusivity decreased according to a power law of time as time increased. They found a solution of the equation of water transport in unsaturated soil with time-dependent diffusivity. Later these authors suggested that the fractional Brownian motion can be a model for such scale-dependent soil water movement (Guerrini & Swartzendruber, 1994).

Our objectives were to: (i) inspect observations of the scale-dependent water movement and anomalous solute dispersion in soils, and (ii) apply and discuss fractal-based modeling approaches that would accommodate these anomalous transport phenomena.

### **EXPERIMENTAL DATA**

# **Solute Dispersion in Soil**

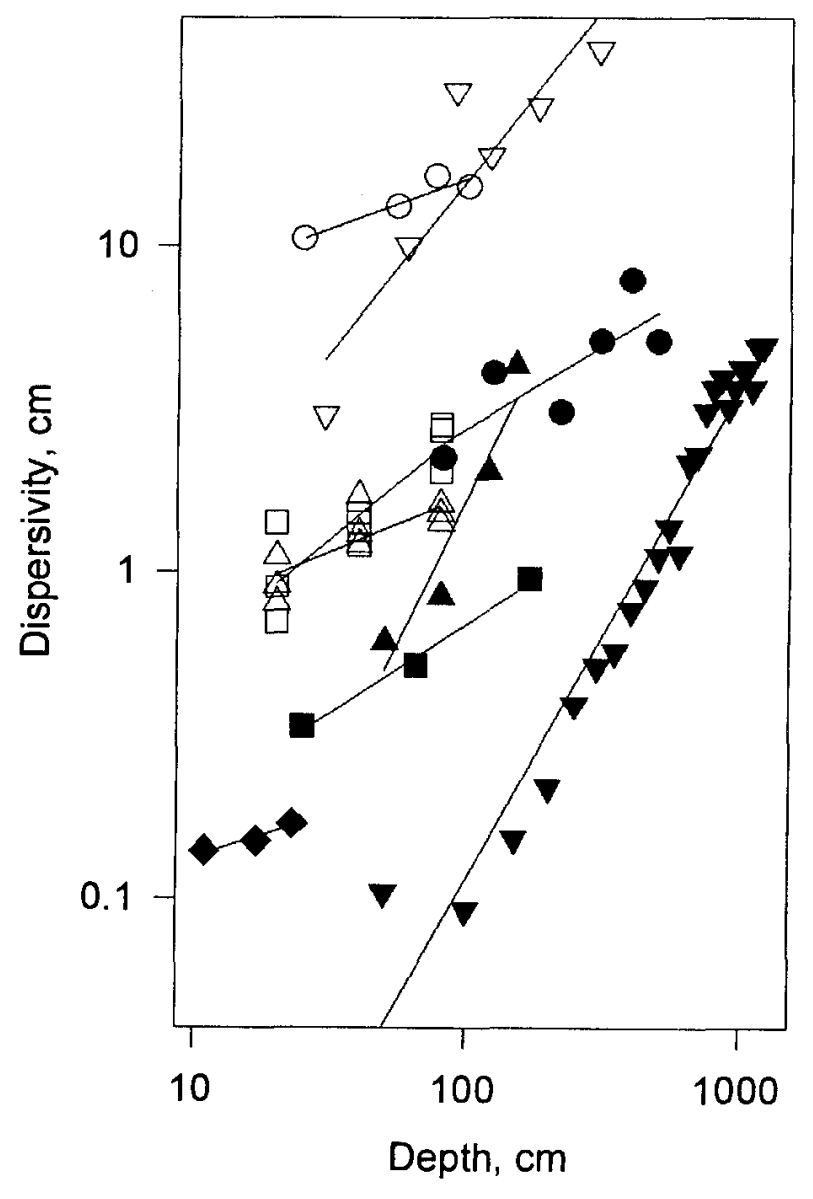
The ADE the was first solute transport model widely and successfully used for soils. For one-dimensional steady state flow of a non-reacting solute in a homogeneous soil layer, the ADE is:

$$(\partial c/\partial t) = D_s (\partial^2 c/\partial x^2) - v (\partial c/\partial x)$$
 [3]

Here c is the solute concentration, [ML<sup>-3</sup>],  $D_s$  is the solute dispersion coefficient, [L<sup>2</sup>T], and v is the average pore-water velocity, [LT<sup>-1</sup>]. This equation describes movement of particles participating in Fickian diffusion-like transport and simultaneously transported with the mean pore velocity.

As the ADE applications accumulated, it became apparent that the ADE might not satisfactorily describe some important features of solute transport in soils. Two phenomena were documented that could result from non-Fickian dispersion. First, the dispersivity defined as the ratio  $D_s/v$  tended to increase as the length of soil column or the soil depth increased (Khan & Jury, 1990; Beven et al., 1993). Second, breakthrough curves of non-reactive solutes had larger tails that those predicted with the ADE, so that the solute appeared sooner and/or was retained in soil longer than the ADE predicted (Van Genuchten & Wierenga, 1976).

Figure 2–1 summarizes published results of column and field experiments in which parameters of Eq. [3] have been estimated from measurements made at sev-



16g. 2. 1. Observed dependencies of the solute dispersivity on depth in soils. Data sources: ●, Porro et al., 1993; ■, Ellsworth et al., 1996; ♠, Yasuda et al., 1994; ▼, Zhang et al., 1994; ♠, Toride et al., 1995; ○, Snow et al., 1994; □, Khan and Jury, 1990; △, Khan and Jury, 1990; ∨, Jury, 1988.

56 PACHEPSKY ET AL.

Table 2–1. Slopes of the log(dispersivity)-log(depth)	dependencies found from field plot and soil col-
umn experiments.	

Data source	Type of the experiment	Maximum depth, cm	Slope	$R^2$
Porro et al., 1993	Column	500	0.513	0.660
Ellsworth et al., 1996	Field plot	170	0.540	0.990
Yasuda et al., 1994	Field plot	150	1.738	0.915
Zhang et al., 1995	Column	1250	1.491	0.948
Toride et al., 1995	Column	24	0.256	0.929
Snow et al., 1995	Field plot	100	0.307	0.875
Khan & Jury, 1990	Column	87	0.683	0.783
Khan & Jury, 1990	Column	87	0.347	0.659
Jury, 1988	Field plot	300	1.069	0.828

eral depths in soil profiles or soil columns. Porro et al. (1993) used a 5-m long soil column, and tritium as a tracer. Elsworth et al. (1996) reported results of a field plot study in which solutes were extracted at 25- and 65-cm depths during an unsaturated steady-state flow experiment, and the plot was excavated to 2-m depth after the experiment. Yasuda et al. (1994) described a field plot experiment in which solute samples were taken at five 0.3- to 1.5-m depths during a ponded infiltration experiment. Zhang et al. (1994) worked with 1250-cm long horizontal sandy soil column and collected electrical conductivity data at 50-cm increments along the column during the steady state saturated flow experiment with NaCl as a tracer. Toride et al. (1995) reported results of Shiozawa who used four-electrode sensors to measure NaCl concentrations at depths of 11, 17, and 23 cm in sand columns with saturated and unsaturated flow. Snow et al. (1994) sampled bromide solution at four depths from a 1-m long lysimeter with a layered soil that was sprinkler-irrigated for 60 d. Khan and Jury (1990) applied pulses of CaCl<sub>2</sub> solution to Tijunga loamy sand soil (mixed, thermic, Typic Xeropsamments) columns 20, 40, and 80 cm long with three different flow rates. Jury (1988) summarized field study in which a plot was irrigated every second day after application of KCl. Tracer and solute concentrations were monitored at depths from 0.3 to 3 m.

Plots of the dispersivity found by application of the ADE to these experiments (Fig. 2–1) show that the dispersivity can be considered as a power function of the mean distance traveled by the solute. Table 2–1 lists the slopes of regression lines in Fig. 2–1. The slopes vary widely, from small values of 0.2 to a relatively large value of 1.7.

Other publications also imply that the authors have encountered an increase of the dispersivity with depth. For example, Jaynes et al. (1988) in a field plot experiment and Wierenga and van Genuchten (1989) in a column experiment observed the increase of the dispersion coefficient with the depth while the velocity decreased.

Some authors did not find a tangible dependence between the dispersivity and depth. For example, Khan and Jury (1990) observed an increase of the dispersivity with depth in undisturbed soil columns but not in columns with repacked soil. Toride et al. (1995) reported an increase in dispersivity with depth in unsaturated sand columns but not in the saturated sand columns. These findings suggest that natural soil structure and the structure of the water-filled space in unsaturated soils lead to anomalous solute dispersion.

The ADE predicts an ideal sigmoidal shape for breakthrough curves (BTC) from soil columns that are sufficiently long. Van Genuchten and Wierenga (1976) pointed out the deviations from this shape in experimental breakthrough curves. They used the term "tail" to describe the last part of nonsigmoidal breakthrough curve that approaches its asymptotic value. Heavy tails of BTC, that is approaching the asymptotic value much slower than Eq. [3] predicts, were observed by a number of authors (e. g., Nielsen et al.; 1986, Vachaud et al., 1990, p. 81–104).

Both depth-dependent dispersivity and heavy tails on breakthrough curves indicate that anomalous dispersion takes place in soils, and that the deviations from ideal Fickian dispersion may be specific to soil structure and degree of saturation.

# **Water Transport in Horizontal Soil Columns**

For one-dimensional horizontal water movement in homogeneous soil, Richards' equation reduces to

$$\frac{\partial \theta}{\partial t} = \frac{\partial}{\partial x} \left( D \mathbf{w} \left( \theta \right) \frac{\partial \theta}{\partial x} \right)$$
 [4]

Here  $\theta$  is the volumetric water content,  $D_{\rm w}$  is the soil water diffusivity, [L<sup>2</sup>T<sup>-1</sup>]. This equation, with boundary and initial conditions

$$\theta = \theta_b, \quad x = 0, \quad t \ge 0$$
  
$$\theta = \theta_i, \quad x > 0, \quad t = 0$$
 [5]

provides the scaling law (Eq. [1]) in which the Boltzmann variable  $\lambda$  is a function of the volumetric water content  $\theta$  only (Philip, 1955). In (Eq. [5]),  $\theta_i$  and  $\theta_b$  are the initial volumetric water content, and the water content on the boundary x = 0, respectively.

A series of experiments with horizontal water flow showed that this equation may not adequately describe water transport so that value of  $\lambda = x/t^{1/2}$  calculated for the same water content at different depths and/or at different times does not remain constant. Figure 2–2 summarizes published results of some experiments on water transport in horizontal soil columns. The companion Table 2–2 contains legends for the graphs. Nielsen et al. (1962) studied transport of water and oil in soil. Airdry soil was packed in columns. A negative pressure was held constant at one end of each column. The largest distance where the wetting front was observed was 50 cm. Positions of the wetting front were measured visually. Figure 2–2a shows the dependence of  $\lambda$  obtained for the wetting front on the distance of the wetting front from the inlet. Rawlins and Gardner (1963) studied movement of water in horizontal soil columns using gamma ray attenuation. The largest distance where the water content was measured was 40 cm. Figure 2–2b shows dependencies of  $\lambda$  on distance from inlet for various water contents! Ferguson and Gardner (1963) studied

<sup>&</sup>lt;sup>1</sup> The method of calculating values of  $\lambda$  for this and following datasets is given in Pachepsky and Fimlin (1998).

AN PACHEPSKY ET AL.

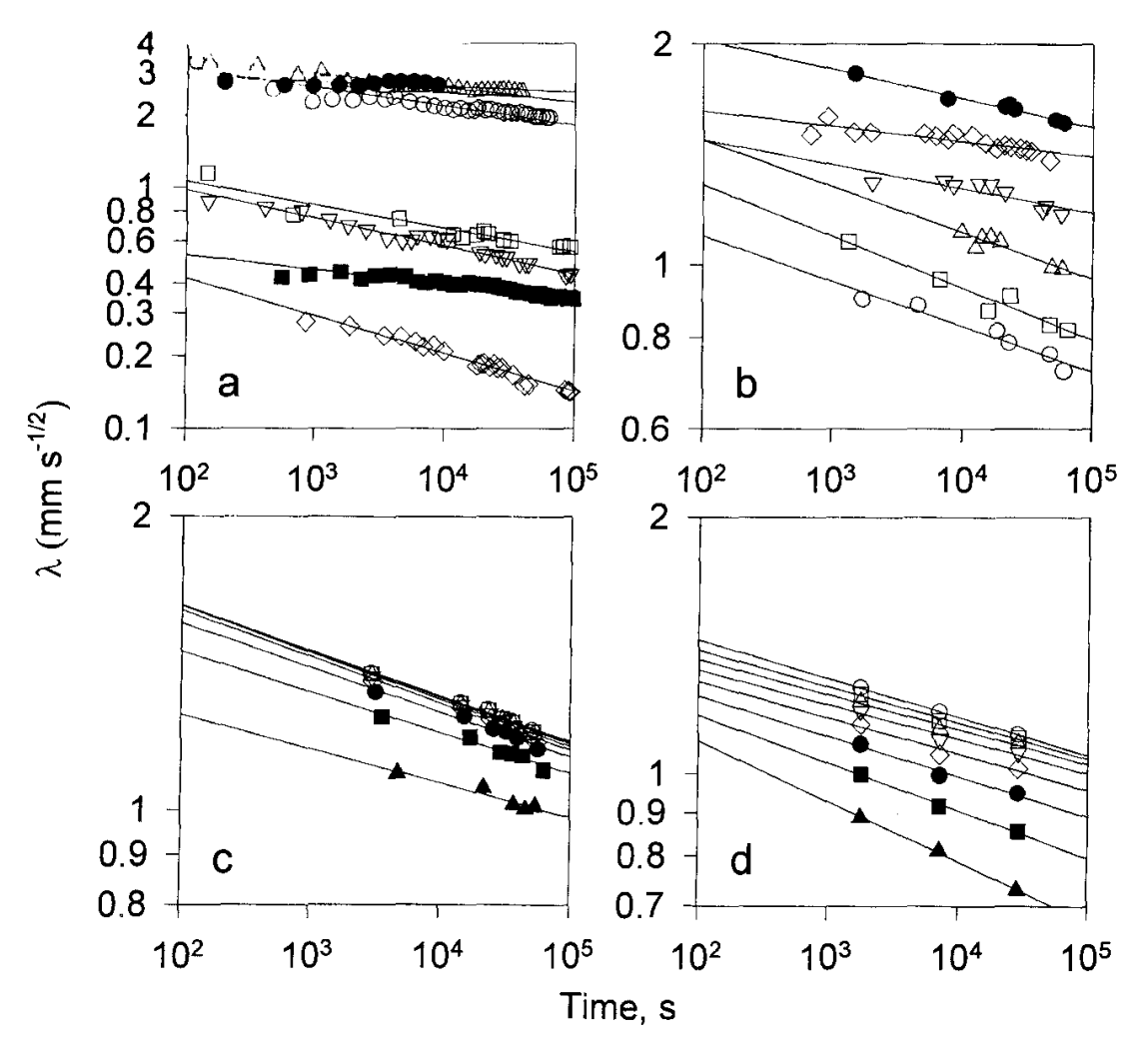


Fig. 2–2. Observed dependencies of the Boltzman variable on time in experiments with horizontal water movement in unsaturated soil columns. Experiments: (a) Nielsen et al. (1962); (b) Rawlins and Gardner (1963); (c) Ferguson and Gardner (1963); and (d) Smiles et al. (1978) (see Table 2–2 for the legend).

movement of water in air dry soil using gamma ray attenuation. The largest distance where the water content was measured was 27.5 cm. They presented dependencies of water content on time for several distances from the inlet. Values of  $\lambda$  for several water contents are shown in Fig. 2–2c. Smiles et al. (1978) studied movement of water and solutes in sand-kaolinite mixtures. The largest observation distance was 22 cm. Figure 2–2d depicts the dependencies of  $\lambda$  on distance from the inlet for the experiment with water in this study.

The remarkable feature of the graphs in Fig. 2–2 is that values of  $\lambda$  did not remain constant as the experiments progressed. Therefore, Eq. [4] was violated. Graphs in Fig. 2–2 are in log-log scale. Points corresponding to the same water content are on straight lines. This means that the scaling law Eq. [2] rather than Eq. [1] was applicable in these experiments. Indeed, if straight lines in the graphs have equations  $\log \lambda = \log \zeta - b \log t$ , and, by definition,  $\log \lambda = \log x - 0.5 \log t$ , then  $\log \zeta = \log x - (0.5-b) \log t$ . Equating 0.5-b to n, we arrive at the scaling law given by Eq. [2]. Table 2–2 contains values of n for the experiments shown in Fig. 2–2. Differences between n and 0.5 are statistically significant.

Table 2–2. Values of parameter n found from data on horizontal movement of water in soil columns.

Data source	n (mean ±	
Soil	standard error)	Graph
Nielsen et al., 1962		
Columbia silt loam† wet at -50 mb	$0.402 \pm 0.003$	Fig. 2–2a ○
Columbia silt loam wet at -100 mb	$0.425 \pm 0.006$	Fig. 2–2a □
Columbia silt loam wet with oil at -2 mb	$0.480 \pm 0.008$	Fig. 2–2a •
Columbia silt loam wet with oil at -38 mb	$0.440 \pm 0.003$	Fig. 2–2a ■
Hesperia sandy loam‡ at −2 mb	$0.440 \pm 0.004$	Fig. 22a △
Hesperia sandy loam at -50 mb	$0.384 \pm 0.002$	Fig. 2–2a ▽
Hesperia sandy loam wet at -100 mb	$0.344 \pm 0.003$	Fig. 2–2a ♦
Rawlins & Gardner, 1963		
Salkum silty clay loam, $\theta = 0.51$	$0.439 \pm 0.007$	Fig. 2–2b ○
Salkum silty clay loam§, $\theta = 0.50$	$0.430 \pm 0.008$	Fig. 2–2b □
Salkum silty clay loam, $\theta = 0.48$	$0.437 \pm 0.011$	Fig. 2–2b △
Salkum silty clay loam, $\theta = 0.45$	$0.467 \pm 0.009$	Fig. 2–2b ∇
Salkum silty clay loam, $\theta = 0.40$	$0.479 \pm 0.003$	Fig. 2–2b ◊
Salkum silty clay loam, $\theta = 0.05$	$0.461 \pm 0.002$	Fig. 2–2b ●
Ferguson & Gardner, 1963		
Salkum silty clay loam, $\theta = 0.05$	$0.454 \pm 0.002$	Fig. 2–2c ○
Salkum silty clay loam, $\theta = 0.10$	$0.453 \pm 0.002$	Fig. 2–2c □
Salkum silty clay loam, $\theta = 0.15$	$0.452 \pm 0.003$	Fig. 22c △
Salkum silty clay loam, $\theta = 0.20$	$0.452 \pm 0.003$	Fig. 2–2c ∇
Salkum silty clay loam, $\theta = 0.25$	$0.452 \pm 0.003$	Fig. 2–2c ♦
Salkum silty clay loam, $\theta = 0.30$	$0.454 \pm 0.003$	Fig. 2–2c •
Salkum silty clay loam, $\theta = 0.35$	$0.458 \pm 0.004$	Fig. 2–2c ■
Salkum silty clay loam, $\theta = 0.40$	$0.465 \pm 0.006$	Fig. 2–2c ▲
Smiles et al., 1978		
Kaoline-sand mixture, $\theta = 0.06$	$0.455 \pm 0.001$	Fig. 2–2d ○
Kaoline-sand mixture, $\theta = 0.08$	$0.458 \pm 0.005$	Fig. 2–2d □
Kaoline-sand mixture, $\theta = 0.10$	$0.459 \pm 0.007$	Fig. 2–2d △
Kaoline-sand mixture, $\theta = 0.12$	$0.459 \pm 0.009$	Fig. 2–2d ∇
Kaoline-sand mixture, $\theta = 0.14$	$0.457 \pm 0.009$	Fig. 2–2d ◊
Kaoline-sand mixture, $\theta = 0.16$	$0.453 \pm 0.007$	Fig. 2–2d •
Kaoline-sand mixture, $\theta = 0.18$	$0.444 \pm 0.004$	Fig. 2–2d <b>■</b>
Kaoline-sand mixture, $\theta = 0.20$	$0.429 \pm 0.003$	Fig. 2–2d ▲

<sup>†</sup> Mixed thermic Xerofluvent.

Some authors did not find statistically significant differences between estimated value of n and 0.5 (Whisler et al., 1968; Selim et al., 1970). It was suggested that the deviations from Boltzmann scaling in horizontal water movement may be related to changes in bulk density (Guerrini & Swartzendruber, 1992) or to changes in wetting front water content with time (Selim et al., 1970). An alternative interpretation explains these deviations by discontinuities in water transport in porous media (Nielsen et al., 1962).

Distance-dependent diffusivity of water indicates that phenomena similar to anomalous diffusion take place in soils, although the deviations from ideal transport predicted by Eq. [3] may be specific to soil structure.

<sup>‡</sup> Mixed thermic Torriorthent.

<sup>§</sup> Kaolinitic mesic Palehumult.

# MODELING ANOMALOUS TRANSPORT OF WATER AND SOLUTES IN SOILS

# **Empirical Approach**

The simplest, purely empirical approach consists in an explicit incorporation of the changes in the dispersivity and the diffusivity coefficients in transport Eq. [3] and [4]. Jury and Roth (1990) suggested that a linear dependence of the dispersion coefficient  $D_s$  on the depth could be included in the ADE. Zhang et al. (1994) found this approach satisfactory for simulation of their depth-dependent dispersivity in the column of 12.5 m length. Guerrini and Swartzendruber (1992) proposed to treat water diffusivity as a time-dependent function,  $D = E(\theta)t^{2n-l}$  where n is the same as in Eq. [2]. Pachepsky and Timlin (1998) evaluated the water diffusivity as a product of a local function  $G(\theta)$  and a scaling function taken as a power function  $x^{-\beta}$  of the distance from the inlet:  $D_w = G(\theta)x^{-\beta}$ . Although the empirical approach can reproduce scaling properties of the dispersivity and diffusivity as shown in Fig. 2–1 and 2–2, it lacks a physical basis and is dimensionally incorrect. Further, this technique is applicable only to unidirectional transport, and a change in the direction of the water flux makes the technique useless.

# **Volumetric or Statistical Averaging**

It is a popular approach to treat scale effects on the solute dispersivity. The stochastic convection model assumes that soil can be represented with a set of streamtubes with lognormal distribution of the velocities (Jury & Roth, 1990). The variance of solute concentration estimated with this model grows with the square of the total infiltration, which is a surrogate for time as the flow progresses (Roth et al., 1991). Adding Taylor dispersion (mixing between the tubes) transforms this model into the stochastic ADE. The latter has a variance that grows linearly with time and yields the Boltzmann scaling given by Eq. [1]. Ward et al. (1995) used 50 soil columns of 15-cm i.d. and were able to show that the ensemble of the columns represented satisfactorily the solute transport over the 65-m<sup>2</sup> field plot. A log-normal distribution is often used for infiltration rates and hydraulic conductivities, so the model grasps some essential physical features of unidimensional solute transport in soil. The two scales of this model, i.e., the microscale of an individual tube and the macroscale of averaging, are not defined clearly. In experiments of Khan and Jury (1990), columns of the same soil having different widths exhibited different dependencies of the solute dispersivity on the column length. In experiments of Parker and Albrecht (1987), soil columns differed in both length and width. The solute dispersivity scaled as the (column length)<sup>2,3</sup>. The exponent 2.3 is much larger than in any of experiments shown in Fig. 2–1 (see Table 2–1). A definition of the micro- and macro-scales, as well as recommendations how to treat intermediate scales, seems to be needed to consider parameters of the stochastic model for particular soil. The model remains unidirectional, and to our knowledge, was never tested for evaporation regimes.

### **Mobile-Immobile Zone Models**

The physical reason for the scale dependence of solute transport parameters is the heterogeneity of soil. It is established in subsurface hydrology that the scale dependence of the dispersivity arises from the way in which an individual solute particle will gradually sample more and more of the velocity fluctuations associated with the heterogeneity of aquifer (Mishra & Parker, 1990; Beven et al., 1993). Differences in solute transport mobilities among different parts of soil pore space have long been recognized. Van Genuchten and Wierenga (1976) developed the first model that explicitly described the variations in solute mobility and divided soil pore space into two zones—mobile and immobile. This MIM (mobile-immobile) model was remarkably successful in describing column experiments and explaining tails on breakthrough curves. Moreover, where the ADE required the depth-dependent dispersivity to simulate the solute transport in soil profile, the MIM model worked with a constant (or, at least, not depth-dependent) dispersivity. Although successful attempts were made to relate parameters of this model to measurable soil properties such as aggregate size (Rao et al., 1980, Montas et al., 1997), in general the parameters, i.e., dispersivity, retardation factor, proportion of the immobile zone in total porosity, and the mass exchange rate between the two zones, are viewed as empirical ones. Determining parameters of this model is a nontrivial task because the parameters appear to be strongly correlated (Beven et al., 1993; Koch & Flühler, 1993; Bronswijk et al., 1995; Montas et al., 1997). The MIM model seems to over-parameterize the solute transport, although it represents the actual distribution of the flow velocities in soil in a piecewise fashion with only two modes: zero and nonzero mean. Introducing more intervals is possible and has been explored by several research groups (Steenhuis et al., 1990; Gwo et al., 1995; Haggerty & Gorelick, 1995; Hutson & Wagenet, 1995). However, as more regions are used, correlation among parameters increases, and it is more difficult to estimate parameters reliably.

#### **Fractal Motion of Particles**

Statistical physics has been successfully used to derive both Richards' equation (Bhatacharrya et al., 1976) and the ADE (Bhatacharya & Gupta, 1990). In both derivations, the authors assumed that solute particles undergo Brownian motion, which is an addition of successive movements that are independent and identically distributed Normal random variables with variance that scales linearly with time. This is a viable assumption provided that the variance is finite, and the total transport length is very large compared to individual movement lengths. The latter may be dependent on correlation length of heterogeneities in the medium.

The movement of solute particles in soils does not generally follow Brownian motion because soil at any scale consists of correlated units. A particle traveling faster than the mean at some instant is likely to still be traveling faster than the mean some later time (Benson, 1998). One may say that particles have a "memory", and the memory of particles is the critical feature required for the occurrence of non-Fickian diffusion (Kinzelbach, 1987). Further, the underlying distribution

of velocity may have infinite variance (Benson et al., 1999) that preclude using Brownian movement model. Guerrini and Swartsendruber (1994) proposed to treat the observed water transport in soils as an integral result of fractal movement of individual particles. Flury and Flühler (1995) simulated solute transport in soils as a diffusion-limited aggregation that is known to obey fractal scaling. These models satisfactorily represent observations of scale dependence in transport.

When particle movements are spatially fractal (e.g., Hughes et al., 1981), they may be described by so-called Lévy motions rather than Brownian motions. A useful analogy here is the dispersion in chaotic flow (Klafter et al., 1987). In these flows, a particle tends to spend long periods of time trapped in vortices that are essentially stagnant with respect to mean flow. A particle can occasionally escape and travel with high velocity between vortices. The relatively rare, high velocity events represent particle excursion probabilities that are more heavy-tailed than the Gaussian distribution. The motion increments have Lévy distributions rather than Gaussian distributions.

Lévy distributions were found to be useful in the description of random physical processes that are characterized by extreme behavior called the "Noah effect" by Mandelbrot and Wallis (1968). The family of Lévy distributions is parameterized with the value  $\alpha$  specifying, in particular, the "weight" in tails of the distribution. The heavier the tail is, the higher is the probability of large deviations from average. The Gaussian distribution is a special case of a Lévy distribution that has  $\alpha = 2$ . Figure 2–3 shows several probability distribution functions from the Lévy family. As the parameter  $\alpha$  decreases from 2, Lévy distributions differ more and more from the Gaussian distribution, and the tails of the distributions become heavier (Fig. 2–3a). The tails of Lévy probability density functions can approach zero much more slowly than the tails of the Gaussian density. As the argument x becomes large, the Gaussian distribution tail decreases exponentially, while the tails of the symmetrical Lévy density follow the power law  $f(x) \approx cx^{-1-\alpha}$ . Lévy statistics have been useful in description of fractal scaling in soils and in aquifers (Painter, 1996; Pachepsky et al., 1997; Liu & Molz, 1997; Benson et al, 1999).

# Fractional Convective-Advective Equation

A differential solute transport equation derived for Lévy motions would facilitate solute transport studies in the same way that the ADE facilitated applications of the Brownian motion model. Recently, Zaslavsky (1994) suggested a procedure to derive such an equation using fractional derivatives that in effect account for the "memory" of solute particles. Zaichev and Zaslavsky (1997), Benson (1998), and Chaves (1998) modified Zaslavsky's procedure to account properly for mathematical properties of fractional derivatives in the one-dimensional case. The simplest form of the one-dimensional equation assumes symmetrical dispersion:

$$\frac{\partial c}{\partial t} = -v \frac{\partial c}{\partial x} + \frac{1}{2} D_{\rm sf} \left( \frac{\partial^{\alpha} c}{\partial x^{\alpha}} + \frac{\partial^{\alpha} c}{\partial (-x)^{\alpha}} \right)$$
 [6]

Here  $D_{\rm sf}$  [L $^{\alpha}$ T $^{-1}$ ] is the fractional dispersion coefficient. The superscript  $\alpha$  is the order of fractional differentiation,  $0 < \alpha \le 2$ , corresponding to the parameter of dis-

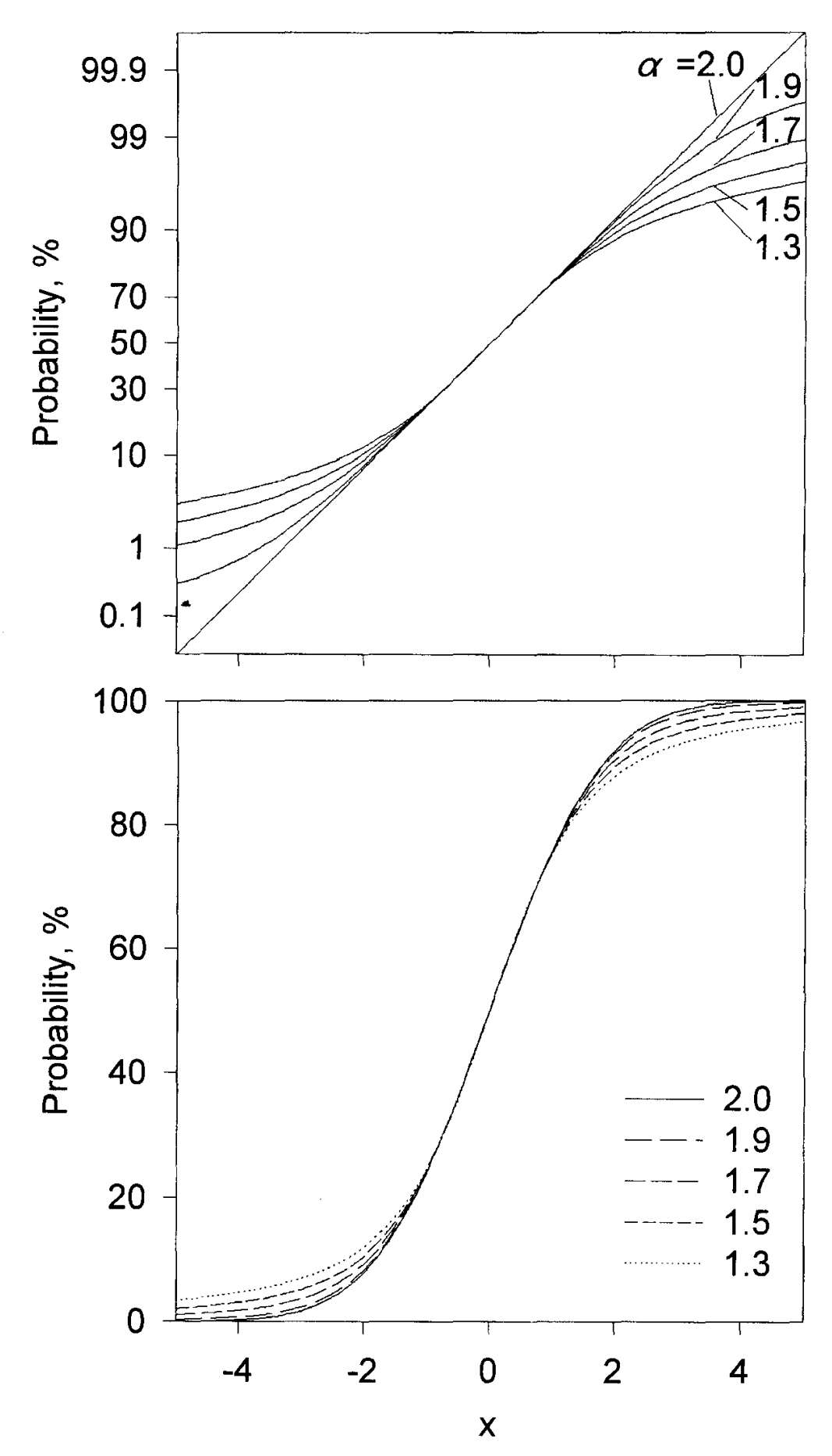


Fig. 2–3. Probability distribution functions for symmetric Levy distributions with (a) linear scaling and (b) probability scaling. The curves differ in values of the distribution parameter  $\alpha$ .

tributions shown in Fig. 2–3. Fractional derivatives are integro-differential operators defined as (Samko et al., 1993):

$$\frac{\partial^{\alpha} c(x,t)}{\partial x^{\alpha}} = \frac{1}{\Gamma(m-a)} \frac{\partial^{m}}{\partial x^{m}} \int_{-\infty}^{x} (x-\xi)^{m-\alpha-1} c(\xi,t) d\xi$$
 [7]

and

$$\frac{\partial^{\alpha} c(x,t)}{\partial (-x)^{\alpha}} = \frac{(-1)^{m}}{\Gamma(m-\alpha)} \frac{\partial^{m}}{\partial x^{m}} \int_{x}^{\infty} (\xi - x)^{m-\alpha-1} c(\xi,t) d\xi$$
 [8]

Here  $\alpha$  is the order of the fractional derivative,  $\alpha > -1$ ,  $\Gamma()$  is the Gamma function, and m is the smallest integer larger than  $\alpha$ . If the value of  $\alpha$  is actually an integer, then fractional derivatives reduce to well-known ordinary derivatives. For example, when  $\alpha = 2$ , the right-hand side expressions in Eq. [7] and [8] will reduce to usual second derivatives. Then Eq. [6] will reduce to the common ADE given in Eq. [3]. This is expected since the Lévy distribution with  $\alpha = 2$  is the Gaussian distribution, and the particles move according to Brownian motion. We use the term FADE (Fractional Advective-dispersive Equation) for Eq. [6], noting that only the dispersion term is fractional. Benson (1998) has shown that the concentration breakthrough curves obey the scaling law Eq. [2] with the exponent  $n = \alpha^{-1}$ . Since  $\alpha \le 2$ , anomalous dispersion can be expected, and the dispersive spreading will increase with time faster than Fick's law predicts. We note, for completeness, that the FADE has been extended to three-dimensional transport, and nonsymmetrical dispersion (Meerschaert et al., 1999)

Equation [6] has analytical solutions, one of which is presented in the Appendix. It can be also solved numerically using finite differences (Benson, 1998). An example of the application of the analytical solutions of the FADE to describe solute transport is given in Fig. 2–4 that contains data on chloride transport in unsaturated sand reported by Toride et al. (1995). Measured and breakthrough curves and their fit with the ADE and the FADE at 11-, 17-, and 23-cm depths are shown. Parameters of the ADE and the FADE were optimized using a modified Marquardt-Levenberg algorithm<sup>2</sup>. Values of parameters and their standard errors are given in Table 2–3.

It can be seen from Table 2–3 that while the ADE requires an increasing dispersivity with depth to simulate the data correctly, the FADE simulates the data with a dispersion coefficient and an order of the fractional derivative ( $\alpha \approx 1.62$ ) that are not statistically different for all depths. Besides, although both the ADE and the FADE capture the shapes of breakthrough curves, inspection of the graphs shows that the FADE simulates the breakthrough curves in unsaturated sand better. Statistics of the model performance shown in Table 2–3 support this observation. The root-mean-square errors are markedly lower for the FADE than for the ADE.

The null hypothesis that both models perform equally well was tested by comparing the mean square lack-of-fit values (Whitmore, 1991):

<sup>&</sup>lt;sup>2</sup> The code is available from the corresponding author upon request.

$$s_{\rm r}^2 = \frac{\sum_{i=1}^{i=N} (c_{i,\rm calc} - c_{i,\rm meas})^2}{N - P}$$

Here N is the number of measurements, P is the number of parameters of the model, and  $c_{i,\text{meas}}$  and  $c_{i,\text{calc}}$  are measured and calculated solute concentrations for the ith observation, respectively. The presence of the number of parameters in the denominator makes the mean square lack-of-fit to be an unbiased estimator of the model's standard error (Whitmore, 1991). To test the null hypothesis, one has to compare the R-ratio of the mean of lack-of fit squares  $F = s_{r,\text{ADE}}^2/s_{r,\text{FADE}}^2$  to the critical value of the Fisher's statistic  $F_{n-P_{\text{ADE}},\,N-P_{\text{FADE}}}$ , where  $P_{\text{ADE}} = 2$ , and  $P_{\text{FADE}} = 3$ . The null hypothesis can be rejected if  $F > F_{n-P_{\text{ADE}},\,N-P_{\text{FADE}}}$ . Data in Table 2–3 show that the F ratio exceeds the critical value taken at the 0.05 significance level, so that the FADE performs better.

Another set of data to compare the performance of the ADE and the FADE was taken from the paper of Dyson and White (1987) who studied Cl<sup>-</sup> transport in structured clay soil (calcareous pelosol) irrigated under a range of constant flow rates from 0.28 cm h<sup>-1</sup> to 2.75 cm h<sup>-1</sup>. Soil cores of  $16.4 \pm 1.5$  cm length were irrigated to maintain unsaturated (0.60 cm<sup>3</sup> cm<sup>-3</sup>)water contents in the soil columns. The sat-

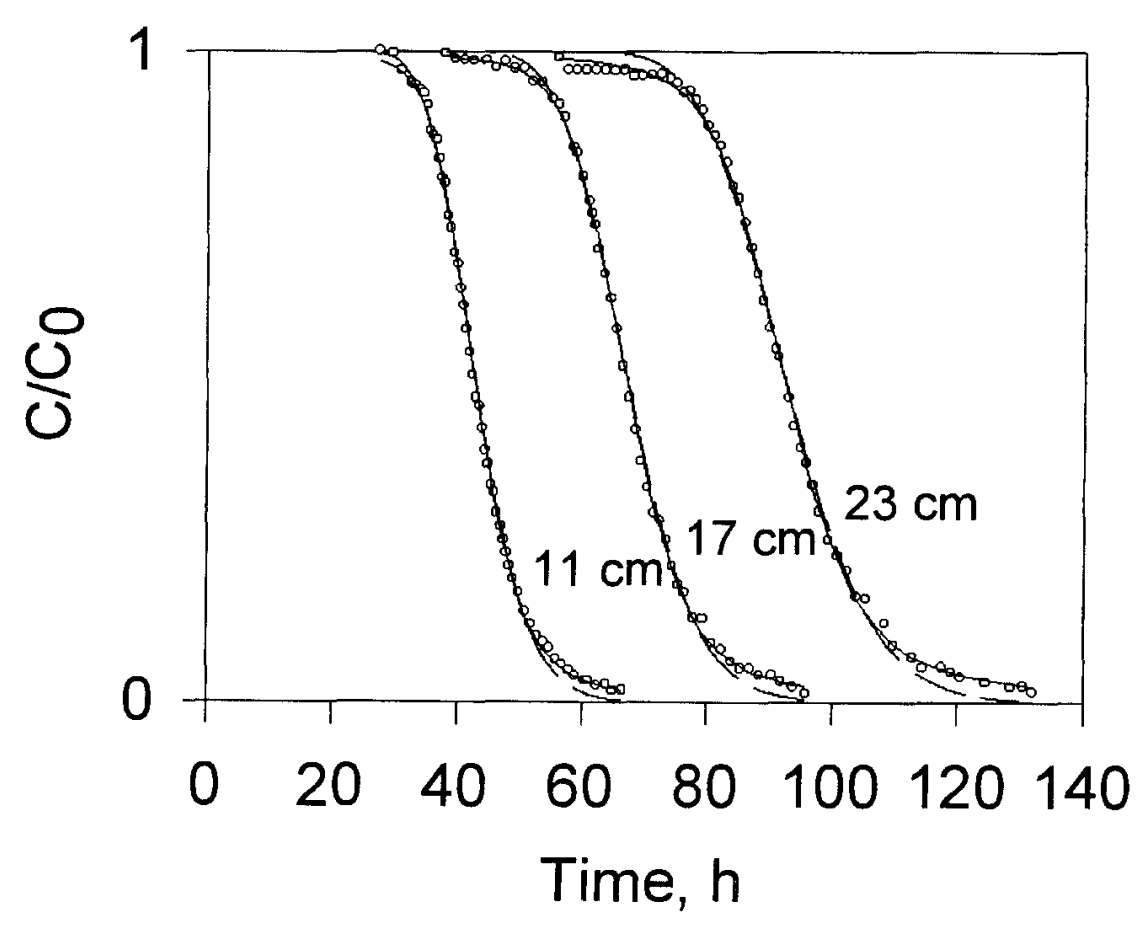


Fig. 2-4. Comparison of measured (•) and calculated with FADE (—) and with ADE (—) chloride breakthrough curves from unsaturated sand columns. Measured values are from Toride et al. (1995).

Table 2-3. Estimated parameters and performance statistics for the advective-dispersive equation (ADE) and fractional advective dispersive equation (FADE) applied to data on Cl<sup>-</sup> breakthrough curves from sand and soil columns.

Data source, soil	Experiment	Length,	Number of points	ADE Parameters		FADE					
							Parameters				
				$D, \text{cm}^2 \text{h}^{-1}$	v, cm h <sup>-1</sup>	RMSE	α	D	v, cm h <sup>-1</sup>	RMSE	<i>F</i> ‡
Toride et al., 1995, sand	Unsaturated	11	52	0.0352 (0.0008)†	0.258 (0.0003)	0.013	1.683 (0.0358)	0.0305 (0.0007)	0.258 (0.0002)	0.0087	2.16 <1.8>
	Unsaturated	17	47	0.0389 (0.0011)	0.254 (0.0003)	0.015	1.615 (0.0294)	0.0291 (0.0008)	0.255 (0.0002)	0.0076	3.79 <1.8>
	Unsaturated	23	53	0.0424 (0.0015)	0.249 (0.0003)	0.019	1.574 (0.0318)	0.0282	0.250 (0.0002)	0.0094	3.96 <1.8>
Dyson & White, 1987, clay soil	$q = 0.28 \text{ cm h}^{-1}$	16.4	22	2.818 (0.147)	0.734 (0.0082)	0.018	1.642 (0.051)	1.209 (0.150)	0.756 (0.0054)	0.0096	3.40 <2.4>
	$q = 2.75 \text{ cm h}^{-1}$	16.4	22	108.3 (7.7)	12.54 (0.26)	0.023	1.696 (0.076)	44.69 (10.03)	12.89 (0.23)	0.0179	1.61 <2.4>

Standard errors of parameters estimates are in parentheses.
 F ratios are calculated as the ratios of square lacks-of-fit F = s<sub>rADE</sub><sup>2</sup>/s<sub>rFADE</sub><sup>2</sup>. The square lack-of-fit s<sub>r</sub> = RMSE<sup>2</sup>[N/(N-P)]<sup>0.5</sup> where N is the number of experimental points, P is the number of fitting parameters in a model, P = 2 in the ADE and P = 3 in the FADE. Critical F values are in angular brackets.

urated water content was estimated to be  $0.67~\rm cm^3~cm^{-3}$ . The model performance statistics F shown in Table 2–3 suggest better performance by the FADE as compared with that of the ADE for the low flow rate experiment with  $q = 0.28~\rm cm~h^{-1}$ . The value of F appears to be less than critical in the high flow rate experiment, so that the hypothesis of similarity in performance between the FADE and the ADE cannot be rejected. Estimated values of the parameter  $\alpha$  do not differ significantly for the two flow rates.

The advantage of using the FADE to describe solute transport in soils is the separation of the scale effect from the values of the transport coefficients. The scale effects are reflected by the order of the fractional derivative, and the transport coefficients need to be found at only one scale.

## **Fractional Equation of Water Transport**

It is also possible (at least, in a formal way) to apply a fractional version of Richards' equation to simulate one-dimensional water transport in horizontal columns. We were able to fit the FADE to data on horizontal water infiltration (data not shown). However, the parameter  $\alpha$  had to be set to values greater than two to fit the experimental data. This range of  $\alpha$  is theoretically unjustified (Benson et al., 1999; Meerschaert et al., 1999). This example serves as a reminder about the danger of drawing analogies between water and solute transport in soils, since the underlying physical processes are different. "Particles" of soil water moving faster than others are affected by the structure of pore surfaces and move in films rather than in bulk volume by convection. One possible way to model the water transport is to use the diffusivity model proposed by Jumarie (1992):

$$\frac{\partial^{\gamma \theta}}{\partial t^{\gamma}} = \frac{\partial}{\partial x} D(\theta) \frac{\partial \theta}{\partial x}$$
 [13]

where  $\gamma \le 1$  and  $D(\theta)$  has units  $L^2 T^{-\gamma}$ . Such a fractional-in-time equation may also have as an underlying physical basis the model of moving particles that are randomly trapped for extended periods of time (Klafter et al., 1987). However, there is an important difference between particle motions resulting in Eq. [13] and in Eq. [6]. Equation [13] presumes Levy walks, i.e., coupling probabilities of the traveling time and traveling distance. Equation [6] does not presume coupled distributions, and the spatial step has not to have a Gaussian or a Levy distribution. However, waiting periods of particles time have to have a power law distribution (Hilfer & Anton, 1995), and a fractional-in-time equation accounts for hierarchical scaling within the time intervals rather than spatial scaling (Jumarie, 1992). The occurrence of rare large movements of the wetting front in unsaturated horizontal columns was documented by Nielsen et al. (1962) who called them "jerky movements". Zaichev and Zaslavsky (1997) indicated that Eq. [13] may, under appropriate conditions, describe fractional Brownian motion. This concurs with the hypothesis of Guerrini and Swartzendruber (1994) about the applicability of the fractional Brownian movement model to horizontal water transport in unsaturated soils.

#### **DISCUSSION AND CONCLUSION**

Observations of anomalous solute dispersion and water diffusivity in soils correspond well to theoretical predictions of the anomalous mass transport in fractal media and accumulated evidence of the fractal nature of soil structure. The spatial arrangement of particles in soils has been successfully described using mass, volume, and surface fractal dimensions. These dimensions, however, may not be relevant for estimating anomalous transport in soils. The extent to which this transport manifests itself must be related to scaling of pore connectivity, which does not have a direct relationship with mass or volume fractal dimensions. Lemaitre and Adler (1990) studied saturated viscous flows through two Menger sponges with similar fractal dimensions and found quite different water transport properties in these sponges. To estimate soil hydraulic conductivity, Crawford (1994) has suggested the use of both mass fractal dimension and the spectral dimension. One method of estimating the spectral dimension was recently suggested by Anderson et al. (1996). It remains to be seen whether this dimension is a good indicator of anomalous transport. Further, estimation of a fractal dimension is only a piece of the puzzle, since the existence of a power law scaling does not imply applicability of a single fractal model. Power law scaling can be usually interpreted using several different fractal and non-fractal models, and the choice of a model depends on a hypothesis about a process causing the observed scaling (Pachepsky et al., 1997). In a purely mathematical example, it is well known that the traces of a fractional Brownian motion (fBm) and a Lévy motion (Lm) may have the same fractal dimension, but the fBm process has Gaussian increments, while Lm has infinite variance. The two traces could be mistaken for each other even visually (Mandelbrot, 1983; Samorodnitsky & Taggu, 1994). Huang and Bradford (1992) give an excellent example of applicability of two different fractal models to simulate the soil surface roughness. It remains to be seen whether the scaling parameters of transport processes can be related to some physical properties of soils that should underlie the occurrence of the fractal scaling because of evidence of fractal geometry of pore space and the space occupied by soil particles.

Diffusion and dispersion in some ideal and computer-simulated fractal porous media demonstrates deviations from the ideal Fick's diffusion (i.e., Grindrod & Impey, 1993, Adler, 1996). However, this does not mean that diffusion and dispersion will necessarily be anomalous in natural porous media, soils among them, that exhibit the fractal scaling only over a range of scales. As the introductory section of this paper shows, fractal scaling of many properties is found in soils. This implies, in particular, that the dispersion may be anomalous, and indeed data in Fig. 2–1 show that this is often true in unsaturated soils. The dispersion in saturated soil has been routinely found to be Fickian and the ADE was a good model. The range of scales as measured by pore radii is much wider in saturated than in unsaturated soils. This situation is similar to the one studied by Salles et al. (1993) who simulated solute transport in a medium characterized by a double structure, i.e., spatially periodic at large scale and fractal at the small scale. The simulations of Salles et al. (1993) showed that in such structures the ADE is a satisfactory model, and the ratio of the dispersion coefficient to the diffusion coefficient is a function of the Peclet number but does not change with the traveled distance.

Effects of the fractal nature of soil on water and solute transport can be further complicated by the differences among fractal dimensions in soils at different scales. Avnir et al. (1986) found at least two ranges of radii with different surface fractal dimensions in studied soils. Dependence of fractal dimension on pore radii was demonstrated (Wu et al., 1993: Perfect et al., 1993). Pachepsky et al.(1995a) found three or four distinct scaling intervals with different fractal dimensions in the range of pore radii from 4 nm to 5  $\mu$ m. Fractal scaling of soil water retention is usually well pronounced at capillary potentials lower than -30 kPa.

Although anomalous diffusion is expected in fractal pore systems, the presence of anomalous diffusion does not prove that the porous media is fractal. A heterogeneity along transport pathways may result in an anomalous transport regardless of the presence or the absence of self-similarity of the pore space (Beven et al., 1993). The physical interpretation of Levy motions does not presume the presence of fractal scaling in the porous media in which the motions occur (Klafter et al., 1990). The applicability of the FADE may be closely related to the distributions of pore-water velocities. In saturated media, the presence of heavy-tailed distributions of the hydraulic conductivity directly implies the validity of the FADE (Meerschaert et al., 1999; Benson et al., 1999). The heavy-tailed hydraulic conductivity distributions were found in geologic media (Painter, 1996; Benson et al., 1999). Heavy-tailed velocity distributions can also be expected in unsaturated and structured soils, and therefore the FADE may be a useful model in these conditions.

Experimental setups limit the ranges of scales within which the transport parameter scaling showed in Fig. 2–1 and 2–2 are valid. The ranges beyond which this scaling changes are not known. There are indications that the anomalous transport in fractal media may not be a stable phenomenon. Pachepsky and Timlin (1998) showed that instability is expected at some stage for the horizontal water transport with the diffusivity scaling shown in Fig. 2–2. Grindrod and Impey (1993) simulated solute transport in saturated two-dimensional fractal porous medium and found that at early stages an anomalous transport occurs whereas the later breakthrough is predominantly Fickian. However, Benson et al. (1999) demonstrate that the FADE is accurate in ground water on the scale of 300 m at a field site.

The external force applied may enhance the anomalous transport in fractal structures (Roman et al., 1989). Therefore, anomalous features can be even more pronounced in the gravity-affected vertical water transport than in the horizontal water transport. General considerations of Roman et al. (1989) imply that the scaling variable  $x/t^n$  in (Eq. [2]) should be in this case replaced by the scaling variable  $x/\log(t)$ . Presence of sharp changes in soil hydraulic and transport properties that can be encountered during vertical flow in soils may make the dispersion/distance relations considerably more complex than they are in the media where the FADE has been shown to be effective. The efficiency of the FADE in such situations remains to be seen.

The anomalous transport of solutes can be an important phenomenon to consider in estimations of the fate of agricultural chemicals. As the dispersivity, used in the traditional ADE, grows with depth, the spreading rate and the tailing of the solute concentrations can be larger than that estimated from short range observations. There may be a potential for chemicals to travel into and within the vadose zone faster than expected from their movement in upper part of soil profile. Anom-

alous transport is an interesting issue to explore, since the movement of water and solutes in soils with fractal properties cannot, in general, be accurately simulated with traditional Richards' and ADE models.

#### **APPENDIX**

The solution of (Eq. [6]) for the initial condition c(x,0) = 0,  $x < 0 < \infty$ , and a continuous source  $c(0,t) = c_0$ , t > 0, is

$$c(x,t) = c_0 \left[ 1 - F_{\alpha} \left( \frac{x - vt}{\sigma} \right) \right]$$

where  $F_{\alpha}(y)$  is a standard symmetric Lévy probability distribution function for parameter  $\alpha$  and  $\sigma = [D_{sf}t | \cos(\pi\alpha/2)|]^{1/\alpha}$  (Benson, 1998). Several methods are available for generating the standard symmetric Lévy distributions including series approximations and integrals that are easily evaluated numerically. McCulloch (1996) lists for symmetric distribution function:

$$F\alpha(y) = C(\alpha) + \frac{\operatorname{sign}(1-\alpha)}{2} \int_{0}^{1} \exp\left[-y^{\alpha/(\alpha-1)} U_{\alpha}(\phi)\right] d\phi$$

where

$$C(\alpha) = \begin{cases} 1, & \alpha > 1 \\ \frac{1}{2}, & \alpha < 1 \quad \text{and} \quad U_{\alpha}(\phi) = \left(\frac{\sin(\pi\alpha\phi/2)}{\cos(\pi\phi/2)}\right)^{\alpha/(1-\alpha)} \end{cases}$$

#### **ACKNOWLEDGMENT**

We are grateful to H.M. Selim for the encouragement of writing this paper. D.A.B. acknowledges support from the DOE-BES grant DE-FG03-98ER14885.

#### REFERENCES

Adler, P.M. 1996. Transports in fractal porous media. J. Hydrol. 187:195–213.

Anderson, A.N., A.B. McBratney, and J.W. Crawford. 1998. Applications of fractals to soil studies. Adv. Agron. 63:1–76.

Anderson, A.N., A.B. McBratney, and E.A. Fitzpatrick. 1996. Soil mass, surface, and spectral fractal dimensions estimated from thin section photographs. Soil Sci. Soc. Am. J. 60:962–969.

Avnir, D., D. Farin, and P. Pfeifer. 1985. Surface geometric irregularity of particulate materials: The fractal approach. J. Coll. Interface Sci. 103:112–123.

Barak, P., C.A. Seybold, and K. McSweeney. 1996. Self-similitude and fractal dimension of sand grains. Soil Sci. Soc. Am. J. 60:72–76.

Bartoli, F., R. Phylippy, M. Doirisse, S. Niquet, and M. Dubuit. 1991. Structure and self-similarity in silty and sandy soils: the fractal approach. J. Soil Sci. 42:167–185.

Baveye, P., J.-Y. Parlange, and B.A. Stewart. 1998. Fractals in soil science. CRC Press. Boca Raton,

- Benson D.A., 1998. The fractional advection-dispersion equation: Development and application. Ph.D. diss. Univ. Nevada, Reno.
- Benson, D.A., R. Schumer, M.M. Meerschaert, and S.W. Wheatcraft. 1999. Fractional dispersion, Lévy motion, and the MADE tracer tests. Desert Res. Inst., Reno, NV.
- Beven, K.J., D.E. Henderson, and A.D. Reeves. 1993. Dispersion parameters for undisturbed partially saturated soil. J. Hydrol. 143:19–43.
- Bhattacharya, R.N., V.K. Gupta, and G. Sposito. 1976. A Markovian stochastic basis for the transport of water through unsaturated soil. Soil Sci. Soc. Am. J. 40:465–467
- Bhatacharya, R., and V.K. Gupta. 1990. Application of the central limit theorem to solute transport in saturated porous media: from kinetic to field scales. p. 97–124. *In* J.H. Cushman (ed.) Dynamics of fluids in hierarchical porous media. Acad. Press, New York.
- Bird, N.R.A., F. Bartoli, and A.R. Dexter. 1996. Water retention models for fractal soil structures. Eur. J. Soil Sci. 47:1–17
- Brakensiek, D.L., W.J. Rawls, S.D. Logsdon, and W.M. Edwards. 1992. Fractal description of macroporosity. Soil Sci. Soc. Am. J. 56:1721–1723.
- Burrough, P.A. 1983a. Multiscale sources of spatial variation in soil. I. The application of fractal concepts to nested levels of soil variation. J. Soil Sci. 34:577–597
- Burrough, P.A. 1983b. Multiscale sources of spatial variation in soil. II. A non-Brownian fractal model and its application in soil survey. J. Soil. Sci. 34:599–620.
- Bronswijk, J.J.B., W. Hamminga, and K. Oostinde. 1995. Field-scale solute transport in a heavy clay soil. Water Resour. Res. 31:517–526.
- Butters, G.L., and W.A. Jury. 1989. Field scale transport of bromide in unsaturated soil. 2. Dispersion modeling. Water. Resour. Res. 25:1575–1581.
- Chaves, A.S. 1998. A fractional diffusion equation to describe Levy flights. Phys. Lett. A 239: 13–16.
- Comegna, V., P. Damiani, and A. Sommella. 1998. Use of a fractal model for determining soil water retention curves. Geoderma 85:307–314.
- Crawford, J.W., K. Ritz, and I.M. Young. 1993. Quantification of fungal morphology, gaseous transport and microbial dynamics in soil: An integrated framework utilizing fractal geometry. Geoderma 56:157–172
- Crawford, J.W. 1994. The relationship between structure and the hydraulic conductivity of soil. Eur. J. Soil Sci. 45:493–502
- Crawford J.W., N. Matsui, and I.M. Young. 1995. The relation between the moisture-release curve and the structure of soil. Eur. J. Soil Sci. 46:369–375.
- Donnelly, D.P., and L. Boddy. 1997. Development of mycelial systems of Stropharia caerulea and Phanerochaete velutina on soil: Effect of temperature and water potential. Mycol. Res. 101: 705–713.
- Dyson, J.S., and R.E. White. 1987. A comparison of the convective dispersion equation and transfer function model for predicting chloride leaching through undisturbed structured clay soil. J. Soil. Sci. 38:157–172.
- Eghball, B., L.N. Mielke, G.A. Calvo, and W.W. Wielhelm. 1993a. Fractal description of soil fragmentation for various tillage methods and crop sequences. Soil Sci. Soc. Am. J. 57:1337–1341.
- Eghball, B., J.R. Settimi, J.W. Maranville, and A.M. Parkhurst. 1993b. Fractal analysis for morphological description of corn roots under nitrogen stress. Agron. J. 85:287–289.
- Ellsworth, T.R., P.J. Shouse, T.H. Scaggs, J.A. Jobes, and J. Fargerlund. 1996. Solute transport in unsaturated soil: Experimental design, parameter estimation, and model discrimination. Soil Sci. Soc. Am. J. 60:397–407.
- Eltz, F.L.F., and L.D. Norton. 1997. Surface roughness changes as affected by rainfall erosivity, tillage, and canopy cover. Soil Sci. Soc. Am. J. 61:1746–1755.
- Ferguson, H., and W.R.Gardner. 1963. Diffusion theory applied to water flow data obtained using gamma ray absorption. Soil Sci. Soc. Am. Proc. 27:243–246
- Fitter, A.H., and T.R. Strickland. 1992. Fractal characterization of root system architecture. Funct. Ecol. 6:632–635.
- Flury, M., and H. Flühler. 1995. Modeling solute leaching in soils by diffusion-limited aggregation: Basic concepts and application to conservative solutes. Water Resour. Res. 31:2443–2452.
- Folorunso, O.A., C.E. Puente, D.E. Rolston, and J.E. Pinzón. 1994. Statistical and fractal evaluation of the spatial characteristics of soil surface strength. Soil Sci. Soc. Am. J. 58:284–294.
- Fuentes, C., M. Vauclin, and R. Haverkamp. 1996. A note on the soil-water conductivity of a fractal soil. Transp. Por. Media 23:31–38.
- Gefen, Y., A. Aharony, and S. Alexander. 1983. Anomalous diffusion on percolating clusters. Phys. Rev. Lett. 50:77–80.

Giménez, D., W. Rawls, E. Perfect, Y. Pachepsky. 1998. Fractal models for predicting soil hydraulic properties: A review. Eng. Geol. 48:161–183.

- Giménez, D., R.R. Allmaras, D.R. Huggins, and E.A. Nater. 1997. Prediction of the saturated hydraulic conductivity-porosity dependence using fractals. Soil Sci. Soc. Am. J. 61:1285–1292.
- Grindrod, P., and M.D. Impey. 1993. Channeling and Fickian dispersion in fractal simulated porous media. Water Resour. Res. 29:4077–4089.
- Grout, H, A.M. Tarquis, and M.R. Wiesner. 1998. Multifractal analysis of particle size distributions in soil. Environ. Sci. Technol. 32:1176–1182.
- Guerrini, I.A., and D. Swartzendruber. 1992. Soil water diffusivity as explicitly dependent on both time and water content. Soil Sci. Soc. Am. J. 56:335–340.
- Guerrini, I.A., and D. Swartzendruber. 1994. Fractal characteristics of the horizontal movement of water in soils. Fractals 2:465–468.
- Gwo, J.P., P.M. Jardine, G.W. Wilson, and G.T. Yeh. 1995. A multiple-pore-region concept to modeling mass transfer in subsurface media. J. Hydrol. 164:217–237.
- Haggerty, R., and S.M. Gorelick. 1995. Multiple-rate mass transfer for modeling diffusion and surface reactions in media with pore-scale heterogeneity. Water Resour. Res. 31:2383–2400.
- Hamlen, C.J., and R.G. Kachanoski. 1992. Field solute transport across a soil horizon boundary. Soil Sci, Soc. Am, J. 56:1716–1720.
- Hatano, R., and H.W.G. Booltink. 1998. Using fractal dimension of stained flow patterns in clay soils to predict bypass flow. p. 261–291. *In P. Baveye et al.* (ed.) Fractals in soil science. CRC, Boca Raton FL.
- Hilfer, R., and L. Anton. 1995. Fractional master equation and fractal time random walks. Phys. Rev. E 51:R848–R851.
- Huang, C.-H., and J. Bradford. 1992. Applications of a laser scanner to quantify soil microtopography. Soil Sci. Soc. Am. J. 56:14–21.
- Hughes, B.D., M.F. Shlesinger, and E.W. Montroll. 1981. Random walks with self-similar clusters. Proc. Natl. Acad. Sci. 78:3287–3291.
- Hutson, J.L., and R.J. Wagenet. 1995. A multiregion model describing water flow and solute transport in heterogeneous soils. Soil Sci. Soc. Am. J. 59:743–751.
- Jaynes, D.B., and R.C. Rice. 1993. Transport of solutes as affected by irrigation method. Soil Sci. Soc. Am. J. 57:1348–1353.
- Jaynes, D.B., R..S. Bowman, and R.C. Rice. 1988. Transport of a conservative tracer in the field under continuous flood irrigation. Soil Sci. Soc. Am. J. 52:618–624.
- Jumarie, G. 1992. A Fokker-Plank equation of fractional order with respect to time. J. Math. Phys. 33:3536–3542.
- Jury, W.A., and K. Roth. 1990. Transfer functions and solute movement through soil: Theory and applications. Birkhauser, Basel.
- Jury, W.A. 1988. Solute transport and dispersion. p. 1–16. *In* W.L. Steffen and O.T. Denmead (ed.) Flow and transport in the natural environment: Advances and applications. Springer Verlag, Berlin.
- Khan, A.U.H., and W.A. Jury. 1990. A laboratory test of the dispersion scale effect. J. Contam. Hydrol. 5:119–132.
- Kinzelbach, W. 1987. Numerische Methoden zur Modelierung des Schadstofftransports im Grundwasser. Oldenburg Verlaf, München.
- Klafter, J., A. Blumen, and M.F. Shlesinger. 1987. Stochastic pathway to anomalous diffusion. Phys. Rev. A 35:3081–3085.
- Klafter, J., A. Blumen, G. Zumofen, and M.F. Shlesinger. 1990. Lévy walk approach to anomalous diffusion. Physica A 168:637–645.
- Koch, S., and H. Flühler. 1993. Solute transport in aggregated porous media: Comparing model independent and dependent parameter estimation. Water Air Soil Pollut. 68:275–289.
- Kozak, E., Ya. Pachepsky, S. Sokolowski, Z. Sokolowska, and W. Stepniewski. 1996. A modified number-based method for estimating fragmentation dimensions of soils. Soil Sci. Soc. Am. J. 60:1291–1297.
- Kravchenko, A., and R. Zhang. 1998. Estimating the soil water retention from particle-size distributions: A fractal approach. Soil Sci. 163:171–179.
- Lemaitre, R., and P.M. Adler. 1990. Fractal porous media. IV: Three-dimensional Stokes flow through random media and regular fractals. Transp. Porous Media 5:325–340.
- Liu, H.H., and F.J. Moltz. 1997. Multifractal analysis of hydraulic conductivity distributions. Water Resour. Res. 33:2483–2488.
- Logsdon, S.D., D. Giménez, and R.R. Allmaras. 1996. Fractal characterization of aggregate-size distribution: The question of scale invariance. Soil Sci. Soc. Am. J. 60 1327, 1330.

- Mandelbrot, B.B., and J.R. Wallis. 1968. Noah, Joseph, and operational hydrology. Water Resour. Res. 4:909–918.
- Mandelbrot, B.B. 1983. Fractal geometry of nature. W.H. Freeman, New York.
- Martin, M.A., and F.J. Taguas. 1998. Fractal modeling, characterization and simulation of particle-size distributions in soil. Proc. R. Soc. Math. Phys. Eng. 454:1457–1471.
- McCuloch, J.H. 1996. Precise tabulation of the maximally-skewed stable distributions and densities. Computat. Stat. Data Anal. 23:307–320.
- Meerschaert, M.M., D.A. Benson, and B. Bäumer. 1999. Multidimensional advection and fractional dispersion. Phys. Rev. E 59:5026–5028.
- Mishra, S., and J.C. Parker. 1990. Analysis of solute transport with a hyperbolic scale-dependent dispersion model. Hydrol. Proc. 4:45–70.
- Montas, H.J., J.D. Eigel, B.A. Engel, and K. Haghighi. 1997. Deterministic modeling of solute transport in soils with preferential flow pathways. 1. Model development. Trans. ASAE 40:1246–1256
- Neuman, S.P. 1995. On advective transport in fractal permeability and velocity fields. Water Resour. Res. 31:1455
- Neuman, S.P. 1990. Universal scaling of hydraulic conductivities and dispersivities in geologic media. Water Resour. Res. 26:1749–1758
- Nielsen, D.R., J.W. Hopmans, and K. Reinhardt. 1998. An emerging technology for scaling field-water behavior. p. 136–166. *In G. Sposito (ed.) Scale dependence and scale invariance in hydrology.* Cambridge Univ. Press, Cambridge, UK.
- Nielsen, D.R., J.W. Biggar, and J.M. Davidson. 1962. Experimental consideration of diffusion analysis in unsaturated flow problem. Soil Sci. Soc. Am. Proc. 26:107–111.
- Nielsen, D.R., M.Th. Van Genuchten, and J.W. Biggar. 1896. Water flow and solute transport processes in the unsaturated zone. Water Resour. Res. 22:89S–108S.
- Niemeyer, J., and C. Ahl. 1991. Die Fractale Verteilung der Minerale und deren Bedeutung für die Sorption. Mitt. Dtsch. Bodenk. Ges. 66:217–274.
- Ogata, A., and R.B. Banks. 1961. A solution of the differential equation of longitudinal dispersion in porous media. USGS Prof. Pap. 411-A. U.S. Gov. Print. Office, Washington, DC.
- Orbach, R. 1986. Dynamics of fractal networks. Science (Washington, DC) 231:814–819.
- Oleschko, K. 1998. Delesse principle and statistical fractal sets: 1. Dimensional equivalents. Soil Till. Res. 49:255–264.
- Pachepsky Y.A., T.A. Polubesova, M. Hajnos, Z. Sokolowska, and G. Jouzefaciuk. 1995a. Fractal parameters of pore surface area as influenced by simulated soil degradation. Soil Sci. Soc. Am. J. 59:58–65.
- Pachepsky, Y.A., R.A. Scherbakov, and L.P. Korsunskaia. 1995b. Scaling of soil water retention using a fractal model. Soil Sci. 159:99–104.
- Pachepsky Y.A., L.P. Korsunskaia, and M. Hajnos. 1996b. Fractal parameters of soil pore surface area under a developing crop. Fractals 4:97–10.
- Pachepsky Y.A., V. Yakovchenko, M.C. Rabenhorst, C. Pooley, and L.J. Sikora. 1996a. Fractal parameters of pore surfaces as derived from micromorphological data: effect of long-term management practices. Geoderma 74:305–325.
- Pachepsky, Y.A., D. Giménez, S. Logsdon, R. Allmaras, and E. Kozak. 1997. On interpretation and misinterpretation of fractal models. Soil Sci. Soc. Am. J. 61:1800–1801.
- Pachepsky, Y., and D. Timlin. 1998. Water transport in soils as in fractal media. J. Hydrol. 204: 98–107.
- Pachepsky, Y.A, J.W. Crawford, and W.J. Rawls (ed.). 1999. Fractal models in soil science. Geoderma Vol. 88.
- Painter, S. 1996. Stochastic interpolation of aquifer properties using fractional Lévy motion. Water Resour. Res. 32:1323–1332.
- Pan, J.-Z., and Z.-X. Lu. 1994. Fractal dimensions of soil strengths for paddy fields in China. J. Terramechan. 31:1–17.
- Pardini, G., and F. Gallart. 1998. A combination of laser technology and fractals to analyze soil surface roughness. Eur. J. Soil. Sci. 49:197–202.
- Parker, J.C., and K.A. Albrecht. 1987. Sample volume effect on solute transport predictions. Water. Resour Res. 23:2293–2301.
- Perfect, E. 1996. An improved fractal equation for the soil water retention curve. Water Resour. Res. 32:281–287.
- Perfect, E., and B.D. Kay. 1991. Fractal theory applied to soil aggregation. Soil Sci. Soc. Am. J. 55:1552–1558.
- Perfect, E. B.D. Kay, and V. Rasiali. 1993. Multifractal model for soil aggregate fragmentation. Soil Sci. Soc. Am. J. 57:896–900.

Perfect, E, and B.D. Kay. 1995. Applications of fractals in soil and tillage research: A review. Soil Tillage Res. 36:1–38.

- Perfect, E. 1999. Estimating soil mass fractal dimension from water retention curves. Geoderma 88:221-232.
- Perrier, E., M. Rieu, G. Sposito, and G. de Marsily. 1996. Models of the water retention curve for soils with a fractal pore size distribution. Water Resour. Res. 32:3025–3031.
- Peyton, R.L., C.J. Gantzer, S.H. Anderson, B.A. Haeffner, and P. Pfeiffer. 1994. Fractal dimension to describe soil macropore structure using X ray computed tomography. Water Resour. Res. 30:691–700.
- Philip, J.R. 1955. Numerical solution of equations of the diffusion type with diffusivity concentration-dependent. Trans. Faraday Soc. 51:885–892.
- Porro, I., P.J. Wierenga, and R.G. Hills. 1993. Solute transport through large uniform and layered soil columns. Water Resour. Res. 29:1321–1330.
- Preston, S., B.S. Griffiths, and I.M. Young. 1997. An investigation into sources of soil crack heterogeneity using fractal geometry. Eur. J. Soil Sci. 48:31–44.
- Rao, P.S.C., D.E. Rolston, R.E. Jessup, and J.M. Davidson. 1980. Solute transport in aggregated porous media: Theoretical and experimental evaluation. Soil Sci. Soc. Am. J. 44:1139–1146.
- Rasiah, V., E. Perfect, and B.D. Kay. 1998. Characterizing the changes in soil porosity by computed tomography and fractal dimension. Soil Sci. 163:203–211.
- Rawlins, S.L., and W.H. Gardner. 1963. A test of the validity of the diffusion equation for unsaturated flow of soil water. Soil Sci. Soc. Am. Proc. 27:507–511.
- Rawls, W.J., D.L. Brakensiek, and S. Logsdon. 1993. Predicting saturated hydraulic conductivity utilizing fractal principles. Soil Sci. Soc. Am. J. 57:1193–1197.
- Rawls, W.J., and D.L. Brakensiek. 1995. Utilizing fractal principles for predicting soil hydraulic properties. J. Soil Water Conserv. 50:463–465.
- Rawls, W.J., D.L. Brakensiek, and S. Logsdon. 1996. Estimation of macropore properties for no-till soils. Trans. ASAE 39:91–95.
- Rasiah, V., E. Perfect, and B.D. Kay. 1995. Linear and nonlinear estimates of fractal dimension for soil aggregate fragmentation. Soil Sci. Soc. Am. J. 59:83–97.
- Rieu, M., and G. Sposito. 1991. Fractal fragmentation, soil porosity, and soil water properties. I. Theory. Soil Sci. Soc. Am. J. 55:1231–1238.
- Roman, H.E., A. Bunde, and S. Havlin. 1989. Anomalous transport on random fractal structures: stretched Gaussians, power-laws, and logarithmic time dependencies. Berichte der Bunsengesellschaft, Phys. Chem. 93:1205–1208.
- Roth, K., W.A. Jury, H. Flühler, and W. Attinger. 1991. Transport of chloride through unsaturated field soil. Water Resour. Res. 27:2533–2541.
- Saichev, A.I., and G.M. Zaslavsky. 1997. Fractional kinetic equations: Solutions and applications. Chaos 7:753–764.
- Salles, J., L. Prérors, R. Delannay, J.-F. Thorert, J.L. Auriault, and P.M. Adler. 1993. Tailor dispersion in random media and regular fractals. Phys. Fluids AS:2348–2376.
- Samko, S.G., A.A. Kilbas, and O.I. Marichev. 2993. Fractional integrals and derivatives: Theory and applications. Gordon and Breach Sci. Publ., London.
- Samorodnitsky, G., and M.S. Taqqu. 1994. Stable non-Gaussian random processes: Stochastic models with infinite variance. Chapman and Hall, New York.
- Selim, H.M., D. Kirkham, and M. Amemiya. 1970. A comparison of two methods for determining soil water diffusivity. Soil Sci. Soc. Am. Proc. 34:14–18.
- Senesi, N., F.R. Rizzi, P. Dellino, and P. Acquafredda. 1996. Fractal dimension of humic acids in aqueous suspension as a function of pH and time. Soil Sci. Soc. Am. J. 60:1773–1780.
- Shepard, J.S. 1993. Using a fractal model to compute the hydraulic conductivity function. Soil Sci. Soc. Am. J. 57:300–306.
- Smiles, D.E., J.R. Philip, J.H. Knight, and D.E. Elrick. 1978. Hydrodynamic dispersion during adsorption of water by soil. Soil Sci. Soc. Am. J. 42:229–234.
- Snow, V.O., B.E. Clothier, D.R. Scotter, and R.E. White. 1994. Solute transport in a layered field soil: experiments and modelling using the convection-dispersion approach. J. Contamin. Hydrol. 16:339–358.
- Sokolowska, Z. 1989. On the role of energetic and geometric heterogeneity in sorption of water vapor by soils: Application of a fractal approach. Geoderma 45:251–265.
- Spek, LY., and M. van Noordwijk. 1994. Proximal root diameter as predictor of total root size for fractal branching models. II. Numerical model. Plant Soil 164:119–127.

- Steenhuis, T.S., J.I. Parlange, and M.S. Andreini. 1990. A numerical model for preferential solute movement in structured soil. Geoderma 46:193–208.
- Toledo, P.G., R.A. Novy, H.T. Davis, and L.E. Scriven. 1990. Hydraulic conductivity of porous media at low water content. Soil Sci. Soc. Am. J. 54:673–679.
- Toride, N, F. Leij, and M.Th. van Genuchten. 1995. The CXTFIT code for estimating transport parameters from laboratory or field tracer experiments. Version 2.0. Res. Rep. 137. U.S. Salinity Lab., Riverside, CA.
- Tyler, S.W., and S.W. Wheatcraft. 1989. Application of fractal mathematics to soil water retention estimation. Soil Sci. Soc. Am. J. 53:987–996.
- Tyler, S.W., and S.W. Wheatcraft. 1992. Fractal scaling of soil particle size distribution: Analysis and limitations. Soil Sci. Soc. Am. J. 56:362–369.
- Vachaud, G., M. Vauclin, and T. M. Addiscott. 1990. Solute transport in the vadose zone: A review of models. *In* Water quality modeling of agricultural of non-point sources, Part1. Symp. Pap., Logan, UT. 19–23 June 1988. USDA ARS.
- Van Damme, H. 1998. Structural hierarchy and molecular accessibility in clayey aggregates. p. 55–74. In Fractals in soil science. Adv. Soil Sci., Boca Raton, FL.
- Van Genuchten, M.Th., and P.J. Wierenga. 1976. Mass transfer in sorbing porous media. I. Analytical solutions. Soil Sci. Soc. Am. J. 40:473–481.
- Ward, A.L., R.G. Kachanoski, A.P. von Bertoldi, and D.E. Elrick. 1995. Field and undisturbed-column measurements for predicting transport in unsaturated layered soil. Soil Sci. Soc. Am. J. 59:52–59.
- Wheatcraft, S., and S. Tyler. 1988. An explanation of scale dependent dispersivity in heterogeneous aquifers using concepts of fractal geometry. Water Resour. Res. 24:566–578.
- Whisler, F.D., A. Klute, and D.B. Peters. 1968. Soil water diffusivity from horizontal infiltration. Soil Sci. Soc. Am. Proc. 32:6–11.
- Whitmore, A.P. 1991. A method for assessing the goodness of computer simulation of soil processes. J. Soil Sci. 42:289–299.
- Wierenga, P.J., and M.Th. Van Genuchten. 1989. Solute transport through small and large unsaturated soil columns. Groundwater 27:35–42.
- Wu, Q., M. Borkovec, and H. Sticher. 1993. On particle-size distribution in soils Soil Sci. Soc. Am. J. 57:883–890.
- Yasuda, H., R. Berndtsson, A. Barri, and K. Jinno. 1994. Plot-scale solute transport in a semiarid agricultural soil. Soil Sci. Soc. Am. J. 58:1052–1060.
- Young, I.M., and J.W. Crawford. 1991. The fractal structure of soil aggregates: Its measurement and interpretation. J. Soil Sci. 42:187–192.
- Zaslavsky, G.M. 1994. Renormalization group theory of anomalous transport in systems with Hamiltonian chaos. Chaos 4:25–33.
- Zeng, Y., C.J. Gantzer, and S.H. Anderson. 1996. Fractal dimension and lacunarity of bulk density determined with x-ray computed tomography. Soil Sci. Soc. Am. J. 60:1718
- Zhang, R., K. Huang, and J. Xiang. 1994. Solute movement through homogeneous and heterogeneous soil columns. Adv. Water Resour. 17:317–324.

# Models Relating Solute Dispersion to Pore Space Geometry in Saturated Media: A Review

Ed Perfect and Michael C. Sukop

University of Kentucky Lexington, Kentucky

This review is concerned with dispersion of nonreactive solutes in saturated porous media. Dispersion can occur as a result of diffusion, interfacial instabilities, mechanical mixing, molecular size effects, and/or turbulence. The focus here is on the combined effects of diffusion and mechanical mixing. Models that predict these processes are either based on an assumed or empirical distribution of pore water velocities, or derived from a geometrical representation of the pore space. Velocity-based models such as the convection-dispersion equation are widely used at present, but lack predictive power because their parameters are generally estimated inversely. Geometrical dispersion models have been neglected in the past because of difficulties in parameterizing the complex structures that occur in natural porous media. However, recent advances in fractal geometry and percolation and network theory may reduce these difficulties, and facilitate the increased use of geometrical models in the future. Such models are attractive because their input parameters can be determined independently from measurements of pore characteristics. Pertinent pore characteristics, including shape, size distribution, and connectivity are defined, and methods of measuring them are discussed. Experimental studies relating dispersion to pore characteristics are reviewed. Theoretical approaches are presented for modeling dispersion in: (i) individual pores, (ii) media with immobile water regions, (iii) spatially periodic media, (iv) capillary bundles, and (v) interacting bond and site networks. In general, these models predict  $K^* \propto P_n^{\alpha}$ , where  $K^*$  is the dimensionless dispersion coefficient,  $P_n$  is the Peclet number, and  $1 \le \alpha$  $\leq$  2. Pore space geometry appears to influence both the prefactor and exponent in this relationship. Work in the emerging areas of prefractal networks, percolation models, numerical simulations, cellular automata, and physical micromodels is reviewed. Finally, some future research opportunities are discussed and approaches for incorporating predictions from geometrical models into macroscopic solute transport simulations are suggested.

#### INTRODUCTION

The spreading of a solute throughout a porous medium during saturated flow is an important physicochemical process, attributable to a combination of diffusive and dispersive mechanisms. This phenomenon has come under the scrutiny of a variety of scientific disciplines, including biophysics, chemical, civil, and petroleum engineering, hydrogeology, applied mathematics, statistical physics, and soil science. In the area of soil science, which constitutes the disciplinary bias of this review, knowledge of the spreading process is critical for predicting the fate of agricultural, industrial, and naturally occurring contaminants that originate, or are spilled, spread or stored, on or within the soil. Contaminants that are not irreversibly adsorbed, taken up by plants, broken down, volatilized, and/or lost in runoff must pass through the soil in order to reach groundwater and any potential receptors.

Solute transport in porous media has been studied intensively during the last 50 yr. Nielsen and Biggar (1961) described a laboratory apparatus and protocol for conducting miscible displacement experiments. Using this basic design, many breakthrough curves (BTC) were determined for solutes flowing through columns of glass beads and "disturbed" (i.e., sieved and repacked) soil samples (Biggar & Nielsen, 1967). However, sieved and repacked samples do not have the same range of pore sizes or connectivity that can be expected under field conditions. As a result, BTC's for "undisturbed" cores (i.e., structured samples) are often quite different from those determined on "disturbed" samples under the same experimental conditions (Elrick & French, 1966; Anderson & Bouma, 1977).

Models that are used to predict transport of chemicals in soil can be grouped into two main categories: those based on an assumed or empirical distribution of pore water velocities, and those derived from a particular geometric representation of the pore space. Velocity-based models are currently the most widely used predictive tools. However, they are unsatisfactory because their parameters generally cannot be measured independently and often depend upon the scale at which the transport experiment is conducted. The focus of this chapter is on pore geometry models for chemical transport. These models are not widely used today. However, recent advances in the characterization of complex pore structures means that they could provide an alternative to velocity based-models in the future. They are particularly attractive because their input parameters can be estimated from independent measurements of pore characteristics. They may also provide a method of inversely estimating pore characteristics from solute transport experiments.

Some geometric transport models are based on solid characteristics rather than on properties of the pore space itself. By assuming a particular packing arrangement it is possible to infer the pore space geometry from information on the size and shape of the solid particles (Coelho et al., 1997). While this approach may be applicable to sieved and repacked soil columns, it is often inappropriate for undisturbed samples, with pore characteristics that depend more on soil structure than on soil texture. Thus, models to predict solute dispersion from the properties of particles in packed beds (e.g., Aris & Amundson, 1957; Koch & Brady, 1985; Rasmuson, 1985) are not the main focus of this review.

Solute dispersion is highly dependent upon water content (Beven et al., 1993; Matsubayashi et al., 1997; Haga et al., 1999) and ion adsorption kinetics

(Brusseau & Rao, 1989; Sugita & Gillham, 1995). To facilitate the establishment of direct relations between pore characteristics and solute spreading, only the transport of conservative, nonreactive chemicals, under steady-state, saturated flow conditions will be considered here. Transient flows de-couple the relationship between solute dispersion and pore space geometry (Sobey, 1982, 1985). Although many soils are only saturated for relatively short periods of time, solute spreading under saturated conditions is a very important process because a large proportion of the total annual movement of water and solutes through the vadose zone can occur during these events. Moreover, solute transport under saturated conditions in groundwater systems is a critical process affecting many environmental contamination and water supply problems. Although only nonreactive transport will be considered, it should be noted that transport parameters derived for nonreactive solutes are often used, in conjunction with experimentally determined or literature-derived adsorption coefficients, to predict the transport of reactive chemicals such as heavy metals and pesticides.

The literature on solute transport in porous media is voluminous. For a general introduction to this subject the reader is referred to Leij and Dane (1989), Elrick and Clothier (1990), and Jury and Flühler (1992). Sahimi (1993) has reviewed some of the advances made in modeling solute transport within complex pore structures. Of the numerous older review articles, those by Bear (1969) and Fried and Combarnous (1971) are especially thorough, and are still relevant today. Other important contributions that discuss aspects of pore geometry as related to solute transport include those by Greenkorn and Kessler (1969), Rose (1977), Brusseau and Rao (1990), and Celia et al. (1995). In addition, several books are relevant to this topic, including those by Bear (1972), Dullien (1992), Adler (1992), and Sahimi (1995).

This chapter is organized as follows. First, velocity-based solute transport models will be reviewed, and their parameters defined. The different mechanisms contributing to the spreading of a conservative nonreactive solute in saturated soil will then be presented. Next, pore characteristics relevant to solute transport will be defined, and methods of measuring them discussed. Experimental studies relating pore characteristics to solute dispersion will be reviewed. The remainder of the chapter will be devoted to theoretical models for solute transport based on various pore characteristics. These models will be presented in order of increasing complexity in their representation of the pore space geometry. Emerging areas of research will be identified. Finally, relationships between solute spreading and pore characteristics will summarized, and the predictive potential of pore-based transport models will be discussed.

#### VELOCITY DISTRIBUTION MODELS

Velocity-based models use the distribution of pore water velocities to predict the spreading of a solute in time and space. No attempt is made to directly link the distribution of pore water velocities or solute spreading to characteristics of the pore space. As a result, the model parameters must be either estimated inversely (Parker & van Genuchten, 1984; Toride et al., 1995) or inferred from the hydraulic conductivity-water content function (Steenhuis et al., 1990; Scotter & Ross, 1994).

The convection-dispersion equation (CDE) is the most widely used of the velocity distribution models. For steady state, one-dimensional water flow, the CDE for a nonreactive solute can be written as (Fried & Combarnous, 1971),

$$\frac{\partial C}{\partial t} = K \frac{\partial^2 C}{\partial x^2} - v \frac{\partial C}{\partial x}$$
 [1]

where C is concentration of solute in the soil water, t is time, x is distance, K is the diffusion-dispersion coefficient, and v is the mean pore water velocity. Analytical solutions to Eq. [1] have been derived for a variety of initial and boundary conditions (van Genuchten & Parker, 1984).

Equation [1] assumes the porous medium is homogeneous and isotropic (i.e., K and v do not vary in space or with direction), that flow is laminar, and that individual solute molecules sample a normal (Gaussian) distribution of pore water velocities in a time-independent fashion (the ergodic hypothesis) (Sposito et al., 1979). It can be shown (e.g., Bear, 1961) that the v and K in Eq. [1] are related to the mean ( $\mu$ ) and variance ( $\sigma^2$ ) of a normal distribution of distances traversed by the solute over the time increment  $\Delta t$  by,

$$v = \mu/\Delta t \tag{2}$$

and

$$K = \sigma^2 / 2\Delta t \tag{3}$$

The tensorial nature of K in multidimensional forms of Eq. [1] is discussed by Bear (1961) and Scheidegger (1957). For purposes of this review, only longitudinal dispersion will be considered; i.e., spreading parallel to the mean direction of flow.

The generally good agreement between predictions made using the CDE and miscible displacement experiments performed on repacked, structureless materials has led to widespread adoption of this model. As a result, solute spreading is commonly quantified in terms of the CDE parameters K and v. The dimensionless diffusion-dispersion coefficient,  $K^*$ , which provides a measure of the role of mechanical mixing in solute spreading relative to diffusion, is defined as (Fried & Combarnous, 1971),

$$K^* = K/D \tag{4}$$

where D is the molecular diffusion coefficient for the solute species. Another dimensionless parameter that is widely used in solute transport studies is the Peclet number,  $P_n$ , which is written as (Fried & Combarnous, 1971),

$$P_{\rm n} = v\ell/D \tag{5}$$

where  $\ell$  is a characteristic mixing length, commonly taken to be the mean pore or particle radius in experiments involving homogeneous porous media. For heterogeneous porous media, however,  $\ell$  is not easily defined. As a result, it is often replaced by L, a characteristic measurement scale, corresponding to the column

length in laboratory miscible displacement experiments. Bolt (1979) suggested that the  $P_n$  defined in this way be called the Brenner number.

The  $P_n$ , like  $K^*$ , provides a measure of the relative importance of convective transport as compared to diffusive transport. The Peclet number as used here and in most of the solute transport literature is a somewhat unusual dimensionless parameter in that it does not serve to non-dimensionalize a governing equation. van Genuchten and Wierenga (1986) use  $P_n = \nu L/K$  to non-dimensionalize the CDE, but this differs from the Peclet number used in this review because it does not explicitly consider diffusion and because L is the length of the system under study rather than some microscopic characteristic length.

Assuming  $K^*$  is directly proportional to  $P_n$  and equating Eq. [4] and [5] results in  $\ell = K/v$ . For this special case, the  $\ell$  parameter is commonly referred to as the dispersivity. In numerical transport modeling, the grid size is used as  $\ell$  in order to define a grid Peclet number, which must be kept small to minimize numerical dispersion.

The definitions presented in Eq. [4] and [5] are ubiquitous in the solute transport literature. They are based on v and K from the CDE. In this chapter, the use of alternative transport models based on different assumptions will be explored. Thus, it is useful to redefine v and K in terms of the experimentally determined BTC, which is independent of the assumptions inherent in the CDE (Skopp, 1984). The empirical v, v', can be calculated from the first time moment  $[t_1 = \Sigma_i C_i(t)t_i/\Sigma_iC_i(t)]$  of the BTC (Jury & Sposito, 1985),

$$v' = L/t_1 \tag{6a}$$

or from,

$$v' = q/\theta \tag{6b}$$

where q is the Darcy velocity and  $\theta$  is the volumetric water content, which is equal to the total porosity in the case of saturated systems. It is interesting to note that practitioners often use an "effective" water content significantly lower than  $\theta$  in estimating the solute velocity (Bear, 1972). This is equivalent to excluding immobile water from the transport process.

The empirical K, K', can be calculated from the first  $(t_1)$  and second  $[t_2 = \sum_i C_i(t)t_i^2/\sum_i C_i(t)]$  time moments of the BTC as follows (Jury & Sposito, 1985),

$$K' = \frac{L^2 (t_2 - t_1^2)}{2t_1^3}$$
 [7]

By substituting Eq. [6] and [7] into Eq. [4] and [5] we obtain definitions of  $K^*$  and  $P_n$  that are independent of the CDE. Thus, when these parameters are mentioned in the context of non-Gaussian models for solute transport, it should be understood that it is the empirical versions that are being referred to.

In addition to the CDE, several other velocity-based models exist in the solute transport literature, including the fractional CDE (Benson, 1998; Pachepsky et al., 2001), mixing cell models (Frissel & Poelstra, 1967a,b; Bolt, 1979), multi-region models (Gwo et al., 1995; Haggerty & Gorelick, 1995; Bai & Roegiers,

1997), kinematic wave models (Charbeneau, 1984; Germann et al., 1987), and transfer function models (Jury, 1982; Jury et al., 1986). As with the CDE, the parameters of these models cannot be explicitly related to pore characteristics. In contrast, the empirical velocity distribution models developed by Scotter and Ross (1994), Durner and Flühler (1996), and Montas et al. (1997a) permit the prediction of solute spreading from independently measured soil physical properties. In these models, the steady saturated flow solute BTC is derived by relating the empirical distribution of pore water velocities to the hydraulic conductivity-water content function,  $k(\theta)$  (Steenhuis et al., 1990). Thus, for the case where  $k(\theta)$  is predicted by the Campbell (1974) water retention function, the effluent BTC for a step change in influent concentration from C = 0 to  $C = C_0$  at time t = 0, is (Scotter & Ross, 1994),

$$\frac{C}{C_0} = 1 - \left[ (2b_c + 3) \frac{t}{t_p} \right]^{-[1/(2b_c + 2) + 1]}$$
 [8]

where  $t_p$  is the time taken for one water-filled pore volume of solution to pass through the soil column, and  $b_c$  is the exponent in the Campbell (1974) water retention function,

$$\frac{\theta}{\theta_{\text{sat}}} = \left(\frac{\Psi}{\Psi_{\text{a}}}\right)^{-1/b_{\text{C}}}$$
 [9]

where  $\theta_{\text{sat}}$  is the volumetric water content at saturation,  $\psi$  is the liquid potential, and  $\psi_a$  is the air-entry value. Predicted solute breakthrough curves for different water retention curves are illustrated in Fig. 3–1. The smaller the Campbell  $b_c$  parameter, the later the first appearance of the solute in the effluent (Fig. 3–1B).

The Scotter and Ross (1994) model provides a means of predicting the solute breakthrough curve directly from the water retention curve or vice versa, without establishing any intermediate relationship between the distribution of pore water velocities and pore space geometry. However, the model generally over-predicts the measured BTC following the first appearance of solute in the effluent (Scotter & Ross, 1994). Using a more sophisticated approach, Montas et al. (1997a,b) were able to accurately predict 8 out of 10 previously published steady flow solute BTCs with independent parameters estimated from the  $k(\theta)$  function.

#### **DISPERSION PROCESSES**

Solute dispersion is the net result of various mixing processes that operate over different spatial and temporal scales. Differential spreading of a conservative, nonreactive tracer can occur as a result of diffusion, interfacial instabilities, mechanical mixing, molecular size effects and/or turbulence. Flow in porous media can generally be treated as laminar, although it is possible that turbulent effects occur in large pores and/or fractures given certain flow boundary conditions. If turbulence is present, laminar flow models may over-predict discharge. Mixing due to turbulent eddy migration will not be considered here. The reader is referred to Greenkorn and Kessler (1969) for a discussion of this topic.

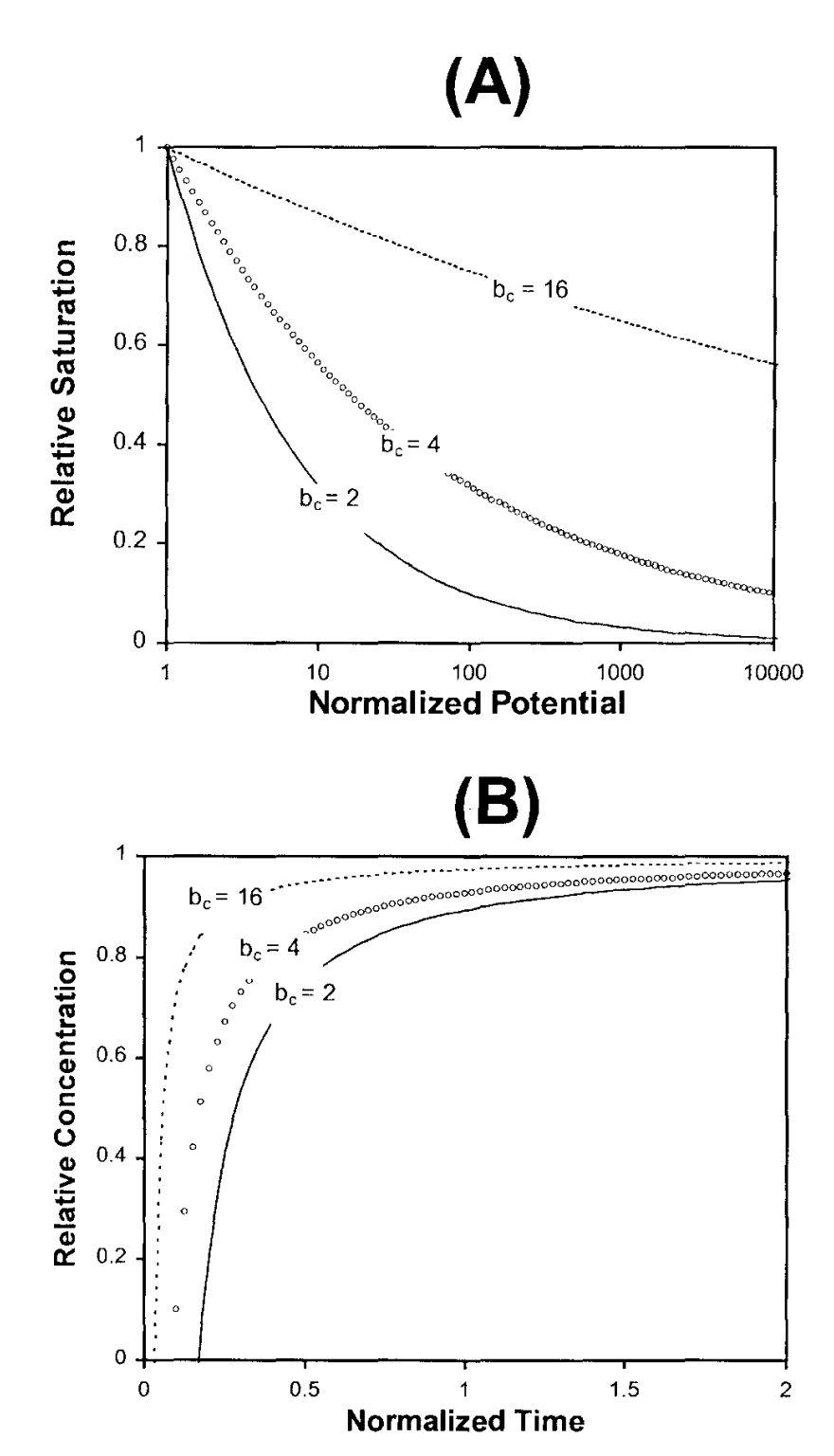


Fig. 3–1. (A) Campbell (1974) water retention curves for different values of b<sub>c</sub>, (B) Corresponding solute breakthrough curves predicted with Eq. [8].

#### **Diffusion**

Solute diffusion is the simplest spreading mechanism in porous media and has been extensively studied (e.g., Fried & Combarnous, 1971; Havlin & Ben-Avraham, 1987). Diffusion occurs as a consequence of random thermal motion (also called Brownian motion), and repeated collisions and deflections of individual molecules in a fluid. This mixing process occurs whether or not there is any convec-

tive flow through the medium. When two miscible fluids are brought into contact, concentration gradients are established, and solutes tend to diffuse down these gradients. The net effect is a tendency to equalize the spatial distribution of diffusible components in any mixed or multicomponent system. In bulk water this mixing process is typically described by Fick's second law of diffusion (Fried & Combarnous, 1971),

$$\frac{\partial C}{\partial t} = D\nabla^2 C \tag{10a}$$

where  $\nabla^2$  is the Laplace operator,

$$\sum_{i=1}^{3} \frac{\partial^2}{\partial x_i^2}$$
 [10b]

and  $x_i$  represent the spatial coordinate axes. For diffusion of solutes in a saturated porous medium, the effective diffusion coefficient,  $D_e$ , is generally less than D for the following reasons,

- 1. liquid water occupies only a fraction of the total volume,
- 2. the connections between pores are tortuous, and increase the mean path length for diffusion,
- 3. interactions occur between solute molecules and the solid phase, and
- 4. changes in the physical properties of water close to solid surfaces.

As a result, for a conservative solute,  $D_e$  can be written as (Sposito, 1989),

$$D_{\rm e} = D\phi/f \tag{11}$$

where  $\phi$  is the porosity and f is the tortuosity, defined as the mean flow path length divided by the sample length. Friedman et al. (1995) have examined the influence of pore space geometry on  $D_e$  using capillary network models.

From the Einstein relation, the mean square displacement of a diffusing species at time t,  $\langle x^2(t) \rangle$ , is related to its effective diffusivity by (Sposito, 1989),

$$D_{\rm e} \sim \frac{\langle x^2(t) \rangle}{t}$$
 [12]

Recent advances in percolation theory and fractal geometry have demonstrated that  $D_e$  is not a constant when diffusion occurs as a result of fractional Brownian motion, i.e., anomalous diffusion (Sahimi, 1993). The time-dependent diffusion coefficient, D(t), for anomalous diffusion in two-dimensional free space is given by (Mandelbrot & Van Ness, 1968),

$$D(t) = Dt^{3-2d_t}$$
 [13]

where  $d_t$  is the fractal dimension of the diffusing particle's trajectory. Note that D(t) = D when  $d_t = 1.5$ ; i.e., classical Brownian motion can be considered a special case

of fractional Brownian motion. Note also that D(t) has dimension  $L^2T^{2-2d_t}$  that is not dimensionally consistent with the diffusion equation when  $d_t \neq 1.5$ . An alternative approach that retains dimensional consistency while incorporating such anomalous behavior is the fractional CDE (Benson, 1998; Pachepsky et al., 2001) based on fractional calculus.

The anomalous diffusivity described by Eq. [13] is due entirely to the fractal nature of the diffusing particle's trajectory in free space. In fractal and multifractal porous media, the diffusing particle's trajectory is further constrained by the geometry of the pore space (Cushman, 1991; Giona et al., 1996; Lovejoy et al., 1998). As a result, when fractional Brownian motion occurs in a two-dimensional fractal porous medium,  $D_e$  becomes scale-dependent, as described by the following equation (Orbach, 1986; Crawford et al., 1993),

$$D_{e}(x) = D_{e}x^{2(d_{m}-d_{t})/d_{t}}$$
 [14]

where  $D_{\rm e}(x)$  is the scale-dependent  $D_{\rm e}$ , and  $d_{\rm m}$  is the mass fractal dimension (defined under "Pore Characteristics") of the porous medium within which the diffusing particle is confined. Note that  $D_{\rm e}(x) = D_{\rm e}$  when  $d_{\rm t} = d_{\rm m}$ . Again, this  $D_{\rm e}$  is generally not dimensionally consistent with the standard diffusion equation.

Anderson et al. (1996) used Eq. [14], in conjunction with digitized images of thin sections, to investigate the influence of pore space geometry on diffusion in soil systems. Giona et al. (1996) applied renormalization analysis to study diffusion and convection on fractal media. Coppens (1997), Santra et al. (1997), and Levitz (1998) have studied the effects of geometrical confinement on diffusion in the Knudsen regime, in which particle collisions with a fractal internal surface dominate over particle-particle collisions.

#### **Interfacial Instabilities**

Fluid properties must also be considered in any mixing process. Interfacial instabilities, or fingers, are driven by differences in liquid density and/or viscosity when two fluids are accelerated in a direction perpendicular to their interface. The density difference provides unbalanced acceleration forces, while the different viscosities account for unequal drag forces (Biggar & Nielsen, 1967). Fingers develop in response to small perturbations. In flow through natural porous media, these perturbations are continuously generated by physical heterogeneities, such as differences in pore geometry (Shikaze et al., 1998), and/or spatial variation in permeability (Moissis & Wheeler, 1990; Liu & Dane, 1997).

Fingering can cause the displacing solution to run ahead of the average displacement front when a concentrated solution displaces a more dilute one during vertical saturated flow (Mulqueen & Kirkham, 1972). Density differences as small as  $0.0002 \text{ g cm}^{-3}$  have been shown to significantly alter the shape of the breakthrough curve, and thus estimates of K (Rose & Passioura, 1971; James & Rubin, 1972).

The most important early work on interfacial instabilities is that of Saffman and Taylor (1958) who considered the stability of an interface between two immiscible fluids moving vertically through a porous medium. Wooding (1959,

1962a,b) and Bachmat and Elrick (1970) investigated free convective mixing of two miscible fluids, that are initially at rest in a saturated column. Biggar and Nielson (1964), Krupp and Elrick (1969), and Rose and Passioura (1971) extended this work to miscible displacement experiments with a uniform velocity distribution. Stockman (1997) and Perea-Reeves and Stockman (1997) used cellular automata to show the increases in dispersion that occur as a result of fluid buoyancy differences. Recently, Bués and Aachib (1991) have established a stability criterion for miscible displacement processes that is defined as a function of two dimensionless numbers,  $G^*$  and  $Rm^*$ . The  $G^*$  parameter reflects the ratio of gravitational forces to viscosity forces, while the  $Rm^*$  parameter is a modification of the Rayleigh number, which is normally used to determine the onset of convection in heated fluids. Additional research is needed to assess whether these stability criteria are applicable to structured porous media as well as to incorporate the impacts of interfacial instabilities in solute transport models.

#### **Molecular Size Effects**

Different-sized nonreactive solutes may experience differential spreading in a porous medium due to molecular sieving and/or differences in their diffusion coefficients. Large solute molecules are more likely to be excluded from small pores than smaller molecules. The diffusion coefficient for a given solute is a function of solute properties such as size or molecular weight. Thus, solute size can affect the diffusive transfer of molecules between regions of mobile and immobile water. Breakthrough curves obtained with solutes of different sizes may be useful for characterizing the pore-size distribution (Hu & Brusseau, 1995; Baltus, 1997).

# **Mechanical Mixing**

Mechanical mixing is caused by the convective flow of a fluid through a porous medium. It occurs at microscopic, mesoscopic, and macroscopic spatial scales, corresponding to the intrapore, interpore, and Darcian flow regimes, respectively. At the microscopic scale, mixing occurs within individual pores due to variations in velocity as a function of distance from the solid surface. For a straight cylindrical tube, the relationship between the velocity distribution, v(y), and the radial distance from the center of the tube, y, is given by Poiseuille's law (Kutílek & Nielsen, 1994),

$$v(y) = 2v \left(1 - \frac{y^2}{r^2}\right)$$
 [15]

where r is the tube radius.

Mixing due to the microscopic distribution of pore water velocities, known as hydrodynamic dispersion, is illustrated in Fig. 3–2. Figure 3–2A shows the pore water velocity profile, v(y) for Poiseuille flow in a uniform capillary tube of radius r. Additional spreading can occur due to the irregular shape of natural pores as compared to ideal cylinders (Fig. 3–2B).

At the mesoscopic scale, differential mixing occurs between individual pores because of differences in pore size and connectivity (Fig. 3–3). Differences in mean

pore water velocity resulting from differences in the radii of uniform capillary tubes are illustrated in Fig. 3–3A, while Fig. 3–3B shows the dispersion that results from flow paths splitting at a junction of three uniform capillaries with the same radii. From Poiseuille's law it is easy to show that  $v \propto r^2$ . Thus, on average, solute particles in large pores will travel greater distances than those in small pores over the same time interval. Because of connections between pores, streamline directions tend to vary with respect to the mean direction of flow. In addition, incomplete connectivity results in autocorrelation of flow paths, i.e., some flow paths become inaccessible to a fluid element once it has entered a particular pore network. Dispersion can also occur in response to recirculation of fluid due to local flow restrictions (Greenkorn & Kessler, 1969). It is the combined effects of microscopic and mesoscopic mechanical mixing processes that are commonly observed with short columns in the laboratory.

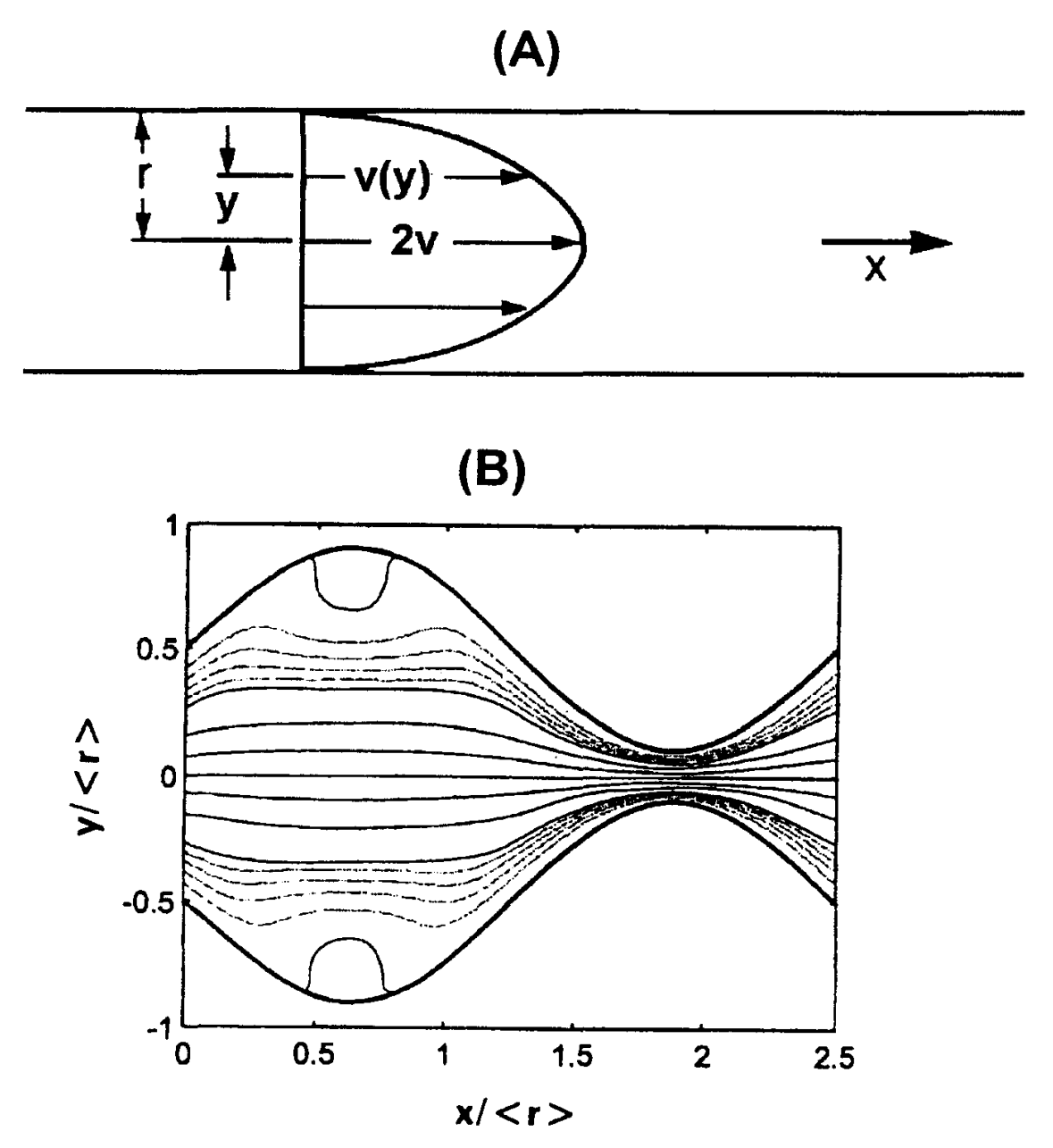


Fig. 3-2. Poiseuille flow in: (A) a uniform capillary, and (B) a sinusoidal capillary (Kitanidis & Dykaar, 1997).

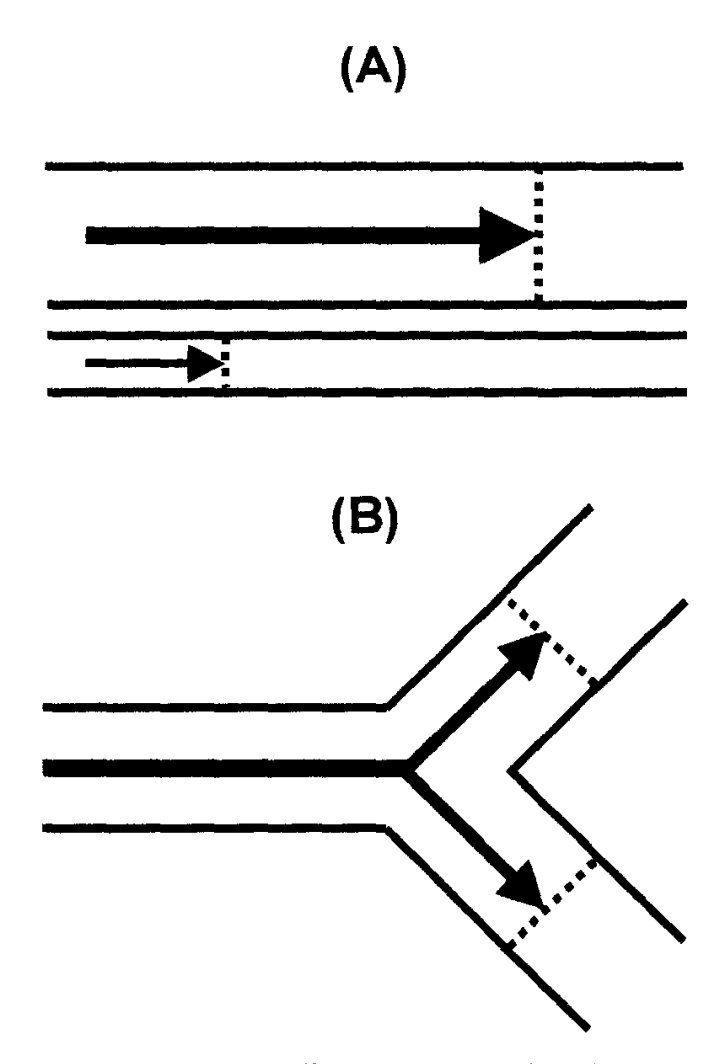


Fig. 3–3. Differential plug flow due to: (A) differences in tube radii, and (B) tube interconnectivity.

Solute spreading also occurs at the macroscopic scale due to heterogeneous permeability fields. Figure 3–4 shows examples of predicted flow lines for spatially periodic and fractal distributions of intrinsic permeability. Dispersion occurs as a result of the spatial variation in flow caused by regions of differing permeability. Macroscopic estimates of dispersivity obtained by fitting the CDE to experimental breakthrough curves tend to increase as a power law function of the length scale over which the transport experiment is conducted (Anderson, 1984; Neuman, 1990; Gelhar et al., 1992). This is because the solute plume experiences increasing variation in the permeability field the further it travels from the source. The fractional CDE appears to account for this phenomenon (Benson, 1998).

Most research on macroscopic dispersion has focused on the prediction of solute spreading from knowledge of the spatial distribution and covariance of the log-transformed saturated hydraulic conductivity,  $\ln(k_{\rm sat})$ . Theoretical models have been developed for exponential and fractal autocorrelation functions (Gelhar & Axness, 1983; Dagan, 1984, 1994; Koch & Brady, 1988; Kemblowski & Wen, 1993; Neuman, 1995; Zhan & Wheatcraft, 1996; Hassan et al., 1997). While these models may explain the scale-dependency observed in dispersivity, they lack predictive power because multiple spatial measurements of  $\ln(k_{\rm sat})$  are needed and such data are not easy to collect. Moreover, they are macroscopic averages that depend

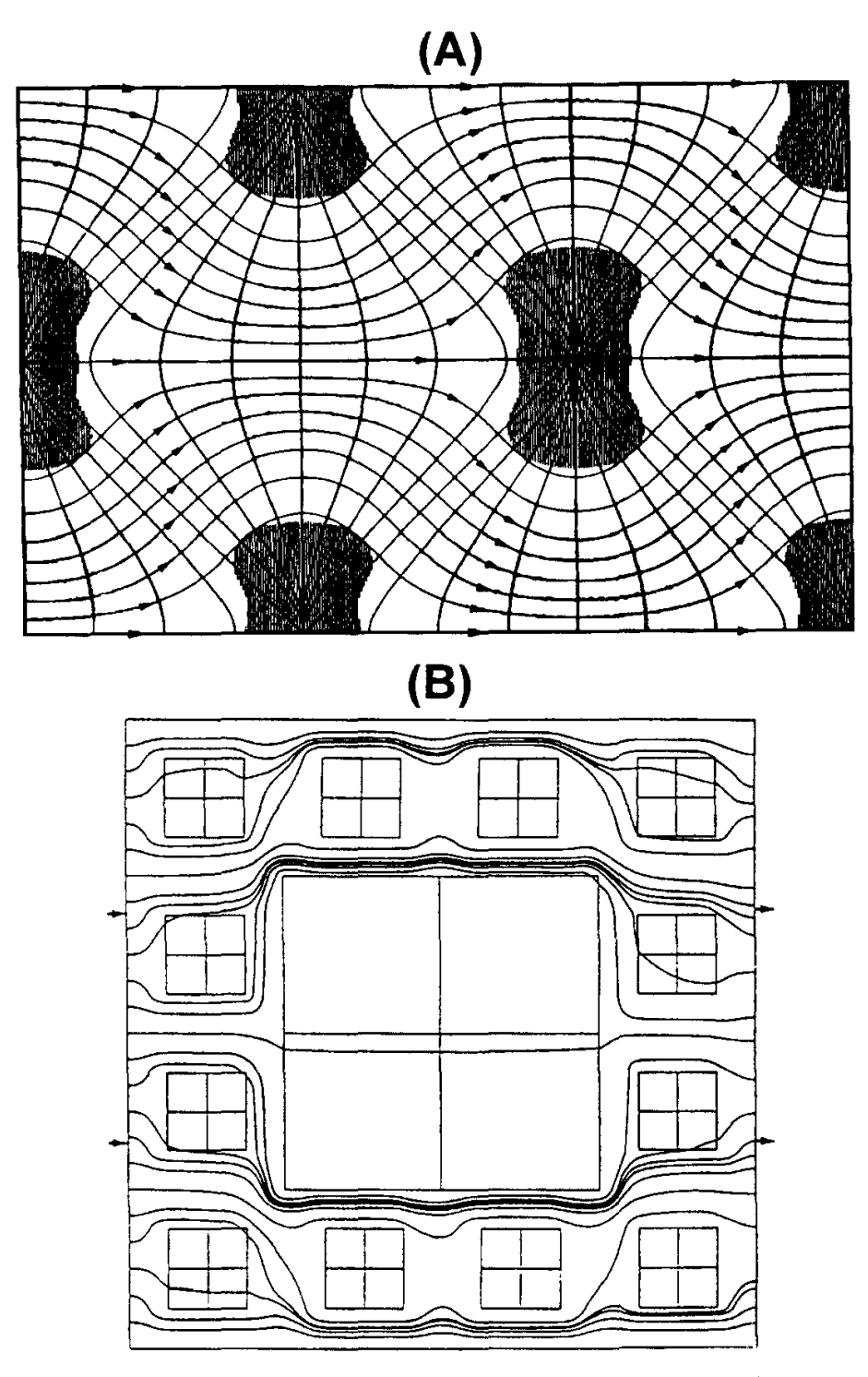


Fig. 3–4. (A) Steamlines in a spatially periodic  $k_{\text{sat}}$  field (Philip, 1986), (B) streamlines in a prefractral  $k_{\text{sat}}$  field (Wheatcraft et al., 1991). The direction of flow is from left to right in both cases.

on the existence of some representative elementary volume (REV), and have not been directly related to pore geometry.

It is not generally possible to separate out the effects of diffusion, interfacial instabilities, and mechanical mixing on solute spreading. However, in any study of the relationship between pore characteristics and solute dispersion, mechanical mixing must be maximized relative to diffusion, and the properties of the displacing and displaced fluids should be matched as closely as possible to avoid interfacial

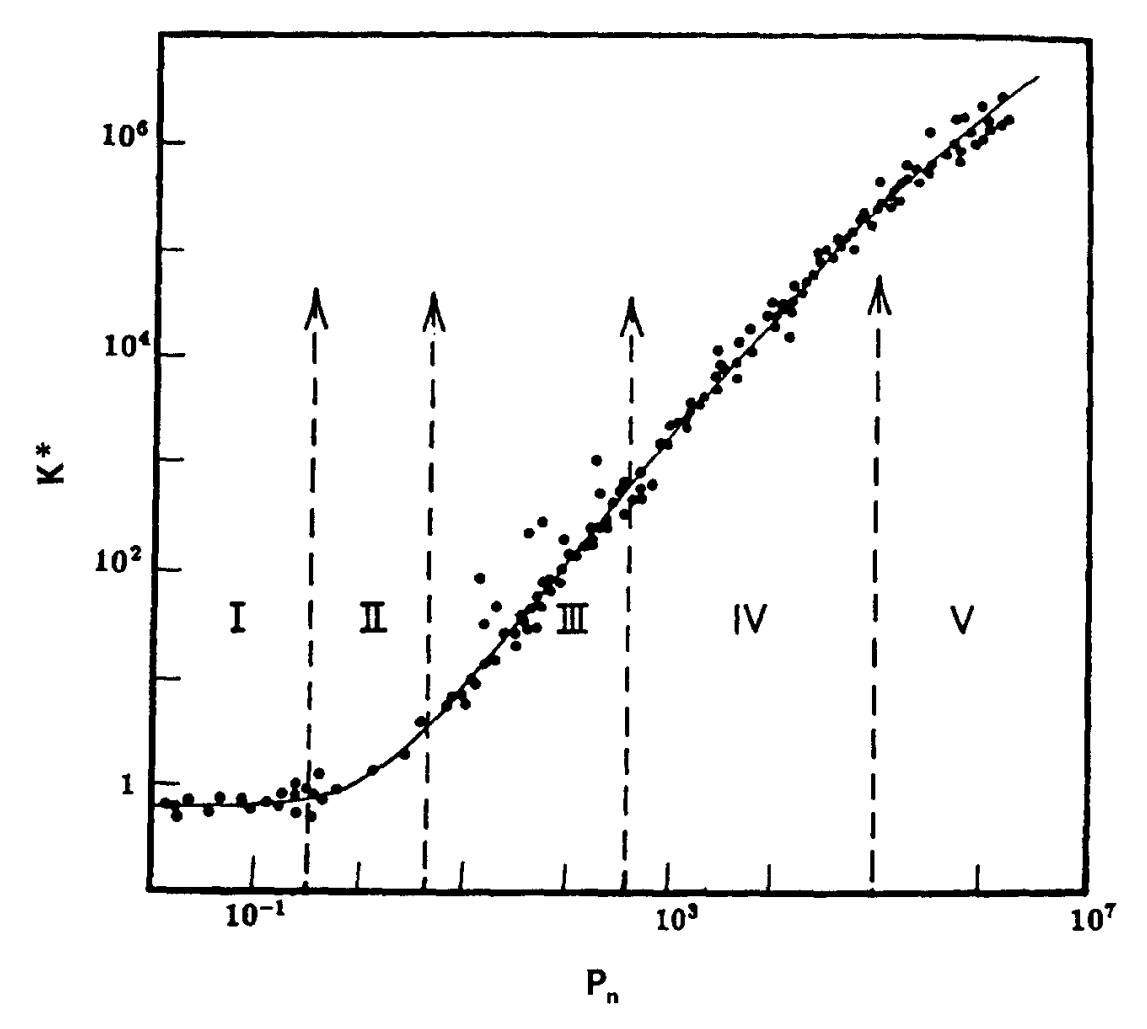


Fig. 3–5. Empirical relationship between the dimensionless longitudinal dispersion coefficient and the Peclet number (Fried & Cornbarnous, 1971).

instabilities. It is also important to maintain steady state flow conditions. Scotter and Raats (1968) and Sobey (1982, 1985) considered convective dispersion in porous media subjected to oscillating flows. The oscillatory nature of the flow regime effectively de-coupled dispersion from pore space geometry. In essence, channel geometry, flow rate, and oscillation frequency interacted to induce vortex formation even though the flow was laminar. Transient flows, which are not considered elsewhere in this review, but are undoubtedly a feature of some natural systems, are likely to enhance dispersion as compared to steady flows.

Experiments on packed beds (as summarized by Fried & Combarnous, 1971, Rose, 1977; Sahimi, 1993) indicate that there are five different dispersion regimes (Fig. 3–5). For  $P_n < 0.3$  (Region I) convection is so slow that diffusion completely controls the mixing process. Region II  $(0.3 < P_n < 5)$  is a transition regime in which the contributions of diffusion and convection are approximately equal and additive. In Region III  $(5 < P_n < 300)$  convection dominates dispersion, but the contribution of diffusion cannot be neglected. Over the range  $300 < P_n < 10^5$  (Region IV) mixing occurs primarily due to convection. For  $P_n > 10^5$  (Region V) flow is turbulent for many fluids, and Darcy's law is no longer valid. This regime is rarely encountered in soils. From the above discussion it is clear that studies that seek to establish relationships between pore characteristics and solute dispersion need to be fo-

cused on Regions III and IV, i.e., within the range  $5 < P_n < 10^5$ . Unfortunately, experimental data similar to those in Fig. 3–5 are not available for more heterogeneous porous media. Furthermore, it is not clear that  $P_n$  can be explicitly defined for such media due to the lack of a well-defined characteristic mixing length,  $\ell$ .

#### PORE CHARACTERISTICS

This section focuses on pore characteristics relevant to solute transport. Soil structural form is often described in qualitative geometrical terms, such as "very coarse prismatic" or "medium subangular blocky" (Soil Surv. Div. Staff, 1993). While observed differences in the shapes of solute breakthrough curves can be related to such descriptions (e.g., Anderson & Bouma, 1977; Vervoort et al., 1999), they are generally unsuitable for inclusion in quantitative transport models. Here we present some geometrical and topological approaches for characterizing irregular pore structures, and briefly discuss methods of measuring key parameters.

Soil pore space is three-dimensional. However, because of methodological constraints, data are often collected in one- or two-dimensions. For some characteristics it is possible infer three-dimensional estimates from data collected in lower dimensions using stereology. Readers are referred to Weibel (1987) and Ringrose-Voase and Nortcliff (1987) for more details on this subject.

# **Total Porosity**

The total porosity,  $\phi$ , is defined as the volume fraction of pore space in a porous medium. It is related to the bulk density  $(\rho_b)$  as follows:

$$\phi = 1 - (\rho_b/\rho_s) \tag{16}$$

where  $\rho_s$  is the particle density, often assumed to be equal to that for quartz (i.e., 2.65 g cm<sup>-3</sup>). The total porosity contains no information about the size, shape and arrangement of pores. In addition, it is a macroscopic variable that depends on the existence of a representative elementary volume. However, it is easily measured and can be theoretically and experimentally related to pore connectivity, and thus to dynamic properties such as  $k_{\text{sat}}$  (Sahimi, 1993; Giménez et al., 1997a). As result, some researchers have sought to link variations in  $\phi$  with macroscopic dispersion in heterogeneous porous media (e.g., Warren & Skiba, 1964; Lin, 1977). Hassan et al. (1998) report that a positive correlation between  $\phi$  and  $k_{\text{sat}}$  decreases macroscopic dispersion as compared to the uncorrelated case. It should be noted that for  $K^* \propto P_n$ , the dimensionless dispersion coefficient is inversely proportional to  $\theta$ , which is equal to  $\phi$  in saturated systems; this can be shown by equating v in Eq. [6b] with v in Eq. [5] and assuming a constant flux and characteristic length.

# Shape

A wide variety of geometrical constructions have been used, both separately and in combination, to model the shape of soil pores (Fig. 3–6). Van Brakel (1975)

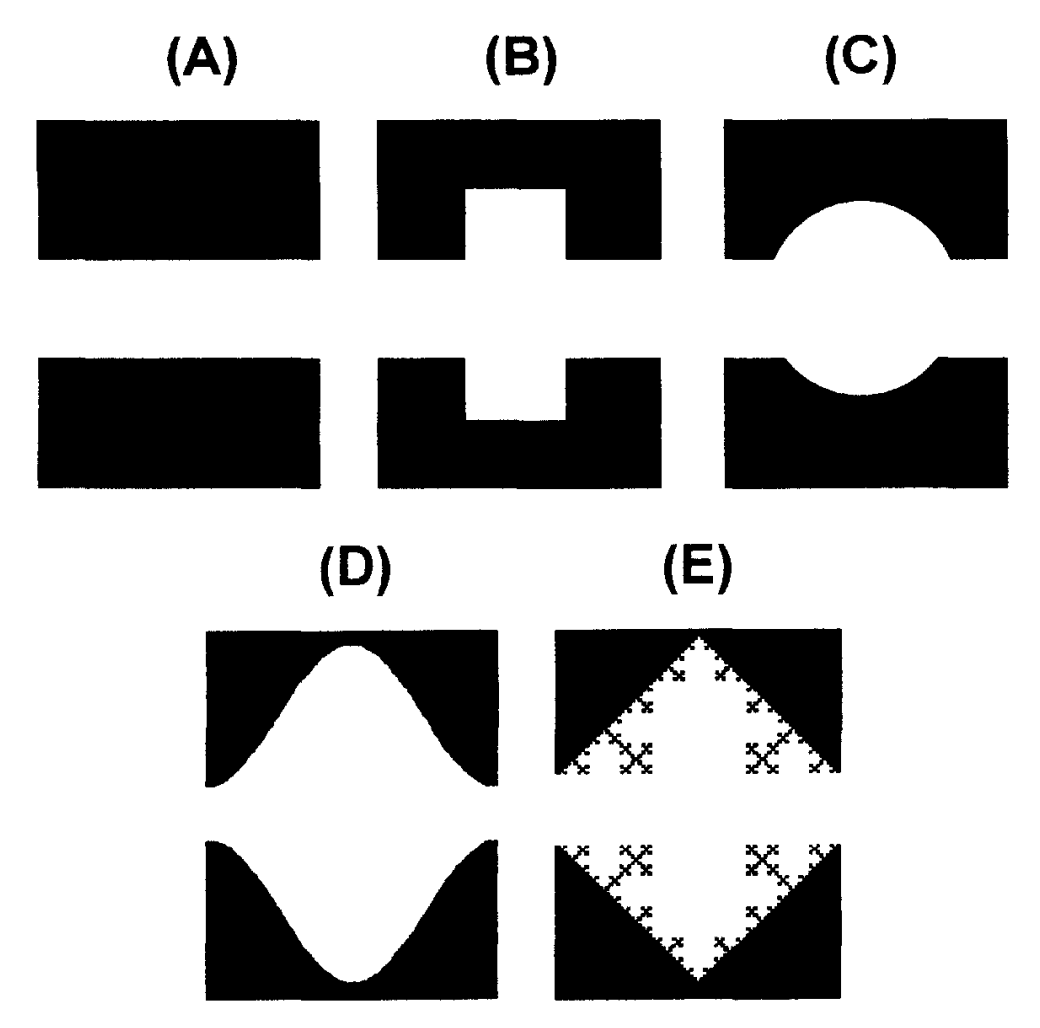


Fig. 3–6. Cross-sections through various geometric pore models: (A) uniform capillary, (B) indented capillary (cylinders with different radii), (C) indented capillary (sphere with cylinders), (D) sinusoidal capillary, and (E) prefractal capillary.

has presented a systematic inventory of the different Euclidean models that have been proposed. The cylinder (Fig. 3–6A) is the simplest and most widely used pore shape model (e.g., Klinkenberg, 1957; Marshall, 1958). More sophisticated Euclidean models include periodically constrained capillary tubes (e.g., Hoagland & Prud'homme, 1985) and spheres with cylindrical appendages (e.g., Chatzis & Dullien, 1985; Ferrand & Celia, 1992). These models (Fig. 3–6B–D) all include the concept of pore bodies being separated from other pore bodies by local minima in the pore size, known as pore throats (Dullien, 1992). In a network representation of porous media, the pore bodies correspond to the sites or nodes of the network, and the pore throats to its bonds (Sahimi, 1993).

Several indices are available for characterizing the extent to which natural pores deviate from the idealized Euclidean models discussed above. The simplest of these is the circularity or compactness,  $\dot{C}$ , defined as (Schwartz, 1980):

$$\dot{C} = 4\pi \left( A/P^2 \right) \tag{17}$$

where A is cross-sectional area, and P is perimeter. For a circle,  $\dot{C}=1$ ; for irregular shapes,  $\dot{C}$  decreases as the irregularity increases. Other methods of characterizing two-dimensional pore outlines, including chart comparisons, aspect ratios,

elongation, and Fourier analysis, have been reviewed by Murphy et al. (1977), Ringrose-Voase and Bullock (1984), Orford and Whalley (1991), and Horgan (1998).

Fractal geometry, as expounded by Mandelbrot (1983), allows for a more detailed representation of natural structures than conventional Euclidean geometry. As a result, fractal models are becoming increasingly popular for simulating soil structure and rock fractures (Thompson, 1991a; Sahimi, 1993; Giménez et al., 1997a; Baveye et al., 1998; Anderson et al., 1998; Pachepsky et al., 2000). True fractals can exist only as mathematical constructs, since they are physically unbounded. In contrast, a prefractal, which exhibits fractal scaling over a certain range of scales, is characterized by well-defined upper and lower scaling limits. There are several types of prefractal geometric models that are applicable to natural porous media, including surface and mass prefractals.

Surface prefractals are most appropriate for modeling the irregular shape of pore surfaces. Schwartz et al. (1989) were the first to simulate pore surface roughness using a surface prefractal model. Fig. 3–6E shows a cross-section through a prefractal capillary similar to their original model. The prefractal cross-section in Fig. 3–6E has a fractal scaling ratio,  $b_{\rm f}$ , of 3, a boundary fractal dimension,  $d_{\rm b}$ , of 1.465, and was iterated to the i=4 level.

A number of different methods are available for obtaining prefractal pore shape characteristics (Sahimi, 1993; Russ, 1994). We will focus on adsorption and image analysis, since these are the most direct and widely used methods. Avnir et al. (1983) and Pfeifer and Avnir (1983) pioneered the development of adsorption techniques to characterize pore surface properties. Their original idea was that different-sized molecules could be used as yardsticks to measure the area of a prefractal surface as a function of the size of the yardstick. Monolayer coverage (that is typically determined from an adsorption isotherm) for various species with different molecular surface areas,  $\omega$ , can then be shown to satisfy the relation,

$$n_{\rm a} \propto \omega^{\rm d_s/2}$$
 [18]

where  $n_a$  is the number of adsorbed molecules and  $d_s$  is the surface fractal dimension. Avnir et al. (1985) later extended the method to describe adsorption of a single molecular species on aggregates from different size fractions. This approach has been applied to a wide variety of rock and soil materials, with estimates of  $d_s$  falling in the expected range from 2 to 3 (Avnir et al., 1985).

Image analysis of soil thin sections is the other method that is commonly used for characterizing pore shape. Because of measurement constraints, these analyses are generally conducted in two dimensions, and thus it is the boundary fractal dimension that is used to quantify pore surface roughness (Kampichler & Hauser, 1993; Anderson et al., 1996; Pachepsky et al., 1996). The  $d_b$  is defined by the following equation (Mandelbrot, 1983),

$$L(\varepsilon) = L_1 \varepsilon^{1 - d_b}$$
 [19]

where  $L(\varepsilon)$  is the measured length using a yardstick of normalized length  $\varepsilon$ , and  $L_1$  is the measured length when  $\varepsilon$  is equal to unity. Assuming an isotropic pore surface,  $d_s$  can be computed from  $d_b$  using the simple relationship,  $d_s = d_b + 1$  (Man-

delbrot, 1983). Allen et al. (1995) have reviewed the different techniques that are available to estimate  $d_b$  from two-dimensional images of pore shapes.

#### Size

Size can refer to volume, area, or length, and therefore pore-size distribution may be defined in terms of any one of these properties. In practice, the definition of size adopted is highly dependent upon the method of measurement. For example, the area size distribution of pores is often measured by image analysis of soil thin sections, while water retention data are usually interpreted in terms of the distribution of pore diameters (Bullock & Thomasson, 1979). For consistency with the definition of the Peclet number, we have chosen to define size in terms of length, L. Dullien (1991) has proposed the following interrelationships between the different definitions of size: L = V/S in three-dimensions or L = A/P in two-dimensions, where V is volume, S is surface area, A is cross-sectional area and P is perimeter. These relations can be used to compare pore-size distributions measured using different methods.

The characteristic length of a pore will depend upon the model of pore shape adopted. Only a few Euclidean shapes can be represented by a single characteristic length (diameter and edge length for spheres and regular polyhedra, respectively). For irregularly shaped pores no single measure of size is possible, and some form of averaging procedure must be employed. For example, star length is the expected value of the length distribution obtained by placing a point at random within a pore, and measuring the distance to the nearest solid surface in one or more randomly chosen directions (Serra, 1982).

Established methods of measuring the size distribution of pores in rocks and soils include water retention, mercury porosimetry, inverse flow procedures, and image analysis (Lawrence, 1977; Dullien, 1992). Methods based on nuclear magnetic resonance (NMR), small angle scattering (SAS), and computer assisted tomography (CAT scanning) are also being developed. The reader is referred to Anderson and Hopmans, (1994) and Sahimi (1995) for more information on these newer techniques.

In the water retention (e.g., Childs, 1940; d'Hollander, 1979) and Hg porosimetry (e.g., Washburn, 1921; Nagpal et al., 1972) methods, length is measured as an equivalent cylindrical radius,  $r_{\rm c}$ , that is calculated according to the following relationship,

$$r_{\rm c} = \frac{2\phi \cos \upsilon}{\Psi g \rho_1} \tag{20}$$

where  $\varphi$  is the liquid-vapor interfacial tension,  $\upsilon$  is the liquid-solid contact angle, g is the constant for gravitational acceleration,  $\rho_l$  is the liquid density, and  $\psi$  is the hydraulic head. Although widely used, Eq. [20] suffers from the same limitations as other idealizations based on non-interacting capillary bundles (see "Geometric Dispersion Models"). Alternative models for estimating size distributions of pore bodies and throats are discussed by Sahimi (1993) and Celia et al. (1995). A simple illustration of the differences between methods based on Eq. [20] and those based on network modeling is given by Zhou and Stenby (1993).

Another measure of length is the equivalent hydraulic radius,  $r_h$ , determined inversely from saturated or unsaturated flow experiments. By comparing Darcy's equation with Poiseuille's law, and invoking a capillary bundle model, one obtains the following definition of  $r_h$  (Kutílek & Nielsen, 1994),

$$r_{\rm h} = \left(\frac{8\eta k_{\rm sat}}{\phi \rho_1 g}\right)^{1/2}$$
 [21]

where  $\eta$  is the dynamic viscosity. Equation [21] can be used to estimate  $r_h$  from measurements of  $k_{\rm sat}$  and  $\phi$ . This approach is most applicable to systems dominated by pores of uniform size and shape. Dunn and Phillips (1991) have investigated the influence of systematic variations in pore shape on estimates of  $r_h$  obtained with Eq. [21]. Philip (1987) proposed an alternative definition of  $r_h$  based on the macroscopic capillary length parameter ( $L_c$ ) determined by fitting an exponential function to the unsaturated hydraulic conductivity-water potential curve,

$$r_{\rm h} = \varphi / \rho_1 g L_{\rm c} \tag{22}$$

With tension infiltrometers it is possible to estimate  $L_{\rm c}$  and thus  $r_{\rm h}$  from field measurements of three-dimensional, unconfined, unsaturated flow (White & Sully, 1987).

Image analysis of digitized thin sections is perhaps the most direct method of quantifying pore-size distributions. This approach involves four steps: thin section preparation, imaging, thresholding, and quantification. Murphy (1986) has summarized the basic methods of thin section preparation. Moran (1994) has reviewed issues related to data acquisition and processing. Recently, McBratney and Moran (1993) and Moran and McBratney (1997) have proposed a conceptual model for simulating gray level images of pore-solid structure based on fuzzy random sets. Binary images are derived from gray-level images by thresholding, a process by which pixels that are lighter or darker than a given value are assigned to the void and solid phases, respectively. The pore size distribution is then obtained directly from the digitized image. Several working definitions of length are available for this purpose, including the Feret diameter (Murphy et al., 1977) and the one-dimensional star length (Serra, 1982; Moran & McBratney, 1992). The mathematical set operations of erosion, dilation, opening, and closing can be used to resolve questions of pore connectivity prior to measuring the length of individual pores (Vogel, 1997; Horgan, 1998).

Binary soil images are readily analyzed using fractal techniques, including the box counting, chord length, and autocorrelation methods (Thompson, 1991a; Garrison et al., 1992, 1993; Sahimi, 1995). The basic objective of such analyses is to characterize the porous medium in terms of the mass fractal dimension,  $d_{\rm m}$ , as defined by the following equation (Mandelbrot, 1983):

$$N(\varepsilon) = N_1 \varepsilon^{\mathbf{d}_{\mathrm{m}}} \tag{23}$$

where  $N(\varepsilon)$  is the number of boxes of length  $\varepsilon$  not containing pores, and  $N_1$  is the number of boxes not containing pores when  $\varepsilon$  is equal to unity. Estimates of  $d_{\rm m}$  ob-

tained by applying Eq. [23] to two-dimensional images of natural porous media range from 1.22 to 1.85 (Giménez et al., 1997b). Spatial variability in the pore-size distribution can be quantified through the use of multifractal spectra (Saucier & Muller, 1993; Muller, 1996). Fractal analyses have also been employed to parameterize the pore-size distribution inferred from water retention and mercury porosimetry measurements (e.g., Friesen & Mikula, 1987; Brakensiek & Rawls, 1992; Perfect, 1999). Discrepancies between estimates of  $d_{\rm m}$  obtained by these different methods have been discussed by Crawford et al. (1995) and Bird and Dexter (1997).

Use of Eq. [23] automatically implies a power law distribution of pore sizes. A variety of other distribution functions, including the log-normal, incomplete Gamma, and Weibull distribution functions, have also been used to characterize natural pore-size distributions (e.g., Brutsaert, 1966). Furthermore, it is possible to parameterize the pore size distribution without resorting to a particular distribution function model using moment analysis (Brutsaert, 1966; Powers et al., 1992).

### **Arrangement and Connectivity**

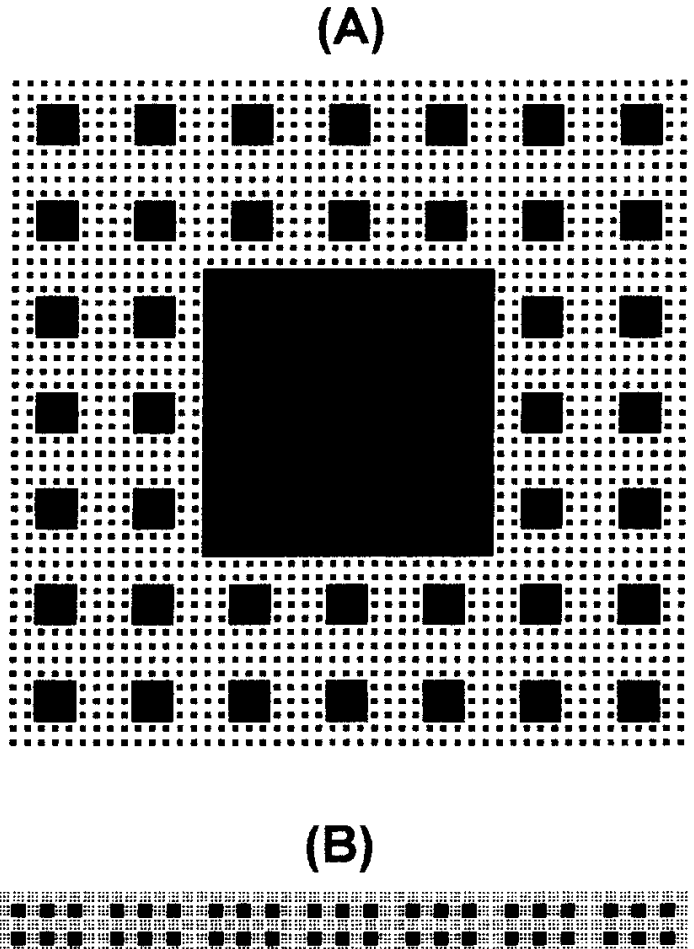
The spatial arrangement and interconnectivity of the pore space in rocks and soils can be characterized using principles derived from topology. Topological properties of structures are invariant under any deformation of their embedding space, and can be related to Euclidean geometrical shapes through the Gauss-Bonnett theorem (Kreyszig, 1959; Alexandroff, 1961). Topologically, the solid and void phases in a porous medium are conjugate; i.e., it is possible to infer the topology of the solid matrix from measurements made on the pore space, and vice versa. Several measures have been used to characterize the topology of natural porous media; these can be classified as either static or dynamic measures.

The simplest static property is the mean coordination number, <Z>, which is loosely defined as the average number of pore throats per pore body (Dullien, 1991). For spatially periodic systems, such as cubic packing of uniform spheres, it is relatively easy to determine <Z>. Methods of estimating <Z> for more heterogeneous porous media are reviewed by Sahimi (1995).

More detailed information about the topology of a porous medium can be obtained from its Betti numbers. Many different Betti numbers can be defined, and for two structures to be topologically equivalent all of their Betti numbers must be equal (Alexandroff, 1961). For applications in the earth sciences, however, it is usually sufficient to consider only the zeroth  $(B_0)$  and first  $(B_1)$  Betti numbers (MacDonald et al., 1986a,b; Scott et al., 1988a,b). The  $B_0$  is a topological measure of the number of isolated pores within the solid matrix, while the  $B_1$  (also called the genus) equates to the number of independent pathways between two points in the pore space. The Euler-Poincaré number,  $E_n$ , defined as  $B_0$  minus the number of solid islands within the pore space, can be used as an estimate of  $B_1$  in images of two-dimensional sections through three-dimensional structures (Chen & Yan, 1988; Vogel & Kretzschmar, 1996). The  $E_n$  provides a static measure of pore connectivity; the more negative the value, the greater the connectivity. The  $E_n$  can be determined from image analysis of serial thin sections (Vogel, 1997) or from a pair of closely spaced parallel sections known as a dissector (Vogel & Kretzschmar, 1996).

Estimates of  $E_n$  vary with pore size and thresholding level (Moran & McBratney, 1997; Vogel, 1997).

Betti numbers can be applied to prefractal systems. For example, Fig. 3–7 shows two deterministic Sierpinski carpets with the same mass fractal dimension,  $d_{\rm m}=1.896$  and Euler-Poincaré number,  $E_{\rm n}=0$ . The two constructions are topo-



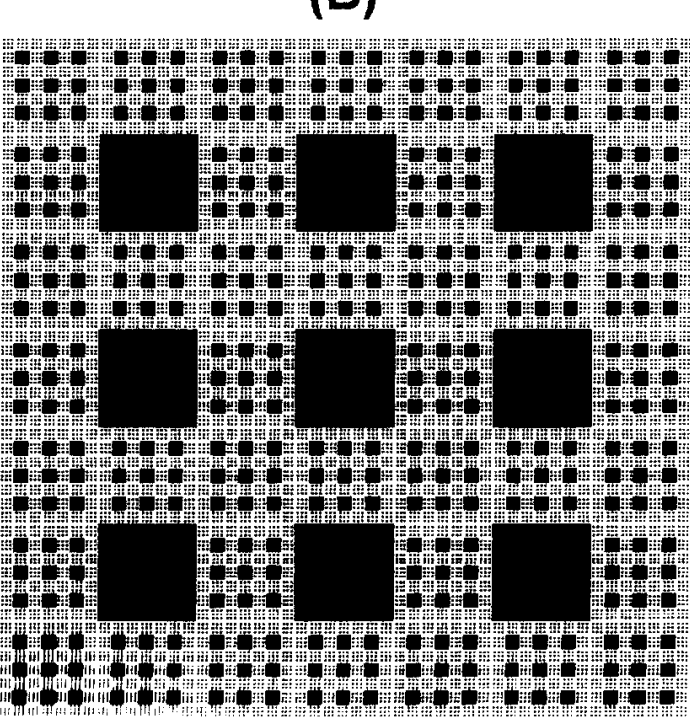


Fig. 3. 7. Examples of Sierpinski carpets with the same fractal dimension ( $d_{\rm in}=1.896$ ), and different zeroth Betti numbers

logically very different. This is because  $B_0 = 1$  for the generator employed in Fig. 3–7A, as compared to  $B_0 = 9$  for the generator in Fig. 3–7B. Values of  $B_0$  and  $E_n$  can be expected to change as a function of iteration level, particularly in the case of randomized prefractals. Further research is needed on the theoretical nature of these relations. Alternatively, it may be possible to apply iterated function systems (Barnsley & Demko, 1985) to deduce the fractal generator for a given system and then use Betti numbers to quantify its topology. The clustering of voids in prefractal porous media has also been characterized by a measure known as lacunarity,  $\Lambda(\varepsilon)$  (Mandelbrot, 1983; Voss, 1986). The  $\Lambda(\varepsilon)$  can be derived from the fluctuations that occur around the power law relationship of Eq. [23] (Gouyet,1996). The  $\Lambda(\varepsilon)$  is periodic in  $\log(\varepsilon)$  for deterministic prefractals obtained by iterating a generator, and aperiodic for randomized prefractals. Zeng et al. (1996) showed that  $\Lambda(\varepsilon)$  was a more sensitive parameter than  $d_m$  for identifying differences in small-scale soil bulk density data collected with x-ray computed tomography.

While static properties are widely used to characterize pore space topology, dynamic approaches are more directly relevant to transport in porous media. Ma and Selim (1994) used the CDE, fitted to tritium BTCs, to estimate tortuosity (f) inversely for various repacked soil materials. Silliman and Wright (1988) utilized a Monte Carlo approach to investigate the existence and structure of continuous flow paths in variable  $k_{\rm sat}$  fields. Eggleston and Pierce (1995) developed a method, based on the principles of dynamic programming, to determine f from digitized images of soil thin sections. Pathways for flow were identified by minimizing a resistance factor, which in this study depended only on path length. Tortuosity was then calculated from the mean primary path length divided by the image length. The f computed in this way is closely related to the spreading dimension, a parameter commonly used to characterize connectivity in fractal systems (Gouyet, 1996).

#### **EXPERIMENTAL STUDIES**

Relatively few experimental studies have been conducted in which the solute breakthrough curve and pore characteristics were determined on the same undisturbed samples, thereby permitting the establishment of empirical relationships. Instead, the majority of studies have been on packed beds (see e.g., Passioura & Rose, 1971; Jensen, 1983; Han et al., 1985). Since it is the geometrical characteristics of the solids or aggregates that are measured in this approach rather than the pore characteristics, the resulting relationships are not directly applicable to undisturbed heterogeneous porous media. Studies on packed beds with constructed macropores of varying size and shape (Kanchanasut et al., 1978; Li & Ghodrati, 1997) and on micromodels (see "Emerging Areas"), may provide more information on the relationship between solute spreading and pore space geometry, but are subject to similar criticisms regarding their applicability to natural systems.

For heterogeneous porous media, Anderson and Bouma (1977) observed greater Cl<sup>-</sup> dispersion in undisturbed soil samples with subangular blocky structure as compared to prismatic structure. Walker and Trudgill (1983) reported significant correlations between solute transport parameters and several pore geometry variables measured by image analysis of soil thin sections. Gist et al. (1990)

showed that tracer dispersion in consolidated rocks was a function of the width of the pore-size distribution determined by mercury porosimetry. Soil dispersivities have also been related to the width of the pore size distribution, as inferred from the slope of the water retention curve (Vervoort et al., 1999).

Several authors have investigated the relationship between pore structures revealed by dye staining patterns and solute transport parameters. Seyfried and Rao (1987) and Vervoort et al. (1999) report increasing solute dispersivity with decreasing percentage dyed area. Percentage dyed area can be thought of as a flow-weighted measure of pore size and connectivity, with small values corresponding to high macropore connectivity and vice versa. Hatano et al. (1992) investigated the relationship between solute dispersion and the fractal geometry of dye staining patterns. These authors conducted Cl<sup>-</sup> miscible displacement experiments on undisturbed soil columns that were later destructively sampled, and their mass and surface fractal dimensions were determined by image analysis of methylene blue dye stains. An empirical equation was obtained by regression analysis relating the Brenner number for Cl<sup>-</sup> breakthrough to both the mass and surface fractal dimensions of the dye stained pore space.

#### **GEOMETRIC DISPERSION MODELS**

These models will be presented in order of increasing complexity in the representation of pore space geometry, from individual uniform pores to interacting nonuniform pore networks.

#### **Discrete Pore Models**

### **Uniform Shape**

The simplest discrete pore model is a straight cylindrical capillary tube of radius r and length l (Fig. 3–6A). Expressed in axisymmetric, cylindrical coordinates, the CDE for this model, incorporating Eq. [15] is (Taylor, 1953):

$$\frac{\partial C}{\partial t} = D \left( \frac{\partial^2 C}{\partial y^2} + \frac{1}{y} \frac{\partial C}{\partial y} + \frac{\partial^2 C}{\partial x^2} \right) - 2v \left( 1 - \frac{y^2}{r^2} \right) \frac{\partial C}{\partial x}$$
 [24]

where D is assumed to be independent of C. While numerical techniques have been employed to solve Eq. [24] directly (Ananthakrishnan et al., 1965; Nunge & Gill, 1970), no exact analytical solutions are available. However, by applying the limiting condition  $\sqrt{48} << P_n << 4l/r$ , and assuming that longitudinal molecular diffusion is negligible, Taylor (1953, 1954) was able to reduce Eq. [24] to:

$$\frac{\partial < C >}{\partial t} \approx K \frac{\partial^2 < C >}{\partial x^2} - v \frac{\partial < C >}{\partial x}$$
 [25]

where  $\langle C \rangle$  is the mean solute concentration at distance x,  $K = DK^*$ , and

$$K^+ = 1 + (1/48) P_0^2$$
 [26]

where  $\ell = r$  in Eq. [5]. Gupta and Bhattacharya (1983) obtained a similar result using Markov process theory. In contrast to Eq. [24], Eq. [25] can be readily solved analytically. The solution for a step increase in solute concentration was derived and experimentally verified by Taylor (1953).

Equation [25] assumes diffusion takes place according to the standard Fickian model, i.e., Eq. [10]. Compte and Camacho (1997) studied the alternative case of a fractal time random walker, i.e., Eq. [13], being dragged by a solvent flowing through a uniform cylindrical capillary tube. The resulting longitudinal dispersion was not the same as the standard asymptotic behavior obtained for a Brownian walker.

Using the method of moments, Aris (1956) was able to generalize Eq. [25] for a straight tube with an aperture of arbitrary cross-section. His expression for the dimensionless dispersion coefficient is:

$$K^* = 1 + \gamma P_n^2$$
 [27]

where  $\gamma$  is a dimensionless number that depends upon the shape of the aperture. For an elliptical aperture, with major and minor semi-axes of a and b respectively, and  $\ell = a$  in Eq. [5],  $\gamma$  is given by (Aris, 1956):

$$\gamma = \frac{1}{48} \left( \frac{24 - 24(1 - b^2/a^2) + 5(1 - b^2/a^2)^2}{24 - 12(1 - b^2/a^2)} \right)$$
 [28]

Note that when b = a,  $\gamma = 1/48$ , as it should for a circle. Equation [27] also applies to unidirectional flow between parallel flat plates, and can be used as a model for solute dispersion in rock fractures. Setting  $\ell$  in Eq. [5] equal to the separation distance between two plates, it can be shown that  $\gamma = 1/210$  (Aris, 1959a; Wooding, 1960). This result has been confirmed by numerical simulations (Koplik et al., 1993) and lattice-gas automata (Perea-Reeves & Stockman, 1997).

# Variable Shape

Natural systems rarely contain perfectly uniform, regular voids. A regular shape model may be unrealistic for macropores and fractures with irregular walls. Thus, it is useful to examine the impact of systematic variations in channel diameter on solute dispersion. Variable shape models are attractive for simulating pore scale dispersion because a single unit cell is often able to capture a wide range of transport processes, from convection in the center of the channel to diffusion in backwater zones near the apex (see Fig. 3–2B). Furthermore, the macroscopic behavior of such models can be predicted from well-defined geometric parameters.

Hoagland and Prud'homme (1985) presented a method of moments analysis of dispersion in a single sinusoidal capillary tube with solid walls (Fig. 3–6C). Their geometric model is defined by the wave length ( $\kappa$ ), the amplitude ( $\mathring{a}$ ) and mean radius ( $\langle r \rangle$ ) of the sine wave (z) that describes the aperture wall:

$$z = \langle r \rangle [1 + \text{å} \sin(2\pi x/\kappa)]$$
 [29]

Using Eq. [29] the following analytical solution was obtained for the dimensionless dispersion coefficient assuming long wavelengths and high Peclet numbers:

$$K^* = \frac{1}{(1 + \mathring{a}^2/2)^3} \left[ 1 + \frac{15}{2} \mathring{a} + \frac{45}{8} \mathring{a}^4 + \frac{5}{16} \mathring{a}^6 \right] + \frac{1}{48(1 + \mathring{a}^2/2)} \left[ 1 + 3\mathring{a}^2 + \frac{3}{8} \mathring{a}^4 \right] P_n^2$$
[30]

where  $\ell = \langle r \rangle$  in Eq. [5]. It should be noted that for a straight tube with å = 0, Eq. [30] properly reduces to Eq. [26]. For 0 < å < 1, dispersion is enhanced in the sinusoidal tube as compared to a straight tube. Equation [30] was confirmed for large Peclet numbers by comparison with results from a numerical Stokes solver (Hoagland & Prud'homme, 1985). Similar numerical simulations were reported by Cao and Kitanidis (1998a,b). Sobey (1982, 1985) extended the numerical approach to predict dispersion in symmetric and asymmetric sinusoidal capillaries during oscillatory flows.

Gill and Ananthakrishnan (1966) and Azzam and Dullien (1977) have numerically simulated flow in an indented cylindrical tube, with periodic step increases and decreases in radius r along its length l (Fig. 3–6B). By assuming water in the indentations is completely immobile, Turner (1958) and Aris (1959b,c) were able to formulate a two-region geometric capacitance model for solute dispersion in this system. By further assuming a parabolic velocity profile within the mobile water region, Aris (1959b) showed that the  $K^*$  for this region is given by Eq. [27], with l = r in Eq. [5] and,

$$\gamma = \frac{1 + 6\beta + 11\beta^2}{48(1+\beta)^2}$$
 [31]

where  $\beta$  is the volume of indentations (or immobile water) per unit volume of main channel (or mobile water). Equation [31] reduces to 1/48, the prefactor in Eq. [26], when  $\beta$  = 0, and predicts increased dispersion relative to the uniform case, when  $\beta$  is large. This trend is physically reasonable since the solute spends more time in the increased stagnant pore space. Predictions using Eq. [27] and [31] agree very well with numerical simulations of dispersion in indented capillaries as long as the elapsed time is sufficiently large (Gill & Ananthakrishnan, 1966). Aris (1959a) and Tsuda et al. (1991) have modified this approach to predict dispersion within cylindrical and parallel plate systems, in which the indentations merge to produce a continuous immobile water zone of uniform thickness immediately adjacent to the channel walls. Recently, Perea-Reeves and Stockman (1997) investigated dispersion in an alveolated channel with lattice gas cellular automata.

It is possible to incorporate fractal concepts into the indented capillary model described previously. Rotation of the cross-section shown in Fig. 3–6E about its central axis generates a three-dimensional prefractal capillary tube. The factor  $\gamma$  for this capillary tube is given by:

$$\gamma = \frac{1 + 6\beta_n + 11\beta_n^2}{48(1 + \beta_n)^2}$$
 [32]

where  $\beta_n$  is the total volume of indentations per unit volume of main channel after n iterations of the fractal generator, defined by:

$$\beta_{n} = \beta b^{2} \sum_{i=1}^{n} b^{(d_{b}-2)i-d_{b}}$$
 [33]

in which  $\beta$  is the Euclidean immobile-mobile water ratio for the first indentation as previously defined,  $b_f$  is the fractal scaling factor, i is the iteration level, and  $d_b$  is the boundary fractal dimension. The series summation in Eq. [33] rapidly converges and gives a constant value of  $\beta_n > \beta$  for n >> 1, e.g., for  $d_b = 1.465$  and  $b_f = 3$ , the limit is  $\beta_n = 2.25\beta$ . As a result of this increase in  $\beta_n$ , longitudinal dispersion is slightly enhanced in the prefractal capillary as compared to the indented capillary. However, this increase is much less than the increase in dispersion that occurs in response to the appearance of the first indentation relative to the uniform capillary tube. This can be seen by comparing  $K^*$  at n = 1 (the indented capillary) with  $K^*$  at n >> 1 (the prefractal capillary) in Fig. 3–8; the corresponding value of  $K^*$  for a uniform capillary is approximately 3. This analysis considers only the volume of the fractal indentations and does not address the likely impact of surface roughness on solute dispersion.

Random and/or natural surface roughness has been incorporated into models to predict solute dispersion. Koplik et al. (1993) numerically simulated solute dispersion in flow through a single two-dimensional channel bounded by parallel plates in which one face presented random rectangular irregularities perpendicular to the direction of flow (Fig. 3–9). They observed a tenfold increase in  $K^*$  between the smooth plate case and the maximum roughness case. Keller et al. (1999) have developed a method of predicting solute breakthrough in natural fractures based on geostatistical and small perturbation analyses of the aperture size distribution.

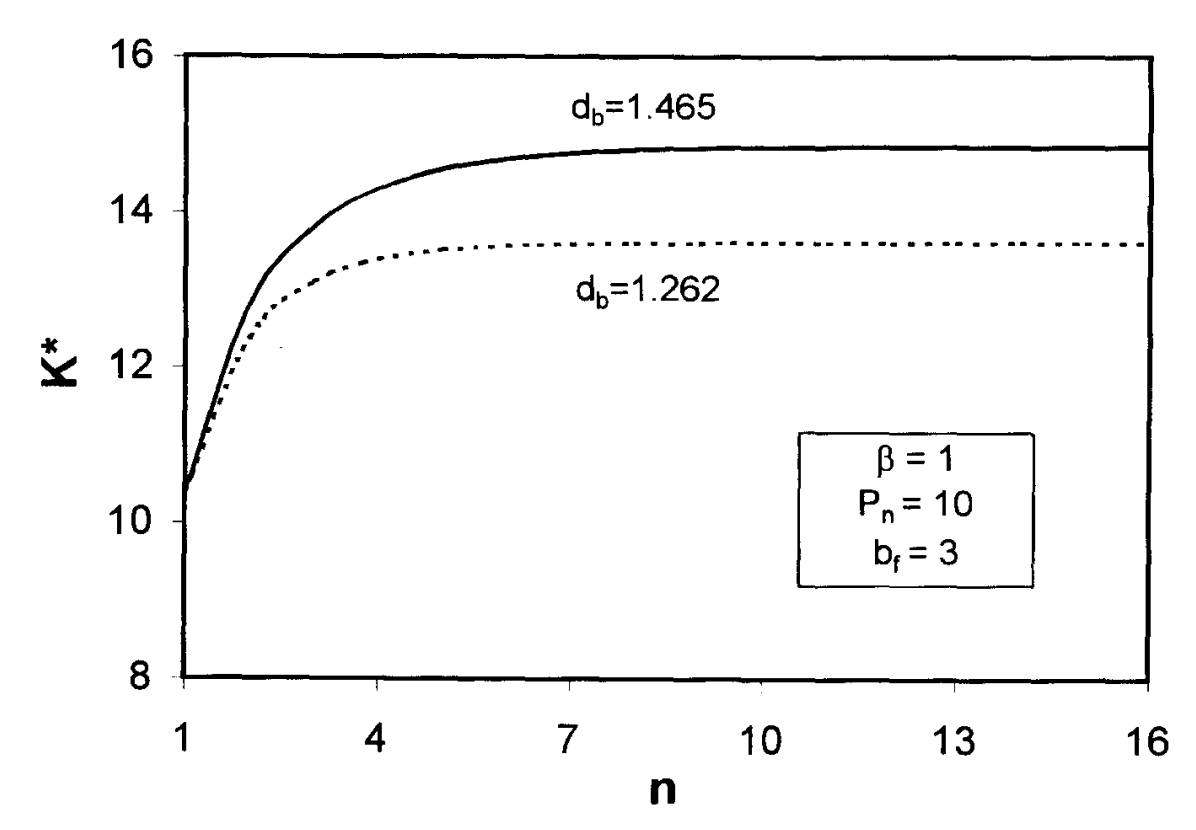


Fig. 3 -8. Dimensionless dispersion coefficients as a function of iteration level for two prefractal capillaries.

The dispersivity of a naturally fractured granite predicted using this approach was within a factor of two of the experimentally determined value.

Prefractal surfaces are a logical extension of the relatively simple Euclidean geometrical structures discussed above. Thompson (1991b), and Amadei and Illangasekare (1994) conducted numerical simulations in fractures with prefractal surfaces. However, it is difficult to identify any clear relationship between the surface fractal dimension and solute dispersion from these studies. Thompson (1991b) employed two surfaces with the same fractal dimension ( $d_s = 2.5$ ) and different separation distances. Amadei and Illangasekare (1994) used pairs of surfaces with different fractal dimensions. Working in two dimensions, Gutfraind et al. (1995) found little dependence of  $K^*$  on the boundary fractal dimension, apparently because of inappropriate scaling of the different fracture profiles.

### **Geometric Capacitance Models**

Capacitance models are a special case of multiregion velocity distribution models, in which the liquid phase is divided into two distinct (mobile and immobile) regions. The CDE for solute transport within the mobile region can then be written as (Coats & Smith, 1964; van Genuchten & Wierenga, 1976):

$$\frac{\partial C_{\rm m}}{\partial t} = K \frac{\partial^2 C_{\rm m}}{\partial x^2} - v_{\rm m} \frac{\partial C_{\rm m}}{\partial x} - \left(\frac{\theta_{\rm im}}{\theta_{\rm m}}\right) \frac{\partial C_{\rm im}}{\partial t}$$
[34]

where the subscripts *m* and *im* refer to the mobile and immobile liquid regions respectively. Equation [34] can be solved analytically without making any assumptions about the spatial arrangement of solids and voids (e.g., Skopp et al., 1981). Geometric capacitance models represent a class of parameterizations of Eq. [34] in which the mobile and immobile liquid regions are explicitly defined in terms of pore space geometry. The majority of these models are for packed beds of uniform porous spheres (Passioura, 1971; Rao et al., 1980a,b; Rasmuson & Neretnieks, 1980). While it is possible to extend this approach to nonuniform and nonspherical aggregates (Rao et al., 1982; van Genuchten & Dalton, 1986; Gerke & van Genuchten, 1996), its predictive capability is limited. This is because the relation-

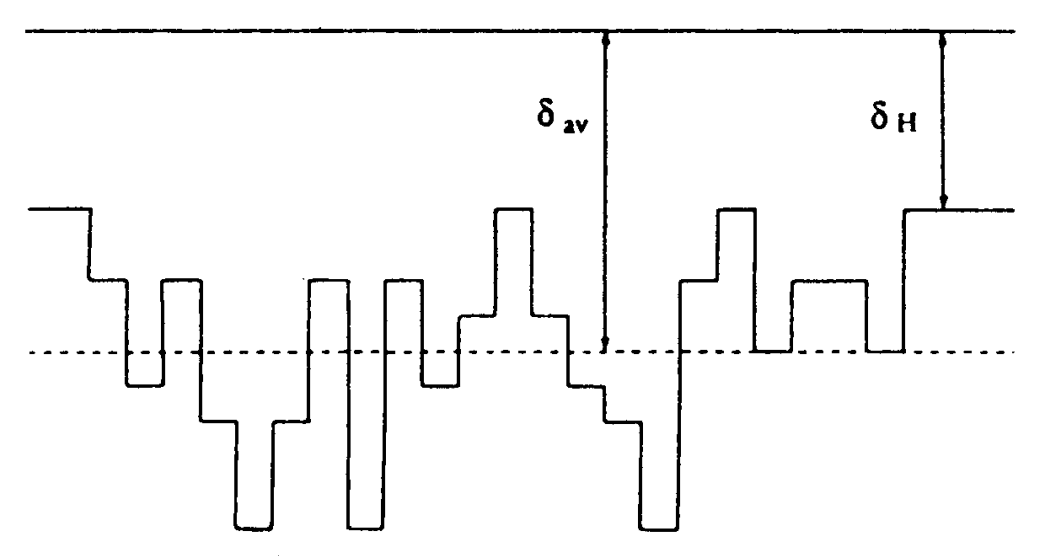


Fig. 3-9. Profile of the irregular channel in the study by Koplik et al. (1993).

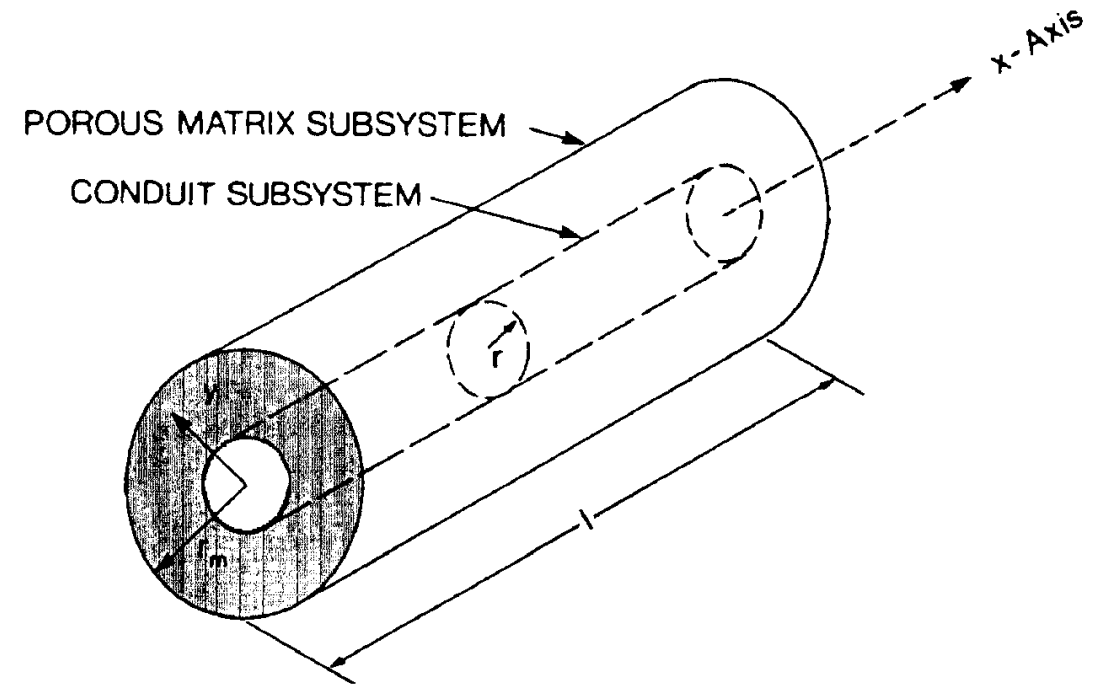


Fig. 3–10. Uniform capillary tube surrounded by an annular porous matrix.

ship between properties of disturbed aggregates and pore characteristics in the undisturbed state is far from clear.

Geometric capacitance models based on macropore geometry offer more promise for predicting solute transport in structured soil and fractured rock systems. The indented capillary tube model (Turner, 1958; Aris, 1959b,c) was discussed previously. This model assumes that the aperture walls are solid. A similar model can be derived for a uniform tube with porous walls (Fig. 3–10). In this case, solute spreading will occur as a result of convective-dispersive transport in the main channel and diffusive exchange with the surrounding matrix. Analytical solutions of Eq. [34] for this condition are available for a variety of macropore shapes and arrangements (Grisak & Pickens, 1981; Tang et al., 1981; Sudicky & Frind, 1982; van Genuchten et al., 1984; Rowe & Booker, 1989). Solute transport in uniform rectangular and cylindrical channels with simultaneous matrix diffusion has also been modeled numerically (Scotter, 1978; Grisak & Pickens, 1980; Bobba, 1989; Sudicky & McLaren, 1992). These studies show that diffusion through pore walls contributes significantly to dispersion. For the 120-µm fracture studied by Grisak and Pickens (1980), matrix porosities as low as 0.05 resulted in an almost 50% reduction in  $C/C_0$  4 d after a step change in concentration at a flow velocity of 0.75 m d<sup>-1</sup>, as compared to complete breakthrough for the nonporous matrix (Fig. 3–11).

# **Spatially Periodic Models**

Spatially periodic porous media are made up of structural elements whose arrangement in space is completely described by a single unit cell (similar to the representative elementary volume concept of Bear, 1969), that is then repeated ad infinitum (Adler, 1992). The structural elements can be discrete voids in a continuous solid phase or vice versa. The simplest spatially periodic models are comprised

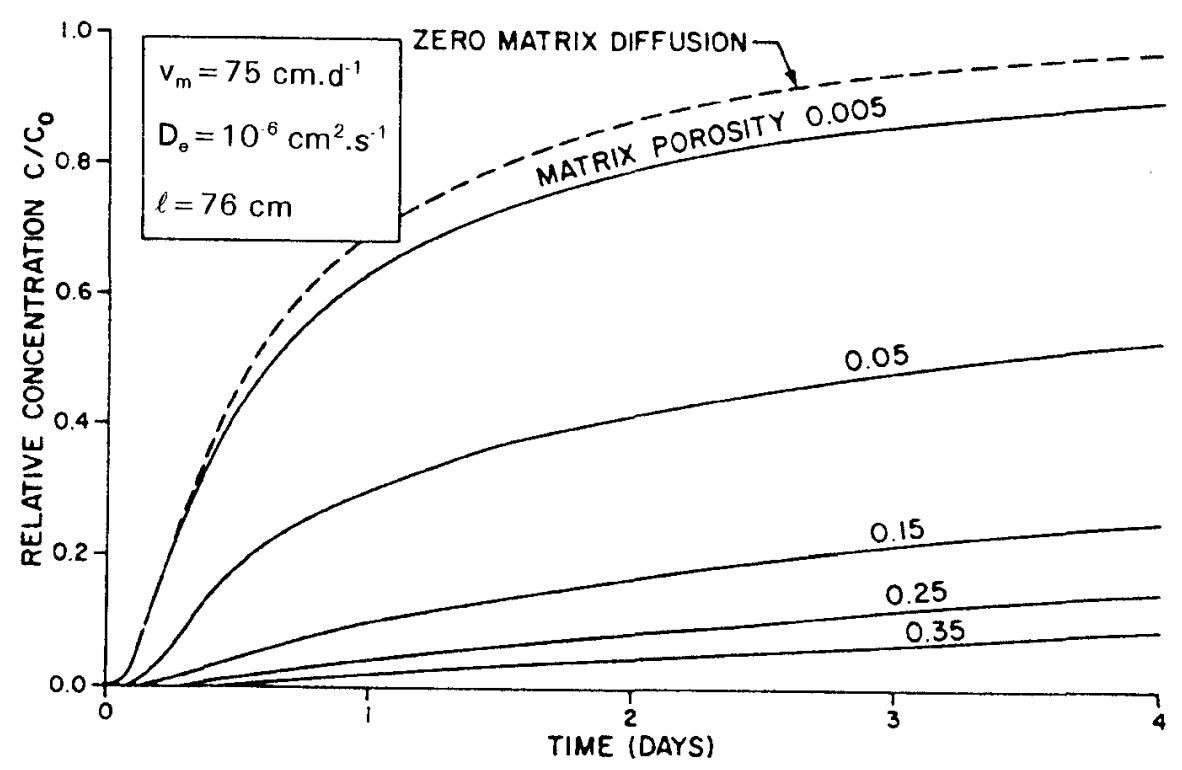


Fig. 3–11. Effect of matrix porosity on solute BTCs obtained for a 120-µm fracture at a distance of 0.76 m (Grisak & Pickens, 1980).

of repetitive arrays of Euclidean geometric structures (Fig. 3–12). However, irregularly shaped structural elements are also possible (Fig. 3–13).

A fundamental characteristic of spatially periodic systems is the existence of a group of translational symmetry operations, by means of which the repeating pattern may be brought into self-coincidence. The translational symmetry of the array, expressing its invariance with respect to parallel displacements in different directions is represented by a lattice. This lattice consists of an array of evenly spaced points (Fig. 3–13), such that the structural elements appear the same and in the same orientation when viewed from each and every one of the lattice points. Another important property of spatially periodic arrays is the existence of two characteristic length scales, corresponding to the average microscopic distance between lattice

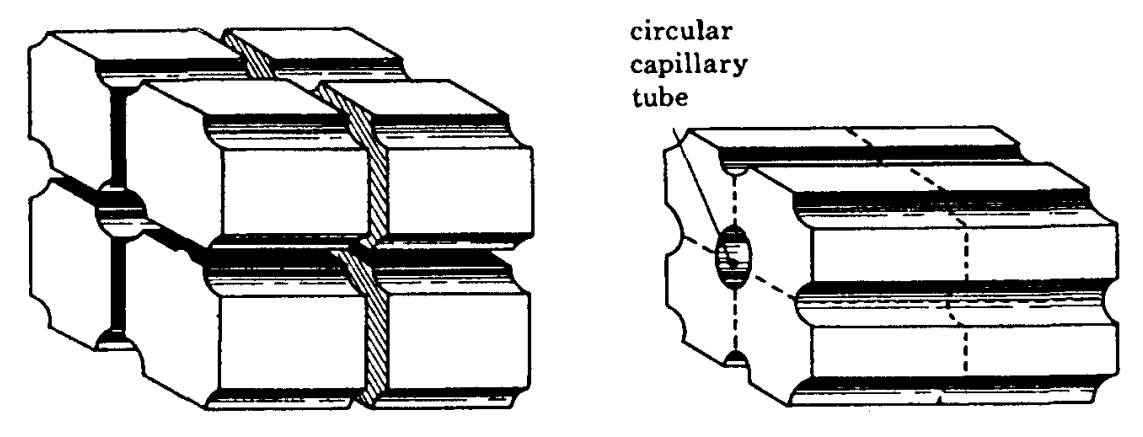


Fig. 3—12. Examples of spatialty periodic media comprised of parallel planes and capillary tubes (Brenner, 1980).

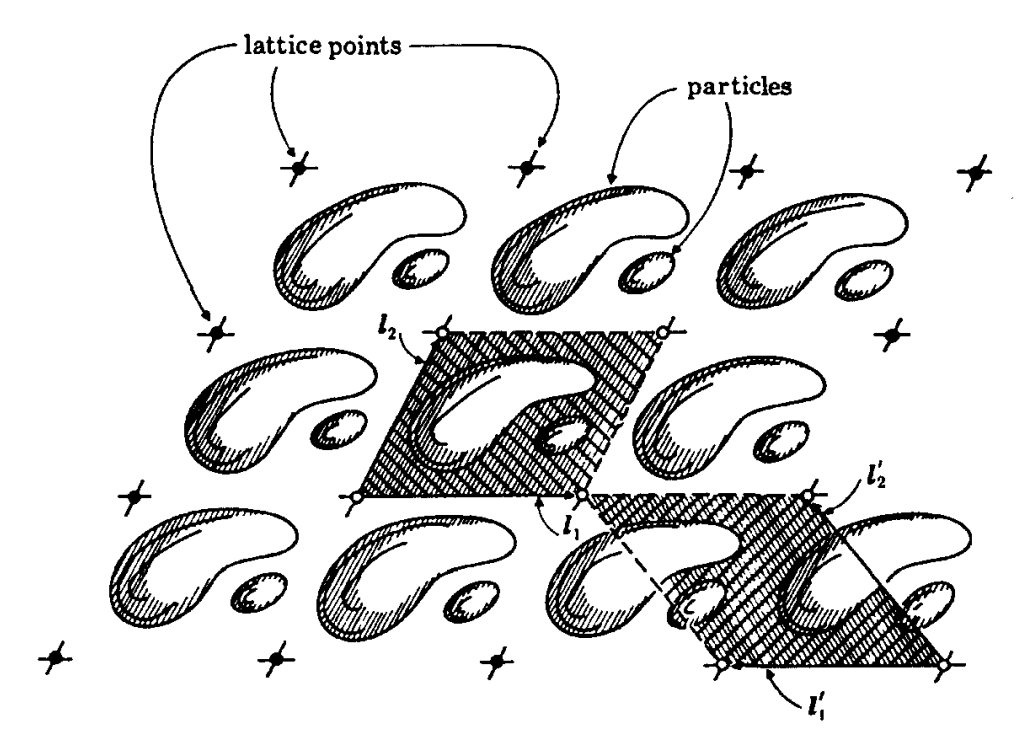


Fig. 3–13. A spatially periodic medium comprised of two irregular particles. The lattice points delineate a unit cell that is invariant with respect to parallel displacements in different directions (Brenner, 1980).

points, and the length of interest, respectively. Application of this type of model to transport problems requires that the latter length be much greater than the former one to ensure mesoscopic homogeneity.

Brenner (1980) has explored the subject of solute dispersion in spatially periodic porous media in considerable detail. Brenner's analysis makes use of the method of moments developed by Aris (1956) and later extended by Horn (1971). Carbonell and Whitaker (1983) and Koch et al. (1989) have addressed the same problem using the method of volume averaging, whereby mesoscopic transport coefficients are derived by averaging the basic conservation equations over a single unit cell. Numerical simulations of solute dispersion, based on lattice scale calculations of the Navier-Stokes velocity fields in spatially periodic structures, have also been performed (Eidsath et al., 1983; Edwards et al., 1991; Salles et al., 1993). These simulations are discussed in detail in the "Emerging Areas" section.

In general, the results of these studies agree well with experimental data for packed beds. This is because the analysis of solute dispersion in spatially periodic media is relatively straightforward when the analytical or numerical calculations are applied to simple Euclidean structures, such as a square array of uniform cylinders. In principle, a unit cell can contain many different sized elements of arbitrary shape (Fig. 3–14). However, the resulting analysis is much more complicated (e.g., Plumb & Whitaker, 1988). As a result, spatially periodic models are mostly used to predict solute dispersion in packed beds of uniform particles. Moreover, because of their repetitive nature and restrictive characteristic lengths, they are unsuitable for modeling natural porous media with evolving heterogeneities. In this respect, they are similar to geometric capacitance models discussed earlier.

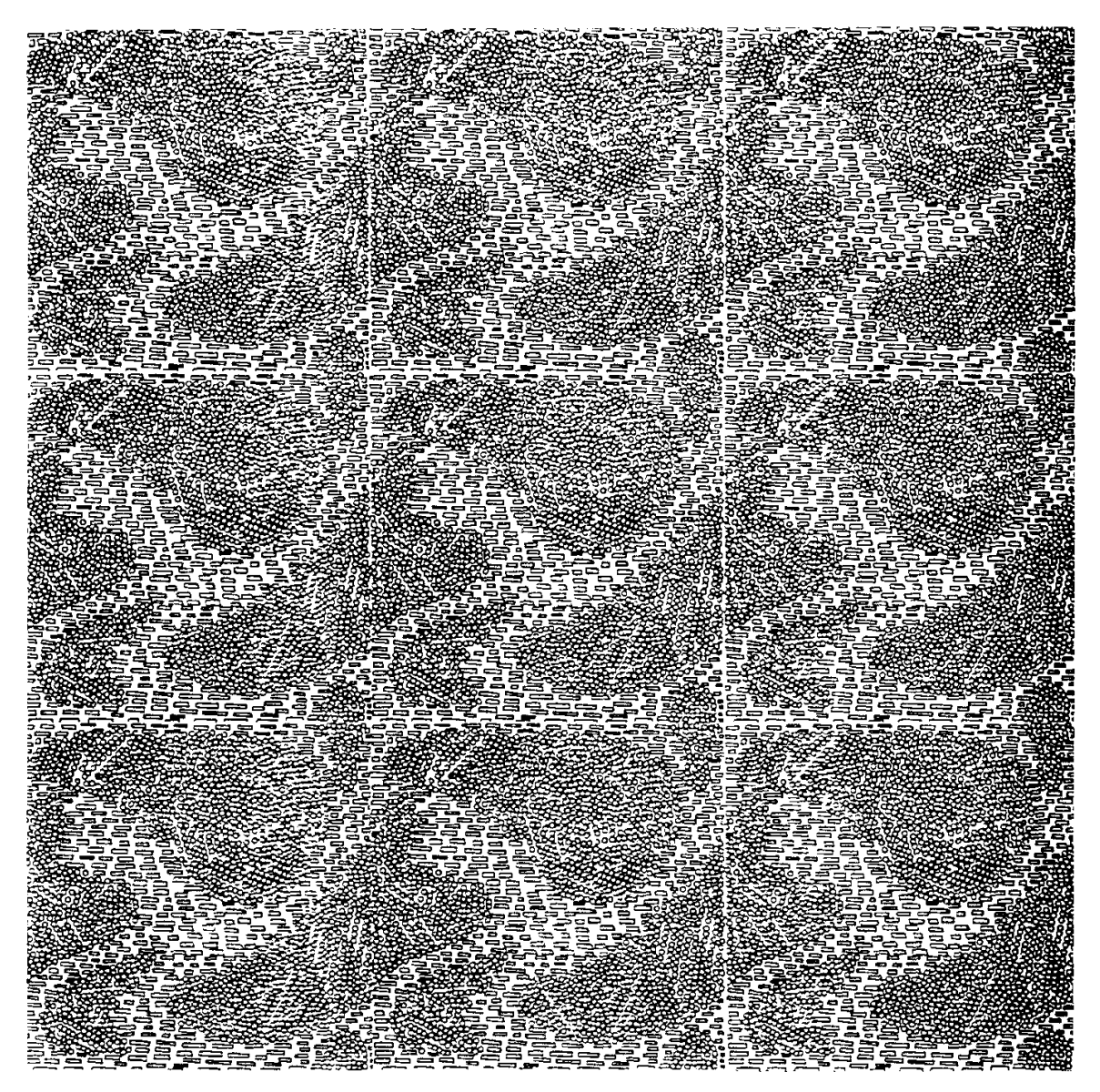


Fig. 3–14. A spatially periodic medium comprised of multiple irregular elements (Plumb & Whitaker, 1988).

### **Capillary Bundle Models**

These models are based on the concept of a porous medium as bundle of non-interacting, uniform capillary tubes with different radii (Fig. 3–15). Expressions for v and K in Eq. [1] are then derived in terms of the frequency distribution of tube radii. This approach was first discussed by Danel (1953). Klinkenberg (1957) and Turner (1958) applied it inversely to predict an equivalent cylindrical pore size distribution from miscible displacement data. Klinkenberg (1957) used Poiseuille's law to relate v to  $r^2$ , and assumed plug flow (i.e., no dispersion) within individual capillary tubes. Assuming dispersion takes place according to the CDE, it is possible to infer the pore-size distribution needed to produce a specific normal distribution of pore water velocities using this approach. The resulting distribution is always skewed towards the largest pore sizes. In contrast, experimental determinations of pore-size distribution based on the capillary bundle concept invariably exhibit the opposite trend (e.g., Nagpal et al., 1972). This discrepancy suggests that the as-

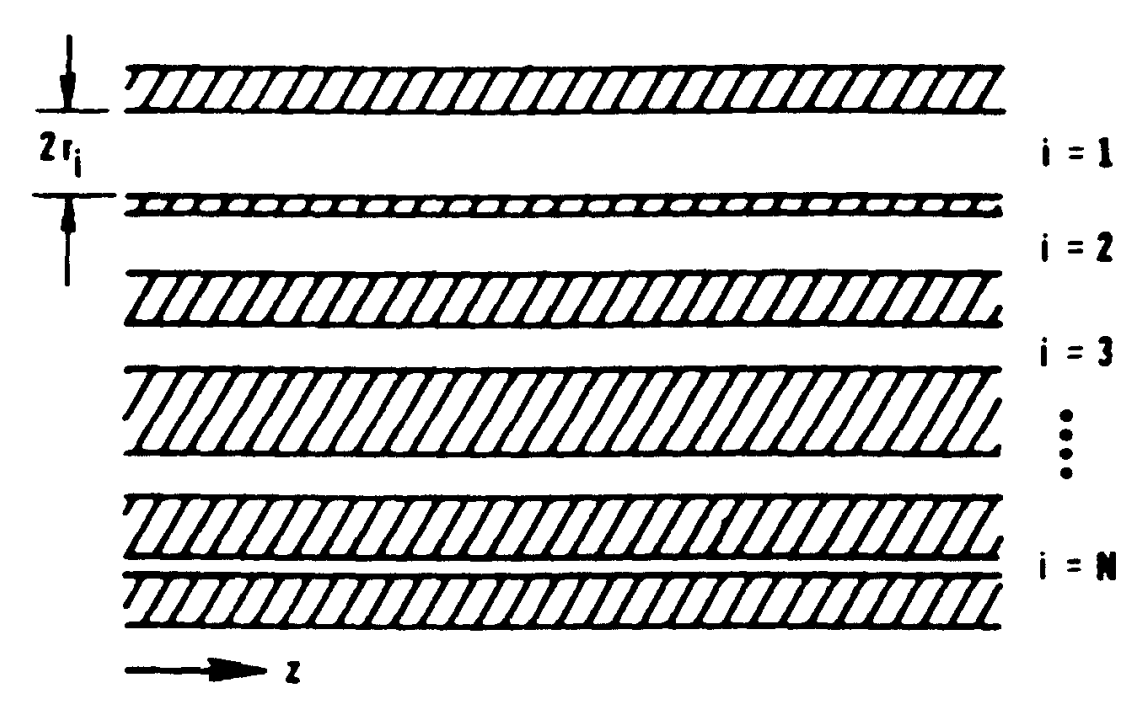


Fig. 3-15. Capillary bundle model (Carbonell, 1979).

sumption of a normal pore-water velocity distribution in the CDE may be erroneous and/or that the representation of natural porous media as equivalent capillary bundles is unrealistic. Turner (1958) proposed a theoretical model for inversely estimating the pore-size distribution of a capillary bundle by measuring effluent concentration as a function of time in response to a sinusoidally varying input concentration. To our knowledge his model has never been tested.

Lindstrom and Boersma (1971) pioneered the prediction of breakthrough curves from equivalent cylindrical pore size distributions, determined by either the water retention or mercury porosimetry methods. The model developed by these authors includes the effects of both intra- and interpore dispersion. In general, dispersion due to differences in tube size has a much greater influence on the shape and position of the breakthrough curve than mixing within tubes due to microscopic velocity profiles (Rao et al., 1976). For completeness, however, it is preferable to include both effects. Lindstrom and Boersma (1971) defined a CDE for each tube, so that  $C/C_0$  for the bundle as a whole is given by:

$$\frac{C}{C_{\rm o}} = \frac{\sum_{j=1}^{N} A_{\rm j} (C_{\rm j}/C_{\rm o})}{\sum_{j=1}^{N} A_{\rm j}}$$
[35]

where  $C_j$  is the solute concentration in the *j*th tube-size increment, N is the total number of increments, and  $A_j$  is the fraction of the bundle occupied by the *j*th tube-size increment. The resulting system of equations is then solved numerically, with the relative contribution of each tube-size increment to the total displacement determined from the empirical frequency distribution of pore sizes.

A similar theoretical approach, with the CDE applied to each noninteracting tube size increment, was proposed by Carbonell (1979). In this method, however, the mesoscopic dispersion coefficient was determined by taking the moments of

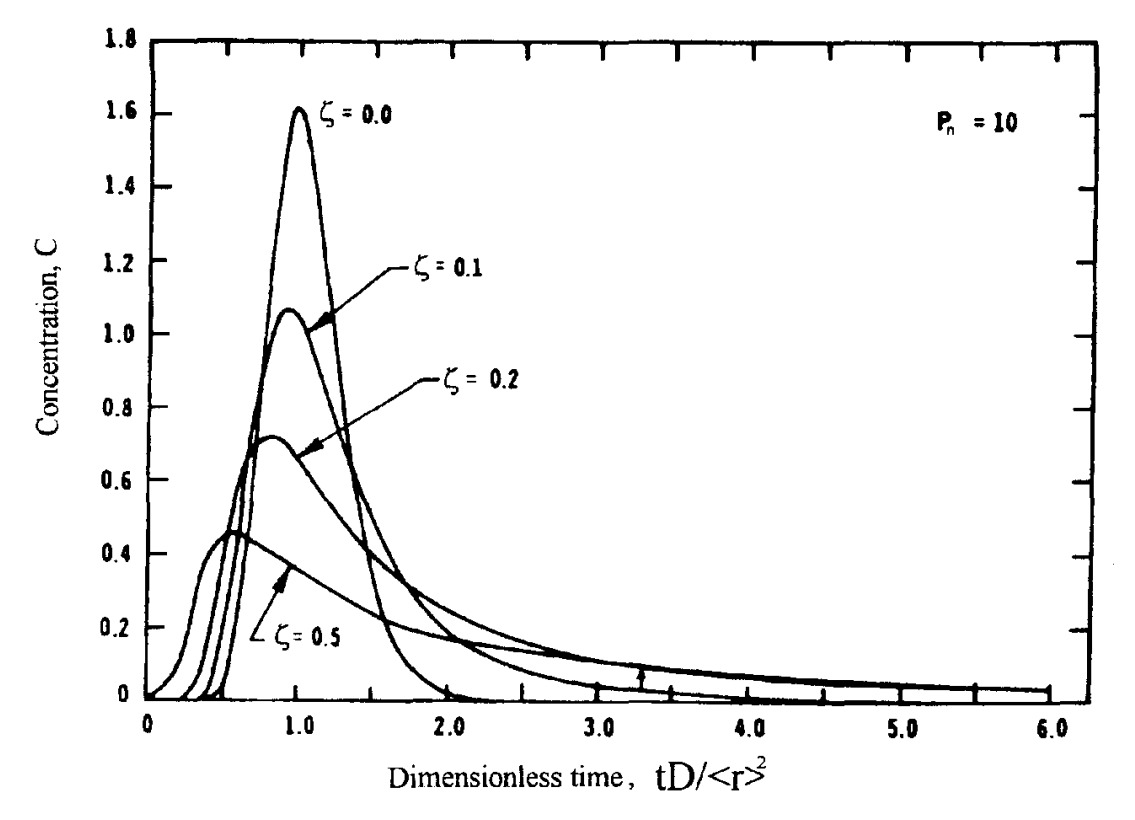


Fig. 3–16. Concentration as a function of dimensionless time for a capillary bundle with a normal distribution of radii and different coefficients of variation (Carbonell, 1979).

the individual concentration profiles, and averaging them over all pore classes. Assuming laminar flow, the resulting expression for  $K^*$  is:

$$K^* = 1 + \frac{v^2}{48D^2} \frac{r_{10}r_2^2}{r_4^3} + \frac{v^2t}{D} \frac{r_2}{r_4^2} \left[ \frac{r_2r_8}{r_4} - r_6 \right]$$
 [36]

where v is the area-averaged pore water velocity, t is time, and  $r_n$  is the nth moment of the pore size distribution as defined by,

$$r_{\rm n} = (1/N) \sum_{i=1}^{N} r_i^{\rm n}, n = 1, 2, 3...$$
 [37]

where N is the number of pore classes. Assuming a normal distribution of pore sizes, the predicted effects of different coefficients of variation ( $\zeta$ ) on the spread of a solute pulse at a given depth are illustrated in Fig. 3–16. The spread of the pulse is greatly magnified as the spread of the pore size distribution, as represented by  $\zeta$ , increases.

The predictions of capillary bundle models have been shown to agree reasonably well with experimental data for packed beds of uniform particles (Carbonell, 1979). However, breakthrough curves computed using this approach appear to underpredict the time of arrival of the peak of the solute pulse in undisturbed soils (Rao et al., 1976; Bouma & Wösten, 1979). This may be due to discrepancies between measured and actual pore size distributions, inappropriate representation of the relationship between  $P_n$  and  $K^*$  within individual pores, or the assumed lack of interconnectivity between pore channels (Lindstrom & Boersma, 1971; Rao et al., 1976).

Carbonell (1979) and Neretnieks (1983) have extended the classic capillary bundle approach to noninteracting, uniform rectangular parallel plates, of infinite extent and variable width. A contrasting approach was proposed by Tsang and Tsang (1987). These authors generated a bundle of statistically equivalent noninteracting one-dimensional channels with the same mean volume, but with variable aperture widths. Solute dispersion takes place due to the resulting distribution of channel residence times during steady state flow. In a subsequent paper Tsang et al. (1988) parameterized the variation in aperture widths along individual channels in terms of the log-normal frequency distribution. Solute dispersion increased as the geometric standard deviation was increased, while keeping the Peclet number constant. The same model was also used inversely to estimate aperture variability from the solute BTC.

### **Network Models**

Network models are closely related to percolation models, which are dealt with under "Emerging Areas". Sahimi (1995) and Berkowitz and Ewing (1998) have traced the development of both types of model, and have summarized the links between them. For the purposes of this review, a network is defined as a system of interconnected elements well above the percolation threshold (i.e., there are many connected paths through the network). Network models can be categorized as: (i) uniform shape and uniform size distribution (Fig. 3–17A), (ii) uniform shape and variable size distribution (Fig. 3–17C).

### **Uniform Shape and Uniform Size Distribution**

Consider a random network of interconnected nonporous cylindrical capillary tubes of uniform radius r and length l. The tubes are connected with one another at their ends, and several tubes may start or end at these junctions (Fig. 3–17A). Thus, the path of a solute molecule introduced into the network can be regarded as a random walk in which the distance, direction, and duration of each step are random variables. This idea was first explored by de Josselin de Jong (1958), whose expression for  $K^*$ , based on a probabilistic analysis of the random walk, is:

$$K^* = (1/6) P_n [f + (3/4) + E]$$
 [38]

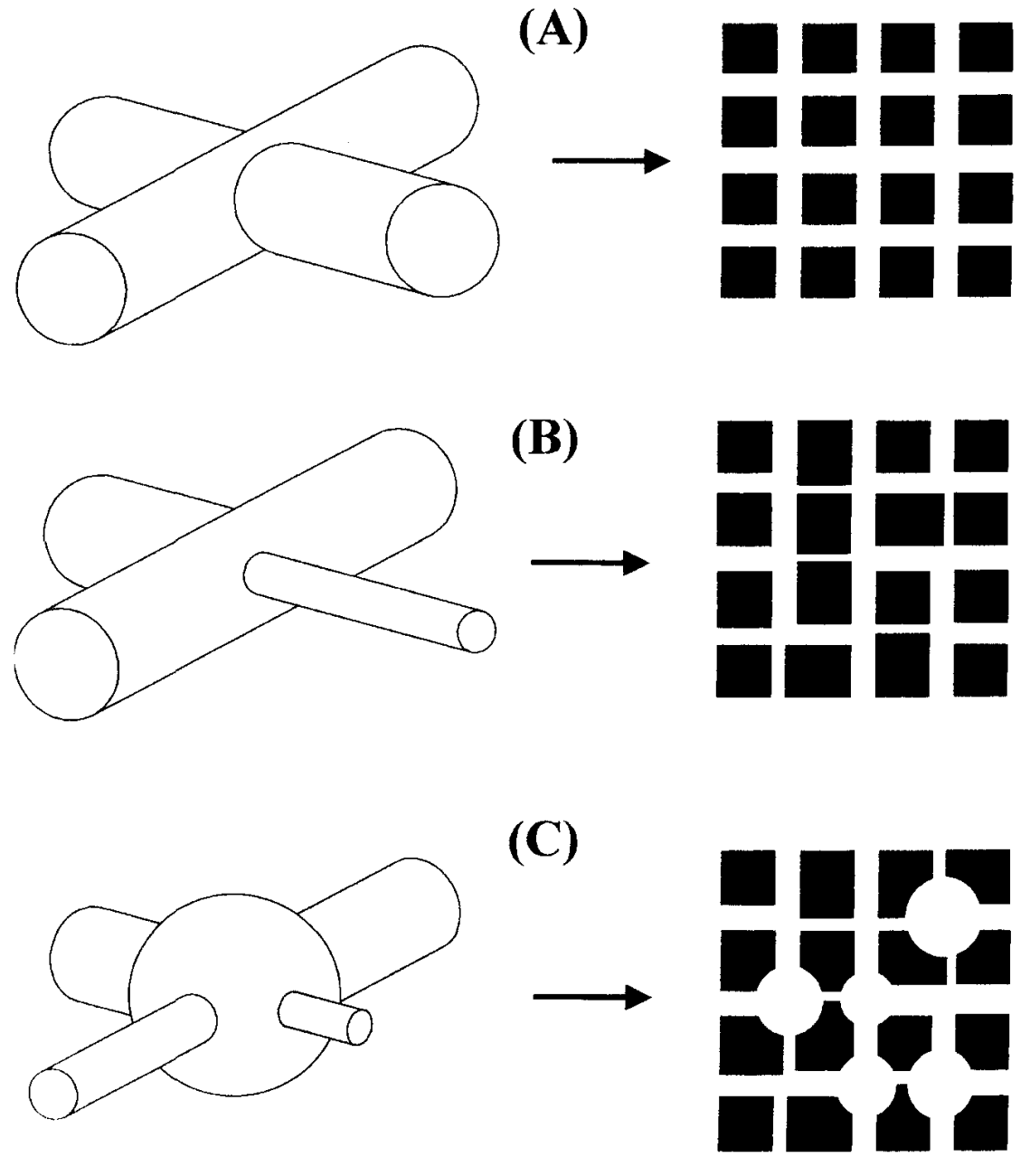
where  $\ell = 1$  in Eq. [5], f is a function of the distance traveled by the solute plume, and E is Euler's constant ( $\approx 0.577$ ). Note that for any given travel distance,  $K \propto v$  in this system, as compared to  $K \propto v^2$  for a single uniform capillary tube (see Eq. [26]). Torelli and Scheidegger (1971) obtained a similar result for a random maze network. Both models neglect the contribution of molecular diffusion and assume a uniform microscopic velocity distribution within individual tubes. Thus, their applicability is restricted to large Peclet numbers.

Saffman (1959) developed a more general network model that accounted for interactions between molecular diffusion and fluid convection within individual tubes. Using the same random walk approach as de Josselin de Jong (1958), he obtained numerical approximations of  $K^*$  for various limiting conditions, including

molecular diffusion dominant, molecular diffusion and convective dispersion of equal importance, and convective dispersion dominant. In a later paper (Saffman, 1960), he extended the range of conditions considered through an alternative analysis based on Lagrangian correlation functions. For the  $P_n$  range of interest, i.e., 1  $<< P_n << 8(l/r)^2$ , his approximate numerical expression for  $K^*$  is (Saffman, 1960; Rose, 1977),

$$K^* = \frac{D_e}{D} + \frac{P_n}{6} \left[ \ln \left( \frac{3P_n}{2} \right) - \frac{P_n}{8} \left( \frac{r}{l} \right)^2 - \frac{17}{12} \right] + \frac{4}{9}$$
 [39]

where  $\ell = 1$  in Eq. [5]. Saffman's model predicts dispersion coefficients over a wide range of Peclet numbers, agreeing well with experimental results for packed beds



1/19 3-17. Network models comprised of (A) uniform cylindrical bonds, (B) variable cylindrical bonds, and (C) variable cylindrical bonds and spherical sites (adapted from Berkowitz & Ewing, 1998).

of spherical particles (Rose, 1977). The predicted values of  $K^*$  are relatively insensitive to r/l when the latter is <1/3.

Torelli (1972) introduced particle tracking for simulating solute dispersion in network models of porous media. The particular model used by Torelli (1972) was a two-dimensional square lattice of uniform capillaries, with a specified number of bonds removed at random. A more sophisticated model was employed by Schwartz et al. (1983). In the particle tracking approach, pressure potential distributions and velocity profiles within individual tubes are established by numerically solving a steady-state flow equation. Rules must also be established for solute mixing at channel intersections (Park & Lee, 1999). For example, solute particles approaching the intersection illustrated in Fig. 3–18 can move in one of three possible directions. In complete mixing, each direction has the same probability (Fig. 3–18A). In streamline routing, the direction is determined by the relative magnitudes of flow away from the intersection (Fig. 3–18B). Breakthrough curves are simulated by monitoring a large number of reference particles released into the network at the upstream boundary. The results of Torelli's (1972) simulations, which ignore mixing due to diffusion, can be summarized as  $K \propto v^{1.2}$ , which is intermediate be-

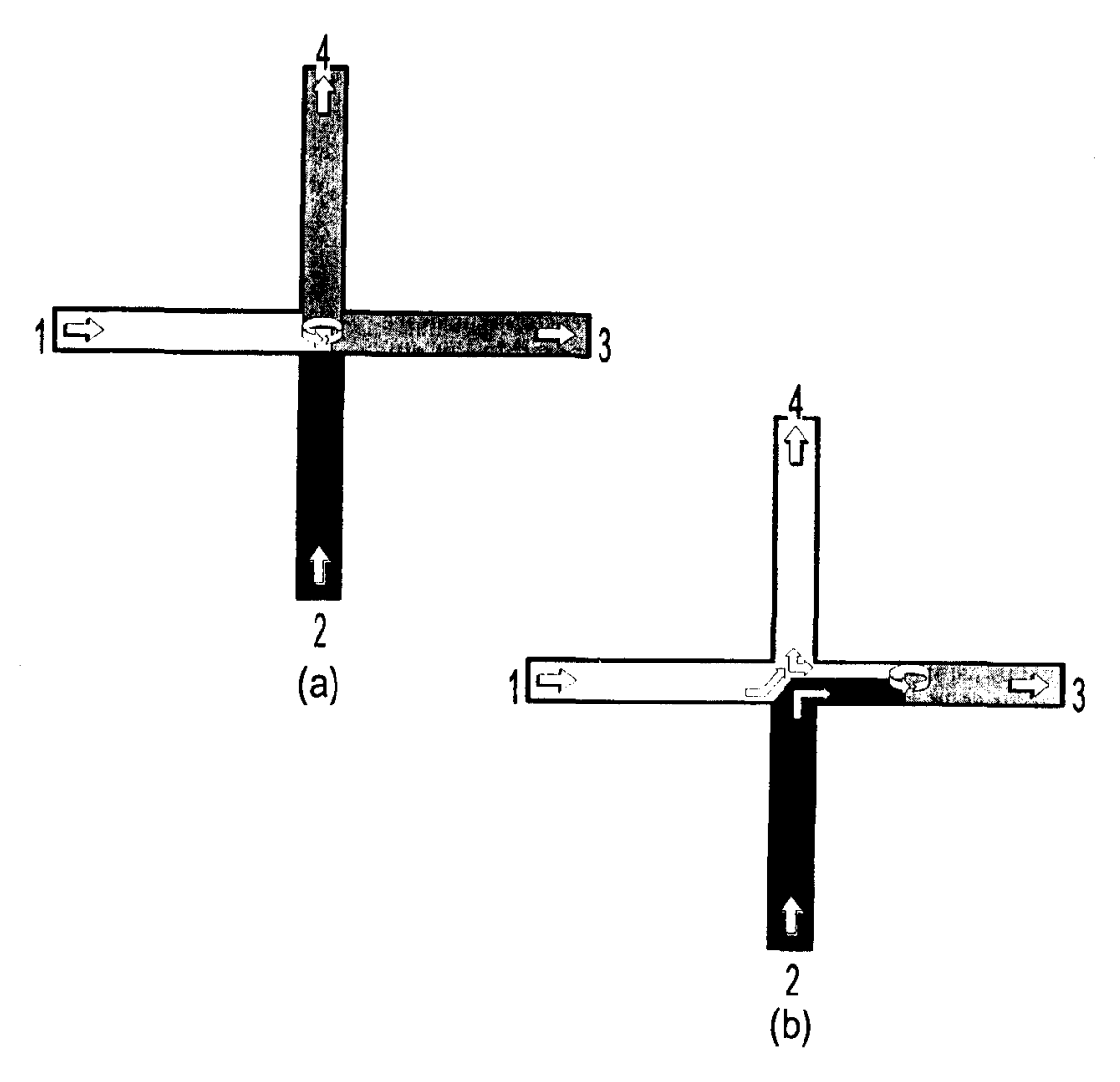


Fig. 3–18. Examples of fluid behavior at an intersection: (A) complete mixing and (B) streamline routing (Park & Lee, 1999).

tween the two extremes of microscopic dispersion  $(K \propto v^2)$  and mesoscopic dispersion  $(K \propto v)$ . Koplik et al. (1988) pointed out that tracking any finite number of particles is subject to limitations because low velocity paths tend to be insufficiently sampled.

### **Uniform Shape and Variable Size Distribution**

These network models are comprised of different-sized, interconnected elements of uniform shape (e.g., Fig 3–17B). The configuration of elements within the network can be either systematic or random. Marle and Defrenne (1960) were the first to use this type of model to predict solute dispersion. Their network was a modified capillary bundle model with regularly spaced interconnections between parallel tubes of radii  $r_1$  and  $r_2$ . This model does not consider diffusion. Spreading of a solute in the model is given by:

$$\sigma^{2}(t) = n \frac{8\eta l_{s}^{2}}{\Delta \psi} \frac{1}{r_{1}^{2} + r_{2}^{2}} \frac{1 - r_{1}^{2}/r_{2}^{2}}{1 + r_{1}^{2}/r_{2}^{2}} + \sigma^{2}(t_{0})$$
 [40]

where n is a large number of interconnections,  $l_s$  is their separation distance,  $\sigma^2(t)$  is the variance at time t, and  $\sigma^2(t_0)$  is the variance at initial time,  $t_0$ . Subsequently, Simon and Kelsey (1971, 1972) investigated dispersion in interconnected capillary tubes of different sizes arranged in square, diamond, and single and double hexagonal patterns. Robinson and Gale (1990) used physical and numerical models to analyze the transport of a conservative solute in diamond lattices with different intersection angles and channel radii. Interacting capillary bundle models have also been developed without explicit reference to the spatial arrangement of their interconnections (e.g., Steenhuis et al., 1990; Grindrod & Impey, 1993; Skopp & Gardner, 1992).

While the above models represent an improvement over classical capillary bundle models, they cannot reproduce the geometrical heterogeneity of natural porous media. As a result, several authors have tried to derive more sophisticated models based on random capillary networks.

Mandel and Weinberger (1972) proposed a two-dimensional network model for solute dispersion based on an irregular hexagonal lattice of intersecting capillary tubes of variable orientation, length, and cross-sectional area. The velocity distribution within individual tubes was neglected, and complete mixing was assumed at each node. A probabilistic analysis of this model, based on the Eulerian point of view, resulted in an expression for longitudinal dispersivity. Comparison of breakthrough curves computed using this approach with those predicted by the model of de Josselin de Jong (1958), which assumes elements of uniform length and cross-sectional area, indicates significant differences only at the extremes of the distribution curves (Mandel & Weinberger, 1972).

Bear (1969, 1972) developed a dispersive flow model based upon the idea of building a continuum at the mesoscopic scale by statistically averaging microscopic quantities over a representative elementary volume, defined with respect to porosity. This geometric model is an assemblage of randomly interconnected tubes

of varying radius r, length l, and orientation. Averaging the resulting mass conservation and transport equations, yields the following approximate expression for  $K^*$  (Bear, 1972; Rose, 1977):

$$K^* \approx \frac{D_e}{D} + P_n \left[ 1 + \frac{2}{P_n} + \frac{4}{P_n} \left( \frac{\langle l \rangle}{\langle r \rangle} \right)^2 \right]^{-1}$$
 [41]

where  $\langle r \rangle$  is the mean pore radius, and  $\langle l \rangle = \ell$  in Eq. [5] is the mean microscopic characteristic length. Bear's model is valid for a wide range of Peclet numbers, but is most sensitive to the value of  $\langle l \rangle / \langle r \rangle$  over the range  $1 \langle P_n \rangle / \langle r \rangle = 1$  (Bear, 1969).

Haring and Greenkorn (1970) developed an alternative statistical model for predicting dispersion in a network of randomly intersecting tubes. In this model, both l and r are assumed to be random variables distributed according to the beta probability distribution function, with parameters  $a_1,b_1$  and  $a_r,b_r$ , respectively. Haring and Greenkorn's (1970) expression for  $K^*$  is:

$$K^* = \frac{1}{12} \frac{(a_1 + 2)(a_1 + b_1 + 2)}{(a_1 + 1)(a_1 + b_1 + 3)J^2} P_n \ln \left[ \frac{27}{2} \frac{(a_1 + b_1 + 2)^2}{(a_1 + 1)^2 J^3} \frac{vt}{\langle l \rangle} \right]$$
 [42]

where  $\ell = \langle l \rangle$  in Eq. [5] and J is a function of  $a_r$  and  $b_r$ . Equation [42] is consistent with Saffman's (1960) model for uniform-sized, interconnected tubes when  $a_l$ ,  $a_r >> 1$  and  $b_l$ ,  $b_r = 0$ . Pakula and Greenkorn (1971) estimated  $a_r$  and  $b_r$  from water retention experiments, and fitted  $a_l$  and  $b_l$  by comparison of Eq. [42] with experimental data obtained for a given Peclet number. Predictions of K based on these parameter estimates were of the same order of magnitude as experimental dispersion coefficients determined at other Peclet numbers. Despite its promise, this model was later retracted because of an apparent error in equating the ensemble average pore water velocity with the spatial average pore water velocity (Guin et al., 1972).

Sahimi et al. (1983) extended the particle tracking method developed by Torelli (1972) to simulate dispersion of a nonreactive tracer in a random tube network of different-sized elements. In their model, one first determines the flow field in the network. A pressure gradient is applied across the network, and the mass of fluid reaching any given node is treated as a conserved quantity. The mean flow rate within each tube is calculated by numerically solving Poiseulle's law for the resulting distribution of nodal pressures. A large number of tracer particles are then randomly introduced into the network at the upstream plane. Complete nodal mixing and zero nodal residence time are assumed. The K is computed from the first passage time distribution of particles as they arrive at the downstream plane using Eq. [3]. Sahimi et al. (1983) showed that K depends linearly on v for this system, which is thus appropriate for simulating pure mechanical dispersion at the mesoscopic scale. Sahimi and Imdakm (1988) modified the original algorithm to allow for particle diffusion among streamlines and into dead end tubes. As soon as diffusion times were included in the total travel time of the particle, the linear dependence of K on v was destroyed, and  $K \propto v^{1.2}$ , as was found by Torelli (1972).

Sorbie and Clifford (1991) used a Monte Carlo method to incorporate diffusion into a network model. Good agreement was found between their method and

experimental data presented in the literature over a wide range of Peclet numbers. In the mixed regime where convection dominates, but diffusion is not negligible, K increased faster than linearly with fluid velocity. For  $K \propto v^{\alpha}$ , their results indicate  $1.19 < \alpha < 1.25$ .

de Arcangelis et al. (1986) proposed another network model for solute dispersion based on the analogy between Poiseuille's law for fluid flow and Ohm's law for random resistor networks. Steady-state electrical currents are used to define the flow field of the background fluid that carries the tracer. Equation [1] is specified for each tube, and the first passage time distribution is computed using an efficient algorithm in the Laplace-transform domain. This approach, which is most appropriate for well-connected networks, gives the probability distribution for a random walk model in which there is a different time for each step, and where each step represents the continuum solution of the traversal time problem for each bond. Applying the technique to a square lattice of interconnected capillary tubes with cross-sectional areas uniformly distributed in the interval  $[1 - \Omega/2, 1 + \Omega/2]$ , where  $\Omega$  determines the degree of disorder in the system, de Arcangelis et al. (1986) were able to predict the entire nonlinear relationship between  $K^*$  and  $P_n$  as a function of  $\Omega$  (Fig. 3–19).

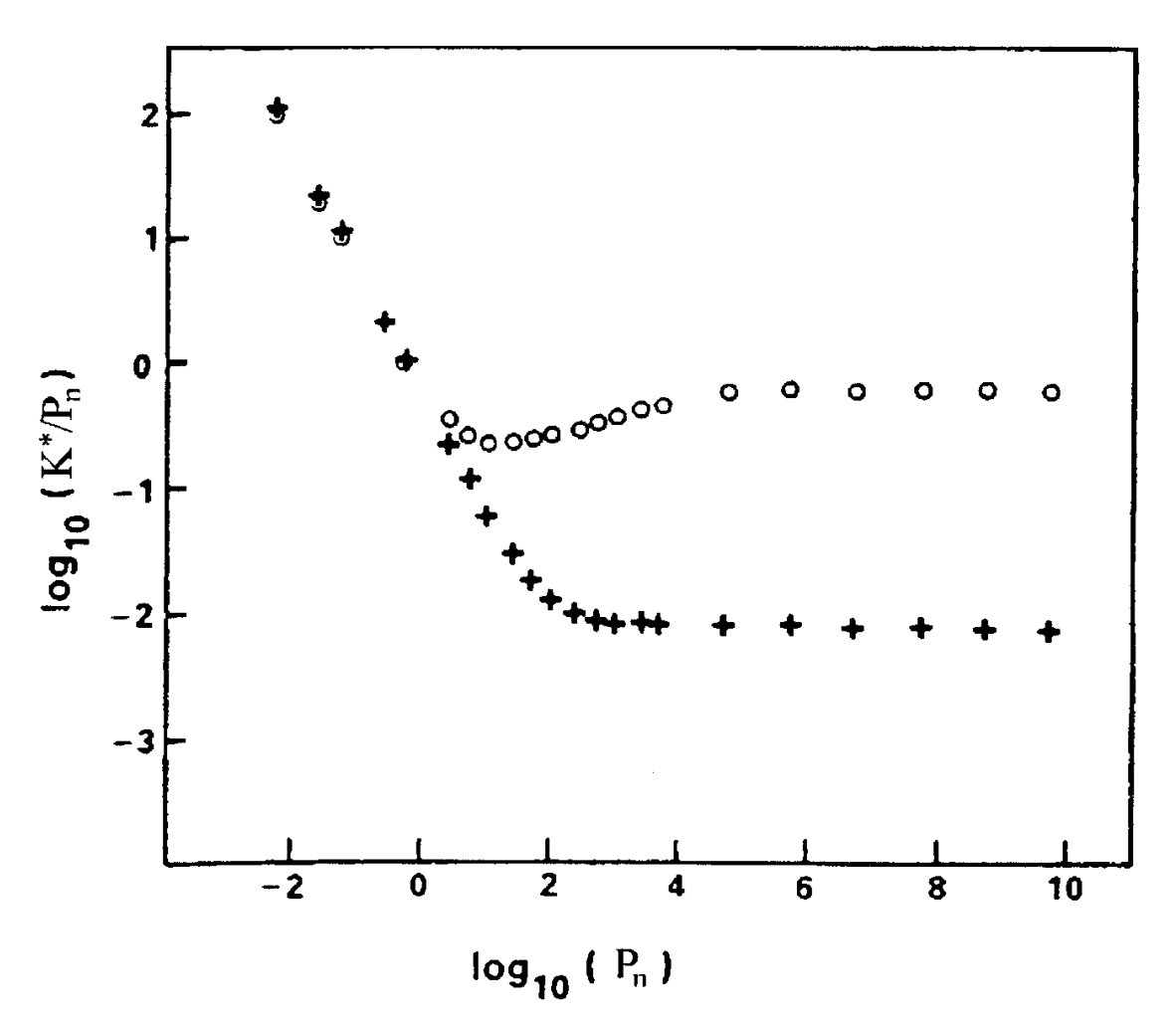


Fig. 3–19. Log-log relationship between normalized longitudinal dispersion coefficient,  $K^*/P_n$  and Peclet number,  $P_n$  for  $\Omega = 0.5$  (crosses) and  $\Omega = 4.5$  (circles) (de Arcangelis, 1986).

Recent particle tracking simulations in soil network models indicate that solute dispersion is more sensitive to the water retention curve than to the particular combination of pore-size distribution and topology that determine its shape (Vogel, 2000). Numerical particle tracking techniques have also been used to simulate solute dispersion in fractured media. Examples for two-dimensional randomly intersecting fracture networks include the models developed by Hull et al. (1987), Smith and Schwartz (1984), Robinson and Gale (1990), and Clemo and Smith (1997). Recently Nordqvist et al. (1996) and Margolin et al. (1998) have extended this approach to three-dimensional fracture networks.

### Variable Shape and Variable Size Distribution

Wendt et al. (1976) proposed a model for solute dispersion in heterogeneous porous media based on nonequilibrium thermodynamics. Their model, which allows for both variable pore shape and size distribution, is constructed from parallel arrays of interacting pores arranged in series. The relative error introduced by assuming the medium can be described by an equivalent uniform pore-size distribution was shown to be small.

Chatzis and Dullien (1977) were the first to use tubular bonds and spherical sites to simulate pore throats and bodies respectively, in network models of porous media. Previously, intersections (sites) were assumed not to have any volume. In their model, individual elements are represented as cylindrical tubes with spherical indentations in the middle (Fig. 3–17C). Bond lengths and bond and site radii can be drawn from independent distribution functions, or as is more common, correlated with each other so that only one distribution function is required (Ioannidis & Chatzis, 1993).

Dullien (1992) and Ferrand (1992) have applied numerical particle tracking methods to compute dispersion coefficients for such networks. In the study by Ferrand (1992) the conductivity of each bond was calculated using an expression that included entrance and exit effects as fluid moves between larger sites and narrower bonds, as well as the resistance of the bond itself. The lattice dispersivity was shown to increase linearly as the geometric standard deviation of the bond-size distribution was increased. Although not widely used at present, this modeling approach offers much promise for future research on the interplay between pore shape and size distribution in determining the relationship between  $K^*$  and  $P_n$ .

#### **EMERGING AREAS**

A number of new approaches to the problem of evaluating dispersion at microand mesoscopic scales have appeared during the past 10 to 15 yr. In particular, cellular automata modeling, advances in numerical simulations, improved physical micromodels, and the development and application of fractal and percolation concepts are significant steps. Most of these approaches are outgrowths of the computer revolution that took place over the same period. In fact, the development of more formal mathematical foundations for some of these approaches has followed their implementation on computers.

#### **Prefractal Networks**

Fractal models for soil structure and rock fractures are becoming increasingly popular (e.g., Sahimi, 1993; Baveye et al., 1998). The primary appeal of these models is their ability to parsimoniously parameterize complex structures. Scale symmetry or scale invariance, in which an object is at least statistically the same after magnification, is a fundamental property of fractals and can also be observed in numerous natural phenomena. Thus, it is logical that some investigators have examined theoretical transport in known prefractals.

Adler (1985) considered Taylor dispersion in fractal capillary networks including a "tree" and a Sierpinski gasket. Dispersion on the tree was solved exactly while a numerical computation was necessary for the Sierpinski gasket. The network tree that Adler considered had every branch splitting into two branches at each vertex. Depending on the value of a parameter  $\Gamma$ , either more ( $\Gamma > 1$ ), less ( $\Gamma < 1$ ), or the same ( $\Gamma = 1$ ) volume is available to the moving fluid at each vertex. Consequently, for  $\Gamma > 1$ , the velocity in each branch decreases as the solute progresses through the network. In this case particle position, x(t), (starting at x = t = 0) is given by

$$x(t) = \frac{\log(qt\log\Gamma + 1)}{\log\Gamma}$$
 [43]

where q is the flow of fluid into the 'trunk' of the network tree. The first moment of the probability density follows a logarithmic increase with time. The mean squared displacement, which is related to the dispersivity, quickly reaches a constant value in this case.

When  $\Gamma$  < 1, the velocity in each new level of branches increases and both moments show an exponential decay with time. Adler (1985) indicated that this type of behavior had not been previously reported. For  $\Gamma$  = 1, the first moment scales as t and the second moment as  $t^2 + t$ , which is consistent with Taylor behavior for spatially periodic media (Brenner, 1980).

By specifying the fluid outflow at two of the three external vertices of a Sierpinski gasket-like network of capillaries (Fig. 3–20), Adler (1985) showed that the internal flows on each of the branches could be computed using Kirchoff's Law. The ratio of the outflows is given by a parameter  $\lambda$ . Adler (1985) demonstrated the seemingly paradoxical result that the anisotropy introduced by  $\lambda$  does not affect the flow in the interior of a large network of this construction. Consequently, Taylor dispersion in such a network was not expected to be sensitive to  $\lambda$ . A numerical solution was used to determine particle transport in a network consisting of 27 triangular elements. Graphs of the time evolution of the first and second moments were presented but no fitted functional representations were provided. The overall conclusion was that Taylor dispersion is nearly independent of the flow field when the size of the network is large enough.

Ross (1986) investigated transport in randomly located and oriented fractures. Each fracture is assumed to be filled with a porous material and is assigned a finite area, and a transmissivity (T = fracture width  $x k_{\text{sat}}$  of filling material) in proportion to its width. Ross presents a model based on random walks that accounts for

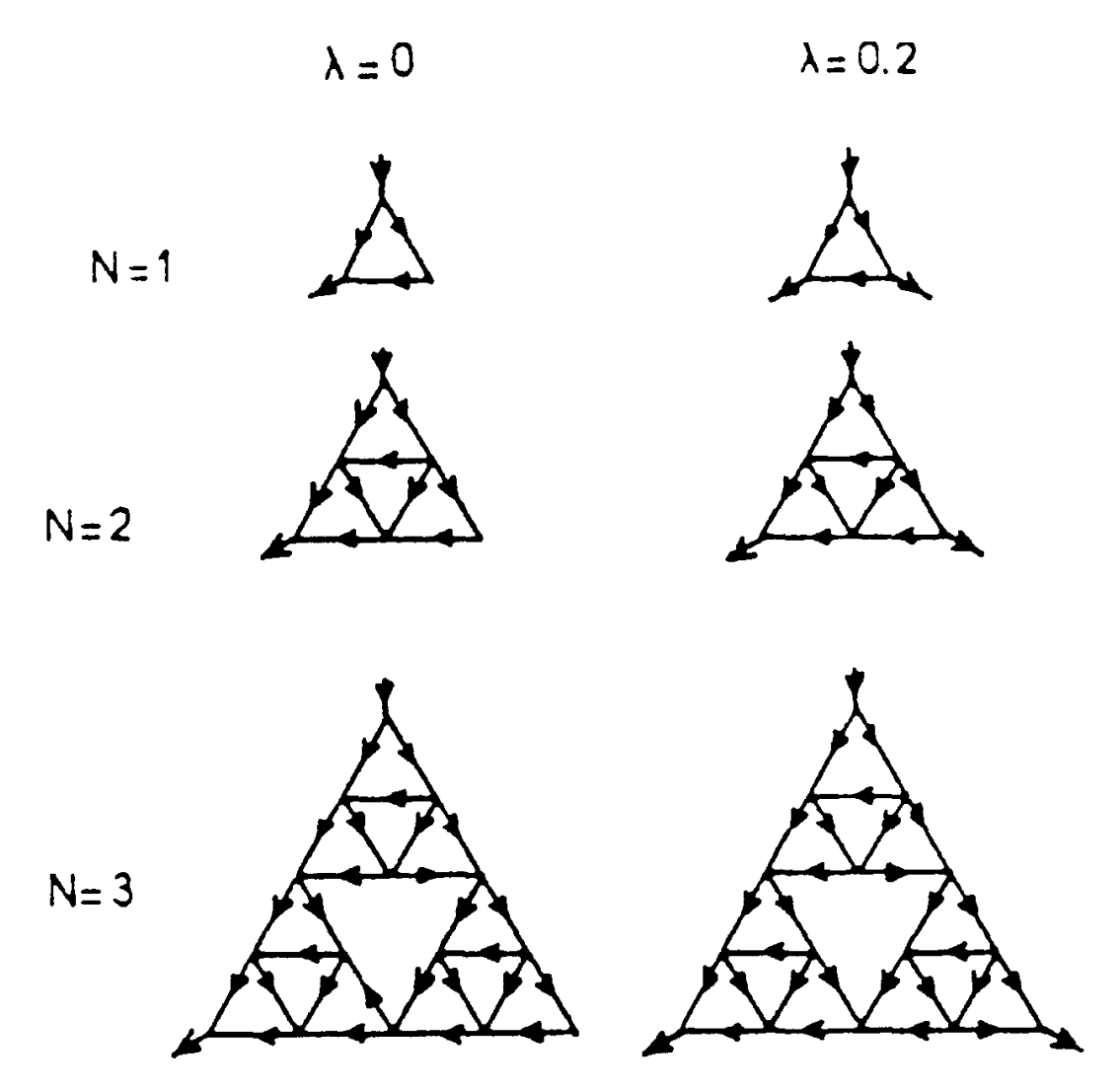


Fig. 3–20. Flow in a Sierpinski gasketlike network of capillaries as a function of iteration level (N) and the  $\lambda$  parameter (Adler, 1985).

the observed relationship between apparent dispersivity and the physical scale of the solute transport system. He points out that because the water velocity in a fracture is in general different from the mean water velocity of the entire network, a particle's motion can be described as the sum of a uniform drift and a random walk component. The random walk is made up of straight steps that represent the particle's residence in a fracture "zone". A fracture zone is defined as the planar area of a fracture bounded by intersecting fractures of the same or greater transmissivity. The linear dimension of a zone is h. The number density function of zones of linear dimension h is defined as N(h), so that N(h)dh is the number of zones per unit volume with linear dimension between h and h + dh. The density function N(h) is assumed to be a power law  $N(h) \propto h^{-p}$ , where p is related to the fractal dimension (Mandelbrot, 1983). Due to the definition of a fracture zone described above, longer fractures are generally more transmissive and an equation of the form  $T(h) \propto h^q$  can be applied. Assuming q = 1 leads to a linear relationship between the standard deviation of particle position and the distance traversed.

Redner et al. (1987) evaluated pure mechanical dispersion (no diffusion) in a self-similar hierarchical model of a porous medium. They expected their model

to be useful in percolation networks near the percolation threshold where the fluid path is fractal (see "Percolation Models" below). Two regimes of behavior were observed depending on the value of an asymmetry parameter that controls the width of the distribution of transit times in the network. In the first regime, spreading occurred at the same rate as the rate of downstream convection (i.e.,  $K^* \propto P_n$ ). In the second regime, dispersion is dominated by small amounts of tracer moving through the slowest bond in the network and is greatly enhanced.

Mazo (1998) studied Taylor dispersion in fractal media and found that the proportionality constant between the spatial spreading of a solute pulse and the time depended on both the fractal dimension of the medium and the dimension of the random walk through it. In normal diffusion the average particle position  $\langle x^2 \rangle$  is directly proportional to the time. Diffusion in fractal media is anomalous with  $\langle x^2 \rangle$  proportional to  $t^{2/d_t}$ , where  $d_t$  is the random walk dimension.

Mazo (1998) points out that when the time is sufficiently long that diffusing particles can sample the entire velocity distribution (e.g., the entire cross-section perpendicular to flow in a capillary tube), the velocity distribution of each particle is the same as that of the distribution of velocities in the flow. In an unbounded flow regime, an infinite time would be required and anomalous dispersion results.

On the basis of a number of assumptions, Mazo (1998) derives an expression for the effective dispersion coefficient in terms of the velocity profile, system geometry, etc., that reduces to Taylor's (1953) formulation for dispersion in a capillary (i.e., where the dimensionless velocity distribution is given by Eq. [15]). Using this approach dispersion for other velocity profiles can be calculated, although no other examples are presented.

### **Percolation Models**

Percolation models are typically based on a network of bonds and sites, which can be thought of as pore necks and pore bodies, respectively. The relationship between percolation models and network models is discussed by Berkowitz and Ewing (1998). In general, percolation models are simply less well connected than network models and the focus of percolation model studies is on transport processes near the percolation threshold.

In two dimensions, the simplest percolation models consist of a uniform array of squares where some fraction of the squares are randomly chosen as conductive pores and the remainder are considered nonconductive solids. Conductive bonds of zero volume occur where adjacent pore sites share edges. In this case, the fraction of conductive pores is the porosity. This type of connection to adjacent pores has a coordination number of four in two dimensions. Alternatively, conductive bonds can also be specified where a diagonal pair of pore sites share single points at their corners (coordination number 6 in two dimensions). Generalization to three dimensions is straightforward.

Extensive empirical studies of percolation networks have revealed "universal" critical percolation thresholds ( $p_c$ ). That is, for percolation to occur across a network, some critical proportion of the squares (or blocks in three-dimensions) must be pores. In two dimensions,  $p_c \neq 0.59$  for conductive bonds at all shared edges (Sahimi, 1995). In three dimensions,  $p_c$  is considerably smaller. Measurements have

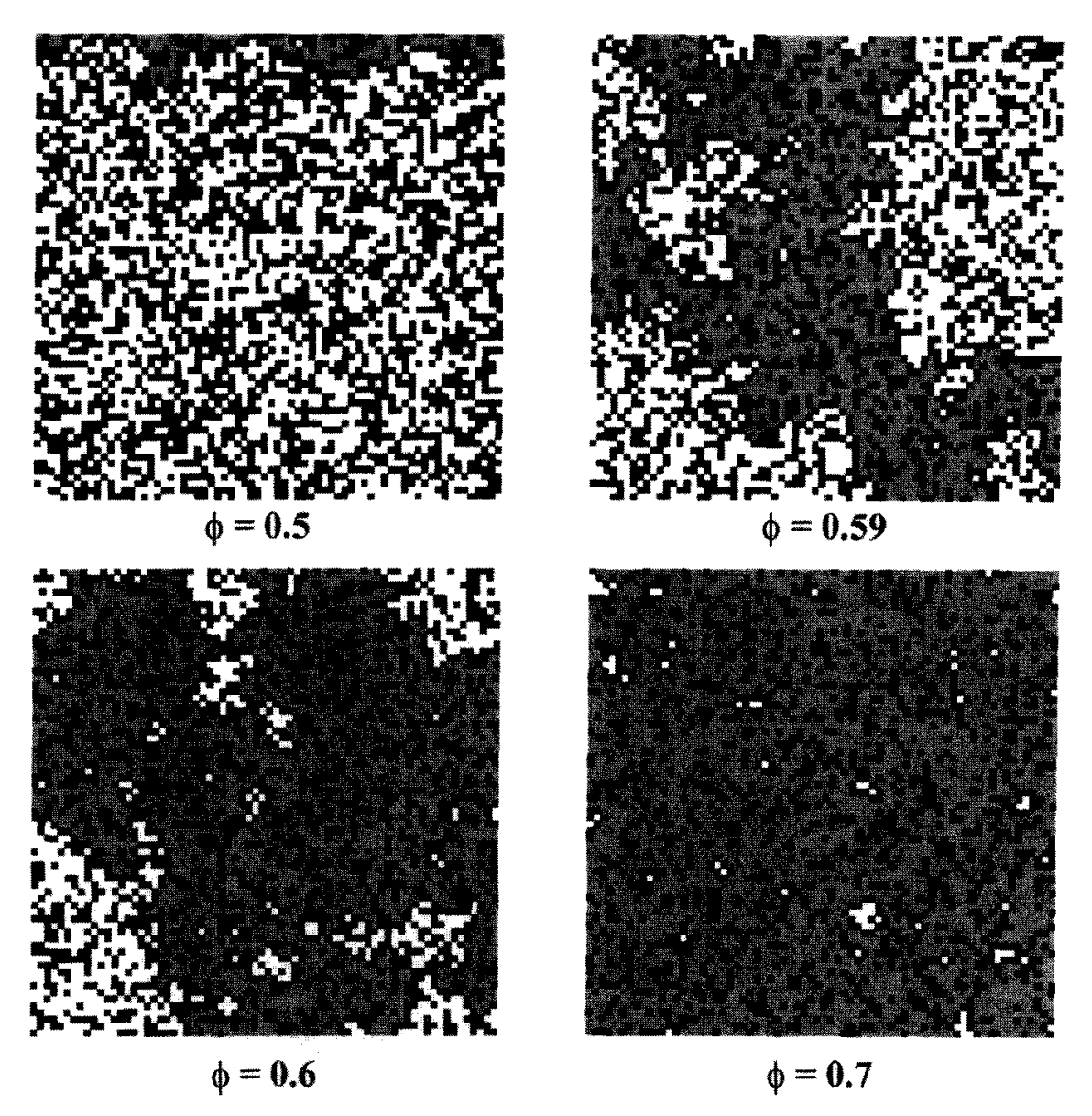


Fig. 3–21. Percolation into random uncorrelated media with varying site occupation probabilities (areal porosities). Solids are black. Continuity of major percolation paths from upper boundary indicated by shading.

also shown that the connected path through a percolation network (the "backbone") is fractal when the porosity is near  $p_c$ . Pores connected to this path are part of the "sample spanning" or percolation cluster. Note that near  $p_c$ , there are many dead-end pores connected to the backbone.

Figure 3–21 illustrates site percolation into the top of 70 by 70 arrays of sites. The percolation process can be thought of as describing the migration of a conservative solute applied to the top boundary. Each of the four networks shown has a different porosity. Below the percolation threshold at  $\phi = 0.5$  (Fig. 3–21A), no connected pathways extend appreciably into the array. Close to the percolation threshold ( $\phi = p_c = 0.59$ , Fig. 3–21B) an open pathway exists between the upper and lower boundaries of the network. Pores connected to the path are known as the percolation cluster. At higher porosities (Fig. 3–21C,D), most of the array is included in the percolation cluster.

E	$\beta_A$	τ	$\beta_{\mathrm{B}}$	d†	$d \ddagger$
2	5/36	4/3	0.48	91/48	1.64
3	0.41	0.88	1.05	2.52	1.8

Table 3–1. Universal constants for percolation networks (Sahimi, 1993).

The correlation length  $\xi_p$  is defined as the average distance between two sites that belong to the same cluster. According to Sahimi (1995), for length scales L >>  $\xi_p$  the percolation system is macroscopically homogeneous and can be modeled with the CDE. For length scales  $l_b << L << \xi_p$ , where  $l_b$  is the length of a bond, the percolation system is macroscopically heterogeneous and fractal.

In addition to the percolation threshold, there are a number of additional universal properties of percolation networks near  $p_c$  These include (Sahimi, 1993):

- 1. the correlation length,  $\xi_p \propto (\phi p_c)^{-\tau}$
- 2. the accessible fraction of open pores (i.e., open pores connected to the sample spanning cluster),  $X^{A} \propto (\phi p_{c})^{\beta_{A}} \propto \xi_{p}^{-\beta_{A}/\tau}$
- 3. the fraction of open pores in the backbone,  $X^{\rm B} \propto (\phi p_{\rm c})^{\beta_{\rm B}} \propto \xi_{\rm p}^{-\beta_{\rm B}/\tau}$
- 4. fractal dimension of sample spanning cluster,  $d = E \beta_A/\tau$
- 5. fractal dimension of backbone,  $d = E \beta_B/\tau$

where E is the topological (conventional) dimension of the network, and the values of the universal constants for two- and three-dimensional systems are summarized in Table 3–1. These properties are independent of the details of the percolation network. For example, the fractal dimension of the sample spanning cluster is the same on square, triangular, honeycomb, Voronoi, and other two-dimensional lattices (Berkowitz & Ewing, 1998).

It is possible to extend standard percolation networks to the case where the porous medium is a prefractal. Such models may allow more realistic simulation of dispersion in heterogeneous porous media. Figure 3–22 illustrates the percolation network approach applied to randomized Sierpinski carpets with the same scaling factor ( $b_f = 10$ ) and iteration level (i = 2), but slightly different fractal dimensions ( $d_m = 1.778$  and 1.748 for Fig. 3–22A,B, respectively). This results in different total porosities ( $\phi = 0.64$  and 0.6864 for Fig. 3–22A,B, respectively). Percolation across the carpet occurs when the porosity exceeds the percolation threshold for these structures. Percolation generally occurs through large pores interconnected by small pores. Expressed in terms of  $d_m$ , percolation thresholds for prefractal porous media increase with increasing  $b_f$  and i (Sukop et al., 2001).

Berkowitz and Ewing (1998) discuss continuum percolation, which differs from percolation on lattice networks. The important differences are:

- 1. the number of connecting bonds per site is variable
- 2. bond lengths vary
- 3. bond directions vary

Figure 3–23 illustrates a continuum percolation network composed of randomly oriented fractures. Such networks might better represent structured soils than standard

<sup>†</sup> Sample spanning cluster.

<sup>#</sup> Backbone.

lattices. In this type of network, the site occupation probability (or porosity)  $\phi$  used previously loses meaning and a new parameter must be defined. Berkowitz and Ewing (1998) demonstrate that the number of bonds per site (or number of intersecting segments per segment), denoted by  $B_s$ , and the critical number of bonds per site ( $B_{sc}$ ) are appropriate substitutes for the  $\phi$  and  $p_c$  respectively of lattice networks.

Berkowitz and Ewing (1998) also describe distinctions between three types of percolation: ordinary, invasion, and invasion with trapping. In ordinary percolation, sites contain tracer simply on the basis of their connection with the source. Figures 3–21 and 3–22 are examples of ordinary percolation. In invasion percolation, sites fill with tracer in the order determined by the size of pore necks. Invasion percolation and invasion percolation with trapping apply primarily to multiphase conditions (e.g., infiltration of water into soil containing air, or water/oil systems) and are not considered further here.

Luxmoore and Ferrand (1993) pointed out that pores that belong to the sample spanning cluster but not the backbone can be thought of as containing stagnant "backwater" zones. Thus, empirical determination of the proportions of backbone and "backwater" porosity in random and nonrandom pore percolation networks could be quite useful. They anticipated that percolation modeling would play an important role in understanding the effects of transient pore scale processes on solute transport.

On the basis of random walk arguments, Koplik et al. (1988) show the relations  $K^* \propto P_n$ ,  $K^* \propto P_n \ln P_n$ , and  $K^* \propto P_n^2$  for: (i) a bundle of uniform stream tubes that meet at perfect mixing chambers separated by a characteristic length l, (ii) nonuniform bond transit times, and (iii) the presence of dead-end pores, respectively. The relationship  $K^* \propto P_n^2$  is also obtained for percolation networks near the percolation threshold when the characteristic length is the percolation correlation length and the molecular diffusion coefficient is adjusted for the presence of the percolation network.

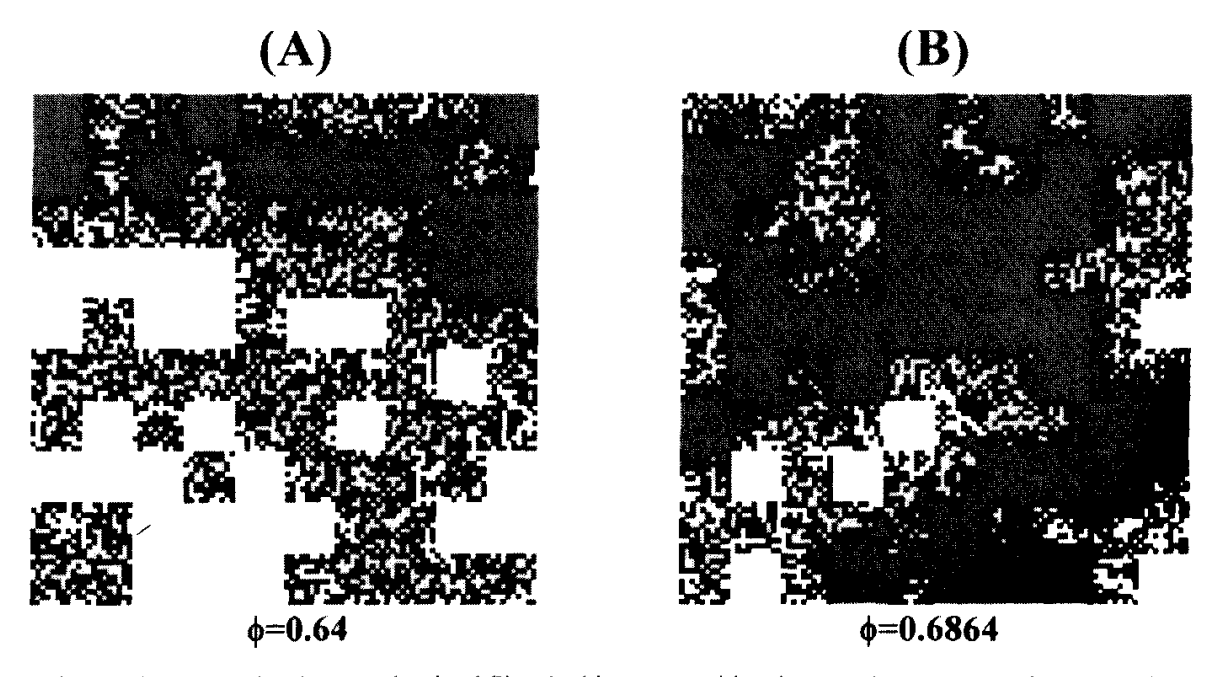


Fig. 3–22. Percolation into randomized Sierpinski carpets with: (Λ) porosity = 0.64, and (Β) porosity = 0.6864. Solids are black. Continuity of major percolation paths from upper boundary indicated by shading.

Koplik et al. (1988) extended the concept of a random walk in a disordered porous medium to account for local fluid velocities by using a CDE with either a diffusion coefficient or a Taylor dispersion coefficient to simulate transport inside each bond of a bond percolation network. This incorporates the convectional bias in the network tubes while retaining unbiased, purely diffusional behavior in the dead-end pores. Using a probability propagation algorithm, they were able to solve for the first-passage probability. According to Koplik et al. (1988), this type of probability propagation is superior to computations that follow the paths of individual particles because low velocity paths, which dominate the higher order moments, tend to be insufficiently sampled in finite simulations.

Working with a small hypothetical network that includes a single dead-end pore, these authors present an argument showing that, at high Peclet number, the mean transit time is the total pore volume divided by the flux. This is equivalent to computing the average velocity as the areal flux q divided by the water content (or porosity for saturated materials) (Eq. [6b]). The implication is that all of the pore water contributes to the average transit time, irrespective of its velocity. This is due to the cancellation of the effects of the probability of entering a particular portion of the medium and the travel time through that portion; the entrance probability is

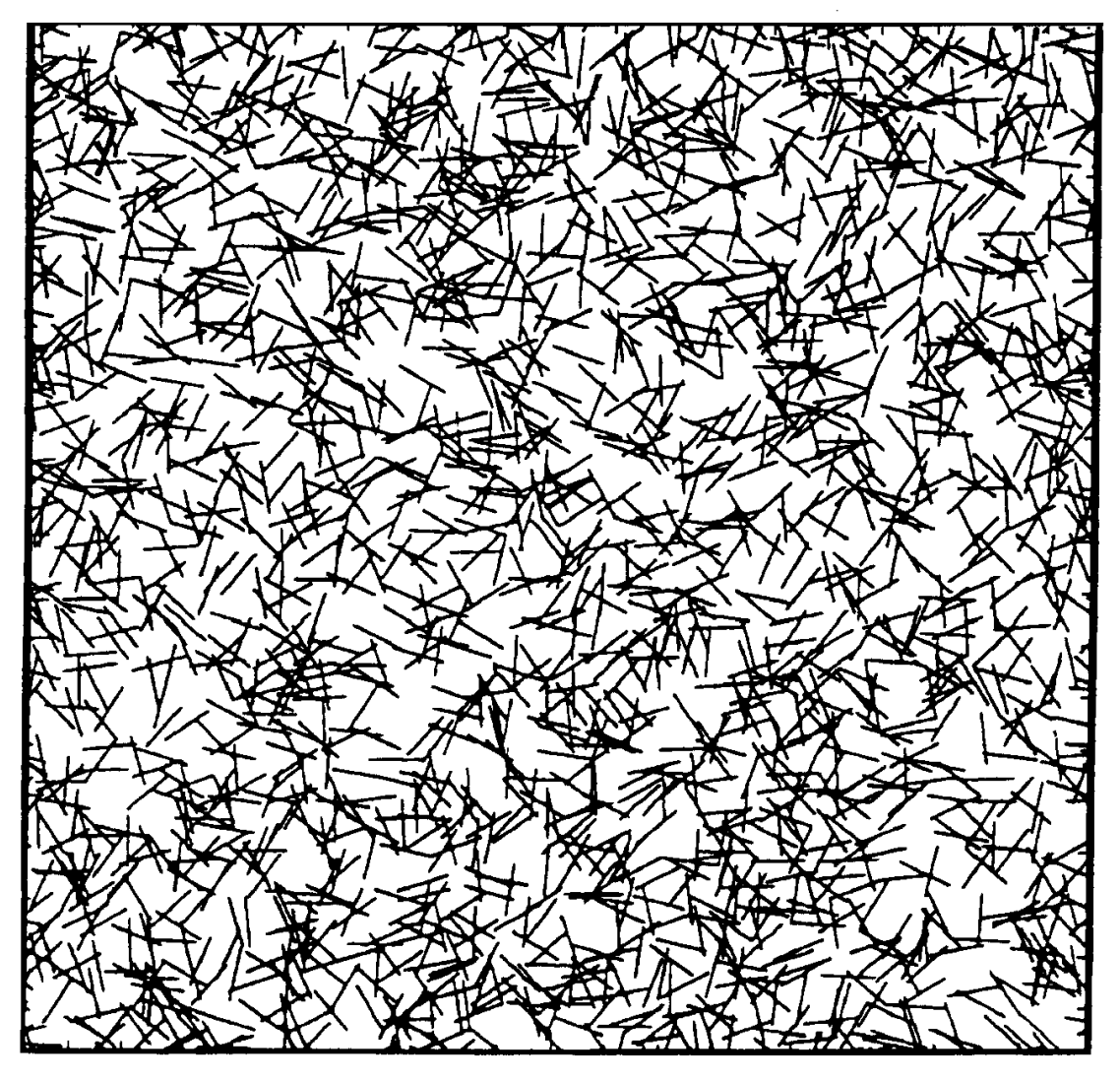


Fig. 3-23. Continuum percolation network comprised of randomly oriented fractures (Berkowitz & Ewing, 1998).

proportional to velocity while the travel time is inversely proportional to velocity. For this system,  $K^* = f_v P_n^2$  where  $f_v$  is the relative volume of dead-end space and the characteristic length is the length of the dead-end pore. Extension of this model to include multiple dead end pores of differing volumes shows that the largest dead-end pores have the most significant effect on the higher order moments.

Koplik et al. (1988) considered flow rates in percolation networks from zero (pure diffusion) to extremely high (the convective limit where the average transit time varies linearly with  $1/\nu$ ). The results obtained for many network realizations were averaged. In the case of  $2 \times 2$  and  $3 \times 3$  network lattices, all possible configurations could be evaluated and hence, the exact averaged transit time moments could be determined. These authors found that anomalous diffusion occurs on networks at the percolation threshold at zero flow. Hence, the CDE does not apply in this case. Koplik et al. (1988) demonstrate that the moments of the transit time distribution for transport near the percolation threshold scale universally.

Yanuka (1992) considered convection-dominated flows on two-dimensional percolation networks. A flow realization was obtained by randomly assigning conductivities to each bond in the network, imposing a pressure gradient across the network, and solving for the flow throughout the network. Two cases were considered; in the first, all bonds between sites were considered open while in the second, the probability of an open bond was near the percolation threshold. Random walks through the networks were weighted by the flow in each bond. In the first case, K is constant and in the second,  $K \propto \langle x \rangle^{1.2}$  as observed previously.

Berkowitz and Braester (1991) presented similar results for fracture networks. Beginning with a regular network of orthogonal, equal length fractures whose apertures followed a lognormal distribution, they created a network near the percolation threshold by removing the fractures having the smallest apertures. A pressure drop was imposed across the network by fluid injection at constant pressure in the center of the domain, and maintaining a constant pressure at the perimeter. Flow in each fracture was calculated with the Hagen-Poiseuille law and flow in the network as a whole was computed by requiring a volume balance at each node. Particles were then tracked along random walks directed by the relative flow in two or more fractures in which flow is away from a node or fracture intersection. Close to the percolation threshold, this procedure gave  $\langle x^2 \rangle \propto t^{1.3}$ , which corresponds closely to the theoretical relationship for length scales shorter than the REV scale and no transverse molecular diffusion. They point out that, because  $\langle x^2 \rangle$  increases faster than linearly with time, dispersion in their network cannot be simulated as a Fickian diffusion process. Sahimi (1993) distinguishes between fractal transport in which  $\langle x^2 \rangle$  increases slower than linearly with time and superdiffusive transport where  $\langle x^2 \rangle$  increases faster than linearly with time. We suspect that there may be a close relationship between the fractional CDE (Benson, 1998) and the superdiffusive case.

## **Numerical Models and Particle Tracking**

Solution of the Navier-Stokes equations of fluid flow is possible using numerical methods. In porous media, considerable simplification is often possible because velocities are generally low and flow is confined to the small spaces between

pore walls. Early examples of the application of numerical solutions of flow in porous media were limited to solutions of flow in highly idealized pores (Ananthakrishnan et al., 1965; Nunge & Gill, 1970; Stark, 1972; Azzam & Dullien, 1977). Solutions for idealized pores can be linked together to simulate spatially periodic media. Because of the explosion in computing power and improvements in numerical methods, numerical solutions of the Navier-Stokes equations subject to more complex boundaries that were once considered intractable can now be computed (e.g., Koplik, et al., 1993).

Cao and Kitanidis (1998a,b) used finite element methods to simulate flow in sinusoidal and indented pores. They reduce the Navier-Stokes equations to the steady Stokes form by considering that the flow is slow and close to no-slip boundaries and by assuming that inertial terms are negligible (i.e., low Reynold's Number). In addition, it is assumed that the reaction to an external impetus is rapid. Hence, time derivatives can be neglected. The simplified equations are:

$$\frac{\partial v_{x}}{\partial x} + \frac{\partial v_{y}}{\partial y} = 0$$
 [44]

$$g \frac{\partial \Psi}{\partial x} = v \left( \frac{\partial^2 v_x}{\partial x^2} + \frac{\partial^2 v_x}{\partial y^2} \right)$$
 [45]

$$g \frac{\partial \Psi}{\partial y} = v \left( \frac{\partial^2 v_y}{\partial x^2} + \frac{\partial^2 v_y}{\partial y^2} \right)$$
 [46]

in which  $v_x$  and  $v_y$  are the velocities in the x and y directions respectively. The first equation is the incompressibility condition, and the second and third are momentum conservation equations. These equations are linear so that if  $(v_x, v_y, \psi)$  is a solution, then  $(av_x, av_y, a\psi + b)$  is also a solution. This means that they have the same behavior as the macroscopic Darcy's equation; an increased head gradient results in a proportional increase in flow velocity. Cao and Kitanidis (1998a,b) use a hierarchical multigrid solver to compute the solutions to Eq. [44] to [46]. Three two-dimensional cases were considered: a "sharp" single sinusoidal pore, a "flat" double sinusoidal pore, and a double indented pore. In the "sharp" sinusoidal pore (length/average width = 1.25 – 1.5), there is a backwater zone that is connected to the main flow only by diffusion. In the flatter pores (length/average width = 2.5), no backwater zones are apparent. Backwater zones with much stronger circulation in them were predicted for the indented pore.

With complete solutions of the velocity distributions in individual pores, solute transport in a series of linked pores could be computed explicitly. This was done for the sharp sinusoidal pore (length/average width = 1.5), in Cao and Kitanidis (1998a). Cao and Kitanidis (1998a) point out that, when the Peclet number is large, strong concentration gradients between main flow zones and backwater zones can develop and be sustained at the front and back of a migrating solute pulse. Using a homogenization technique, they were able to estimate the macroscopic dispersion coefficient for a spatially periodic array of pores from the solution to a steady

	Square array		Hexagonal array	
φ	С	α	c	α
0.804 0.599 0.400	0.109 0.109 0.174	1.734 1.789 1.760	0.0594 0.0650 0.0319	1.820 1.765 1.659
Avg.	0.130	1.761	0.0520	1.748

Table 3–2. Prefactor c and exponent  $\alpha$  in  $K^* = cP_n^{\alpha}$  for different  $\phi$  and packings (Edwards et al., 1991).

convection dispersion equation for a single pore. The results of this approach compared favorably with direct numerical solutions of transport in the pores.

Eidsath et al. (1983) used finite element methods to numerically investigate dispersion in two dimensional, low Reynolds number flow through spatially periodic arrays of cylinders with a porosity of 0.37. They found that  $\alpha \cong 1.7$  in  $K^* \propto P_n^{\alpha}$ . Edwards et al. (1991) also used finite element methods to compute the longitudinal and transverse dispersion coefficients for a two-dimensional, spatially periodic array of cylinders. Their results differed from the results of Eidsath et al. (1983), possibly due to differences in the details of the numerical methods.

Edwards et al. (1991) found that the longitudinal dispersivity increased at a rate less than proportional to  $P_n^2$ , although  $P_n^2$  dependence was reached asymptotically for large Peclet numbers. Packing of the cylinders had the strongest impact on solute spreading, with arrangements that lead to more curvature in the streamlines having lower longitudinal dispersivities. Reducing the total porosity in a square array of cylinders caused an increase in dispersivity that was attributed to increased velocity gradients between the cylinders as porosity declined. The packings (staggered and hexagonal) that have more tortuous flow paths showed reduced dispersivity on reducing the porosity. Edwards et al. (1991) also found that  $K^*$  could be fitted to a power-law function of the Peclet number. The exponents and prefactors for different packings and porosities estimated by least squares regression are listed in Table 3–2. The effect of the Reynolds number was also considered; longitudinal dispersivity increased with increasing Reynolds number.

Salles et al. (1993) determined the dispersion coefficient as a function of Peclet number for spatially periodic assemblages of deterministic, fractal, random, and reconstructed porous media unit cells. Dispersion was computed by numerically solving a vectorial steady-state convection diffusion equation. For the spatially periodic media considered, the long-time behavior was shown to be Gaussian (i.e., to follow the CDE). However, they suggest that the pre-Gaussian transient may persist for a very long time, and that experimental samples used to estimate the dispersion are generally too small.

Giona et al. (1995) studied diffusion in the presence of a constant convective field in percolation clusters with stochastic differential equations and a coupled exittime equation. On the basis of numerical studies on percolation clusters near the percolation threshold, they found that the volume-averaged exit time as a function of  $P_n$  did not follow the normal relationship (in which it is proportional to  $1/P_n$ ) but instead increased monotonically with  $P_n$ . Their approach needs generalization to more realistic convective fields. They also present exit-time analyses for transport on diffusion limited aggregates and in deterministic fractals.

Numerical models have also been applied to simulate macrodispersion in spatially variable  $k_{\text{sat}}$  fields (e.g., Thompson & Gelhar, 1990; Moissis & Wheeler, 1990; Wheatcraft et al., 1991). This "Darcian" approach requires averaging of flow over some Representative Elementary Volume (REV).

Moissis and Wheeler (1990) used finite element methods to compute unstable, miscible displacement in  $k_{\rm sat}$  fields where  $\ln k_{\rm sat}$  followed an isotropic normal distribution with a mean  $\ln k_{\rm sat} = 0$ , variance  $\sigma^2$ , and a correlation length  $\xi$ . Instabilities in the flow leading to fingering were due to viscosity differences between the displaced and displacing fluids. The distribution of permeabilities near the inflow end of the simulation domain determined the location, initial number, and growth rates of the fingers. Highly correlated permeabilities caused fewer fingers to form initially, and their numbers were further reduced by mergers as displacement progressed.

Thompson and Gelhar (1990) investigated transport in similar three-dimensional spatially correlated  $\ln k_{\rm sat}$  fields. The flow problem was solved using an iterative seven-point finite difference scheme. The solute transport was evaluated using random walk particle tracking methods, with a large number of particles moved in discrete time steps by convective and diffusive forces. The results indicated that the longitudinal dispersivities grew at a rate proportional to the standard deviation of the  $\ln k_{\rm sat}$  field to the 1.3-power.

Wheatcraft et al. (1991) considered flow and solute transport in a medium composed of high and low  $k_{\rm sat}$  distributed according to a Sierpinski carpet fractal, reminiscent of low permeability pebbles distributed in a high permeability matrix. A multigrid solver was used to compute the flow field (Fig. 3–4B) and a particle-tracking algorithm was used to determine the tracer motion. No diffusion was considered. They found that dispersion increased with the scale of the simulation faster than could be predicted with other models.

#### Cellular Automata

Cellular automata are essentially algorithmic entities capable of interacting with their neighbors. The interactions give rise to complex behavior and allow ensembles of automata to "compute" solutions to boundary value problems that may be intractable for traditional analytical and numerical solutions of differential equations. Our particular interest is in the solution of fluid flow (Navier-Stokes equations) and solute transport in complex porous media. Much of the literature describing cellular automata applications to these problems has appeared in physics journals and workshop proceedings (e.g., Frisch et al., 1986; Baudet et al., 1989; Verheggen, 1992; Boghosian, 1993; Gutfraind et al., 1995). Rothman and Zalesky (1997) recently published a book on the topic.

Simulation of fluids using cellular automata is frequently referred to as "Lattice Gas" simulation because the automata exist on a lattice and carry out their computation by accounting for momentum exchange in collisions between "gas" molecules. Figure 3–24 illustrates the collision rules for a two-dimensional triangular lattice (Boghosian, 1993). Early simulations of fluid flow in a two-dimensional porous medium were carried out by Rothman (1988). Figure 3–25 shows fluid velocity vectors in a random porous medium. Complex patterns of the flow velocity

field in the two-dimensional porous medium including Poiseuille-like parabolic velocity distributions across flow channels and flow bifurcations and convergences are illustrated. A small eddy is observed in a dead-end pore near the lower right-hand side of the domain.

Galilean invariance (Rothman & Zalesky, 1997) is a fundamental tenet of Newtonian mechanics. It is invariance under the transformation x' = x - wt, where w is the constant velocity of a moving frame of reference, and embodies the concept that only the relative velocities and positions of two bodies determine their interaction. Galilean invariance is lost in lattice gas simulations because every particle has only one possible speed. This loss is an artifact that can be eliminated for incompressible fluids by re-scaling the velocity. According to Boghosian (1993), more sophisticated lattice gas models overcome this problem. Appropriate application of lattice gas models also requires certain restrictions on the mean free path of a particle (Rothman, 1988).

Baudet et al. (1989) used lattice gas automata to simulate flow and solute transport between two flat, parallel plates. They demonstrated good agreement between the lattice gas simulations and an analytical solution to the CDE based on the work of Aris (1959a) and Wooding (1960).

Gutfraind et al. (1995) extended the work of Baudet et al. (1989) with lattice gas simulations of solute transport in a channel bounded by symmetrical, self-affine (prefractal) surfaces. They found that, for Peclet numbers in the range of 20 to 50, the CDE described solute concentration profiles adequately. Increasing roughness

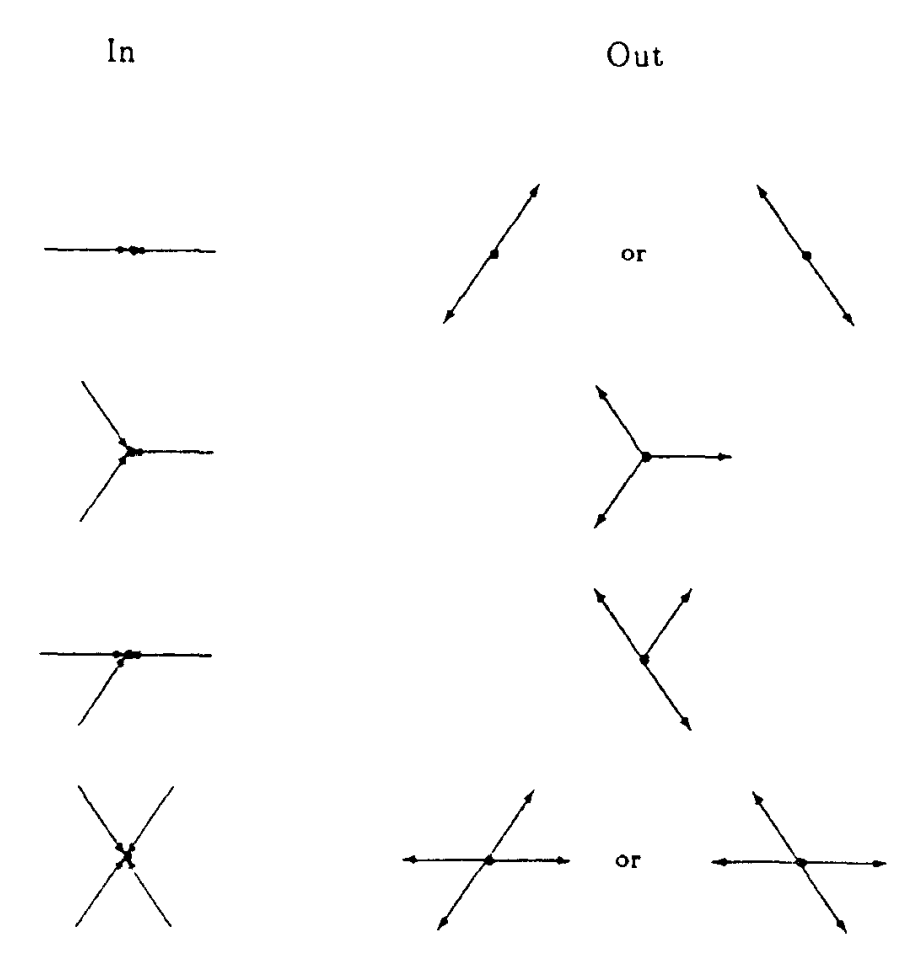


Fig. 3-24. Two-dimensional lattice gas collision rules (Boghosian, 1993)

of the boundaries increased dispersion. For the range of Peclet numbers investigated, they found that the effective dispersion coefficient varied as  $(\delta_{av}/\delta_H)^2$  where  $\delta_{av}$  is an average aperture size and  $\delta_H$  is the hydraulic diameter (see Fig. 3–9). The aperture size controls the transverse diffusion length and the hydraulic radius controls the flow velocity. Overall, they found that the effect of small surface irregularities on flow and solute transport was negligible, possibly due to incorrect scaling of the different profiles. The largest irregularities had the most important influence. This result is in accordance with analytical solutions for dispersion in indented and prefractal capillaries presented above.

Stockman (1997) considered dispersion in fractures using a lattice gas simulation incorporating sorption kinetics and buoyancy factors. He advocated the use of solute slugs over step changes in concentration because moment calculations are simplified and noise in the computation of second moments is reduced.

Perea-Reeves and Stockman (1997) applied a lattice-gas cellular automaton model to study solute dispersion, including the effect of fluid buoyancy arising from solution density differences, in a pocketed channel. They found good agreement with the indented capillary model discussed in the "Variable Shape, Discrete Pore Models" section. For Peclet numbers smaller than 3 however, they found that *K* was actually smaller than the molecular diffusion coefficient. They attributed this to the restriction to diffusion in the direction of flow imposed by the pocket walls. They also observed that density differences between the existing and introduced fluids

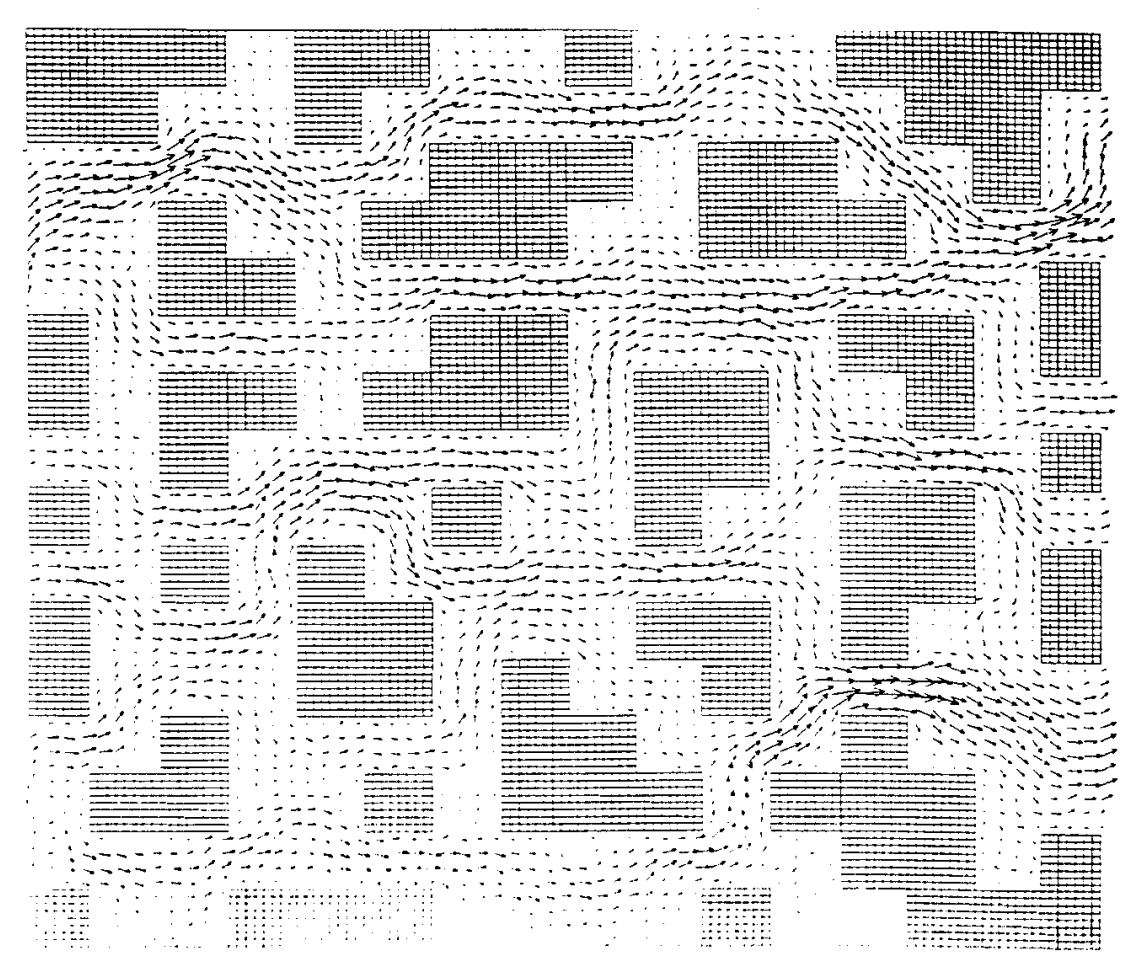


Fig. 3-25. Flow lines in a random porous medium computed with cellular automata (Rothman, 1988).

increased dispersion for a step increase in inlet concentration, and decreased dispersion when a pulse of denser fluid was injected into the system.

Stockman et al. (1997) provide details on the practical problems and limitations of lattice gas and lattice Boltzmann methods in flow and transport simulation. In particular, they focus on errors associated with boundary conditions, the accuracy required for useful comparison with experimental data, programming, and problem size and run-time issues. For lattice gas methods, they find that averaging over a large number of time steps is sometimes needed to resolve the flow velocity field. This limits the applicability of lattice gas methods to flow simulation under steady state or slowly varying conditions. In contrast, dispersive processes alone can be adequately simulated with lattice gasses by averaging a much smaller number of time steps. Lattice Boltzmann methods do not require averaging.

The bounce-back collision typically employed at fluid-solid boundaries, where fluid particles are turned back in the direction they came from following collision with a solid wall, causes the effective wall position to extend one half lattice unit into the fluid from the solid surface (Stockman et al., 1997). This is not a serious problem for velocity computations in slow flows, but has the potential to be a significant problem for tracer/dispersion simulations. Increasing the number of lattice points inside a flow channel can reduce this error, but is computationally very expensive.

There are also limits on the range of Peclet numbers that are achievable using lattice gas and Lattice Boltzmann methods. For lattice gasses, the achievable range depends primarily on the practical velocity range (0.001–0.1 lattice units per time step) and the characteristic length (usually the channel width). This is because the molecular diffusion coefficient is fixed by the lattice size and time step. Stockman et al. (1997) have found that varying the fluid velocity, the channel width, the viscosity, and the molecular diffusion coefficient independently and maintaining numerical stability is not always possible for Lattice Boltzmann methods.

All of the lattice gas applications discussed above are in two dimensions. Three-dimensional lattice gas simulations of fluids require a four-dimensional lattice (face-centered hypercubic or FCHC lattice) (Rothman & Zaleski, 1997).

# **Physical Micro-Models**

Researchers have used physical models of porous media to study flow problems for many years. For example, the Hele-Shaw cell appeared in the late 1800s (Sahimi, 1993). The first reported use of such models for two-phase systems is attributed to Chatenever and Calhoun (1952), who used Lucite and glass bead packs to view immiscible displacement of brine and crude oil (Buckley, 1991). Subsequently, etched and photo-etched glass were used to construct physical models. The use of molded resins for model construction was introduced in the 1970s (Buckley, 1991).

Generally, these physical "micromodels" are very thin (e.g., 0.2 mm) and are intended to approximate two-dimensional conditions. Corapcioglu et al. (1997) combined video recording and image analysis technology to quantify the results of micromodel solute transport simulations. Transport in the micromodel could be simulated accurately as a porous medium or as a network of discrete fractures. The frac-

ture model neglected the pores formed at the intersection of fractures however, and gave excessive dispersion.

Charlaix et al. (1987) used glass beads and various degrees of sintering to reduce the porosity and modify the pore space. They found that in unsintered glass beads (37% porosity), the dispersion of CaCl<sub>2</sub> solutions could be described by a Gaussian model, while "anomalous" dispersion with long-tailed BTC was observed when even slight modifications (reduction to 34% porosity) were induced by sintering. The BTC data were evaluated with a capacitance model and a linear relationship between the characteristic exchange time between the mobile and immobile zones was found to vary inversely with the flow velocity.

In a related study, Hulin et al. (1988) studied dispersion of CaCl<sub>2</sub> solutions in mixtures of glass beads of two different sizes that were subjected to sintering. At the percentage of small beads that yielded close to the smallest porosity, nearly Gaussian behavior was observed and the dispersion coefficient was close to that in a monosized beads of similar porosity. Together with the results of Charlaix et al. (1987), this suggests that small-scale details of the pore structure were not as important in determining the dispersion characteristics as the reduction in connectivity induced by sintering.

Charlaix et al. (1988) also conducted a study of NaCl and dye transport in etched transparent lattices. A fully connected square lattice with a lognormal distribution of channel widths and a partially connected hexagonal lattice (a percolation network) were considered. They concluded that the disorder and heterogeneity of the medium determined the characteristic dispersion length. From experimental data on the percolation network, they showed that this dispersion length was close to the percolation correlation length  $\xi_p$ .

#### **DISCUSSION AND CONCLUSIONS**

There are many different models for predicting solute dispersion from pore geometrical characteristics. Despite the diversity of approaches, some general trends have emerged. The following discussion applies mainly to the range  $5 < P_n < 10^5$ , and assumes that mixing due to convection dominates over diffusive processes.

Relating  $K^*$  to  $P_n$  implies that a characteristic length,  $\ell$ , can be defined and measured for the system under investigation. For individual pores,  $\ell$  is usually taken to be the radius in capillary tube models; we recommend use of an equivalent cylindrical radius based on the star length concept (Serra, 1982) for irregularly shaped pores. For multipore systems, with a range of pore sizes, one possibility is that  $\ell$  be defined as the equivalent cylindrical radius of the largest pores that are present. The largest pore size might be preferable to the mean pore size, which has been widely used in the past, because it does not assume any particular pore size distribution function (e.g., normal or log-normal) and can accommodate fractal porous media, which do not have a characteristic mean length scale. Furthermore, the size of the largest pore present is readily obtainable from image analysis or water retention measurements.

Within individual pores the microscopic distribution of flow lines results in  $K^* \propto P_n^2$  (Taylor, 1953, 1954). Differences in pore space geometry are manifested in the constant of proportionality or prefactor in this relationship, which increases in magnitude as pore shape becomes more irregular (Aris, 1956, 1959b). In contrast, mechanical mixing in multipore systems, with a single (mean) pore water velocity assigned to each pore, results in  $K^* \propto P_n$  (Day & Forsythe, 1957; Torelli, 1972). The prefactor in this relationship also increases with increasing pore space heterogeneity.

Solute dispersion at the mesoscopic scale is a combination of both intra- and interpore water velocity differences, coupled with the small but important contribution of diffusion into and out of stagnant water regions. As a result, the relationship between  $K^*$  and  $P_n$  is expected to be intermediate between  $K^* \propto P_n^2$  and  $K^* \propto P_n$ . The actual form of this relationship has not been derived definitively. Two different relationships,  $K^* \propto P_n \ln(P_n)$  and  $K^* \propto P_n^\alpha$ , where  $1 < \alpha < 2$ , have been proposed (Sahimi, 1993). It can be shown that these relationships are similar when  $\alpha = 1.2$ . Some authors contend that  $\alpha = 1.2$  is a universal constant, and that both relationships are acceptable. If this is true, only the prefactor will change in response to pore characteristics and arrangement (e.g., Biggar & Nielsen, 1976). However, particle tracking simulations suggest that  $\alpha$  also depends upon network configuration (Salles et al., 1993; Sahimi, 1993), and most recent studies favor the power law relationship with a variable exponent. In this case, both parameters become functions of the pore space geometry.

We recommend that future research in this area focus on establishing theoretical and/or empirical relations between the prefactor and exponent in the power law relating  $K^*$  to  $P_n$ , and quantitative pore characteristics, such as the mass fractal dimension and Betti numbers. In particular, there is an urgent need for additional experimental studies, in which  $K^*$  is determined over a wide range of  $P_n$  on undisturbed samples of natural porous media that are well-characterized in terms of their pore space geometry. Such data are required for model testing.

A final consideration is how parameters from geometrical models might be incorporated into models to better predict solute dispersion at the macroscopic scale. One approach involves the development of effective continuum models for structured soils and fractured rocks (de Josselin de Jong & Way, 1972; Long et al., 1982; Berkowitz et al., 1988). Another approach is the inclusion of dispersion due to porosity variations in Monte Carlo simulations of solute transport in random conductivity fields (Fiori, 1998; Hassan et al., 1998). It is also possible to embed geometrical models within multiregion velocity based models (Gwo et al., 1998).

The last approach to be considered is upscaling (also known as block averaging, coarse graining, and renormalization), whereby effective macroscale properties are determined by aggregating distributions of micro- and meso-scale properties (see McBratney, 1998, for a general introduction to this topic). Mishra and Parker (1990) computed an effective macroscopic dispersivity from variable local dispersivities by simple spatial averaging. However, local values of  $K^*$  tend to be log-normally distributed (Biggar & Nielsen, 1976). Thus, use of the geometric mean is probably more appropriate than the arithmetic mean in this context. Spatial averaging assumes that the property of interest is not autocorrelated. In the likely event

that core-scale estimates of the dispersivity are shown to be spatially autocorrelated, more sophisticated upscaling procedures will be needed.

Rubin and Gómez-Hernández (1990) and Indelman and Dagan, (1993) have developed analytical expressions for apscaling both the mean and the variance of spatially autocorrelated  $\ln(k_{\rm sat})$  data. Since macroscale dispersion can be related to the variance of  $\ln(k_{\rm sat})$ , it may be possible to apply their expressions for predicting variance as a function of block size to the problem of upscaling estimates of  $K^*$  determined in the laboratory to the field scale. Unfortunately, numerical simulations based upon this approach are likely to be computationally expensive.

Real space renormalization is an alternative upscaling technique that has been found to be computationally efficient and accurate when used to predict single phase flow (King et al., 1993; Sahami, 1995). In this approach the effective properties of small regions are computed and mapped onto a coarse grid. The grid is then further coarsened and the process repeated until a single effective property is obtained. Real space renormalization has recently been applied to miscible and immiscible flows (Morris & Ball, 1990; King et al., 1993). Further research into the feasibility of predicting dispersion at the reservoir scale by renormalizing core-scale dispersivity measurements may prove fruitful.

#### APPENDIX A

# **List of Symbols**

a, b = major and minor semi-axes, respectively

å = sine wave amplitude

 $a_1,b_1$  and

 $a_r,b_r$  = Beta distribution parameters

A = cross-sectional area

 $A_i$  = fraction of the bundle occupied by the jth tube-size increment

 $b_{\rm c}$  = exponent in the Campbell water retention function

 $b_{\rm f}$  = fractal scaling factor

 $B_0$  = zeroth Betti number or number of isolated pores within the solid matrix

 $B_1$  = first Betti number (also the genus) or number of independent pathways between two points in the pore space

 $B_{\rm s}$  = number of bonds per site (or number of intersecting segments per segment)

 $B_{\rm sc}$  = critical number of bonds

c= prefactor in relationship between  $P_n$  and  $K^*$ 

C =concentration of solute in pore water

 $C_0$  = concentration at time t = 0

 $C_{\rm im}$  = concentration of solute in immobile soil water

 $C_i$  = solute concentration in the *j*th tube-size increment

 $C_{\rm m}$  = concentration of solute in mobile soil water

C = circularity or compactness

 $\langle C \rangle$  = mean solute concentration

d = fractal dimension of backbone or sample spanning cluster

 $d_{\rm b}$  = boundary fractal dimension

 $d_{\rm m}$  = mass fractal dimension

 $d_{\rm s}$  = surface fractal dimension

 $d_1$  = fractal dimension of a diffusing particle's trajectory

D =molecular diffusion coefficient  $D_{\rm e}$  = effective diffusion coefficient E = topological or conventional Euclidean dimension  $E_n$  = Euler-Poincaré number f = tortuosity $f_{\rm v}$  = relative volume of dead-end pore space f = function of distance traveled by solute g = constant for gravitational acceleration  $G^*$  = dimensionless number that represents the ratio of gravitational forces to viscosity forces h = linear dimension of a fracture zonei = iteration level $J = f(a_r, b_r)$ k = hydraulic conductivity $k_{\text{sat}}$  = saturated hydraulic conductivity  $K^*$  = dimensionless diffusion-dispersion coefficient  $K' = \text{empirical } K \text{ calculated from } t_1 \text{ and } t_2$ l = capillary tube length $l_{\rm b}$  = length of a bond  $l_s$  = separation distance = mean microscopic characteristic length  $\ell$  = characteristic mixing length or dispersivity L = lengthL = characteristic measurement scale  $L_1$  = measured length when is equal to unity  $L_{\rm c}$  = macroscopic capillary length parameter  $n_{\rm a}$  = number of adsorbed molecules n, N = number  $N_1$  = number of boxes not containing pores when  $\varepsilon$  is equal to unity P = perimeterp = power law exponent related to the fractal dimension $p_{\rm c}$  = critical percolation threshold  $P_{\rm n}$  = Peclet number q = Darcy velocityr = radius $r_{\rm c}$  = equivalent cylindrical radius  $r_{\rm h}$  = equivalent hydraulic radius  $r_{\rm n}$  = nth moment of the pore size distribution  $\langle r \rangle$  = mean pore radius  $Rm^*$  = modified Rayleigh number, dimensionless number used to determine the onset of convection in heated fluids S = surface areat = time $t_1$  = first time moment of solute breakthrough curve  $t_2$  = second time moment of solute breakthrough curve  $t_p$  = time taken for one pore volume to pass through the medium  $\hat{T}$  = transmissivity (= fracture width ×  $k_{\text{sat}}$  of filling material) v = mean pore water velocity v(y) = streamline velocity as a function of y v' = empirical v calculated from  $t_1$  $v_x$  and  $v_y$  = streamline velocity components in the x and y directions respectively V = volume

w = constant velocity of a moving frame of reference

x = distance

 $\langle x \rangle$  = mean distance

 $X^{A}$  = accessible fraction of open pores (i.e., open pores connected to the sample spanning cluster)

 $X^{\rm B}$  = fraction of open pores in backbone

y = radial coordinate

z =sinusoidal aperture wall coordinate

<Z> = mean coordination number or average number of pore throats per pore body

 $\alpha$  = exponent of  $P_n$  in relationship with  $K^*$ 

 $\beta$  = volume of indentations (or immobile water) per unit volume of main channel (or mobile water)

 $\beta_A$ ,  $\beta_B$  = percolation exponents

 $\beta_n$  = total volume of indentations per unit volume of main channel after n iterations of the fractal generator

 $\gamma$  = shape factor in relationship between  $K^*$  and  $P_n^2$  $\Gamma$  = ratio of volume available to moving fluid at vertex

 $\delta_{av}$  = average aperture size

 $\delta_{\rm H}$  = hydraulic diameter

 $\varepsilon$  = normalized length

E = Euler's constant

 $\zeta$  = coefficient of variation

 $\eta$  = dynamic viscosity

 $\theta$  = volumetric water content

 $\theta_{sat}$  = volumetric water content at saturation

 $\theta_{im}$  = immobile water content

 $\theta_{\rm m}$  = mobile water content

 $\kappa$  = sine wave length

 $\lambda$  = ratio of the outflows from network branches

 $\Lambda = lacunarity$ 

 $\mu$  = mean value

 $\xi$  = correlation length

 $\xi_p$  = percolation correlation length

 $\rho_b$  = bulk density

 $\rho_{l}$  = liquid density

 $\rho_s$  = particle density

 $\sigma^2$  = variance

 $\sigma^2(t)$  = variance at time t

 $\sigma^2(t_0)$  = variance at initial time,  $t_0$ 

 $\tau$  = percolation exponent

v = liquid-solid contact angle

 $\phi = porosity$ 

 $\phi$  = liquid-vapor interfacial tension

 $\psi$  = liquid potential

 $\psi_a$  = air-entry potential

 $\omega$  = molecular surface area

 $\Omega$  = degree of disorder in network

#### REFERENCES

Adler, P.M. 1985. Transport processes in fractals. III. Taylor dispersion in two examples of fractal capillary networks. Int. J. Multiphase Flow 11:241–254.

Adler, P.M. 1992. Porous media: Geometry and transports. Butterworth-Heinemann, Boston, MA.

Alexandroff, P. 1961. Elementary concepts of topology. Dover Publ., New York.

Allen, M., G.J. Brown, and N.J. Miles. 1995. Measurement of boundary fractal dimensions: review of current techniques. Powder Technol. 84:1–14.

Amadei, B., and T. Illangasekare. 1994. A mathematical model for flow and solute transport in nonhomogeneous rock fractures. Int. J. Rock Mech., Mining Sci. Geomech. Abstr. 31:719–731.

- Ananthakrishnan, V., W.N. Gill, and A.J. Barduhn. 1965. Laminar dispersion in capillaries: Part I. Mathematical analysis. AIChE J. 11:1063–1072.
- Anderson, A.N., A.B. McBratney, and E.A. FitzPatrick. 1996. Soil mass, surface, and spectral fractal dimensions estimated from thin section photographs. Soil Sci. Am. J. 60:962–969.
- Anderson, A.N., A.B. McBratney, and J.W. Crawford. 1998. Applications of fractals to soil studies. Adv. Agron. 63:1–76.
- Anderson, J.L., and J. Bouma. 1977. Water movement through pedal soils. I. Saturated flow. Soil Sci. Soc. Am. J. 41:413–418.
- Anderson, M.P. 1984. Movement of contaminants in groundwater: groundwater transport—advection and dispersion. Groundwat. Contam. 6:37–45.
- Anderson, S.H., and J.W. Hopmans (ed.). 1994. Tomography of soil-water-root processes. SSSA Spec. Publ. 36. SSSA, Madison, WI.
- Aris, R. 1956. On the dispersion of a solute in a fluid flowing through a tube. Proc. R. Soc. London Ser. A 235:67–77.
- Aris, R. 1959a. On the dispersion of a solute by diffusion, convection and exchange between phases Proc. R. Soc. London Ser. A 252:538–550.
- Aris, R. 1959b. The longitudinal diffusion coefficient in flow through a tube with stagnant air pockets. Chem. Eng. Sci. 11:194–198.
- Aris, R. 1959c. Diffusion and reaction in flow systems of Turner's structures. Chem Eng. Sci. 10:80-87.
- Aris, R., and R. Amundson. 1957. Some remarks on longitudinal mixing or diffusion in fixed beds. AIChE J. 3:280–282.
- Avnir, D., D. Farin, and P. Pfeifer. 1983. Chemistry in noninteger dimensions between two and three. II. Fractal surfaces of adsorbents. J. Chem. Phys. 79:3566–3571.
- Avnir, D., D. Farin, and P. Pfeifer. 1985. Surface geometric irregularity of particulate materials: the fractal approach. J. Colloid Interface Sci. 103:112–123.
- Azzam, M.I.S., and F.A.L. Dullien. 1977. Flow in tubes with periodic step changes in diameter: A numerical solution. Chem. Eng. Sci. 32:1445–1455.
- Bachmat, Y., and D.E. Elrick. 1970. Hydrodynamic instability of miscible fluids in a vertical porous column. Water Resour. Res. 6:156–171.
- Bai, M., and J-C. Roegiers. 1997. Triple-porosity analysis of solute transport. J. Contam. Hydrol. 28:247–266.
- Baltus, R.E. 1997. Characterization of the pore area distribution in porous membranes using transport measurements. J. Membrane Sci. 123:165–184.
- Barnsley, M.F., and S. Demko. 1985. Iterated function systems and the global construction of fractals. Proc. R. Soc. London Ser. A 399:243–275.
- Baudet, C., and J.P. Hulin. 1989. Lattice-gas automata: A model for the simulation of dispersion phenomena. Phys. Fluids A1:507–512.
- Baveye, P., J.-Y. Parlange, and B.A. Stewart (ed.). 1998. Fractals in soil science. CRC Press, Boca Raton, FL.
- Bear, J. 1961. On the tensor form of dispersion in porous media. J. Geophys. Res. 66:1185–1197.
- Bear, J. 1969. Hydrodynamic dispersion. p. 109–199. *In R.J.M.* de Wiest (ed.) Flow through porous media. Acad. Press, New York.
- Bear, J. 1972. Dynamics of flow in porous media. Am. Elsevier Publ., New York.
- Benson, D.A. 1998. The fractional advection-dispersion equation: Development and application. Ph.D. diss. Univ. Nevada, Reno.
- Berkowitz, B., and C. Braester. 1991. Dispersion in sub-representative elementary volume fracture networks: Percolation theory and random walk approaches. Water Resour. Res 27:3159–3164.
- Berkowitz, B., and R.P. Ewing. 1998. Percolation theory and network modeling applications in soil physics. Surv. Geophys. 19:23–72.
- Berkowitz, B., J. Bear, and C. Braester. 1988. Continuum models for contaminant transport in fractured porous formations. Water Resour. Res. 24:1225–1236.
- Beven, K.J., D.E. Henderson, and A.D. Reeves. 1993. Dispersion parameters for undisturbed partially saturated soil. J. Hydrol. 143:19–43.
- Biggar, J.W., and D.R. Nielsen. 1964. Chloride-36 diffusion during stable and unstable flow through glass beads. Soil Sci. Soc. Am. Proc. 28:591–595.
- Biggar, J.W., and D.R. Nielsen. 1967. Miscible displacement and leaching phenomenon. p. 254–274. In R.M. Hagan et al. (ed.) Irrigation of agricultural lands. Agron. Monogr. 11. ASA, Madison, WI

- Biggar, J.W., and D.R. Nielsen. 1976. Spatial variability of the leaching characteristics of a field soil. Water Resour. Res. 12:78–84.
- Bird, N.R.A., and A.R. Dexter. 1997. Simulation of soil water retention using random fractal networks. Eur. J. Soil Sci. 48:633–641.
- Bobba, A.G. 1989. Numerical model of contaminant transport through conduit-porous matrix system. Math. Geol. 21:861–890.
- Boghosian, B.M. 1993. Lattice gas hydrodynamics. Nucl. Phys. B 30:204–210.
- Bolt, G.H. 1979. Movement of solutes in soil: Principles of adsorption/exchange chromatography. p. 285–348. *In* G.H. Bolt (ed.) Soil chemistry. Elsevier Sci., New York.
- Bouma, J., and J.H.M. Wösten. 1979. Flow patterns during extended saturated flow in two, undisturbed swelling clay soils with different macrostructures. Soil Sci. Soc. Am. J. 43:16–22.
- Brakensiek, D.L., and W.J. Rawls. 1992. Comment on "Fractal Processes in Soil Water Retention" by S. W. Tyler and S.W. Wheatcraft. Water Resour. Res. 28:601–602.
- Brenner, H. 1980. Dispersion resulting from flow through spatially periodic porous media. Phil. Trans. R. Soc. London Ser. A 297:81–133.
- Brusseau, M.L., and P.S.C. Rao. 1989. Sorption non-ideality during organic contaminant transport in porous media. CRC Crit. Rev. Environ. Control 19:33–99.
- Brusseau, M.L., and P.S.C. Rao. 1990. Modeling solute transport in structured soils: A review. Geoderma 46:169–192.
- Brutsaert, W. 1966. Probability laws for pore-size distributions. Soil Sci. 101:85-92.
- Buckley, J.S. 1991. Multiphase displacements in micromodels. p. 157–189. *In* N.R. Murrow (ed.) Interfacial phenomena in petroleum recovery. Vol. 36. Marcel Dekker, New York.
- Bués, M.A., and M. Aachib. 1991. Influence of the heterogeneity of the solutions on the parameters of miscible displacement in saturated porous medium. I. Stable displacement with density and viscosity contrasts. Exp. Fluids 11:25–32.
- Bullock, P., and A.J. Thomasson. 1979. Rothamsted studies of soil structure. II. Measurement and characterisation of macroporosity by image analysis and comparison with data from water retention measurements. J. Soil Sci. 30:391–413.
- Campbell, G.S. 1974. A simple method for determining unsaturated hydraulic conductivity from moisture retention data. Soil Sci. 117:311–314.
- Cao, J., and P.K. Kitanidis. 1998a. Pore-scale dilution of conservative solutes: An example. Water Resour. Res. 34:1941–1949.
- Cao, J., and P.K. Kitanidis. 1998b. Adaptive finite element simulation of Stokes flow in porous media. Adv. Water Resour. 22:17–32.
- Carbonell, R.G. 1979. Effect of pore distribution and flow segregation on dispersion in porous media. Chem. Eng. Sci. 14:1031–1039.
- Carbonell, R.G., and S. Whitaker. 1983. Dispersion in pulsed systems. II. Theoretical developments for passive dispersion in porous media. Chem. Eng. Sci. 18:1795–1802.
- Celia, M.A., P.C. Reeves, and L. A. Ferrand. 1995. Recent advances in pore scale models for multiphase flow in porous media. Rev. Geophys. 33(July Suppl.):1049–1057.
- Charbeneau, R.J. 1984. Kinematic models for soil moisture and solute transport. Water Resour. Res. 20:699–706.
- Charlaix, E., J.P. Hulin, and T.J. Plona. 1987. Experimental study of tracer dispersion in sintered glass porous materials of variable compaction. Phys. Fluids 30:1690–1698.
- Charlaix, E., J.P. Hulin, C. Leroy, and C. Zarcone. 1988. Experimental study of tracer dispersion in flow through two-dimensional networks of etched capillaries. J. Phys. D. 21:1727–1732.
- Chatenever, A., and J.C. Calhoun. 1952. Visual examinations of fluid behavior in porous media. I. Trans. Am. Inst. Min. Metall. Petrol. Eng. 195:149–156.
- Chatzis, I., and F.A.L. Dullien. 1977. Modelling pore structures by 2-d and 3-d networks with application to sandstones. Can. J. Petrol. Tech. 16:97–108.
- Chatzis, I., and F.A.L. Dullien.1985. The modeling of mercury porosimetry and the relative permeability of mercury in sandstones using percolation theory. Int. Chem. Eng. 25:47–66.
- Chen, M.-H., and P.F. Yan. 1988. A fast algorithm to calculate the Euler number for binary images. Patt. Recognit. Lett. 8:295–297.
- Childs, E.C. 1940. The use of soil moisture characteristics in soil studies. Soil Sci. 50:239–252.
- Clemo, T., and L. Smith. 1997. A hierarchical model for solute transport in fractured media. Water Resour. Res. 33:1763–1783.
- Coats, K.H., and B.D. Smith 1964. Dead end pore volume and dispersion in porous media. Soc. Petrol. Eng. J. 4:73–84.

Coelho, D., J.F. Thovert, and P.M. Adler. 1997. Geometrical and transport properties of random packings of spheres and aspherical particles. Phys. Rev. E 55:1959–1978.

- Compte, A., and J. Camacho. 1997. Levy statistics in Taylor dispersion. Phys. Rev. E 56:5445–5449.
- Coppens, M.-O. 1997. Accessibility of a catalyst's fractal surface to diffusing and reacting molecules. p. 336–349. *In* J.L. Véhel et al. (ed.) Fractals in engineering. From theory to industrial applications. Springer-Verlag, New York.
- Corapcioglu, M.Y., S Chowdhury, and S.E. Roosevelt. 1997. Micromodel visualization and quantification of solute transport in porous media. Water Resour. Res. 33:2547–2558.
- Crawford, J.W., K. Ritz, and I.M. Young. 1993. Quantification of fungal morphology, gaseous transport and microbial dynamics in soil: an integrated framework utilizing fractal geometry. Geoderma 56:157–172.
- Crawford, J.W., H. Matsui, and I.M. Young. 1995. The relation between the moisture release curve and the structure of soil. Eur. J. Soil Sci. 46:369–375.
- Cushman, J.H. 1991. On diffusion in fractal porous media. Water Resour. Res. 27:643-644.
- Dagan, G. 1984. Solute transport in heterogeneous porous formations. J. Fluid Mech. 145:151-177.
- Dagan, G. 1994. The significance of heterogeneity of evolving scales to transport in porous formations. Water Resour. Res. 30:3327–3336.
- Danel, P. 1953. The measurement of ground-water flow. p. 99–107. *In* Proc. Ankara Symp. Arid Zone Hydrol. no. 2, Ankara, Turkey. UNESCO, Paris.
- Day, P.R., and W.M. Forsythe. 1957. Hydrodynamic dispersion of solutes in the soil moisture stream. Soil Sci. Soc. Am. Proc. 21:477–480.
- de Arcangelis, L., J. Koplik, S. Redner, and D. Wilkinson. 1986. Hydrodynamic dispersion in network models of porous media. Phys. Rev. Lett. 57:996–999.
- de Josselin de Jong, G. 1958. Longitudinal and traverse diffusion in granular deposits. Trans. Am. Geophys. Union 39:67–74.
- de Josselin de Jong, G., and S.C. Way. 1972. Dispersion in fissured rock, report. New Mexico Inst. Miner. Technol., Soccoro, NM.
- d'Hollander, E.H. 1979. Estimation of the pore-size distribution from the moisture characteristic. Water Resour. Res. 15:107–112.
- Dullien, F.A.L. 1991. Characterization of porous media—pore level. Trans. Porous Media 6:581–606.
- Dullien, F.A.L. 1992. Porous media: Fluid transport and pore structure. 2nd ed. Acad. Press, New York.
- Dunn, G.H., and R.E. Phillips. 1991. Equivalent diameter of simulated macropores during saturated flow. Soil Sci. Soc. Am. J. 55:1244–1248.
- Durner, W., and H. Flühler. 1996. Multi-domain model for pore-size dependent transport of solutes in soils. Geoderma 70:281–297.
- Edwards, D.A., M. Shapiro, H. Brenner, and M. Shapira. 1991. Dispersion of inert solutes in spatially periodic, two-dimensional model porous media. Transp. Por. Media 6:337–358.
- Eggleston, J.R., and J.J. Pierce. 1995. Dynamic programming analysis of pore space. Eur. J. Soil Sci. 46:581–590.
- Eidsath, A., R.G. Carbonell, S. Whitaker, and R. Herrmann. 1983. Dispersion in pulsed systems. III Comparison between theory and experiments for packed beds. Chem. Eng. Sci. 18:1803–1816.
- Elrick, D.E., and L.K. French. 1966. Miscible displacement patterns on disturbed and undisturbed soil cores. Soil Sci. Soc. Am. Proc. 30:153–156.
- Elrick, D.E., and B.E. Clothier. 1990. Solute transport and leaching. p. 93–126. *In M.D. Thorne* (ed.) Agronomists and food: Contributions and challenges. Agron. Monogr. 30. ASA, Madison, WI.
- Ferrand, L.A. 1992. A pore-scale computational model for chemical transport in porous media. p. 401–408. *In* T.F. Russel et al. (ed.) Mathematical modeling in water resources. Proc. 9th Int. Conf. Computat. Methods Water Resour., Vol. 2, Denver, CO. 9–12 June. Computational Mechanics Publ., Southampton, UK.
- Ferrand, L.A., and M.A. Celia. 1992. The effect of heterogeneity on the drainage capillary pressure-saturation relation. Water Resour. Res. 28:859–870.
- Fiori, A. 1998. On the influence of pore-scale dispersion in nonergodic transport in heterogeneous formations. Transp. Por. Media 30:57–73.
- Fried, J.J., and M.A. Combarnous. 1971. Dispersion in porous media. Adv. Hydrosci. 7:169-282.
- Friedman, S.P., L. Zhang, and N.A. Seaton. 1995. Gas and solute diffusion coefficients in pore networks and their description by a simple capillary model. Transp. Por. Media 19:281–301.
- Friesen, W.I., and R.J. Mikula. 1987. Fractal dimension of coal particles. J. Colloid Interface Sci. 120:263–271.
- Frisch, U., B. Hasslacher, and Y. Pomeau. 1986. Lattice-gas automata for the Navier Stokes equation. Phys. Rev. Lett. 56:1505–1508.

- Frissel, M.J., and P. Poelstra. 1967a. Chromatographic transport through soils. I. Theoretical evaluations. Plant Soil 26:285–302.
- Frissel, M.J., and P. Poelstra. 1967b. Chromatographic transport through soils. II. Column experiments with Sr-and Ca-isotopes. Plant Soil 27:20–32.
- Garrison, J.R., Jr., W.C. Pearn, and D.U. Rosenberg. 1992. The fractal Menger sponge and Sierpinski carpet as models for reservoir rock/pore systems: I. Theory and image analysis of Sierpinski carpets. In Situ 16:351–406.
- Garrison, J.R., Jr., W.C. Pearn, and D.U. Rosenberg. 1993. The fractal Menger sponge and Sierpinski carpet as models for reservoir rock/pore systems: II. Image analysis of natural fractal reservoir rocks. In Situ 17:1–53.
- Gelhar, L.W., and C.L. Axness. 1983. Three-dimensional stochastic analysis of macrodispersion in aquifers. Water Resour. Res. 19:161–180.
- Gelhar, L.W., C. Welty, and K.R. Rehfeldt. 1992. A critical review of data on field-scale dispersion in aquifers. Water Resour. Res. 28:1955–1974.
- Gerke, H.H., and M.Th. van Genuchten. 1996. Macroscopic representation of structural geometry for simulating water and solute movement in dual-porosity media. Adv. Water Resour. 19:343–357.
- Germann, P.F., M.S. Smith, and G.W. Thomas. 1987. Kinematic wave approximation to the transport of *Escherichia Coli* in the vadose zone. Water Resour. Res. 23:1281–1287.
- Gill, W.N., and V. Ananthakrishnan. 1966. Laminar dispersion in capillaries: Part II. Effect of inlet boundary conditions and turner type of system capacitance. AIChE J. 12:906–915.
- Giona, M., A. Adrover, and A.R. Giona. 1995. Convection-diffusion transport in disordered structures: Numerical analysis based on the exit-time equation. Chem. Eng. Sci. 50:1001–1011.
- Giona, M., W.A. Schwalm, M.K. Schwalm, and A. Adrover. 1996. Exact solution of linear transport equations in fractal media. II. Diffusion and convection. Chem. Eng. Sci. 51:4731–4744.
- Giménez, D., E. Perfect, W.J. Rawls, and Y. Pachepsky. 1997a. Fractal models for predicting soil hydraulic properties: A review. Eng. Geol. 48:161–183.
- Giménez, D., R.R. Allmaras, E.A. Nater, and D.R. Huggins. 1997b. Fractal dimensions for volume and surface of interaggregate pores—scale effects. Geoderma 77:19–38.
- Gist, G.A., A.H. Thompson, A.J. Katz, and R.L. Higgins. 1990. Hydrodynamic dispersion and pore geometry in consolidated rock. Phys. Fluids A 2:1533–1544.
- Gouyet, J.-F. 1996. Physics and fractal structures. Springer-Verlag. New York.
- Greenkorn, R.A., and D.P. Kessler. 1969. Dispersion in heterogeneous, nonuniform, anisotropic porous media. Ind. Eng. Chem. 61:14–32.
- Grindrod, P., and M.D. Impey. 1993. Channeling and Fickian dispersion in fractal simulated porous media. Water Resour. Res. 29:4077–4089.
- Grisak, G.E., and J.F. Pickens. 1980. Solute transport through fractured media. I. The effect of matrix diffusion. Water Resour. Res. 16:719–730.
- Grisak, G.E., and J.F. Pickens. 1981. An analytical solution for solute transport through fractured media with matrix diffusion. J. Hydrol. 52:47–57.
- Guin, J.A., D.P. Kessler, and R.A. Greenkorn. 1972. The dispersion tensor in anisotropic porous media. Ind. Eng. Chem. Fund. 11:477–482.
- Gupta, V.K., and R.N. Bhattacharya. 1983. A new derivation of the Taylor-Aris theory of solute dispersion in a capillary. Water Resour. Res. 19:945–951.
- Gutfraind, R., I. Ippolito, and A. Hansen. 1995. Study of tracer dispersion in self-affine fractures using lattice-gas automata. Phys. Fluids 7:1938–1948.
- Gwo, J.P., P.M. Jardine, G.V. Wilson, and G.T. Yeh. 1995. A multiple-pore-region concept to modeling mass transfer in subsurface media. J. Hydrol. 164:217–237.
- Gwo, J.P., R. O'Brien, and P.M. Jardine. 1998. Mass transfer in structured porous media: Embedding mesoscale structure and microscale hydrodynamics in a two-region model. J. Hydrol. 208:204–222.
- Haga, D., Y. Niibori, and T. Chida. 1999. Hydrodynamic dispersion and mass transfer in unsaturated flow. Wat. Resour. Res. 35:1065–1077.
- Haggerty, R., and S.M. Gorelick. 1995. Multiple-rate mass transfer for modeling diffusion and surface reactions in media with pore scale heterogeneity. Water Resour. Res. 31:2383–2400.
- Han, N., J. Bhakta, and R.G. Carbonell. 1985. Longitudinal and lateral dispersion in packed beds: effect of column length and particle size distribution. AIChE J. 31:277–288.
- Haring, R.E., and R.A. Greenkorn. 1970. A statistical model of a porous medium with nonuniform pores. AIChE J. 16:477–483.

Hassan, A.E., J.H. Cushman, and J.W. Delleur. 1997. Monte Carlo studies of flow and transport in fractal conductivity fields: comparison with stochastic perturbation theory. Water Resour. Res. 33:2519–2534.

- Hassan, A.E., J.H. Cushman, and J.W. Delleur. 1998. Significance of porosity variability to transport in heterogeneous porous media. Water Resour. Res. 34:2249–2259.
- Hatano, R., N. Kawamura, J. Ikeda, and T. Sakuma. 1992. Evaluation of the effect of morphological features of flow paths on solute transport by using fractal dimensions of methylene blue staining pattern. Geoderma 53:31–44.
- Havlin, S., and D. Ben-Avraham. 1987. Diffusion in disordered media. Adv. Phys. 36:695–798.
- Hoagland, D.A., and R.K. Prud'homme. 1985. Taylor-Aris dispersion arising from flow in a sinusoidal tube. AIChE J. 31:236–244.
- Horgan, G.W. 1998. Mathematical morphology for analysing soil structure from images. Eur. J. Soil Sci. 49:161–173.
- Horn, F.J.M. 1971. Calculation of dispersion coefficients by means of moments. AIChE J. 17:613–620.
- Hu, Q., and M.L. Brusseau. 1995. Effect of solute size on transport in structured porous media. Water Resour. Res. 31:1637–1646.
- Hulin, J.P., E. Charlaix, T.J. Plona, L. Oger, and E. Guyon. 1988. Tracer dispersion in sintered glass beads with a bidisperse size distribution. AIChE J. 34:610–617.
- Hull, L.C., J.D. Miller, and T.M. Clemo. 1987. Laboratory and simulation studies of solute transport in fracture networks. Water Resour. Res. 23:1505–1513.
- Indelman, P., and G. Dagan. 1993. Upscaling of conductivity of heterogeneous formations: General approach and application to isotropic media. Transp. Por. Media 12:161–183.
- Ioannidis, M.A., and I. Chatzis. 1993. Network modeling of pore structure and transport properties of porous media. Chem. Eng. Sci. 48:951–972.
- James, R.V., and J. Rubin. 1972. Accounting for apparatus-induced dispersion in analyses of miscible displacement experiments. Water Resour. Res. 8:717–721.
- Jensen, J.R. 1983. Chloride dispersion in packed columns during saturated, steady flow. J. Soil Sci. 34:249–262.
- Jury, W.A. 1982. Simulation of solute transport using a transfer function. Water Resour. Res. 18:363–368.
- Jury, W.A., and G. Sposito. 1985. Field calibration and validation of solute transport models for the unsaturated zone. Soil Sci. Soc. Am. J. 49:1331–1341.
- Jury, W.A., and H. Flühler. 1992. Transport of chemicals through soil: Mechanisms, models, and field applications. Adv. Agron. 47:141–201.
- Jury, W.A., G. Sposito, and R.E. White. 1986. A transfer function model of solute transport through soil.

  1. Fundamental concepts. Water Resour. Res. 22:243–247.
- Kampichler, C., and M. Hauser. 1993. Roughness of soil pore surface and its effect on available habitat space of microarthropods. Geoderma 56:223–232.
- Kanchanasut, P., D.R. Scotter, and R.W. Tillman. 1978. Preferential solute movement through larger soil voids. II. Experiments with saturated soil. Aust. J. Soil Res. 16:269–276.
- Keller, A.A., P.V. Roberts, and M.J. Blunt. 1999. Effect of fracture aperture variations on the dispersion of contaminants. Water Resour. Res. 35:55–63.
- Kemblowski, M.W., and J.-C. Wen. 1993. Contaminant spreading in stratified soils with fractal permeability distribution. Water Resour. Res. 29:419–425.
- King, P.R., A. H. Muggeridge, and W.G. Price. 1993. Renormalization calculations of immiscible flow. Transp. Por. Media 12:237–260.
- Kitanidis, P.K., and B.B. Dykaar. 1997. Stokes flow in a slowly varying two-dimensional periodic pore. Transp. Por. Media 26:89–98.
- Klinkenberg, I.J. 1957. Pore size distribution of porous media and displacement experiments with miscible liquids. Petrol. Trans. AIME 2:366–369.
- Koch, D.L., and J.F. Brady. 1985. Dispersion in fixed beds. J. Fluid Mech. 154:399–427.
- Koch, D.L., and J.F. Brady. 1988. Anomalous diffusion in heterogeneous porous media. Phys. Fluids 31:965–973.
- Koch, D.L., R.G. Cox, H. Brenner, and J. F. Brady. 1989. The effect of order on dispersion in porous media. J. Fluid Mech. 200:173–188.
- Koplik, J., I. Ippolito, and J.P. Hulin. 1993. Tracer dispersion in rough channels: A two-dimensional numerical study. Phys. Fluids A 5:1333–1343.
- Koplik, J., S. Redner, and D. Wilkinson. 1988. Transport and dispersion in random networks with percolation disorder. Phys. Rev. A 37:2619 (2636).
- Kreyszig, E. 1959. Differential geometry. Univ. Toronto Press, Toronto, Canada

- Krupp, H.K., and D.E. Elrick. 1969. Density effects in miscible displacement experiments. Soil Sci. 107:372–380.
- Kutílek, M., and D.R. Nielsen. 1994. Soil hydrology. Catena Verlag, Cremlingen-Destedt, Germany.
- Lawrence, G.P. 1977. Measurement of pore sizes in fine-textured soils: A review of existing techniques. J. Soil Sci. 28:527–540.
- Leij, F.J., and J.H. Dane. 1989. A review of physical and chemical processes pertaining to solute transport. Alabama Agric. Exp. Stn. Agron. Soils Dep. Ser. no. 132.
- Levitz, P. 1998. Off-lattice reconstruction of porous media: critical evaluation, geometrical confinement and molecular transport. Adv. Colloid Interface Sci. 77:71–106.
- Li, Y., and M. Ghodrati. 1997. Preferential transport of solute through soil columns containing constructed macropores. Soil Sci. Soc. Am. J. 61:1308–1317.
- Lin, S.H. 1977. Longitudinal dispersion in porous media with variable porosity. J. Hydrol. 34:13–19.
- Lindstrom. F.T., and L. Boersma. 1971. A theory on the mass transport of previously distributed chemicals in a water saturated sorbing porous medium. Soil Sci. 111:192–199.
- Liu, H.H., and J.H. Dane. 1997. A numerical study on gravitational instabilities of dense aqueous phase plumes in three-dimensional porous media. J. Hydrol. 194:126–142.
- Long, J.C.S., J.S. Remer, C.R. Wilson, and P.A. Witherspoon. 1982. Porous media equivalents for networks of discontinuous fractures. Water Resour. Res. 18:645–658.
- Lovejoy, S., D. Schertzer, and P. Silas. 1998. Diffusion in one-dimensional multifractal porous media. Water Resour. Res. 34:3283–3291.
- Luxmoore, R.J., and L.A. Ferrand. 1993. Towards pore-scale analysis of preferential flow and chemical transport. p. 45–60. *In* D. Russo and G. Dagan (ed.) Water flow and solute transport in soils. Springer-Verlag, New York.
- Ma, L., and H.M. Selim. 1994. Tortuosity, mean residence time, and deformation of tritium breakthrough from soil columns. Soil Sci. Soc. Am. J. 58:1076–1085.
- MacDonald, I., P. Kaufmann, and F.A.L. Dullien. 1986a. Quantitative image analysis of finite porous media. I. Development of genus and pore map software. J. Micros. 144:277–296.
- MacDonald, I., P. Kaufmann, and F.A.L. Dullien. 1986b. Quantitative image analysis of finite porous media. II. Specific genus of cubic lattice models and Bera sandstone J. Micros. 144:297–316.
- Mandel, S., and Z. Weinberger. 1972. Analysis of a network-model for dispersive flow. J. Hydrol. 16:147–157.
- Mandelbrot, B.B., and J. Van Ness. 1968. Fractional Brownian motion, fractional noises and applications. SIAM Rev. 10:422–437.
- Mandlebrot, B.B. 1983. The fractal geometry of nature. W.H. Freeman, New York.
- Margolin, G., B. Berkowitz, and H. Scher. 1998. Structure, flow, and generalized conductivity scaling in fracture networks. Water Resour. Res. 34:2103–2121.
- Marle, C., and P. Defrenne. 1960. La description mathématique du déplacement de fluides miscibles dans un milieu poreux. Rapp. Inst. Fr. Pétrole No. 5433.
- Marshall, T.J. 1958. A relationship between permeability and size distribution of pores. J. Soil Sci. 9:1–8.
- Matsubayashi, U., L.P. Devkota, and F. Takagi. 1997. Characteristics of the dispersion coefficient in miscible displacement through a glass beads medium. J. Hydrol. 192:51–64.
- Mazo, R.M. 1998. Taylor dispersion on a fractal. Acta Phys. Polon. B 29:1539–1549.
- McBratney, A.B. 1998. Some considerations on methods for spatially aggregating and disaggregating soil information. Nutr. Cycl. Agroecosyst. 50:51–62.
- McBratney, A.B., and C.J. Moran. 1993. Soil pore structure modeling using fuzzy random pseudofractal sets. p. 495–506. *In A.J. Ringrose-Voase and G. Humphreys (ed.) Studies in management and genesis. Proc. 9th Int. Work. Meet. Soil Micromorphol., Townsville, Australia. July 1992. Elsevier, Amsterdam.*
- Mishra, S., and J.C. Parker. 1990. Analysis of solute transport with a hyperbolic scale-dependent model. Hydrol. Process. 4:45–57.
- Moissis, D.E., and M.F. Wheeler. 1990. Effect of the structure of the porous medium on unstable miscible displacement. p. 243–271. *In* J.H. Cushman (ed.) Dynamics of fluids in hierarchical porous media. Acad. Press, San Diego, CA.
- Montas, H.J., J.D. Eigel, B.A. Engel, and K. Haghighi. 1997a. Deterministic modeling of solute transport in soils with preferential flow pathways. I. Model development. Trans. ASAE 40:1245–1256.
- Montas, H.J., J.E. Eigel, B.A. Engel, and K. Haghighi. 1997b. Deterministic modeling of solute transport in soils with preferential flow pathway. II. Model validation. Trans. ASAE 40:1257–1265.
- Moran, C.J. 1994. Image processing and soil micromorphology. Dev. Soil Sci. 22:459–482.
- Moran, C.J., and A.B. McBratney. 1992. Acquisition and analysis of three-component digital images of soil pore structure. I. Method. J. Soil Sci. 43:541-549.

Moran, C.J., and A.B. McBratney. 1997. A two-dimensional fuzzy random model of soil pore structure. Math. Geol. 29:755–777.

- Morris, M.I., and R.C. Ball. 1990. Renormalization of miscible flow functions. J. Phys. A 23:4199–4204.
- Muller, J. 1996. Characterization of pore space in chalk by multifractal analysis. J. Hydrol. 187:215–222.
- Mulqueen, J., and D. Kirkham. 1972. Leaching of a surface layer of sodium chloride into tile drains in a sand-tank model. Soil Sci. Soc. Am. J. 36:3–4.
- Murphy, C.P. 1986. Thin section preparation of soils and sediments. A.B. Acad., Berkhamsted, UK.
- Murphy, C.P., P. Bullock, and R.H. Turner. 1977. The measurement and characterization of voids in soil thin sections by image analysis. Part I. Principles and techniques. J. Soil Sci. 28:498–508.
- Nagpal, N.K., L. Boersma, L.W. DeBacker. 1972. Pore size distributions from mercury intrusion porosimeter data. Soil Sci. Soc. Am. Proc. 36:264–267.
- Neretnieks, I. 1983. A note on fracture flow dispersion mechanisms in the ground. Water Resour. Res. 19:364–370.
- Neuman, S.P. 1990. Universal scaling of hydraulic conductivities and dispersivities in geologic media. Water Resour. Res. 26:1749–1758.
- Neuman, S.P. 1995. On advective transport in fractal permeability and velocity fields. Water Resour. Res. 31:1455–1460.
- Nielsen, D.R., and J.W. Biggar. 1961. Miscible displacement in soils: I. Experimental information. Soil Sci. Soc. Am. Proc. 25:1–5.
- Nordqvist, A.W., Y.W. Tsang, C.F. Tsang, B. Dverstorp, and J. Andersson. 1996. Effects of high variance of fracture transmissivity on transport and sorption at different scales in a discrete model for fractured rocks. J. Contamin. Hydrol. 22:39–66.
- Nunge, R.J., and W.N. Gill. 1970. Mechanisms affecting dispersion and miscible displacement. p. 179–195. *In* Flow through porous media. ACS, Washington, DC.
- Orbach, R. 1986. Dynamics of fractal networks. Science (Washington, DC) 231:814–819.
- Orford, J.D., and W.B. Whalley. 1991. Quantitative grain form analysis. p. 88–108. *In J.P.M. Syvitski* (ed.) Principles, methods, and application of particle size analysis. Cambridge Univ. Press, Cambridge, UK.
- Pachepsky, Y., V. Yakovchenko, M.C. Rabenhorst, C. Pooley, and L.J. Sikora. 1996. Fractal parameters of pore surfaces as derived from micromorphological data: effect of long-term management practices. Geoderma 74:305–319.
- Pachepsky, Y., J.W. Crawford, and W.J. Rawls (ed.). 2000. Fractals in soil science. Elsevier, Amsterdam, The Netherlands.
- Pachepsky, Y., D.A. Benson, and D.J. Timlin. 2001. Transport of water and solutes in soils as in fractal porous media. p. 51–75. *In* H.M. Selim and D.L. Sparks (ed.) Physical and chemical processes of water and solute transport /retention in soil. SSSA Special Publ. 56, Madison, WI.
- Pakula, R.J., and R.A. Greenkorn. 1971. An experimental investigation of a porous medium model with nonuniform pores. AIChE J. 17:1265–1268.
- Park, Y.-J., and K.-K. Lee. 1999. Analytical solutions for solute transfer characteristics at continuous fracture junctions. Water Resour. Res. 35:1531–1537.
- Parker, J.C., and M.Th. van Genuchten. 1984. Determining transport parameters from laboratory and field tracer experiments. Virginia Agric. Exp. Stn. Bull. 84-3.
- Passioura, J.B. 1971. Hydrodynamic dispersion in aggregated Media. 1. Theory. Soil Sci. 111:339–344.
- Passioura, J.B., and D.A. Rose. 1971. Hydrodynamic dispersion in aggregated media 2. Effects of velocity and aggregate size. Soil Sci.111:345–351.
- Perea-Reeves, S.J., and H.W. Stockman. 1997. A lattice-gas study of dispersion in alveolated channels. Chem Eng. Sci. 52:3277–3286.
- Perfect, E. 1999. Estimating soil mass fractal dimensions from water retention curves. Geoderma 88:221-231.
- Pfeifer, P., and D. Avnir. 1983. Chemistry in noninteger dimensions between two and three. I. Fractal theory of heterogeneous surfaces. J. Chem. Phys. 79:3558–3565.
- Philip, J.R. 1986. Issues in flow and transport in heterogeneous porous media. Transp. Por. Media 1:319–338.
- Philip, J.R. 1987. The quasilinear analysis, the scattering analog, and other aspects of infiltration and seepage. p. 1–27. *In* Y.-S. Fok (ed.) Infiltration development and application. Water Resour. Res. Center, Honolulu, HI.
- Plumb, O.A., and S. Whitaker. 1988. Dispersion in heterogeneous porous media 1. Local volume averaging and large-scale averaging. Water Resour. Res. 24:913–926.
- Powers, W.L., J.U. Baer, and J. Skopp. 1992. Alternative soil water release parameters for distinguishing tillage effects. Soil Sci. Soc. Am. J. 56:873–878.

- Rao, P.S.C., R.E. Green, L.R. Ahuja, and J.M. Davidson. 1976. Evaluation of a capillary bundle model for describing solute dispersion in aggregated soils. Soil Sci. Soc. Am. J. 40:815–820.
- Rao, P.S.C., R.E. Jessup, D.E. Rolston, J.M. Davidson, and D.P. Kilcrease. 1980a. Experimental and mathematical description of nonadsorbed solute transfer by diffusion in spherical aggregates. Soil Sci. Soc. Am. J. 44:684–688.
- Rao, P.S.C., D.E. Rolston, R.E. Jessup, and J.M. Davidson. 1980b. Solute transport in aggregated porous media: Theoretical and experimental evaluation. Soil Sci. Soc. Am. J. 44:1139–1146.
- Rao, P.S.C., R.E. Jessup, and T.M. Addiscott. 1982. Experimental and theoretical aspects of solute diffusion in spherical and nonspherical aggregates. Soil Sci. 133:342–349.
- Rasmuson, A. 1985. The effect of particles of variable size, shape and properties on the dynamics of fixed beds. Chem. Eng. Sci. 40:621–629.
- Rasmuson, A., and I. Neretnieks. 1980. Exact solution of a model for diffusion in particles and longitudinal dispersion in packed beds. AIChE J. 26:686–690.
- Redner, S., J. Koplik, and D. Wilkinson. 1987. Hydrodynamic dispersion in a self-similar geometry. J. Phys. A 20:1543–1555.
- Ringrose-Voase, A.J., and P. Bullock. 1984. The automatic recognition and measurement of soil pore types by image analysis and computer programs. J. Soil Sci. 35:673–684.
- Ringrose-Voase, A.J., and S. Nortcliff. 1987. The application of stereology to the estimation of soil structural properties: A preview. p. 81–88. *In* N. Fedoroff et al. (ed.) Soil micromorphology. Proc. 7th Int. Work. Meet. Soil Micromorphol., Paris. July 1985. Assoc. française pour l'étude du sol, Plaisir, France.
- Robinson, J.W., and J.E. Gale. 1990. A laboratory and numerical investigation of solute transport in discontinuous fracture system. Ground Water 28:25–36.
- Rose, D.A. 1977. Hydrodynamic dispersion in porous materials. Soil Sci. 123:277-283.
- Rose, D.A., and J.B. Passioura. 1971. Gravity segregation during miscible displacement. Soil Sci. 111:258-265.
- Ross, B. 1986. Dispersion in fractal fracture networks. Water Resour. Res. 22:823-827.
- Rothman, D.H. 1988. Cellular-automaton fluids: A model for flow in porous media. Geophysics 53:509–518.
- Rothman, D.H., and S. Zalesky. 1997. Lattice-gas cellular automata. Cambridge Univ. Press, Cambridge, UK.
- Rowe, R.K., and J.R. Booker. 1989. A semi-analytic model for contaminant migration in a regular twoor three-dimensional fractured network: Conservative contaminants. Int. J. Numer. Anal. Meth. Geomechan. 13:531–550.
- Rubin, Y., and J.J. Gómez-Hernández. 1990. A stochastic approach to the problem of upscaling of conductivity in disordered media: theory and unconditional numerical simulations. Water Resour. Res. 36:691–701.
- Russ, J.C. 1994. Fractal surfaces. Plenum Press, New York.
- Saffman, P.G. 1959. A theory of dispersion in a porous medium. J. Fluid Mech. 6:321–349.
- Saffman, P.G. 1960. Dispersion due to molecular diffusion and macroscopic mixing in flow through a network of capillaries. J. Fluid Mech. 7:194–208
- Saffman, P.G., and G.I. Taylor. 1958. The penetration of a fluid into a porous medium or Hele-Shaw cell containing a more viscous liquid. Proc. R. Soc. London Ser. A 245:312–329.
- Sahimi, M. 1993. Flow phenomena in rocks: From continuum models to fractals, percolation, cellular automata, and simulated annealing. Rev. Modern Phys. 65:1393–1534.
- Sahimi, M. 1995. Flow and transport in porous media and fractured rock. VCH Verlagsgesellschaft mbH, Weinheim, Germany.
- Sahimi, M., and A.O. Imdakm. 1988. The effect of morphological disorder on hydrodynamic dispersion in flow through porous media. J. Phys. Ser. A 21:3833–3870.
- Sahimi, M., B.D. Hughes, L.E. Scriven, and H.T. Davis. 1983. Stochastic transport in disordered systems. J. Chem. Phys. 78:6849–6864.
- Salles, J., J.F. Thovert, R. Delannay, L. Prevors, J.L. Auriault, and P.M. Adler. 1993. Taylor dispersion in porous media: Determination of the dispersion tensor. Phys. Fluids A 5:2348–2376.
- Santra, S.B., B. Sapoval, and O. Haeberlé. 1997. Lévy distribution of collisions for Knudsen diffusion in fractal pores. p. 350–355. *In J.L.* Véhel et al. (ed.) Fractals in engineering. From theory to industrial applications. Springer-Verlag, New York.
- Saucier, A., and J. Muller. 1993. Characterization of porous media with geometrical multifractals. Fractals 1:894–903.
- Scheidegger, A.E. 1957. The physics of flow through porous media. Univ. Toronto Press, Macmillan, New York.

Schwartz, F.W., L. Smith, and A.S. Crowe. 1983. A stochastic analysis of macroscopic dispersion in fractured media. Water Res. 19:1253–1265.

- Schwartz, H. 1980. Two dimensional feature shape indices. Mikroskopie (supplement) 37:64-67.
- Schwartz, L.M., P.N. Sen, and D.L. Johnson. 1989. Influence of rough surfaces on electrolytic conduction in porous media. Phys. Rev. B 40:2450–2458.
- Scott, G.J.T., R. Webster, and S. Nortcliff. 1988a. The topology of pore structure in cracking clay soil. I. The estimation of numerical density. J. Soil Sci. 39:303–314.
- Scott, G.J.T., R. Webster, and S. Nortcliff. 1988b. The topology of pore structure in cracking clay soil. II. Connectivity density and its estimation. J. Soil Sci. 39:315–326.
- Scotter, D.R. 1978. Preferential solute movement through larger soil voids. I Some computations using simple theory. Aust. J. Soil Res. 16:257–267.
- Scotter, D.R., and P.A.C. Raats. 1968. Dispersion in porous mediums due to oscillating flow. Water Resour. Res. 6:1201–1206.
- Scotter, D.R., and P.J. Ross. 1994. The upper limit of solute dispersion and soil hydraulic properties. Soil Sci. Soc. Am. J. 58:659–663.
- Serra, J. 1982. Image analysis and mathematical morphology. Acad. Press, London, UK.
- Seyfried, M.S., and P.S.C. Rao. 1987. Solute transport in undisturbed columns of an aggregated tropical soil: Preferential flow effects. Soil Sci. Soc. Am. J. 51:1434–1444.
- Shikaze, S.G., E.A. Sudicky, and F.W. Schwartz. 1998. Density-dependent solute transport in discretely-fractured geologic media: Is prediction possible? J. Contam. Hydrol. 34:273–291.
- Silliman, S.E., and A.L. Wright. 1988. Stochastic analysis of paths of high hydraulic conductivity in poorer media. Water Resour. Res. 24:1901–1910.
- Simon, R., and F.J. Kelsey. 1971. The use of capillary tube networks in reservoir performance studies: I. Equal-viscosity miscible displacements. Soc. Petrol. Eng. J. 11:99–112.
- Simon, R., and F.J. Kelsey. 1972. The use of capillary tube networks in reservoir performance studies: II. Effect of heterogeneity and mobility on miscible displacement efficiency. Soc. Petrol. Eng. J. 12:345–351.
- Skopp, J. 1984. Analysis of solute movement in structured soils. p. 220–227. *In J.* Bouma and P.A.C. Raats (ed.) Proc. ISSS Symp. Water Solute Movement in Heavy Clay Soils, Wageningen, The Netherlands. 27–31 August. ILRI, Wageningen, the Netherlands.
- Skopp, J., and W.R. Gardner. 1992. Miscible displacement: An interacting flow region model. Soil Sci. Soc. Am. J. 56:1680–1686.
- Skopp, J., W.R. Gardner, and E.J. Tyler. 1981. Solute movement in structured soils: Two-region model with small interaction. Soil Sci. Soc. Am. J. 45:837–842.
- Smith, L., and F.W. Schwartz. 1984. An analysis of the influence of fracture geometry on mass transport in fractured media. Water Resour. Res. 20:1241–1252.
- Sobey, I.J. 1982. Oscillatory flows at intermediate Strouhal number in asymmetric channels. J. Fluid Mech. 125:359–373.
- Sobey, I.J. 1985. Dispersion caused by separation during oscillatory flows through a furrowed channel. Chem. Eng. Sci. 40:2129–2134.
- Soil Survey Division Staff. 1993. Soil survey manual. USDA Handb. 18. U.S. Gov. Print. Office, Washington, DC.
- Sorbie, K.S., and P.J. Clifford. 1991. The inclusion of molecular diffusion effects in the network modelling of hydrodynamic dispersion in porous media. Chem. Eng. Sci. 46:2525–2542.
- Sposito, G. 1989. The chemistry of soils. Oxford Univ. Press, Oxford, UK.
- Sposito, G., V.K. Gupta, and R.N. Bhattacharya. 1979. Foundation theories of solute transport in porous media: A critical review. Adv. Water Resour. 2:59–68.
- Stark, K.P. 1972. A numerical study of the nonlinear laminar regime of flow in an idealised porous medium. p. 86–102. *In* Fundamentals of transport phenomena in porous media. Int. Assoc. Hydraulic Res., Elsevier, New York.
- Steenhuis, T.S., J.-Y. Parlange, and M.S. Andreini. 1990. A numerical model for preferential solute movement in structured soils. Geoderma 46:193–208.
- Stockman, H.W. 1997. A lattice gas study of retardation and dispersion in fractures: Assessment of errors from desorption kinetics and buoyancy. Water Resour. Res. 33:1823–1831.
- Stockman, H.W., C. Cooper, C. Li, and S.J. Perea-Reeves. 1997. Practical application of lattice-gas and lattice Boltzmann methods to dispersion problems. Int. J. Complex Syst. Pap. 90. Available at http://www.wizard.com/~hwstock/saltfing.htm.
- Sudicky, E.A., and E.O. Frind. 1982. Contaminant transport in fractured porous media: Analytical solutions for a system of parallel fractures. Water Resour. Res. 18:1634–1642

- Sudicky, E.A., and R.G. McLaren. 1992. The Laplace transform Galerkin technique for large-scale simulation of mass transport in discretely fractured porous formations. Water Resour. Res. 28:499-514.
- Sugita, F., and R.W. Gillham. 1995. Pore scale variation in retardation factor as a cause of nonideal reactive breakthrough curves. 3. Column investigations. Water Resour. Res. 31:121–128.
- Sukop, M.C., G.-J. van Dijk, E. Perfect, and W.K.P. van Loon. 2001. Percolation thresholds in 2-dimensional prefractal models of porous media. Transp. Por. Media. (In press.)
- Tang, D.H., E.O. Frind, and E.A. Sudicky. 1981. Contaminant transport in fractured porous media: Analytical solution for a single fracture. Water Resour. Res. 17:555–564.
- Taylor, G.1953. Dispersion of soluble matter in solvent flowing slowly through a tube. Proc. R. Soc. London Ser. A 219:186–203.
- Taylor, G. 1954. Conditions under which dispersion of a solute in a stream of solvent can be used to measure molecular diffusion. Proc. R. Soc. London Ser. A 225:473–477.
- Thompson, A.F.B., and L.W. Gelhar. 1990. Numerical simulation of solute transport in three-dimensional, randomly heterogeneous porous media. Water Resour. Res. 26:2541–2562.
- Thompson, A.H. 1991a. Fractals in rock physics. Ann. Rev. Earth Planet Sci. 19:237–262.
- Thompson, M.E. 1991b. Numerical simulation of solute transport in rough fractures. J. Geophys. Res. 96:4157–4166.
- Torelli, L. 1972. Computer simulation of the dispersion phenomena occurring during flow through porous media, using a random maze model. Pure Appl. Geophys. 96:875–888.
- Torelli, L., and A.E. Scheidegger. 1971. Random maze models of flow through porous media. Pure Appl. Geophys. 89:32–44.
- Toride, N., F.J. Leij, and M. Th. van Genuchten. 1995. The CXTFIT Code for estimating transport parameters from laboratory or field tracer experiments. Res. Rep. 137. U.S. Salinity Lab., USDA-ARS, Riverside, CA.
- Tsang, Y.W., and C.F. Tsang. 1987. Channel model of flow through fractured media. Water Resour. Res. 23:467–479.
- Tsang, Y.W., C.F. Tsang, I. Neretnieks, and L. Moreno. 1988. Flow and tracer transport in fractured media: a variable aperture channel model and its properties. Water Resour. Res. 24:2049–2060.
- Tsuda, A., W.J. Federspiel, P.A. Grant Jr., and J.J. Fredberg. 1991. Axial dispersion of inert species in alveolated channels. Chem. Eng. Sci. 46:1419–1426.
- Turner, G.A. 1958. The flow-structure in packed beds. Chem. Eng. Sci. 7:156–165.
- van Brakel, J. 1975. Pore space models for transport phenomena in porous media: Review and evaluation with special emphasis on capillary liquid transport. Powder Technol. 11:205–236.
- van Genuchten, M.Th., and J.C. Parker. 1984. Boundary conditions for displacement experiments through short laboratory soil columns. Soil Sci. Soc. Am. J. 48:703–708.
- van Genuchten, M.Th., and P.J. Wierenga. 1976. Mass transfer studies in sorbing porous media I. Analytical solutions. Soil Sci. Soc. Am. J. 40:473–480.
- van Genuchten, M.Th., and F.N. Dalton. 1986. Models for simulating salt movements in aggregated field soils. Geoderma 38:165–183.
- van Genuchten, M.Th., D.H. Tang, and R. Guennelon. 1984. Some exact solutions for solute transport through soils containing large cylindrical macropores. Water Resour. Res. 20:335–347.
- van Genuchten, M.Th., and P.J. Wierenga. 1986. Solute dispersion coefficients and retardation factors. p. 1025–1054. *In A. Klute* (ed.) Methods of soil analysis. Part 1. 2nd ed. Agron. Monogr. 9. ASA and SSSA, Madison, WI.
- Verheggen, T.M.M. (ed.). 1992. Numerical methods for the simulation of multi-phase and complex flow. Springer-Verlag, New York.
- Vervoort, R.W., D.E. Radcliffe, and L.T. West. 1999. Soil structure development and preferential solute flow. Water Resour. Res. 35:913–928.
- Vogel, H.J. 1997. Morphological determination of pore connectivity as a function of pore size using serial sections. Eur. J. Soil Sci. 48:365–377.
- Vogel, H.J. 2000. A numerical experiment on pore size, connectivity, water retention, permeability, and solute transport using network models. Eur. J. Soil Sci. 51:99–105.
- Vogel, H.J., and A. Kretzschmar. 1996. Topological characterization of pore space in soil—sample preparation and digital image-processing. Geoderma 73:23–38.
- Voss, R.F. 1986, Random fractals: Characterization and measurement, p. 1–11. *In* R. Pynn and A. Skeltorp (ed.) Scaling phenomena in disordered systems. Plenum Press, New York.
- Walker, P.J.C., and S.T. Trudgill. 1983. Quantimet image analysis of soil pore geometry: Comparison with tracer breakthrough curves. Earth Surf. Process. Landforms 8:465–472.

Warren, J.E., and F.F. Skiba. 1964. Macroscopic dispersion. Trans. Am. Min. Metall. Petrol. Eng. 231:215-230.

- Washburn, E.W. 1921. The dynamics of capillary flow. Phys. Rev. 17:273–283.
- Weibel, E.R. 1987. Ideas and tools: The invention of stereology. Acta Stereol. 6:23-33.
- Wendt, R.P., E.A. Mason, and E.H. Bresler. 1976. Effect of heteroporosity on flux equations for membranes. Biophys. Chem. 4:237–247.
- Wheatcraft, S.W., G.A. Sharp, and S.W. Tyler. 1991. Fluid flow and solute transport in fractal heterogeneous porous media. p. 695–722. *In J.* Bear and M.Y. Corapcioglu (ed.) Transport processes in porous media. Kluwer Acad., Dordrecht, The Netherlands.
- White, I., and M.J. Sully. 1987. Macroscopic and microscopic capillary length and time scales from field infiltration. Water Resour. Res. 23:1514–1522.
- Wooding, R.A. 1959. The stability of a viscous liquid in a vertical tube containing porous material. Proc. R. Soc. London Ser. A 252:120–134.
- Wooding, R.A. 1960. Instability of a viscous liquid of variable density in a vertical Hele-Shaw cell. J. Fluid Mech. 7:501–515.
- Wooding, R.A. 1962a. Free convection of fluid in a vertical tube filled with porous material. J. Fluid Mech. 13:129–144.
- Wooding, R.A. 1962b. The stability of an interface between miscible fluids in a porous medium. Z. Angew. Math. Phys. 13:255–265.
- Yanuka, M. 1992. Percolation theory approach to transport phenomena in porous media. Transp. Por. Media 7:265–282.
- Zeng, Y., C.J. Gantzer, R.L. Payton, and S.H. Anderson. 1996. Fractal dimension and lacunarity of bulk density determined with x-ray computed tomography. Soil Sci. Soc. Am. J. 60:1718–1724.
- Zhan, H., and S.W. Wheatcraft. 1996. Macrodispersivity tensor for nonreactive solute transport in isotropic and anisotropic fractal porous media: Analytical solutions. Water Resour. Res. 32:3461-3474.
- Zhou, D., and E.H. Stenby. 1993. Interpretation of capillary pressure curves using invasion percolation theory. Transp. Por. Media 11:17–31.

# Testing Kinematic Wave Solutions for Flow in Macroporous Soils Against a Lattice-Gas Simulation

## Liliana Di Pietro

Institut National de la Recherche Agronomique Avignon, France

## Peter F. Germann

University of Bern Bern, Switzerland

Soil structure, antecedent soil moisture and input flow rate control rapid flow along preferential pathways in well-structured soils. The amount of preferential flow may be significant for high input rates, mainly in the intermediate to high ranges of moisture. We use a three-dimensional lattice-gas model to simulate infiltration in a cracked porous medium as a function of rainfall intensity. We compute flow velocities and water contents during infiltration. The dispersion mechanisms of the rapid front in the crack are analyzed as a function of rainfall intensity. The numerical lattice-gas solutions for flow are compared with the analytical solution of the kinematic wave approach. The process is better described by the kinematic wave approach for high input flow intensities, but fails to adequately predict the front attenuation showed by the lattice-gas solution.

## INTRODUCTION

Many of the operational approaches to infiltration in structured soils are based on a double porosity approach (Hosang, 1993; Jarvis, 1994). The porous medium is viewed as the superposition of two interacting continua. One continuum is the matrix or microporosity where capillary-driven flow, governed by Richards' equation (Richards, 1931) is dominant; the other is the macroporosity where the main force is gravity and water flows freely. Generally, a diffusive sink-source term accounts for the mass exchange between the two continua. Most of these models require a priori assumptions either on the spatial arrangements of macropores or on their temporal hydraulic activity. A more conceptual approach based on kinematic waves has been proposed (Germann, 1985; Germann, 1990) for describing macropore flow.

The wave equation derives from the assumption that the macropore volume flux is a nonlinear single valued function of the volumetric water content. It has been shown (Di Pietro & Lafolie, 1991) that this approach applies reasonably well to water content profiles for high water input rates and high degrees of saturation. Yet the meaning of the parameters involved in the equation and the limits of application of this approach are not well assessed. A kinematic wave approximation has been also derived as an asymptotic limit of Richard's transport equation based on the assumption of a unit gradient of the total potential head (Sisson et al., 1980; Smith, 1983; Raats, 1983). This approximation applies during redistribution and drainage when the soil profile is draining freely. Both kinematic equations are derived from very different conceptual basis and the parameters involved are defined at different space and time scales. Whatever interpretation of these parameters, the underlying physical process unifying both approaches is the predominance of gravity driven flow over the dispersive capillary flow. The validity of these approximations and particularly the meaningful interpretation of model parameters require accurate experiments. Usually, problems arise when trying to measure flow variables and structural properties during rapid flow. Although sophisticated experimental systems have been implemented, information obtained about the process is incomplete in most cases.

Lattice-gas algorithms have shown to provide useful information about the dynamics of flow in porous media and particularly in multiple-scaled porous media (Di Pietro, 1996; Di Pietro et al., 1994). These models reproduce fluid behavior within the incompressible limit, because they are automata for the Navier-Stokes equations. Lattice-gases allow the study of hydrodynamic phenomena at the pore scale, but they also recover transport laws at a macroscopic scale (Di Pietro, 1998).

In this chapter, we use the results of numerical infiltration experiments in dual porosity media performed with a three-dimensional lattice-gas model to characterize preferential flow as response to rainfall intensity. From the temporal and spatial evolution of the water content during infiltration and drainage, we evaluate the adequacy of a kinematic wave approximation to describe the flow. We also discuss the conceptual basis of the asymptotic kinematic approach to Richards' equation in comparison with the macropore kinematic equation.

#### THEORETICAL APPROACHES

### **Lattice-Gas Models**

Traditional methods of simulation in hydrodynamics are based on the description of a fluid field obeying to partial differential equations. Finite difference, finite elements, spectral methods are generally used to approximate the equations and they are represented in the computer by floating point numbers. The implementation of the boundary conditions is the main difficulty of these methods.

Cellular automata (CA) are an alternative method to solve differential equations. They can be considered as discrete approximations to partial differential equations. Cellular automata are mathematical systems consisting of many identical components or cells. Each cell is a kind of virtual robot that responds to signals according

to a set of transition rules. Despite the simplicity of their construction the whole system is capable of complex behavior. From their analysis it is possible to develop specific models for particular systems. The evolution of the cellular automaton involves sequential processing of the information associated with the states of the cell. The transition rules determine the macroscopic behavior of the system. The evolution of the whole system is analyzed statistically. The large-scale dynamic equations describing the behavior of the system are obtained as a statistical average in space and time of the corresponding microscopic variables under the assumption of statistical equilibrium. The form of the large-scale equations is quite insensitive to microscopic details (Wolfram, 1986). The microscopic transition rules can only affect the value of the macroscopic coefficients.

Cellular automata techniques show several advantages. The whole system and rules are expressible in Boolean algebra and then no floating point calculations are involved. They are well adapted for massively parallel computers. Nonlinearity is a natural component of the system, thus no special treatment is required. Models based on cellular automata are more appropriate in highly nonlinear regimes of physical systems (Wolfram, 1984). Various field equations can be approximated by the large-scale behavior of suitably chosen cellular automata. In particular, it has been shown (Frisch et al., 1986, 1987) that the two-dimensional and three-dimensional Navier-Stokes equations can be simulated with lattice-gas models. Frisch et al. (1986) developed the first cellular automaton (called lattice-gas) that behaves at a large-scale like a viscous fluid in the incompressible limit. This behavior hails from the physical principle that states that macroscopic laws do not depend on the detailed microscopic interactions but they depend on microscopic conservation laws and on the symmetry of the underlying space. Since 1986, numerous lattice-gases have been developed for two-dimensional and three-dimensional hydrodynamic applications. Most of these applications are mentioned and discussed by Boon et al. (1993).

# **Structure and General Properties of Lattice Gases**

On a microscopic level, physical fluids consist of discrete particles. The system can be described by a deterministic system of equations, called the micro dynamic equations. These equations are obtained by describing the evolution of each individual molecule in space and time. For practical reasons, a probabilistic description is normally used. In this latter approach an ensemble of microscopic particle configurations are described by a probability distribution function. At the macroscopic scale, the fluid may be seen as a continuum and can be described by the partial differential equations of hydrodynamics. These macro-dynamic equations are derived from the microscopic conservation relations of the microscopic mean quantities, namely mass and momentum, for large space scale and for long time scale. By analogy with statistical mechanics, the microscopic and macroscopic dynamics of lattice-gases can be described in the same way. Lattice-gases may be viewed as a completely discrete model of a fluid at the molecular level of description. Each cell on the lattice plays the role of a volume element that is large enough to contain a number of particles, but is small compared to all macroscopic lengths % ales in the system. When the lattice has suitable symmetries to ensure the isotropy

of macroscopic tensor quantities, the large-scale equations differ only by irrelevant terms from the Navier-Stokes equations in the low-speed incompressible limit. The collision rules will determine the magnitude of the macroscopic transport coefficients such as viscosity, but they do not change the form of the macroscopic equations. We briefly describe below the structure and the main equations of latticesgases. For a detailed derivation of the master equations see, for instance, Frisch et al. (1987).

# **Deterministic Micro-dynamic Equations**

In a lattice-gas the individual cells are the structural units of a D-dimensional regular lattice. Each cell is defined by its position vector  $r_*$  on the discrete space, a finite number of states  $s(r_*)$  and a set of transition rules E that map the state of the cell at time t into the state at time t+1. A finite number of particles reside in each cell. A discrete velocity  $c_i$  with  $i=1,\ldots,k$  is associated to each particle. This velocity is chosen such that the particle can propagate to a neighboring cell in unit time. Each velocity direction is subject to an exclusion principle of utmost single occupancy. The combinations of occupancies define the set of possible states associated with each cell. The configuration of each cell is defined by the Boolean field

$$s(r_*,t) = \{s_i(r_*,t), i = 1...k\}$$
 [1]

where the  $s_i$ 's are Boolean variables that take the value 1 or 0, respectively if a particle with velocity  $c_k$  is present or not.

Alternating propagation and collision steps update the lattice. The propagation operator S performs spatial shifting of particles by  $c_i$  and it is defined by

$$S: s_i(r_*,t) \longrightarrow s_i(r_* + c_i, t+1)$$
 [2]

Collision is a local exchange of the linear momentum of the particles. The momentum exchange rules are chosen such that they conserve the total mass and linear momentum, like real elastic collisions. The collision operator may be written as

$$C: s_i(r_*, t+1) \longrightarrow s_i(r_*, t) + \Delta_i(s_i)$$
 [3]

where  $\Delta_i$  ( $s_i$ ) is the collision function. Its form depends on the particular imposed rules.

The evolution operator is the composition of the propagation and collision operators  $E = C \cdot S$ . The entire updating of the system can be described by the following equation:

$$s(*,t+1) = E[s(*,t)],$$
 [4]

where the symbol \* stands for all the space variables. Equation [4] is called the deterministic micro dynamic evolution equation of the lattice-gas. The mass and momentum conservation equations for the Boolean field are, respectively, written as

$$\sum_{i} s_{i}(r_{*},t) = \sum_{i} s_{i}(r_{*} + c_{i},t+1),$$
 [5]

and

$$\sum_{i} c_{i} s_{i} (r_{*}, t) = \sum_{i} c_{i} s_{i} (r_{*} + c_{i}, t+1),$$
 [6]

## **Probabilistic Description**

Let P[s(\*,t)] be the probability for the entire lattice gas to have the configuration s(\*) at time t. Mean quantities, such as the mean population and the mean momentum, are given by ensemble averaging over the probability distribution.

Using the Boltzmann molecular chaos assumption, which states that the configuration of cells are uncorrelated in space and time, P[s(\*,t)] may be completely factorized over all cells. It is expressed as the product of the probabilities of the configurations of each cell

$$P[s(*,t)] = \prod_{r_*} P[s(r_*,t)]$$
 [7]

The molecular chaos assumption implies that the system is at statistical equilibrium. As in traditional kinetic theory this probability distribution function represents the maximum entropy state of the system.

When the lattice is updated, conservation of probability implies that

$$P[s(*,t+1)] = P\{[E[s(*,t)]\}$$
 [8]

for all the possible configurations. Equation [8] is the probabilistic evolution equation of the lattice gas.

It has been shown (see Frisch et al., 1987) that Eq. [8] admits equilibrium solutions that lead to a Fermi-Dirac distribution for the mean population of particles  $N_i$ . This distribution is expressed by

$$N_{\rm i} = \frac{1}{1 + \exp(h + q.c_{\rm i})}$$
 [9]

where h is an arbitrary real number and q is an arbitrary one-dimensional vector.

Averaging of the micro-dynamic conservation relations 5 and 6 leads to the following conservation relations for the mean population and for the mean momentum

$$\sum_{i} N_{i}(r_{*},t) = \sum_{i} N_{i}(r_{*} + c_{i},t+1),$$
[10]

$$\sum_{i} c_{i} N_{i} (r_{*}, t) = \sum_{i} c_{i} N_{i} (r_{*} + c_{i}, t+1),$$
[11]

The total mean mass density  $\rho(r_*,t)$  and the total mean momentum  $J(r_*,t)$  per cell are, respectively, defined by

$$\rho(r_*,t) = \sum_{i} N_i$$
 [12]

$$J(r_{*},t) = \sum_{i} c_{i} N_{i} = \rho(r_{*},t) u(r_{*},t)$$
[13]

where u is the mean velocity at position  $r_*$  and time t.

Equations [12] and [13] allows us to write the conservation Relations [10] and [11] in terms of the mean variables  $\rho$  and u.

## The Large-scale Behavior of Lattice-gases

To derive the macroscopic transport equations, the conservation Relation [10] and [11] must be converted to differential equations. The main assumption needed is that the mean density and the mean velocity vary slowly in space and in time. Starting from Eq. [10] and [11], the macro dynamic equations describing the large-scale behavior of the lattice gas are obtained by multiple-scale perturbation expansion technique (Frisch et al., 1987). We shall not derive this formalism here. In the continuous limit, Eq. [10] leads to the macro dynamical conservation of mass or Euler equation

$$(\partial \rho / \partial t) + \nabla \cdot (\rho u) = 0$$
 [14]

The second-order expansion of Eq. [11] leads to a macroscopic momentum conservation equation that differs from Navier-Stokes equations only in irrelevant terms of higher order provided that the mean velocity u is small. Thus lattice-gases may be used as models for fluids.

## Applications of Lattice-gas to Transport in Porous Media

For a single fluid, existing two-dimensional models are all variations of the original FHP lattice-gas (Frisch et al., 1986). The cellular space is built as a hexagonal lattice. At most, six moving particles may reside in a cell at a time. Several variants have been constructed differing in the number of particles at rest and in the collision rules.

Three-dimensional regular lattices do not have enough symmetry to ensure macroscopic isotropy. To model three-dimensional fluids, a suitable three-dimensional projection of a four-dimensional model, the face-centered-hypercube (FCHC), is used (see, for instance, Sommers & Rem, 1992). Each node in the lattice is connected via links to 24 nearest neighbors. In this case, up to 24 moving particles may occupy the cells.

Generalizations of the lattice-gas models into two or more species have also been developed to model the dynamics of interfaces coupled with fluid motion (i.e., Rothman & Keller, 1988).

Because lattice-gases are entirely encoded with bit operations, they very efficiently employ computer memory, rendering their applications to fluid transport in porous media very attractive. These models have been successfully used to study flow in porous media for single and multiphase fluid flow, and for steady state and transient regimes (Balashubramanian et al., 1987; Rothman, 1988, 1989).

A lattice gas model for liquid-vapor transition has also been proposed, the interacting liquid-gas model (ILG) of Appert and Zaleski (1990, 1993). The authors

added long-range attractive interactions to the evolution rules. These interactions act like Van der Waals forces in real fluids and lead to a liquid-gas transition. Both the collision and the long-range interaction leave the total momentum and the mass invariant. The model has at equilibrium two coexisting phases of high and low density, the interface showing surface tension. The viscosity of the dense and light phases and their equilibrium densities can be estimated from numerical simulations.

It has been shown that the ILG model can adequately simulate well-established macroscopic flow regimes, like Poiseuille's law (Di Pietro et al., 1994). The ILG model was also applied to study evaporation in porous media (Pot, 1994), infiltration in two-dimensional saturated and non-saturated porous media with macropores (Di Pietro, 1996) and water storage in roughed infiltrating and non-infiltrating surfaces (Garcia Sanchez et al., 1996).

For these latter applications the geometry of the solid medium was introduced by selecting sites that fluid particles cannot visit. Particular collision rules are defined between solid and fluid sites. During the collision step particles are bounced back from the solid sites with a given probability returning to the site where they were coming from. This probability controls the fluid wetting properties, as it regulates the degree of attraction of liquid particles by the solid. Forcing fluid particles to preferentially travel in a selected direction with a given probability simulates external forces such as gravity. In order to simulate flow in unsaturated porous media, the liquid and gas phases are introduced by initializing selected regions of the pore space with either the denser or the lighter phases at their respective equilibrium densities. Proper scaling of the lattice variables such as length, time, pressure, density, viscosity and velocity may provide for the link between simulations and real situations by using the hydrodynamic similarity principle.

In this chapter we use a three-dimensional version of the ILG model to simulate liquid infiltration in double porosity porous media. Our objective is to compare this approach with the kinematic wave analytical solution. Lattice gas methodology provide information that we are not able to obtain with available experimental methods.

# Kinematic Wave Approximation to Transport in Porous Media

A complete mathematical description of the evolution of a physical quantity in a macroscopic continuous system usually arises from the combination of fundamental conservation laws, like conservation of mass and linear momentum. For a systematic study of systems of conservation laws see Majda (1984). A conservation law states the physical balance between the local variation of the density of a physical quantity  $\phi({\bf r},t)$  within a given region  $\Omega\in\Re^3$  of the space and the flux  $F_\phi$  of this quantity across the external boundary  $\partial\Omega\in\Omega$ . This law may be written as

$$(\partial \varphi / \partial t) + \nabla . \mathbf{F}_{\varphi} = 0$$
 [15]

To completely describe the system we further need a law relating  $\mathbf{F}_{\varphi}$  with  $\varphi$ , which leads to a differential transport equation when combined with Eq. [15]. It characterizes the evolution of  $\varphi$  in space and time. When  $\mathbf{F}_{\varphi}$  depends on the spatial co-

ordinates  $\mathbf{r}$  and on  $\phi$ , but it does not depend on the derivatives of  $\phi$ , a first-order kinematic wave equation is obtained (Lighthill & Whitman, 1955; Lax, 1972). In this particular case

$$\mathbf{F}_{\varphi} = f(\mathbf{r}, \varphi) \tag{16}$$

and then

$$\nabla . \mathbf{F}_{\mathbf{\phi}} = (\partial f / \partial \mathbf{\phi})|_{\mathbf{r}} \nabla \mathbf{\phi}.$$
 [17]

By introducing Eq. [17] in Eq. [15] the following kinematic wave equation is obtained:

$$(\partial \mathbf{\phi}/\partial t) + c(\mathbf{\phi}, \mathbf{r}) \nabla \mathbf{\phi} = 0,$$
 [18]

where  $c(\mathbf{r}, \varphi) = (\partial f/\partial \varphi)|_{\mathbf{r}}$  is the signal speed at which  $\varphi$  propagates. The propagation paths in the  $\mathbf{r} - t$  space are called characteristics and are given by  $d\mathbf{r} = c(\varphi, \mathbf{r})dt$ . Along each characteristic  $\varphi$  is constant. When f is a linear function, the wave travels with no distortion. For nonlinear relations the waves may spread out fanwise or may sharpen allowing for shock wave formation. Numerous physical phenomena are approximated with kinematic wave theory, like flow of nonviscous compressible fluids and flood movements in rivers. Such a description physically means that no dissipative mechanisms are considered at the chosen scale. Mathematically, dispersive effects usually appear as an implicit or explicit dependence of the flux on one or more derivatives of the considered quantity. In these cases the transport equation is usually of higher order. This is the case of Richards' equation for transport in porous media, which is derived from the combination of the conservation law (Eq. [15]) by replacing the physical quantities  $\varphi$  and  $\mathbf{F}_{\varphi}$  with the volumetric water content  $\theta$ , and with the volumetric water flux  $\mathbf{J}$ , respectively,

$$(\partial \theta / \partial t) + \nabla . \mathbf{J} = 0, \tag{19}$$

and including Darcy's law. Darcy's law for unsaturated conditions may be written as

$$\mathbf{J} = K(\theta) - D(\theta)\nabla\theta, \tag{20}$$

where  $K(\theta)$  and  $D(\theta)$  are, respectively, the hydraulic conductivity and the diffusivity. Equation [20] shows the volumetric flux depending explicitly on a derivative of  $\theta$ . The Richards' transport equation, written in the Fokker-Planck nonlinear diffusion form, is obtained by replacing Eq. [20] in Eq. [19]

$$(\partial \theta / \partial t) + (\partial K / \partial \theta) \nabla \theta = \nabla \cdot (D \nabla \theta).$$
 [21]

Equation [21] shows water transport as a diffusion-convection process. If the diffusive term  $\nabla \cdot (D\nabla\theta)$  is neglected, Eq. [21] reduces to Eq. [18] with  $c(\theta, \mathbf{r}) = (\partial K/\partial \theta)|_{\Gamma}$ . This type of kinematic approximation to water transport has been used

to describe the drainage process of a uniform profile under the assumption of unit potential gradient (Sisson et al., 1980; Raats, 1983). Smith (1983) compared the solutions of the complete Richard's equation with those of the kinematic approximation for predicting the location of moving water fronts during infiltration and drainage. The kinematic solution predicted rather well the location of the waterfront as well as the general pattern of  $\theta$  behind the front, but a loss of much of the details due to diffusion was observed. He used the Peclet number

$$Pn = K(\theta)/D\nabla\theta \tag{22}$$

to assess the accuracy of the approximation. The larger the value of Pn, the better was the approximation.

Equation [21] does not apply to the entire porous medium domain if continuous macropores are present. If we consider a domain  $\Omega$  of the porous medium, a conservation equation of the form 19 for the total water content  $\theta$  is applicable, but Eq. [20] holds only in the microporous domain where the REV concept applies. The hydraulic conductivity is ill defined elsewhere. Durner (1994), among others, introduced bi- and multimodal shaped potential functions to extend the hydraulic conductivity function for multiporosity systems. The underlying assumption is the validity of Darcy's law in the macropore domain. Although this assumption is inaccurate at the macroscopic scale, the use of multimodal functions ameliorates the description of flow near saturation. It has been shown (Levy, 1988; Ene, 1990) that the validity of Darcy's law is recovered by increasing conveniently the volume  $\Omega$ to include at least one megascopic elementary volume where the continuity hypothesis may be applied. This involves upscaling from the medium scale of observation, where we can distinguish the micropore from the macropore domain, to a larger scale. The difficulties determining megascopic elementary volumes and measuring the megascopic transport coefficients render the large-approach impractical in most cases.

Beven and Germann (1981) first proposed a relation between the macropore volumetric flux  $J_{mac}$  and macropore water content  $\theta_{mac}$  of the following form

$$\mathbf{J}_{\text{mac}} = b\Theta_{\text{mac}}^{\text{a}} \tag{23}$$

where a and b are two coefficients. When considering that the medium is only formed by a distribution of macropores carrying all the flow, the combination of Eq. [23] with the continuity equation leads to a kinematic wave equation

$$(\partial \theta_{\text{mac}}/\partial t) + c_{\text{mac}} \nabla \theta_{\text{mac}} = 0$$
 [24]

where  $c_{\text{mac}} = (\partial \mathbf{J}_{\text{mac}}/\partial \theta_{\text{mac}})|_{\text{r}}$ . Germann (1985) developed the solutions of Eq. [24] for infiltration and drainage for a square input water pulse of volumetric flux density  $\mathbf{J}_{\text{s}}$  and duration  $t_{\text{s}}$ . The following boundary and initial conditions were considered

$$\begin{cases} \theta_{\text{mac}}(0,t) = 0, & t \le 0, t \ge t_{\text{s}} \\ \theta_{\text{mac}}(0,t) = \theta_{\text{s}}, & 0 \le t \le t_{\text{s}} \\ \theta_{\text{mac}}(z,0) = 0, & 0 \le z \le \infty \end{cases}$$
 [25]

The solution for  $\theta_{\text{mac}}(x,t)$ , for all  $z \le z_{\text{I}}$ , where  $z_{\text{I}}$  is the depth at which the draining front intercepts the wetting front, is

$$\begin{cases} \theta_{\text{mac}}(z,t) = 0, & 0 \le t \le t_{\text{w}}(z) \\ \theta_{\text{mac}}(z,t) = \theta_{\text{s}}, & t_{\text{w}}(z) \le t \le t_{\text{D}}(z) \\ \theta_{\text{mac}}(z,t) = \theta_{\text{s}} & \left(\frac{t_{\text{D}}(z) - t_{\text{s}}}{t - t_{\text{s}}}\right)^{1/(a-1)} & t \ge t_{\text{D}}(z) \end{cases}$$
[26]

where  $t_w(z)$  and  $t_D(z)$  are the arrival times of the wetting and draining fronts at depth z respectively. Equation [26] indicate that the square pulse infiltrates as a shock wave without being spread. After input has ceased, the water content at the surface drops to zero and a draining front develops behind the wetting front. The draining front travels with velocity  $c_I = ac_{\text{max}}$ , which is greater than  $c_{\text{mac}}$ . After the draining front intercepts the wetting front,  $\theta_{\text{mac}}(z,t)$  results in a single-crested function of time for depths  $z \ge z_I$ , and the water content of the peak begins to decrease. For details on the derivation of the flow equations see Germann (1985). For  $z \le z_I$  the characteristics of the wetting and draining fronts are straight lines intersecting at  $(z_I,t_I)$  as shown in Fig. 4–1. The characteristics correspond to the evolution of two shock waves, respectively, one originating from the applied water content  $\theta_s$  at time t = 0 and the other one from the reduction to zero water content at the surface when input ceases at time  $t = t_s$ .

As discussed by Germann and Di Pietro (1996) the kinematic wave model applies in two modes. The  $\theta$ -mode presented above and the **J**-mode that is obtained by writing Eq. [26] in terms of **J** using relation 23. To test the validity of the kinematic approach, the **J**-mode allows for input-output experiments. Typically, these experiments consist of raining on the surface of a soil and measuring the drainage

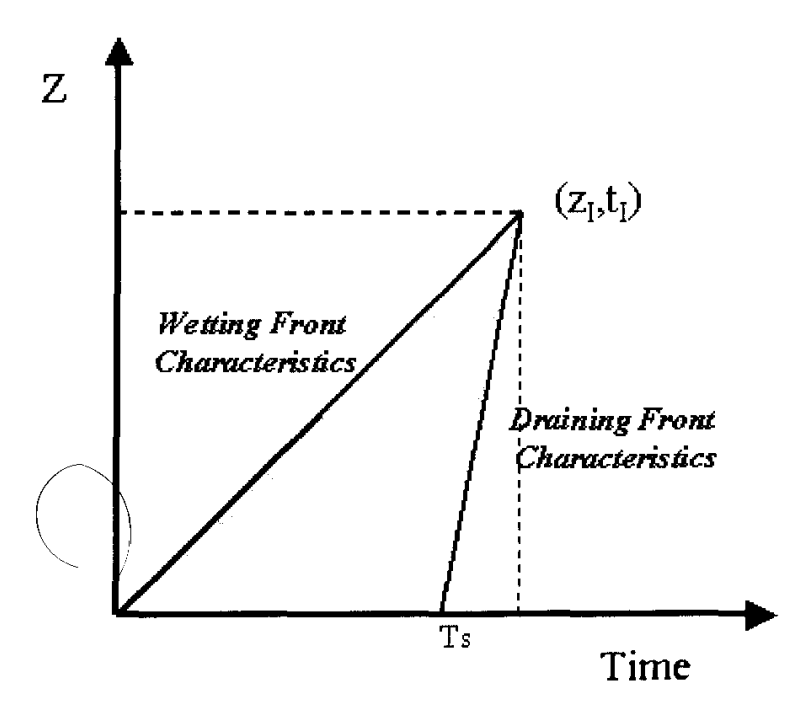


Fig. 4–1. Theoretical wetting and draining front characteristics for the kinematic wave model for a square pulse of duration  $T_k$  at z=0.

hydrograph at a given depth. The  $\theta$ -mode requires rapid measurement of soil moisture at a given depth. The model parameters a and b are estimated through a nonlinear curve fitting procedure (see for instance Germann et al., 1997) from the  $\theta(z,t)$  or  $\mathbf{J}(z,t)$  curves for times  $t \geq t_{\mathbf{D}}(z)$ . We note that we normally measure total water content or volumetric fluxes, while the kinematic Eq. [24] applies to noncapillary or mobile water flow. This represents a first difficulty when trying to validate the approach as the distinction between nonmobile and mobile water content is usually ambiguous.

Several tests of the accuracy of the approach to predict infiltration and drainage in media with macropores have been carried out by using either the  $\theta$  or the **J**-modes (Mdaghri, 1997). The kinematic description is legitimate for water inputs of intensity and duration high enough to sustain gravity dominant flow with respect to capillary dispersion. A first insight on the possible mechanisms controlling dispersive and preferential flow based on the analysis of the dissipation of linear momentum have been proposed (Germann & Di Pietro, 1999). However, not enough experimental data exist and no accurate method has been implemented for distinguishing the types of flow.

When comparing the kinematic limit of Eq. [21] with Eq. [24], we note similitude; both derive from a conservation law and from a structural relation and both apply when gravity driven flow is dominant. But the first one is limited to macroscopic continuum media where the hydraulic conductivity is well defined everywhere. The other one is more general as the structural relation between the flux and the volumetric content is not dependent on the existence of a REV. Equation [24] does not account for waterfront dispersion, nevertheless dispersive effects have been experimentally observed for low input intensities (Di Pietro & Lafolie, 1991).

#### DESCRIPTION OF NUMERICAL EXPERIMENTS

Four different three-dimensional numerical infiltration experiments were carried out in a simulated porous medium with a central parallel crack as shown in Fig. 4–2. The lattice size is 10 by 100 by 150 sites in the x, y and z directions, respectively. Solid sites are represented in red. A probabilistic algorithm generated at random the solid distribution of the microporous matrix. The mean microporosity and macroporosity are 0.52, and 0.192, respectively, of the total volume of the medium. A gravity force was simulated as described in Di Pietro et al. (1994), oriented parallel to the crack in the z-downward direction. Void sites (white color in Fig. 4–2) are initially filled with gas. All quantities are expressed in arbitrary lattice units.

A rainfall event of constant intensity lasting 4000 time steps was simulated at the surface of the medium by injecting liquid particles at a constant rate. Applied input rates were 0.01, 0.55, 0.77 and 1.47 sites per time step, respectively, for simulations 1 to 4. Each simulation was run over 10 000 time steps.

Special code modules were developed to compute the water content and the liquid velocity field. We obtained the macroscopic mean values of micropore and macropore water contents, respectively,  $\theta_{\rm mic}(z_i,t)$  and  $\theta_{\rm mac}(z_i,t)$  by averaging over 50 time steps, and over spatial steps of 5 sites in the z-direction and over all the mi-

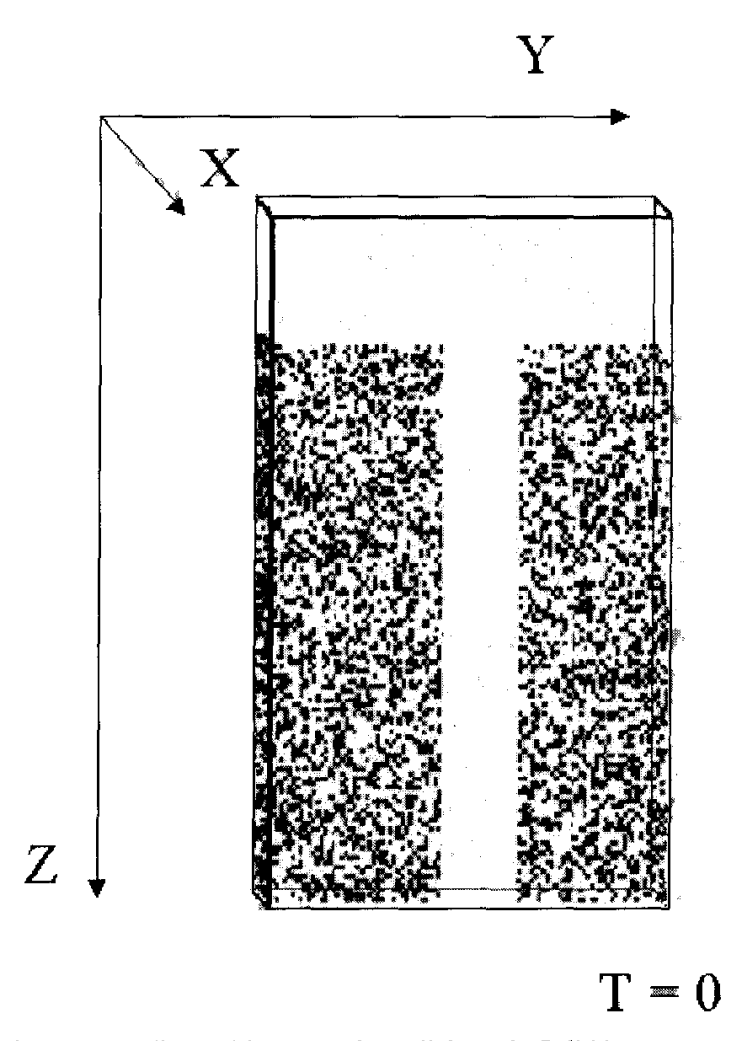


Fig. 4-2. Simulated porous medium with a central parallel crack. Solid is represented in red.

cropore or macropore sites in the x-y plane. The total macroscopic water content  $\theta(z_i,t_i)$  results from

$$\theta(z_{i},t) = \theta_{\text{mic}}(z_{i},t) + \theta_{\text{mac}}(z_{i},t)$$
 [27]

Even if we computed the microscopic velocity field in the x, y and z directions, we only considered the macroscopic averages in the y and z directions, as no heterogeneity is considered in the x-direction. The macroscopic fluxes were calculated by averaging the microscopic velocities over 50 time steps, over five sites in the z-direction, and over half-cross sections of the micropore matrix and of the crack, multiplied by the respective mean water contents.

## RESULTS AND DISCUSSION

## **Numerical Infiltration Patterns and Water Content Profiles**

A typical infiltration pattern is shown in Fig. 4–3. The global waterfront is irregular. Water advances more rapidly within the crack than in the micropore matrix, but water redistributes into the matrix all along the micropore walls. For the

T = 2600

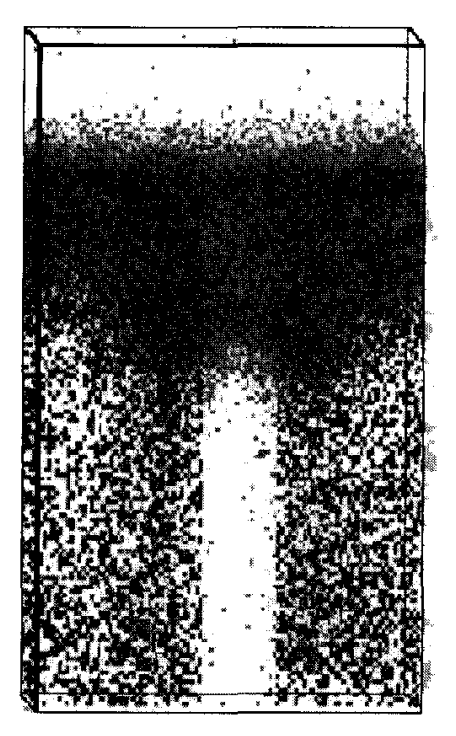


Fig. 4–3. Liquid infiltration into porous medium with a central crack at time T = 2600 for simulation 4. Solid, liquid and gas phases are represented in red, blue and white, respectively.

lowest input intensity (simulation 1), no macropore flow was observed, water infiltrates homogeneously into the micropore matrix, and the successive first layers gradually saturate. Preferential flow along the macropore occurred for the other three input intensities. Figures 4–4 and 4–5 show the comparative water profiles in time for four selected depths. Total, macropore and micropore water contents are represented in black, medium gray, and light gray, respectively. The vertical line indicates the time when input ceases at the surface.

Initially, just a water film pours along the macropore walls. It wets the macropore walls and infiltrates into the micropore matrix. Water enters progressively into the crack and eventually saturates it. The input lasted long enough to observe saturation of the upper layers of the macropore in the three last experiments. The higher the input intensity, the longer and deeper the macropore carries water. When input ceases, the macropore begins to drain, while the microporosity water content does not significantly change.

# Computation of the Flux Field

We calculated the flux vectors  $\mathbf{J}_i(z,t) = \theta_i(z,t)\mathbf{v}_i(z,t)$ , where  $\mathbf{v}$  is the mean flow velocity at time t and depth z, and the index i denote macropore or micropore, respectively. Figures 4–6 and 4–7 show the computed flux fields for one of the numerical experiments. During rainfall, infiltration is dominated by the macropore. Lateral infiltration into the matrix occurs as water advances within the macropore (see the direction of vectors in Fig. 4–6). As soon as the nearby walls are saturated,

they behave as impervious and the water flux in the macropore is vertical in the downward direction and lateral infiltration is observed only in the wetting front of the macropore. For simulations 2, 3 and 4, water availability at the surface was not a limiting factor. In these conditions the crack conducts all the liquid it can. When input ceases (Fig. 4–7) water redistributes within the matrix. The macropore empties progressively, and the mean macropore flow velocity slows down. Deep outflow due to macropore flow occurs mainly during rainfall and when input intensity is high enough (no macropore flow was observed for the lowest applied in-

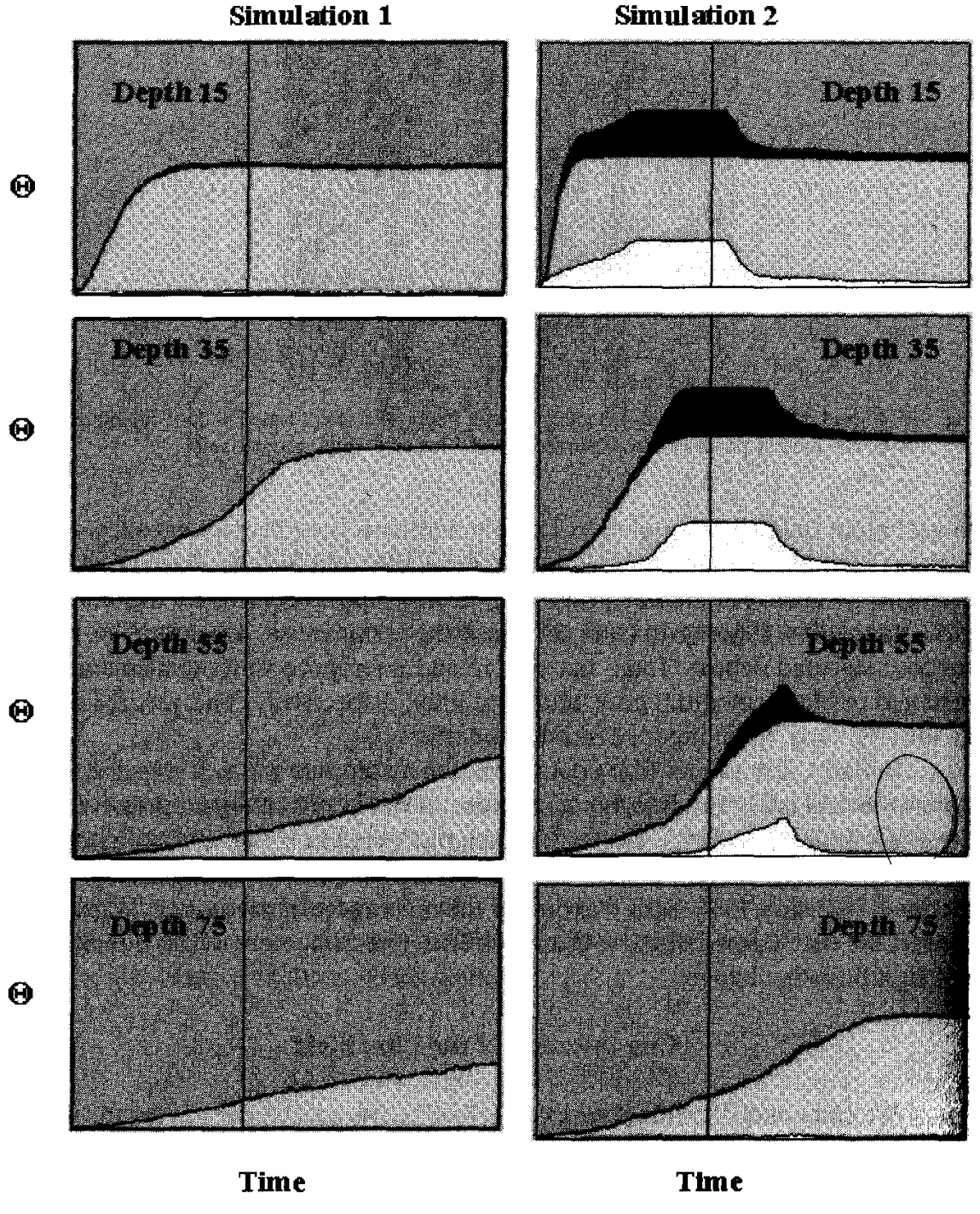
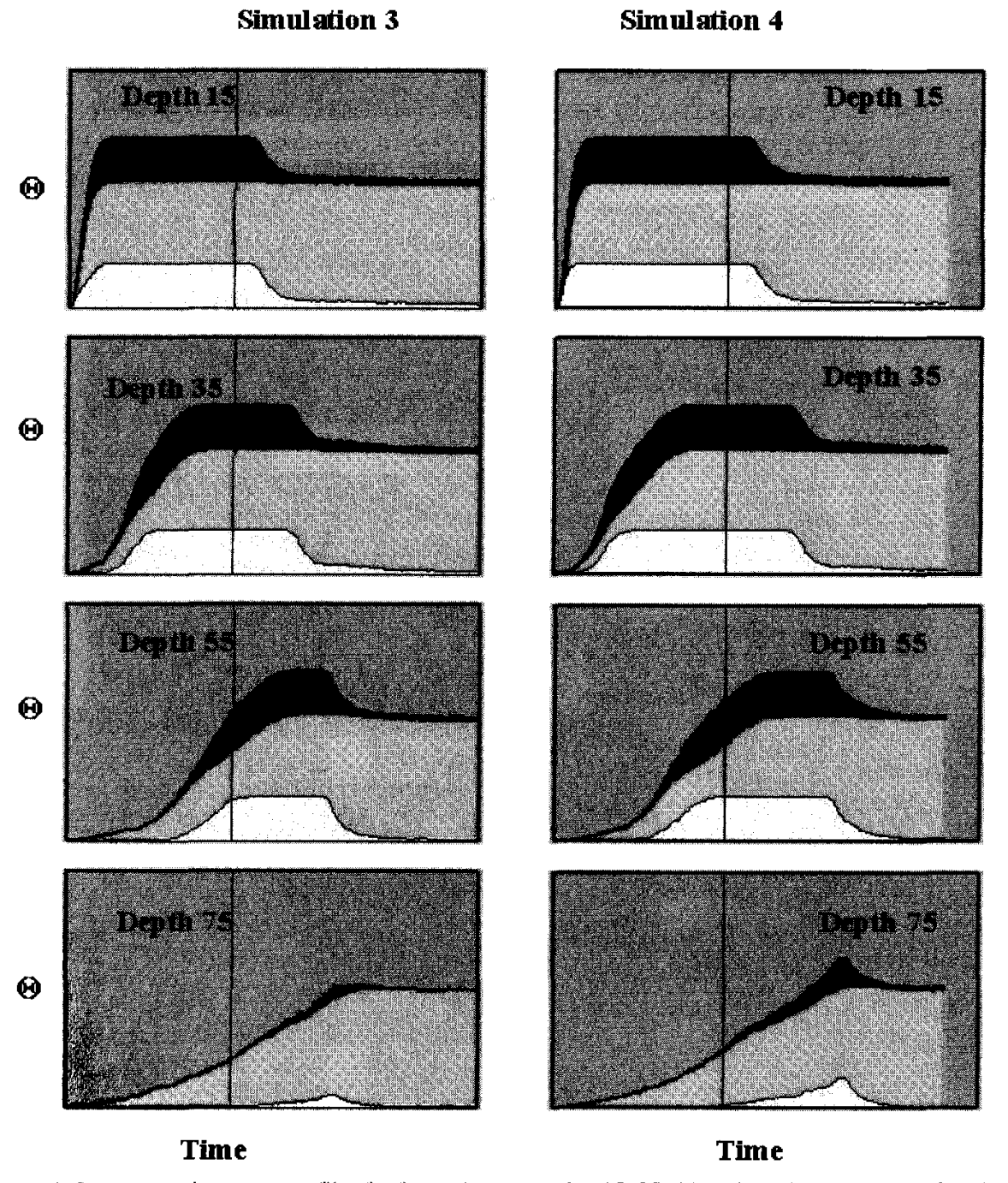


Fig. 4–4. Comparative water profiles for four selected depths (15, 35, 55, and 75) for simulations 1 and 2. Total, micropore and macropore water contents are represented in black, medium gray and light gray, respectively. The vertical ligne indicates the time when surface input ceases at  $T_{\rm k}$ .

tensity). More simulations at intermediate rainfall intensities are needed to determine the limit intensity originating macropore flow for this geometry.

# COMPARISON OF KINEMATIC WAVE AND LATTICE GAS SOLUTIONS

We want to see if a kinematic wave (KW) approximation fits with the numerical solutions  $\theta(z,t)$  obtained with the lattice-gas model. Figure 4–8 shows the



4. 5. Comparative water profiles for four selected depths (15, 35, 55, and 75) for simulations 3 and
 4. Total, micropore and macropore water content are represented in blue, green and yellow, respectively. Vertical ligne indicates the time when input ceases at the surface.

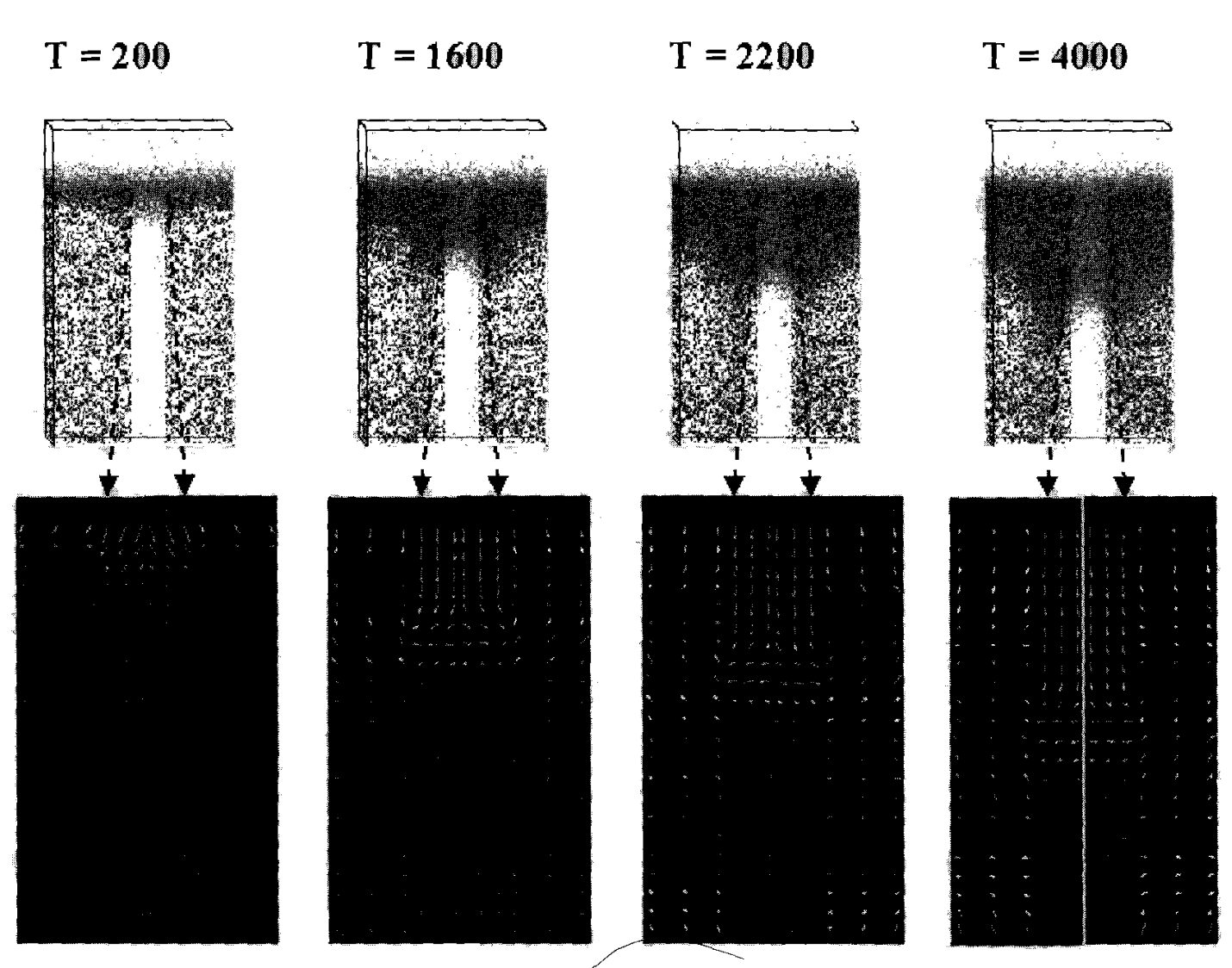


Fig. 4-6. Four infiltration stages and the corresponding liquid flux vector fields during rainfall (numerical simulation 4).

general form of the graphical solutions for  $\theta(z,t)$  obtained by the lattice gas method (Fig. 4–8a) and by analytically solving the kinematic Eq. [24] (Fig. 4–8b) for an input pulse at the surface of duration  $T_s$ . Note that if  $\theta(z,t)$  is the integral surface of the kinematic Eq. [24], the projection of this integral surface in the (z,t) plane are the characteristics of the partial differential equation. The same is valid for  $\mathbf{J}(z,t)$  if we use the  $\mathbf{J}$ -mode of Eq. [24].

We calculated the wetting (WC) and drainage front characteristics (DC) from the four sets of numerical data in J-mode. The points of the WC correspond to the path of the applied input flux signal in the (z, t) plane. The DC are calculated as the paths of the onset of the decay input signal in the same plane. The calculated curves are shown in Fig. 4–9 for the four numerical LG experiments (dots in the figure). No drainage characteristics exists for simulation 1, where no macropore flow occurred.

If these characteristics correspond to those of a shock wave they should be straight lines with slopes equal to the kinematic velocities as shown in Fig. 4–1. From the estimated LG characteristics we observe that a linear shock wave develops after

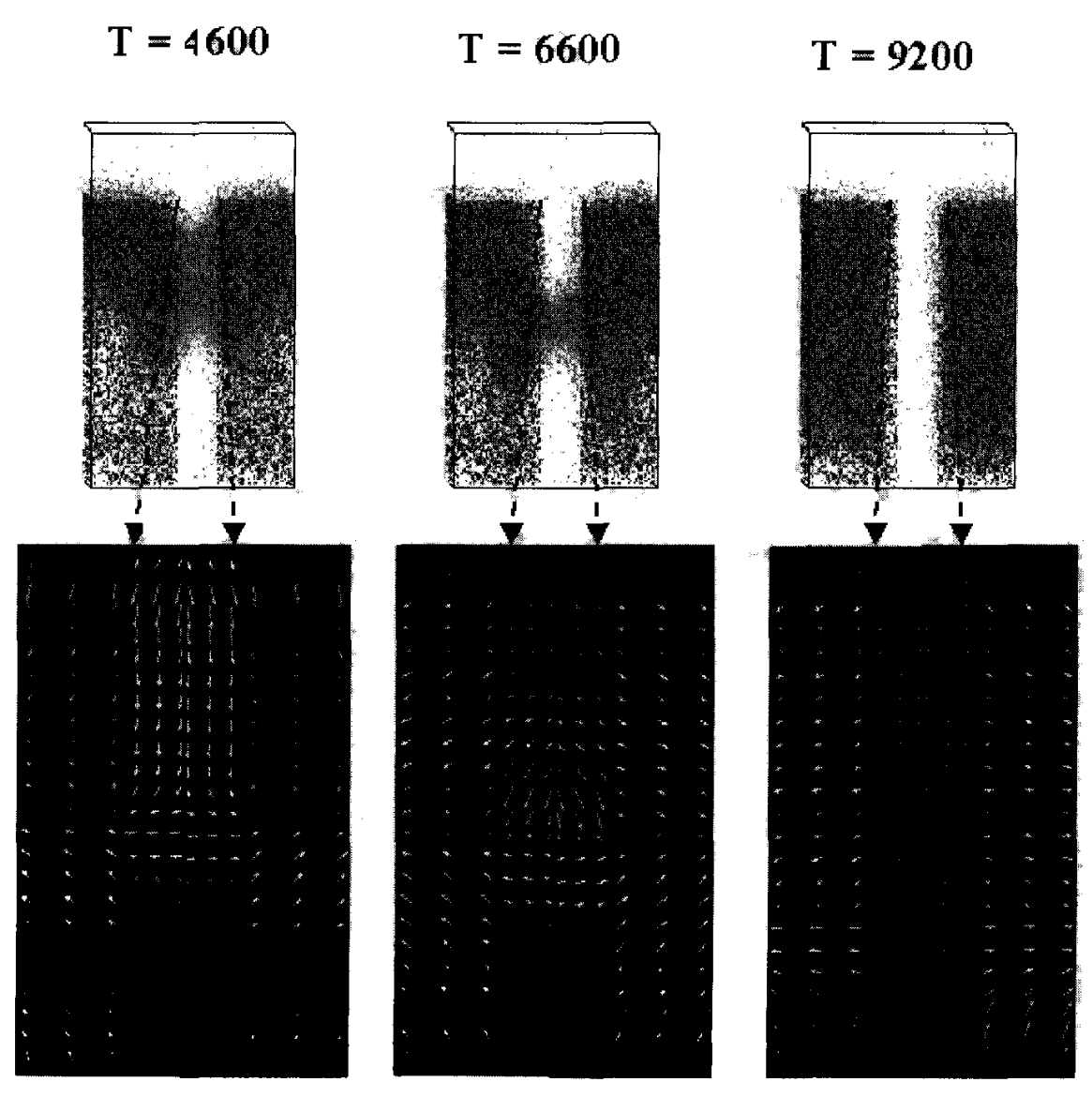


Fig. 4-7. Three infiltration stages after the cessation of surface input and their corresponding liquid flux vector fields (numerical simulation 4)

a time lag. This time increases inversely to input intensity. Capillary effects seem to dominate flow in the initial stages of infiltration and this effect is more marked for the lower intensities.

To calculate the velocities of the wetting and drainage signals, we fitted, when statistically significant, a linear model to LG data (Fig. 4–9). The fitted wetting characteristics are lines of slope  $c_{\rm w2} = 0.0082 \pm 0.0003$ ,  $c_{\rm w3} = 0.0093 \pm 0.0002$ ,  $c_{\rm w4} = 0.0109 \pm 0.0002$  for simulations 2, 3 and 4, respectively. The fitted LG drainage characteristics do not differ significantly and the estimated mean slope is  $c_{\rm d} = 0.0209 \pm 0.008$ . From the relation  $c_{\rm d} = ac_{\rm w}$  we can estimate the value of the coefficient a

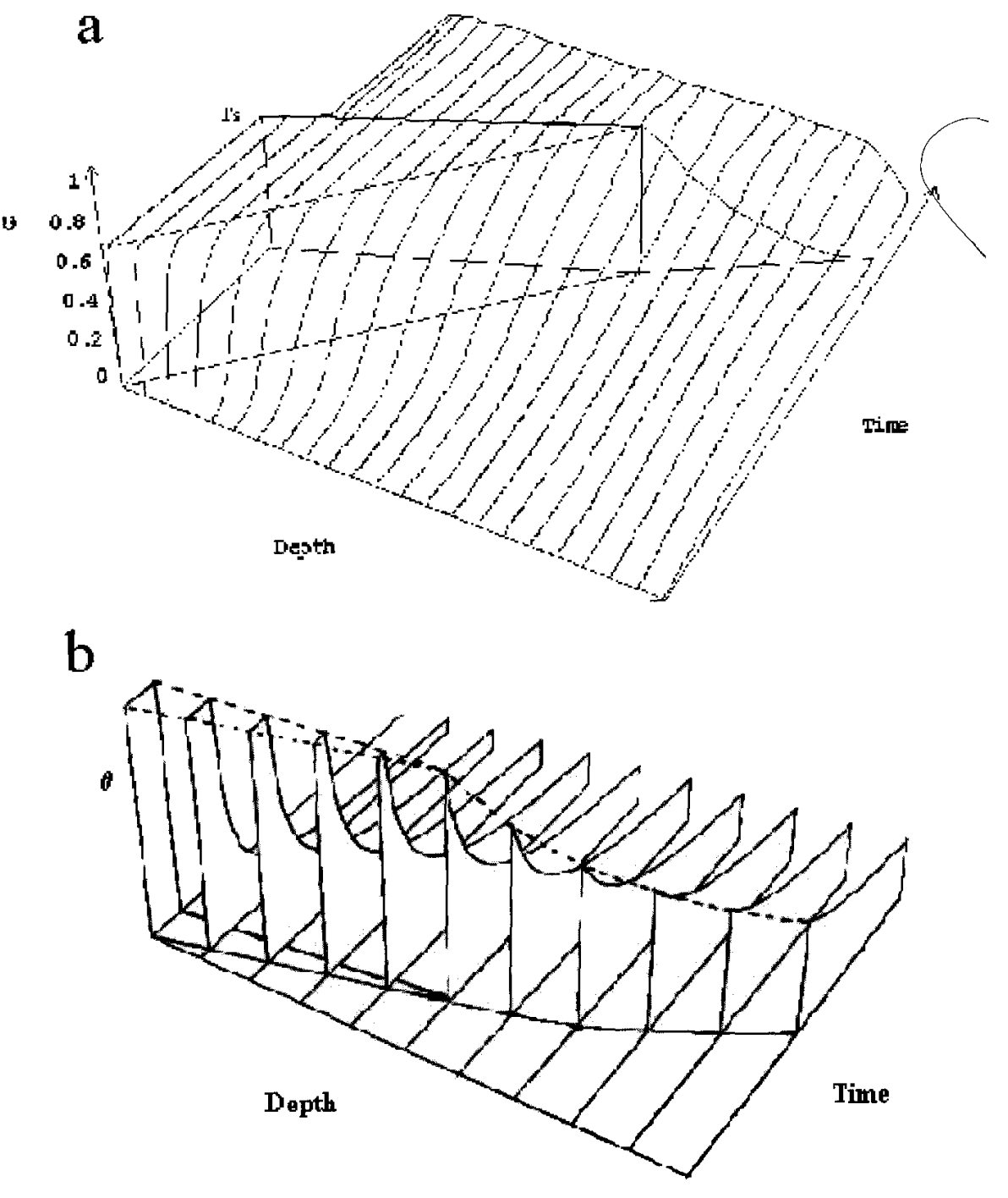


Fig. 4–8. Schematic form of the water content as a function of depth and time for a square pulse input: (a) LG solution, and (b) KW solution.

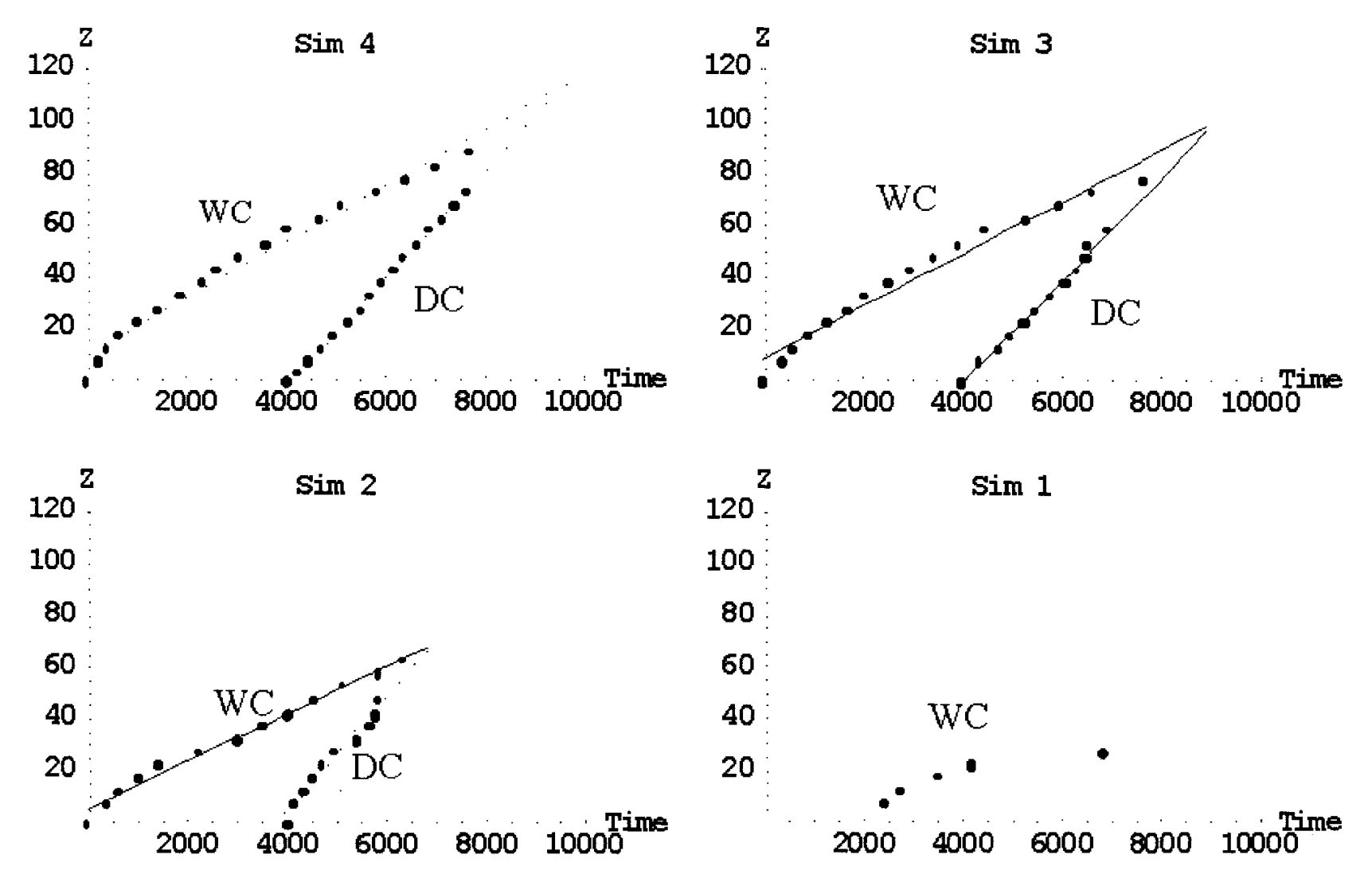


Fig. 4-9. Wetting and drainage front characteristics obtained from the LG numerical solutions for the four simulations [calculated values (dots) and linear model fit (full-ligne)].

for each numerical experiment. The estimated values are, 2.54, 2.25, and 1.92, respectively, for simulations 2, 3 and 4.

Using these values for a in Eq. [26] we estimated the water content profiles according to kinematic theory. The KW estimated water content profiles and LG data for two depths are presented in Fig. 4–10 for simulations 2, 3 and 4. The times of beginning of drainage are rather well predicted by the KW approach. The differences between the KW and LG draining curves are due to the fact that we have assumed that all of the water participates in the drainage process whereas in reality only macropore (i.e., mobile) water drains at this time scale. The KW approach better predicts the arrival times of the wetting front at the higher intensities and for the upper layers. The initial dominance of capillary effects and lateral infiltration from the macropore into the matrix result in a distortion of the mean waterfront, which gradually decreases its velocity. The kinematic approach does not consider

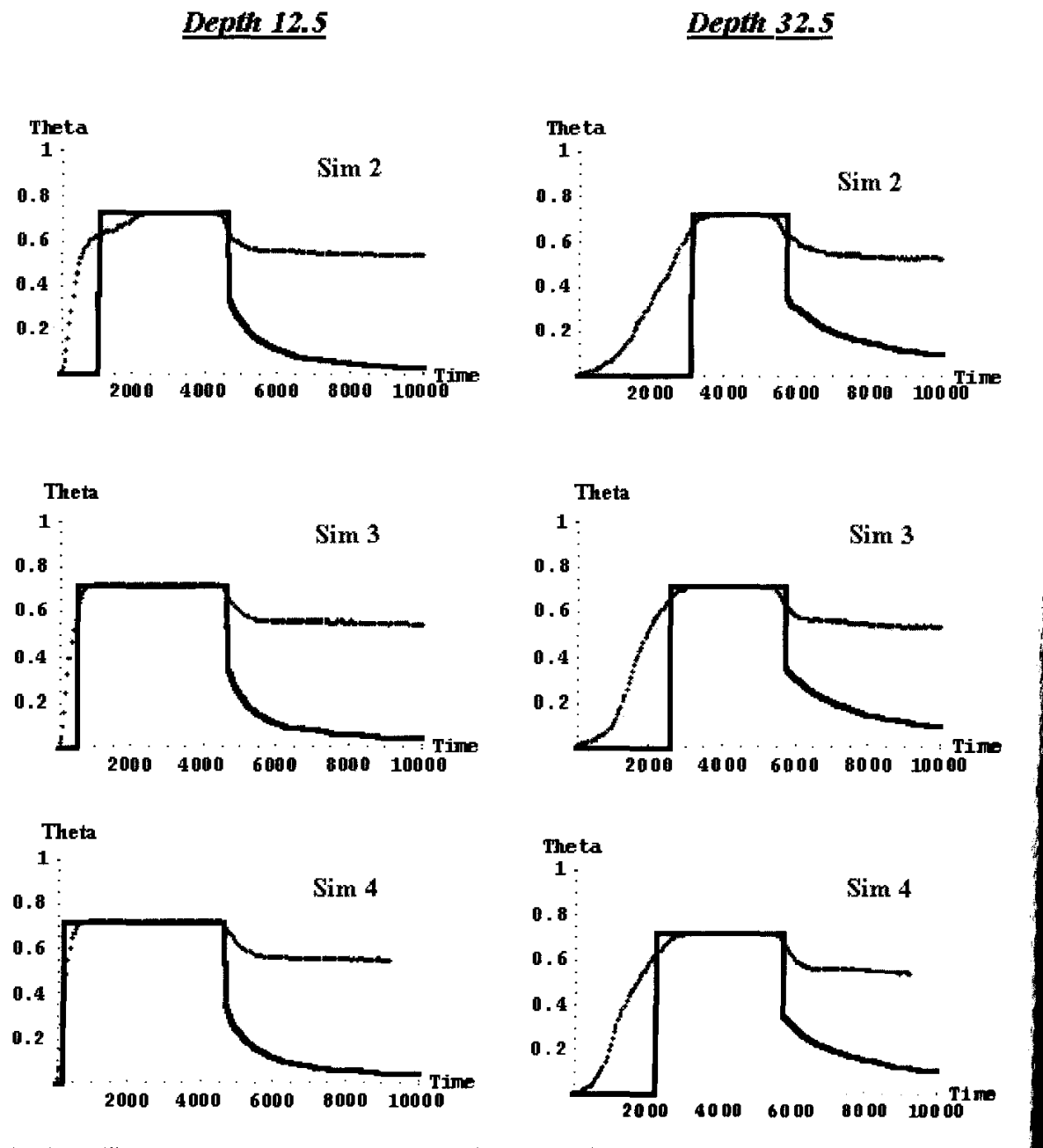


Fig. 4-10. Total water content at depths 12.5 and 32.5 [LG data (black) and KW prediction (blue)].

dissipation mechanisms. We hypothesize that the dispersive effects showed by the LG solution could be modeled by a kinematic dispersive approach. Our future research efforts will be oriented in this direction.

#### CONCLUSIONS

We have used a lattice-gas model to analyze preferential flow mechanisms in porous media. This numerical approach provides information that most experimental methods are presently unable to supply. The need for simple macroscopic models of preferential flow oriented us to test the kinematic wave approach. The comparison of the lattice gas solution with the kinematic approximation has shown the limitations of the latter approach and the possible ways of ameliorating it.

## REFERENCES

- Appert, C., and S. Zaleski. 1990. Lattice-gas with a liquid-gas transition. Phys. Rev. Lett. 64:1-4.
- Appert, C., and S. Zaleski. 1993. Dynamical liquid-gas transition. J. Phys. II (France) 3:309–337.
- Balasubramanian, K., F. Hayot, and W.F. Saam. 1987. Darcy's law from lattice-gas hydrodynamics. Phys. Rev. A 36:2248–2253.
- Beven, K., and P. Germann. 1981. Water flow in soil macropores. II: A combined flow model. J. Soil Sci. 32:15–29.
- Boon J., U. Frisch, and D. D'Humières. 1993. L'hydrodynamique modélisée sur réseau. La Recherche 24:391–399.
- Di Pietro, L. 1996. Application of a lattice gas numerical algorithm to modelling water transport in fractured porous media. Transp. Por. Media 22:307–325.
- Di Pietro, L. 1998. Strategies for describing preferential flow: The continuum approach and cellular automaton fluids. p. 437–453. *In* H.M. Selim and L. Ma (ed.) Physical non-equilibrium in soils, modelling and applications. Ann Arbor Press, MI.
- Di Pietro, L., and F. Lafolie. 1991. Water flow characterization and test of a kinematic wave model for macropore flow in a highly contrasted and irregular double porosity medium. J. Soil Sci. 42:551-563.
- Di Pietro, L., A. Melayah, and S. Zaleski. 1994. Modeling water infiltration in porous media by interacting lattice-gas cellular automata. Wat. Resour. Res. 30:2785–2792.
- Durner, W. 1994. Hydraulic conductivity estimation for soils with heterogeneous porous structure. Water Resour. Res. 30:211–223.
- Ene, H.I. 1990. Application of the homogeneization method to transport in porous media. p. 223–241. In J.H. Cushman (ed.) Dynamics of flow in hierarchical porous media. Acad. Press, London.
- Frisch, U., B. Hasslacher, and Y. Pommeau. 1986. Lattice-gas automata for the Navier-Stokes equation. Phys. Rev. Lett. 56:1505–1508.
- Frisch, U., D. d'Humieres, B. Hasslascher, P. Lallemand, Y. Pommeau, and J. Rivet. 1987. Lattice gas hydrodynamics in two and three dimensions. Complex Syst. 1:649–707.
- Garcia Sanchez L., L. Di Pietro, and P. Germann. 1996. Lattice-gas approach to surface runoff after rain. Eur. J. Soil Sci. 47:453–462.
- Germann, P. 1985. Kinematic wave approximation to infiltration and drainage into and from soil macropores. Trans. ASAE 28:745–749.
- Germann, P. 1990. Preferential flow and the generation of runoff. I: Boundary layer theory. Water Resour. Res. 26:3055–3063.
- Germann, P., and L. Di Pietro. 1996. When is porous media preferential? A hydromechanical perspective. Geoderma 74:1–21.
- Germann, P.F., and L. Di Pietro. 1999. Scales and dimensions of momentum dissipation during preferential flow in soils. Water Resour. Res. 35:1443--1454.
- Germann, P., L. Di Pietro, and V. Singh. 1997. Momentum of flow in soils assessed with TDR-moisture readings. Geoderma 80 153-168

- Hosang, J. 1993. Modelling preferential flow of water in soils—a two phase approach for field conditions. Geoderma 58:149–163.
- Jarvis, N.J. 1994. The MACRO model: Technical description and sample simulations. Rep. Diss. 19. Swed. Univ. Agric. Sci., Upsala.
- Lax, P.D. 1972. The formation and decay of shock waves. Am. Math. Monthly 79:227-241.
- Levy, T. 1988. Ecoulement d'un fluide dans un milieux poreux fissuré. C.R. Acad. Sci. Paris II 306;1413-1417.
- Lightill, M.J., and G.B. Whitman. 1955. On kinematic waves. I: Flood movement in long rivers. Proc. R. Soc. London A 229:281–316.
- Majda, A. 1984. Compressible fluid flow and systems of conservation laws in several space variables. Springer-Verlag, New York.
- Mdaghri, A. 1997. Transferts d'eau et de substances (bromides, chlorides et bactériographes) dans des milieux non saturés à porosité bimodale: Expérimentation et modélisation. Ph.D. diss. Bern Univ, Switzerland.
- Pot, V. 1994. Etude microscopique du transport et du changement de phase en milieux poreux par la méthode de gaz sur réseau. Thése de Doctorat, Université Pierre et Marie Curie, Paris VI, France.
- Raats, P.A.C. 1983. Implications of some analytical solutions for drainage of soil water. Agric. Water Manage. 6:191–175.
- Richards, L.A. 1931. Capillary conduction of liquids in porous medium. Physics 1:318-333.
- Rothman, D.H. 1988. Cellular-automaton fluids: A model for flow in porous media. Geophysics 53:509–518.
- Rothman, D.H., and J.M. Keller. 1989. Immiscible cellular-automaton fluids. J. Stat. Phys. 52:1119–1127.
- Sisson, J.B., A.H. Fergurson, and M.Th. Van Genuchten. 1980. Simple method for predicting drainage from field plots. Soil Sci. Soc. Am. J. 44:1147–1152.
- Smith, R.E. 1983. Approximate soil water movement by kinematic characteristics. Soil Sci. Soc. Am. J. 47:3–8.
- Sommers, J.A., and P.C. Rem. 1992. Obtaining numerical results from the 3D FCHC-lattice gas. p. 59–78. In T.M.M. Verheggen (ed.) Workshop for numerical methods for the simulation of multi-phase flow, Amsterdam. 30 May–1 June 1990. Springer, Berlin.
- Wolfram, S. 1984. Cellular automata as models of complexity. Nature (London) 311:419-424.
- Wolfram, S. 1986. Cellular automaton fluids 1: Basic theory. J. Stat. Phys. 45(3/4):471-526.

## Tracer Transport in a Soil Column for Sine Wave Loading

#### Donald Dean Adrian and Senda Ozkan

Louisiana State University Baton Rouge, Louisiana

#### Akram N. Alshawabkeh

Northeastern University Boston, Massachusetts

Tracer transport modeling in a soil column involves developing and solving the governing equation subject to appropriate initial and boundary conditions. The major processes affecting the unsteady state tracer concentration are convection, dispersion, sorption and decay. A periodic loading function that varies as a sine or cosine curve (sinusoid) enlarges the number of variations of tracer input to a soil column for which there are analytical solutions. However, the development of an analytical solution of the governing equation for the appropriate boundary conditions is complicated. The governing equation is solved by applying the Laplace transform and the convolution integral. The integral is evaluated by introducing complex variables, so that the analytical solution can be completed. The resulting equation is a new analytical solution for quasi steady-state or unsteady state sinusoidally varying tracer loading. Discussion of applications tells how the analytical solution may be useful in conducting tracer transport experiments to measure soil and tracer transport parameters.

#### INTRODUCTION

Tracer modeling in a soil column could well be dated from the pioneering work of Lapidus and Amundson (1952) who developed the relationship for the unsteady state transport of a tracer in a column subject to convection, dispersion, and linear equilibrium adsorption. They included the convective (or advective) term in their tracer transport model that marked a departure from viewing the soil column and the water it contained as a solid with tracers transported by diffusion. For example, earlier studies of progressive waves in confined and unconfined aquifers due to cyclical changes in river stage provided insight into solution of diffusion-type equations subject to sinusoidally varying boundary conditions (Werner & Noren,

1951; Ferris, 1952; Cooper & Rorabaugh, 1963). Although results of these analytical solutions were applied to infer aquifer properties based on measurements of river stage and water levels in observation wells, they had little application to tracer transport in soils as the convective term is not a part of the model. The usefulness of the Lapidus and Amundson (1952) model encouraged additional analytical solutions applicable to tracer transport in soils, with solutions being developed for impulse loadings, step changes in concentration, and exponential changes in concentration. These analytical solutions for simple initial and boundary conditions were developed by a number of authors and were tabulated in van Genuchten and Alves (1982). A review of inorganic solute transport in soil columns with nonequilibrium reaction was presented by Jardine (1991), while Harmon et al. (1989) and Brusseau and Rao (1991) reviewed nonequilibrium transport of organic solutes. Several studies of contaminant transport in rivers provide insight into soil column studies because of the similarity of governing differential equations although in a river the porosity and retardation coefficient are unity (Li, 1972; Thomann, 1974, p. 140; Thomann & Mueller, 1987). Holley and Harleman (1965), Harleman et al. (1966), and Holley (1968) published solutions for a time series of slug-type releases of an organic waste into a river, an approach that left the solution for the concentration in the form of an integral that usually had to be integrated numerically. Likewise, Bennett (1971) prepared a convolution integral solution for a time series of waste discharges to a river, but numerical evaluation of the integral was a drawback to this approach. Yu et al. (1991) introduced a method of solution in which superposition of analytical solutions described the biochemical oxygen demand (BOD) in a river due to a time series of inputs while a similar approach for a tracer in a soil column was presented by Ge and Lu (1996).

Cyclical boundary conditions represented by sinusoidal loading functions may result in some confusion when the terms steady-state, quasi steady-state, and unsteady state are used to describe the concentration profile. Steady-state, of course, means that there is no change in the concentration profile with time. Steady-state concentration profiles appear to involve a contradiction in terms when applied to tracer transport in a soil column with a cyclical boundary condition. Unsteady state appears to be the alternative if a concentration profile is not steady-state. However, in the engineering literature the term "quasi steady-state" has been used to describe the unsteady state concentration profile as time goes to infinity. In other words, the quasi steady-state is reached with a cyclical boundary condition when the concentration profile replicates itself within an acceptable error tolerance with the frequency of the cyclical loading. A characteristic of the quasi steady-state condition is that it is achieved when the initial condition no longer influences the concentration profile. Obviously, the quasi steady-state concentration profile propagates with time inward from the cyclical boundary. Thus, the concentration profile in a soil column may be described as being quasi steady-state for a certain distance from the boundary into the soil column, while for a larger distance from the boundary the concentration profile is unsteady state. Yet, further reflection suggests that a long column that has been subject to a cyclic boundary condition for a long, but not infinite, period of time may be divided into three zones: for some distance inward from the boundary the quasi steady-state concentration profile prevails, further from the boundary the concentration profile may appear to be steady state, then still further

from the boundary the influence of the initial condition prevails so that an unsteady-state concentration profile provides a transition from the apparent steady-state value to the initial condition value. Normally, the quasi steady-state and the steady-state concentration profiles would not be separated, but would be considered together in a model. Yu et al. (1991) used the term "memory time" to provide a practical measure of when the quasi steady-state condition had been attained at a certain location. They also used the term "memory length" to measure the distance from the boundary for which the quasi steady-state concentration profile was applicable at a certain time. Logan and Zlotnik (1995) provided an asymptotic estimate for the time required for transients to decay. Their estimate is of the order  $O(dl/\sqrt{t})$  where d is a constant depending on the distance from the inlet boundary. Oppenheimer et al. (1999) recently proved that a periodic loading function, or boundary condition, admits a unique asymptotically attracting solution. In other words, the unsteady state solution will approach with time the quasi steady-state solution.

Li (1972a,b) developed a perturbation solution and a method of characteristics solution to describe the concentration of BOD in a river for which the loading function followed a sine wave. For the perturbation solution advective transport in a river was considered much larger than dispersive transport, an assumption that was similar to one employed by Logan et al. (1996) for flow in a fractured porous medium subject to a periodic boundary condition. Adrian et al. (1994) and Adrian and Alshawabkeh (1997) developed quasi steady-state solutions for a BOD loading to a river in which the input function varied as a sine or a cosine wave. The solutions were applicable after the river forgot its initial condition. An exact analytical unsteady state solution was published by Alshawabkeh and Adrian (1997) who applied the Laplace transform method to the problem of BOD transport and decay in a river after the transport equations had been expressed in terms of complex functions. A noteworthy feature of their method of solution was that the inverse Laplace transforms were not based on the convolution integral but they were found from inverse Laplace transforms of complex functions. The dispersion coefficient for a river is taken as a constant, while some recent studies of dispersion in a soil have explored expressing it as a function of distance (Logan & Zlotnik, 1996). There are other mathematical approaches that can be employed to develop analytical solutions to the boundary value problem that describes tracer transport in a soil column subject to a cyclic boundary condition. The approaches differ depending upon whether the problem is formulated as a quasi steady-state problem or as an unsteadystate problem. A partial list of approaches includes: applying Green's functions (Beck et al., 1992), formulating a solution based on applying Duhammel's principle (Tikhonov & Samarskii, 1963; Özisik, 1968), using the principle of superposition (Luikov, 1968, p. 660–668), and obtaining the solution by using integral transforms (Sneddon, 1961).

Developing concentration profiles in a soil column for cyclical boundary loading functions is important for several reasons. One reason is that the solution increases the repertoire of mathematical models that are available for which someone may find a use. A second reason is that the solution can be used by those who set up experiments to estimate parameters such as the dispersion coefficient. Another reason is that analytical solutions to tracer transport equations are desired because they can be used easily for some simple flow cases to quickly estimate what

may take place in an experiment. A final justification for analytical solutions is that they can be applied for testing numerical models.

The objective of this study is to develop an analytical model for a soil column's response to a sinusoidally varying tracer loading function by applying the familiar Laplace transform method in which the convolution integral is used to obtain the inverse transformation. The solution methodology will use Laplace transforms and their inverses that are available in most introductory texts on Laplace transforms to develop both the quasi steady-state and unsteady-state solutions. Applications of the solutions will be listed and explained.

#### MATHEMATICAL DERIVATION

Consider a soil column for which the solute is uniformly distributed through any cross-section so that a one-dimensional model is applicable. The governing equation for solute transport, obtained by mass balance, is

$$\frac{\partial C}{\partial t} + U \frac{\partial C}{\partial x} = E \frac{\partial^2 C}{\partial x^2} - K_1 C - \frac{\rho_b}{\theta} \frac{\partial q}{\partial t}$$
 [1]

where  $K_1$  is the first-order transformation constant  $(T^{-1})$ ; C is the solute concentration (mol L<sup>-3</sup>); t is time (T); U is the convective (or advective) or travel time (Darcy velocity/volumetric water content) velocity  $(LT^{-1})$ ; x is the distance from the inlet boundary in the flow direction (L); E is the apparent diffusion coefficient, usually called the dispersion coefficient,  $(L^2T^{-1})$ ;  $\rho_b$  is the soil bulk density  $(M L^{-3})$ ;  $\theta$  is porosity; and q is the adsorbed solute concentration (mol M<sup>-1</sup>). For linear equilibrium adsorption the retardation coefficient,  $R' = 1 + \rho_b K_d/\theta$ , transforms the transport equation to

$$\frac{\partial C}{\partial t} + u \frac{\partial C}{\partial x} = D \frac{\partial^2 C}{\partial x^2} - k_1 C$$
 [2]

where  $k_1$  is the modified first-order decay constant,  $K_1/R$ ,  $(T^{-1})$ ; C is the tracer concentration (mol L<sup>-3</sup>); t is time (T); u is the modified travel time velocity, U/R,  $(LT^{-1})$ ; x is the distance from the upstream boundary in the flow direction (L); and D is the modified apparent diffusion or dispersion coefficient, E/R,  $(L^2T^{-1})$ .

#### **Solution for Unsteady-State Case**

The initial and boundary conditions for a sinusoidal loading of tracer are

$$C\left( x,0\right) =0 \tag{3}$$

$$C(0,t) = C_1 + C_0 \sin(\omega t)$$
 [4]

$$\lim_{x \to \infty} C(x,t) \to 0 \tag{5}$$

where  $C_1$  is the average tracer concentration (mol L<sup>-3</sup>);  $C_0$  is the amplitude of the variation from the average tracer concentration (mol L<sup>-3</sup>); and  $\omega$  is the frequency  $(T^{-1})$ . To make the problem realistic and without loss of generality,  $C_0$  and  $C_1$  are positive or zero with the constraint that  $C_1 \ge C_0$  while D is positive. In the following solution that uses superposition  $C_0$  or  $C_1$  may be set equal to zero. Yet, when the final solution is obtained by superposing the individual solutions  $C_1 \ge C_0$ , while U and U are positive or zero. When U is zero, the solution is well known (van Genuchten & Alves, 1982)

$$C(x,t) = \frac{C_1}{2} \exp\left[\frac{ux}{2D} - \sqrt{\frac{\lambda}{D}} x\right] erfc \left[\frac{x}{\sqrt{4Dt}} - \sqrt{\lambda t}\right] + \frac{C_1}{2} \exp\left[\frac{ux}{2D} + \sqrt{\frac{\lambda}{D}} x\right] erfc \left[\frac{x}{\sqrt{4Dt}} + \sqrt{\lambda t}\right]$$
[6]

where  $\lambda = u^2/4D + k_1$ . We will now look for the solution to the case  $C_1 = 0$  and  $C_0 \neq 0$  that is not solved in van Genuchten and Alves (1982). It has been discussed but not solved by Thomann (1974, p. 140) and an early numerical solution was presented by Dresnack and Dobbins (1968). Adrian et al. (1994) and Adrian and Alshawabkeh (1997) presented solutions for the quasi steady-state case. The following transform of the dependent variable (Kirkham & Powers, 1972, p. 526–527)

$$C(x,t) = Y(x,t) \exp \left[\frac{ux}{2D} - \frac{u^2t}{4D} - k_1t\right]$$
 [7]

reduces the problem of Eq. [2] to

$$\frac{\partial Y}{\partial t} = D \frac{\partial^2 Y}{\partial x^2}$$
 [8]

subject to

$$Y(x,0) = 0 ag{9}$$

$$Y(0, t) = C_0 e^{\lambda t} \sin(\omega t)$$
 [10]

$$\lim_{x \to \infty} Y(x, t) \to 0$$

The solution to Eq. [8] along with conditions [9] through [11] may be obtained by the Laplace transform method with convolution (Carslaw & Jaeger, 1963) or a solution for a less restrictive initial condition, Eq. [9], may be obtained by following the methods presented by Logan and Zlotnik (1995). Following the methods of Scott (1955), Carslaw and Jaeger (1959), and Oberhettinger and Badii (1973) the Laplace transform solution with convolution becomes

$$Y(x,t) = \frac{C_0 x \sin(\omega \tau) e^{\lambda t}}{\sqrt{4\pi D}} \int_0^t \frac{\cos(\omega t) \exp\left[-\left(\lambda \tau + \frac{x^2}{4D\tau}\right)\right]}{\tau^{3/2}} d\tau$$

$$-\frac{C_0 x \cos(\omega \tau) e^{\lambda t}}{\sqrt{4\pi D}} \int_0^t \frac{\sin(\omega t) \exp\left[-\left(\lambda \tau + \frac{x^2}{4D\tau}\right)\right]}{\tau^{3/2}} d\tau$$
[[12]

where  $\tau$  is a dummy variable of integration.

The integrals in Eq. [12] are not tabulated in widely used mathematical references (Petit Bois, 1961, Abramowitz & Stegun, 1965; Gradshteyn & Ryzhik, 1980, p. 128–129). They appear to present an insurmountable difficulty to solution of the problem of describing the tracer concentration in a soil column due to a sinusoidal loading boundary concentration by applying the Laplace transform method with the readily applied convolution rule.

We now turn to an alternative to direct integration of the two integrals by noting that the argument of the integrals differs only by a  $\cos(\omega \tau)$  or  $\sin(\omega \tau)$ . This suggests that the Euler equation for the exponential with a complex argument (Franklin, 1958, p. 52) can combine the two integrals into a single integral. Thus, we will examine the following integral where  $i = \sqrt{-1}$ , a complex number,

$$I_{-3/2,t} = \int_0^t \frac{\exp(i\omega \tau) \exp\left[-\left(\lambda \tau + \frac{x^2}{4D\tau}\right)\right]}{\tau^{3/2}} d\tau$$
 [13]

that can be expressed as

$$I_{-3/2,t} = \int_0^t \frac{\exp\left[-\left([\lambda - i\omega]\tau + \frac{x^2}{4D\tau}\right)\right]}{\tau^{3/2}} d\tau.$$
 [14]

This integral has been evaluated by Horenstein (1945) as referenced by Turner (1972, p. 196–200) to result in

$$I_{-3/2,t} = \frac{\sqrt{\pi}}{a} \cosh(2ab) + \frac{\sqrt{\pi}}{2a} f(t)$$
 [15]

where

 $f(t) = \exp(-2 ab)[erf(bt^{1/2} - at^{-1/2})]$ 

$$-\exp(2ab)[erf(bt^{1/2} + at^{-1/2})]$$
 [16]  
$$b^2 = \lambda - i \omega$$
 [17]

and

$$b^2 = \lambda - i \, \omega \tag{17}$$

and

$$a^2 = (x^2/4D)$$
 [18]

Turner (1972, p. 196–200) also states a result that will be used later by noting that when  $t \rightarrow \infty$ 

$$I_{-3/2,\infty} = (\sqrt{\pi/a}) \exp(-2ab)$$
 [19]

With these results Eq. [12] can be rewritten as

$$Y(x,t) = \frac{C_0 x \sin(\omega t)e^{\lambda t}}{\sqrt{4\pi D}} Re (I_{-3/2,t})$$

$$- \frac{C_0 x \cos(\omega t)e^{\lambda t}}{\sqrt{4\pi D}} Im (I_{-3/2,t})$$
[20]

where the notation  $Re(L_{3/2},t)$  is read "the real part of  $I_{-3/2},t$ " and  $Im(I_{-3/2},t)$  is read "the imaginary part of  $I_{-3/2},t$ ". Then Eq. [7] and [20] are combined to provide the value of C(x,t) for the case  $C_1 = 0$  and  $C_0 \neq 0$ . This result is added to Eq. [6] to give the solution to the original problem stated in Eq. [2] to [5]

$$C(x,t) = \frac{C_1}{2} \exp\left[\frac{ux}{2D} - \sqrt{\frac{\lambda}{D}} x\right] erfc \left[\frac{x}{\sqrt{4Dt}} - \sqrt{\lambda t}\right]$$

$$+ \frac{C_1}{2} \exp\left[\frac{ux}{2D} + \sqrt{\frac{\lambda}{D}} x\right] erfc \left[\frac{x}{\sqrt{4Dt}} + \sqrt{\lambda t}\right]$$

$$+ \frac{C_0 x \exp(ux/2D)}{\sqrt{4\pi D}} \left\{\sin(\omega t) Re\left(I_{-3/2,t}\right) - \cos(\omega t) Im\left(I_{-3/2,t}\right)\right\}$$
[21]

The formal solution to the problem of describing the unsteady-state concentration distribution in a soil column has now been completed. Equation [21] can be used directly for computations using computers that have the software to evaluate the real and complex parts of a complex function such as  $I_{-3/2,t}$ . If such software is not available the real and imaginary parts of  $I_{-3/2,t}$  are presented in Appendix 2, in terms of elementary functions that do not involve complex variables, as Eq. [A24] and [A25], respectively.

#### Solution for Quasi Steady-State Case

While Eq. [21] is applicable for any time, it is useful to have available the solution to Eq. [2] to [5] for the quasi steady-state case. The quasi steady-state solution is obtained by letting  $t \to \infty$  in Eq. [21]. The result is

$$C(x,t) = C_1 \exp\left[\frac{ux}{2D} - \sqrt{\frac{\lambda}{D}} x\right] + \frac{C_0 x \exp(ux/2D)}{\sqrt{4\pi D}} \left\{\sin(\omega t) \operatorname{Re}\left(I_{-3/2,\infty}\right) - \cos(\omega t) \operatorname{Im}\left(I_{-3/2,\infty}\right)\right\}$$
[22]

where  $I_{-3/2,\infty}$  was presented in Eq. [19]. Equation [22] can be used directly for computations using computers with software to evaluate the real and complex parts of a complex function, such as  $I_{-3/2,\infty}$ . The steps that show that the function  $I_{-3/2,\infty}$  can be expressed in terms of elementary functions that do not involve complex variables are shown next.

Equation [19], the function  $I_{-3/2,\infty}$ , must be divided into its real and imaginary parts as

$$I_{-3/2,\infty} = \frac{2\sqrt{\pi D}}{x} \exp\left[-\frac{x}{\sqrt{D}} (\lambda - i\omega)^{1/2}\right].$$
 [23]

The term  $(\lambda - i\omega)$  is expressed in an alternative form for complex numbers (Churchill, 1958) as  $r \exp(i\theta)$  where

$$r = (\lambda^2 + \omega^2)^{1/2} \tag{24}$$

and

$$\theta = \arctan\left(-\frac{\omega}{\lambda}\right)$$
 [25]

with the result that Eq. [23] becomes

$$I_{-3/2,\infty} = \frac{2\sqrt{\pi D}}{x} \exp\left\{-\sqrt{\frac{r}{D}} x \left[\cos\left(\frac{\theta}{2}\right) + i \sin\left(\frac{\theta}{2}\right)\right]\right\}.$$
 [26]

Equation [26] is simplified by applying Euler's rule, then separating the real and imaginary parts, so Eq. [22] becomes the solution for the quasi steady-state case

$$C(x,t) = C_1 \exp\left[\left(\frac{u}{2D} - \sqrt{\frac{\lambda}{D}}\right)x\right] + C_0 \exp\left\{\left[\frac{u}{2D} - \sqrt{\frac{r}{D}}\cos\left(\frac{\theta}{2}\right)\right]x\right\} \sin\left[\omega t + \sqrt{\frac{r}{D}}x\sin\left(\frac{\theta}{2}\right)\right]$$
 [27]

after applying the law of sine addition.

#### **ILLUSTRATIVE EXAMPLES**

### Effect of Time, Loading Frequency, and Dispersion on Solute Distribution

Three figures of solute transport in a soil column will be discussed to contrast unsteady-state and quasi steady-state behavior, to illustrate the effect of loading frequency on solute distribution in a soil column, and to show the effect of the magnitude of the dispersion coefficient on decreasing the magnitude of the ampli-

tude of concentration fluctuations with distance from the inlet. While the equations developed in this manuscript have been for a column of infinite length, any real column will have a finite length. The figures can be interpreted as showing the concentration distribution of tracer in the first 500 cm of a longer column, but there may be some deviation in behavior of a tracer near the outlet of a finite length column.

Figure 5–1 shows the behavior of both the quasi steady-state solution, Eq. [27], for t = 100 d, and the unsteady-state solution, Eq. [21], for t = 1, 10, 20 and 100 d. Equations [A24] and [A25] have been incorporated into Eq. [21] to develop the concentration curves. The values of the parameters are presented on Fig. 5–1, except  $\omega = 1/24 \, h^{-1}$  and R = 1. For t = 100 d, the quasi steady-state solution, Eq. [27], gives the same results as are given by Eq. [21], the unsteady-state solution. Obviously, 100 d is a long enough time for the unsteady-state effects to disappear from the 500 cm length of column in Fig. 5–1. Dispersion acts to reduce the height of the peaks and fill in the valleys of the concentration vs. distance curve. Although the sinusoidal fluctuations in concentration amplitude are dampened by dispersion, they are still visible after the solute travels 500 cm.

Figure 5–2 shows the effect of frequency on the concentration distribution. All three curves are for t = 100 d, which is the quasi steady-state case for a 500-cm long column. A low frequency of concentration change,  $\omega = 1/48 \, h^{-1}$ , is attenuated by dispersion, but propagates with only a small change in shape. By contrast, the highest frequency concentration loading with  $\omega = 1/12 \, h^{-1}$  approaches a quasi

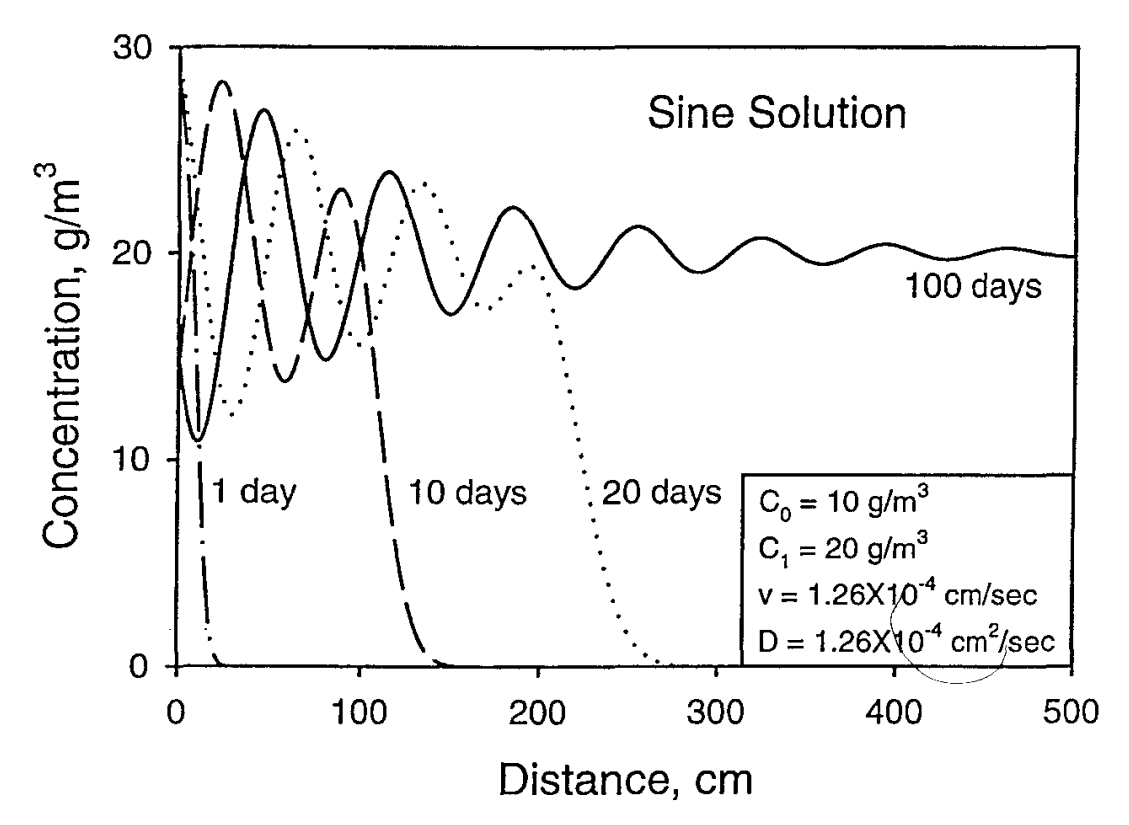


Fig. 5–1. Concentration tracer distribution in a soil column for four different sinusoidally varying tracer loading concentrations at the column inlet. Unsteady state tracer distribution curves are shown for t = 1, 10, 20 and  $100 \, d$ , while a quasi steady-state tracer distribution curve is shown for  $t = 100 \, d$ , where it is noted it is identical to the unsteady state curve for  $t = 100 \, d$ . The retardation coefficient, R = 1, and the sinusoidal loading frequency,  $t = 1/24 \, h^{-1}$ , for all figures.

steady-state concentration of 20 g m<sup>-3</sup> within a distance of about 200 cm. Figure 5–2 shows that attenuation of the amplitude of a peak in concentration is a nonlinear function of frequency and distance.

Figure 5–2 is of interest in planning experiments where the sinusoidal loading of a tracer might be used to calculate the dispersion coefficient. If the loading frequency is selected too large then the concentration may become dampened so quickly that at the column outlet one will have no concentration change with time information with which to calculate the dispersion coefficient. On the other hand, selecting a low frequency of oscillation of tracer loading will insure a larger contrast in the concentration between the peak and an adjacent valley, but there will be fewer tracer cycles observed at the outlet in a given observation time. One of the advantages of the sinusoidal loading of a tracer to a column is the opportunity to observe a sequence of tracer transport "experiments". In effect, a tracer transport experiment is repeated each period of the loading function. The period of a loading cycle is given by  $T = 1/\omega$ , and the wave length is  $L = \mu T$ . These relationships between the frequency, the period and the wave length can be useful in planning experiments. By contrast, if a conventional tracer transport experiment is conducted using a slug-type input of a step change in tracer concentration, one does not measure the replications of output data for increasing the precision of parameter estimates.

Figure 5–3 shows the effect of the dispersion coefficient on the tracer distribution in a soil column. Of course, the figure shows a 10-fold increase in dispersion coefficient quickly dampens out fluctuations in the concentration distribution curve leading to a near steady-state concentration profile for x > 200 cm. By con-

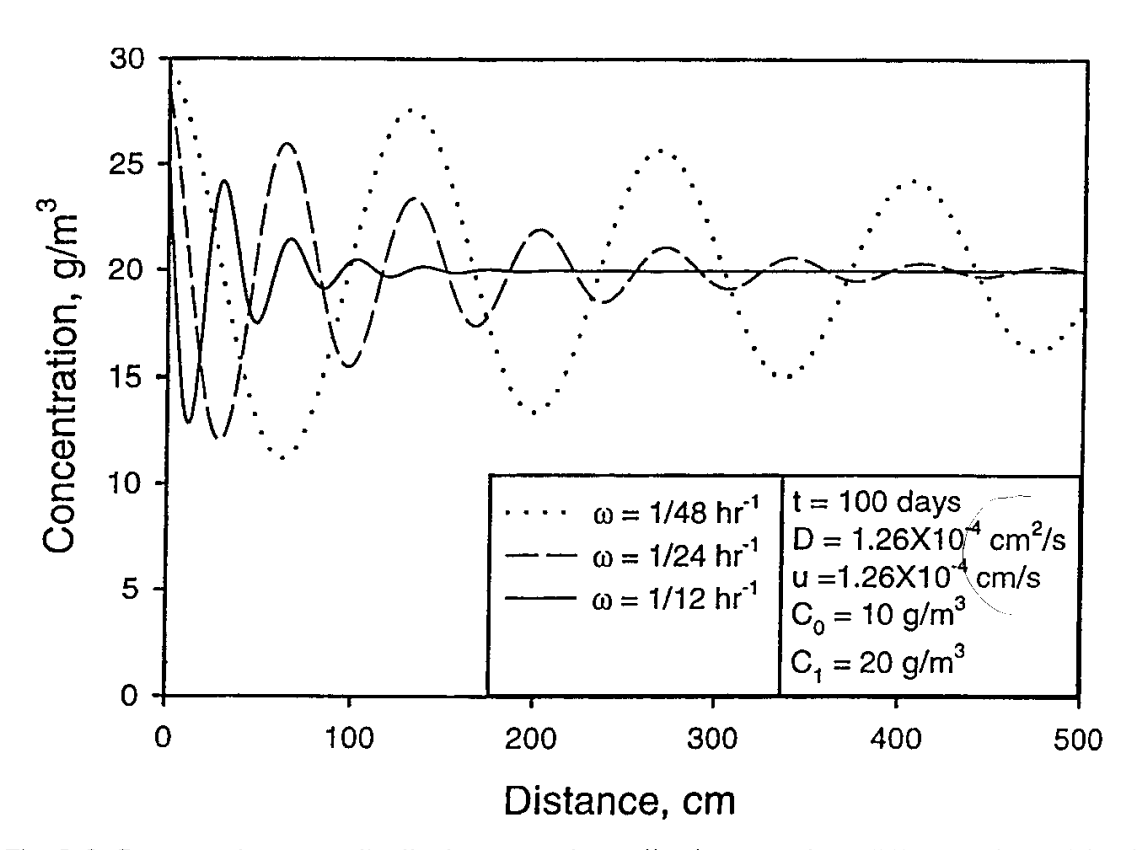


Fig. 5–2. Concentration tracer distribution curves in a soil column for three different values of the sinusoidal tracer loading frequency.

trast, a 10-fold lower dispersion coefficient sharply decreases the dampening effect. The dispersion coefficient is not under the control of the experimenter except indirectly through packing and selection of the advective velocity. This figure emphasizes the importance of carrying out preliminary experiments prior to selecting the final experimental configuration.

#### **Improving the Estimate of Dispersion Coefficient**

Suppose an experiment with the objective of estimating the dispersion coefficient takes place using a tracer in a soil column of length L. Also, suppose that the conservative, nonsorbing solute concentration entering the soil column conforms to the sinusoidal loading pattern described by boundary condition Eq. [4]. Also suppose that the experiment has been run for a number of loading cycles with a time series of effluent concentration measurements being recorded. Then it would be reasonable to assume that the quasi steady-state concentration distribution Eq. [27] was applicable to model the time series of data after x in Eq. [27] had been replaced by L. If there were no experimental and model error, each loading cycle would produce an identical set of data. Of course, that won't happen so that a measurement taken at time  $t_i$ ,  $C(L, t_i)$ , will contain some error. If the data had been collected for a time period that represented N loading cycles, and measurements were taken at regularly spaced intervals, 1/M, where M is an integer, then there would be N values of concentration for each time increment of the loading cycle. In effect, there would be N replications of the experiment (contrast this situation that produces replicated data against an experiment in which a slug or a pulse loading had been ap-

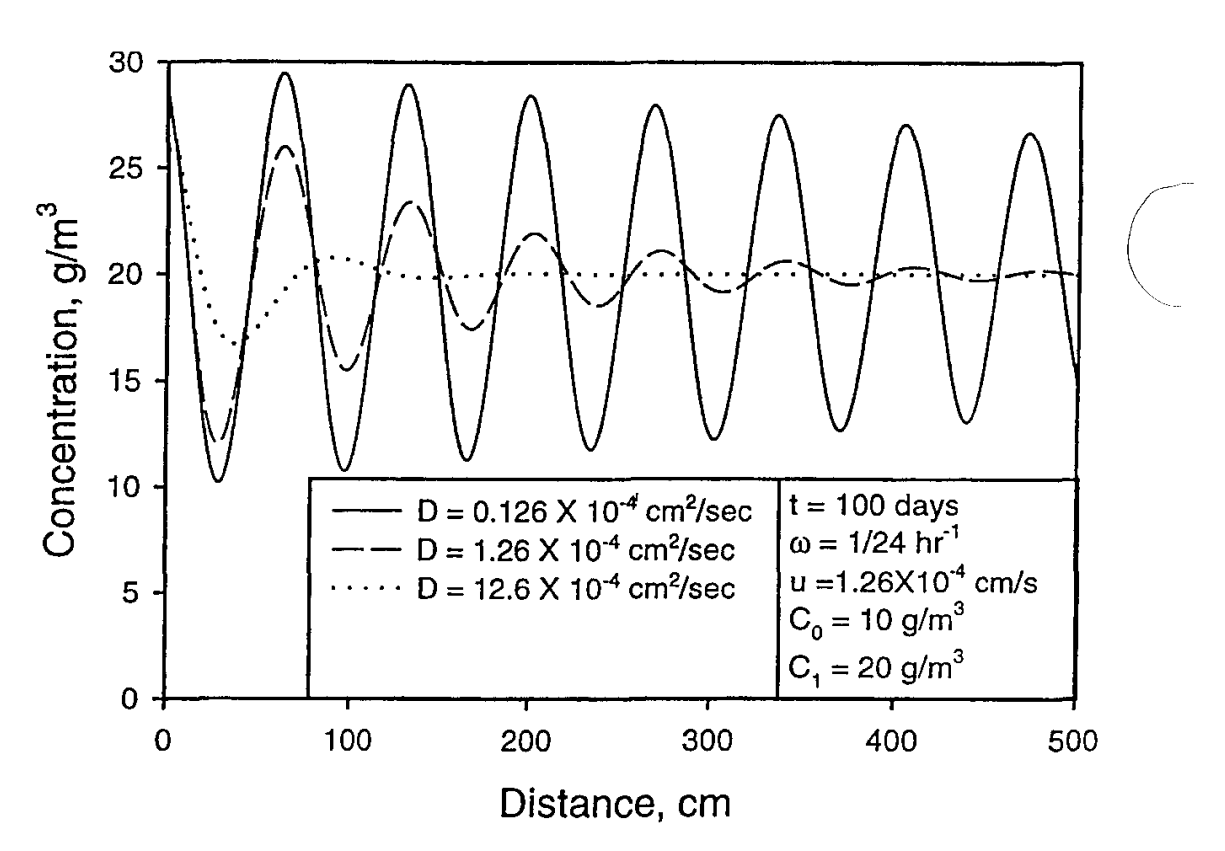


Fig. 5–3. Concentration tracer distribution curves in a soil column which has a sinusoidally varying inlet tracer concentration for three different values of the dispersion coefficient.

plied to a soil column). The expectation is that the replication of data should result in more precise estimates of the dispersion coefficient (Berthouex & Brown, 1994, p. 201–212). In many experiments, the data will be collected at regular intervals but the spacing between measurements will not divide a loading cycle evenly. This data collection scheme should still yield an improved precision of the estimate of the dispersion coefficient as contrasted with data from slug tests or pulse loadings of tracer.

There are problems in selecting the time interval at which data will be collected from an experiment with sinusoidal loading. One of the problems is that the data should be collected frequently enough to describe the outlet concentration curve. One can picture certain data collection frequencies to avoid, such as collecting data only at the peak, neutral point, or trough of the concentration curve. Problems occur when few samples are collected resulting in an inability to reconstruct sinusoidal curves from the data. References on spectral analysis of data discuss in detail such points as the Nyquist frequency (Blackman & Tukey, 1958; Gunnerson, 1966). Another problem that may be encountered is with a time series of noisy data. Noisy data may make it difficult to estimate a starting value of the dispersion coefficient for use in a numerical optimization procedure such as a least squares procedure to estimate the dispersion coefficient. Jandel Scientific (Jandel Corp., 1995, p. 6-67–6-86) discusses the use of filtering algorithms to apply with noisy data. Experience has shown that straightforward least squares procedures may not be efficient estimators of sinusoidal wave properties when data errors are present (Jandel Corp., 1996, p. 3-37–3-44). Turner (1972, p. 196–200) discusses the merits of alternative methods of determining parameters from sinusoidal data, and points out that one may fit the peaks and valleys of the tracer curve (frequency domain analysis), the values of concentration at various times (time domain analysis), the Laplace transformed data (Laplace domain analysis), or use the moments of the data (moment analysis). Jandel Scientific (Jandel Corp., 1995, p. 6-67–6-86) discusses problems that may develop when estimating parameters from a time series of data and a model such as Eq. [27].

#### How are Sinusoidal Loading Boundary Conditions Developed?

Generating a sinusoidally variation of concentration with time to match the boundary condition Eq. [4] can be carried out by using a digital controller or an analog device (Turner, 1972, p. 196–200). A digital controller will change the pumping rate of the tracer solution that is applied to the column inlet. Some digital controllers do not provide a smooth change in concentration to simulate a sine curve, but carry out the simulation through a series of step changes in concentration, for example, representing a single sine wave curve as a series of 16 steps. Yu et al. (1991) showed that representing a sine input curve by 12 steps in concentration resulted in considerable error, while representing the some curve by 24 steps in concentration provided a good fit. An analog device can be constructed to change rotary motion into linear motion. Two reservoirs of water can be connected to a soil column through a capillary tube with the result that the flow rate through each tube is proportional to the reservoir's elevation. If one reservoir contains a tracer and the other reservoir contains dilution water, then a sinusoidal variation in concentration of the

flow into the column can be achieved. Turner (1972, p. 196–200) discusses placing the reservoirs on a Scotch yoke or an oscillating beam to fulfill the requirement for sinusoidal variation in concentration.

#### **CONCLUSIONS**

A quasi steady-state solution for the tracer distribution in a soil column has been developed for the inlet boundary concentration being a constant plus a sinusoidal component. Then an unsteady state solution for tracer distribution in a soil column was developed for the same inlet boundary condition as above. The unsteady-state tracer concentration distribution applies to the section of a soil column that still remembers the initial condition. The two solutions may be applicable to those planning experiments to measure parameters such as the dispersion coefficient from tracer tests. A sinusoidal loading of tracer at the inlet boundary may enable one to obtain repeated data traces at the column outlet as part of an extended experiment. Continued collection of tracer concentration vs. time data at the column outlet over a number of periods would enable one to collect data from repeated experiments, for each period of the sine wave would represent another experiment. This should enable one to obtain more replicates of data to improve statistical estimates of the dispersion coefficient than could be obtained by experimental methods that use a slug loading or a step change of concentration at the column inlet.

Several mathematical methods were drawn upon to aid in solving the governing equations for the problem discussed herein. Superposition enabled the inlet boundary condition and the related boundary value problem to be separated into two subproblems, one of which had been solved previously in the literature, while the other subproblem with the sine loading was the major focus of this study. First, a transform of dependent variable, Eq. [7], removed the convective and decay terms and left a diffusion equation to solve. Then, the Laplace transform method was applied to determine the solution to the governing equations, Eq. [8] to [11]. However, when the convolution integral theorem was applied to determine the inverse of the Laplace transform solution, two difficult-to-evaluate integrals were produced in Eq. [12]. This difficulty was overcome by the introduction of complex variables and application of Euler's equation that resulted in combining the two integrals of Eq. [12] into a single integral in Eq. [14]. Fortunately, the integral in Eq. [14] had been evaluated by Horenstein (1945) so that an analytical solution to the original problem could be obtained, Eq. [21] for unsteady state, and Eq. [27] for quasi steadystate.

One area of frustration for those applying the solutions that have been developed is that computer error messages may occur referring to a calculated quantity being too large. These messages are associated with the combination of functions that appear in Eq. [6] and [21] when an exponential function with a positive argument is multiplied by a complementary error function with a positive argument. The exponential function will grow in magnitude as the positive argument increases; likewise, the complementary error function will decrease in magnitude as its argument increases. As discussed in van Genuchten and Alves (1982) the product of the two functions will go to zero, not infinity. The authors have learned to

look to this combination of terms when error messages, or strange results, appear in computations. A simple, easy, practical—but not necessarily rigorous—solution to the problem is to check the magnitude of the argument of the complementary error function that has the plus sign in its argument. When the argument is larger than three, then set the product of the exponential function with the plus sign in its argument and the complementary error function with the plus sign in its argument equal to zero. Again, it should be noted that the problem discussed above arises only with the arguments that contain a plus sign. A rigorous alternative to the procedure just outlined is to use the asymptotic form for the product which approaches zero for large arguments.

The final conclusion is that the solutions that have been presented herein should encourage investigators to consider carrying out experiments in soil columns with sinusoidal inlet boundary conditions. With the ability to obtain repeated sets of data at the column outlet, one set of data for each period of the sine wave, should be an attractive and economical method for improving the precision of estimates of dispersion coefficients.

#### ACKNOWLEDGMENTS

The work was supported by the U.S. Army Engineer Research and Development Center, Vicksburg, Mississippi, through Projects 127-15-5101 and 127-15-5191, Louisiana Transportation Research Center Project 127-15-4106, and the University of New Orleans Urban Waste Management and Research Center Project 127-15-5188. Helpful suggestions were provided by Fang Xin Yu, Donald Barbe, Dean Muirhead, Babak Naghavi, Ben Hill and two anonymous reviewers.

#### APPENDIX 1

#### **Nomenclature**

C(x,t) = solute concentration at distance x and time t, g m<sup>-3</sup>

 $C_1$  = average solute concentration at x = 0, g m<sup>-3</sup>

 $C_0$  = solute concentration amplitude at x = 0, g m<sup>-3</sup>

 $D = \text{reduced dispersion coefficient, cm}^2 \text{ s}^{-1}$ 

 $E = dispersion coefficient, cm^2 s^{-1}$ 

 $i = \text{imaginary unit where } i^2 = -1$ 

 $K_1$  = transformation rate constant,  $d^{-1}$ 

 $k_1$  = reduced transformation rate constant,  $d^{-1}$ 

 $K_{\rm d} = {\rm distribution\ coefficient,\ cm^3\ g^{-1}}$ 

L = length dimension, also liter

M =mass dimension

n = index of summation

 $q = adsorbed solute concentration, mg kg^{-1}$ 

r =inverse of time

R = retardation coefficient

t = time

T = time dimension

 $U = \text{average convective travel time, cm s}^{-1}$ 

 $u = \text{reduced average convective travel time, cm s}^{-1}$ 

x =distance from the inlet, cm

 $Y = \text{transformed concentration function, g m}^{-3}$ 

 $\lambda$  = frequency constant,  $h^{-1}$ 

 $\theta$  = porosity, also angle in radians

 $\omega$  = loading frequency, h<sup>-1</sup>

#### **APPENDIX 2**

The objective of this appendix is to obtain  $Re(I_{-3/2,t})$  and  $Im(I_{-3/2,t})$  in terms of elementary functions that do not contain complex variables, where  $I_{-3/2,t}$  is given by Eq. [15] to [18]. Equations [15] to [18] are

$$I_{-3/2,t} = \frac{\sqrt{\pi}}{a} \cosh(2ab) + \frac{\sqrt{\pi}}{2a} f(t)$$
 [A1]

where

$$f(t) = \exp(-2ab) \left[ erf(bt^{1/2} - at^{-1/2}) \right] - \exp(2ab) \left[ erf(bt^{1/2} + at^{-1/2}) \right]$$
 [A2]

and

$$b^2 = \lambda - i\omega \tag{A3}$$

and

$$a^2 = (x^2/4D).$$
 [A4]

Each of the terms in Eq. [A1] to [A3] will be separated into its real and imaginary parts. Equation [A4] is already a real expression so it needs no attention.

The term  $\cosh(2ab)$  becomes

$$\cosh (2ab) = 1/2 \left\{ \exp[2a (\lambda - i\omega)^{1/2}] + \exp[-2a (\lambda - i\omega)^{1/2}] \right\}$$
 [A5]

after substituting Eq. [A3]. Then applying Eq. [24], [25], and Euler's equation to Eq. [A5] and simplifying, yields the real and imaginary parts

$$\cosh(2ab) = \cos\left[2a\sqrt{r}\sin\left(\frac{\theta}{2}\right)\right] \cosh\left[2a\sqrt{r}\cos\left(\frac{\theta}{2}\right)\right]$$

$$+ i\sin\left[2a\sqrt{r}\sin\left(\frac{\theta}{2}\right)\right] \sinh\left[2a\sqrt{r}\cos\left(\frac{\theta}{2}\right)\right]$$
[A6]

Next, one separates  $\exp(-2ab)$  and  $\exp(2ab)$  into their real and imaginary parts. Equation [19] and Euler's equation yield

$$\exp(-2ab) = \exp\left[-2a\sqrt{r}\cos\left(\frac{\theta}{2}\right)\right]\cos\left[2a\sqrt{r}\sin\left(\frac{\theta}{2}\right)\right]$$
$$-i\exp\left[-2a\sqrt{r}\cos\left(\frac{\theta}{2}\right)\right]\sin\left[2a\sqrt{r}\sin\left(\frac{\theta}{2}\right)\right]$$
[A7]

where the definition of cosine function as an even function and the sine function as an odd function were employed. Similarly,

$$\exp(2ab) = \exp\left[2a\sqrt{r}\cos\left(\frac{\theta}{2}\right)\right]\cos\left[2a\sqrt{r}\sin\left(\frac{\theta}{2}\right)\right] + i\exp\left[2a\sqrt{r}\cos\left(\frac{\theta}{2}\right)\right]\sin\left[2a\sqrt{r}\sin\left(\frac{\theta}{2}\right)\right]$$
[A8]

The error functions are more difficult to separate into real and complex parts. The procedure used by Alshawabkeh and Adrian (1997) is followed.

$$erf(bt^{1/2} - at^{-1/2}) = erf\left\{ \left[ \sqrt{rt}\cos\left(\frac{\Theta}{2}\right) - \frac{a}{\sqrt{t}} \right] + i\sqrt{rt}\sin\left(\frac{\Theta}{2}\right) \right\}$$
 [A9]

after applying Eq. [17] and Euler's rule. Equation [A9] has the form

$$erf(bt^{1/2} - at^{-1/2}) = erf(R1 + iI1)$$
 [A10]

where

$$R1 = \sqrt{rt}\cos\left(\frac{\theta}{2}\right) - \frac{a}{\sqrt{t}}$$
 [A11]

and

$$I1 = \sqrt{rt} \sin\left(\frac{\theta}{2}\right).$$
 [A12]

The other error function in Eq. [A2] becomes

$$erf\left(bt^{1/2} + at^{-1/2}\right) = erf\left\{ \left[ \sqrt{rt}\cos\left(\frac{\theta}{2}\right) + at^{-1/2} \right] + i\sqrt{rt}\sin\left(\frac{\theta}{2}\right) \right\}$$
 [A13]

that has the form

$$erf(bt^{1/2} + at^{-1/2}) = erf(R2 + iI1)$$
 [A14]

where

$$R2 = \sqrt{rt} \cos\left(\frac{\theta}{2}\right) + \frac{a}{\sqrt{t}}$$
 [A15]

Alshawabkeh and Adrian (1997) followed a procedure presented by Abramowitz and Stegun (1965) by which Eq. [A9] and [A13] are evaluated. They noted

$$erf(R + iI) = F(R, I) + iG(R, I) + \varepsilon(R, I)$$
 [A16]

where  $\varepsilon$  (R, I) is an error term

$$\varepsilon(R, I) \approx 10^{-16} | erf(R + iI) |.$$
 [A17]

As the error function is bounded by  $\pm 1$  the error term is negligible and will be omitted in subsequent calculations. The function F(R, I) and G(R, I) will be defined subsequently due to their length.

Equation [A2] contains the product of a complex exponential multiplied by a complex error function. Thus, the product of Eq. [A7] and [A16] must be separated into its real and imaginary parts as well as the product of Eq. [A8] and [A16]. The product of Eq. [A7] and [A16] produces

$$\begin{cases} \exp\left[-2a\sqrt{r}\cos\left(\frac{\theta}{2}\right)\right]\cos\left[2a\sqrt{r}\sin\left(\frac{\theta}{2}\right)\right] \\ -i\exp\left[-2a\sqrt{r}\cos\left(\frac{\theta}{2}\right)\right]\sin\left[2a\sqrt{r}\sin\left(\frac{\theta}{2}\right)\right] \end{cases} \\ \left\{F\left(R1,I1\right)+iG\left(R1,I1\right)\right\} = \\ \exp\left[-2a\sqrt{r}\cos\left(\frac{\theta}{2}\right)\right]\cos\left[2a\sqrt{r}\sin\left(\frac{\theta}{2}\right)\right]F\left(R1,I1\right) \\ +\exp\left[-2a\sqrt{r}\cos\left(\frac{\theta}{2}\right)\right]\sin\left[2a\sqrt{r}\sin\left(\frac{\theta}{2}\right)\right]G\left(R1,I1\right) \\ +i\left\{\exp\left[-2a\sqrt{r}\cos\left(\frac{\theta}{2}\right)\right]\cos\left[2a\sqrt{r}\sin\left(\frac{\theta}{2}\right)\right]G\left(R1,I1\right) \\ -\exp\left[-2a\sqrt{r}\cos\left(\frac{\theta}{2}\right)\right]\sin\left[2a\sqrt{r}\sin\left(\frac{\theta}{2}\right)\right]F\left(R1,I1\right) \end{cases}$$

$$\left[A18\right]$$

Then the product of Eq. [A8] and [A16] results in

$$\left\{ \exp\left[2a\sqrt{r}\cos\left(\frac{\theta}{2}\right)\right]\cos\left[2a\sqrt{r}\sin\left(\frac{\theta}{2}\right)\right] + i\exp\left[2a\sqrt{r}\cos\left(\frac{\theta}{2}\right)\right]\sin\left[2a\sqrt{r}\sin\left(\frac{\theta}{2}\right)\right] \right\}$$

$$\{F(R2, I1) + iG(R2, I1)\} =$$

$$\exp\left[2a\sqrt{r}\cos\left(\frac{\theta}{2}\right)\right]\cos\left[2a\sqrt{r}\sin\left(\frac{\theta}{2}\right)\right]F(R2, I1)$$

$$-\exp\left[2a\sqrt{r}\cos\left(\frac{\theta}{2}\right)\right]\sin\left[2a\sqrt{r}\sin\left(\frac{\theta}{2}\right)\right]G(R2, I1)$$

$$+i\left\{\exp\left[2a\sqrt{r}\cos\left(\frac{\theta}{2}\right)\right]\cos\left[2a\sqrt{r}\sin\left(\frac{\theta}{2}\right)\right]G(R2, I1)\right\}$$

$$+\exp\left[2a\sqrt{r}\cos\left(\frac{\theta}{2}\right)\right]\sin\left[2a\sqrt{r}\sin\left(\frac{\theta}{2}\right)\right]F(R2, I1)$$

$$+\exp\left[2a\sqrt{r}\cos\left(\frac{\theta}{2}\right)\right]\sin\left[2a\sqrt{r}\sin\left(\frac{\theta}{2}\right)\right]F(R2, I1)$$
[A19]

Abramowitz and Stegun (1965) define the functions F(R, I) and G(R, I) as

$$F(R, I) = erf(R) + \frac{\exp(-R^2)}{2\pi R} [1 - \cos(2RI)]$$

$$+ \frac{2}{\pi} \exp(-R^2) \sum_{n=1}^{\infty} \frac{\exp(-n^2/4)}{n^2 + 4R^2} f_n(R, I)$$

$$G(R, I) = \sin(2RI) + \frac{2}{\pi} \exp(-R^2) \sum_{n=1}^{\infty} \frac{\exp(-n^2/4)}{n^2 + 4R^2} g_n(R, I)$$
[A20]

where  $f_n(R, I)$  and  $g_n(R, I)$  are defined as

$$f_n(R, I) = 2R - 2R \cosh(nI) \cos(2RI) + n \sinh(nI) \sin(2RI)$$
 [A22]

$$g_n(R, I) = 2R \cosh(nI) \sin(2RI) + n \sinh(nI) \cos(2RI).$$
 [A23]

Finally, the components of  $Re(I_{-3/2,t})$  have been identified. The real part of  $I_{-3/2,t}$  is obtained by substituting the real parts of Eq. [A6], [A 18] and [A19] into Eq. [A1] and [A2] to obtain

$$Re (I_{-3/2,t}) = \frac{\sqrt{\pi}}{a} \cos \left[ 2a\sqrt{r} \sin \left( \frac{\theta}{2} \right) \right] \cosh \left[ 2a\sqrt{r} \cos \left( \frac{\theta}{2} \right) \right]$$

$$+ \frac{\sqrt{\pi}}{2a} \left\{ \exp \left[ -2a\sqrt{r} \cos \left( \frac{\theta}{2} \right) \right] \cos \left[ 2a\sqrt{r} \sin \left( \frac{\theta}{2} \right) \right] F(R1, I1) \right.$$

$$+ \exp \left[ -2a\sqrt{r} \cos \left( \frac{\theta}{2} \right) \right] \sin \left[ 2a\sqrt{r} \sin \left( \frac{\theta}{2} \right) \right] G(R1, I1)$$

$$- \exp \left[ 2a\sqrt{r} \cos \left( \frac{\theta}{2} \right) \right] \cos \left[ 2a\sqrt{r} \sin \left( \frac{\theta}{2} \right) \right] F(R2, I1)$$

$$+\exp\left[2a\sqrt{r}\cos\left(\frac{\theta}{2}\right)\right]\sin\left[2a\sqrt{r}\sin\left(\frac{\theta}{2}\right)\right]G\left(R2,I1\right)$$
 [A24]

Next, the imaginary part of  $I_{-3/2,t}$  is obtained by substituting the imaginary parts of Eq. [A6], [A18] and [A19] into Eq. [A1] and [A2] to obtain

$$Im (I_{-3/2,l}) = \frac{\sqrt{\pi}}{a} \sin \left[ 2a\sqrt{r} \sin \left( \frac{\theta}{2} \right) \right] \sinh \left[ 2a\sqrt{r} \cos \left( \frac{\theta}{2} \right) \right]$$

$$+ \frac{\sqrt{\pi}}{2a} \left\{ \exp \left[ -2a\sqrt{r} \cos \left( \frac{\theta}{2} \right) \right] \cos \left[ 2a\sqrt{r} \sin \left( \frac{\theta}{2} \right) \right] G(R1, I1) \right.$$

$$- \exp \left[ -2a\sqrt{r} \cos \left( \frac{\theta}{2} \right) \right] \sin \left[ 2a\sqrt{r} \sin \left( \frac{\theta}{2} \right) \right] F(R1, I1)$$

$$- \exp \left[ 2a\sqrt{r} \cos \left( \frac{\theta}{2} \right) \right] \cos \left[ 2a\sqrt{r} \sin \left( \frac{\theta}{2} \right) \right] G(R2, I1)$$

$$- \exp \left[ 2a\sqrt{r} \cos \left( \frac{\theta}{2} \right) \right] \sin \left[ 2a\sqrt{r} \sin \left( \frac{\theta}{2} \right) \right] F(R2, I1) \right\}.$$

$$[A25]$$

The objective of this appendix has now been satisfied.

#### REFERENCES

- Abramowitz, M., and I.A. Stegun (ed.). 1965. Handbook of mathematical functions. Dover Publ., New York.
- Adrian, D.D., and A. Alshawabkeh. 1997. Analytical dissolved oxygen model for sinusoidally varying BOD. J. Hydrol. Eng. 2(4):180–187.
- Adrian, D.D., F.X. Yu, and D. Barbe. 1994. Water quality modeling for a sinusoidally varying waste discharge concentration. Water Res. 28:1167–1174.
- Alshawabkeh, A., and D.D. Adrian. 1997. Analytical water quality model for a sinusoidally varying bod discharge concentration. Water Res. 31:1207–1215.
- Beck, J.V., K.D. Cole, A. Haji-Sheikh, and B. Litkouhi. 1992. Heat conduction using Green's functions. Hemisphere Publ. Co., Washington, DC.
- Bennett, J.P. 1971. Convolution approach to the solution for the dissolved oxygen balance equation in a stream. Water Resour. Res. 7:530–590.
- Berthouex, P.M., and L.C. Brown. 1994. Statistics for environmental engineers. Lewis Publ., Boca Raton, FL.
- Blackman, R.B., and J.W. Tukey. 1958. The measurement of power spectra. Dover Publ., Inc., New York.
- Brusseau, M.L., and P.S.C. Rao. 1991. Sorption kinetics of organic chemicals: Methods, models and mechanisms. p. 281–302. *In D.L. Sparks* and D.L. Suarez (ed.) Rates of soil chemical processes. SSSA Spec. Publ. 27. SSSA, Madison, WI.
- Carslaw, H.S., and J.C. Jaeger. 1959. Conduction of heat in solids. 2nd ed. Oxford Univ. Press, London, UK.
- Carslaw, H.S., and J.C. Jaeger. 1963. Operational methods in applied mathematics. Dover Publ. Inc., New York.
- Churchill, R.V. 1958. Complex variables and applications. McGraw-Hill, New York.
- Cooper, H.H., and M.I. Rorabaugh. 1963. Ground-water movements and bank storage due to flood stages in surface streams. p. 343–366. *In* Geological survey water-supply paper 1536-J. U.S. Gov. Print. Office, Washington, DC.
- Dresnack, R., and W.E. Dobbins. 1968. Numerical analysis of BOD and DO profiles, J. Sanit. Eng. Div. (ASCE) 94:789–807.

Ferris, J.J. 1952. Cyclic fluctuations of water level as a basis for determining aquifer transmissibility. p. 1–17. *In* Contribution number 1. Ground Water Hydraul. Sect., Ground Water Branch, U.S. Geol. Surv., Washington, DC.

- Franklin, P. 1958, Functions of complex variables. Prentice-Hall, Englewood Cliffs, NJ.
- Ge, S., and N. Lu. 1996. A semianalytical solution of one-dimensional advective-dispersive Solute transport under arbitrary concentration boundary conditions. Ground Water 32:1449–1454.
- Gradshteyn, I.S., and I.M. Ryzhik. 1980. Table of integrals, series, and products. Rev. ed. Acad. Press, New York.
- Gunnerson, C.G. 1966. Optimizing the sampling interval in tidal estuaries. J. Sanit. Eng. 92:103–125.
- Harleman, D.R.F., E.R. Holley, and W.C. Huber. 1966. Interpretation of water pollution data from tidal estuary models. p. 1–11. *In* Paper no. 3, Sect. III. Proc. 3rd Int. Conf. Water Pollut. Res., Munich. September. Pergamon Press.
- Harmon, T.C., W.P. Ball, and P.V. Roberts. 1989. Nonequilibrium transport of organic contaminants in groundwater. p. 405–437. *In* B.L. Sawhney and K. Brown (ed.) Reactions and movement of organic chemicals in soils. SSSA Spec. Publ. 22. SSSA, Madison, WI.
- Holley, E.R., and D.R.F. Harleman. 1965. Dispersion of pollutants in estuary-type flows. Hydrodynam. Lab. Rep. 74. MIT, Cambridge, MA.
- Holley, E.R. 1969. Discussion to "Difference modeling of stream pollution," by D.A. Bella and W.E. Dobbins. J. Sanit. Eng. 95:968–972.
- Horenstein, W. 1945. Q. Appl. Math. 3:183.
- Jardine, P. M. 1991. Modeling nonequilibrium reactions in inorganic solute in soil columns. p. 255–279. In D.L. Sparks and D.L. Suarez (ed.) Rates of soil chemical processes. SSSA Spec. Publ. 27. SSSA, Madison, WI.
- Jandel Corporation. 1995. Transforms & nonlinear regressions for windows, user's manual. Jandel Corp., San Rafael, CA.
- Jandel Corporation. 1996. TableCurve 2D v 4.0 software, user's manual. Jandel Corp., San Rafael, CA.
- Kirkham, D., and W.L. Powers. 1972. Advanced soil physics. Wiley-Interscience, New York.
- Lapidus, L., and N.R. Amundson. 1952. Mathematics of adsorption in beds. VI. The effects of longitudinal diffusion in ion exchange and chromatographic columns. J. Phys. Chem. 56:984–988.
- Li, W.H. 1972a. Effects of dispersion on DO-SAG in uniform flow, J. Sanit, Eng. 98:169–182.
- Li, W.H. 1972b. Differential equations of hydraulic transients, dispersion, and groundwater flow. Prentice-Hall, Inc., Englewood Cliffs, NJ.
- Logan, J.D., and V. Zlotnik. 1995. The convective-diffusion equation with periodic boundary conditions. Appl. Math. Lett. 8:55–61.
- Logan, J.D., and V. Zlotnik. 1996. Time-periodic transport in heterogeneous porous media. Appl. Math. Comput. 75:119–138.
- Logan, J.D., V.A. Zlotnik, and S. Cohn. 1996. Transport in fractured porous media with time-periodic boundary conditions. Math. Comput. Model. 24:1–9.
- Luikov, A.V. 1968. Analytical heat diffusion theory. Acad. Press, New York.
- Oberhettinger, F., and L. Badii. 1973. Tables of Laplace transforms. Springer-Verlag, New York.
- Oppenheimer, S.F., D.D. Adrian, and A.N. Alshawabkeh. 1999. A river water quality model for time varying BOD discharge concentration. Math. Probl. Eng. 5:193–221.
- Özisik, M.N. 1968. Boundary value problems of heat conduction. Int. Textbook Co., Scranton, PA.
- Petit Bois, G. 1961. Tables of indefinite integrals. Dover Publ. Inc., New York.
- Scott, E.J. 1955. Transform calculus with an introduction to complex variables. Harper & Brothers, New York.
- Sneddon, I.N. 1961. Elements of partial differential equations. McGraw-Hill Book Co., New York.
- Tikhonov, A.N., and A.A. Samarskii. 1963. Equations of mathematical physics. D.M. Brink (ed.) Pergamon Press, Oxford, UK.
- Thomann, R.V. 1974. Systems analysis and water quality management. McGraw-Hill, New York.
- Thomann, R.V., and J.A. Mueller. 1987. Principles of surface water quality modeling and control. Harper and Row, New York.
- Turner, G. A. 1972. Heat and concentration waves. Acad. Press, New York.
- van Genuchten, M.T., and W.J. Alves. 1982. Analytical solutions of the one-dimensional convective-dispersive solute transport equation. USDA ARS Tech. Bull. 1661. U.S. Gov. Print. Office, Washington, DC.
- Yu, F.X., D. D. Adrian, and V.P. Singh. 1991. Modeling river quality by superposition method J. Environ. Syst. 20:1–16.
- Werner, P.W., and D. Noren. 1951. Progressive waves in non artesian aquiters. Trans. Am. Geophys. Union 32:238–244.

# Modeling Nonlinear Kinetic Behavior of Copper Adsorption-Desorption in Soil

H. M. Selim

Louisiana Stae University Baton Rouge, Louisiana

Liwang Ma

USDA-ARS Great Plains Systems Research Fort Collins, Colorado

The retention of heavy metals resulting from acid mine waste, application of sewage sludge, and waste from timber preservation industry has become a major environmental concern. The problem of identifying the fate and transport of heavy metals in soils must account for retention reactions and transport of the various species in the soil environment. Specifically, the development of mechanistic models for describing the fate and transport of heavy metals is a key component for environmental impact assessment. Heavy metals in soils can be involved in a series of complex chemical and biological interactions. Such reactions include oxidation-reduction, precipitation and dissolution, volatilization, and surface and solution phase complexation. A number of scientists have studied soil properties that significantly affect the behavior of heavy metals such as Cu in soils (e.g., Aringhieri et al., 1985; Buchter et al., 1989).

Amacher et al. (1986, 1988) showed that sorption-desorption of several heavy metals from batch studies on several soils was not adequately described by use of single reaction of the equilibrium Langmuir or Freundlich isotherms. They also found that a first-order kinetic reaction was not capable of describing changes in Cd, Cr, and Hg concentrations in the soil solution with time. Aringhieri et al. (1985) showed that retention of Cd and Cu on an organic soil was strongly time-dependent. Cernik et al. (1994) described Cu and Zn distribution with depth in a contaminated soil near a metal smelter. They used a modified (equilibrium) Freundlich equation incorporated into the convective-dispersion equation. Montero et al. (1994) described the movement of Cu in soil columns based on equilibrium adsorption-desorption, coupled with kinetic solubilization. In addition, models based on nonlinear kinetic adsorption or ion exchange and specific sorption have been proposed in the literature. A number of such modeling efforts were used with mixed

190 SELIM & MA

success to describe Cd, Zn, and Cu movement through soils (Selim et al., 1992; Hinz & Selim, 1994; Buchter et al., 1996). Where failure occurred, it was attributed to nonequilibrium kinetic adsorption processes and/or inaccurate representation of mechanisms associated with heavy metal fractions that are strongly sorbed by soils.

Copper is a heavy metal exploited in large quantities for economic value and often leaves many abandoned Cu mines around the world. Drainage water from the abandoned mines often contains high Cu concentrations and can be of environmental concern (Amacher et al., 1995). An understanding of the retention and transport of Cu in mine soils is necessary for minimizing possible adverse effects from Cu mining. For several heavy metals (e.g., Cu, Hg, Cr, Cd, and Zn), retention/release reactions in the soil solution have been observed to be strongly time dependent. In fact, heavy metals in the soil environment can be involved in a series of complex chemical and biological interactions. Several of the reactions include oxidation-reduction, precipitation and dissolution, volatilization, and surface and solution phase complexation. A number of scientists studied soil properties that significantly affect the behavior of heavy metals such as Cd in the soil. The problem of identifying the fate of heavy metals in soils must account for retention reactions and transport of the various species in the soil environment.

Since the soil system is heterogeneous in nature, a number of studies investigated the interaction of Cu and other heavy metals with different soil constituents. For example, Sequi and Aringhieri (1977) reported that removal of organic matter released new sorption sites on soil. In contrast, Cavallaro and McBride (1984) found that treatment of the clays by removal of organics tended to either enhance or have little effect on sorption and fixation of Cu and Zn. They attributed this behavior to dominance of oxides of the soil clays to sorption and fixation of heavy metals compared to the organic component in soil. Atanassova (1995) investigated Cu adsorption-desorption for a vertisol and a planosol and their clay fractions and found that Cu sorption was well described using Freundlich and Langmuir isotherms. It was suggested that observed decreases of the distribution coefficient  $(K_d)$  with increasing Cu concentration is due to high affinities at low surface coverage. One may regard dependency of  $K_d$  on concentration as manifestation of the heterogeneity of sorption and clear indication of the nonlinearity of Cu sorption isotherms. Atanassova (1995) also showed that desorption was non-hysteretic and fully reversible for Planosol whereas strong desorption hysteresis was observed for the vertisol soil with significantly higher organic matter content. Recently, Wu et al. (1999) found that Cu was preferentially sorbed on organic matter associated with the coarse clay fraction. They also suggested that iron oxides may block available sites by coating lateral surfaces of layer silicates. Wu et al. (1999) also suggested that observed adsorption-desorption hysteresis is probably due to extremely high energy bonding with organic matter and layer silicate surfaces.

A literature search reveals that Cu isotherms for different soils as well as clay fractions often exhibit a nonlinear shape. Moreover, most investigations do not consider the kinetic retention behavior of Cu retention during adsorption. Since the nonlinear nature of Cu retention directly influences its mobility in soils, knowledge of the time-dependence nature of Cu behavior is significant. Therefore, the primary objective of this investigation was to study the kinetics of Cu adsorption as well as

release or desorption over a wide range of concentrations. Specifically, we investigated the extent of nonlinearity and kinetics of Cu retention behavior in a McLaren soil (coarse-loamy over sandy or sandy-skeletal, mixed, super active, Typic Eutrocryepts). To achieve these goals, we employed several nonlinear approaches based on the assumption of single and multiple reaction site mechanisms. The approaches implemented include single reactions, multireaction and second-order models of the nonlinear kinetic type. Limitations of these approaches and the experimental data sets are also discussed.

#### Multireaction Model

The two-site equilibrium-kinetic model of Selim et al. (1976) is perhaps one of the earliest multireaction approaches for describing retention and transport behavior of reactive solutes in porous media. Basis to the multisite approach is that the soil solid phase is made up of different constituents (soil minerals, organic matter, iron and aluminum oxides), and that a solute species is likely to react with various constituents (sites) through different mechanisms (Amacher et al., 1988). As reported by Hinz et al. (1994) heavy metals are assumed to react at different rates with different sites on matrix surfaces. Therefore, a multireaction kinetic approach may be considered to describe Cu retention kinetics in soils. The multireaction model (MRM) used here considers several interactions of one reactive solute species with soil matrix surfaces. Specifically, the model assumes that a fraction of the total sites is kinetic in nature whereas the remaining fractions interact rapidly or instantaneously with solute in the soil solution.

As illustrated in Fig. 6–1, the model accounts for reversible as well as irreversible retention reactions of the concurrent and consecutive type. We assumed Cu to be present in the soil solution phase, C (mg L<sup>-1</sup>), and in several phases representing Cu retained by the soil matrix as  $S_e$ ,  $S_1$ ,  $S_2$ ,  $S_s$  and  $S_{irr}$  (mg kg<sup>-1</sup> soil). We further considered the sorbed phases  $S_e$ ,  $S_1$ , and  $S_2$  are in direct contact with the solution phase (C) and are governed by concurrent reactions. Specifically C is assumed to react rapidly and reversibly with the equilibrium phase ( $S_e$ ) such that

$$S_{\rm e} = K_{\rm e} (\theta/\rho) C_{\rm n}$$
 [1]

where  $k_e$  is a distribution coefficient (m<sup>3</sup> Mg<sup>-1</sup>),  $\rho$  is soil bulk density (Mg m<sup>-3</sup>),  $\Theta$  is water content (m<sup>3</sup> m<sup>-3</sup>), and n is the reaction order (dimensionless). Moreover, n represents a nonlinearity parameter that is commonly less than unity (Buchter et al., 1989). This parameter represents the heterogeneity of sorption sites with different affinity to heavy metal retention on matrix surfaces (Kinniburgh, 1986).

The relations between C and  $S_1$  and  $S_2$  were assumed to be governed by a non-linear kinetic reaction expressed as

$$(\partial S_1/\partial t) = k_1 (\Theta/\rho) C^{m} - k_2 S_1$$
 [2]

$$(\partial S_2/\partial t) = [k_3 (\Theta/\pi) C^m - k_4 S_2] - k_5 S_2$$
 [3]

where t is time (h),  $k_1$  and  $k_2$  are the rate coefficients (h<sup>-1</sup>) associated with  $S_1$  and m is the reaction order. Similarly, for the reversible reaction between C and  $S_2$ ,  $k_3$ ,

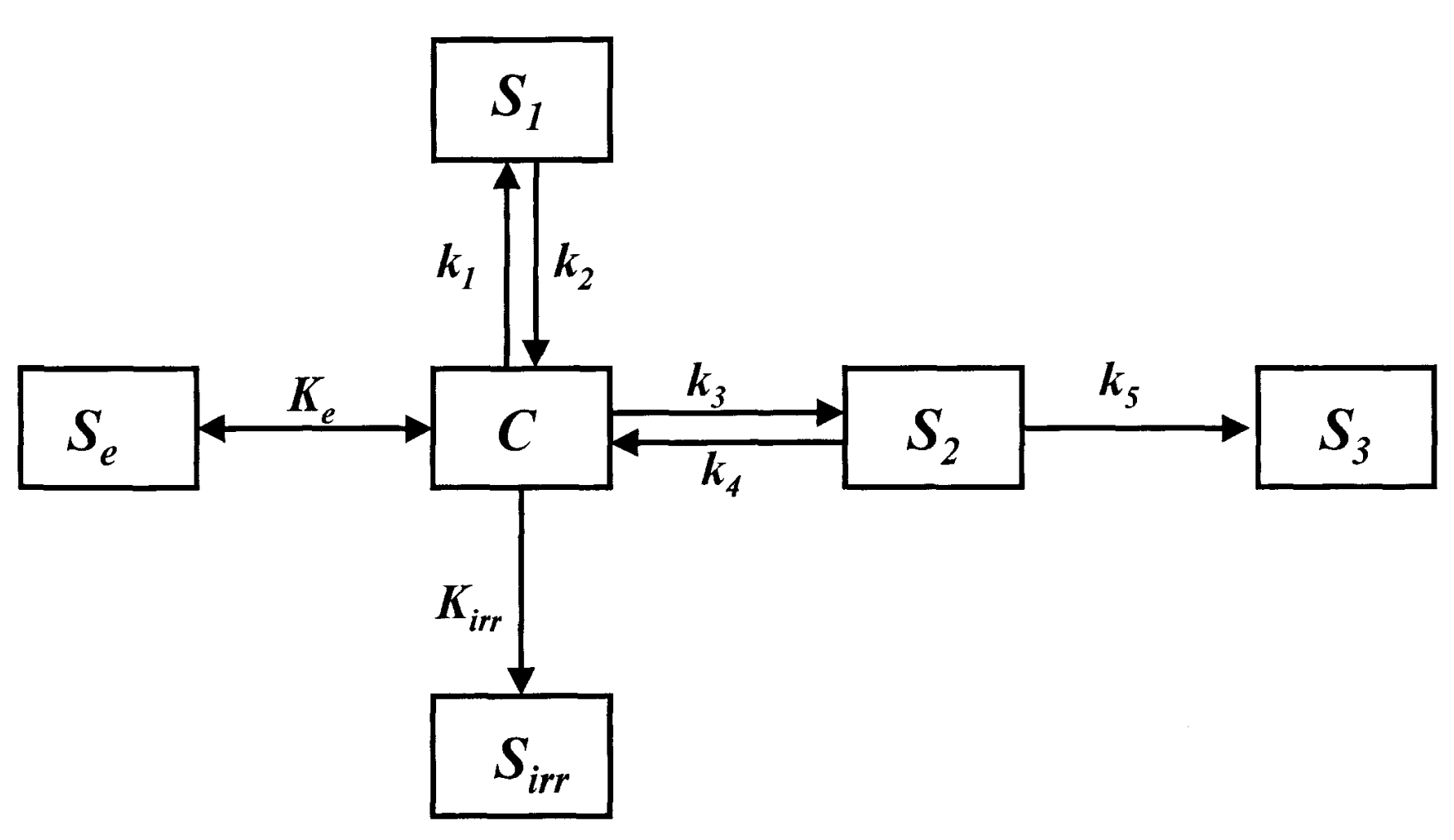


Fig. 6–1. Schematic of the proposed Cu adsorption-desorption mechanisms.

and  $k_4$  are the respective rate coefficients (h<sup>-1</sup>). In the above equations we assumed n = m since there is no known method for estimating n and/or m independently.

The multireaction model accounts for irreversible retention in two ways. First as a sink term Q with direct reaction with the solution phase C and  $S_{\rm irr}$ , e.g., precipitation/dissolution, and immobilization, as first-order kinetic process

$$Q = \rho \left( \partial S_{irr} / \partial t \right) = k_{irr} \Theta C$$
 [4]

where  $k_{irr}$  is the associated rate coefficient (h<sup>-1</sup>). Irreversible retention was also considered as a result of subsequent reaction of the  $S_2$  phase into a less accessible or strongly retained phase  $S_3$  such that,

$$\partial S_3/\partial t = k_5 S_2 \tag{5}$$

One may regard the slowly reversible phase  $S_3$  as a consequence of rearrangement of that retained on matrix surfaces.

#### Second-Order Two-Site Model

The basic assumption of the second-order modeling approach is that there exists at least two types of retention sites for heavy metal on soil matrix surfaces. Moreover, the primary difference between these two types of sites is based on the rate of the proposed kinetic retention reactions. Furthermore, the retention mechanisms are site specific where the rate of reaction is a function of not only the solute concentration present in the soil solution phase but also the amount of available retention sites on matrix surfaces.

The original second-order approach (SOTS) was first proposed to describe Cr retention and transport in several soils by Selim and Amacher (1988). Here two types of sites were considered, the first was of the equilibrium type and the second was kinetically controlled type sites. Moreover,  $S_{\text{max}}$  (µg g<sup>-1</sup> of soil) was considered to represent the total retention capacity or total amount of sites on matrix surfaces. It is also assumed that  $S_{\text{max}}$  is an intrinsic soil property that is time invariant. Therefore based on the two-site approach, the total adsorption sites,

$$S_{\text{max}} = (S_{\text{e}})_{\text{max}} + (S_{\text{k}})_{\text{max}}$$
 [6]

where  $S_{\rm max}$  is adsorption maximum,  $(S_{\rm e})_{\rm max}$  and  $(S_{\rm k})_{\rm max}$  are the total amount or adsorption maxima for equilibrium and kinetic type sites, respectively (µg g<sup>-1</sup> of soil). If f represents the fraction of equilibrium type sites  $(S_{\rm e})_{\rm max}$  to the total sites, we thus have,

$$(S_e)_{\text{max}} = f S_{\text{max}}$$

$$(S_k)_{\text{max}} = (1 - f) S_{\text{max}}$$
[7]

Assuming  $\phi_c$  and  $\phi_k$  as the vacant or available sites ( $\mu$ g g<sup>-1</sup> of soil) for adsorption on equilibrium and kinetic type sites ( $S_c$  and  $S_k$ ), respectively, we have

194 SELIM & MA

$$\phi_{e} = (S_{e})_{\text{max}} - S_{e} = f S_{\text{max}} - S_{e}$$

$$\phi_{k} = (S_{k})_{\text{max}} - S_{k} = (1 - f) S_{\text{max}} - S_{k}$$
[8]

with the total available sites of  $\phi = \phi_e + \phi_k$ . As the sites become filled or occupied by the retained solute, the amount of vacant sites approaches zero,  $(\phi_e + \phi_k) \to 0$ . In the meantime, the amount of solute retained by the soil matrix approaches the total capacity or sorption maxima  $(S_e + S_k) \to S_{max}$ .

The second-order approach was successfully used for Cr retention and transport predictions by Selim and Amacher (1988) and for Zn retention by Hinz et al. (1992). This model was recently modified such that the total adsorption sites  $S_{\text{max}}$  were not partitioned between  $S_{\text{e}}$  and  $S_{\text{k}}$  phases based on a fraction of sites f (Selim & Amacher, 1997; Ma & Selim, 1998). Instead it was assumed that the vacant sites are available to both types of  $S_{\text{e}}$  and  $S_{\text{k}}$ . Therefore, f is no longer required and the amount of solute adsorbed on each type of sites is only determined by the rate coefficients associated with each type of sites. As a result, sites associates with equilibrium or instantaneous type reactions will compete for available sites prior to slow or kinetic type sites are filled. Perhaps such mechanism is in line with observations where rapid (equilibrium type) sorption is first encountered and followed by slow types of retention reactions. We are not aware of the use of this second-order approach to describe heavy metal retention kinetics and transport in soils.

In the following analysis we followed similar overall structure for the second-order formulation to that described for the multireaction approach where three types of retention sites are considered with one equilibrium type sites  $(S_e)$  and two kinetic type sites, namely  $S_1$  and  $S_2$ . Therefore, we have  $\phi$  now related to the sorption capacity  $(S_{\text{max}})$  by

$$S_{\text{max}} = \phi + S_{\text{e}} + S_1 + S_2$$
 [9]

The governing retention reactions can be expressed as (Ma & Selim, 1998):

$$S_{e} = K_{e} \Theta C \Phi$$
 [10]

$$(\partial S_1/\partial t) = k_1 \Theta C \Phi - k_2 S_1$$
 [11]

$$(\partial S_2/\partial t) = [k_3 \Theta C \Phi - k_4 S_2] - K_5 S_2$$
 [12]

$$(\partial S_3/\partial t) = k_5 S_2 \tag{13}$$

$$(\partial S_{irr}/\partial t) = k_{irr} \Theta C$$
 [14]

The unit for  $K_e$  is cm<sup>3</sup>  $\mu$ g<sup>-1</sup>,  $k_1$  and  $k_3$  have a derived unit of cm<sup>3</sup>  $\mu$ g<sup>-1</sup> h<sup>-1</sup>;  $k_2$ ,  $k_4$ ,  $k_5$  and  $k_{irr}$  are assigned with the unit of hours (h<sup>-1</sup>).

#### MATERIALS AND METHODS

McLaren surface soil (unclassified) with pH of 4.1, organic matter content of 3.03%, and cation exchange capacity (CEC) of 33.0 mmol<sub>c</sub>kg<sup>-1</sup>. McLaren soil was obtained from a site near an abandoned Cu mine on Fisher mountain, Montana. Acid mine drainage from the abandoned mine flows into Daisy Creek below the mine that is located about 3.2 km (2 mi) from Cooke City, Montana (Amacher et al., 1995). Results from undisturbed soils near the minespoil are reported here. The minespoil is characterized by high Cu contents and low pH.

Kinetic retention of Cu was studied using the batch method described by Amacher et al. (1988). Triplicate 3 g of soil was placed in polypropylene tubes and mixed with 30-mL solutions of known initial Cu concentrations. Initial concentrations ( $C_0$ ) of Cu were 5, 10, 20, 50, and 100 mg L<sup>-1</sup>. Reagent-grade copper perchlorate was used. Background solution composition was 0.005 M Mg(ClO<sub>4</sub>)<sub>2</sub>. The soil slurry was shaken 15 min every 2 h. After 2, 4, 8, 12, 20, 48, 96, and 192 h of reaction time, samples were centrifuged and aliquots of 1.0 mL of the supernatant were withdrawn for Cu concentrations analysis using inductively coupled plasma spectroscopy (ICP). The samples were reweighed, vortex mixed, and returned to shaker. The amount adsorbed were calculated as the decrease in Cu concentration in soil solution. For each concentration, the means of triplicate samples are reported throughout.

Following adsorption, Cu desorption was carried out using successive dilutions. Here, the soil residue with initial Cu concentrations ( $C_0$ ) of 50 and 100 mg L<sup>-1</sup> was extracted with 0.005 M Mg(ClO<sub>4</sub>)<sub>2</sub> several times. Each extraction was conducted by adding 30 mL of 0.005 M Mg(ClO<sub>4</sub>)<sub>2</sub> solution after decanting the supernatant. The first four extractions were completed in 2 h in order to evaluate the equilibrium adsorption sites. The subsequent four extractions were conducted with a three-dimensional equilibration time interval between each desorption step in order to assess the affinity of retention sites for Cu during desorption.

#### RESULTS AND DISCUSSION

#### **Single Reaction Models**

Several sorption isotherms representing the total amount of Cu retained (S) vs. Cu in soil solution (C) are shown in Fig. 6–2. These results were obtained for selected reaction times from the batch experiments and show the kinetics of Cu retention in this soil. In addition, Cu retention is not only time dependent but nonlinear in nature. Similar kinetic and nonlinear behavior of other heavy metal retention has been observed by numerous investigators. The concave sorption nonlinearity implies that Cu mobility in the soil solution tends to increase as the concentration increases. A simple way to describe the above sorption isotherms is by use of the Freundlich equation;

196 SELIM & MA

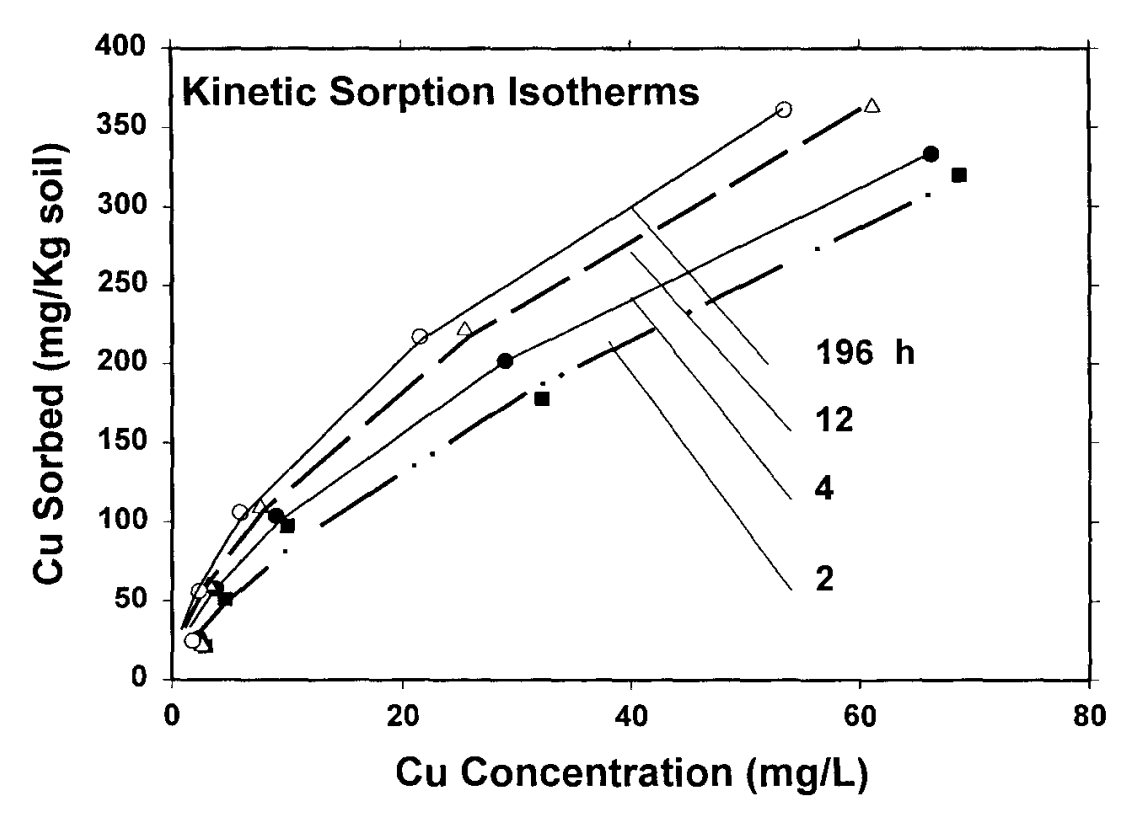


Fig. 6–2. Adsorption isotherms for Cu on McLaren soil at different retention times. The solid curves are based on the Freundlich equation.

was used where  $K_f$  is the distribution coefficient (cm<sup>3</sup> g<sup>-1</sup>) and b is an exponential parameter. A set of  $K_f$  and b values was obtained for each S vs. C data set. Examples of isotherms calculated using Eq. [15] are shown by the solid curves in Fig. 6–2. The parameters obtained indicate that  $K_f$  was strongly time dependent (see Fig. 6–3). The  $K_d$  values along with their standard errors are also given in Table 6–1. The goodness of fit of the model to the data is given by the  $r^2$  values. The  $K_f$  value increased from 16.7 to 42.1 m<sup>3</sup> Mg<sup>-1</sup> with retention time from 2 and 196 h, respectively. The parameter b was less than unity for all isotherms and ranged from 0.601 to 0.696 with a mean value of 0.629. No consistent trend for b vs. reaction time was observed, however. In fact, these b values did not vary appreciably for the different reaction times. Similar behavior was observed for Cd by Hinz and Selim (1994) who found b to vary from 0.60 to 0.74 for Cd for a time range of 2 to 240 h.

The extent of nonlinearity of Cu isotherms can thus be compared with Cu isotherms obtained by other investigators. For example, Buchter et al. (1989) measured  $K_f$  and b for Cu after 1 d of retention for 11 soils having a wide range of properties. They reported a range of b values from 0.47 to 1.42 with a mean value of 0.76. Recently, a somewhat lower value for b of 0.42 was reported by Houng and Lee (1998). These investigators also reported that b for Cu was not affected by the presence of Cd as a competing heavy metal. It should be emphasized, for most studies, adsorption isotherms represent one-dimensional retention where the kinetics of the sorption processes is not investigated.

The results shown in Fig. 6–3 indicate that for a given reaction time, the Freundlich Eq. [15] was capable of describing the overall shape of the isotherms. Nevertheless, the time dependency of  $K_f$  implies that the model given by Eq. [15] rep-

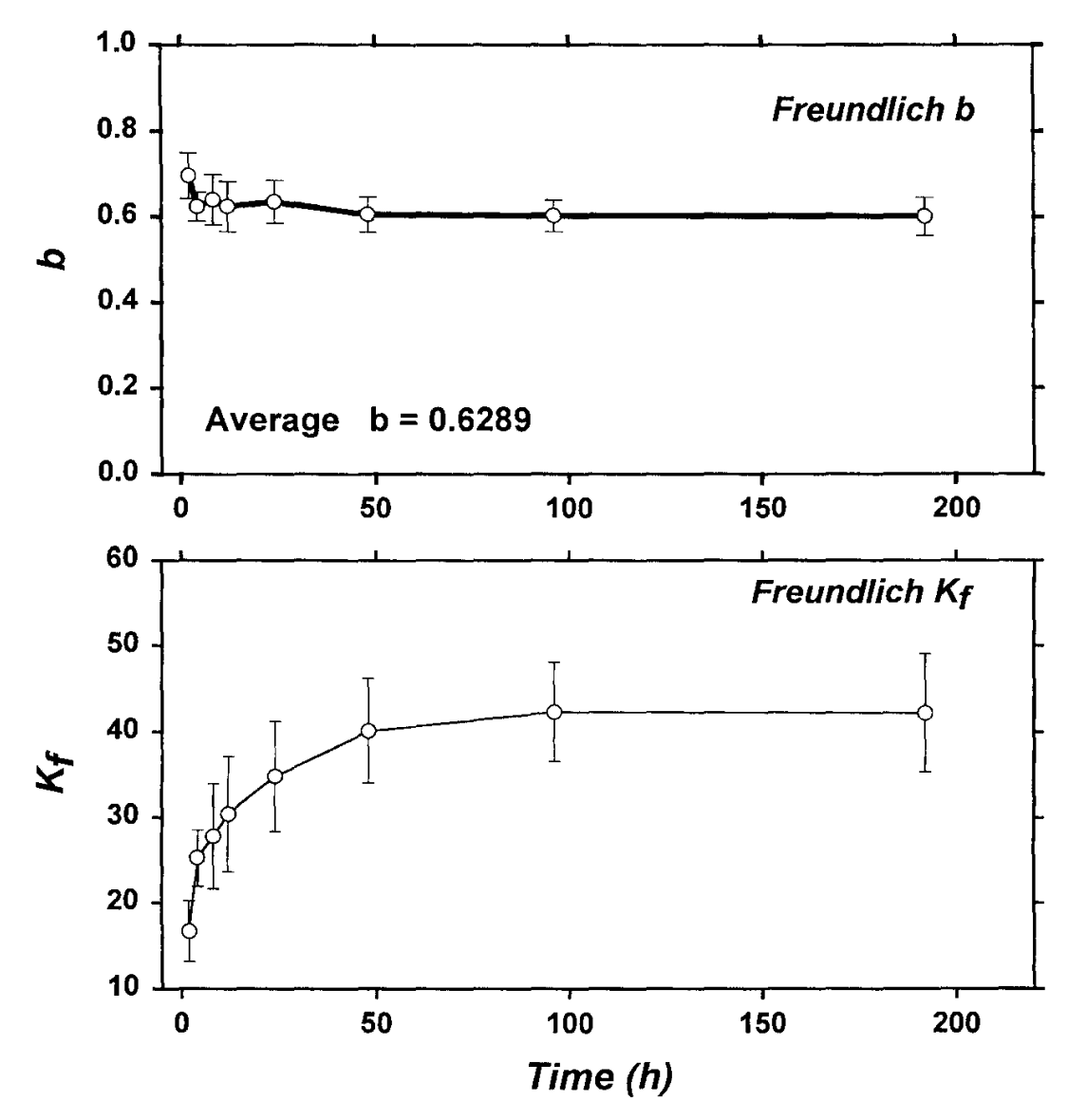


Fig. 6–3. Freundlich parameters  $K_f$  and b vs. retention time.

resents an over simplification of the retention mechanisms in the soil. Specifically, a single equilibrium reaction was incapable of describing the kinetic behavior shown.

Measured isotherms of the type shown in Fig. 6–2 are frequently described using the Langmuir approach. In fact, several investigators indicated that one-di-

Table 6–1. Parameter estimates, standard errors, and coefficient of correlation  $r^2$ ) for the Langmuir and Freundlich equations at various reaction times.

Time	$S_{max}$	ω	$r^2$	$K_{f}$	b	$r^2$	
h	mg	kg <sup>-1</sup> ———		L mg <sup>-1</sup>			
2	$637.8 \pm 163.7$	$71.2 \pm 30.9$	0.976	$16.71 \pm 3.51$	$0.696 \pm 0.053$	0.988	
4	$554.2 \pm 71.6$	$42.4 \pm 10.9$	0.986	$25.25 \pm 3.32$	$0.624 \pm 0.634$	0.994	
8	$634.9 \pm 83.9$	$41.1 \pm 10.7$	0.987	$27.82 \pm 6.15$	$0.640 \pm 0.058$	0.983	
12	$619.6 \pm 75.9$	$36.7 \pm 9.2$	0.987	$30.41 \pm 6.76$	$0.625 \pm 0.058$	0.981	
24	$721.9 \pm 85.9$	$36.2 \pm 8.5$	0.989	$34.79 \pm 6.44$	$0.636 \pm 0.050$	0.987	
48	$683.2 \pm 62.9$	$30.0 \pm 5.9$	0.992	$40.09 \pm 6.10$	$0.606 \pm 0.041$	0.993	
96	$701.8 \pm 78.3$	29.3 ± 6.96	0.988	$42.31 \pm 5.75$	$0.603 \pm 0.037$	0.994	
196	$689.6 \pm 82.7$	$28.5 \pm 7.40$	0.986	$42.16 \pm 6.86$	$0.601 \pm 0.045$	0.989	

198 SELIM & MA

mensional isotherms for Cu and other heavy metals can be well described using Freundlich and Langmuir approaches (Cavallaro & McCbride, 1978; Harter, 1984; Amacher et al., 1986; Schulte & Beese, 1994; Aassova, 1995; Houng & Lee, 1998). Although the Langmuir form is not strictly recommended over the Freundlich equation, it is often preferred since it provides a sorption maxima  $S_{\text{max}}$  that can be correlated to intrinsic soil properties such as the type of clay, specific surface area, etc. Therefore, the isotherms shown in Fig. 6–2, were also described based on the Langmuir form,

$$S = S_{\text{max}}C/(\omega + C)$$
 [16]

where the parameter  $\omega$  (mg L<sup>-1</sup>) is a Langmuir coefficient that represents a measure of the affinity of sites or bonding strength. Based on nonlinear linear least squares, best-fit Langmuir parameters for the different adsorption times were obtained and are given in Table 6–1 and  $\omega$  and  $S_{\text{max}}$  vs. retention time are shown in Fig. 6–4. Based on  $r^2$  and root mean square errors (rmse), the Langmuir formula-

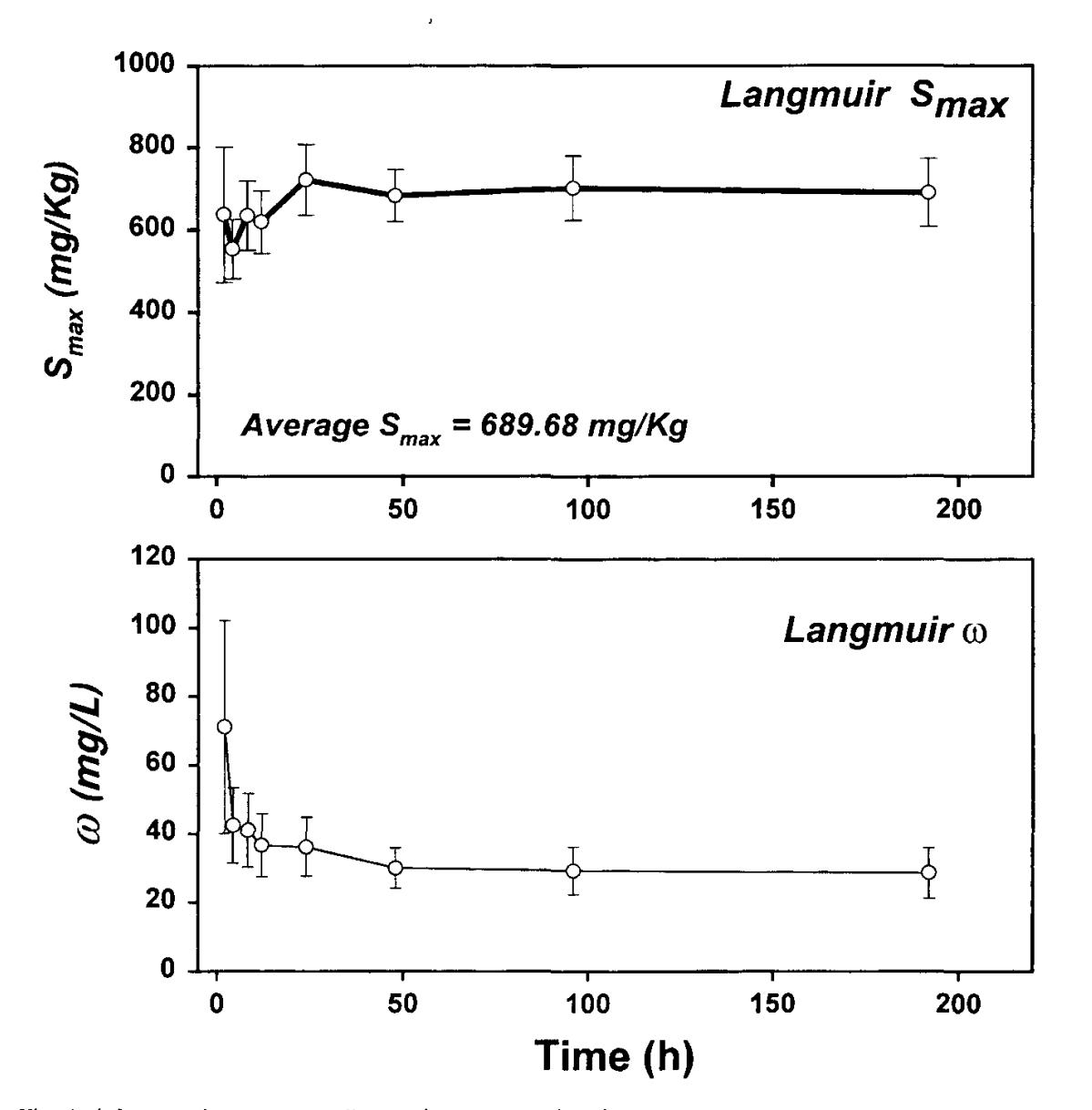


Fig. 6–4. Langmuir parameters  $S_{\text{max}}$  and  $\omega$  vs. retention time.

tion is capable of describing our Cu adsorption data. In fact, the Langmuir approach was successfully used to describe several heavy metals including Cu isotherms for several soils (Cavallaro & McCbride, 1978; Harter, 1984; Amacher et al., 1986; Atanassova, 1995; Houng & Lee, 1998). Unlike the isotherms presented here, the time of reaction for most Cu isotherms reported in the literature is limited to 1 d of adsorption.

The fact that the sorption capacity term  $(S_{\rm max})$  given in Table 6–1 did not appreciably change with retention time gives credence to the Langmuir model in describing our Cu results. This is a significant finding if the sorption capacity is to be used in describing the retention behavior as well as the potential mobility of a heavy metal such as Cu in soils. If  $S_{\rm max}$  is not a unique value and varies with time or concentration, the use of such term in modeling efforts becomes questionable. We recognize that based on parameter estimation alone, we cannot conclude that the Langmuir equation is uniquely applicable to our Cu sorption data. In fact, as argued by Sposito (1982) and Amacher et al. (1988) isotherm equations such as those of Eq. [15] and [16] should be regarded as empirical equations and that their use constitutes primarily curve-fitting procedure.

The consequence of the above is that based on goodness of fit of the sorption data, both the Freundlich and the Langmuir approaches described the data equally well for all reaction times (see Table 6–1). It is also conceivable that such a finding is expected since both approaches result from the general isotherm equation (Kinniburgh, 1986)

$$\frac{S}{S_{\text{max}}} = \sum_{i=1}^{j} F_{i} \left[ \frac{(\kappa_{i}C_{i})^{\lambda_{i}}}{1 + \varepsilon_{i} (\kappa_{i}C_{i})^{\lambda_{i}}} \right]^{\beta_{i}}$$
[17]

where j = 1,  $F_i = 1$ ,  $\beta_i = 1$ ,  $\lambda_i = 1$ , and  $\varepsilon_i = 1$  for the Langmuir equation. Whereas for the Freundlich equation. we have j = 1,  $F_i = 1$ ,  $\beta_i = 1$ , and  $\varepsilon_i = 0$ .

#### **Multiple Reaction Models**

Results from the kinetic batch experiments for our soil are presented in order to illustrate the changes in Cu concentration (C) vs. time for the various initial (input) concentrations  $(C_0)$ . Retention of Cu by the soil matrix was rapid during the initial stages of reaction and was then followed by slow and continued Cu retention as depicted by the changes of C vs. time results. The capability of the multireaction approach discussed above in describing the experimental batch data is shown by the solid curves of Fig. 6–5 for the various initial concentrations  $(C_0$ 's). Good model predictions were observed for the wide range of input concentrations values considered.

The multireaction model used here accounts several interactions of the reactive solute species (Cu) within the soil system. Specifically, the model assumes that a fraction of the total sites is highly kinetic whereas the remaining fraction interacts slowly or instantaneously with solute in the soil solution. As illustrated in Fig. 6–1, the model also accounts for irreversible reactions of the concurrent and consecutive type. As a result, different versions of the multireaction model shown in Fig. 6–1 represent different reactions from which one can deduce Cu retention

200 SELIM & MA

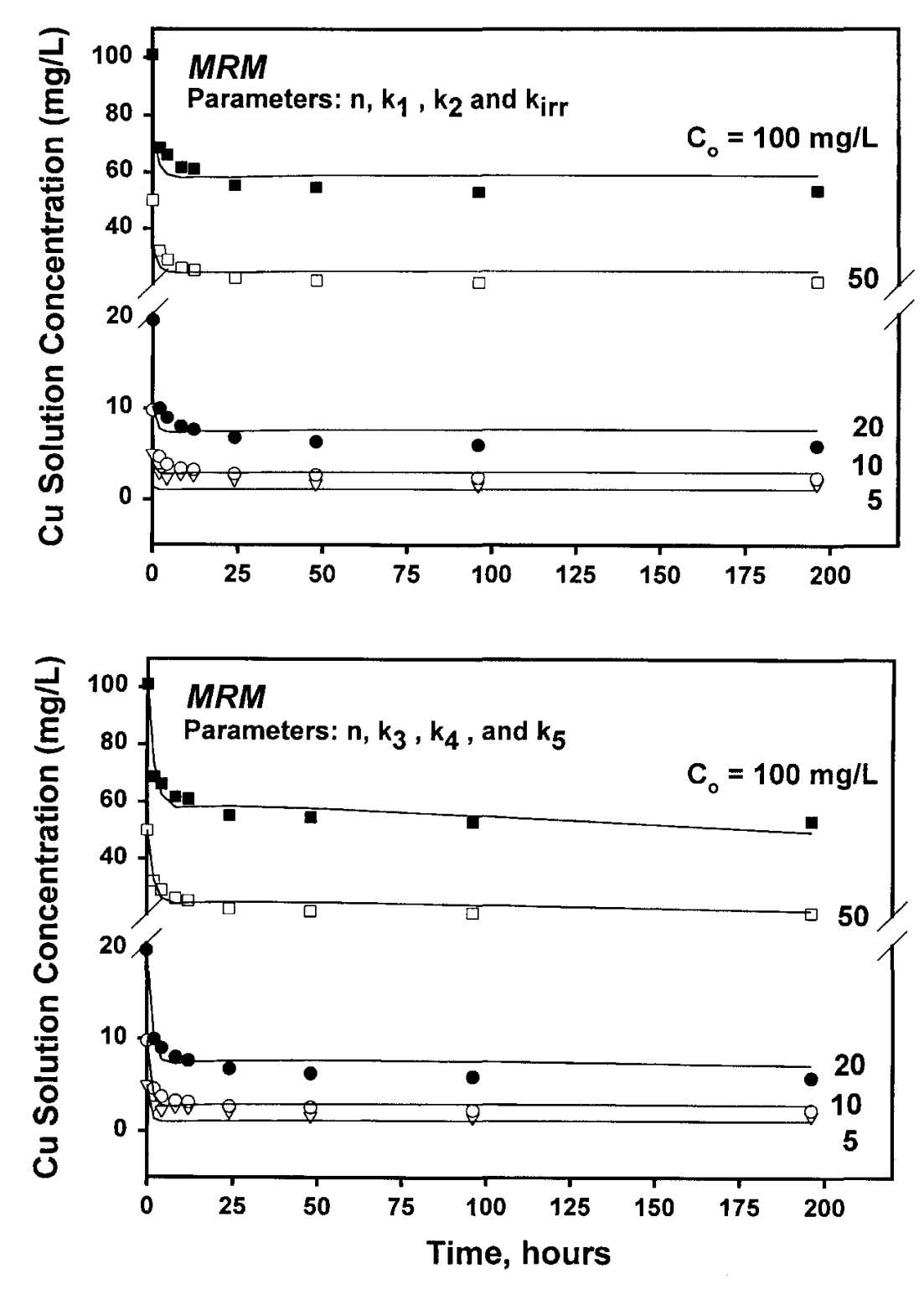


Fig. 6-5. Experimental results of Cu in soil solution for McLaren soil vs. time for a wide range of initial concentrations ( $C_0$ 's). The solid curves were obtained using the multireaction model with concurrent (top figure) and consecutive (bottom figure) irreversible reactions. Fitted parameters were n,  $k_1$ ,  $k_2$ , and  $k_{irr}$  (top) and n,  $k_3$ ,  $k_4$ , and  $k_5$  (bottom) and are given in Table 6-4.

mechanisms. Several variations were examined: (i) a two-parameter model with  $k_e$  and  $k_{irr}$ ; (ii) a four-parameter model with  $k_e$ ,  $k_1$  and  $k_2$ , and  $k_{irr}$ ; (iii) another four-parameter model with  $k_e$ ,  $k_3$ ,  $k_4$  and  $k_5$ ; and (iv) a five-parameter model with  $k_1$ ,  $k_2$ ,  $k_3$ ,  $k_4$ , and  $k_{irr}$ . These variations were chosen based on our observations of C vs. time and assumes the presence of at least a fraction of retention sites that interacts

$C_{\mathrm{o}}$	Model $r^2$	RMSE	n	SE	K <sub>e</sub>	SE	K <sub>irr</sub>	SE
mg L <sup>-1</sup>					— m <sup>3</sup> N	⁄lg L <sup>-1</sup> ──	h	-1
5	0.747	2.024	0.244	831.6	0.010	19.28	0.0138	0.053 5
10	0.641	5.460	0.594	15 338.0	0.002	98.49	0.0113	0.103 3
20	0.757	9.349	0.221	4 200.0	0.002	39.46	0.147	0.027 7
50	0.501	23.034	0.212	11 609.0	0.006	394.9	0.0043	0.030 5
100	0.550	38.126	0.295	9 265.0	0.004	273.8	0.003 5	0.007 7
Overall-A	0.981	3.098	0.584	0.065 5	3.605	0.917	0.0028	0.0004
Overall-B	0.981	3.075	0.629†		3.041	0.135	0.002 8	0.0004

Table 10–2. Comparison of goodness of fit of the multireaction model with  $S_e$  and  $S_{irr}$  for McLaren soil. All  $C_o$ 's were used for the "overall" fit.

slowly (kinetic) and another which is kinetic but irreversible or slowly reversible in nature. Each model variation was fitted to the experimental data using a nonlinear, least-squares, parameter optimization scheme (van Genuchten, 1981, p. 80). Criteria used for estimating the goodness-of-fit of the model to the data were the  $r^2$  and the root mean square error (rmse) statistics (Kinniburgh, 1986),

$$rmse = [rss/(N-P)]^{1/2}$$
 [18]

where rss is the residual sum of squares, N is the number of data points, and P is the number of parameters.

In our simulations, the multireaction model was fitted to Cu vs. time for all input concentrations ( $C_0$ ) simultaneously. As a result an "overall" set of model parameters for the appropriate rate coefficients, applicable for the entire data set, was achieved. Generally, individually fitted parameters had large standard errors due to small degrees of freedom. Several model variations even failed to fit Cu concentration vs. time for most  $C_0$ 's and convergence was often not achieved. In addition, large variations existed among fitted model parameters. The example shown in Table 6–2 is for the simplest case where only two sorbed phases were considered; a reversible ( $S_e$ ) and an irreversible ( $S_{irr}$ ) where three model parameters were estimated (n,  $k_e$ , and  $k_{irr}$ ). For most  $C_0$ 's, parameter optimization failed to fit the data. Moreover, the nonlinear parameter n was particularly difficult to estimate due to extremely high standard errors. We also found that when other versions of the multireaction model were tested, poor parameter estimates were obtained. Therefore, the use of a data set from an initial input concentration was not recommended in our study for the purpose of parameter estimation of the multireaction model.

In order to overcome this difficulty, the entire data set consisting of all input concentrations ( $C_0$ 's) was used in the nonlinear least-square optimization. The resulting overall set of parameter estimates for our simplest model version (e.g., n,  $k_e$ , and  $k_{irr}$ ) are given in Table 6–2. This use of the entire data set resulted in increased degrees of freedom. Specifically, this resulted in a decrease of the root mean square error (rmse) and improved  $r^2$  value as well as a decrease in parameter standard errors. In addition, the overall shape of C vs. time observations for the different  $C_0$ 's were improved using this overall fitting strategy. The estimated value for n was 0.584 that is within the confidence interval of the Freundlich b (=0.629) obtained earlier

 $<sup>\</sup>dagger n$  was derived from Freundlich Eq. [15].

202 SELIM & MA

the Freuhanch equation $(n = b = 0.029)$ for mulvidual as well as overall $C_0$ s.											
$C_{\mathrm{o}}$	Model r <sup>2</sup>	RMSE	$k_1$	SE	$K_2$	SE	K <sub>irr</sub>	SE			
mg <sub>.</sub> L <sup>-1</sup>					h	-1					
6	0.601	0.3601	0.682	0.225	0.429	0.167	0.0062	0.0022			
10	0.849	0.3668	0.922	0.109	0.270	0.043	0.0079	0.0022			

0.179

0.163

0.252

0.089

0.315

0.273

0.357

0.323

0.063

0.056

0.087

0.031

0.0059

0.0028

0.0019

0.0020

0.0018

0.0010

0.0007

0.0003

20

50

100

Overall

0.762

0.802

0.663

0.992

0.8887

2.1709

4.3336

2.0635

1.133

0.994

1.217

1.131

Table 6–3. Goodness of fit of the multireaction model when the nonlinear parameter n was derived from the Freundlich equation (n = b = 0.629) for individual as well as overall  $C_0$ 's.

(see Fig. 6–2, Table 6–1). Consequently, we tested whether the value of Freundlich b can be used in place of the parameter n in the multireaction model. Therefore, for this model version, only two parameters were estimated ( $k_e$  and  $k_{irr}$ ) that resulted in equally good description of C vs. time for all  $C_o$ 's (figure not shown). Moreover, when n = b was assumed, the resulting rmse and  $r^2$  values were comparable to those when n was estimated (see Table 6–2).

Based on the above findings, we tested other versions of the multireaction model where n = b was assumed (see Tables 6–3 and 6–4). The examples shown in Figs. 6–5 and 6–6 (see also Table 6–3) are for the case where a kinetic phase  $(S_1)$ and an irreversible phase  $(S_{irr})$  were considered. Based on goodness of fit of the model to the experimental results, the use of Freundlich b in place of n is recommended only if the entire data set (for all  $C_0$ 's) is simultaneously used in the optimization method (see Table 6–3). Obviously, the use of n = b reduces the number of total parameters to be estimated that is advantageous because the parameter n is, in general, difficult to estimate as discussed above. Simulations, where n = b was assumed, are shown in Fig. 6-6 for two model versions. It is obvious from the simulations shown in Figs. 6–5 and 6–6, a number of model versions were capable of producing indistinguishable simulations of the data. Similar conclusions were made by Amacher et al. (1988, 1990) for Cd, Cr(VI), and Hg for several soils. They also stated that it was not possible to determine whether the irreversible reaction is concurrent or consecutive, since both model versions provided similar fit of their batch data. Contrary to their findings, we found that the use of a consecutive irreversible reaction provided an improved fit of our Cu data than other model versions. This finding is based not only on  $r^2$  and rmse values but also on visual observation of model simulations.

#### **Second-Order Two-Site**

The adsorption maximum, which is often used to characterize heavy meta adsorption, can be quite misleading if the experimental data do not cover a sufficient range of solution concentration and if other conditions such as the amount initially sorbed prevail (Houng & Lee, 1998). Harter (1984) emphasized that isotherms should be examined in the original form and if they do not show the correct shapes and only the low concentrations are used, the Langmuir equation car provide estimates of the adsorption maximum that are in error by 50% or more. In our study, we have shown that, for reaction times greater than 20 to 30 h,  $S_{max}$  was

Table 10—4. Goodness of fit of several versions of the multireaction model for describing Cu adsorption on McLaren soil. Model versions A-1 and A-2 are based on consument irreversible reaction whereas versions B-1 and B-2 are based on the consecutive type.

Model version	Model r <sup>2</sup>	RMSE‡	n	SE‡	$K_1$	SE	$K_2$	SE	k <sub>3</sub>	SE	$k_4$	SE	k <sub>5</sub>	SE	K <sub>irr</sub>	SE
					h-1											<del></del>
A-1 A-2÷	0.992 0.992	2.071 2.062	0.592 0.629	0.042	1.318 1.131	0.256 0.089	0.327 0.323	0.302 0.031	 	 		 	 	 	0.0020 0.0020	0.0003 0.0003
B-1 B-2÷	0.999 0.992	2.000 1.987	0.619 0.629	0.0375					1.1980 1.1871	0.2104 0.0951	0.3264 0.3496	0.0304 0.0021	0.0024 0.0021	0.0004 0.0004	 	

<sup>†</sup> *n* value derived from the Freundlich Eq. [15]. ‡ RMSE = root mean square error, SE = standard error.

SELIM & MA

not time dependent (see Fig. 6–3). To further test its validity, the average Langmuir  $S_{\text{max}}$  from Table 6–1 was utilized as an input parameter in the second-order two-site formulation (SOTS). Since SOTS relies on the assumption that rate of retention is a function of the amount of unoccupied or vacant sites, the choice of the ap-

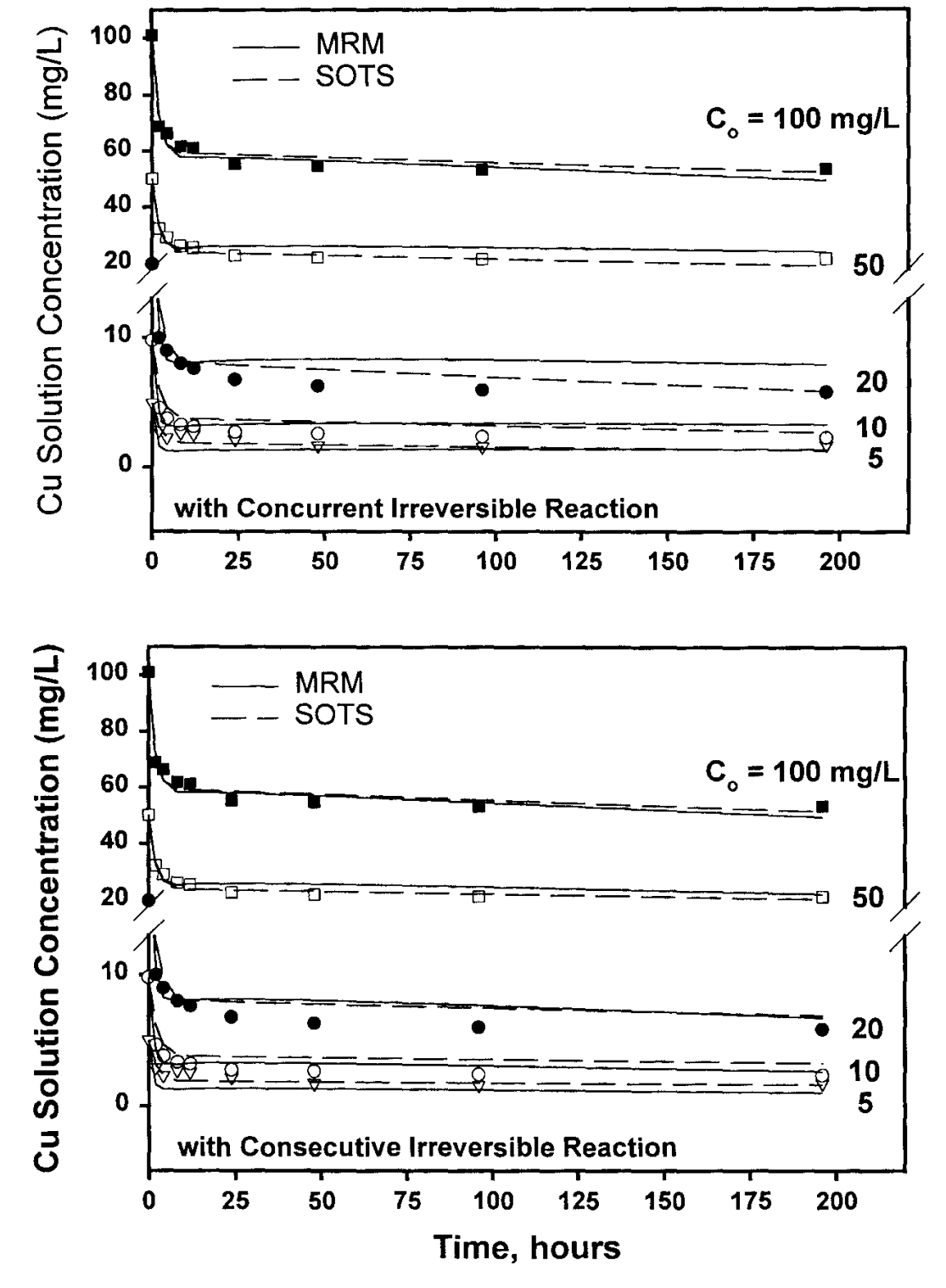


Fig. 6–6. Experimental results of Cu in soil solution for McLaren soil vs. time. The solid and dashed curves were obtained using the multireaction and second-order models, respectively. The irreversible mechanism was accounted for based on concurrent (top) and consecutive (bottom) reactions. Fitted parameters were  $k_1$ ,  $k_2$ , and  $k_m$  (top) and  $k_3$ ,  $k_4$ , and  $k_5$  (bottom) and are given in Tables 6–4 and 6–5.

propriate  $S_{max}$  is essential in simulation and prediction of adsorption-desorption as well as transport behavior of heavy metals in soils.

Figure 6–6 shows adsorption results using the SOTS model based on two model versions. The associated estimates of the parameters that provided model results along with their standard errors are given in Table 6–5. For both model versions,  $S_{\text{max}}$  was not estimated rather the values used was 689.67 mg kg<sup>-1</sup> which was obtained from the Langmuir formulation (see Table 6–1). The goodness of fit of the model to the data is once gain based on  $r^2$  and rmse values that illustrate the versatility of the model. The question arises when we relaxed our assumption of the use of Langmuir  $S_{\text{max}}$  and utilized the SOTS with the optimization scheme to arrive at best estimate of the rate coefficients ( $k_1$ ,  $k_2$ , etc.) as well as  $S_{\text{max}}$ . The results of the optimization for the two model versions are also given in Table 6–5. Based on these results, it is clear that the use of Langmuir  $S_{\text{max}}$  as an input parameter provides reliable predictions of our adsorption kinetic results.

The success of the second-order approach in describing the Cu results is significant since, to our knowledge, the SOTS formulation described in this chapter has net been applied for heavy metals. Previous use of the second-order formulation that included a partitioning of the sites indicated that for Cr and Zn the rate coefficients were highly concentration dependent (Selim & Amacher, 1988; Hinz et al., 1992). In contrast, important features of the SOTS approach used here include the fact that the reaction rate coefficients are not concentration dependent, rather only one *overall* set of parameters is needed to describe the data. In addition, a prior knowledge of the fraction of the equilibrium to kinetic sites from total available is not needed. Moreover, the use of Langmuir  $S_{\text{max}}$  as an input parameter provided equally good prediction of our batch data.

# Hysteresis

Adsorption-desorption results are presented as isotherms in the traditional manner in Fig. 6-7 that clearly indicate considerable hysteresis for Cu. This hysteretic behavior resulting from discrepancy between adsorption and desorption isotherms was not surprising in view of the kinetic retention behavior of Cu in our soil. Several studies indicated that observed hysteresis in batch experiments may be due to kinetic retention behavior and slow release and/or irreversible adsorption conditions. Adsorption-desorption isotherms indicate that the amount of irreversible or nondesorbable phases increased with time of reaction. Copper may be retained by heterogeneous type sites having a wide range of binding energies. At low concentrations, binding may be irreversible. The irreversible amount almost always increased with time (Lehman & Harter, 1984). Recently, Wu et al. (1999) suggested that Cu hysteresis is probably due to extremely high energy bonding with organic matter and layer silicate surfaces. The fraction of nondesorbable Cu was referred to as specifically sorbed. Atanassova (1995) showed that desorption was non-hysteretic for a Planosol whereas strong desorption hysteresis was observed for a Vertisol. It was suggested that Cu was fixed in a nonexchangeable form that resulted in lack of reversibility as well as hysteretic behavior.

Many researchers reported that the magnitude of hysteresis increases with longer sorption incubation periods. Ainsworth et al. (1994) found that despite in-

Table 10–5. Goodness of fit of several versions of the second-order model for describing Cu adsorption on McLaren soil. Model versions A-1 and A-2 are based on concurrent irreversible reaction whereas versions B-1 and B-2 are based on the consecutive type.

Model version	Model r <sup>2</sup>	RMSE‡	$S_{\max}$	SE‡	$K_{l}$	SE	$K_2$	SE	$k_3$	SE	$k_4$	SE	<i>k</i> <sub>5</sub>	SE_	$K_{ m irr}$	SE
			- mg k	.g-1						—— h	1		<u> </u>			
A-1 A-2†	0.995 0.995	1.629 1.607	690.88 689.67			0.000 45 0.000 32		0.021 7 0.018 1		 		<del></del> 	 			0.000 020 0.000 013
B-1 B-2÷	0.995 0.995	1.623 1.621	642.16 689.67	44.80 				 		0.000 51 0.000 32			0.001 18 0.004 36			 

<sup>†</sup> S<sub>max</sub> is provided from Langmuir Eq. [16]. ‡ RMSE = root mean square error, SE= standard error.

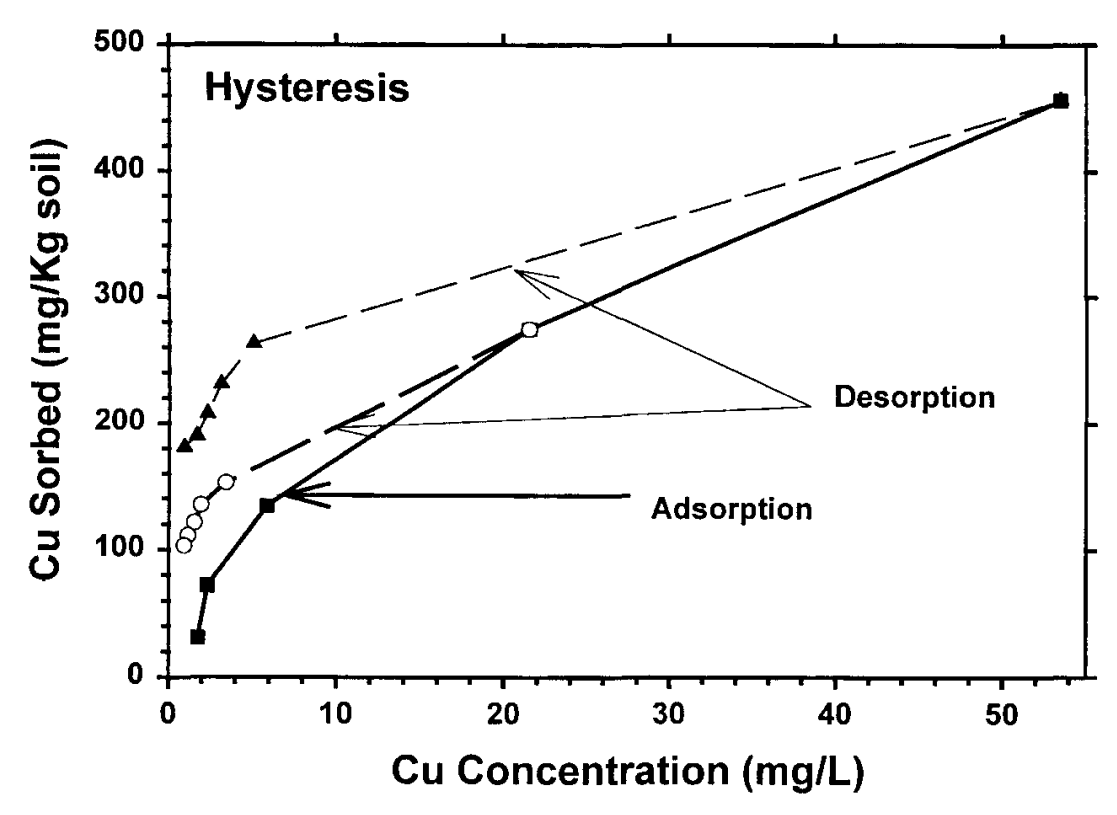


Fig. 6–7. Adsorption and desorption isotherms illustrating hysteresis behavior of Cu retention in McLaren soil.

creasing the desorption times from 16 h to 9 wk, hysteresis persisted for Co and Cd sorbed on hydrous ferric oxide. They also found that Cd and Co displayed increasing hysteretic behavior upon aging from 2 to 16 wk while Pb sorption/desorption behavior was reversible. Hysteresis has also been observed in ion exchange reactions for several cations, where the exchange of one sorbed cation with another is not completely reversible, i.e., the forward and reverse exchange reactions do not result in the same isotherms. The hysteretic behavior of cation exchange is abundantly reported in the literature; a critical review of this literature was published by Verburg and Baveye (1994). From a survey of the literature they were able to categorize several elements into three categories. The elements in each category were found to show hysteretic exchange between groups, but not within groups. Verburg and Baveye (1994) proposed that exchange reactions are most likely a multistage kinetic process in which the later rate-limiting processes are a result of physical transformation in the system, e.g., surface heterogeneity, swelling hysteresis, and formation of quasi-crystals, rather than simply a slow kinetic exchange process where there exists a unique thermodynamic relationship for forward and reverse reactions. While this may be true in some circumstances, an apparent (pseudo) hysteresis also can result from slow sorption and desorption reactions, i.e., lack of equilibrium (Selim et al., 1976). Regardless of the different reasons for hysteresis, it is evident that kinetic models such as those proposed in this study need to be complimented by detailed information on the mechanism(s) responsible for the slow kinetic reaction(s).

208 SELIM & MA

#### Validation

Validation of models such as the second-order and multireaction model requires model parameters to be estimated independently. Such a validation should be carried out prior to model adoption for prediction of retention and mobility of heavy metals in soils. This validation is also necessary for the use of a model for different soils and for a wide range of conditions. This requirement is not always achieved because independent parameters are not often available, however. As a result, evaluation of a model is sometimes restricted to goodness of fit of the model results to experimental measurements.

Validation of our proposed kinetic model is illustrated by the solid and dashed curves shown by the C vs time results shown in Figs. 6–8 and 6–9 for  $C_o$  of 50 and 100 mg L<sup>-1</sup>. Here all model parameters for both the multireaction and second-order models were based on adsorption data only. With the exception of  $\rho$  and  $\theta$ , initial conditions for this initial-value problem were the only input required. Based on these predictions, we can conclude that both models predicted Cu desorption or release behavior satisfactorily. However, predictions of desorption isotherms were not considered adequate at the initial stages of desorption following adsorption. In addition, the model underpredicted amount sorbed that directly influences subsequent predicted are expected if the amounts of Cu in the various phases (C,  $S_e$ ,  $S_1$ , and  $S_2$ ) at each desorption step were significantly different. These underpredictions also may be due to the inherent assumptions of the model. Specifically, the models may

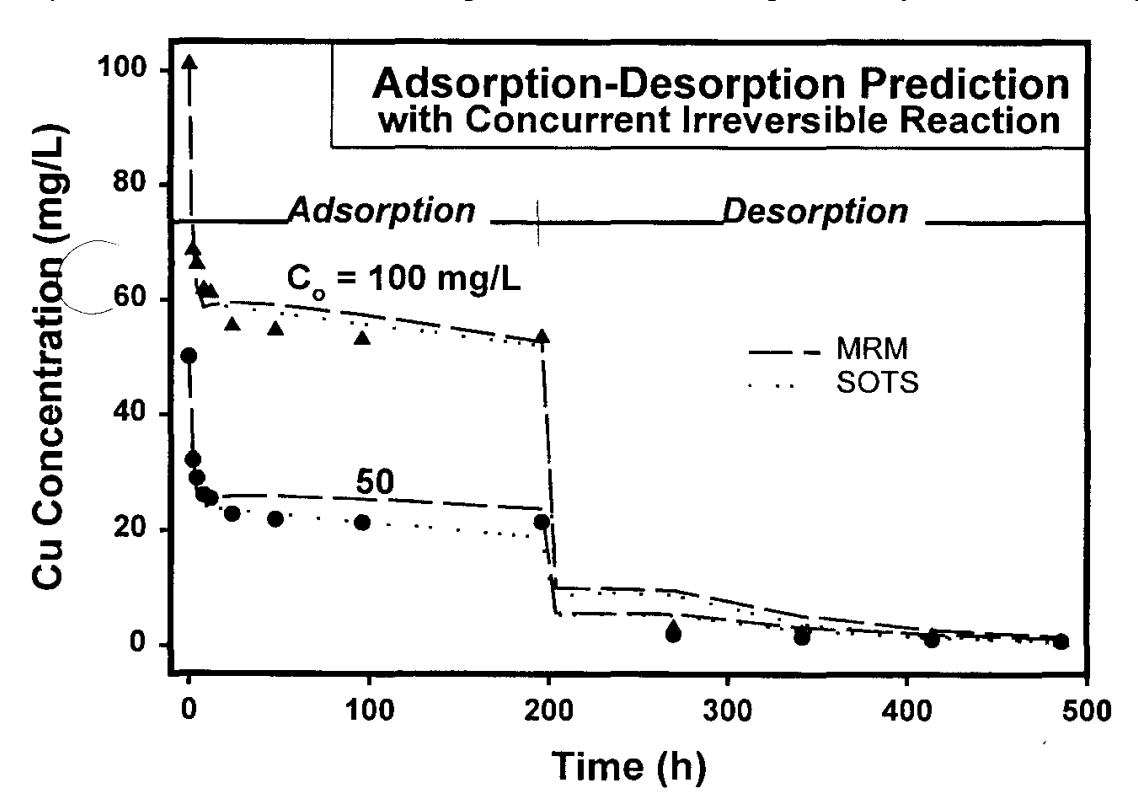


Fig. 6–8. Experimental results of Cu in soil solution for McLaren soil vs. time during adsorption and desorption for initial concentration  $C_0 = 50$  and 100 mg L. <sup>1</sup>. The solid and dashed curves are predictions based on parameters from adsorption data using the multireaction and second-order models given in Tables 6–4 and 6–5, respectively. The irreversible mechanism was accounted for based on concurrent reactions.

not account for all retention or provide incomplete description of Cu reactions in soils.

Finally, based on literature review, most retention experiments were designed for adsorption measurements where desorption data were not always sought. Therefore, kinetic retention models, such as those proposed in this study, which are capable of *predicting* desorption behavior of heavy in soils based solely on adsorption parameters are of practical importance. Based on our results, the overall goodness of our model predictions are considered adequate and provides added credence to the applicability of our proposed model approaches. Moreover, adsorption as well as desorption results, the second-order model was superior compared to the multireaction model. Furthermore, model formulations with consecutive irreversible retention, for MRM as well as SOTS, provided better Cu description than other model versions.

#### SUMMARY AND CONCLUSIONS

The kinetic behavior of Cu in McLaren soil, during adsorption and desorption, is consistent with observation for other heavy metals and soils. In fact, several researchers have noted that not only are heavy metals strongly sorbed and exhibit slow desorption kinetics, but that the rate of desorption decreases with increasing reaction. Padmanabham (1983) conducted desorption experiments of Cu from goethite and concluded that Cu was sorbed in two different ways: a fraction

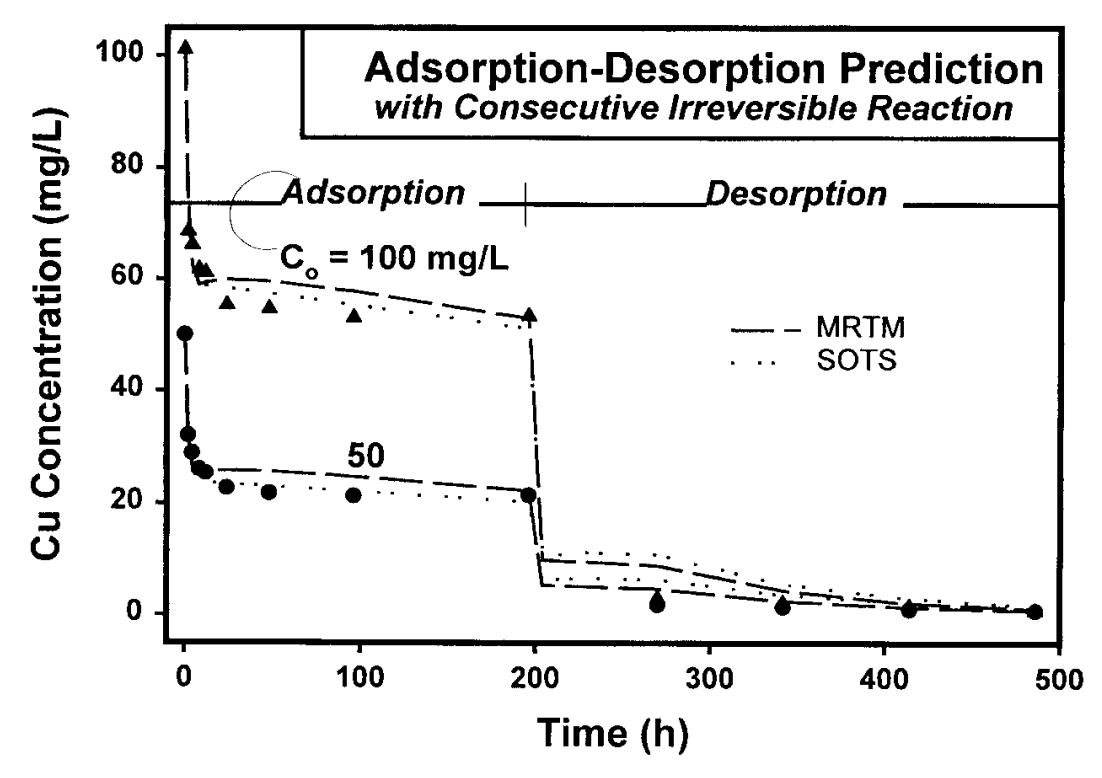


Fig. 6–9. Experimental results of Cu in soil solution for McLaren soil vs. time during adsorption and desorption for initial concentration  $C_0 = 50$  and  $100 \text{ mg L}^{-1}$ . The solid and dashed curves are predictions based on parameters from adsorption data using the multireaction and second-order models given in Tables 6–4 and 6–5, respectively. The irreversible mechanism was accounted for based on consecutive fractions

210 SELIM & MA

was associated with low bonding energy and the rest was associated with high bonding energy. It was observed that a gradual interchange with increasing incubation time occurs between the readily desorbed fraction (low energy) and the less readily desorbed fraction (high energy). Smith and Comans (1996) observed an increase in the slowly desorbed fraction of sorbed Cs from sediments with increasing incubation time. Modeling of their data using a two compartment model suggests that there exist an exchangeable sorbed fraction and a fixed fraction. Slow transfer between the two fractions was responsible for slow kinetics of sorption and desorption.

Mechanisms associated with our modeling efforts using MRM and SOTS consider at least two sorbed phases: a fully reversible phase and one which is fixed or characterized by slow release or irreversible. The reversible phase  $(S_1)$  and/or  $S_2$  represent kinetic type sites and  $S_e$  for equilibrium type sites. Adsorption reactions associated with  $S_e$ ,  $S_1$ , and  $S_2$  may include mechanisms such as inner-sphere complexes, outer-sphere complexes, and diffuse ions (Sposito, 1989). Outer-sphere bonds consist of a solvated ion that forms a complex with a charged functional group, the primary bonding force is electrostatic. An inner-sphere complex is partially dehydrated, the ion forms a direct ionic or covalent bond with the surface functional groups. A diffuse ion exists in the water layers near the surface, and is held by electrostatic attraction from permanent charges that exist in the solid structure. A major difference between the outer-sphere complex and the diffuse ion complex is in the strength of the electrostatic force, which is directly correlated to the proximity of the ion to the surface (McBride, 1994).

Mechanisms associated with irreversible reactions include different types of surface precipitation that accounts for the formation or sorption of metal polymers on the surface, a solid solution or coprecipitate that involves coions dissolved from the sorbent; and a homogeneous precipitate formed on the surface composed of ions from the bulk solution, or their hydrolysis products (Farley et al., 1985). The continuum between surface precipitation and chemisorption is controlled by several factors, including: (i) the ratio of the number of sites vs. the number of metal ions in solution; (ii) the strength of the metal-oxide bond; and (iii) the degree to which the bulk solution is undersaturated with respect to the metal hydroxide precipitate. Such mechanisms are consistent with one or more irreversible reactions associated with our model presented in Fig. 6–1. Based on the goodness of fit to our experimental results, irreversible retention of the consecutive type appears to be the dominant mechanism. This finding is equally applicable for the multireaction model as well as the second-order model.

Although, the above studies consider several possible forms of heavy metals species to be present in the soil environment, such do not provide the controlling mechanisms among the various species. However, the work of Lehman and Harter (1984) supports our assumption of a consecutive rather than a concurrent reaction for irreversible sorption. Lehman and Harter (1984) measured the kinetics of chelate promoted Cu release from a soil to assess the strength of the bond formed. Their sorption/desorption data were multisite, which they attributed to high and low energy bonding sites. They also found that with increased residence time, 30 min to 24 h, there was a transition of the Cu from low energy sites to high energy sites (as evaluated by release kinetics). Incubations for up to four days showed a con-

tinued uptake of Cu and a decrease in the fraction released within the first three minutes, which was referred to as the low energy adsorbed fraction. Kim et al. (1996) used nuclear magnetic resonance (NMR) spectroscopy to make microscopic observations of Cs sorption mechanisms on kaolinite, boehmite, silica gel, and illite. Their experiments coincide with those of Lehman and Harter (1984), suggesting that Cs formed two distinct types of complexes on the surfaces of the minerals: innersphere, and outer-sphere.

In conclusion, we presented clearly the kinetics of both sorption and desorption processes. The models are based on speculation of possible mechanism(s) that governs reaction kinetics. However, these hypotheses are based primarily on macroscopic data, while sorption and desorption processes are microscopic phenomena. At best, macroscopic investigations suggest a particular mechanism may be occurring; they provide little evidence that other mechanisms are not involved (Strawn & Sparks, 1999). Despite such difficulties, adequate predictions of sorption mechanisms based on macroscopic observations are presented. Based on our studies, to better predict the mechanisms responsible for the kinetic processes governing adsorption-desorption reactions, microscopic as well as macroscopic data are needed.

#### ACKNOWLEDGMENT

The authors express their thanks to Dr. Michael C. Amacher for his assistance in this study.

#### REFERENCES

- Ainsworth C.C., J.L. Pilon, P.L. Gassman, and W. G. Van der Sluys. 1994. Cobalt, cadmium, and lead sorption to hydrous iron oxide: Residence time effect. Soil Sci. Soc. Am. J. 58:1615–1623.
- Amacher, M.C., R.W. Brown, R.W. Sidle, and J. Kotuby-Amacher. 1995. Effect of mine waste on element speciation in headwater streams. p. 275–309. *In* H.E. Allen et al. (ed.) Metal speciation and contamination of soil. Lewis Publ., Boca Raton, FL.
- Amacher, M.C., J. Kotuby-Amacher, H.M. Selim, and I.K. Iskandar. 1986. Retention and release of metals by soils: Evaluation of several models. Geoderma 38:131–154.
- Amacher, M.C., H.M. Selim, and I.K. Iskandar. 1988. Kinetics of chromium(VI) and cadmium retention in soils: A nonlinear multireaction model. Soil Sci. Soc. Am. J. 52:398–408.
- Amacher, M.C., H.M. Selim, and I.K. Iskandar. 1990. Kinetics of mercuric chloride retention in soils. J. Environ. Qual. 19:382–388.
- Aringhieri, R., P. Carrai, and G. Petruzzelli. 1985. Kinetics of Cu<sup>2+</sup> and Ca<sup>+2</sup> adsorption by an Italian soil. Soil Sci. 139:197–204.
- Atanassova, I.D. 1995. Adsorption and desorption of Cu at high equilibrium concentrations by soil and clay samples from Bulgaria. Environ. Pollut. 87:17–21.
- Buchter, B., B. Davidoff, M.C. Amacher, C. Hinz, I.K. Iskandar, and H.M. Selim. 1989. Correlation of Freundlich K<sub>d</sub> and n retention parameters with soils and elements. Soil Sci. 148:370–379.
- Buchter, N., C. Hinz, M. Gfeller, and H. Hinz. 1996. Cadmium transport in an unsaturated stony subsoil monolith. Soil Sci. Soc. Am. J. 60:716–721.
- Cernik, M., P. Federer, M. Borkovec, and H. Sticher. 1994. Modeling of heavy metal transport in a contaminated soil. Soil Sci. Soc. Am. J. 58:1239–1248.
- Cavallaro, N, and M.B. McBride. 1978. Copper and cadmium adsorption characteristics of selected acid and calcarcous soils. Soil Sci. Soc. Am. J. 42:550–556.
- Cavallaro, N., and M.B. McBride. 1984. Zine and copper sorption and fixation by an acid soil clay: Effect of selective dissolution. Soil Sci. Soc. Am. J. 48:1050–1054.

212 SELIM & MA

Farley K.J., D.A. Dzombak, and F.M.M. Morel. 1985. A surface precipitation model for the sorption of cations on metal oxides. J. Colloid Interface Sci. 106:226–242.

- Harter, R.D. 1984. Curve-fit errors in Langmuir adsorption maxima. Soil Sci. Soc. Am. J. 48:749-752.
- Hinz, C., B. Buchter, and H.M. Selim. 1992. Heavy metal retention in soils: Application of multisite models to zinc sorption. p. 141–170. *In* I.K. Iskandar and H.M. Selim (ed.) Engineering aspects of metal-waste management. Lewis Publ., Boca Raton, FL.
- Hinz, C., and H.M. Selim. 1994. Transport of Zn and Cd in Soils: Experimental evidence and modelling approaches. Soil Sci. Soc. Am. J. 58:1316–1327.
- Hinz, C., H.M. Selim, and L. A. Gaston. 1994. Effect of sorption isotherm type on predictions of solute mobility in soil. Water Resour. Res. 30:3013–3021.
- Houng, K.-H., and D.-Y. Lee. 1998. Comparison of linear and nonlinear Langmuir and Freundlich Curvefit in the study of Cu, Cd, and Pb adsoption on Taiwan soils. Soi. Sci. 163:115–121.
- Kim Y., R.J. Kirkpatrick, and R.T. Cygan. 1996. <sup>133</sup>Cs NMR study of cesium on the surfaces of kaolinite and illite. Geochim. Cosmochim. Acta 60:4059–4074.
- Kinniburgh, D.G. 1986. General purpose adsorption isotherms. Environ. Sci. Technol. 20:895–904.
- Lehman, R.G., and R.D. Harter. 1984. Assessment of Copper-soil bond strength by desorption kinetics. Soil Sci. Soc. Am. J. 48:769–772.
- Ma, L., and H.M. Selim. 1997. Evaluation of nonequilibrium models for predicting atrazine transport in soils. Soil Sci. Soc. Am. J. 61:1299-1307.
- McBride M.M. 1994. Environmental chemistry of soils. Oxford Univ. Press, New York.
- Montero, J.P., J.O. Munoz, R. Abeliuk, and M. Vauclin. 1994. A solute transport model for the acid leaching of copper in soil columns. Soil Sci. Soc. Am. J. 58:678–686.
- Padmanabham, M. 1983. adsorption-desorption behavior of copper (ii) at the goethite solution interface. Aust. J. Soil Res. 21:209–320.
- Schulte, A., and F. Beese. 1994. Isotherms of cadmium sorption dernsity. J. Environ. Qual. 23:712–718.
- Selim, H.M., and M.C. Amacher. 1988. A second-order kinetic approach for modeling solute retention and transport in soils. Water Resour. Res. 24:2061–2075.
- Selim, H.M., and M.C. Amacher. 1997. Reactivity and transport of heavy metals in soils/CRC/Lewis Publ., Boca Raton, FL.
- Selim, H.M., B. Buchter, C, Hinz, and L. Ma. 1992. Modeling the transport and retention of cadmium in soils: Multireaction and multicomponent approaches. Soil Sci. Soc. Am. J. 56:1004–1015.
- Selim, H.M., J.M. Davidson, and R.S. Mansell. 1976. Evaluation of a two-site adsorption-desorption model for describing solute transport in soils. p. 444–448. *In* Proc. Summer Comput. Simulat. Conf., Washington, DC. 12–14 July. Simulat. Counc., LaJolla, CA.
- Sequi, P., and R. Aringhieri. 1977. Destruction of organic matter by hydrogen peroxide in the presence of pyrophosphate and its effect on soil specific surface area. Soil Sci. Soc. Am. J 41:340–342.
- Strawn, D.G., and D.L. Sparks. 1999. Sorption kinetics of trace metals in soils and soil materials. p. 1–28. In H.M. Selim and I.K. Iskandar (ed.) Fate and transport of heavy metals in the vadose zone. CRC/Lewis Publ., Boca Raton, FL.
- Smith J.T., and R.N.J. Comans. 1996. Modeling the diffusive transport and remobilization of cs<sup>137</sup> in sediments: The effects of sorption kinetics and reversibility. Geochim. Cosmochim. Acta 60:995–1004.
- Sposito, G. 1982. On the use of the Langmuir equation in the interpretation of "adsorption" phenomena. II. The "two-surface" Langmuir equation. Soil Sci. Soc. Am. J. 46:1157–1152.
- Sposito, G. 1989. The chemistry of soils. Oxford Univ. Press, New York.
- van Genuchten, M.Th. 1981. Non-equilibrium transport parameters from miscible displacement experiments. Res. Rep. no. 119. U.S. Salinity Lab., Riverside, CA.
- Verburg K., and P. Baveye. 1994. Hysteresis in the binary exchange of cations on 2:1 clay minerals: A critical review. Clays Clay Miner. 42:207–220.
- Wu, J., D.A. Laird, and M.L. Thompson. 1999. Sorption and desorption of copper on soil clays components. J. Environ. Qual. 28:334–338.

# Application of Spectroscopic Methods to Sorption Model Parameter Estimation

Lynn E. Katz

University of Texas Austin, Texas

Eric J. Boyle-Wight

University of Maine Orono, Maine

Macroscopic data for the sorption of Co(II), Cd(II) and Sr(II) to  $\alpha$ -Al<sub>2</sub>O<sub>3</sub> were used in conjunction with x-ray absorption spectroscopy (XAS) data to estimate triple layer (TLM) surface complexation model parameters. The XAS results showed that Co(II) and Cd(II) sorbed as inner-sphere surface complexes and that Sr(II) sorbed as an outer-sphere complex. In addition, surface precipitation was observed only in the case of Co(II) sorption. Surface complexation model reactions were selected based on the XAS results for each divalent metal ion, and surface acidity constants were determined using potentiometric titration data. A solid solution version of the TLM that appears to be consistent with the spectroscopic data was used to describe the sorption of Co(II). The modeling results predicted that Co(II) sorption is dominated by mononuclear surface complexes at low surface coverage and by Co(II)/Al(III) surface precipitates at high surface coverage. In order to model the Cd(II) sorption data throughout the range of data presented by Honeyman (1984), it was necessary to incorporate a second high energy surface hydroxyl site. In contrast to the Co(II) data, it was not necessary to incorporate a solid solution model to predict sorption data collected at high coverage. The effects of ionic strength on Sr(II) adsorption to  $\alpha$ -Al<sub>2</sub>O<sub>3</sub> could be described using two outer sphere reactions. The results shown in this chapter demonstrate the effectiveness of surface complexation models when the selection of surface reactions and parameter estimation are constrained by independent measurements.

## INTRODUCTION

The prevalence of toxic metal ions in contaminated aqueous and terrestrial environments represents a significant environmental risk. Effective pollution con-

trol and remediation strategies for toxic metal ions require accurate descriptions of their fate and transport in the environment. Inorganic species present in soil and aqueous systems may undergo a range of reactions that will affect their mobility and bioavailability in the environment. These reactions include complexation, precipitation-dissolution, oxidation/reduction and phase partitioning processes. The least understood and perhaps most dominant of these reactions are those associated with partitioning of the contaminants to soil surfaces, commonly referred to as sorption processes. Sorption of a contaminant to soil may occur by adsorption at the mineral/water interface, absorption within soil organic matter, or through formation of a surface or co-precipitate. The type of sorption process that dominates in a particular system is highly dependent on the type of mineral phases present and the properties of the sorbing species. Solution conditions such as pH, ionic strength, metal ion concentration, and the presence and concentration of other sorbing or complexing species can also control the extent and type of operative sorption process.

While the rates and extent of sorption will differ significantly for each of these sorption processes, approaches commonly employed to describe metal ion sorption often fail to distinguish among them. Indeed, the most common approach to describing metal ion sorption has been to fit data to empirical isotherm models that relate the total concentration of solute in solution phase to its total sorbed concentration. The simplicity of implementing these empirical descriptions of sorption into field-scale transport models makes them an attractive alternative. Unfortunately, these empirical models exhibit limited ability to predict sorption outside of the range of conditions (i.e., pH, sorbate and sorbent concentrations, ionic strength, and solution composition) for which they were calibrated, and therefore are not adequate predictive tools. Over the past several decades there has been a substantial research effort directed toward developing mechanistic models capable of describing sorption reaction phenomena over a range of field-scale behavior. These research efforts have led to the development and refinement of modeling approaches that attempt to accurately depict the reaction of sorbates with mineral surfaces.

Surface complexation models (SCM) have emerged at the forefront of these more thermodynamic descriptions of adsorption and many geochemical speciation models have incorporated various SCM into their code's behavior (Davis et al., 1978; Davis & Leckie, 1978, 1980; Stumm et al., 1980; Barrow et al., 1980, 1981; Hayes & Leckie, 1986; Hiemstra et al., 1989a,b; Dzombak & Morel, 1990; Robertson & Leckie; 1997; Goldberg, 1992). All SCM are based on the assumption that reactions between surface functional groups and sorbing species are analogous to aqueous solution complexation reactions. Differences among the various models stem primarily from their description of the surface/water interfacial region. While SCM were originally developed and applied to describe sorption of cations and anions to oxide, hydroxides and oxyhydroxides, they have since been applied to sorption of metal cations, oxyacids, organic acids and metal-ligand complexes to pure mineral phases, mixed mineral assemblages, clays, and natural soils.

During the early development of these surface complexation models, the selection of a particular reaction was based on its ability to fit adsorption data collected in macroscopic experiments in which the extent of sorption was expressed by quantifying the mass of solute lost from solution as a function of pH. Model refinements were based on attempts to more accurately describe surface charge behavior, ionic strength effects, proton release and sorption over a large range of total solute/sorbent ratios. Unfortunately, the selection of the appropriate reaction was often dependent on the selection of the particular model and a number of different model reactions were able to fit selected data sets reasonably well. However, the ability to extend sorption predictions beyond the range of experimental data used to derive the reaction constants was tenuous.

In order for SCM to serve as predictive tools in natural systems, operative reaction phenomena must be described accurately over the range of conditions expected in field-scale scenarios. This requirement is even more evident in light of studies showing that sorption of metal ions can affect the subsequent sorption of other solution species (McBride, 1985a,b; Stahl & James, 1991), the surface charge characteristics of the mineral phase (Hendershot & Lakkluich, 1983; Hansmann & Anderson, 1985; Anderson & Benjamin, 1990; Ryan & Gschewend, 1992; Herrera-Urbina & Furstenau, 1995), the morphology of the mineral phase (Johnsson, 1994), the rate of surface enhanced oxidation and hydrolysis (Fendorf et al., 1993; Torrents & Stone, 1994; Baolin & Stone, 1996); the rate of mineral dissolution (Bondietti et al., 1993; House, 1994; Stumm, 1997) and the coagulation properties of mineral phases (Liang & Morgan, 1990).

Over the past several decades, molecular spectroscopy and microscopy have emerged as the most promising tools for confirming: (i) the types of functional groups present on mineral surfaces; (ii) the location of sorbed species with respect to the surface; and, (iii) the molecular structure of sorbed complexes and surface precipitates. Over the past 10 yr the most promising of these spectroscopic tools has been synchrotron-based XAS. XAS can provide quantitative structural data of the coordination environment of sorbing metal ions on pure minerals and natural sorbents in systems containing metal ion concentrations as low as 10 g cm<sup>-3</sup> (Brown, 1990). Specifically, extended x-ray absorption fine structure (EXAFS) data can yield the identity of first and second nearest neighbors, coordination numbers, and distances from the sorbing metal ion and the first and second nearest neighbors. Because the technique does not require a vacuum for analysis of transition metals, sorption samples can be analyzed in an aqueous environment. This tool has been applied to differentiate between inner-sphere and outer-sphere complexes (Hayes & Leckie, 1986), mononuclear, polynuclear complexes and surface precipitates (Chisholm-Brause et al., 1990; Charlet & Manceau, 1992, 1994; O'Day et al., 1994a,b, 1996; Papelis et al., 1995; Hayes & Katz, 1996; Towle et al., 1997; Schiedegger et al., 1997, 1998; Thompson et al., 1999), monodentate and bidentate surface complexes (Chisholm-Brause, 1991; Bargar et al., 1997; Brown et al., 1999), internal and external sorption on clays (Papelis & Hayes, 1996; Chen & Hayes, 1999) and binary and ternary complex formation (Bargar et al., 1998).

The incorporation of this information into surface complexation models will allow their application to more complex systems and will provide scientists and engineers with the tools necessary to accurately predict metal ion sorption at field-scale. Thus, the goal of this chapter is to demonstrate a methodology for calibrating a surface complexation model using spectroscopic information to guide the selection of model reactions. A brief review of divalent metal cation sorption and the dependence of sorption processes on solution conditions is provided to establish the basis for surface complexation modeling. Background information on the the-

oretical framework of the SCM approach is also provided to introduce the number and type of parameters that must be evaluated for applying SCM. The modeling approach previously developed and applied to the cobalt/ $\alpha$ -Al<sub>2</sub>O<sub>3</sub> system is then reviewed and applied to two different divalent metal cation/ $\alpha$ -Al<sub>2</sub>O<sub>3</sub> systems.

## **BACKGROUND**

The dependence of mineral surface charge and metal ion sorption on the properties of mineral oxides, metal ions, and solution conditions has been summarized in a number of previous reviews (see, e.g., James & Parks, 1982; Schindler & Stumm, 1987; Dzombak & Morel, 1990; Davis & Kent, 1990; Stumm, 1992; McBride, 1994; Hayes & Katz, 1996). The surface charge of many minerals is known to vary as a function of pH and is typically characterized by the point of zero charge of the mineral (pH<sub>pzc</sub>). Below the pH<sub>pzc</sub>, a mineral carries a net positive charge and above the pH<sub>pzc</sub> the mineral carries a negative surface charge. The variable charge associated with oxide, hydroxide and oxyhydroxide minerals derives from the acid/base characteristics of hydroxyl groups on the surface.

In general,  $pH_{pzc}$  values for silica and manganese oxides are below pH 7 and values for aluminum and iron oxides are greater than pH 7. Therefore, the electrostatic attraction of a divalent metal ion for a particular mineral will vary with pH. The adsorption of divalent cations is expected to increase with increasing pH as the surface becomes less positively charged. For example, Fig. 7–1 demonstrates the shift in the fractional pH adsorption edge of cadmium (Cd(II)) with pH<sub>pzc</sub> of the sorbent. Reported pH<sub>pzc</sub> values of rutile, ferrihydrite and corundum ( $\alpha$ -Al<sub>2</sub>O<sub>3</sub>) are 5.8, 8.5 and 8.9, respectively (Davis & Kent, 1990; Stumm, 1992; Hayes et al., 1990). Adsorption of Cd(II) for all of the minerals shown occurs below its reported pH<sub>pzc</sub>.

This ability to sorb against a positive surface charge is common for many strongly sorbing divalent metal ions and suggests that adsorption to the oxide surface cannot be solely attributed to ion pair formation with surface sites. Strongly sorbing metal ions are found in the middle of the periodic table and include the divalent transition (e.g., Zn Cu, Ni, Co, Fe, and Mn) and other heavy metal cations (e.g., Cd and Pb). For these divalent cations, sorption has been found to occur through inner-sphere coordination of the metal ions with surface hydroxyls. The XAS studies conducted by a number of investigators have confirmed the formation of inner-sphere surface complexes with a number of these divalent metal ions (Chisholm-Brause et al., 1990; Fendorf et al., 1994; O'Day et al., 1994a,b, 1996; Towle et al., 1997; Bargar et al., 1997a,b; Strawn et al., 1998). For example, EXAFS has demonstrated that cobalt (Co(II)) sorbs to  $\alpha$ -Al<sub>2</sub>O<sub>3</sub>,  $\gamma$ -Al<sub>2</sub>O<sub>3</sub>, and kaolinite through an inner-sphere reaction in which Co(II) is bonded directly to the surface (Chisholm-Brause, 1991; O'Day et al., 1994a,b, 1996; Bargar et al., 1997b). Similarly, Bargar et al. (1997a), and Strawn et al. (1998) have shown that Pb sorbs to  $\alpha$ -Al<sub>2</sub>O<sub>3</sub>,  $\gamma$ -Al<sub>2</sub>O<sub>3</sub>, hematite and goethite primarily as inner-sphere complexes.

In contrast to the transition metals, divalent alkaline earth metal ions typically sorb at pH values above the pH<sub>pzc</sub>. For these cations, sorption is believed to occur primarily through relatively weak ion pair formation (outer sphere complexes). The relative affinity to form complexes with surface hydroxyls can be correlated with

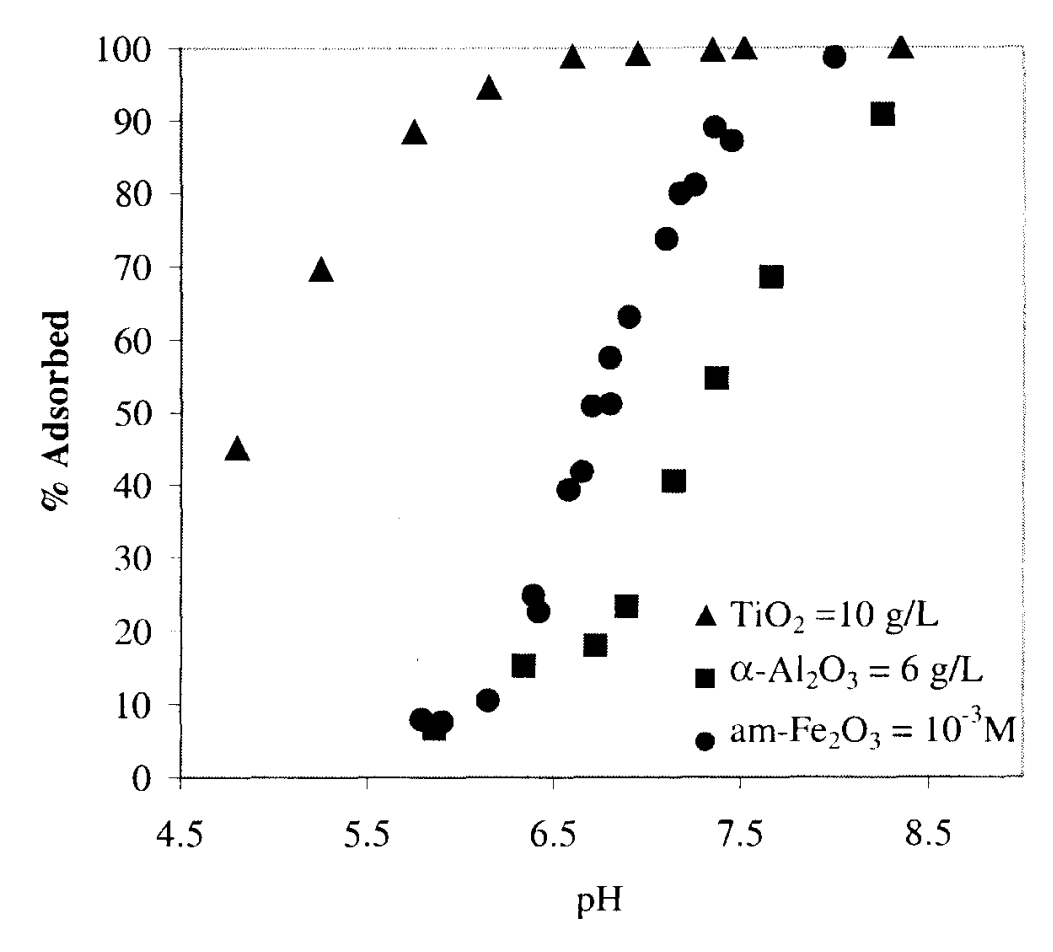


Fig. 7–1. Fractional pH adsorption edges for Cd sorption [10<sup>-6</sup> M Cd(II) added to solution] to corundum, ferrihydrite (am-Fe<sub>2</sub>O<sub>3</sub>) and rutile (adapted from Honeyman, 1984).

the inverse of the ionic radii if coulombic forces dominate over ion-dipole and ion induced-dipole interactions between the counter ions and water molecules (Eisenmann, 1962). Based on the ionic radii shown in Table 7–1, the following selectivity trends are expected for the alkaline earth ions assuming that coulombic forces dominate:

$$Mg^{2+} > Ca^{2+} > Sr^{2+} > Ba^{2+}$$
.

Table 7–1. Ionic radii of selected divalent metal ions.

Divalent metal ion	Ionic radius (pm)†	
Cd	95.0	
Co	74.5	
Cr	61.5	
Ni	69.0	
Pb	119.0	
Al	53.5	
Mg	72.0	
Ca	100.0	
Sr	118.0	
Ba	135.0	

ERadii are for a coordination number of six (data are from Shannon, 1976).

The above sequence has been observed in studies of alkaline earth adsorption on  $\gamma$ -Al<sub>2</sub>O<sub>3</sub> (Huang & Stumm, 1973). The trend is also consistent with the expectation based on the expected preference of harder Lewis acids for hard Lewis bases like surface hydroxyls. Limited spectroscopic evidence is available for sorption of alkaline earth metals because many of these metals do not exhibit sufficiently high K-shell fluorescence energies to be studied in the presence of corundum and water using current EXAFS methods. Chen and Hayes (1999) have shown that Sr(II) sorbs to montmorillonite, illite, and hectorite primarily as a weakly associated outersphere complex. Similar findings have been reported for sorption of Sr(II) to clay minerals (Parkman et al., 1998; O'Day et al., 2000; Sahai et al., 2000).

It has also become commonly accepted that the dependence of sorption on ionic strength is also a function of the strength of bonding and whether an inner-or outer-sphere complex forms (Hayes & Leckie, 1986). For example, as shown in Fig. 7–2, strontium (Sr(II)) sorption to α-Al<sub>2</sub>O<sub>3</sub> is highly dependent on the concentration of the background electrolyte, NaNO<sub>3</sub>, whereas Co(II) sorption appears to be unaffected by increases in NaNO<sub>3</sub> concentrations. The lack of ionic strength effect for Co(II) adsorption is consistent with spectroscopic data (Hayes & Katz, 1996; Towle et al., 1997; Bargar et al., 1997) indicating that Co(II) forms an innersphere complex with surface hydroxyl groups. The EXAFS data for Sr(II) on corundum has yet to be reported in the literature, however, the Sr(II) data is consistent with the findings for clay minerals (Parkman et al., 1998: Chen & Hayes, 1999; O'Day et al., 1999a,b).

While many of these hypotheses have become commonly accepted axioms, it must be recognized that these generalizations are oversimplifications. Outer-sphere complexes have been observed in systems for which macroscopic data showed a lack of ionic strength dependence, and there are examples in the literature in which strongly sorbing metal ions exhibit ionic strength dependence (Kosmulski, 1996; Bargar et al., 1997b). For example, studies reported by Bargar et al. (1997b) on single crystals indicate that Pb can form both inner- and outer-sphere complexes depending on the crystallographic surface. In studies with an oriented single crystal of  $\gamma$ -Al<sub>2</sub>O<sub>3</sub>, Pb(II) formed outer-sphere complexes on the  $\gamma$ -Al<sub>2</sub>O<sub>3</sub> (0001) surface and inner-sphere complexes on the  $\gamma$ -Al<sub>2</sub>O<sub>3</sub> (1102) surface. These differences have been explained using bond valence theory to distinguish between the affinity of Pb(II) for the different crystal faces. These findings further highlight the deficiencies associated with relying solely on macroscopic sorption data to guide the selection of surface complexes in SCM applications and reiterate the need for spectroscopic identification of surface complexes.

The utility of EXAFS has been especially evident in recent studies examining the formation of surface precipitates. A number of investigators have suggested the formation of surface precipitates to explain poor SCM model fits in data ranges for which the surface concentration of sorbed metal ion is high, but the system is undersaturated with respect to bulk metal ion solubility (Farley et al., 1985; Dzombak & Morel, 1990; Charlet & Manceau, 1992). Recent research in the geochemical, soil science, and environmental literature has confirmed the formation of polynuclear sorbate structures with varying surface loadings of Co(III), Cr(II), Cu(II), Ni(II), and Pb(II) on a wide variety of metal oxide and clay mineral surfaces (Chisholm-Brause et al., 1990; Charlet & Manceau, 1992, 1994; Fendorf et al., 1994;

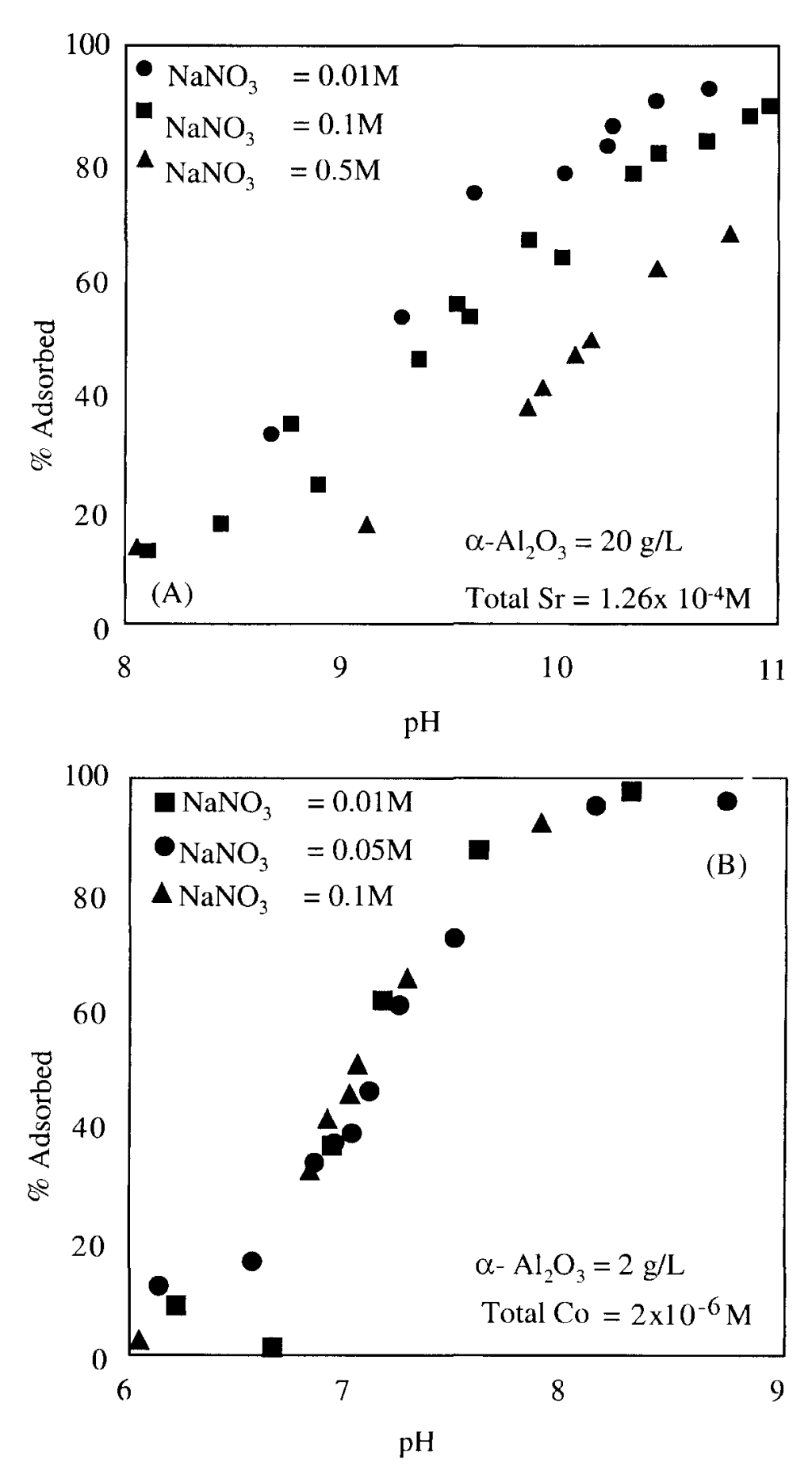


Fig. 7—2. Effect of increasing ionic strength on pH adsorption edges for (A) a weakly sorbing divalent metal, Sr(II); and (B) a strongly sorbing divalent metal ion, Co(II).

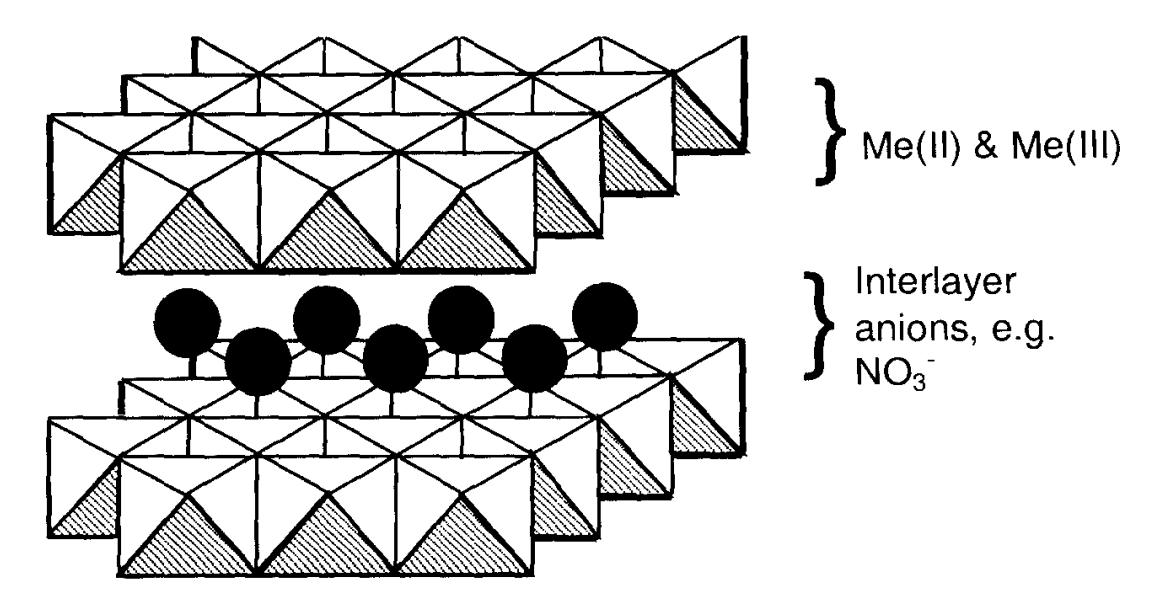


Fig. 7–3. Representative hydrotalcite structure. The charge imparted by Al<sup>3+</sup> incorporation into the edge-sharing octahedra of the brucite sheets is compensated by charge balancing anions in the interlayer.

O'Day et al., 1994a,b, 1996; Hayes & Katz, 1996; Papelis & Hayes, 1996; Scheidegger et al., 1997, 1998; Towle et al., 1997; Xia, 1997). The formation of these surface precipitates occurs below bulk solution saturation for precipitation of pure metal hydroxide phases and at submonolayer surface coverages in many of the cases cited above.

Surface precipitates formed during sorption of Co(II) and Ni(II) to aluminum oxide and clay systems are similar to the hydrotalcite group of minerals identified in geologic weathering environments (Bish, 1980) and consist of brucitelike layers of edge-sharing metal octahedra interlayered by charge-compensating anions (see Fig. 7–3). The general structural formula can be expressed [Me(II)<sub>1-x</sub> Me(III)<sub>x</sub>(OH)<sub>2</sub>]<sup>x+</sup> [A<sup>n-</sup><sub>x/n</sub> YH<sub>2</sub>O]<sup>x-</sup> (Brindley & Kikkawa, 1979; Hashi et al., 1983; Taylor, 1984) where the presence of interlayer anions, A<sup>n-</sup>, is required to compensate the excess positive charge imparted by Al<sup>3+</sup> substitution into the octahedral layer (Fig. 7–3). EXAFS can be used to analytically distinguish these phases from pure metal hydroxides because Al<sup>3+</sup> incorporation leads to a contraction in the average Me-O-Me bond and reduction in the number of nearest-neighbor Me ions (de la Caillerie et al., 1995; Bellotto et al., 1996, Scheidegger et al., 1997; Towle et al., 1997).

The formation of mixed metal hydroxide precipitates is not expected for all divalent metal ions. In a recent paper by Bargar et al. (1997) examining sorption of Pb(II) on α-Al<sub>2</sub>O<sub>3</sub> using EXAFS, the formation of small multinuclear clusters observed at high coverage were not consistent with the formation of a mixed metal hydroxide precipitate. Similar results were obtained by Strawn et al. (1998) in the study of Pb(II) sorption complexes on γ-Al<sub>2</sub>O<sub>3</sub>. In this study, no surface precipitates were detected after 23 d of equilibration and EXAFS data suggested that Pb(II) primarily formed a monomeric inner-sphere complex with Al(III) hydroxyl functional groups. It was hypothesized that the lack of formation of a surface precipitate for Pb was due to the large ionic radius of Pb relative to Al(III). In a study of Cd(II) adsorption to porous transition aluminas (Papelis et al., 1995), there was also no evidence supporting the formation of polynuclear cadmium surface complexes

Parameter	Description
$\overline{N_{\rm s}}$	Site density
$K^{+}$	Mass law formation constant for SOH <sup>2+</sup>
$K^-$	Mass law formation constant for SO <sup>-</sup>
$K_{\mathrm{cat}}$	Mass law formation constant for background electrolyte cation
$K_{\rm an}$	Mass law formation constant for background electrolyte anion
$C_1$	Inner layer capacitance for describing relationship between charge and potential
$C_2$	Outer layer capacitance for describing relationship between charge and potential
$\tilde{K_{ m Me}}$	Mass law formation constant for complexation between metal ion and surface hydroxyl

Table 7–2. TLM parameters and potential metal ion sorption reactions.

Hypothetical reaction	Complex formed
$SOH + Me^{2+} \Leftrightarrow SO^{-} - Me^{2+} + H^{+}$	(Outer-sphere)
$SOH + Me^{2+} + H_2O \Leftrightarrow SO^MeOH^+ + 2H^+$	(Outer-sphere)
$SOH + Me^{2+} \Leftrightarrow SOMe^{+} + H^{+}$	(Inner-sphere, mononuclear, -dentate)
$SOH + Me^{2+} + H_2O \Leftrightarrow SOMeOH + 2H^+$	(Inner-sphere, mononuclear, -dentate)
$SOH + Me^{2+} + An^{-} \Leftrightarrow SOMeAn + H^{+}$	(Inner-sphere, mononuclear, ternary)
$SOH + Me^{2+} + An^{-} \Leftrightarrow SOHMeAn^{+}$	(Inner-sphere, mononuclear, ternary)
$SOH + Me^{2+} + An^- \Leftrightarrow SOMe^+ - An^- + H^+$	(Inner-sphere, mononuclear, ternary)
$2SOH + Me^{2+} + H_2O \Leftrightarrow (SO)_2Me + 2H^+$	(Multidentate)
$SOH + 4Me^{2+} + 3H_2O \Leftrightarrow SO(Me)_4(OH)_3^{4+} + 4H^+$	(Multinuclear)
$SOH + Me^{2+} + 2H_2O \Leftrightarrow (SOH)Me(OH)_{2(s)} + 2H^+$	(Surface precipitate)

in systems that were undersaturated. However, in systems that were well oversaturated with respect to cadmium hydroxide solubility, precipitate formation was observed during sample preparation and was apparent in the EXAFS spectra. Re-examination of Table 7–1 suggests that the lack of surface precipitation in this system may also be due to the large ionic radius of Cd(II) relative to Al(III).

These results suggest that the sorption mechanisms of Sr(II), Cd(II) and Co(II) to aluminum oxides are distinctly different. Spectroscopic data for Sr(II) adsorption to clays and to iron oxide suggest that Sr(II) adsorbs as an outer-sphere complex. Spectroscopic data for Co(II) adsorption to  $\gamma$ - $Al_2O_3$  suggest that Co(II) adsorbs as an inner-sphere complex and at high coverage a hydrotalcitelike surface precipitate forms that incorporates Al(III) from the sorbent phase. In contrast, the EXAFS data for Cd(II) sorption to aluminum oxides suggest that Cd(II) does not form surface precipitates, presumably due to its large ionic radius. Thus, these three compounds serve as excellent probes for evaluating SCM capabilities for describing sorption over a range of expected surface behavior.

#### SURFACE COMPLEXATION MODELS

A number of different surface complexation models have been applied to describe and predict divalent metal ion sorption data over the past 20 to 30 yr. All of the models incorporate surface acidity and the formation of metal ion complexes with surface hydroxyl groups via equilibrium mass law expressions such at those presented in Table 7–2. In addition, each model employs a description of the electrical double layer to correct for electrostatic effects at the mineral/water interface (as shown in Fig. 7–4 for the triple layer model and described in Table 7–3). These electrostatic effects arise from the presence of surface charge generated electrostatic

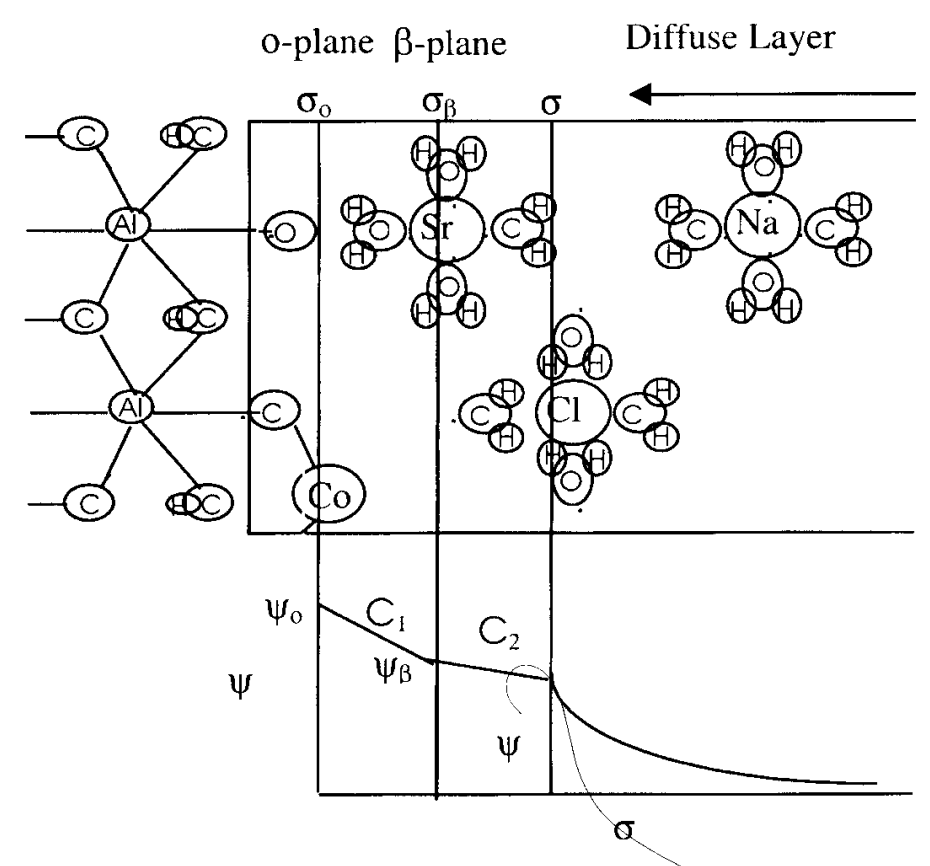


Fig. 7–4. Schematic representation of the triple layer surface complexation model showing the three planes of adsorption and the charge/potential relationship for each adsorption plane. In this modified version of the TLM (Hayes & Leckie, 1986), adsorption can occur either in the o-plane or the  $\beta$ -plane depending on the binding strength of the metal cation.

potential that diminishes as a function of distance from the surface. Each of the models offers a different conceptualization of the interfacial region. The models differ with respect to the type and location of sorbed surface species and in the formulations used to describe the relationship between surface charge and surface potential across the interfacial region (see Table 7–3). In addition, some models assume surface hydroxyl site heterogeneity. Model comparisons are provided in a number of reviews (Westall & Hohl, 1980; Davis & Kent, 1990; Goldberg, 1992; Hayes & Katz, 1996; Venema et al., 1996; Robertson & Leckie, 1997).

The most simplistic surface complexation models that incorporate electrical double layer theory are the diffuse layer model (DLM) and the constant capacitance model (CCM). In both of these models, all divalent metal ions sorb directly to the surface hydroxyl groups (at the o plane) and specific adsorption of electrolyte ions is ignored. The diffuse layer model has been widely used due to its simplicity and the development of an extensive database of metal ion binding constants for sorption to hydrous ferric oxide (Dzombak & Morel, 1990). In addition to the metal ion binding constants, it requires only three adjustable parameters to describe adsorption behavior; two surface acidity constants and the site density. The relationship between charge and potential is described by the Guoy/Chapman expression. The CCM requires one additional parameter to fit adsorption data, namely, a capacitance term to describe the charge/potential relationship and the parameters are strictly valid at only one ionic strength.

**Table** 7-3. Surface complexation reactions and model parameters.

			Location of complex		
Protolysis reactions	Mass law	Constant capacitance model	Diffuse layer model	Triple layer model	
Constant					
$SOH + H^+ = SOH_2^+$	<i>K</i> +		ø-plane	ø-plane	
$SOH = SO^- + H^+$	<i>K</i> <sup>-</sup>	ø-plane	ø-plane	ø-plane	
Surface complexation reactions					
$SOH + Me^{2+} = SOMe^{+}H^{+}$	$K_{ m Me}$	ø-plane	ø-plane	ø-or β-plane	
$SOH + L^{-} = SL + OH^{-}$	$K_{ m L}$	ø-plane	øplane	ø-or β-plane	
$SOH + Cat^+ = SO^ Cat^+ + H^+$	K <sub>Cat</sub>			β-plane	
$SOH + An^{-} + H^{+} = SOH_{2}^{+} - An^{-}$	$K_{An}$			β-plane	
Charge/potential relationships					
Location		Relationship	Relationship	Relationship	
$\sigma_{o}$ -plane		$C_1 \Psi_o$	$0.1174\sqrt{I} \sinh(zF\psi_{\rm d}/2RT)$	$/(\psi_{\rm o} - \psi_{\rm \beta})C_1$	
$\sigma_{ extsf{d}^-}$ plane			$0.1174\sqrt{I} \sinh(zF\psi_{\rm d}/2RT)$	$0.1174\sqrt{I} \sinh(zF\psi_d/2RT)$	
				$= -(\psi - \psi_{\rm d})C_2$	
Model parameters		$K^+, K^-, N_s C_1$	$K^+, K^-, N_s$	$K^+, K^-, K_{CAT}, K_{AN}, N_s, C_1, C_2$	

The triple layer model is one of the most commonly used models. It is more complex than either the DLM or CCM in that it allows adsorption to occur at various locations within the interfacial region depending on the type of complex formed as shown in Fig 7–4. As a result, it requires seven adjustable parameters in addition to the metal ion binding constants. These parameters include two capacitance values, two surface acidity constants, binding constants for the anion and cation of the background electrolyte, and site density. The model was initially developed and applied by Davis and Leckie (Davis et al., 1978; Davis & Leckie, 1978, 1980) and Morel et al. (1981) based on the works of Yates and Chan (Yates et al., 1974; Chan et al., 1975). Over the years, the model has undergone various modifications and extensions. The initial version of the TLM did not allow sorption directly to surface hydroxyls in the o-plane. One of the most significant modifications was to allow inner-sphere sorption at the o-plane (Hayes & Leckie, 1986a). Hayes and Leckie (1987) also modified the approach used to incorporate activity corrections; however, this modification has been criticized in recent literature (Criscenti & Sverjensky, 1999).

Thus, current versions of the model allow sorption of inner-sphere complexes directly to surface hydroxyls whereas outer-sphere complexes are located at the  $\beta$ -plane. Recent modifications have included an extension to allow parameter estimation of surface site densities, surface acidity constants and site densities using Born solvation and crystal chemical theory (Sverjensky, 1993, 1994; Sverjensky & Sahai, 1996; Sahai & Sverjensky, 1997a,b) and to treat electrolyte ions as non-specific adsorbing species that screen charge in the  $\beta$ -plane (Robertson & Leckie, 1997).

Offshoots of the TLM incorporate site heterogeneity and more complex representations of the interfacial region. In the CD-MUSIC surface complexation model, the charging mechanism of the surface oxygens was modified to allow the protonated surface oxygens to have fractional charge and to allow site heterogeneity (Hiemstra et al., 1989a,b). Model extensions were also made to account for differences between pH<sub>pzc</sub> and isoelectric point measurements in the "four layer model" (Bowden et al., 1980; Barrow et al., 1980, 1981; Bousse et al., 1991; Charmas et al., 1998). This model allows only potential determining ions (H<sup>+</sup> and OH<sup>-</sup>) at the o-plane. A new plane is provided to disallow adsorption of strongly sorbing cations directly to the surface and to distinguish between adsorption of cations and anions of the electrolyte. While these model extensions may provide a better representation of the electrical double layer region, they do so at the cost of adding even more parameters to the model. The selection of an appropriate model, therefore, typically represents a compromise between the accuracy of the model construct and the reliability of the model parameters. In many cases, models with fewer parameters can provide reasonable representations of experimental data over a fairly broad range of data.

The goal in applying any SCM is to develop a self-consistent methodology for parameter estimation such that a set of standard parameters to describe surface acidity, site density, and the charge/potential relationships for different minerals can be developed and can be used in conjunction with spectroscopic data to guide the selection of appropriate adsorption reactions for the formation of metal ion surface complexes (i.e., inner vs. outer sphere, mono vs. bidentate, mononuclear vs.

polynuclear adsorption). Dzombak and Morel (1990) made significant progress on this front for the DLM. After determining a representative site density and surface equilibrium constants for protonation of the surface of hydrous ferric oxide, they used FITEQL a nonlinear optimization program to determine surface binding constants for a wide range of metal cations and oxyanions (Westall, 1982). The limitation of their work with respect to the proposed methodology is that the metal ion surface binding reactions were not based on spectroscopic data. More recently, Hayes and Katz (1996) and Katz and Hayes (1995a,b) applied this methodology to the TLM for the adsorption of Co(II) to  $\gamma$ -Al<sub>2</sub>O<sub>3</sub>. In the remaining sections of this chapter the methodology for determining surface complexation modeling parameters for the TLM for Co(II) adsorption will be reviewed and then applied to Sr(II) and Cd(II) sorption.

#### METHODOLOGY

The TLM surface complexation model (modified by Hayes & Leckie, 1986a) contains a number of adjustable parameters to describe surface acidity, electrolyte surface binding, inner- and outer-layer capacitances and metal ion adsorption. These parameters are described in Table 7–2. In previous research, Hayes et al. (1990) and Hayes and Katz (1995a,b) developed a methodology for estimating these parameters for Co(II) adsorption to α-Al<sub>2</sub>O<sub>3</sub>. The methodology is described in detail in Katz and Hayes (1996). A similar approach is used here to describe Sr(II) sorption and Cd(II) sorption. Briefly, the approach involved characterizing the sorbent material and collecting potentiometric titration data for α-Al<sub>2</sub>O<sub>3</sub>, macroscopic sorption data for the metal ion sorption to  $\alpha$ -Al<sub>2</sub>O<sub>3</sub> and XAS spectroscopy data of the sorbate/sorbent phase. The potentiometric titration data were used in conjunction with an objective fitting routine (FITEQL, Westall, 1982) to determine the  $pH_{nzc}$ and to obtain the surface hydroxyl site density,  $N_s$ , the values for the two surface protolysis equilibrium constants,  $K^+$  and  $K^-$ , and the values for the electrolyte binding equilibrium constants,  $K_{AN}$  and  $K_{CAT}$ . The results of the XAS experiments were used to: (i) select appropriate SCM metal sorption reactions; and, (ii) an appropriate data set for calibrating the metal ion sorption equilibrium constants. The model parameters were then evaluated for their ability to predict the effects of ionic strength and surface coverage for a range of macroscopic sorption data sets. The experimental and modeling procedures used in this work are outlined below.

## **MATERIALS**

All of the experimental data to be modeled in this work utilized  $\alpha$ -Al<sub>2</sub>O<sub>3</sub> (Buehler LTD, Evanston, IL). This oxide has been subjected to previous SCM surface characterization (Honeyman, 1984; Hayes et al., 1991; Katz, 1993; Katz & Hayes, 1995a) and has similar sorption properties to other aluminum oxide minerals. The surface area of the material was determined to be  $12.6 \times 10^3$  m<sup>2</sup> kg<sup>-1</sup> using the N<sub>2</sub> BET method.

Points of zero charge can be determined experimentally through potentiometric titration at different ionic strengths, index ion adsorption or through elec-

Reaction	$\log K$	Source
$Co^{2+} + H_2O = CoOH^+ + H^+$	-9.7	Smith & Martell, 1993
$Co^{2+} + 2H_2O = Co(OH)_2^0 + 2H^+$	-18.8	Smith & Martell, 1993
$Co^{2+} + 3H_2O = Co(OH)_3^- + 3H^+$	-31.5	Smith & Martell, 1993
$2\text{Co}^{2+} + \text{H}_2\text{O} = \text{Co}_2\text{OH}^{3+} + \text{H}^+$	-11.2	Baes & Mesmer, 1976
$4\text{Co}^{2+} + 4\text{H}_2\text{O} = \text{Co}_4(\text{OH})_4^{4+} + 4\text{H}^+$	-30.5	Baes & Mesmer, 1976
$Co^{2+} + NO = CoNO_3^+ + H^+$	0.2	Smith & Martell, 1993
$Co^{2+} + 2NO = Co(NO_3)_2^0 + H^+$	-0.3(ionic strength = 0.5)	Smith & Martell, 1993
$Co^{2+} + 2H_2O = Co(OH)_{2(s)} + 2H^+$	-13.1	Smith & Martell, 1993
$Al^{3+} + 3H_2O = 0.5\alpha - Al_2O_3 + 3H^+$	-9.73	Lindsay, 1979
$Cd^{2+} + H_2O = CdOH^+ + H^+$	-10.1	Smith & Martell, 1993
$Cd^{2+} + 2H_2O = Cd(OH)_2^0 + 2H^+$	-20.3	Smith & Martell, 1993
$Cd^{2+} + 3H_2O = Cd(OH)_3^{-1} + 3H^+$	-31.7	Smith & Martell, 1993
$Cd^{2+} + NO_3^- = CdNO_3^+$	0.5	Smith & Martell, 1993
$Cd^{2+} + 2NO_3^- = Cd(NO_3)_2^0$	0.2	Smith & Martell, 1993
$Cd^{2+} + 2H_2O = Cd(OH)_{2(s)} + 2H_+$	-13.7	Smith & Martell, 1993
$Sr^{2+} + H_2O = SrOH^+ + H^+$	-13.2	Smith & Martell, 1993

Table 7–4. Thermodynamic constants for aqueous speciation.

trophoretic mobility measurements. All of these methods provide only estimates of the point of zero charge and each method has potential drawbacks (Sposito, 1998). In addition to these experimental methods, significant progress has been made in the development of theoretically based determinations of points of zero charge from mineral properties such as dielectric constant, Pauling electrostatic bond strength and cation hydroxyl bond length (Severjensky, 1994; Felmy et al., 1998). In this work, a pH<sub>pzc</sub> of 8.9 was previously estimated by Hayes et al. (1991) from the crossover point of a series of potentiometric titrations conducted at varying ionic strength (known as the pH of the point of zero salt effect).

Co(II), Cd(II) and Sr(II) were selected as sorbates because they are either toxic or radioactive contaminants and their sorption behavior is representative of many other environmentally relevant divalent metal cations. In addition, the solutes vary with respect to their ionic size as shown in Table 7–1, and, as discussed previously, exhibit varying sorption behavior on oxide minerals. In addition, all of these metal ions have sufficiently high K-shell fluorescence energies that they can be studied using XAS in the presence of aluminum oxide and water. Relevant solution reactions and thermodynamic constants for calculating metal ion solution speciation and solubility are summarized in Table 7–4.

## **EXPERIMENTAL METHODS**

Some of the experimental data modeled in this chapter were obtained from the literature and the experimental methods are reported therein. In all cases, sodium nitrate was used as the background electrolyte. The Co(II) adsorption data were collected by Katz and Hayes (1995a,b). Macroscopic and XAS sorption data for Cd(II) were collected previously by Honeyman (1984) and Papelis et al. (1995), respectively. The spectroscopic data from Papelis et al. (1995) were collected on

transition alumina rather than  $\alpha$ -Al<sub>2</sub>O<sub>3</sub> and is used in this research to guide the selection of SCM reactions for modeling of Honeyman's Cd(II) data (1984). The Sr(II) data were collected as part of this work. Except as noted below, experimental solution conditions were adjusted to avoid precipitation of metal oxide, carbonate, or hydroxide phases. In addition to the complexation and precipitation reactions shown, Co(II) also undergoes oxidation reactions at high pH and high solute concentrations. Therefore, caution was exercised to avoid reaching these conditions in the experiments conducted by Katz and Hayes (1995a,b).

# **Titration Experiments**

Potentiometric titration data for the corundum used for SCM surface parameter evaluation were taken from Hayes et al. (1991). Titrations were conducted for three ionic strength conditions, varying over two orders of magnitude. The experiments were carried out at 25 °C while maintaining an argon atmosphere at all times. The NaNO<sub>3</sub> and HNO<sub>3</sub> were initially added to adjust the ionic strength to the lowest level to be studied and the pH to an arbitrary starting value at least two pH units away from the point of zero salt effect (PZSE), the crossover point of a family of constant ionic-strength titration curves (Sposito, 1984). Then, the titration was carried out by incremental base addition using equilibration times ranging from 2 to 10 min. The final pH of the base titration never exceeded 11 in order to minimize dissolution. An acid titration was performed to return the suspension to the original starting pH, additional electrolyte was added to increase the ionic strength, and the titration was repeated following the same protocol. Based on extensive titration studies, no significant hysterisis was observed between acid and base titration "legs" using the above approach. In addition, comparison of results for titration experiments conducted over longer periods of time (24–48 h) to these data showed no significant differences between the techniques (Katz, 1993).

# Sorption Experiments

For Co(II) and Sr(II) sorption experiments, 10-mL polyethylene centrifuge tubes were used as reactors. Each centrifuge tube containing the solid suspensions was mixed by end-over-end rotation at 0.84 rad s<sup>-1</sup> (8 rpm) in a constant temperature room maintained at 25 °C. Mixing times were normally fixed at 48 h to allow sufficient time to achieve equilibrium conditions. The pH was measured at 25 °C using a Ross combination semi-microelectrode and an Orion Model 720 pH meter (Orion Research Inc., Boston, MA). The amount of metal ion sorbed was determined by analyzing the supernatant for solute following solid/liquid separation. Solid/liquid separation was accomplished by centrifugation. Several control samples, which did not contain solid, were carried through each procedure to monitor system losses and, in several cases, control samples that did not contain solute were also monitored. The Cd(II) data were collected using similar procedures that are described in detail by Honeyman (1984). Notable exceptions are that the experiments were conducted in 40-mL polycarbonate tubes, and a 4-h equilibration time was employed based on kinetic studies showing that adsorption was complete within

this time frame. Batch equilibrium data for sorption of the metal ions covered a range of pH values for different initial solute concentrations, solid concentrations and ionic strengths [except that all of the Cd(II) data were collected at a 0.1 *M* ionic strength].

# X-Ray Adsorption Fine Structure Data Collection and Analysis

Sorption samples were prepared for XAS using the same procedures described above for generating the pH edges and isotherm data. All samples were equilibrated for a minimum of 24 h prior to pH measurement and centrifugation. An aliquot of supernatant was then removed and stored in acid prior to subsequent analysis for metal ion content. Most of the remaining supernatant solution was then removed and the remaining wet pastes were placed into aluminum sample holders, sealed with mylar or Kapton tape windows for XAS analysis.

X-ray absorption spectra were collected at Stanford Synchrotron Radiation Laboratory (SSRL) on wiggler beam lines. The Cd(II) data and solution samples were collected at room temperature. The Sr(II) and Co(II) data were collected at cryogenic temperatures (20 K) to minimize static disorder. The results obtained for Co(II) were consistent with results obtained at room temperature. Beam current ranged from 40 to 95 mA at  $4.8 \times 10^{-10}$  J (3 GeV) with a wiggler magnetic field of 1.8 T (18 kG). Energy selection was achieved using a Si(220) crystal monochromator with incoming beam flux detuned 30 to 50% to reject high-order harmonic reflections. Beam energy was calibrated to the K-edge of a metallic cadmium foil, cobalt foil, or elemental Bi foil for Sr. Fluorescence spectra for low temperature samples were collected using a 13-element Ge detector with a Be window at a 45° angle to the sample. Fluorescence spectrum for Cd(II) samples and the solution sample were collected using a Stern-Heald-type detector (Lytle et al., 1984) with soller slits and an aluminum filter. Sorption samples typically required 6 to 12 scans depending on concentration. Model compounds typically required two to four scans.

Specific details of the Co(II) and Cd(II) data analysis are provided elsewhere (Hayes & Katz, 1996; Papelis et al., 1995). The Sr(II) data analysis was accomplished using a suite of programs developed at SSRL called EXAFSPAK (George & Pickering, 1995). Background below the edge was subtracted using a Gaussian fit through the pre-edge region. Background above the edge was subtracted using a fourth-order, three-segmented spline fit through the EXAFS region using a Victoreen polynomial and tabulated McMaster coefficients (McMaster et al., 1969; Teo, 1986; Brown et al., 1990). Weighting with a factor of  $k^3$  compensated damping of the spectra. A k-space EXAFS range was selected using points at which chi was zero, typically 3.0 to 11.0 for Sr(II). The k-window range was then Fourier transformed to distance space, producing radial structure functions (RSF). Individual peaks were isolated with a window in R-space and back-transformed. Generally, an experimental model compound is first analyzed to determine spline conditions and R-windows, which are altered minimally for the unknowns.

Fitting was accomplished by nonlinear least squares techniques with four adjustable parameters per component: N, R,  $\sigma^2$  and  $\Delta E_0$  where N is the coordination number, R is the distance,  $\sigma^2$  is the Debye-Waller factor and  $\Delta E_0$  is the difference between the reference functions and unknown spectra. The  $\Delta E_0$  variable was floated in the first shell only and fixed in subsequent shells. Experimental or the-

oretical FEFF 7.0 (Rehr et al., 1991; Zabinsky et al., 1995) phase-shift and amplitude functions from known compounds were used for fitting unknown spectra. Fits were first performed on individual back-transformed peak regions. During the final step, parameter data for all shells were combined to fit the original  $k^3$  EXAFS spectra.

# **Modeling Approach**

Modeling divalent metal ion sorption requires estimation of the proton stoichiometry (the number of protons released per metal ion sorbed), the type of surface complex (inner or outer sphere) formed, and the formation constants for each reaction selected. Table 7–2 presents a list of various reactions that may be incorporated into the TLM. Because a variety of combinations of different sorption reactions and constants may fit various aspects of the sorption data equally well (see, e.g., Westall & Hohl, 1980; Hayes et al., 1991; Katz & Hayes, 1995a), protocols are needed to insure the best choice of reactions and a more universally accepted set of guidelines to allow reproducibility from one laboratory to another. The strategy used in modeling Co(II) sorption to  $\alpha$ -Al<sub>2</sub>O<sub>3</sub> involved:

- 1. Estimation of the SCM metal oxide surface parameters using surface titration data and the objective curve fitting routine FITEQL (Westall, 1982). (A range of valid parameters sets were generated assuming various values of site density,  $\Delta p K_a$ , and  $C_1$ ,  $C_2$ , to be later optimized with metal cation sorption data.)
- 2. Evaluation of spectroscopic data and ionic-strength dependence to guide the selection of divalent cation sorption reactions at low to moderate coverage where mononuclear sorption is the dominant reaction process.
- 3. Estimation of surface complexation constants for the selected mononuclear surface reactions using one set of low coverage sorption data (<0.25 μmol m<sup>-2</sup>) in conjunction with the objective curve fitting routine FITEQL (Westall, 1982).
- 4. Analysis of the predictive capabilities of the ionic-strength dependence for valid sets of surface acidity parameters determined in step 1, and selection of optimal SCM parameters sets based on metal ion sorption data fits.
- 5. Analysis of the predictive capabilities of the monomer surface complexation constants over a range of moderate and high surface coverage data. Model failure at high coverage was indicative of the formation of surface precipitates.
- 6. Re-evaluation of XAS data to guide the selection of multinuclear SCM reactions.
- 7. Incorporation of multinuclear species formation and surface precipitation reactions into SCM to accurately account for their formation.
- 8. Re-analysis of predictive capabilities of the SCM model over a wide range of surface coverages and conditions using the valid set of parameters determined in steps 3 and 4.

FITEQL (Westall, 1982), a least-squares, fitting program, was used to find optimum SCM parameter values from sets of titration or metal ion sorption data.

Parameter optimization is attained by changing the values of the adjustable parameters until the sum-of-the-squares of the residuals between the measured sorption data and FITEQL calculated values is minimized. Optimization can be performed using single or multiple sets of data.

For estimation of the appropriate SCM surface parameters, combined titration data covering over two orders of magnitude in ionic strength were used. In our procedure, the two electrolyte surface binding constants were optimized using FITEQL for a given set of surface acidity, site density and capacitance values. In order to identify appropriate parameter sets, FITEQL optimization was performed for more than 100 different sets of parameters. In the case of metal ion sorption at moderate coverage, FITEQL was used to obtain the sorption constants using a minimum set of pH-edge data in conjunction with the parameters obtained from the potentiometric titration data optimizations. In turn, each of these surface complexation constants was then tested for its ability to predict data collected under other system conditions including pH edges collected at different surface coverage and different ionic strengths.

#### **RESULTS AND DISCUSSION**

## **Potentiometric Titration Data**

A detailed discussion of the FITEQL optimization of TLM surface parameters for  $\alpha$ -Al<sub>2</sub>O<sub>3</sub> has been discussed previously (Hayes et al., 1991). The analysis demonstrated that the TLM version of the surface complexation model can fit titration data reasonably well using a range of TLM surface parameter sets (see Fig. 7–5 as an example). While it was not possible to identify a single optimum set of parameters, it was possible to narrow the range of parameters. Valid sets of surface parameters for the TLM were found for  $\Delta pK_a$  between 0 and 6,  $C_1$  between 0.8 and 2.0 F m<sup>-2</sup>, and  $N_s$  between 1 and 10 sites nm<sup>-2</sup>. In all cases the value of  $C_2$  was set equal to 0.2 F m<sup>-2</sup>.

# **Cobalt Sorption Model Calibration and Predictions**

A detailed discussion of the FITEQL optimization of TLM sorption parameters for Co(II) sorption on  $\alpha$ -Al<sub>2</sub>O<sub>3</sub> has also been discussed previously (Katz & Hayes, 1995a,b; Hayes & Katz, 1996). The first step in modeling Co(II) sorption to  $\alpha$ -Al<sub>2</sub>O<sub>3</sub> was to select an appropriate mononuclear species reaction and reaction constant at low to moderate coverage (step 2 above). The postulated reactions should include those that are structurally consistent with crystal structure, proton reaction stoichiometry, and EXAFS analysis. A stiochiometry of one proton released per metal ion sorbed has been found to be appropriate for strongly sorbing divalent metal ions (Huang & Stumm, 1973; Hohl & Stumm, 1976; Hayes & Leckie, 1987; Dzombak & Morel, 1990). A lack of ionic strength effect on the location of the adsorption edge was shown in Fig. 7–2 and spectroscopic data have indicated that sorption of Co(II) to  $\alpha$ -Al<sub>2</sub>O<sub>3</sub> and  $\gamma$ -Al<sub>2</sub>O<sub>3</sub> leads to inner-sphere surface complexes at surface coverages less than 0.25  $\mu$ mol m  $^2$  (Brown et al., 1999). The evidence sup-

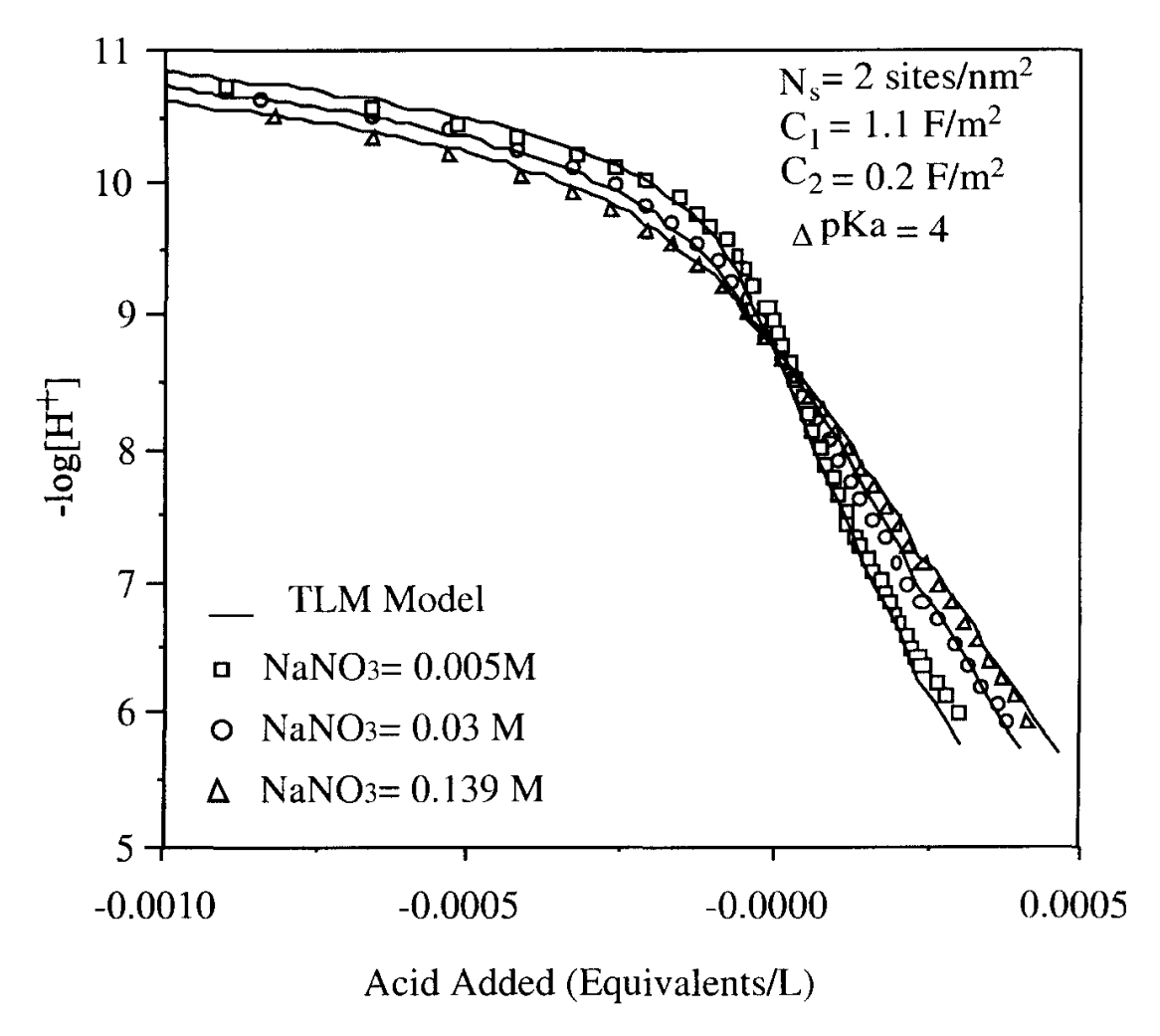


Fig. 7-5.  $\alpha$ -Al<sub>2</sub>O<sub>3</sub> titration data and TLM optimization fits for  $C_1 = 1.1 \text{ F m}^{-2}$ ,  $C_2 = 0.2 \text{ F m}^{-2}$ ,  $N_s = 2 \text{ sites nm}^{-2}$ , and  $\Delta p K_a = 4$  as a function of ionic strength data from Hayes et al., 1990).

porting inner-sphere, mononuclear surface complexes for Co(II) sorption at low coverage included EXAFS fits of a Co-Al interaction at 0.31 nm (3.1 Å) and the absence of Co second nearest neighbors at these low surface coverages (Brown et al., 1999). Based on these results, the following inner-sphere monomer reaction was selected for calibration of the moderate-coverage data:

$$\equiv SOH + Co^{2+} \Leftrightarrow \equiv SOCo^{+} + H^{+}$$
 [1]

Although we selected a monodentate inner-sphere surface complex involving just one surface hydroxyl, more recent modeling of the  $\text{Co}/\gamma\text{-}\text{Al}_2\text{O}_3$  system by Brown et al. (1998) incorporated a bidentate surface complex with two surface hydroxyl groups bound to a single  $\text{Co}^+$ . In their work two inner-sphere bi-dentate monomeric reactions were used to describe Co(II) sorption to  $\gamma\text{-}\text{Al}_2\text{O}_3$  at low coverage:

$$2(\equiv SOH) + Co^{2+} + H_2O \Leftrightarrow [(\equiv SOH)_2CoOH]^+ + H^+$$
 [2]

and

$$2(\pm SOH) + Co^{2+} + 2H_2O \Leftrightarrow [(\pm SOH)_2Co(OH)_2]^0 + 2H^+$$
 [3]

In terms of proton release, the first of these models is consistent with the monodentate reaction that we proposed, but their reaction incorporates an additional surface hydroxyl site. If the formation of a bidentate complex involves coordination of a metal ion to different types of surface hydroxyl sites, monodentate representation may be more consistent with the potentiometric titration approach used to quantify the sorbent surface sites. For example, based on EXAFS analysis of sorbed samples and the polyhedral approach for selecting feasible surface sites, it has been proposed that at low coverage, a bidentate complex of Co(II) may be formed on kaolinite by sharing a terminal Al-OH and a nearby bridging Al-OH-Si (O'Day et al., 1994a). Because proton release from bridging hydroxyls is unlikely (Hiemstra et al., 1989a,b), only one proton exchangeable terminal hydroxyl site is involved. Since the titration data used to determine the SCM parameters only quantify the total number of proton exchangeable sites (e.g., terminal surface hydroxyls), a monodentate surface reaction may be more reasonable. In contrast, if crystallographic data are used to quantify the site density, then it may be more reasonable to use the bidentate reactions proposed by Brown et al. (1999). Clearly, more work is needed to provide a link between the most thermodynamically favorable sites and XAS data. Recent efforts to utilize valance bond theory in conjunction with EXAFS data (Bargar et al., 1997a,b) and to develop methods for estimating surface complexation model parameters from first principles may provide the tools for accomplishing this task (Sverjensky, 1994; Sverjensky & Sahai, 1996).

The TLM calibration was performed on data collected for the system containing  $10^{-6}$  mol L<sup>-1</sup> Co(II), 0.01 M NaNO<sub>3</sub> and 20 g L<sup>-1</sup>  $\alpha$ -Al<sub>2</sub>O<sub>3</sub> using the innersphere monomer monodentate reaction. These data were selected because surface precipitate formation is not expected in this coverage range (<0.25 mol m<sup>-2</sup>) based on EXAFS results. The model calibration was performed for a range of valid TLM parameter sets ( $N_s$ ,  $\Delta p K_a$ ,  $C_1$ ,  $C_2$ ,  $K_{an}$ ,  $K_{cat}$ ) optimized from potentiometric titration data (step 1). The results of the calibration step indicated that a range of SCM surface parameters provided similar fits to the  $2 \times 10^{-6}$  mol L<sup>-1</sup> Co(II), 0.01 M NaNO<sub>3</sub> and 20 g L<sup>-1</sup>  $\alpha$ -Al<sub>2</sub>O<sub>3</sub> sorption edge (see Fig. 7–6, and Katz & Hayes, 1995a). However, in general, TLM parameter sets with  $N_s$  values between 1.0 and 10 sites nm<sup>-2</sup>,  $C_1$  values greater than 0.8 up to 2.0 F m<sup>-2</sup>, and  $\Delta p K_a$  values less than or equal to four were needed to predict the data collected at different ionic strengths reasonably well. The TLM parameters derived from the 20 g L<sup>-1</sup> data and consistent with ionic strength data were subsequently used to predict sorption for a variety of data that varied over a range of surface coverage as shown in Fig. 7–7.

Based on that analysis, it was found that most of the surface parameter sets that worked well for the calibration and ionic strength dependence step did not adequately predict the data over moderate ranges in surface coverage and pH. Two TLM parameters sets, however, did predict sorption data well up to about 0.4  $\mu$ mol m<sup>-2</sup> (see Table 7–5). These two sets were  $C_1 = 1.1$  F m<sup>-2</sup>,  $N_s = 3$  sites nm<sup>-2</sup> and  $\Delta p K_a = 4$ , and  $C_1 = 1.1$  F m<sup>-2</sup>,  $N_s = 2$  sites nm<sup>-2</sup> and  $\Delta p K_a = 4$ . As illustrated in Fig. 7–7, using these parameters, the TLM gives excellent predictions of the 2 g L<sup>-1</sup>  $\alpha$ -Al<sub>2</sub>O<sub>3</sub>, 2 × 10<sup>-6</sup> M data, reasonable predictions of the 20 g L<sup>-1</sup>  $\alpha$ -Al<sub>2</sub>O<sub>3</sub>, 1 × 10<sup>-4</sup> M data, and underpredicts the 2 g L<sup>-1</sup>  $\alpha$ -Al<sub>2</sub>O<sub>3</sub>, 1 × 10<sup>-4</sup> M total Co(II) data. These results suggest that the model is capable of predicting sorption data for surface coverages less than approximately 0.4  $\mu$ mol 1. in reasonable agreement

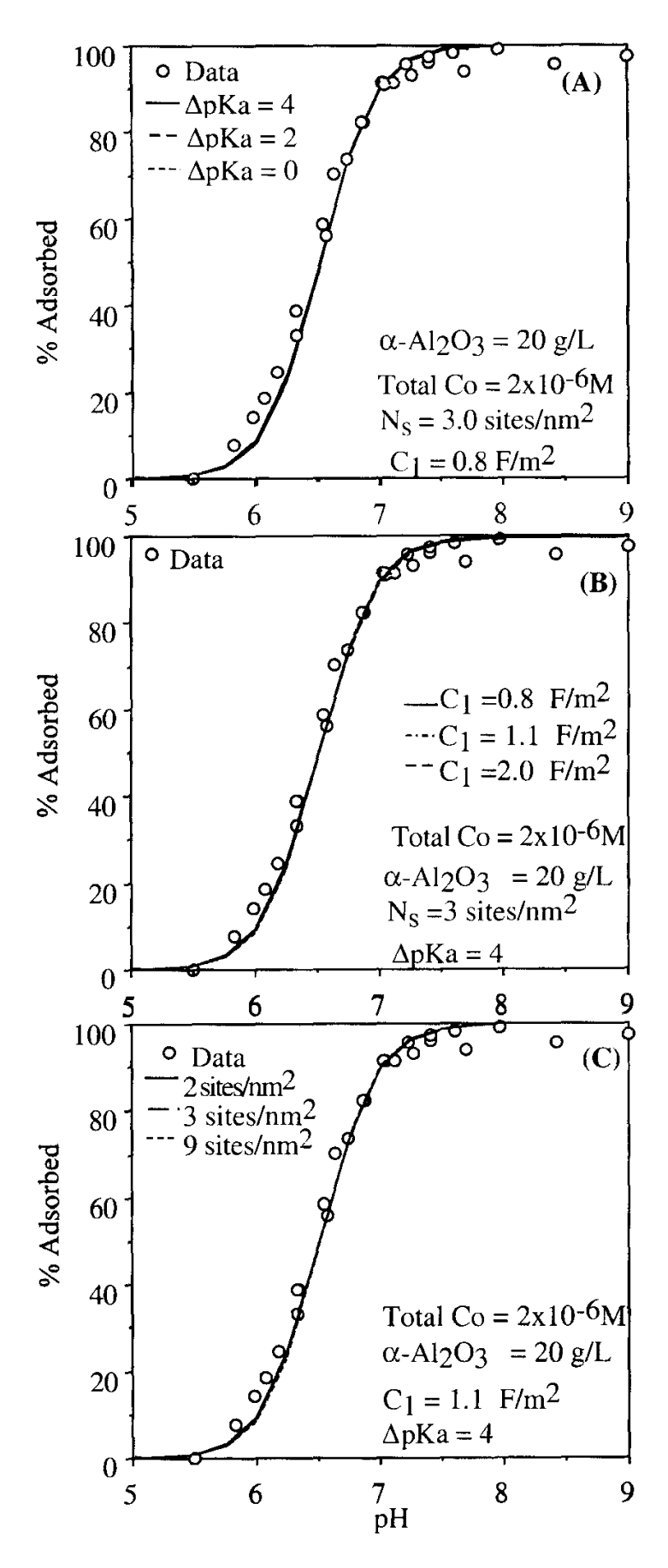


Fig. 7-6. TLM calibration (FITEQL optimization fits) of Co(II) sorption to  $\alpha$ -Al<sub>2</sub>O<sub>3</sub> for a range of TLM surface parameters: (A) effect of  $\Delta p K_n$ , (B) effect of  $C_1$ , (C) effect of  $N_s$ . In all cases the value of  $C_2$  was set equal to 0.2 F m<sup>-2</sup> (after Hayes & Katz, 1996).

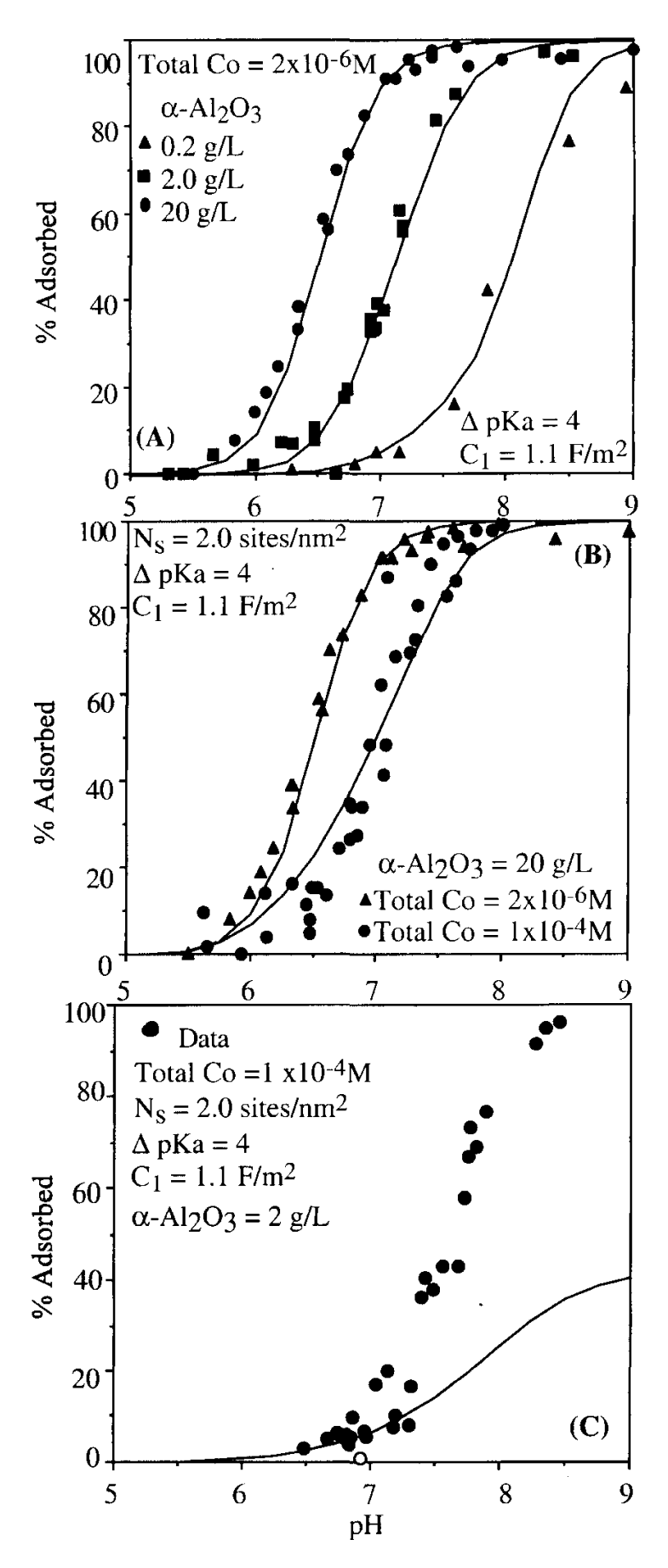


Fig. 7–7. TLM predictions of Co(II) sorption to  $\alpha$ -Al<sub>2</sub>O<sub>3</sub>: (A) effect of sorbent concentration, (B) effect of solute concentration, (C) high coverage data. In all cases the value of  $C_2$  was set equal to 0.2 F m<sup>-2</sup> (after Hayes & Katz, 1996).

Table 7–5. TLM surface	ionization and metal	ion adcorntion na	rametere
Table 1-5. I Livi sulface	TOTILLATION and metal	TOIL austripuon pa	raniculs.

Parameter Description		Parameter values	
$\overline{N_{\rm s}}$	Site density	2	3
	Log formation constant for $\equiv SOH^{2+}$	6.9	6.9
log K	Log formation constant for $\equiv SO^-$	-10.9	-10.9
$\log K_{\text{CAT}}$	Log formation constant for background electrolyte cation (≡SO <sup>-</sup> -CAT <sup>2+</sup> )	-8.08	-8.29
$\log K_{\rm An}$	Log formation constant for background electrolyte anion $(\equiv SOH_2^+ + An^-)$	9.58	9.35
$C_1$	Inner layer capacitance for describing relationship between charge and potential	1.1	1.1
$C_2$	Outer layer capacitance for describing relationship between charge and potential	0.2	0.2
$\log K_{\mathrm{Co}} \ \log K_{\mathrm{Cd1}}$	Log formation inner-sphere Co(II) surface complex (≡SOCo) Log formation inner-sphere Cd(II) surface complex to high	-1.1	-1.2
<i>8</i> Cai	energy sites (≡SOCd <sup>+</sup> )	1.25	1.00
$\log K_{\text{Cd2}}$	Log formation inner-sphere ternary Cd(II) surface complex to high energy sites (≡SOHCdNO <sub>3</sub> )	9.00	8.75
$\log K_{\text{Cd3}}$	Log formation inner-sphere Cd(II) surface complex to low energy sites (≡SOCd <sup>+</sup> )	-1.1	-2.95
$\log K_{\rm Sr1}$	Log formation outer-sphere Cd surface complex (≡SO <sup>-</sup> –Sr <sup>2+</sup> )	-14.96	
$\log K_{\rm Sr2}$	Log formation outer-sphere Sr(II) surface complex (≡SO <sup>-</sup> –SrOH <sup>+</sup> )	-5.29	

with the range for which monodentate sites are expected based on EXAFS analyses presented by Chisholm-Brause (1991) for sorption of Co(II) to  $\gamma$ -Al<sub>2</sub>O<sub>3</sub>. Her EXAFS results suggest that the onset of multinuclear surface complexes occurred between 0.25 and 0.61  $\mu$ mol m<sup>-2</sup>. Above this coverage, the formation of multinuclear surface complexes is suggested by the Fourier transforms of EXAFS spectra showing the presence of second- and fourth-shell neighbor Co-Co interactions at 0.307 nm (3.07 Å) and 0.614 nm (6.14 Å), respectively (see Towle et al., 1997, and Fig. 7–8 showing Fourier transforms of data uncorrected for phase shift and presented in Hayes & Katz, 1996).

Several methods have been postulated for modeling sorption data that is dominated by multinuclear surface reactions and surface precipitation. Katz and Hayes (1995b) and Brown et al. (1998) have proposed the use of polynuclear species based on EXAFS results such as those shown in Fig. 7-8. The Co-Co interactions observed at high coverage, and the increase in the coordination number with coverage is consistent with an increase in the size of the multinuclear complexes as the surface coverage increases. In the latter work, polynuclear species incorporated into the TLM were calibrated to fit the EXAFS derived coordination numbers for second-shell Co-Co interactions. Katz and Hayes (1995b) also adapted the DLM version of the surface precipitation model developed by Farley et al. (1985) to the TLM. This model is based on the assumption that an ideal solid solution forms from the dissolution of the sorbent phase and the sorbing metal ion making it thermodynamically feasible for a precipitate to form below the solubility of the pure cobalt hydroxide phase. The composition of the precipitate is expected to vary as a function of the relative amounts of sorbent and sorbing material participating in the reaction. Based on recent EXAFS data suggesting the formation of a hydrotalcite type surface precipitate that is comprised of Co(II) and Al(III) derived from the sorbent phase, this model would seem appropriate (Towle et al., 1997).

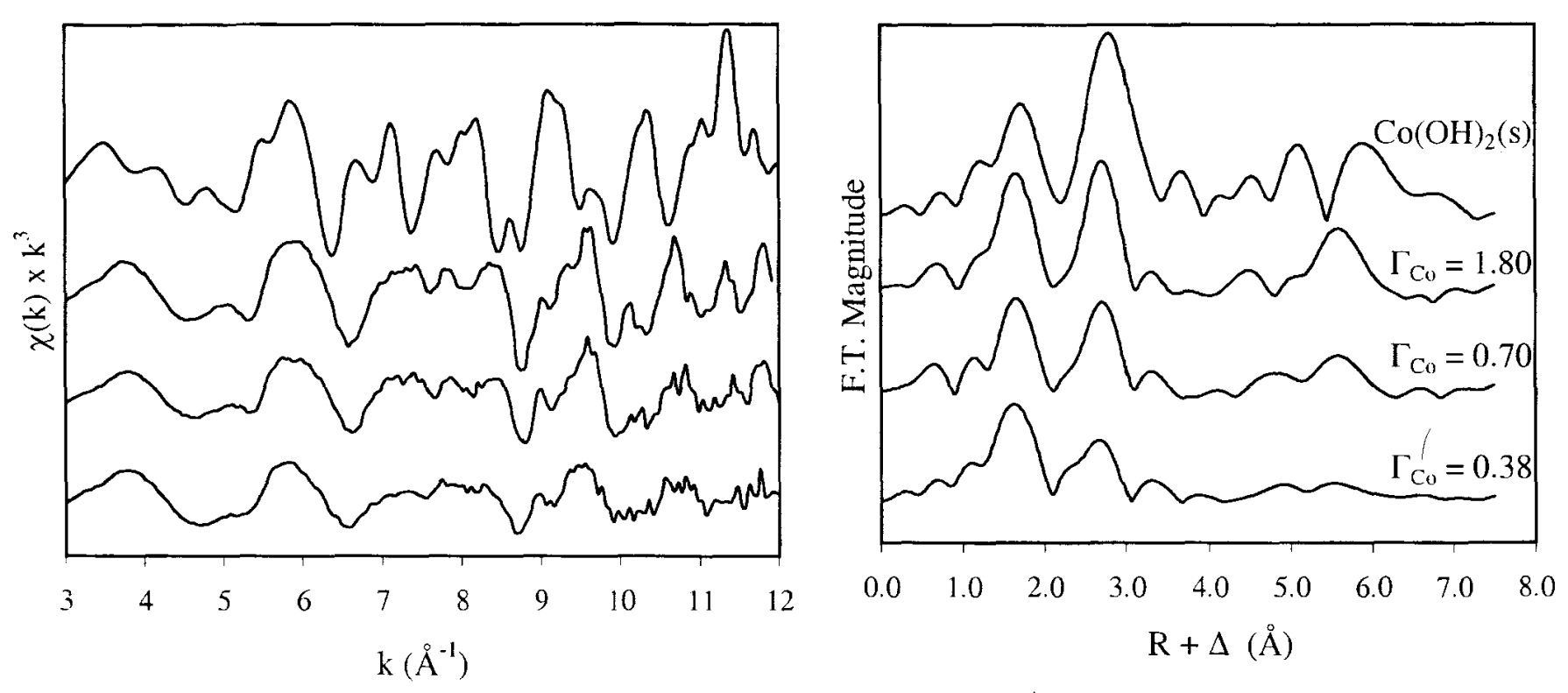


Fig. 7-8. Co XAS results for sorption to α-Al<sub>2</sub>O<sub>3</sub>: (A) background subtracted  $k^3$  Co(II) EXAFS spectra as a function of surface coverage,  $\gamma$ , (B) fast Fourier transformed radial structure functions of Co(II) EXAFS, uncorrected for phase shift. Uncorrected peaks at approximately 2600 and 5500 pm in the sorption samples are primarily due to Co-Co second shell and Co-Co fourth-shell interactions, respectively (after Hayes & Katz, 1996).

The solid solution model implemented by Farley et al. (1985) allows for surface complexation at low surface coverages and co-precipitation of the metal hydroxide phase as a solid solution containing sorbing and sorbent ions. In an ideal solid solution, the solid phase activities are given by:

$${Me(OH)_{2(s)}} = \frac{[Me(OH)_{2(s)}]}{T_s}$$
 [4]

and

$$\{S(OH)_{3(s)}\} = \frac{[S(OH)_{3(s)}]}{T_s}$$
 [5]

where the {} denotes activities, [] denotes concentration,  $S(OH)_{3(s)}$  represents a trivalent oxide or hydroxide sorbent phase,  $Me(OH)_{2(s)}$  represents a divalent hydroxide sorbing phase and  $T_s$  represents the total mass of solid material in solid solution and is given by:

$$T_{s} = [Me(OH)_{2(s)}] + [S(OH)_{3(s)}]$$
 [6]

In addition, because an ideal solid solution is assumed:

$${S(OH)_{3(s)}} + {Me(OH)_{2(s)}} = 1$$
 [7]

This representation allows the solubility of the sorbing metal hydroxide phase to change as a function of surface coverage because the solubility will be exceeded according to:

$${Me^{2+}}{OH^{-}}^{2} \ge {Me(OH)_{2(s)}}K_{sp}$$
 [8]

where  $K_{\rm sp}$  is the thermodynamic solubility product constant.

There are no additional parameters required for implementation of the equations above if all of the sorbent material is able to participate in the formation of the solid solution. However, an additional parameter is required if only a fraction of the sorbent phase can participate in the solid solution. In the case of a crystalline solid material, this parameter is expected to be a small fraction of the total solid added to the system, accounting for the fact that only the surface and some of the first few layers of the sorbent will participate in the formation of a solid solution with the co-precipitating metal ion. The value chosen for this parameter is likely to depend on the dissolution properties of the sorbent and can be considered a fitting parameter.

The surface precipitation model was implemented using MICROQL+ (Dzombak, 1989) using the  $K_{\rm sp}$  values shown in Table 7–4 and assuming that approximately 2% of the aluminum oxide added to the system was able to participate in the formation of the solid solution. Representative results of the surface precipitation modeling, shown in Fig. 7–9, suggest that the model can provide a reasonable representation of the sorption process over a range of solution conditions.

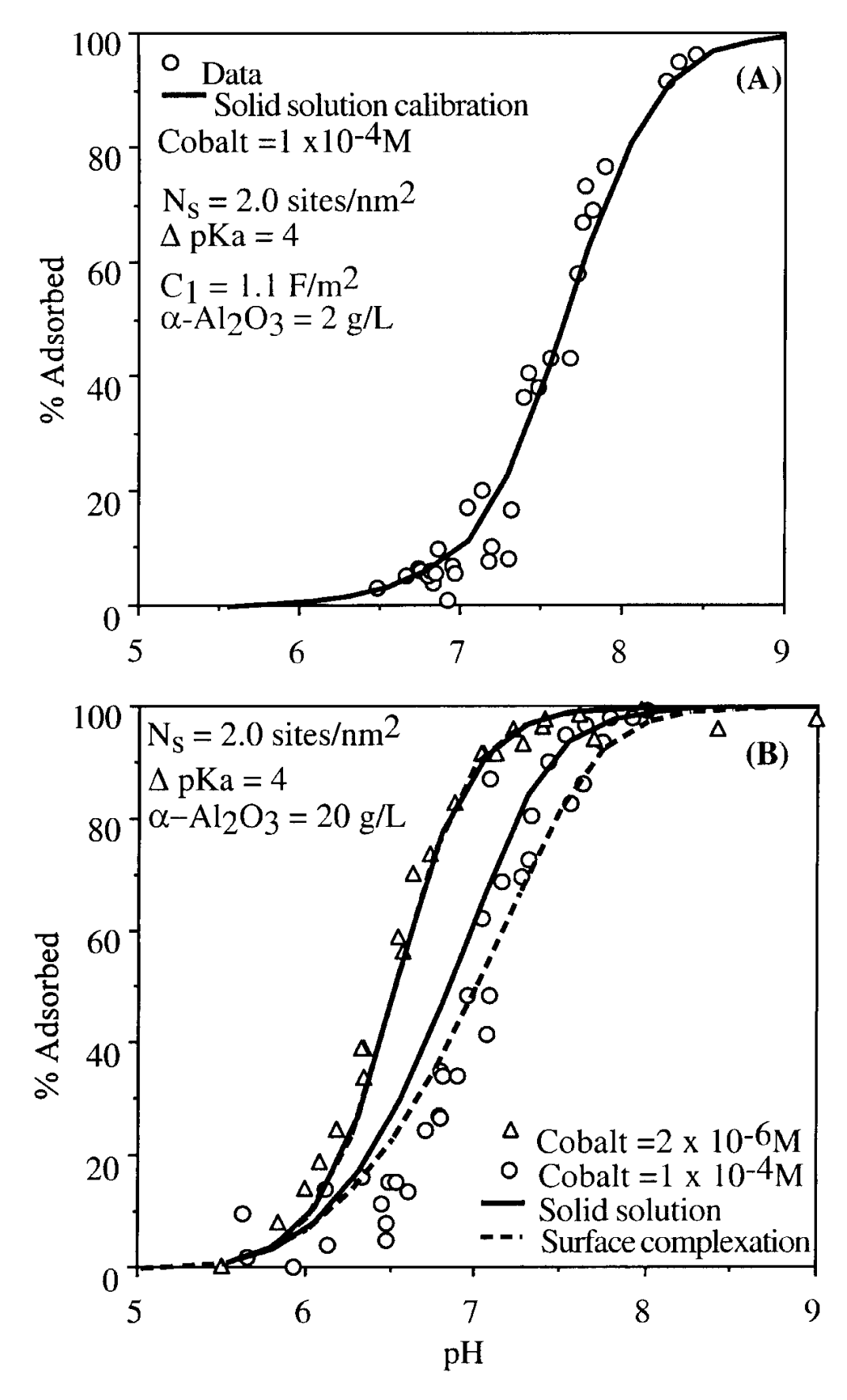


Fig. 7–9. TLM solid solution model calibration and predictions for Co(II) sorption to α-Al<sub>2</sub>O<sub>3</sub> at low and high surface coverage: (A) model calibration to high coverage data, (B) Surface complexation and solid solution model predictions of representative pH sorption edges, (C) surface complexation and solid solution model predictions of a sorption isotherms at pH 7.6, and (D) surface complexation and solid solution model predictions of a sorption isotherm at pH 6.9 (after Katz & Hayes, 1995b).

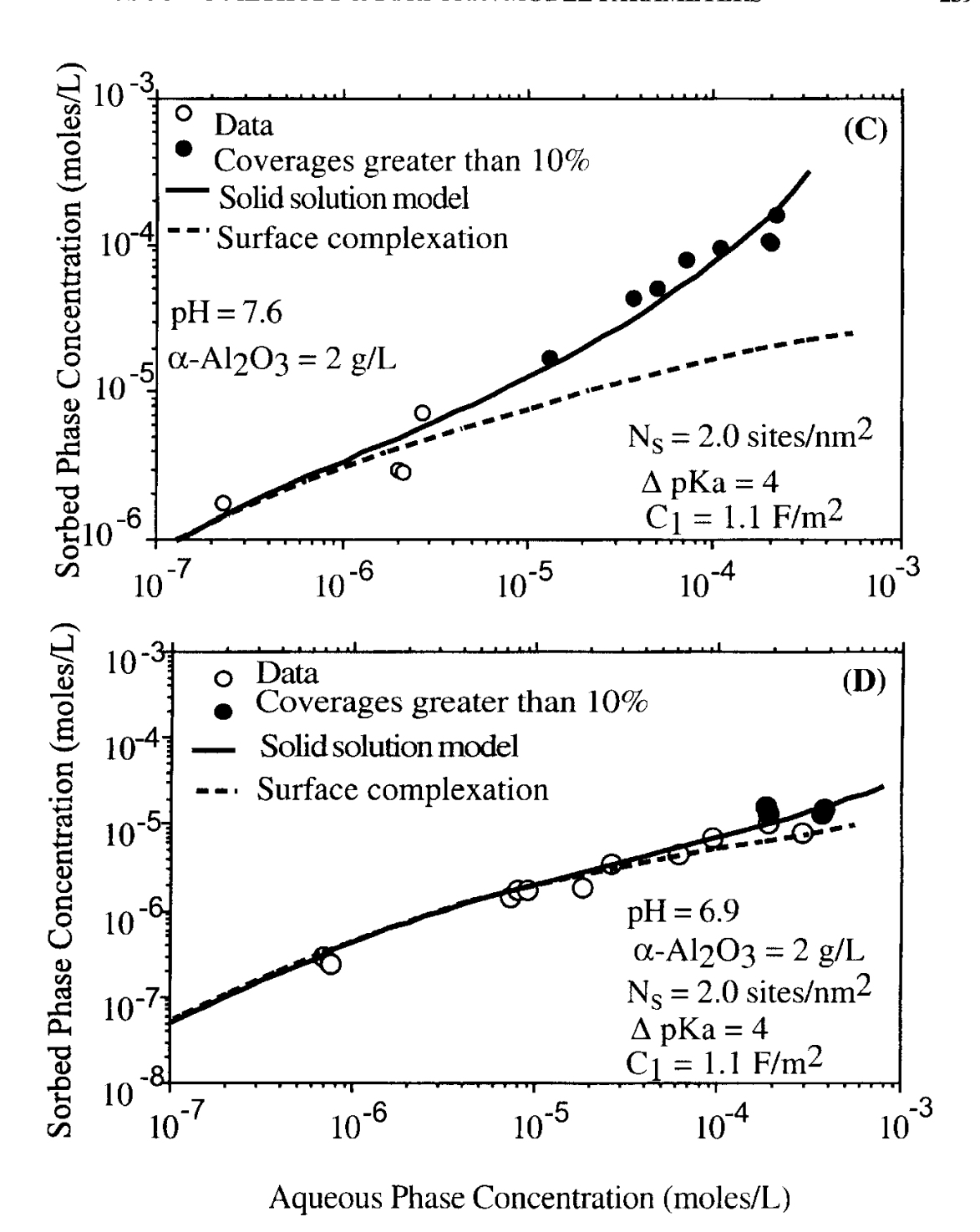


Fig. 7–9. Continued.

# **Cadmium Sorption Model Calibration and Predictions**

The next task in the evaluation of SCM for predicting sorption behavior was to assess its ability to predict sorption for other divalent metal ions. This aspect of research was conducted to test the extensibility of the surface ionization constants derived for Co(II) to cations with varying sorption behavior. To this end, results are presented in this section for modeling data collected by Honeyman (1984) for sorption of Cd(II) by  $\alpha$ -AlO using the TLM. The selection of Cd(II) was based on previous EXAFS research conducted by Papelis et al. (1995) indicating that Cd(II)

Solid concentration	Solution concentration	Surface coverage µmol m <sup>-2</sup>	
g L <sup>-1</sup>	mole L <sup>-1</sup>		
2.0	$1.0 \times 10^{-6}$	0.040	
6.0	$1.0 \times 10^{-6}$	0.013	
10.0	$1.0 \times 10^{-6}$	0.0080	
30.0	$1.0 \times 10^{-6}$	0.002 6	
50.0	$1.0 \times 10^{-6}$	0.001 6	
2.0	$5.0 \times 10^{-5}$	2.0	
10.0	$5.0 \times 10^{-5}$	0.40	
20.0	$5.0 \times 10^{-5}$	0.20	
2.0	$1.0 \times 10^{-5}$	0.40	
10.0	$1.0 \times 10^{-5}$	0.080	
20.0	$1.0 \times 10^{-5}$	0.040	
20.0	$8.0 \times 10^{-8}$	0.000 32	
20.0	$4.1 \times 10^{-8}$	0.000 16	
20.0	$1.6 \times 10^{-8}$	0.000 06	
20.0	$1.0 \times 10^{-7}$	0.0004	

Table 7-6. Surface coverages for Cd sorption pH edges.

forms only mononuclear surface complexes. This conclusion was based on the absence of second-shell Cd neighbors in samples containing 1.2  $\mu$ M Cd m<sup>-2</sup> aluminum oxide. Second-shell nearest neighbors were observed in a pH 9.0 sample containing  $10^{-4}$  M of Cd(II) and with a surface coverage of 12  $\mu$ M Cd(II) m<sup>-2</sup> aluminum oxide. However, the formation of a bulk precipitate was observed during the sample preparation above pH 7.5.

The absence of surface precipitate formation was also observed by Bargar et al. (1997a,b) and Strawn et al. (1998) for Pb(II) sorption to aluminum oxide, and no evidence exists in the literature to support the incorporation of Pb into hydrotalcitelike structures (Cavani et al., 1991), most likely due to the large ionic radius of Pb(II) (119 pm) relative to that of Al (III) (53.5 pm). The ionic radius of Cd(II) is also relatively large (95 pm). Macroscopic sorption data also support the absence of surface precipitation of Pb(II) and Cd(II). In systems aged up to 60 wk, studies by Lothenbach et al. (1997) indicated potential formation of a solid solution between Ni(II), Zn(II), or Cu(II) and precipitated Al(III) (added in a dissolved form) in montmorillonite suspensions. In contrast, the behavior of Cd(II) and Pb(II) appeared to be consistent with formation of a strict adsorption complex. Thus, in modeling Cd(II) sorption to  $\alpha$ -Al<sub>2</sub>O<sub>3</sub> only mononuclear adsorption reactions were considered.

The experimental conditions for Cd(II) data collected by Honeyman (1984) are presented in Table 7–6, along with the surface coverages assuming 100% of the initial Cd(II) added to the system was adsorbed. As indicated by the data in this table, some of the experiments in these systems represented extremely low surface coverages. As shown in Fig. 7–10a, the position of the edge for experiments conducted below  $1 \times 10^{-7} \, M$  solution concentration and 20 g L<sup>-1</sup>  $\alpha$ -Al<sub>2</sub>O<sub>3</sub> was invariant with respect to pH. The surface coverages for data from these experiments ranged from approximately  $6 \times 10^{-6} \, \mu mol \, m^{-2}$  to  $3 \times 10^{-4} \, \mu mol \, m^{-2}$  (corresponding to approximately 10% adsorbed for the lowest total concentration and 100% adsorption for the highest total concentration shown in Fig. 7–10a). Invariance of the pH edge at low coverage is indicative of saturation of a small number of high energy sites sorption. Thus, the approach used to fit the data in this system was to incorporate

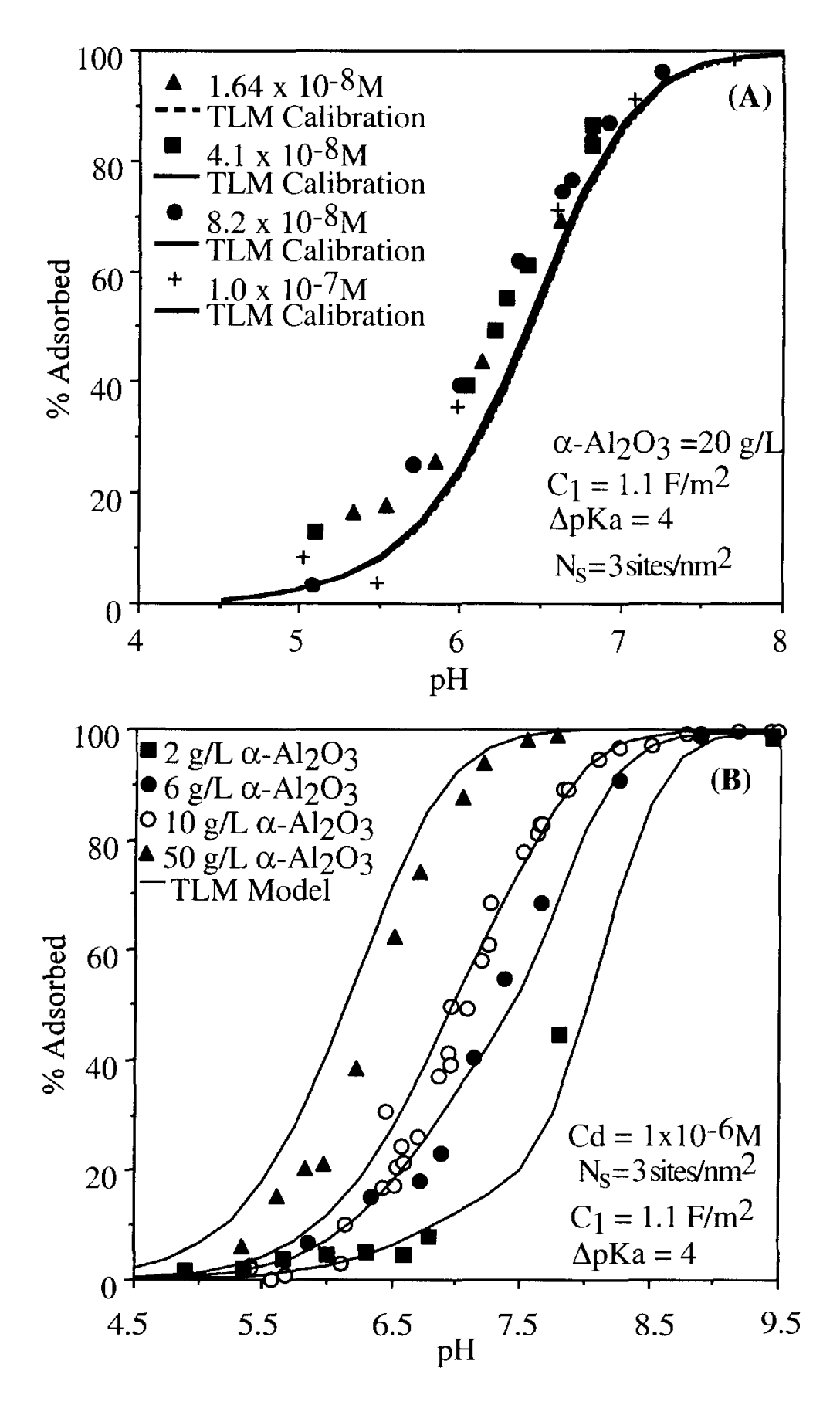


Fig. 7–40. TLM model calibration and predictions of Cd(II) sorption to  $\alpha$ -Al<sub>2</sub>O<sub>3</sub>: (A) low coverage data and model calibration to high energy sorption sites,  $N_{S2}$ , (B) TLM calibration (open circles) to low energy sorption sites,  $N_S$  and model predictions of the effect of solid concentration on sorption of  $10^{-6} M$  Cd(II) to  $\alpha$ -Al-O<sub>3</sub>.

into the TLM, a second, lower energy site having identical surface protolysis and electrolyte complexation reaction constants as those used for Co(II) sorption. A number of potential inner-sphere reactions were evaluated using FITEQL for their ability to predict the slope and location of the sorption edges shown in Fig. 7–10 and 7–11. The following two reactions provided the best fit to the low coverage data assuming sorption to high energy sites:

$$SOH + Cd^{2+} = (SOCd)^{+} + H^{+} K_{Cd1}$$
 [9]

$$SOH + Cd^{2+} + NO_3^- = (SOHCdNO_3) K_{Cd2}$$
 [10]

The first reaction incorporating the (SO-Cd)<sup>+</sup> surface complex was also used to describe sorption to the remaining weaker binding sites; however, the equilibrium constant for sorption to the high energy sites,  $K_{\text{Cd3}}$ , was significantly smaller. While no spectroscopic data have been presented to substantiate the selection of these reactions, the second reaction was required to match the slope of the pH adsorption edge (corresponding to the proton release) at the lower coverages.

Calibration of the model required estimation of the three equilibrium constants for Cd(II) sorption to the high and low energy sites as well as an estimation of the number of high energy sites. The surface parameters for the low energy sites were the same as those used for Co(II) sorption data. In addition, valid sets of surface parameters determined from the α-Al<sub>2</sub>O<sub>3</sub> potentiometric titration data and Co(II) sorption data were also used for the high energy sites ( $C_1 = 1.1 \text{ F m}^{-2}$ ,  $N_s = 3 \text{ sites}$ nm<sup>-2</sup>, and  $\Delta pK_a = 4$ , and  $C_1 = 1.1 \text{ F m}^{-2}$ ,  $N_s = 2 \text{ sites nm}^{-2}$ , and  $\Delta pK_a = 4$ ), except the value of the high energy site density was reduced to fit the data. Calibration of the site density for the high energy sites and the sorption equilibrium constants and  $(N_{S2}, K_{Cd1})$  and  $K_{Cd2}$  was performed separately from the equilibrium constant for the low energy sites by calibrating with only the low coverage data. FITEQL was used to estimate the values for the equilibrium constants for the reactions, although it was not possible to incorporate the high energy site density as a fitting parameter into FITEQL and achieve convergence. As a result, the value of high density sites  $(N_{s2})$  was determined by manually changing the value of  $N_{s2}$  during FITEQL optimization of the low coverage data. The values of  $N_{\rm S2}$ ,  $K_{\rm Cd1}$  and  $K_{\rm Cd2}$  determined are shown in Table 7-5. Plotted in Fig. 7-10 is the TLM simulation for the data set used to determine the equilibrium constants and site density for the low coverage data.

After the values of  $N_{\rm S2}$ ,  $K_{\rm Cd1}$  and  $K_{\rm Cd2}$  were determined, the value of  $K_{\rm Cd3}$  was determined using the data collected for  $1 \times 10^{-6}$  M Cd(II) and 10 g L<sup>-1</sup>  $\alpha$ -Al<sub>2</sub>O<sub>3</sub>, the calibrated values of  $N_{\rm S2}$ ,  $K_{\rm Cd1}$ , and  $K_{\rm Cd2}$  and the surface acidity constants determined from  $C_1 = 1.1$  F m<sup>-2</sup>,  $N_{\rm s} =$  three sites nm<sup>-2</sup>, and  $\Delta p K_a =$  four. The value for  $K_{\rm Cd3}$  is presented in Table 7–5, and the model calibration is shown in Fig. 7–10b along with predictions using these constants.

Predictions for Cd(II) sorption by  $\alpha$ -Al<sub>2</sub>O<sub>3</sub> provide reasonable agreement over a range of solute and solid concentrations, as shown in Fig. 7–10 and 7–11. However, the model slightly underpredicts sorption in the system containing 2 g L<sup>-1</sup>  $\alpha$ -Al<sub>2</sub>O<sub>3</sub> and 5 × 10<sup>-5</sup> M Cd(II). There are three possible reasons for the lack of fit in this region. First, the coverages in this region are consistent with the surface pre-

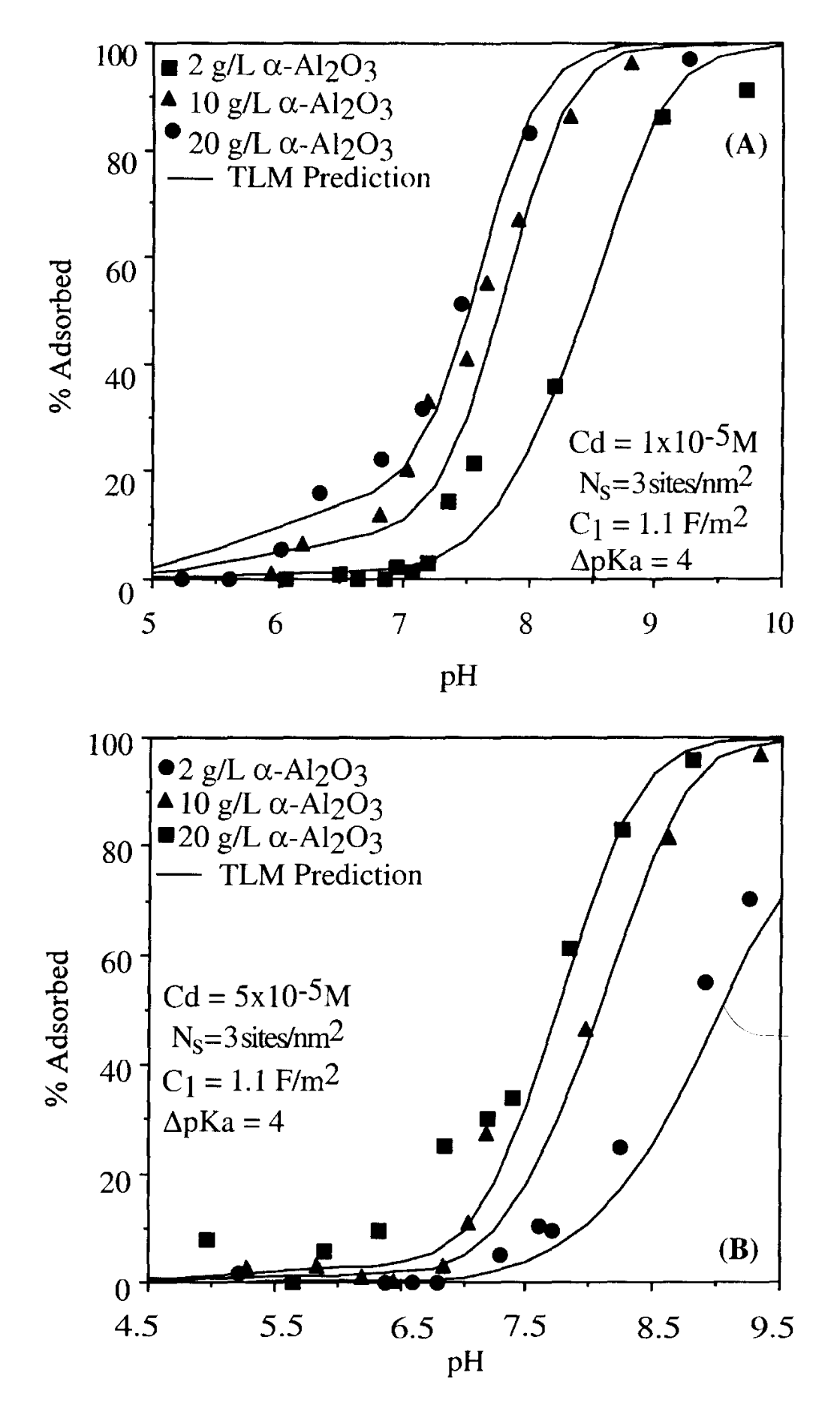


Fig. 7. 11. TLM model predictions of the effect of solid concentration on Cd(II) sorption to  $\alpha$ -Al<sub>2</sub>O<sub>3</sub>: (A) total Cd(II) concentration  $\sim 1 \times 10^{-5} M_{\odot}$  (B) total Cd(II) concentration  $\approx 5 \times 10^{-5} M_{\odot}$ 

cipitate coverages observed for Co(II). However, spectroscopic data available for Cd(II) sorption to aluminum oxide were not consistent with surface precipitate formation.

A second possible explanation is that using a site density of 3 sites nm<sup>-2</sup>, the system is reaching site saturation. In order to maintain consistency between the parameters obtained for Co(II) and the parameters used to model other divalent metal ions, only valid parameter sets obtained with Co(II) can be applied in this analysis  $(C_1 = 1.1 \text{ F m}^{-2}, N_s = 3 \text{ sites nm}^{-2}, \text{ and } \Delta p K_a = 4 \text{ or } C_1 = 1.1 \text{ F m}^{-2}, N_s = 2 \text{ sites nm}^{-2}, \text{ and } \Delta p K_a = 4)$ . Comparison of model fits for the surface acidity parameters derived using two sites nm<sup>-2</sup> instead of three sites nm<sup>-2</sup> led to an even greater underprediction of the data so this explanation cannot be ruled out.

A third possible explanation for the slight underprediction of sorption in this region, is the presence of bulk precipitation. Equilibrium calculations using the solubility constant presented in Table 7–4, an ionic strength of 0.1 M and a Cd(II) concentration of  $5 \times 10^{-5} M$  indicate that precipitation should occur above pH 9.1. In the experiments conducted by Papelis et al. (1995) bulk precipitation was observed in systems containing  $1 \times 10^{-4} M$  Cd(II) and 0.01 M ionic strength above pH 7.5. This corresponds to a solubility constant of ( $K_{so}$ ) of  $10^{-10.9}$ . Using this value of the solubility constant, bulk precipitation will occur in the  $5 \times 10^{-5} M$  system (in the absence of adsorption) at pH values greater than 7.8. Thus, it is possible that bulk precipitation is contributing to removal of Cd(II) from solution in this region.

In summary, the analysis of the data collected by Honeyman (1984) shows that at very low surface coverages incorporation of a second high energy site could be used to describe the sorption behavior over a range of low coverage conditions. With the incorporation of a second site, it was possible to describe sorption of Cd(II) over a range of solid concentrations from 2 g L<sup>-1</sup> to 50 g L<sup>-1</sup>. At high coverages (in excess of 0.5 µmol m<sup>-2</sup> percentage surface coverage) the model slightly underpredicted sorption. The underprediction at higher coverages may be due to bulk precipitation of an amorphous cadmium hydroxide or cadmium hydroxycarbonate phase or due to the selection of a low site density.

# Strontium Spectroscopy and Sorption Model Calibration and Predictions

The final task in the evaluation of SCM for predicting sorption behavior was to assess its ability to predict sorption for a weakly sorbing (outer-sphere) divalent metal ion. Because previous studies reporting EXAFS results for Sr(II) sorption to aluminum oxides were not available in the literature prior to our modeling efforts, Sr(II) XAS data were collected as part of this work. The Sr(II) XAS data were collected for a strontium nitrate solution and the samples shown in Table 7–7.

The background-subtracted, normalized  $k^3$ -weighted EXAFS spectra for a strontium nitrate solution and the three sorption samples are shown in Fig. 7–12. Only one frequency is visible in all of the spectra corresponding to the oxygen first-shell neighbors as shown in the Fourier transforms in Fig. 7–12. The Sr-O distance and coordination numbers were determined by fitting the back transformed first-shell peak using phase and amplitude parameters derived from the SrO model compound. An example fit of the background-subtracted,  $k^3$ -weighted Sr(II) EXAFS is shown in Fig. 7–13. The results presented in Table 7–7 and Fig. 7–14 are in good

Sample	рН	Initial concentration	N†	R†	$\Delta\sigma^2$ †	$\Delta E_{ m o}\dagger$
Sr Solution	7.49	0.0010 M	9.17	2.52	0.0098	-5.65
$\Gamma = 0.17$	8.79	0.0002 M	9.48	2.58	0.0105	-2.21
$\Gamma = 0.38$	9.75	0.0002 M	8.27	2.57	0.0077	-2.46
$\Gamma = 1.25$	9.62	0.0006 M	8.42	2.58	0.0080	-2.46

Table 7–7. Sr-O fit parameters for Sr sorption to 20 g  $L^{-1}$   $\alpha$ -Al<sub>2</sub>O<sub>3</sub>, 0.1 M NaNO<sub>3</sub>.

agreement with the strontium nitrate solution sample suggesting that the coordination environment for Sr(II) is consistent with an outer-sphere reaction. In addition, the strong ionic strength dependence presented in Fig. 7–2 for Sr(II) adsorption is also consistent with outer-sphere adsorption. As a result, model calibration of Sr(II) adsorption to  $\alpha$ - $Al_2O_3$  utilized the following two surface complexation reactions, which could not be distinguished spectroscopically:

$$\equiv SOH + Sr^{2+} + H_2O \Leftrightarrow \equiv SO^- - Sr^{2+} + H^+ \qquad K_{Sr1}$$
 [11]

$$\equiv$$
SOH + Sr<sup>2+</sup> + H<sub>2</sub>O  $\Leftrightarrow \equiv$ SO<sup>-</sup>-SrOH<sup>+</sup> + 2H<sup>+</sup>  $K_{Sr2}$  [12]

Model calibration of these reactions was performed on data collected at  $5.0 \times 10^{-5}$  M Sr(II) and ionic strengths of 0.01 and 0.5 M. The optimized equilibrium constants for the reactions are shown in Table 7–5, and the model calibration is shown in Fig. 7–14 along with predictions of data collected at ionic strengths of 0.003 M and 0.1 M. Predictions of data collected at higher solute concentration (Fig. 7–15) indicate that the model appears to be able to predict both ionic strength effects and solute concentration effects, at least for the limited range of data shown here.

# CONCLUSIONS

This chapter has illustrated a methodology for modeling divalent cation sorption at metal oxide-water interfaces using SCM. The methodology was applied to simulate and predict sorption data over a wide range of solution conditions and surface coverage for three divalent metal ions that differ with respect to their binding strength and their ability to form surface precipitates. The keystone of the methodology relies on the use of spectroscopic data to guide the selection of appropriate model reactions. In the case of Cd(II) and Co(II), XAS data were consistent with the formation of inner-sphere surface complexes for sorption to α-Al<sub>2</sub>O<sub>3</sub>. A single mononuclear inner-sphere reaction, however, was unable to account for sorption except over a limited range of conditions in both cases. For Co(II), spectroscopic data have indicated the formation of a surface precipitate comprised of Co(II) and Al(III) derived from the sorbent surface. Incorporation of an ideal solid solution model into the TLM was capable of describing Co(II) sorption throughout a fairly large range of data. Consistent with the spectroscopy, the model predicts that mononneclear species dominate at low surface coverage and that the ex-

<sup>†</sup> N = coordination number, R = distance,  $\sigma^2 = \text{the Debye-Waller factor}$ ,  $E_0 = \text{the difference between}$  the energy at which wave vector K was set to zero for reference functions and unknown spectra.

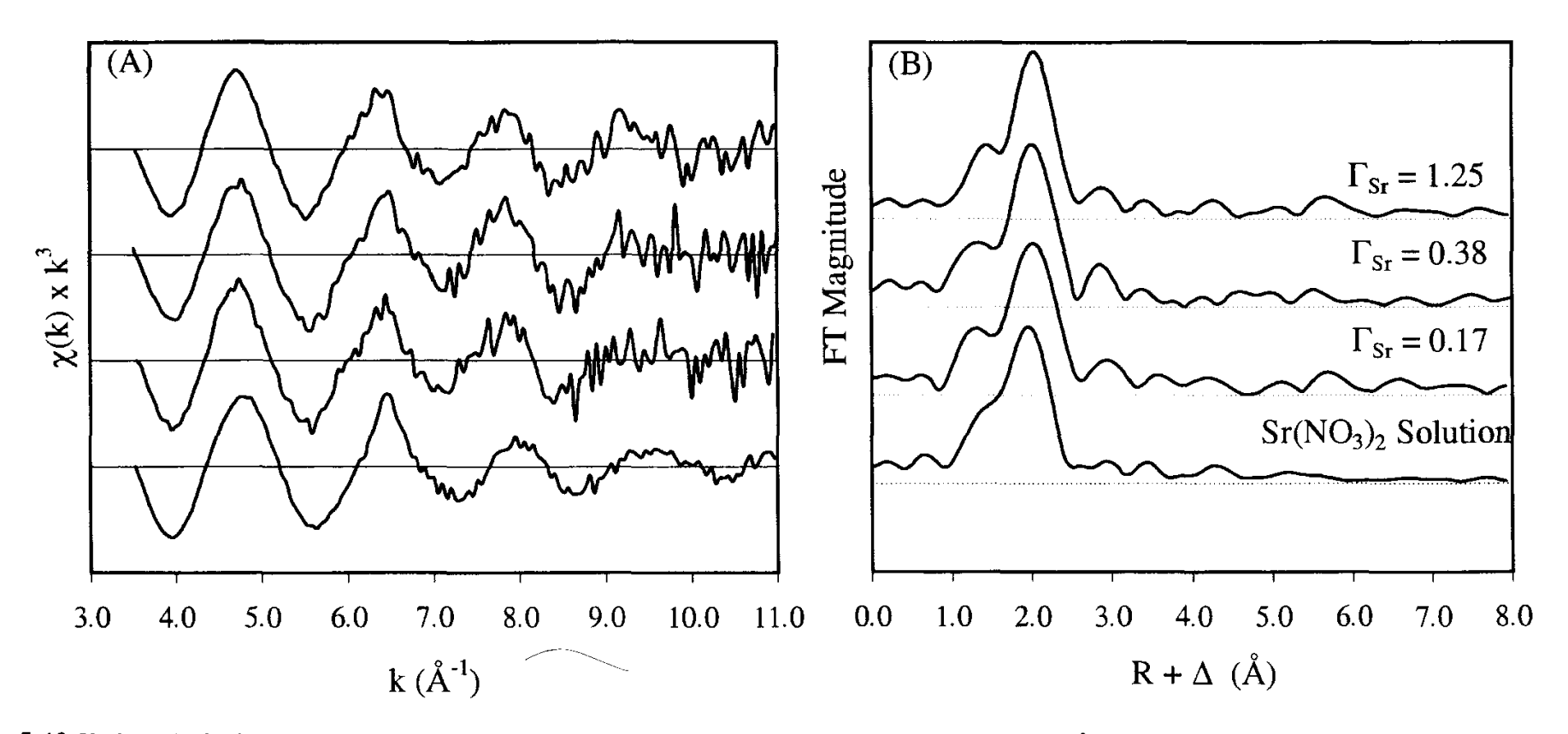


Fig. 7-12. XAS results for Sr(II) sorption samples as a function of surface coverage, γ: (A) background subtracted k³ Sr EXAFS spectra, (B) fast Fourier transformed RSF uncorrected for phase shift. Peaks shown in the Fourier transform correspond to first shell Sr-O interactions.

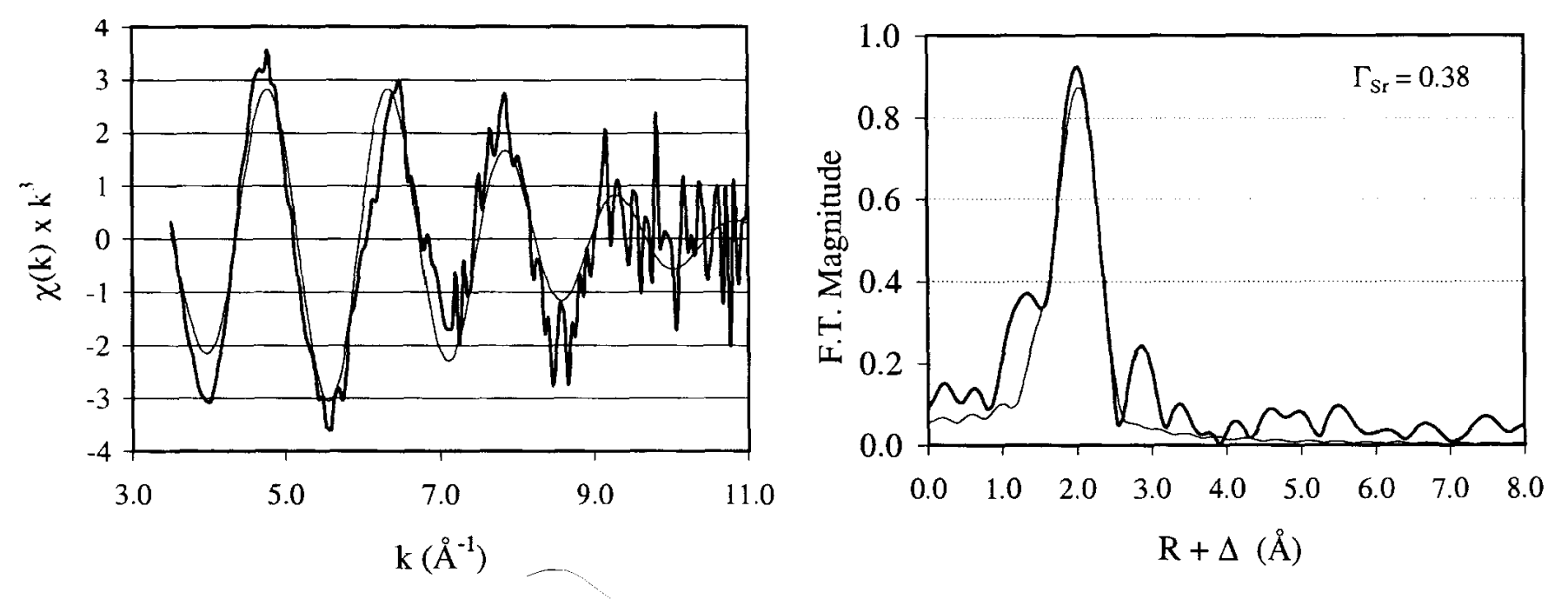


Fig. 7–13. Example fits of Sr(II) EXAFS data. Thick lines are the data and fine lines are the fits using parameters in Table 7–7. These fits are representative of the fit quality for all of the sorption samples.

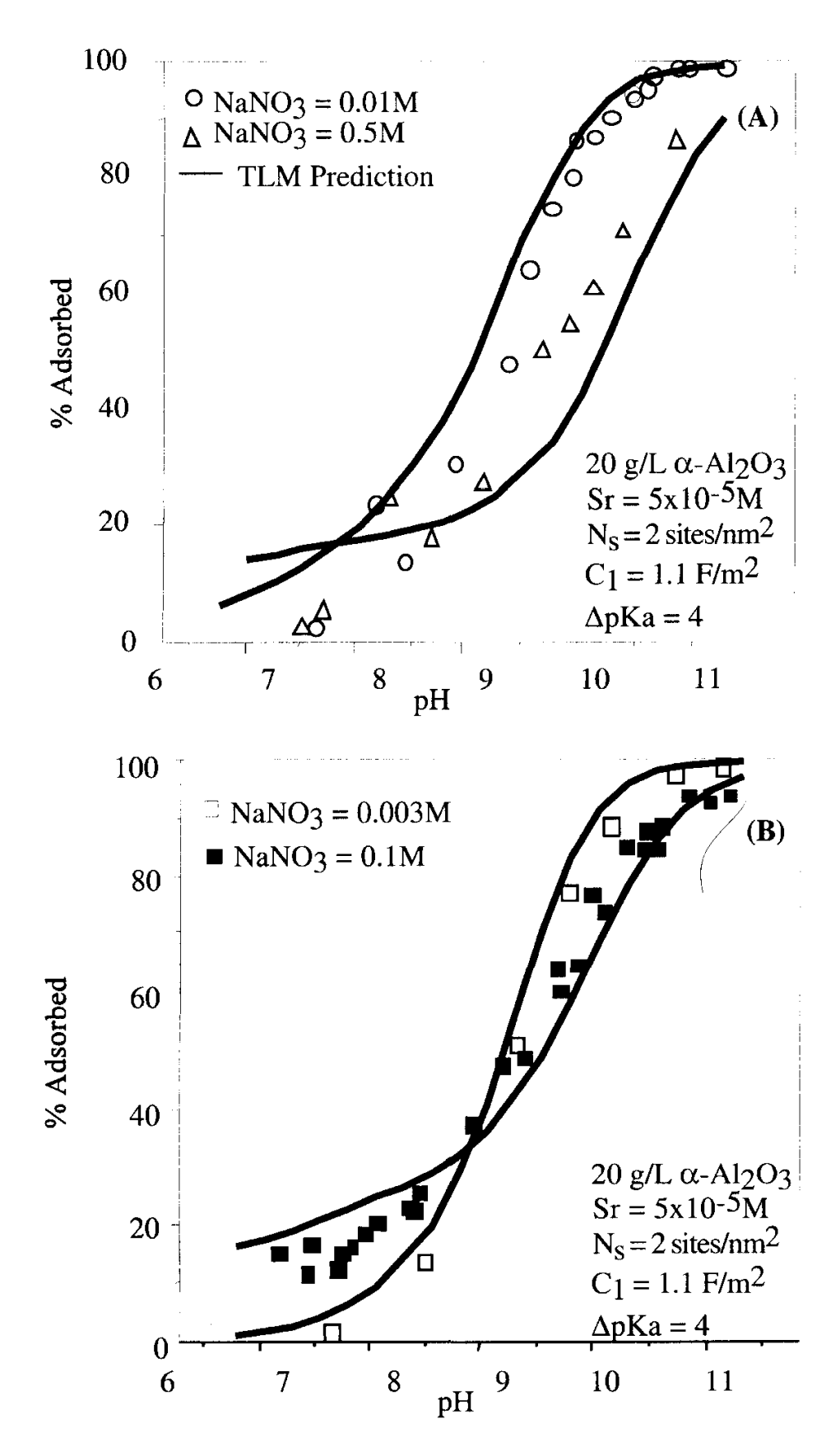


Fig. 7–14. TLM model calibration and predictions for outer sphere Sr(II) to α-Al<sub>2</sub>O<sub>3</sub>: (A) model calibration (optimization using FITEQL), (B) predictions of Sr(II) sorption ionic strength dependency.

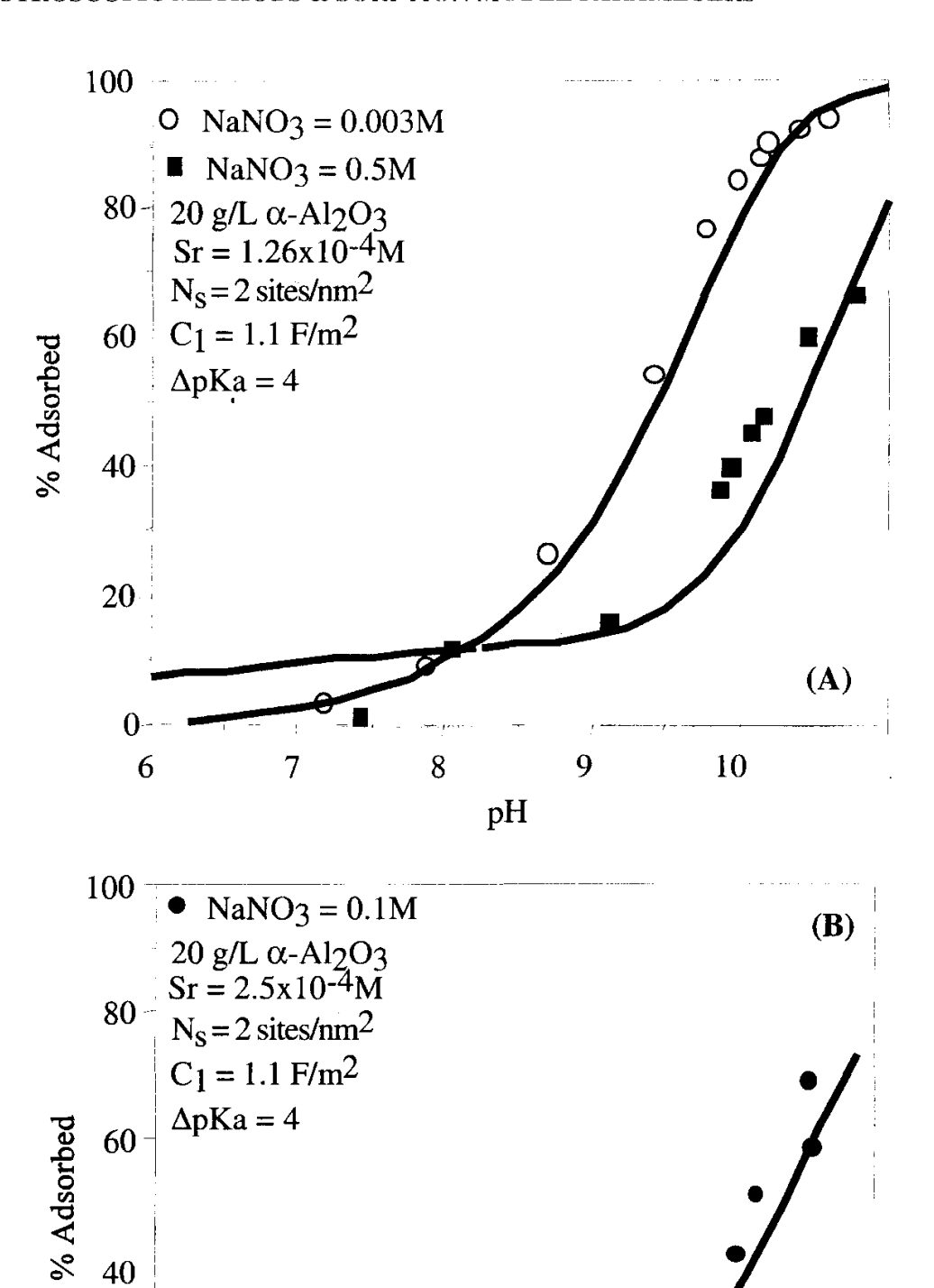


Fig. 7–15. TLM model predictions of the effects of solute concentration on Sr(II): (A) total Sr(II) concentration =  $1.26 \times 10^{-4} M$ , (B) total Sr(II) concentration =  $2.5 \times 10^{-4} M$ .

pН

tent of surface precipitation increases with increasing surface coverage and increasing pH.

The Cd(II) sorption data were available over an even larger range of surface coverage than Co(II). In this case, the spectroscopic data did not provide evidence for the formation of a surface precipitate, and the TLM was able to predict sorption at high coverage reasonably well without incorporating surface precipitation. However, the TLM was not capable of predicting data at very low surface coverages using a single monomeric reaction. It was necessary to account for site heterogeneity by incorporating a second surface hydroxyl site into the model. Due to current limitations of XAS and other spectroscopies, it was not possible to identify the structure of the surface complex at low coverage, nor was it possible to independently estimate the surface hydroxyl site density of the high-energy sites. Not surprisingly, it was possible to predict the data in the low coverage range by incorporating a second high-energy surface site and two Cd(II) surface reactions. However, the reactions that were used to describe the behavior in this range of data were not unique, and the accuracy of the modeling description in this range of data is tenuous at best.

Spectroscopic data for Sr(II) were consistent with the selection of outer-sphere reactions to describe adsorption. Two outer-sphere reactions were employed to describe the trends in pH, ionic strength and surface coverage. One of the significant components of the modeling approach was that the TLM parameters used for Cd(II) and Sr(II) were constrained to employ the same model constants derived previously for Co(II). In both cases, it was possible to describe the adsorption behavior of these solutes using the same values of the surface hydroxyl site density, surface protolysis equilibrium constants, and electrolyte binding equilibrium constants.

While this chapter has illustrated the utility of SCM for predicting sorption behavior of divalent metal ions using the methodology described, much still remains to be accomplished before SCM can be more universally applied. For example, while this study focused on single-solute adsorption onto pure oxides, more research needs to address the use of SCM in multisolute systems containing other sorbing anions and cations, and to evaluate sorption in heterogeneous soils. A limited amount of research conducted in this area suggest that SCM show promise in this regard (Wang et al., 1997) but more research is needed prior to field-scale application (e.g., Davis et al., 1998).

# **ACKNOWLEDGMENTS**

We thank H. Magdi Selim and Donald Sparks for inviting us to participate in the SSSA symposium that resulted in this volume and for their patience in waiting for our manuscript. We would also like to thank Donald Sparks, and Noel Scrivner and James Dyer at Dupont Engineering, for their sabbatical support of the senior author while preparing aspects of this chapter. The staff at SSRL (supported by the Department of Energy and the National Institutes of Health), especially Dr. Britt Hedman, were extremely helpful during our XAS beamtime. Chia-Chen Chen, Lambis Papelis, Sam Traina and Kim Hayes have been invaluable members of our research team at SSRL. The comments of two anonymous reviewers were

extremely helpful. This research was supported by the National Science Foundation, Grant Nos. BES-9625047 and BES-9896214.

### REFERENCES

- Anderson, P.R., and M.M. Benjamin. 1990. Modeling adsorption in aluminum-iron binary oxide suspension. Environ. Sci. Technol. 24:1586–1592.
- Baes, C.F., and R.E. Mesmer. 1976. The hydrolysis of cations. Krieger Publ. Co., Malabar, FL.
- Baolin, D., and A.T. Stone. 1996. Surface-catalyzed chromium(VI) reduction: The TiO<sub>2</sub> –Cr(VI)-mandelic acid system. Environ. Sci. Technol. 30:463–467.
- Bargar, J.R., G.E. Brown, Jr., and G.A. Parks. 1997a. Surface complexation of Pb(II) at oxide water interfaces: I. XAFS and bond-valence determination of mononuclear Pb(II) sorption products on aluminum oxides. Geochim. Cosmochim. Acta 61:2617–2637.
- Bargar, J.R., G.E. Brown, Jr., and G.A. Parks. 1998. Surface complexation of Pb(II) at oxide-water interfaces: III. XAFS determination of Pb(II) and Pb(II)-chloro adsorption complexes on goethite and alumina. Geochim. Cosmochim. Acta 62:193–207.
- Bargar, J.R., S.N. Towle, G.E. Brown, Jr., and G.A. Parks. 1997b. XAFS and bond-valence determination of the structures and compositions of surface functional groups and Pb(II) and Co(II) sorption products on single-crystal α-Al<sub>2</sub>O<sub>3</sub>. J. Colloid Interf. Sci. 185:473–492.
- Barrow, N.J., J.W. Bowden, A.M. Posner, and J.P. Quirk. 1980. An objective method for fitting models of ion adsorption on variable charge surfaces. Aust. J. Soil Res. 18:37–47.
- Barrow, N.J., J.W. Bowden, A.M. Posner, and J.P. Quirk. 1981. Describing the adsorption of copper, zinc and lead on a variable charge mineral surface. Aust. J. Soil Res. 19:309–321.
- Bellotto, M., B. Rebours, O. Clause, J. Lynch,, D. Bazin, and E. Elkaim. 1996. Hydrotalcite decompostion mechanism: A clue to the structure and reactivity of spinel-like mixed oxides. J. Phys. Chem. 100:8535–8542.
- Bish, DL. 1980. Anion-exchange in takovite: Applications to other hydroxide minerals. Bull. Mineral. 103:170–175.
- Bondietti, G., J. Sinniger, and W. Stumm. 1993. Reactivity of Fe(III) (hydr)oxides. Effects of ligands in inhibiting the dissolution. Colloids Surf. 79(A):157–161.
- Bowden, J.W., S. Nagarajah, N.J. Barrow, A.M. Posner, and J.P. Quirk. 1980. Describing the adsorption of copper, zinc and lead on a variable charge mineral surface. Aust. J. Soil Res. 18:49–51.
- Brindley, G.W., and S. Kikkawa. 1979. A crystal-chemical study of Mg, Al and Ni, Al hydroxy-per-chlorates and hydroxy-carbonates. Am. Mineral. 64:836–843.
- Brown, Jr., G.E. 1990. Spectroscopic studies of chemisorption reaction mechanisms at oxide-water interfaces. p. 23, 309–363. *In* M.F. Hochella and A.F. White (ed.) Mineral water interface geochemistry. Mineral. Soc. Am., Washington, DC.
- Brown, Jr., G.E., G. Calas, G.A. Waychunas, and J. Petiau. 1990. X-ray absorption spectroscopy and its applications in mineralogy and geochemistry. p. 431–512. *In* F.C. Hawthorne (ed.) Spectroscopic methods in mineralogy and geology. Reviews in mineralogy. Vol. 18. Mineral. Soc. Am., Washington, DC.
- Brown, Jr., G.E., G.A. Parks, J.R. Bargar, and S.N. Towle. 1999. Use of x-ray absorption spectroscopy to study reaction mechanisms at metal oxide-water interfaces. p. 14–36. *In* D.L. Sparks and T.J. Grundl (ed.) Kinetics and mechanisms of reactions at the mineral/water interface. ACS Symp. Ser. no. 715. ACS, Washington, DC.
- Cavani, F., F. Trifiro, and A. Vaccari 1991. Hydrotalcite-like anionic clays: Preparation, properties and applications. Catal. Today 11:173–301.
- Chan, D., J.W. Perram, L R. White, and T.W. Healy. 1975. Regulation of surface potential at amphoteric surfaces during particle-particle interaction. J. Chem. Soc. Faraday Trans. 71:1046–1057.
- Charlet, L., and A. Manceau. 1992. X-ray absorption spectroscopic study of the sorption of chromium(III) at the oxide-water interface. II. Adsorption, coprecipitation, and surface precipitation on hydrous ferric oxide. J. Colloid Interf. Sci. 148:443–58.
- Charlet, L., and A. Manceau. 1994. Evidence for the neoformation of clays upon sorption of Co(II) and Ni(II) on silicates. Geochim. Cosmochim. Acta 58:2577–2582.
- Charmas, R., W. Paisecki, and W. Rudzinski. 1995. Four layer complexation model for ion adsorption at electrolyte/water interface: Theoretical foundations. Langmuir 11:3199–3210.
- Chen, C.C., and K.F. Hayes. 1999. X-ray absorption spectroscopy investigation of aqueous Co(II) And Sr(II) sorption at clay water interfaces, Geochim. Cosmochim. Acta 58:3205–3216.

- Chisholm-Brause, C.J. 1991. Spectroscopic and equilibrium study of cobalt (II) sorption complexes at oxide/water interfaces. Ph.D. diss. Stanford Univ., Stanford, CA.
- Chisholm-Brause, C.J., P.A. O'Day, and G.E. Brown, Jr. 1990. Evidence for multinuclear metal-ion complexes at solid/water interfaces from x-ray absorption spectroscopy. Nature (London) 348;528–530.
- Criscenti, L.J., and D.A. Sverjensky. 1999. The role of electrolyte anions (ClO<sup>4-</sup>, NO<sup>3-</sup>, and Cl<sup>-</sup>) in divalent metal (M<sup>2+</sup>) adsorption on oxide -and hydroxide surfaces in salt solutions. Am. J. Sci. 299:828–899.
- Davis, J.A., J.A. Coston, D.B. Kent, and C.C. Fuller. 1998. Application of the surface complexation concept to complex mineral assemblages. Environ. Sci. Technol. 32:2820–2828.
- Davis, J.A., R.O. James, and J.O. Leckie. 1978. Surface ionization and complexation at the oxide/water interface. I. Computation of electrical double layer properties in simple electrolytes. J. Colloid Interf. Sci. 63:480–499.
- Davis, J.A., and D.B. Kent 1990. Surface complexation modeling in aqueous geochemistry. p. 177–260. *In* M.F. Hochella and A.F. White (ed.) Mineral water interface geochemistry. Vol. 23. Mineral. Soc. Am., Washington, DC.
- Davis, J.A., and J.O. Leckie. 1978. Surface ionization and complexation at the oxide/water interface. II. Surface properties of amorphous iron oxyhydroxide and adsorption of metal ions. J. Colloid Interf. Sci. 67:90–107.
- Davis, J.A., and J.O. Leckie. 1980. Surface ionization and complexation at the oxide/water interface. III. Adsorption of anions. J. Colloid Interf. Sci. 74:32–43.
- de la Caillerie, J.B., M. Kermarec, and O. Clause. 1995. Impregnation of gamma-alumina with Ni(II) or Co(II) ions at neutral pH: Hydrotalcite-type coprecipitate formation and characterization. J. Am. Chem. Soc. 117:11471–11481.
- Dzombak, D.A 1989. Computer programs for implementation of the generalized two-layer model. Dep. Civil Eng. Tech. Rep. Carnegie-Mellon Univ., Pittsburgh, PA.
- Dzombak, D.A., and F.M.M. Morel. 1990. Surface complexation modeling: Hydrous ferric oxide. Wiley Intersci., New York.
- Eisenmann, G. 1962. Cation selective glass electrodes and their mode of operation. Biophys. J. 2:259–323.
- Farley, K.J., D.A. Dzombak, and F.M.M. Morel. 1985. A surface precipitation model for the sorption of cations on metal oxides. J. Colloid Interf. Sci. 106:226–242.
- Felmy, A.R., and J.R. Rustad. 1998. Molecular statics calculations of proton binding to goethite surfaces: Thermodynamic modeling of the surface charging and protonation of goethite in aqueous solution. Geochim. Cosmochim. Acta 62:25–31.
- Fendorf, S.E., G.M. Gamble, M.G. Stapleton, M.J. Kelley, and D.L. Sparks. 1994. Mechanisms of chromium (III) sorption on silica. 1. Cr(III) surface structure derived by extended x-ray absorption fine structure spectroscopy. Environ. Sci. Technol. 28:284–289.
- Fendorf, S.E., R.J. Zasoski, and R.G. Burau. 1993. Competing metal ion influences on chromium (III) oxidation by birnessite. Soil Sci. Soc. Am. J. 57:1508–1515.
- Ford, R.J., A.C. Scheinost, K.G. Scheckel, and D.L. Sparks. 1999. The link between clay mineral weathering and the stabilization of Ni surface precipitates. Environ. Sci. Technol. 33:3140–3144.
- Goldberg, S. 1992. Use of surface complexation models in mineralogy and geology. Adv. Agron. 47:233–329.
- Hansmann, P.D., and M.A. Anderson. 1985. Using electrophoresis in modeling sulfate, selenite, and phosphate adsorption onto geothite. Environ. Sci. Technol. 19:544–551.
- Hashi, K., S. Kikkawa, and M. Koizumi. 1983. Preparation and properties of pyroaurite-like hydroxy minerals. Clays Clay Miner. 31:152–154.
- Hayes, K.F., and L.E. Katz. 1996. Application of x-ray absorption spectroscopy for surface complexation modeling of metal ion sorption. p. 147–223. *In* P.V. Brady (ed.) Physics and chemistry of mineral surfaces. CRC Press, Boca Raton, FL.
- Hayes, K.F., and J.O. Leckie 1986. Modeling ionic strength effects on cation adsorption at hydrous oxide/solution interfaces. J. Colloid Interf. Sci. 115:564–572.
- Hayes, K.F., J.O. Redden, W. Ela, and J.O. Leckie. 1991. Surface complexation models. I. An evaluation of model parameter estimation using FITEQL and oxide mineral titration data. J. Colloid Interf. Sci. 142:448–469.
- Hayes, K.F., L.A. Roe, G.E. Brown, Jr., K.O. Hodgson, J.O. Leckie, and G.A. Parks. 1987. In-situ x-ray absorption study of surface complexes at oxide/water interfaces: Selenium oxyanions on α-FeOOH. Science (Washington, DC) 238:783–786.
- Hendershot, W.H., and L.M. Lavkulich. 1983. Effect of sesquioxide coatings on surface charge of standard mineral and soil samples. Soil Sci. Soc. Am. J. 47(1252) 4260

- Herrera,-Urbina, R., and D.W. Fuerstenau. 1995. The effect of Pb(II) species, pH and dissolved carbonate on the zeta potential at the quartz/aqueous solution interface. Colloids Surf. 98(A):25–33.
- Hiemstra, T., J.C.M. De Wit, and W.H. Van Riemsdijk. 1989a. Multi proton adsorption modeling at the solid/solution interface of (hydr)oxides: A new approach. II. Application to various important (hydr)oxides. J. Colloid Interf. Sci. 133:105–117.
- Hiemstra, T., W.H. Van Riemsdijk, and G.H. Bolt. 1989b. Multisite proton adsorption modeling at the solid/solution interface of (hydr)oxides: A new approach. I. Model description and evaluation of intrinsic reaction constants. J. Colloid Interf. Sci. 133:91–104.
- Hohl, H., and W. Stumm. 1976. Interaction of Pb<sup>2+</sup> with hydrous γ-Al<sub>2</sub>O<sub>3</sub>. J. Colloid Interf. Sci. 55:281–288.
- Honeyman, B.D. 1984. Cation and anion adsorption at the oxide/solution interface in systems containing binary mixtures of adsorbents: An investigation of the concept on adsorptive additivity. Ph.D. diss. Stanford Univ., Stanford, CA.
- House, W.A. 1994. The role of surface complexation in the dissolution kinetics of silica: effects of monovalent and divalent ions at 25°C. J. Colloid Interf. Sci. 163:379–390.
- Huang, C.P., and W. Stumm. 1973. Specific adsorption of cations on hydrous γ-Al<sub>2</sub>O<sub>3</sub>. J. Colloid Interf. Sci. 43:409–420.
- James, R.O., and T.W. Healy. 1972a. Adsorption of hydrolyzable metals ions at the oxide/water interface. I. Co (II) adsorption on SiO<sub>2</sub> and TiO<sub>2</sub> model systems. J. Colloid Interf. Sci. 40:42–52.
- James, R.O., and T.W. Healy. 1972b. Adsorption of hydrolyzable metal ions at the oxide-water interface. II. Charge reversal of SiO<sub>2</sub>- and TiO<sub>2</sub>-colloids by adsorbed Co(II), La(III), and Th(IV) as model systems. J. Colloid Interf. Sci. 40:53–64.
- James, R.O., and T.W. Healy. 1972c. Adsorption of hydrolyzable metal ions at the oxide-water interface. III A thermodynamic model of adsorption. J. Colloid Interf. Sci. 40:65–81.
- James, R.O., and G.A. Parks. 1982. Characterization of aqueous colloids by their electrical double-layer and intrinsic surface chemical properties. p. 119–216. *In* E. Matijevic (ed.) Surfaces and colloid science. Vol. 12. Plenum Press, New York.
- Johnsson, P.A. 1994. Hematite dissolution in natural organic acids. Ph.D. diss. Stanford Univ., Stanford, CA.
- Katz, L.E. 1993. Surface complexation modeling of cobalt ion sorption at the  $\alpha$ -Al<sub>2</sub>O<sub>3</sub>-water interface: Monomer, polymer and precipitation reactions. Ph.D. diss. Univ. Michigan, Ann Arbor, MI.
- Katz, L.E., and K.F. Hayes. 1995a. Surface Complexation modeling: I Strategy for modeling monomeric complex formation at moderate surface coverage. J. Colloid Interf. Sci. 170:477-490.
- Katz, L.E., and K.F. Hayes. 1995b. Surface complexation modeling: II. Strategy for modeling polymer and precipitation reactions at high surface coverage. J. Colloid Interf. Sci. 170:491–501.
- Kosmulski, M. 1996. Adsorption of cadmium on alumina and silica: Analysis of the values of stability constants of surface complexes calculated for different parameters of triple layer model. Colloid Surf. 117:201–214.
- Liang, L., and J.J. Morgan. 1990. Chemical aspects of iron oxide coagulation in water: Laboratory studies and implications in natural systems. Aquat. Sci. 52:32–55.
- Lindsay, W.L. 1979. Chemical equilibria in soils. John Wiley & Sons, Inc., New York.
- Lothenbach B., G. Furrer, and R. Schulin. 1997. Immobilization of heavy metals by polynuclear aluminum and montmorillonite compounds. Environ. Sci. Technol. 31:1452–1462.
- Lytle, F.W., D.R. Sandstrom, E.C. Marques, J. Wong, C.L. Spiro, G.P. Huffman, and F.E. Huggins. 1984. Measurements of soft x-ray absorption spectra with fluorescence ion chamber detector. Nucl. Instr. Meth. 226:542–548.
- Manceau A., and L. Charlet. 1992. X-ray absorption spectroscopic study of the sorption of chromium(III) at the oxide-water interface. I. Molecular mechanism of Cr(III) oxidation on manganese oxides. J. Colloid Interf. Sci. 148:425–429.
- McBride, M.B. 1982. Cu<sup>2+</sup>-adsorption characteristics of aluminum hydroxide and oxyhydroxides. Clays Clay Miner. 30:21–28.
- McBride, M.B. 1985a. Influence of glycine on Cu<sup>2+</sup> adsorption by microcrystalline gibbsite and boehmite. Clays Clay Miner. 33:397–402.
- McBride, M.B. 1985b Sorption of copper (II) on aluminum hydroxide as affected by phosphate. Soil Sci. Soc. Am. J. 49:843–846.
- McBride, M.B. 1994. Environmental chemistry of soils. Oxford Univ. Press, New York.
- McBride, M.B., A.R. Fraser, and W.J. McHardy. 1984. Cu<sup>2+</sup> Interaction with microcrystalline gibbsite. Evidence for oriented chemisorbed copper ions. Clays Clay Miner. 32:12–18.
- McKenzie, R.M. 1970. The reaction of cobalt with manganese dioxide minerals. Aust. J. Soil Res. 8:97–106.

- McMaster, W.H., N. Nerr del Grande, and J.H. Mallett. 1969. Compilation of x-ray cross sections. Rep. UCRL-50174. Sect. 2. Rev. 1. Lawerence Radiat. Lab., Univ. California, Livermore, CA.
- Morel, F.M.M., J.G. Yeasted, and J.C. Westall. 1981. Adsorption models: A mathematical analysis in the framework of general equilibrium calculations. p. 263–294. *In* M.A. Anderson and A.J. Rubin (ed.) Adsorption of inorganics at solid-liquid interfaces. Ann Arbor Sci., Ann Arbor, MI.
- O'Day, P.A., G.E. Brown, and G.A. Parks. 1994a. X-ray absorption spectroscopy of Cobalt(II) multinuclear surface complexes and surface precipitates on kaolinite. J. Colloid Interf. Sci. 165:269–289.
- O'Day, P.A., C.J. Chisholm-Brause, S.N. Towle, G.A. Parks, and G.E. Brown, Jr. 1996. X-ray absorption spectroscopy of Co(II) sorption complexes on quartz (-SiO<sub>2</sub>) and rutile (TiO<sub>2</sub>). Geochim. Cosmochim. Acta 60:2515–2532.
- O'Day, P.A., M. Newville, P.S. Neuhoff, N. Sahai, and S.A. Carroll. 2000. X-ray absorption spectroscopy of strontium (II) coordination. I. Static and thermal disorder in crystalline, hydrated, and precipitated solids and in aqueous solution. J. Colloid Interf. Sci. 222:198–212.
- O'Day, P.A., G.A. Parks, and G.E. Brown. 1994b. Molecular structure and binding sites of cobalt(II) Surface complexes on kaolinite from x-ray absorption spectroscopy. Clays Clay Miner. 42:337–355.
- Papelis, C., G.E. Brown, Jr., G.A. Parks, and J.O. Leckie. 1995. X-ray absorption spectroscopic studies of cadmium and selenite adsorption on aluminum oxides. Langmuir 11:2041–2048.
- Papelis, C., and K.F. Hayes. 1996. Distinguishing between interlayer and external sorption sites of clay minerals using x-ray absorption spectroscopy. Colloids Surf. Aspects 107:89–96.
- Papeilis, C., K.F. Hayes, and J.O. Leckie. 1988. Hydraql: A program for the computation of chemical equilibrium of aqueous batch systems including surface-complexation modeling of ion adsorption at the oxide/water interface. Dep. Civil Eng. Tech. Rep. no. 306. Stanford Univ., Stanford, CA.
- Parkman, R.H., J.M. Charnock, F.R. Livens, and D.J. Vaughan. 1998. A study of the interaction of strontium ions in aqueous solution with the surfaces of calcite and kaolinite. Geochim. Cosmochim. Acta 62:1481–1492.
- Parks, G.A. 1965. The isoelectric points of solid oxides, solid hydroxides and aqueous hydroxo complex systems. Chem. Rev. 65:177–198.
- Rehr, J.J., J. Mustre de Leon,, S.I. Zabinski, and R.C. Albers. 1991. Theoretical x-ray absorption fine structure standards. J. Am. Chem. Soc. 113:5135–5140.
- Robertson, A.P., and J.O. Leckie. 1997. Cation binding predictions of surface complexation models: Effects of pH, ionic strength, cation loading, surface complex and model fit. J. Colloid Interf. Sci. 188:444–472.
- Ryan, J.N., and P.M. Gschwend. 1992. Effect of diagenesis on the transport of colloidal clay in an unconfined sand aquifer. Geochim. Cosmochim. Acta 56:1507–1521.
- Sahai, N., S.A. Carroll, S. Roberts, and P.A. O'Day. 2000. X-ray absorption spectroscopy of strontium(II) coordination. II. Sorption and precipitation at kaolinite, silica gel, and goethite surfaces. J. Colloid Interf. Sci. 222:184–197.
- Sahai, N., and D.A. Sverjensky. 1997a. Evaluation of internally consistent parameters for the triple layer model by the systematic analysis of oxide surface titration data. Geochim. Cosmochim. Acta 61:2801–2826.
- Sahai, N., and D.A. Sverjensky. 1997b. Solvation and electrostatic model for specific electrolyte adsorption. Geochim. Cosmochim. Acta 61:2827–2848.
- Scheidegger, A.M., G.M. Lamble, and D.L. Sparks. 1997. Spectroscopic evidence for the formation of mixed-cation hydroxide phases upon metal sorption on clays and aluminum oxides. J. Colloid Interf. Sci. 186:118–128.
- Scheidegger, A.M., D.G. Strawn, G.M. Lamble, and D.L. Sparks. 1998. The kinetics of mixed Ni-Al hydroxide formation on clays and aluminum oxides: A time-resolved XAFS study. Geochim. Cosmochim. Acta 62:2233–2402.
- Schindler, P.W., and W. Stumm. 1987. The surface chemistry of oxides, hydroxides, and oxide minerals. p. 83–110. *In* W. Stumm (ed.) Aquatic surface chemistry. Wiley-Intersci., New York.
- Shannon, R.D. 1976. Revised effective ionic radii and systematic studies of interatomic distances in halides and chalcogenides. Acta Cryst. B25:925–946.
- Smith, R.M., and A.E. Martell. 1993. Critical stability constants of metal complexes database. Companion CD-ROM [CD-ROM computer file]. NIST, Gaithersburg, MD.
- Sposito, G. 1984. The surface chemistry of soils. Oxford Univ. Press, New York...
- Sposito, G. 1998. On points of zero charge. Environ. Sci. Technol. 32:2815–2819.
- Stahl, R.A., and B.R. James. 1991. Zinc sorption by iron oxide coated sand as a function of pH. Soil. Sci. Soc. Am. J. 55:1287–1290.

- Strawn, D.G., A.M. Scheidegger, and D.L. Sparks. 1998. Kinetics and mechanisms of Pb(II) sorption and desorption at the aluminum oxide/water interface. Environ. Sci. Technol. 32:2596–2601.
- Stumm, W. 1992. Chemistry of the solid-water interface: Processes at the mineral-water and particle water interface in natural systems. John Wiley & Sons, Inc., New York.
- Stumm, W. 1997. Reactivity at the mineral/water interface: Dissolution and inhibition. Colloid Surf. 120:143–166.
- Stumm, W., R. Kummert, and L. Sigg. 1980. A ligand exchange model for the adsorption of inorganic and organic ligands at hydrous oxide interfaces. Croat. Chem. Acta 53:291–312.
- Sverjensky, D.A. 1993. Physical surface complexation models for sorption at the mineral water interface. Nature (London) 364:776–780.
- Sverjensky, D.A. 1994. Zero-point of charge prediction from crystal chemistry and solvation theory. Geochim. Cosmochim. Acta 58:3123–3129.
- Sverjensky, D.A., and N. Sahai. 1996. Theoretical prediction of single-site surface protonation equilibrium constants for oxides and silicates in water. Geochim. Cosmochim. Acta 55:989–1004.
- Taylor, R.M. 1984. The rapid formation of crystalline double hydroxy salts and other compounds by controlled hydrolysis. Clay Miner. 19:591–603.
- Teo, B.-K. 1986. EXAFS: Basic principles and data analysis. *In* Inorganic chemistry concepts. Vol. 9. Springer-Verlag, New York.
- Teo, B.-K., and D.C. Joy. 1981. EXAFS spectroscopy. Plenum Press, New York.
- Thompson, H.A., G.A. Parks, and G.E. Brown, Jr. 1999a. Ambient-temperature synthesis, evolution, and characterization of cobalt-aluminum hydrotalcite-like solids. Clays Clay Miner. 47:425–438
- Thompson, H.A., G.A. Parks, and G.E. Brown, Jr. 1999b. Dynamic interactions of dissolution, surface adsorption, and precipitation in an aging cobalt(II)-clay-water system. Geochim. Cosmochim. Acta 63:1767–1780.
- Torrents, A., and A.T. Stone. 1994. Oxide surface catalyzed hydrolysis of barboxylate esters and phosphorothioate esters. Soil Sci. Soc. Am. J. 58:3.
- Towle, S.N., J.R. Bargar, G.E. Brown, Jr., and G.A. Parks. 1997. Surface precipitation of Co(II)(aq) on Al<sub>2</sub>O<sub>3</sub>. J. Colloid Interf. Sci. 187:62–82.
- Venema, P., T. Hiemstra, and W.H. van Riemsdijk. 1996. Comparison of different site binding models for cation sorption: Description of pH dependency, salt dependency, and cation-proton exchange. J. Colloid Interf. Sci. 181:45–59.
- Wang, F., C. Jingsheng, and F. Willis. 1997. Modeling sorption of trace metals on natural sediments by surface complexation model. Environ. Sci. Technol. 31:448–453.
- Westall, J.C. 1982. FITEQL: A computer program for determination of chemical equilibrium constants from experimental data. Rep. 82-01. Dep. Chem., Oregon State Univ., Corvallis, OR.
- Westall, J.C., and H. Hohl. 1980. A comparison of electrostatic models for the oxide/solution interface. Adv. Colloid Interf. Sci. 12:265–294.
- Xia, K., A. Mehadi, R.W. Taylor, and W.F. Bleam. 1997. X-ray absorption and electron paramagnetic resonance studies of Cu(II) sorbed to silica: Surface-induced precipitation at low surface coverages. J. Colloid Interf. Sci. 185:252–257.
- Yates, D.E., S. Levine, and T.W. Healy. 1974. Site binding model of the electrical double layer at the oxide/water interface. Chem. Soc. Faraday Trans. 70:1807–1818.
- Zabinsky S.I., J.J. Rehr, A. Ankudinov, R.C. Albers, and M.J. Eller. 1995. Multiple-scattering calculations of x-ray-absorption spectra. Phys. Rev. (B) 52:2995–3009

# Molecular Dynamics Simulations of Adsorption Processes at the Clay Mineral/Aqueous Solution Interface

David M. Miller, Ching-Hsing Yu, and Lothar Schäfer

University of Arkansas Fayetteville, Arkansas

Brian J. Teppen

Michigan State University East Lansing, Michigan

In 1808 the great French chemist Gay-Lussac predicted that "we are perhaps not far removed from the time when we shall be able to submit the bulk of chemical phenomena to calculation" (Gay-Lussac, 1808). Today, almost 200 yr later, we are on the verge of realizing Gay-Lussacs vision. The widespread availability of high-speed computers and the development of efficient software packages have caused phenomenal growth in a subdiscipline now generally referred to as computational chemistry. What began as an esoteric chemical exercise has evolved into a powerful tool used increasingly by chemists to solve a wide array of problems in applied fields such as pharmaceuticals development, nanomaterials, and soil chemistry.

To a large extent soil chemistry has traditionally been a phenomenological science. That is, various important bulk properties of soils, such as the thermodynamics and kinetics of adsorption, have been studied extensively and successfully, but detailed mechanistic explanations of such phenomena in molecular terms are largely unavailable, even though they are highly desirable. In an attempt to provide molecular descriptions of such phenomena as adsorption in soils, during the past decades soil chemists have increasingly employed spectroscopic techniques. In support of these efforts and in the hope of aiding in the interpretation of experimental data, we have explored the possibilities of using atomic scale computer simulations to arrive at general mechanistic models that can rationalize the large body of empirical data that have been accumulated for important soil chemical processes.

The molecular computational techniques that we chose to perform the desired tasks are based on classical potential energy functions that allow one to approximate the forces influencing a collection of atoms. In the case of polar solutes and

water near clays, the dominant forces arise from electrostatics and hydrogen bonding, while dispersion forces are dominant in the adsorption of nonpolar molecules by clays. Thus, effective and useful potential energy parameters must accurately describe clay electrostatics, the hydrogen bonding of surface hydroxyls, and the dispersion/repulsion characteristics of clay surface atoms. If these parameters are properly calibrated, then the computational techniques can effectively describe adsorption reactions that are governed by nonbonded forces, such as those for cations and neutral organics. In order for such methods to be successful, it is of course a prerequisite that the basic structural features of the clay systems involved are known from experimental studies, such as x-ray crystallography.

Within the framework of classical computational procedures, molecular dynamics (MD) simulations are an effective tool for providing insight into the properties of large molecular systems. Such simulations typically generate a collection of molecular states or configurations that approximately represent a statistical mechanical ensemble, and they are characterized by the fact that optimized potential energy is not sought for in a static way but, rather, the atoms and molecules in a given ensemble are allowed to move freely, approaching an equilibrium state without any restraints other than those imposed by the potential energy functions and the state variables, such as temperature and pressure. Standard formulae from statistical thermodynamics can then be used to calculate ensemble averages, which in turn can be related to the macroscopic properties of interest. In the recent past we have developed potential energy functions that make it possible to apply MD simulation techniques to study adsorption phenomena at the clay mineral/aqueous solution interface. It is the purpose of this chapter to provide a short introduction to the procedures involved, to illustrate their capabilities by describing some of our recent results, and to provide an outlook by describing some of our current and planned projects.

### SOME ASPECTS OF MOLECULAR FORCE FIELDS

In order to perform MD simulations of an ensemble of molecules, the potential energy of the system has to be known. When the latter is formulated in terms of a valence type potential, the total potential energy of a molecule,  $V_{\text{tot}}$ , can be expressed as the sum of potential energy terms corresponding to bond stretching, angle bending, angle torsion, electrostatic interactions, and van der Waals interactions:

$$V_{\text{tot}} = V_{\text{bond stretch}} + V_{\text{angle bend}} + V_{\text{angle torsion}} + V_{\text{electrostatic}} + V_{\text{vdW}} + cross terms$$
[1]

The parameter-coupling cross terms model correlations between coordinates of different type, such as between bond stretching and angle bending.

The individual terms of Eq. [1] can be expressed by various functionalities. As representative examples we present, in Eq. [2] to [6], the specific functional expressions that we are using in our work. These expressions are the same as those used in the force field developed by Maple et al. (1994), and they form the operational basis of the MSI/Insight/Discover software suite (MSI, 1997).

The bond stretch potential in this force field (Maple et al., 1994) is:

$$V_{\text{bond stretch}} = k_2 (r - r_0)^2 + k_3 (r - r_0)^3 + k_4 (r - r_0)^4$$
 [2]

where  $r_0$  is the equilibrium separation distance between two bonded atoms, r is the actual separation distance, and  $k_2$ ,  $k_3$ , and  $k_4$  are potential parameters. A complete set of parameters ( $k_2$ ,  $k_3$ ,  $k_4$  and  $r_0$ ) is required for each unique pair of bonded atom types. For example, the values of these parameters will be different for a bond between Al in octahedral coordination and triply coordinated O in the octahedral sheet, or between Al in tetrahedral coordination and O in a Si-O-Al linkage.

The functional form of the angle bending potential in this force field (Maple et al., 1994) is:

$$V_{\text{angle}} = c_2(\theta - \theta_0)^2 + c_3(\theta - \theta_0)^3 + c_4(\theta - \theta_0)^4$$
 [3]

where  $\theta_0$  is the equilibrium bond angle and  $c_2$ ,  $c_3$ , and  $c_4$  are potential parameters. Similarly, for the torsional potential:

$$V_{\text{torsion}} = T_1 [1 + \cos(\phi - \phi_{01})] + T_2 [1 + \cos(2\phi - \phi_{02})] + T_3 [1 + \cos(3\phi - \phi_{03})]$$
 [4]

where the  $\phi_{0i}$  are equilibrium torsion angles and the  $T_i$  are the potential parameters. The potential energy possessed by a molecule that results from nonbonded interactions between atoms is described by van der Waals and electrostatic potentials:

$$V_{\text{vdW}} = (A_{i}A_{j}/r_{lj}^{9}) - (B_{i}B_{j}/r_{lj}^{6})$$
 [5]

$$V_{\text{electrostatic}} = q_i q_j / \varepsilon r_{ij}$$
 [6]

where the  $A_i$  and  $B_i$  are van der Waals repulsion and attraction parameters, respectively,  $r_{ij}$  is the distance between atoms i and j, the  $q_i$  are partial atomic charges,  $\varepsilon$  is the dielectric constant of the intervening medium, and the subscripts refer to atoms i and j.

A collection of atom types, potential energy equations, and all associated parameters is collectively referred to as a force field. Historically, force fields were parameterized by comparing simulated molecular structures and conformational energies with experimentally determined structures and energies and adjusting the parameters until differences between simulated and experimental values were minimized. In part because experimental data of high quality are sparse, increased use is now being made of quantum mechanical calculations to supplement the experimental data base available for force field parameter development. In order to proceed in this way, the structures and energies of representative molecules are calculated ab initio, and the force field parameters are adjusted in such a way as to reproduce the ab initio results as accurately as possible.

In addition to providing reference molecular structures, quantum mechanical calculations also yield direct estimates of other molecular properties, such as force constants and partial atomic charges, which are of direct utility in force field

parameter development. To serve this purpose, the ab initio calculations must be performed at a level that is in close agreement with experimental data. This means that, for example, nonbonded parameters must be obtained from ab initio calculations that include electron correlation (Teppen et al., 1994; Ramek et al., 1996).

All the results described below were obtained with the force field supplied with the MSI/Insight/Discover software suite (MSI, 1997). More precisely, this force field consists of the cff91 parameters (Maple et al., 1994) for standard organic and inorganic compounds, augmented with parameters for silicates and zeolites developed by Hill and Sauer (1994, 1995). Since zeolites do not contain octahedrally coordinated Al, we had to derive (Teppen et al., 1997) new potential parameters that make it possible to perform molecular dynamics simulations of phyllosilicates. Specifically, it was necessary to derive an angle bending potential for octahedral O-Al-O angles that is able to produce dual minima at 90 and 180°. In addition, since the force field by Hill and Sauer (1994, 1995) was based in part on the results of ab initio calculations that did not include electron correlation, a new set of nonbonded parameters and partial atomic charges was derived from the results of new, electron-correlated ab initio calculations of molecular structures representing fragments of phyllosilicates. The resulting potential parameters (Teppen et al., 1997) were further refined to reproduce as closely as possible the x-ray crystal structures of some oxides and phyllosilicate minerals.

To illustrate this approach, the simulated and experimental structures of gibbsite, kaolinite and pyrophyllite are compared in Fig. 8–1. The experimental crystal structures are those of Saalfeld and Wedde (1974) for gibbsite, Bish (1993) for kaolinite, and Lee and Guggenheim (1981) for pyrophyllite. In Table 8–1 structural parameters of pyrophyllite obtained with our force field are compared with the corresponding x-ray crystallographic values of Lee and Guggenheim (1981). Details on how the mineral structures were calculated can be found in the original paper (Teppen et al., 1997). Furthermore, information on the procedural details involved in performing molecular dynamics simulations can be found in a number of standard texts, such as the one by Allen and Tildesley (1987).

# A BRIEF REVIEW OF RELATED WORK CONDUCTED BY OTHER RESEARCH GROUPS

While the focus of this chapter is on research conducted by our group, there are numerous other research groups performing computer simulations of the molecular properties of clay minerals. Several of these groups are using methods that are different from those used by us. A brief summary of the work being conducted by these groups follows.

The bulk structures of most minerals important to soil chemists are well known from x-ray and neutron diffraction studies. Exceptions to this generality would be the various amorphous oxides and mixed oxide precipitates. Methods pioneered by Catlow's group should find increasing applicability to the structural study of these amorphous soil minerals and mixed phases. Their approach has been to develop ionic-type force fields for performing static energy minimizations of general oxide and halide minerals. Since ionic force fields require far fewer parameters than va-

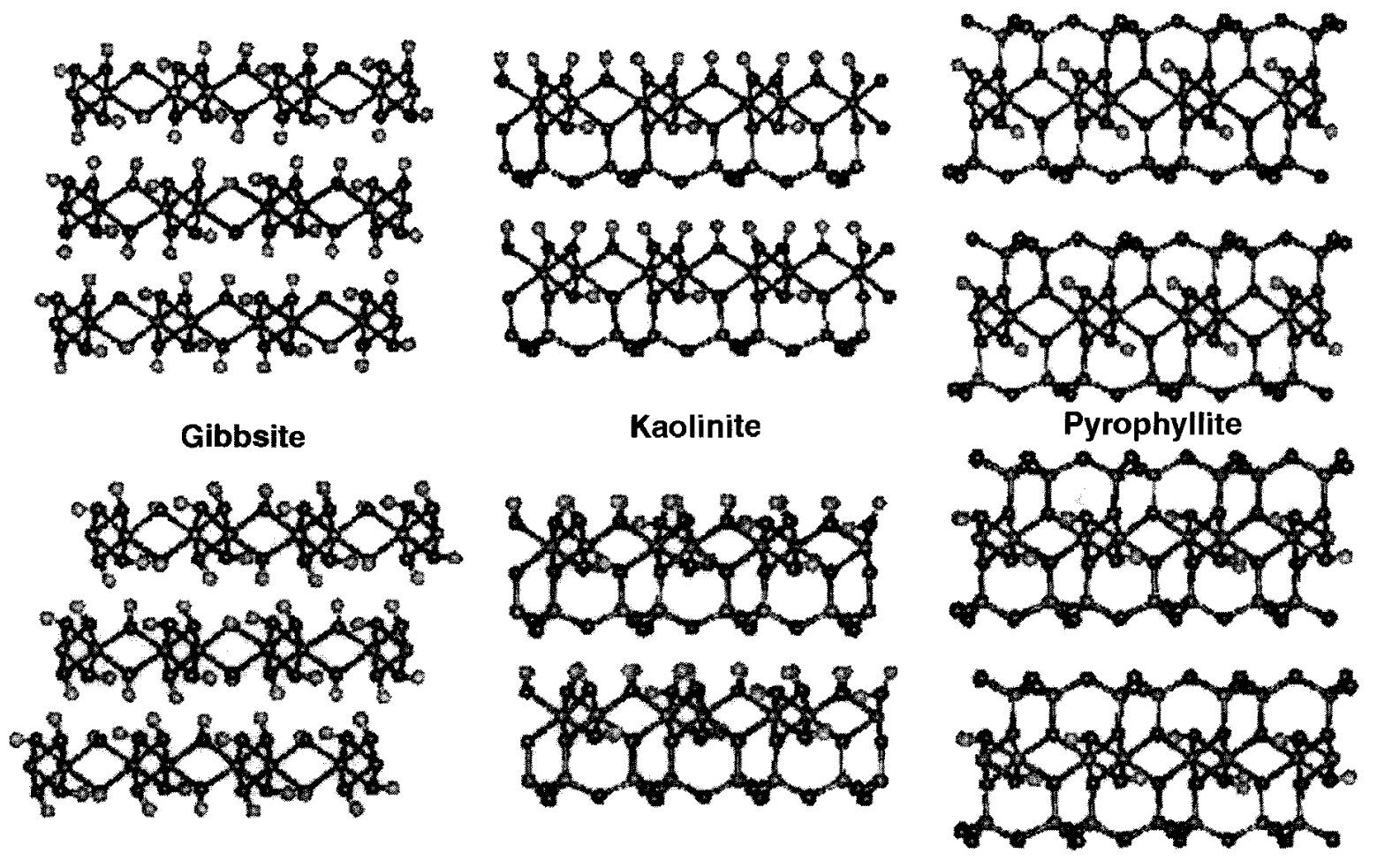


Fig. 8–1. Comparison of experimentally determined crystal structures (top) with typical snapshots from constant-pressure MD simulations (bottom) for gibbsite (left), kaolinite (center) and pyrophyllite (right). The crystal structures used were by Saalfeld and Wedde (1974) for gibbsite, Bish (1983) for kaolinite, and Lee and Guggenheim (1981) for pyrophyllite.

Mineral parameter	Simulated	Experimental†	
a axis length	$0.518 \pm 0.002$	0.5160	
b axis length	$0.902 \pm 0.007$	0.8966	
layer d spacing	$0.931 \pm 0.004$	0.9190	
density (Mg m <sup>-3</sup> )	$2.75 \pm 0.02$	2.815	
Al-O bond length	$0.192 \pm 0.003$	0.1911	
Si-O bond length	$0.163 \pm 0.003$	0.1618	
O-H bond length	$0.097 \pm 0.002$	0.0970	

Table 8–1. Comparison of simulated and experimental crystal structure parameters for pyrophyllite (all distances in nm).

lence force fields, they have generally been able to derive their force fields from experimental data for simple oxides (Sanders et al., 1984; Collins & Catlow, 1990), although they have had occasion to employ quantum calculations, too (Gale et al., 1992; Purton et al., 1993). They have tested their overall force field for its applicability to mixed oxides (Bush et al., 1992, 1994; Battle et al., 1995; Lewis et al., 1995), mica (Collins & Catlow, 1990, 1991, 1992; Collins et al., 1993) and smectite clay minerals (Breu & Catlow, 1995).

For the study of adsorption to general oxide surfaces, the ideal ionic force-field would be consistent with a molecular mechanics model for dissociable water. Such a forcefield has indeed been developed and has been applied to the study of silicate (Rustad & Hay, 1995) and iron(III) (Rustad et al., 1995) hydrolysis in solution, to bulk iron oxyhydroxide structures (Rustad et al., 1996a) and to the protonation of goethite surfaces (Rustad et al., 1996b).

In many instances, we believe that the forces causing adsorption are almost entirely of a nonbonded nature, as in the case of clays interacting with hydrated cations or nonpolar organics. For these cases, valence force fields are ideally suited for simulating adsorption, and they have the advantage that good parameters already exist for water, organic solutes, and some inorganic solutes. Among soil mineral surfaces, it is the basal surfaces of phyllosilicate clays that have been most extensively studied by both experimental and theoretical methods. A variety of adsorbates have now been simulated in the clay interlayer space, including aqueous alkali cations (Delville, 1991, 1992, 1993; Delville & Sokolowski, 1993; Skipper, 1998a; Skipper et al., 1991, 1995a,b; Chang et al., 1995, 1997, 1999; Boek et al., 1995a,b; Karaborni et al., 1996; Greathouse & Sposito, 1998; Cygan, 1998; Cygan et al., 1998; Smith, 1998), aluminum polymers (Capková et al., 1997, 1998a,b), ammonium cations (Janeba et al., 1998), several metal chelates (Sato et al., 1992a,b, 1996; Breu & Catlow, 1995; Breu et al., 1999; Park et al., 1997) and alkanes (Keldsen et al., 1994; Skipper, 1998b). These simulations have normally been done by holding the clay lattice rigid and allowing the interlayer space to relax through various Monte Carlo or molecular dynamics methods. On the other hand, Breu and Catlow (1995) and Breu et al. (1999) observed "chiral recognition" of an organometallic intercalate by a smectite when they allowed the entire system, including the clay lattice, to relax.

<sup>†</sup> Taken from Lee and Guggenheim (1981).

# THE ADSORPTION OF ORGANIC MATERIALS AT THE CLAY MINERAL/AQUEOUS SOLUTION INTERFACE

The adsorption of organic compounds by clay mineral surfaces is a process of immense interest to soil and environmental chemists. For example, the adsorption of naturally occurring organic compounds such as humic acids by clays is thought to protect the organic from microbial degradation while enhancing the hydrophobicity of the clay mineral surface. In addition, the adsorption of organic molecules has been used in various analytical techniques, such as in the determination of clay layer charge by the alkyl ammonium ion method and in the determination of cation exchange capacity by methylene blue adsorption. In each of these cases, details of the structural and energetic interactions of the organic compounds with the mineral surfaces are important to know and estimates can be obtained from MD simulations.

In this section we shall briefly review three different cases taken from our recent work: the adsorption of trichloroethene by clay minerals, the adsorption of methylene blue by clay minerals, and studies dealing with the alkyl ammonium ion method for layer charge determination.

# **Adsorption Studies of Trichloroethene**

# Scope

Chlorinated hydrocarbons dominate lists of the 10 most commonly detected organic contaminants in groundwaters of the USA and Western Europe (Kerndorff et al., 1992). Among them, trichloroethene (TCE) has perhaps the greatest potential to spread (Schleyer et al., 1992) from waste disposal sites to drinking water sources because of its relatively high water solubility, high vapor pressure, and long persistence in subsurface environments. Toxicological concerns have resulted in regulations (CFR, 1993) placing an upper limit of 0.005 mg L<sup>-1</sup> for concentrations of TCE in American drinking water. The water solubility of TCE is 1385 mg L<sup>-1</sup> (West, 1992), which is more than five orders of magnitude greater than the drinking water limit. Thus, a concerted effort to characterize, understand, contain, and remediate waste plumes of chlorinated hydrocarbons is needed before the plumes further contaminate major aquifers.

From 10 to 10<sup>4</sup> mg kg<sup>-1</sup> TCE sorb to low-organic-matter minerals (Estes et al., 1988; Farrell & Reinhard, 1994a,b), so all contaminated aquifer materials are potential long-term sinks and longer-term sources of TCE, but little or nothing is known about the mechanisms of adsorption. Clay minerals often comprise the bulk of the surface area in low-organic-matter aquifer materials, so the interactions of TCE and clays are of special interest.

The considerations presented above prompted us to explore the behavior of TCE on hydrated clay surfaces (Teppen et al., 1998a,b,c).

**Some Computational Aspects of the Trichloroethene Simulations.** To model the properties of TCE on clay surfaces, in one series of calculations the 1:1 clay mineral knotinite was constructed using experimental coordinates (Bish, 1993). From this, a supercell [composition  $Al_{32}Si_{32}O_{80}(OH)_{64}$ ] was built with a

nearly rectangular repeat unit of 2.061 by 1.788 nm in the *ab*-plane. Unlike smectites, kaolinite does not typically swell along the *c*-axis upon hydration. We nevertheless separated the layers for the purpose of simulation. We increased the *c* axis from 0.74 to 2.0 nm in order to create a 1.2-nm interlayer space where the behavior of water and TCE could be modeled. Here kaolinite proves itself to be an interesting model mineral, since it presents two very different types of surfaces to aqueous solutions. Artificially expanding the interlayer space creates a pore that provides the opportunity to use a single simulation to study adsorption to both types of basal external surface that would be found on a kaolinite mineral grain. Slit-pores of this type are found in the environment, for example in kaolinite books (Dixon, 1989) and perhaps at interfaces between silicate grains and aluminum oxide coatings.

If a system with an artificially and permanently expanded interlayer space was to be modeled (in order to model an external surface, for example), all calculations were performed under NVT (constant mass, volume, and temperature) conditions. In certain other situations such as those described below, the artificially expanded systems were first allowed to equilibrate under NVT conditions and subsequently subjected to NPT (constant mass, pressure, and temperature) conditions, whereupon the separated layers spontaneously reannealed, thereby restoring the equilibrium interlayer spacing characteristic of that particular system.

The kaolinite surfaces were hydrated at two different levels. Either 55 or 89 water molecules were added to the supercell pore and distributed on the surfaces during 15 ps of molecular dynamics simulations to create hydrated mineral surfaces. On a dry clay basis, these systems contained 24 and 39% water, respectively. Then, four TCE molecules were added to the center of each slit-pore and each system was equilibrated for at least 50 ps. In this and all other calculations a time step of 0.5 fs was used.

In another series of MD simulations of TCE on clay mineral surfaces, the clay mineral pyrophyllite, an uncharged, 2:1, dioctahedral phyllosilicate, was constructed using experimental data (Lee & Guggenheim, 1981). We chose pyrophyllite for study because it has the same structure as the smectites, but it is a neutral clay and the interlayer space is thus devoid of the hydrated counterions that would typically be present to complicate simulations.

Six unit cells of pyrophyllite were fused to produce an Al<sub>24</sub>Si<sub>48</sub>O<sub>120</sub>(OH)<sub>24</sub> supercell of neutral, idealized 2:1 clay. Again, we expanded the interlayer space, in this case to 3.0 nm, and inserted 76 water molecules to give a water content of 32% by weight. We equilibrated the water for 15 ps at constant volume, and then inserted eight TCE molecules into the center of the interlayer space. This time, the molecular dynamics were run in the isothermal-isobaric (NPT) ensemble to simulate TCE in a fully hydrated micropore environment with no liquid-gas interfaces.

**Some Mechanistic Aspects of Trichloroethene Sorption.** The simulations described above have so far yielded the following results (Teppen et al., 1998a,b,c):

1. Water was found to outcompete C<sub>2</sub>HCl<sub>3</sub> for clay surface sites. At the lowest water content, the kaolin surfaces were not covered by a complete monolayer, and all TCE molecules were able to adsorb directly to the clay surface. From this state desorption was slow.

2. Three distinct mechanisms coexist for TCE adsorption on clay mineral surfaces. The most stable interaction of C<sub>2</sub>HCl<sub>3</sub> with clay surfaces is by full molecular contact, coplanar with the basal surface. This kind of interaction is suppressed by increasing water loads. This mechanism is preferred more on the hydroxylated aluminalike surface of kaolinite than on the siloxane surface. A second, less stable and more reversible interaction involves adsorption through single-atom contact between one Cl atom of TCE and the clay mineral surface. At higher water contents, TCE cannot sorb parallel to the surface, but inserts one Cl atom through the water monolayer, from both the H-C-Cl and Cl-C-Cl ends, to make contact with the clay surface. In this state the sorbate is rather mobile and can move between different adsorption sites along the mineral surface. In a third mechanism, adsorbed C<sub>2</sub>HCl<sub>3</sub> never contacts the clay directly but sorbs onto the first water layer. This kind of interaction is observed when enough water is present to form a complete water monolayer on the mineral surfaces.

We have also studied the desorption of TCE (Teppen et al., 1998a,c) from kaolinite surfaces. In these studies, a monolayer of TCE was first equilibrated with a kaolinite external (hydroxylated aluminol) surface, and then water was added. After 350 ps of MD simulation (NVT, 5.0-nm interlayer separation, 0.5-fs timestep), 60% of the TCE had desorbed (Fig. 8–2). In this process TCE first changed its interaction with the mineral surface from a planar association to one in which only one or two atoms contacted the clay. Subsequently the TCE desorbed into the water layer.

When the same process was repeated by first equilibrating a monolayer of TCE with a kaolinite siloxane surface and then adding water, after 350 ps of MD simulation only 20% of the TCE had desorbed. As this example shows, MD simulations can be employed in this way to explore the relative kinetics of adsorption/desorption of solutes at the clay mineral/aqueous solution interface.

Ongoing investigations involve capillary phase separation of TCE and water. When condensed phases of TCE and water are created within the interlayer region of pyrophyllite, chosen to represent a generic slioxane-lined slit pore, after 200 ps of molecular dynamics at 298 K and 1 bar, no mixing between the two phases had occurred. Further simulations are underway to assess the likelihood that such capillary phase separation actually will occur spontaneously.

The methods described above for the study of TCE are representative of the methods we are currently using to study the adsorption of a variety of organic molecules by clay mineral surfaces. We shall briefly summarize the results obtained so far in two other cases, one dealing with the adsorption of methylene blue to clays and the other dealing with a recalibration of the alkyl ammonium ion method for surface charge determination. In both of these studies, essentially the same computational techniques as those described above were used.

# The Adsorption of Methylene Blue

# Scope

Methylene blue (MB) was selected for study by MD simulations because it has been widely used for the determination of both surface areas and cation exchange

capacities (CEC) of clay minerals (Brindley & Thompson, 1970; Hang & Brindley, 1970). Surface area estimates are made by noting the MB surface coverage that produces the most rapid flocculation of the clay and by assuming that each MB

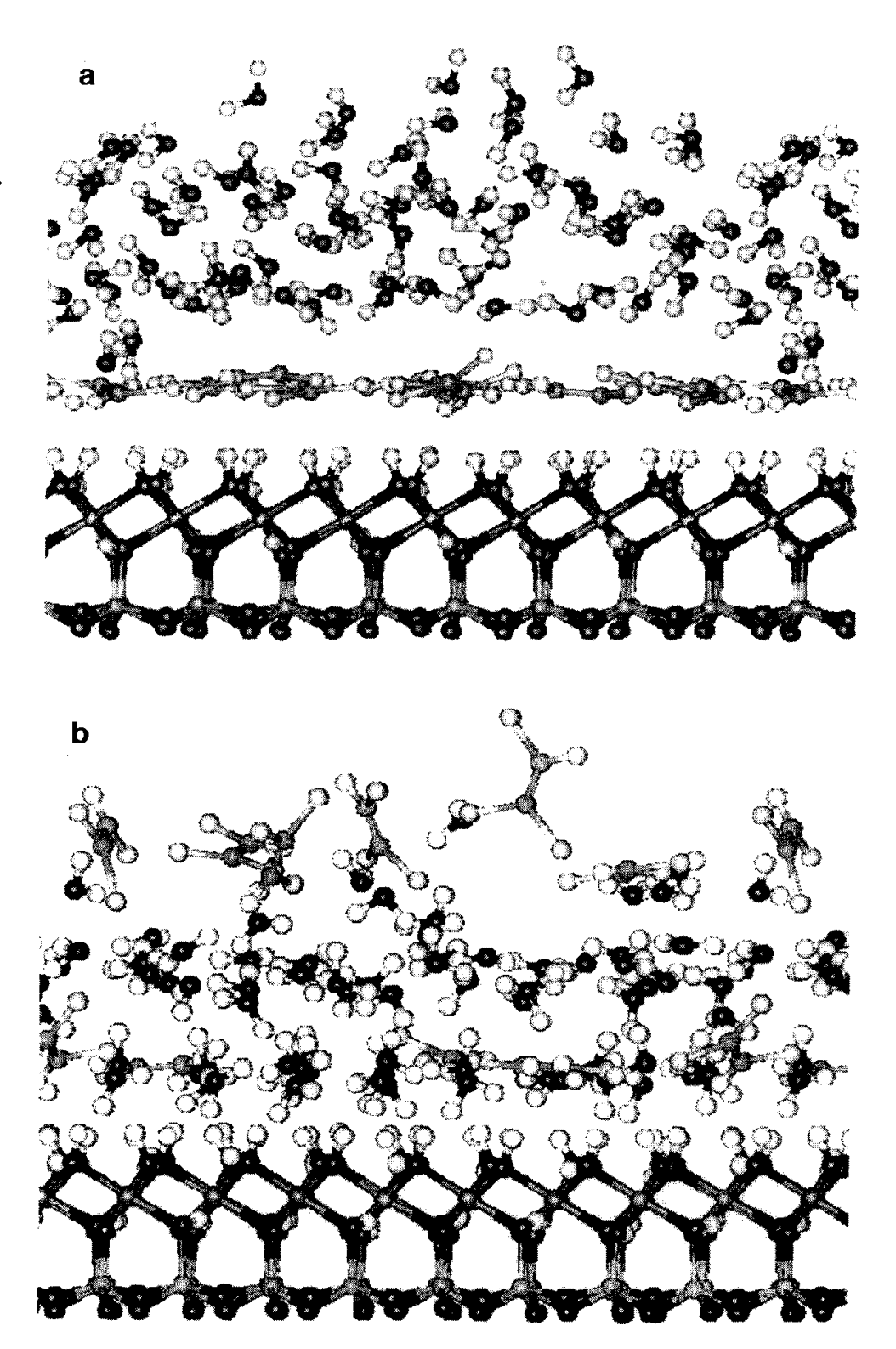


Fig. 8–2. (a) A monolayer of TCE was equilibrated with a hydroxylated aluminol kaolinite surface, then water was added. (b) After 350 ps of molecular dynamics simulation, 60% of the TCE had desorbed. Desorption occurred in two steps: first the TCE molecule "stood up" on the surface so that only one or two atoms contacted the clay, and then after some time detachment occurred and the TCE moved very quickly to the external water surface. When the same procedure was repeated at the siloxane kaolinite surface, after 350 ps of molecular dynamics simulation only 20% of the TCE had desorbed.

cation lies flat on the clay basal surface, covering approximately 0.55 nm<sup>2</sup>. Cation exchange capacities are estimated from the plateaus of MB adsorption isotherms, assuming that inorganic cations are fully exchanged. The procedure has been most successful in measuring sodium-clays (Brindley & Thompson, 1970; Lagaly, 1981) and has been widely used in industry as a simple means of estimating the relative smectite contents of bentonite deposits.

It is a characteristic aspect of the MB method that it frequently overestimates the values of both surface area and CEC (Hähner et al.,1996). Typical explanations for this phenomenon are that MB adsorbs in multiple layers (Hang & Brindley, 1970) or that it does not lie flat on the mineral surface (De et al., 1974; Shelden et al.,1993; Hähner et al.,1996; Bujdák & Komadel, 1997). The exact reason remains unclear because the mechanisms of MB adsorption to clay minerals are largely unknown and expected to be rather complex (Bodenheimer & Heller, 1968). Thus, the problem of MB adsorption is basically a structural one and of the kind for which MD simulations are particularly well suited.

For this reason we performed MD simulations of MB sorption at relatively high (~105 cmol of MB kg<sup>-1</sup> clay), intermediate (~70 cmol of MB kg<sup>-1</sup> clay), and low (~35 cmol of MB kg<sup>-1</sup> clay) loadings on various clay mineral surfaces, including a model beidellite and a model mica surface, with variable amounts of water. As a result of these calculations it must be concluded that MB ions can arrange in a large number of ways on silicate surfaces. Structures found on dry beidellite include: (i) single layers parallel to the interlayer surfaces; (ii) stacks in which the ions are approximately parallel to one another but at an angle with respect to the basal plane; and (iii) bilayers parallel to the clay basal planes. In each case the addition of water perturbs the regular stacking found in the absence of water.

Simulations with mica yielded similar results. At low loadings, when sufficient surface area is available, the molecules attach flat on the mica. At higher loadings some of the molecules begin to assume a tilted orientation with respect to the basal plane, finally forming irregular clusters with flat, tilted, and random orientations in which the molecules are piled on top of each other.

From all these findings it follows that MB adsorption does not involve a single, well-defined arrangement on clay surfaces, and the surface area occupied by an individual adsorbate molecule can vary over a broad range.

# Molecular Dynamics Simulations Concerning the Alkylammonium Ion Exchange Method

As a final example, we shall briefly summarize the results of investigations (Teppen, 1997) performed to determine mechanistic aspects of the alkylammonium ion-exchange method.

The alkylammonium ion-exchange (AAIE) method for layer-charge determination of smectitic and vermiculitic clays was pioneered in the 1960s by Lagaly and Weiss (see the review by Lagaly, 1994). It has the practical advantage that it allows determination of the layer charge (i.e., structural cation exchange capacities) for impure clays such as are found in soils. However, when the method is tested (Laird et al., 1989; Senkayi et al., 1985; Mermut, 1994) on pure clays and the results are compared with layer charges derived from elemental analyses, it is found

to systematically underpredict the layer charge (Laird, 1994). Many hypotheses have been advanced to explain this disparity (Lagaly, 1994; Laird, 1994), including charge heterogeneity, mineral-edge effects, and incomplete saturation of the CEC by the organic cations. To some extent, MD simulations can be used to test, on a molecular level, the plausibility of each of these hypotheses. For this purpose a series of some 30 MD simulations of alkylammonium ions were performed (Teppen, 1997) on muscovite mica and on a dioctahedral vermiculite.

Central to the AAIE method are assumptions made concerning the average surface areas and the average interlayer volumes occupied by the alkylammonium ions. These assumptions can be directly tested by inspecting the results of MD simulations. Indeed, when we inspected the arrangement of alkylammonium ions in the interlayer space of the vermiculite and the mica, we found that their arrangements were much less rigid and regular than usually assumed. Specifically, molecular dynamics simulations were performed testing the adsorption of alkylammonium ions on a dioctahedral vermiculite, composition  $(Si_{40}Al_8)Al_{24}O_{120}(OH)_{24}$ , with a tetrahedral charge of -8 balanced by eight alkylammonium ions. The CEC is therefore  $187 \text{ cmol}_c \text{ kg}^{-1}$ . Additional studies were done on a muscovite mica,  $(Si_{24}Al_8)Al_{16}O_{80}(OH)_{16}$ , with a tetrahedral charge of -8 balanced by eight alkylammonium ions. The CEC is therefore  $262 \text{ cmol}_c \text{ kg}^{-1}$ .

Detailed analyses of the structural results obtained by the calculations show (Teppen, 1997) that the disparity between the AAIE method and layer charge determinations by elemental analysis can be explained simply by demonstrating that the customary estimates of the occupied surface area and interlayer volume are inaccurate. The MD simulations can be used to derive expressions for the average surface areas and average interlayer volumes occupied by cations of a given alkyl chain length. These expressions can in turn be used to calibrate the alkylammonium ion method. In Fig. 8–3 it is shown that, when the AAIE method is recalibrated in accordance with the computed results, using improved estimates for occupied average surface areas and interlayer volumes, the discrepancies between AAIE layer charges and those determined by elemental analysis are essentially resolved (Teppen, 1997). Basically the calculations show that standard assumptions typically overestimate the size of the ammonium head group, underestimate the size of incremental CH<sub>2</sub>-groups, and overestimate the rigidity of alkyl chains.

# ONGOING RESEARCH

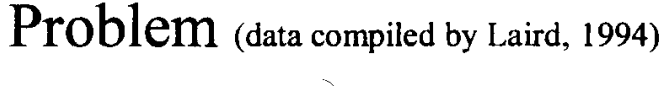
In this section several examples will be presented that are representative of ongoing research projects. Even though the results are still preliminary, the projects selected further illustrate the utility of MD simulations in soil chemistry. Topics include the calculation of free energy changes associated with cation exchange and the adsorption of proteins on clay mineral surfaces.

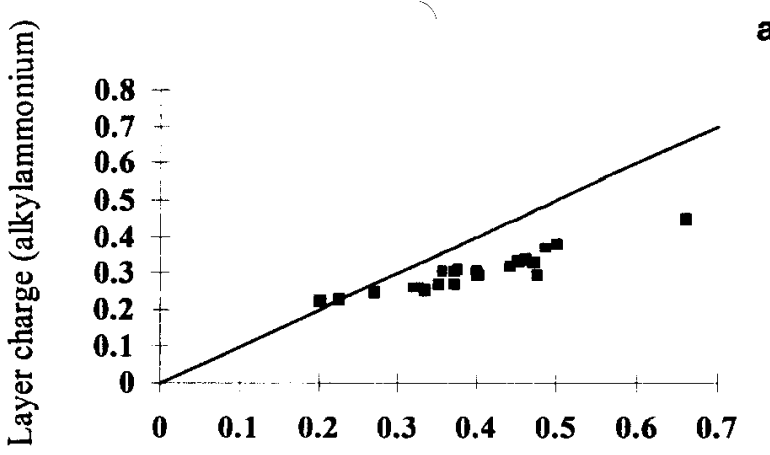
# **Cation Exchange Simulations**

# Theory

Simulations of  $K^+ \Rightarrow Rb^+$  and  $Rb^+ \Rightarrow Cs^+$  exchange were performed on an idealized montmorillonite  $(X^+Si_8Al_3MgO_{20}(OH)_4, CEC - 1.35 \text{ cmol}_c \text{ kg}^{-1})$  with a

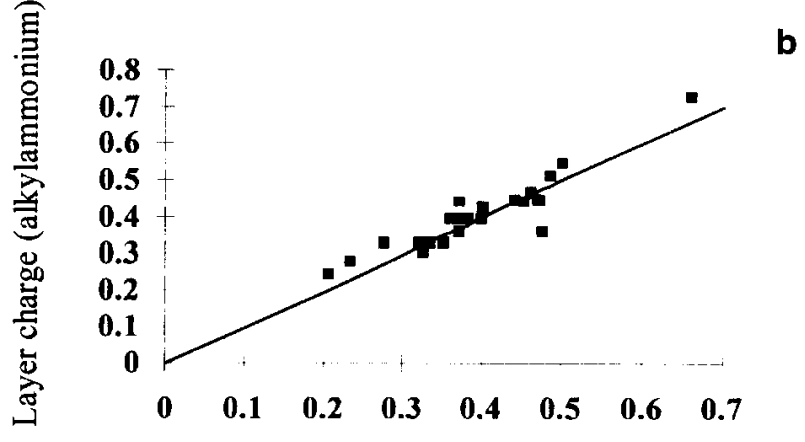
water content of 150 g kg<sup>-1</sup> (approximately equivalent to monolayer coverage). The overall exchange reaction was treated as the sum of two component reactions, the first corresponding to a change in the identity of the ion on the clay surface, and the second corresponding to a change in the identity of the ion in the bulk aqueous solution. In this way the overall reaction for the exchange of two ions  $A^+ \Rightarrow B^+$ ,





Layer charge (elemental analysis)

# Recalculation of Experimental Data Using New Calibration



Layer charge (elemental analysis)

Fig. 8–3. (a) When compared with layer charges determined by elemental analysis for pure clays, the alkylammonium ion-exchange method systematically underpredicts the charge. (b) When the alkylammonium method is recalibrated with expressions derived from MD simulations for the average surface areas and average interlayer volumes occupied by cations of a given alkyl chain length, and the new calibration is applied to experimental data sets (Laird et al., 1989; Senkayi et al., 1985; Mermut et al., 1994), the systematic differences between the results of the alkylammonium method and the elemental analysis are almost eliminated.

$$A^{+}-X + B^{+}_{(aq)} \Rightarrow A^{+}_{(aq)} + B^{+}-X \qquad \Delta G_{ex}$$
 [7]

can be written as the sum of two steps:

$$A^+-X \Rightarrow B^+-X \qquad \Delta G_{\text{clay}}$$
 [8]

$$B_{(aq)}^+ \Rightarrow A_{(aq)}^+ \qquad \Delta G_{soln}$$
 [9]

where X represents the clay lattice bearing 1 mole of negative charge. Thus, the Gibbs free energy change for the exchange reaction can be written as  $\Delta G_{\rm ex} = \Delta G_{\rm clay} + \Delta G_{\rm soln}$ .

To calculate the free energy terms, we used the free energy perturbation technique (Bash et al., 1987; Jorgensen & Ravimohan, 1985; Straatsma et al., 1986; MSI, 1997). In this procedure, the Gibbs free energy of a chemical reaction is obtained by mutating the parameters of the reactants into those of the products. This is done in a series of steps during which the parameters of the initial system are changed incrementally into those of the final system. The number of steps, n, is determined by the requirement that energy differences between neighboring steps should be  $\langle 2RT \rangle$  (Bash et al., 1987; Jorgensen & Ravimohan, 1985; Straatsma et al., 1986), i.e.,  $n = (\Delta G_{rx}/2RT)$ , where  $\Delta G_{rx}$  is the reaction Gibbs free energy. For example, in the case of the exchange reaction  $K^+ \Rightarrow Rb^+$ , 10 steps were required to mutate the parameters of  $K^+$  into  $Rb^+$  and vice versa, in order to calculate  $\Delta G_{clay}$  or  $\Delta G_{soln}$  (Eq. [8] and [9]).

The total number of steps, n, can be used to define a coupling parameter,  $\lambda$ :

$$\delta \lambda = 1/n \text{ and } \lambda = i(\delta \lambda)$$
 [10]

where *i* is the number (i = 0, 1,...n) of an individual step. At the *i*th step of the mutation of A<sup>+</sup> into B<sup>+</sup>, the potential energy of the system is calculated with force field parameters,  $P_{\lambda}$ , defined by the equation:

$$P_{\lambda} = P_{A} + \lambda (P_{B} - P_{A})$$
 [11]

where  $P_A$  and  $P_B$  are the potential parameters for  $A^+$  and  $B^+$ , respectively.

In order to calculate  $\Delta G_{\rm clay}$  or  $\Delta G_{\rm soln}$  (Eq. [8] and [9]) with the free energy perturbation technique, it is necessary to compute and sum the relative free energy differences between adjacent mutation steps. A procedure that can be used for this purpose is readily derived from standard statistical thermodynamic formulae.

In an NPT (constant mass, pressure and temperature) ensemble of clay-water systems the Gibbs free energy, G, is related to the partition function, Q, by the formula:

$$G = -kT(\ln Q) \tag{12}$$

where k is the Boltzmann constant. The difference in Gibbs free energy between two states i and j is therefore:

$$\Delta G_{ij} = G_i - G_i = -kT[\ln(Q_i/Q_i)]$$
 [13]

In Eq. [13] the ratio of partition functions can be expressed as:

$$Q_i/Q_i = [\exp(-\Delta E_{ii}/kT)]$$
 [14]

where E is internal energy, the brackets denote expectation value, and the subscripts identify the states involved in the difference. Combining Eq. [13] and [14] will yield:

$$\Delta G_{ij} = -kT\{\ln\left[\exp(-\Delta E_{ij}/kT)\right]\}$$
 [15]

Thus, the free energy difference between two states, or between two steps in the free energy perturbation scheme, can be obtained from the ensemble averages of the internal energy differences.

If the states *i* and *j* have approximately the same kinetic energy, KE, then  $\Delta E \approx \Delta V$ . For the systems dealt with in this work this is a good approximation, since kinetic energy differences,  $\Delta KE$ , between adjacent steps can be expected to be close to zero. Equation [15] can thus be rewritten as:

$$\Delta G_{ii} = -kT \{ \ln \left[ \exp(-\Delta V_{ii}/kT) \right] \}$$
 [16]

The important aspect of Eq. [16] is that  $[\exp(\Delta V_{ij}/kT)]$  and, hence,  $\Delta G_{ij}$ , for two steps i and j can be determined from the MD simulations.

In our current work, expectation values of  $\exp(-\Delta V/kT)$  are calculated by performing MD simulations (50 ps with a 0.5 fs time step) at individual steps i, defined by  $\lambda = i(\Delta \lambda)$ . It was determined that in order to establish an ensemble of clay/water systems at each step, it was sufficient to select several hundred (~400) instantaneous molecular configurations at random from the second half of each MD run. The collection of molecular configurations in each ensemble was then used to compute, according to Eq. [16],  $\Delta G$  for each subinterval ( $\lambda + \delta \lambda$  or  $\lambda - \delta \lambda$ ) along the mutation path.

In all simulations of clay mineral systems we apply periodic boundary conditions at constant pressure and temperature (constant NPT). This allows the system volume to change freely at 100 kPa (1 bar) external pressure and 298 K. Furthermore we employ Ewald summation to compute both electrostatic potentials and dispersive van der Waals interactions, and the simulations are fully dynamic, using the *Discover* module and *Insight II* graphical user interface of the MSI molecular modeling suite (MSI, 1997). The free energy perturbation technique is not implemented in this software per se so that many of the aforementioned calculations have to be performed with spreadsheet software (e.g., Microsoft Excel).

# **Cation Exchange Free Energy Calculations**

Using the formalism described above, we are calculating the free energy changes for the half reactions (Eq. [8] and [9]) of the exchange reactions

$$K^{+}-X + Rb^{+}_{(aq)} \Rightarrow K^{+}_{(aq)} + Rb^{+}-X$$
 [17]

and

$$Rb^+ X + Cs^+_{(aq)} \Rightarrow Rb^+_{(aq)} + Cs^+ X$$
 [18]

To perform the calculations corresponding to the reaction represented by Eq. [8], a montmorillonite supercell of composition  $K_4Si_{32}(Al_{12}Mg_4)O_{80}(OH)_{16}$  was created. The crystal structure of muscovite mica (Comodi & Zanazzi, 1995; Liang & Hawthorne, 1996) was modified by converting all tetrahedral cations to Si and substituting Mg for each of four  $Al^{3+}$  ions in the octahedral sheet, to create a high-charge montmorillonite with CEC of 135 cmol<sub>c</sub> kg<sup>-1</sup>. The substitution was implemented in such a way as to avoid charges on adjacent octahedral sites. Subsequently, the interlayer was expanded and enough water added to the interlayer space to form a monolayer (equilibrated  $d_{001}$  was  $1.209 \pm 0.005$  for K montmorillonite). To perform calculations corresponding to the reaction represented by Eq. [9], one cation, initially K<sup>+</sup>, was placed with one Cl<sup>-</sup> into a water box containing 254 water molecules.

Calculations of free energy differences are much more difficult and ambitious to attempt than simulations of other molecular properties, such as basic features of molecular structure. This is so because the resulting energy values are small differences between large numbers, and the results are acutely sensitive to the particular values assumed for the force field parameters. Since our force field parameters are still subject to ongoing refinements (see, e.g., Schäfer et al., 1999), the currently available cation exchange results are strictly preliminary. Nevertheless, the calculations performed so far suggest the following aspects of cation exchange processes on clay mineral surfaces.

First of all, the calculations suggest that the exchange reactions  $K^+ \Rightarrow Rb^+$ ,  $Rb^+ \Rightarrow Cs^+$  and  $K^+ \Rightarrow Cs^+$  are spontaneous at the clay mineral/aqueous solution interface. That is, the simulations correctly reproduce the well-known (Gast, 1969, 1972; Maes & Cremers, 1978; Sposito, 1984) selectivity sequence  $Cs^+ > Rb^+ > K^+$  on montmorillonite. In addition, the  $\Delta G_{clay}$  values available so far indicate that  $K^+ \Rightarrow Cs^+$ ,  $Rb^+ \Rightarrow Cs^+$  and  $K^+ \Rightarrow Cs^+$  are nonspontaneous processes on dry clay surfaces. That is, the driving force for the overall exchange reactions (Eq. [17] and [18]) does not lie in the ion-clay interactions but, rather, in the ion-water interactions. It is the fact that  $Rb^+$  is more hydrophobic than  $K^+$ , and  $Cs^+$  is more hydrophobic than either  $Rb^+$  or  $K^+$ , that causes the selectivity sequence  $Cs^+ > Rb^+ > K^+$  on montmorillonite. This finding is consistent with the Eisenman (1961) model of cation exchange as described by McBride (1994).

These conclusions are proposed on the basis of the following numerical results, which are somewhat tentative due to ongoing developments of our force field parameters. Transforming Rb<sup>+</sup> and Cs<sup>+</sup> into K<sup>+</sup> (Eq. [9]) in a water box (~250 water molecules with four cations and four Cl<sup>-</sup>) yielded free energy changes ( $\Delta G_{\rm soln}$ ) of -4.0 kcal mol<sup>-1</sup> for the Rb<sup>+</sup> to K<sup>+</sup> transformation and -9.4 kcal mol<sup>-1</sup> for the Cs<sup>+</sup> to K<sup>+</sup> transformation. This compares to experimental hydration free energy differences (Åqvist, 1990) of -5.1 kcal mol<sup>-1</sup> and -12.8 kcal mol<sup>-1</sup> for these two transformations, respectively. Combining these values with the free energy changes ( $\Delta G_{\rm clay}$ ) calculated for the corresponding transformation of ions adsorbed on clay (Eq. [8]), the calculated free energy changes for the overall exchange reactions ( $\Delta G_{\rm ex}$ ) were -1.3 kcal mol<sup>-1</sup> for K  $\Rightarrow$  Rb exchange and -2.7 kcal mol<sup>-1</sup> for K  $\Rightarrow$  Cs exchange. These values compare to experimental free energies of exchange (Gast, 1969, 1972; Maes & Cremers, 1978) found on Chambers and Camp Berteau montmorillonites (CEC 100 cmol<sub>c</sub> kg<sup>-1</sup>) of -0.6 to -1.11 kcal mol<sup>-1</sup> for K  $\Rightarrow$  Rb exchange and -1.16 to -1.66 kcal mol<sup>-1</sup> for K  $\Rightarrow$  Cs exchange.

# Some Structural Aspects of Cation Arrangements on Clay Surfaces

Another interesting aspect of the simulation results concerns the location of the counterions in the interlayer space. The (001) perspective of simulated Cs<sup>+</sup>-montmorillonite (Fig. 8–4) shows that, at a water content [150 g H<sub>2</sub>O kg<sup>-1</sup>] approximately corresponding to a monolayer, the cations always adopted locations such that they were aligned with the center of a siloxane ditrigonal cavity on the basal surface of one clay layer and with the base of an SiO<sub>4</sub> tetrahedron on the basal surface of the opposing clay layer. At lower water contents this configuration was not stable, and the interlayer counterions tended to align themselves with the centers of siloxane cavities on the basal surfaces of both clay layers.

All surface complexes between counterions and the clay mineral surfaces were inner sphere due to our use of a monolayer of water. When present, water molecules tended to position themselves in such a way as to be in equatorial association with the counterions, i.e., they did not interpose themselves between a counterion and a clay surface. The equilibrium  $d_{001}$  spacings between hydrated montmorillonite layers in these simulations were reasonable [see, e.g., Brindley (1980) for experimental values], varying from 1.209  $\pm$  0.005 nm (K) to 1.214  $\pm$  0.004 nm (Rb) to 1.223  $\pm$  0.005 nm (Cs).

# The Adsorption of Proteins on Clay Mineral Surfaces

It is well known that much of the organic matter in soils occurs not in a free state, but in intimate association with the surfaces of clay minerals. These organic/clay complexes are of great interest because of the role that they play in regulating the movement of anthropogenic organic compounds through the soil. Thus, in studying the fate of pollutants in soils, it is not sufficient only to investigate their interactions with clay mineral surfaces, but also with organic matter/clay complexes.

Humic acids are ubiquitous in soils and are among the most important compounds that coat clay mineral surfaces. For this reason, some time ago we started MD simulations of humic acid/clay mineral complexes. It is a difficulty of such modeling calculations that the structures of humic acids are ill defined and highly variable from one molecule to the next, so that it is difficult to design a humic molecule that is representative of the entire class.

In contrast to humic acids, proteins constitute a class of compounds that are chemically well defined, prevalent in soils, and able to form complexes with clay surfaces. Therefore, in order to study the interactions of anthropogenic chemicals with organic matter/clay complexes, we have started a series of MD simulations dealing with the adsorption of proteins by phyllosilicate surfaces. These investigations can be extended to humic acid coated clays, because many of the functional groups in proteins are the same as those in humic acids.

Some of the results of our MD simulations of proteins on clay mineral surfaces are summarized in Fig. 8–5. When proteins are placed in the interlayer space of clay minerals, interactions between the surface and the protein compete with intramolecular protein nonbonded interactions. As a result, a protein molecule can get stretched out along the mineral surface, significantly denatured from its native state. In the case of subredoxin adsorbed by pyrophyllite, for example, the mole-

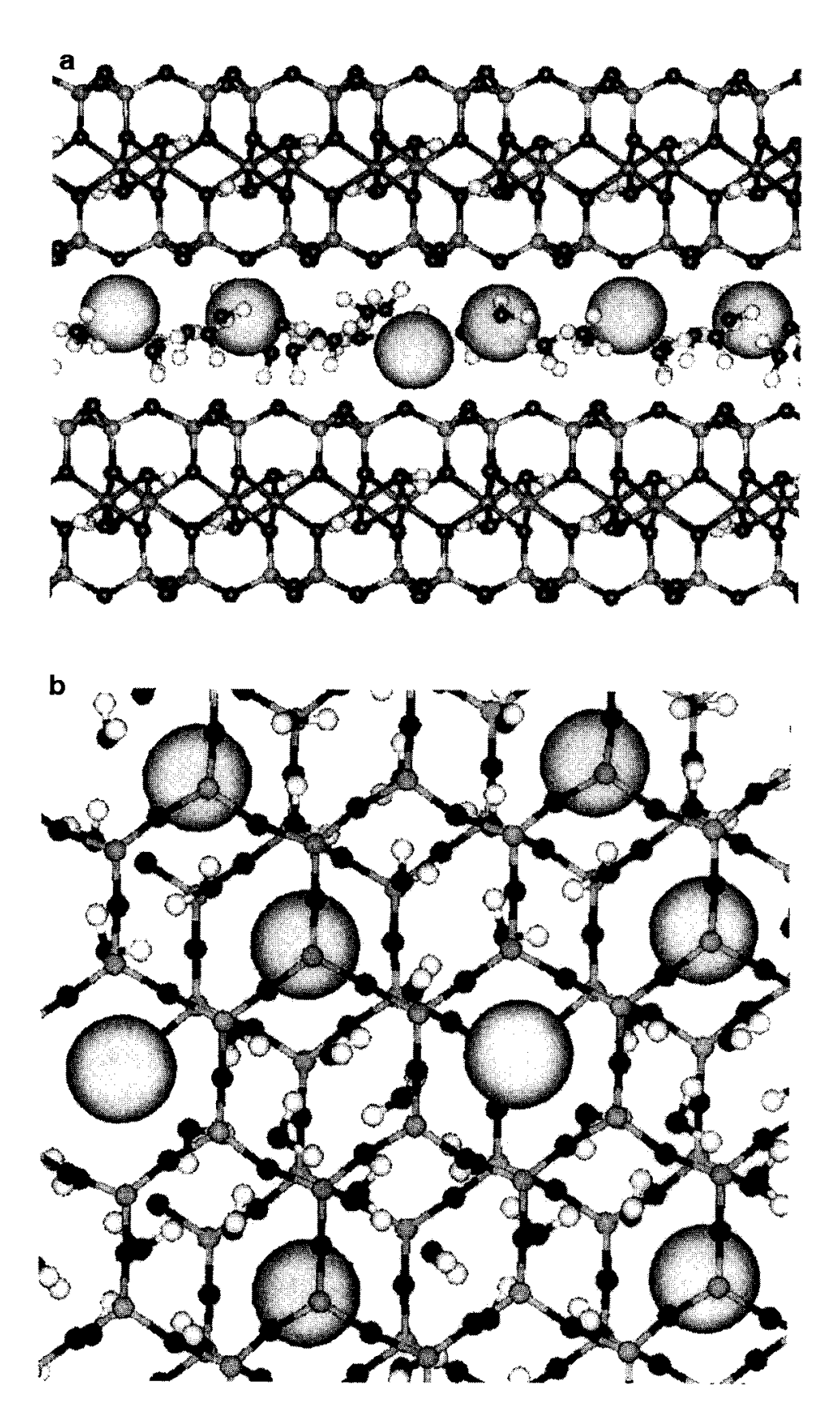


Fig. 8–4. (a) Representative snapshots of equilibrated Cs-montmorillonite. The cations and clay were solvated by a monolayer of water, as shown in the (010) view. (b) The (001) perspective shows that the aqueous cations adopted locations where they always bridged between a siloxane ditrigonal cavity on one crystal layer and a tetrahedral site on the opposing layer. Dehydrating the system caused the cations to align themselves with the centers of siloxane cavities on both layers.

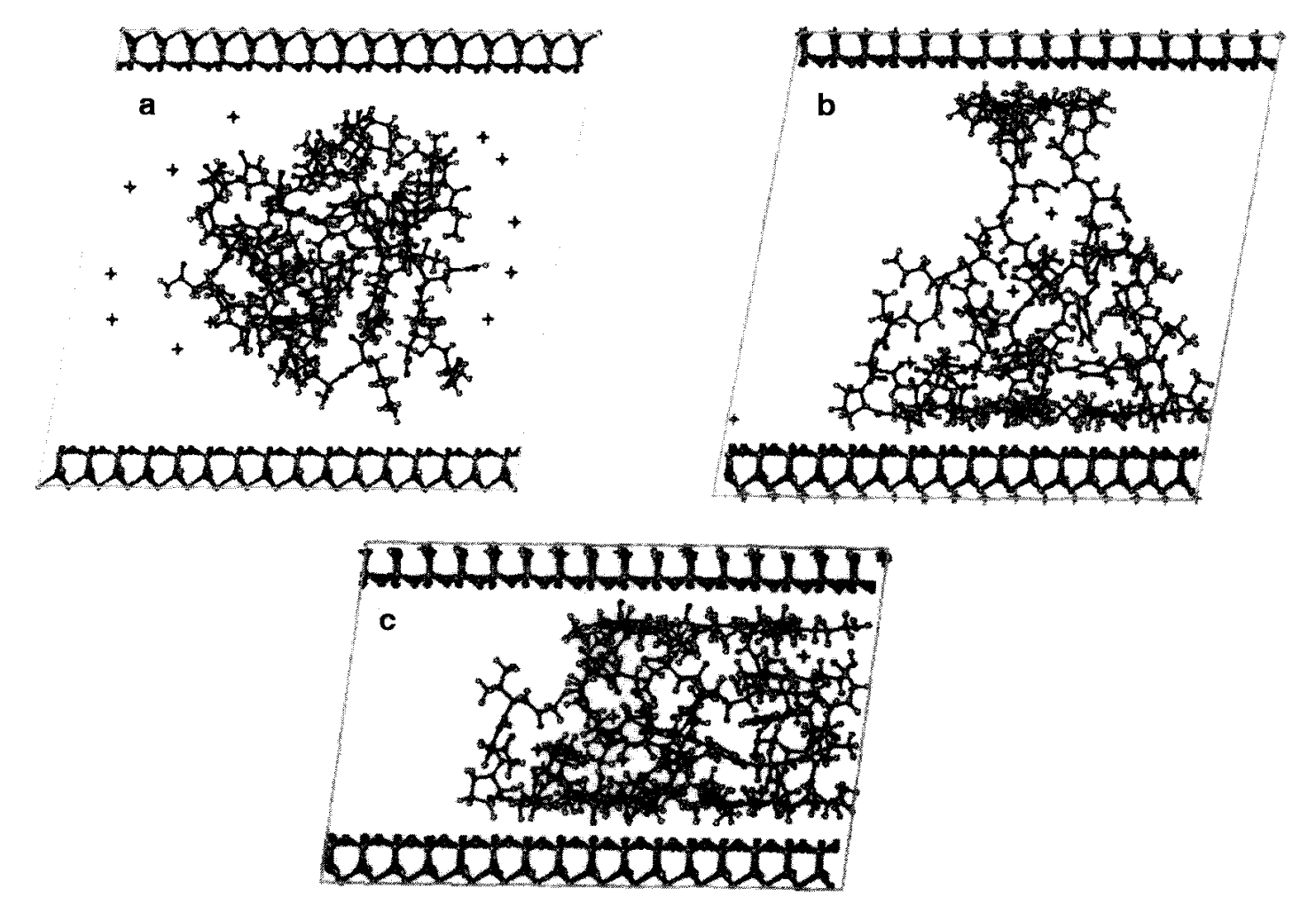


Fig. 8–5. Rubredoxin on pyrophyllite. When proteins are placed into the interlayer space of a 2:1 clay mineral, the interactions of the protein with the mineral surface compete with intraprotein nonbonded interactions. (a) The crystal structure of rubredoxin taken from the Brookhaven Protein Data Bank is shown in the interlayer space of pyrophyllite, which has been artificially expanded to 5 nm. (b) During the course of NVT molecular dynamics simulation, end groups of the protein begin to interact with, and migrate along, the mineral surface. (c) When the system is then subjected to NPT molecular dynamics, the interlayer space collapses, compressing the protein from a diameter of 3.6 to 2.4 nm.

cule was found to change its diameter from ~3.6 nm to ~2.4 nm, indicating that systems of this kind can form strong complexes with clay surfaces. Ongoing MD simulations are exploring the role of water in this process.

# **CONCLUSIONS AND SUMMARY**

The examples presented above illustrate that empirical molecular modeling and molecular dynamics techniques have matured to the extent that they may now be used in a productive manner to examine a variety of phenomena relevant to soil and environmental chemistry. Ultimately, all physical and chemical processes in soils are molecular by nature, and it must be possible for them to be modeled in terms of molecular properties.

At its current stage of development, computer modeling of adsorption phenomena at the clay mineral/aqueous solution interface is perhaps most reliable in shedding light on questions of structural chemistry. For example, can MB adsorb flat on a mineral surface? Can it form double layers in addition to single layers? Do TCE and other anthropogenic pollutants sorb preferentially to mineral surfaces or do they tend to remain in the aqueous phase? What is the average volume of alkylammonium ions in the interlayer space as a function of chain length? Such questions can be answered, we feel, rather reliably.

At the same time, when experimental problems involve small energy differences between competing states, the results of empirical molecular modeling calculations must be accepted with some caution because calculated energy differences are highly dependent on the parameters of a given force field. For this reason, the free energies of ion exchange described above have been presented as tentative. They illustrate that while calculations of this kind are technically possible, further development of our clay mineral force field parameters is needed in order to make calculated free energy differences or enthalpies reliable at the level of a few tenths of a kilocalorie per mole. The current situation of empirical molecular modeling and dynamics is thus very similar to that of molecular quantum mechanics one or two decades ago (Schäfer, 1983), when it was possible to determine details of molecular structure with great accuracy, but calculated energy differences were not so reliable.

It is at this point where molecular modeling procedures can be further improved. We see opportunities for improvement mainly in two areas. First, by enhancing the available molecular data base, for example by adding results from high quality ab initio calculations, it will be possible to further improve the parameterization of existing molecular force fields. Second, the direct application of quantum mechanical procedures to adsorption phenomena on mineral surfaces is becoming increasingly facilitated by the availability of faster computers and more efficient software. The program CASTEP (Payne et al., 1992), for example, allows energy minimizations of molecular species adsorbed on fully periodic systems. Quantum molecular dynamics of large systems is currently not possible, but may very well become possible in the not so distant future.

Thus, in a variety of applications—such as in soil remediation, studies of catalytic processes on clay mineral surfaces, determinations of the strength of ad-

sorption of pesticides on pristine or humic-coated surfaces, determinations of the conformational or structural properties of humics and their dependence on pH, studies of the structure and properties of interfacial water, and many others—it seems safe to predict that computer modeling with atomic scale resolution will become an increasingly useful and important tool in the study of soil chemical phenomena.

## REFERENCES

- Allen, M.P., and D.J. Tildesley. 1987. Computer simulation of liquids. Oxford Univ. Press, Oxford, UK. Åqvist, J. 1990. Ion-water interaction potentials derived from free energy perturbation simulations. J. Phys. Chem. 94:8021–8024.
- Bash, P.A., U.C. Singh, R. Langridge, and P.A. Kollman. 1987. Free-energy calculations by computer-simulation. Science (Washington, DC) 236:564–568.
- Battle, P.D., T.S. Bush, and C.R.A. Catlow. 1995. Structures of quaternary Ru and Sb oxides by computer simulation. J. Am. Chem. Soc. 117:6292–6296.
- Bish, D.L. 1993. Rietveld refinement of the kaolinite structure at 1.5 K. Clay Clay Miner. 41:738–744.
- Bodenheimer, W., and L. Heller. 1968. Sorption of methylene blue by montmorillonite saturated with different cations. Isr. J. Chem. 6:307–314.
- Boek, E.S., P.V. Coveney, and N.T. Skipper. 1995a. Molecular modeling of clay hydration: A study of hysteresis loops in the swelling curves of sodium montmorillonites. Langmuir 11:4629–4631.
- Boek, E.S., P.V. Coveney, and N.T. Skipper. 1995b. Monte Carlo molecular modeling studies of hydrated Li-, Na-, and K-smectites: Understanding the role of potassium as a clay swelling inhibitor. J. Am. Chem. Soc. 117:12 608–12 617.
- Breu, J., and C.R.A. Catlow. 1995. Chiral recognition among tris(diimine)-metal complexes. 4. Atomistic computer modeling of a monolayer of [Ru(bpy)<sub>3</sub>]<sup>2+</sup> intercalated into a smectite clay. Inorg. Chem. 34:4504–4510.
- Breu, J., N. Raj, and C.R.A. Catlow. 1999. Chiral recognition among trisdiimine-metal complexes, Part 4. Atomistic computer modeling of [Ru(bpy)<sub>3</sub>]<sup>2+</sup> and [Ru(phen)<sub>3</sub>]<sup>2+</sup> intercalated into low charged smectites. J. Chem. Soc. Dalton 1999(no. 6):835-845.
- Brindley, G.W. 1980. Order-disorder in clay mineral structures. p. 125–195. *In* G.W. Brindley and G. Brown (ed.) Crystal structures of clay minerals and their x-ray identification. Miner. Soc., London
- Brindley, G.W., and T.D. Thompson. 1970. Methylene blue adsorption by montmorillonite. Determination of surface areas and exchange capacities with different initial cation saturations. Isr. J. Chem. 8:409-415.
- Bujdák, J., and P. Komadel. 1997. Interaction of methylene blue with reduced charge montmorillonite. J. Phys. Chem. B 101:9065–9068.
- Bush, T.S., C.R.A. Catlow, A.V. Chadwick, M. Cole, R.M. Geatches, G.N. Greaves, and S.M. Tomlinson. 1992. Studies of cation dopant sites in metal oxides by EXAFS and computer-simulation techniques. J. Mater. Chem. 2:309–316.
- Bush, T.S., J.D. Gale, C.R.A. Catlow, and P.D. Battle. 1994. Self-consistent interatomic potentials for the simulation of binary and ternary oxides. J. Mater. Chem. 4:831–837.
- Capkov, P., R.A.J. Driessen, M. Numan, H. Schenk, Z. Weiss, and Z. Klika. 1998a. Molecular simulations of montmorillonite intercalated with aluminum complex cations. Part I. Intercalation with  $[Al_{13}O_4(OH)_{24+x}(H_2O)_{12-x}]^{(7-x)+}$ . Clay Clay Miner. 46:232–239.
- Capkov, P., R.A.J. Driessen, M. Numan, H. Schenk, Z. Weiss, and Z. Klika. 1998b. Molecular simulations of montmorillonite intercalated with aluminum complex cations. Part II. Intercalation with Al(OH)<sub>3</sub>-fragment polymers. Clay Clay Miner. 46:240–244.
- Capkov, P., R.A.J. Driessen, H. Schenk, and Z. Weiss. 1997. Interlayer porosity in montmorillonite intercalated with keggin-like cations. Studies by molecular mechanics simulation. J. Molec. Model. 3:467–472.
- Chang, F.-R.C., N.T. Skipper, K. Refson, J.A. Greathouse, and G. Sposito. 1999. Interlayer molecular structure and dynamics in Li-, Na-, and K-montmorillonite-water systems. p. 88–106. *In D.L. Sparks* and T.J. Grundl (ed.) Mineral water interfacial: Kinetics and mechanisms. ACS, Columbus, OH.
- Chang, F. R.C., N.T. Skipper, and G. Sposito. 1995. Computer simulation of interlayer molecular structure in sodium montmoriflonite hydrates. Langmuir 11:2734–2741.

Chang, F.-R.C., N.T. Skipper, and G. Sposito. 1997. Monte Carlo and molecular dynamics simulations of interfacial structure in lithium-montmorillonite hydrates. Langmuir 13:2074–2082.

- Code of Federal Regulations. 1993. National primary drinking water regulations. 40 CFR. Part 141. U.S. Gov. Print. Office, Washington, DC.
- Collins, D.R., and C.R.A. Catlow. 1990. Interatomic potentials for micas. Molec. Sim. 4:341–346.
- Collins, D.R., and C.R.A. Catlow. 1991. Energy-minimized hydrogen-atom position of kaolinite. Acta Crystall. B 47:678–682.
- Collins, D.R., and C.R.A. Catlow. 1992. Computer simulation of structures and cohesive properties of micas. Am. Miner. 77:1172–1181.
- Collins, D.R., W.G. Stirling, C.R.A. Catlow, and G. Rowbotham. 1993. Determination of acoustic phonon dispersion curves in layer silicates by inelastic neutron scattering and computer simulation techniques. Phys. Chem. Miner. 19:520–527.
- Comodi, P., and P.F. Zanazzi. 1995. High-pressure structural study of muscovite. Phys. Chem. Miner. 22:170–177.
- Cygan, R.T. 1998. Molecular models of metal sorption on clay minerals. p. 127–176. *In J.D. Kubicki* and W.F. Bleam (ed.) Molecular modeling of clays and mineral surfaces. Clay Miner. Soc., Boulder, CO.
- Cygan, R.T., K.L. Nagy, and P.V. Brady. 1998. Molecular models of cesium sorption on kaolinite. p. 383–399. *In* E.A. Jenne (ed.) Adsorption of metals by geomedia. Acad. Press, San Diego, CA.
- De, D.K., J.L. das Kanugo, and S.K. Chakravarty. 1974. Adsorption of methylene blue, crystal violet and malachite green on bentonite, vermiculite, kaolinite, asbestos, and feldspar. Ind. J. Chem. 12:1187–1189.
- Delville, A. 1991. Modeling the clay-water interface. Langmuir 7:547–555.
- Delville, A. 1992. Structure of liquids at a solid interface: An application to the swelling of clay by water. Langmuir 8:1796–1805.
- Delville, A. 1993. Structure and properties of confined liquids: A molecular model of the clay-water interface. J. Phys. Chem. 97:9703–9712.
- Delville, A., and S. Sokolowski. 1993. Adsorption of vapor at a solid interface: A molecular model of clay wetting. J. Phys. Chem. 97:6261–6271.
- Dixon, J.B. 1989. Kaolin and serpentine group minerals. p. 468–526. *In J.B. Dixon and S.B. Weed (ed.)* Minerals in soil environments. 2nd ed. SSSA, Madison, WI.
- Eisenman, G. 1961. On the elementary origin of equilibrium ionic specificity. p. 163–179. *In A. Kleinzeller and A. Kotyk (ed.) Symposium on membrane transport and metabolism. Acad. Press, New York.*
- Estes, T. J., R.V. Shah, and V.L. Vilker. 1988. Adsorption of low molecular weight halocarbons by montmorillonite. Environ. Sci. Technol. 22:377–381.
- Farrell, J., and M. Reinhard. 1994a. Desorption of halogenated organics from model solids, sediments, and soil under unsaturated conditions. 1. Isotherms. Environ. Sci. Technol. 28:53–62.
- Farrell, J., and M. Reinhard. 1994b. Desorption of halogenated organics from model solids, sediments, and soil under unsaturated conditions. 2. Kinetics. Environ. Sci. Technol. 28:63–72.
- Gale, J.D., C.R.A. Catlow, and W.C. Mackrodt. 1992. Periodic ab initio determination of interatomic potentials for alumina. Model. Simul. Mater. Sci. Eng. 1:73–81.
- Gast, R.G. 1969. Standard free energies of exchange for alkali metal cations on Wyoming bentonite. Soil Sci. Soc. Am. J. 33:37–41.
- Gast, R.G. 1972. Alkali metal cation exchange on Chambers montmorillonite. Soil Sci. Soc. Am. J. 36:14–19.
- Gay-Lussac, J.L. 1808. Memoires de la Societe d'Arcueil 2:207.
- Greathouse, J., and G. Sposito. 1998. Monte Carlo and molecular dynamics studies of interlayer structure in Li(H<sub>2</sub>O)<sub>3</sub>-smectites. J. Phys. Chem. B 102:2406–2414.
- Hähner, G., A. Marti, N.D. Spencer, and W.R. Caseri. 1996. Orientation and electronic structure of methylene blue on mica: A near edge x-ray absorption fine structure spectroscopic study. J. Chem. Phys. 104:7749–7757.
- Hang, P.T., and G.W. Brindley. 1970. Methylene blue adsorption by clay minerals. Determination of surface areas and cation exchange capacities. Clay Clay Miner. 18:203–212
- Hill, J.-R., and J. Sauer. 1994. Molecular mechanics potential for silica and zeolite catalysts based on ab initio calculations. 1. Dense and microporous silica. J. Phys. Chem. 98:1238-1244.
- Hill, J.-R., and J. Sauer. 1995. Molecular mechanics potential for silica and zeolite catalysts based on ab initio calculations. 2. Aluminosilicates. J. Phys. Chem. 99:9536–9550.
- Janeba, D., P. Capkov, and Z. Weiss. 1998. Molecular mechanics studies of montmorillonite intercalated with tetramethylammonium and trimethylphenylammonium. J. Molec. Model. 4:176–182.

- Jorgensen, W. L., and C. Ravimohan. 1985. Monte-Carlo simulation of differences in free-energies of hydration. J. Chem. Phys. 83:3050–3054.
- Karaborni, S., B. Smit, W. Heidug, J. Urai, and E. van Oort. 1996. The swelling of clays: Molecular simulations of the hydration of montmorillonite. Science (Washington, DC) 271:1102–1104.
- Keldsen, G.L., J.B. Nicholas, K.A. Carrado, and R.E. Winans. 1994. Molecular modeling of the enthalpies of adsorption of hydrocarbons on smectite clay. J. Phys. Chem. 98:279–284.
- Kerndorff, H., R. Schleyer, G. Milde, and R.H. Plumb, Jr. 1992. Geochemistry of groundwater pollutants at German waste disposal sites. p. 245–271. *In* S. Lesage and R.E. Jackson (ed.) Groundwater contamination and analysis at hazardous waste sites. Marcel Dekker, New York.
- Lagaly, G. 1981. Characterization of clays by organic compounds. Clay Miner. 16:1–21.
- Lagaly, G. 1994. Layer charge determination by alkylammonium ions. p. 1–46. *In A.R. Mermut* (ed.) Layer charge characteristics of 2:1 silicate clay minerals. Clay Miner. Soc., Boulder, CO.
- Laird, D.A., A.D. Scott, and T.E. Fenton. 1989. Evaluation of the alkylammonium method of determining layer charge. Clay Clay Miner. 37:41–46.
- Laird, D.A. 1994. Evaluation of the structural formula and alkylammonium methods of determining layer charge. p. 79–103. *In* A.R. Mermut (ed.) Layer charge characteristics of 2:1 silicate clay minerals. Clay Miner. Soc., Boulder, CO.
- Lee, J.H., and S. Guggenheim. 1981. Single crystal x-ray refinement of pyrophyllite-1*Tc*. Am. Miner. 66:350–357.
- Lewis, D.W., C.R.A. Catlow, G. Sankar, and S.W. Carr. 1995. Structure of iron-substituted ZSM-5. J. Phys. Chem. 99:2377–2383.
- Liang, J.-J., and F.C. Hawthorne. 1996. Rietveld refinement of micaceous materials: Muscovite-2M<sub>1</sub>, a comparison with single-crystal structure refinement. Can. Miner. 34:115–122.
- Maes, A., and A. Cremers. 1978. Charge density effects in ion exchange. Part 2. Homovalent exchange equilibria. J.C.S. Faraday I 74:1234–1241.
- Maple, J.R., M.-J. Hwang, T.P. Stockfish, U. Dinur, M. Waldman, C.S. Ewig, and A.T. Hagler. 1994. Derivation of Class II force fields. I. Methodology and quantum force field for the alkyl functional group and alkane molecules. J. Comp. Chem. 15:162–182.
- McBride, M.B. 1994. Environmental chemistry of soils. Oxford Univ. Press, New York.
- Mermut, A.R. 1994. Problems associated with layer charge characterization of 2:1 phyllosilicates. p. 105–122. *In* A.R. Mermut (ed.) Layer charge characteristics of 2:1 silicate clay minerals. Clay Miner. Soc., Boulder, CO.
- Molecular Simulations, Inc. 1997. Discover user guide, September, 1997. MSI, San Diego, CA.
- Park, S., A. Fitch, and Y. Wang. 1997. Computational studies compared to electrochemical measurements of intercalation of cationic compounds in Wyoming montmorillonite. J. Phys. Chem. B101:4889–4896.
- Payne, M.C., M.D. Teter, D.C. Allan, T.A. Arias, and J.D. Joannopoulos. 1992. Iterative minimization techniques for *ab initio* total energy calculations, molecular dynamics and conjugate gradients. Rev. Mod. Phys. 64:1045–1097.
- Purton, J., R. Jones, C.R.A. Catlow, and M. Leslie. 1993. Ab initio potentials for the calculation of the dynamical and elastic properties of α-quartz. Phys. Chem. Min. 19:392–400.
- Ramek, M., F.A. Momany, D.M. Miller, and L. Schäfer. 1996. On the importance of full geometry optimization in correlation-level ab initio molecular conformational analysis. J. Molec. Struct. 375:189–191.
- Rustad, J.R., A.R. Felmy, and B.P. Hay. 1996a. Molecular statics calculations for iron oxide and hydroxide minerals: Toward a flexible model of the reactive mineral-water interface. Geochim. Cosmochim. Acta 60:1553–1562.
- Rustad, J.R., A.R. Felmy, and B.P. Hay. 1996b. Molecular statics calculations of proton binding to goethite surfaces: A new approach to estimation of stability constants for multisite surface complexation models. Geochim. Cosmochim. Acta 60:1563–1576.
- Rustad, J.R., and B.P. Hay. 1995. A molecular dynamics study of solvated orthosilicic acid and orthosilicate anion using parameterized potentials. Geochim. Cosmochim. Acta 59:1251–1257.
- Rustad, J.R., B.P. Hay, and J.W. Halley. 1995. Molecular dynamics simulation of iron(III) and its hydrolysis products in aqueous solution. J. Chem. Phys. 102:427–431.
- Saalfeld, H., and M. Wedde. 1974. Refinement of the crystal structure of gibbsite, Al(OH)<sub>3</sub>. Z. Kristallogr. 139:129–135.
- Sanders, M.J., M. Leslie, and C.R.A. Catlow. 1984. Interatomic potentials for SiO<sub>2</sub>, J.C.S. Chem. Comm. 1984:1271–1273.
- Sato, H., A. Yannagishi, and S. Kato. 1992a. Theoretical study on the interactions between a metal chelate and a clay. Monte Carlo simulations. J. Phys. Chem. 96:9377–9382.

Sato, H., A. Yamagishi, and S. Kato. 1992b. Theoretical study on racemic adsorption of tris(1,10-phenanthroline)metal(II) by a clay: Monte Carlo simulations. J. Phys. Chem. 96:9382–9387.

- Sato, H., A. Yamagishi, K. Nata, and S. Kato. 1996. Monte Carlo simulations on intercalation of tris(1,10-phenanthroline)metal(II) by saponite clay. J. Phys. Chem. 100:1711–1717.
- Schäfer, L. 1983. The ab initio gradient revolution in structural chemistry: The importance of local molecular geometries and the efficacy of joint quantum mechanical and experimental procedures. J. Molec. Struct. 100:51–73.
- Schäfer, L., C.-H. Yu, B.J. Teppen, D.M. Miller, and K. Rasmussen. 1999. Refinements of water parameters for molecular dynamics simulations of adsorption at the clay mineral/aqueous solution interface. p. 541–546. *In* H. Kodama et al. (ed.) Clays for our future. Proc. 11th Int. Clay Conf. 1999, Ottawa, Can. 15–21 June 1997. ICC97 Organiz. Committ., Ottawa, Canada.
- Schleyer, R., H. Kerndorff, and G. Milde. 1992. Detection and evaluation of groundwater contamination caused by waste sites. p. 273–291. *In S. Lesage and R.E. Jackson (ed.)* Groundwater contamination and analysis at hazardous waste sites. Marcel Dekker, New York.
- Senkayi, A.L., J.B. Dixon, L.R. Hossner, and L.A. Kippenberger. 1985. Layer charge evaluation of expandable soil clays by an alkylammonium method. Soil Sci. Soc. Am. J. 49:1054–1060.
- Shelden, R.A., W.R. Caseri, and U.W. Suter. 1993. Ion exchange on muscovite mica with ultrahigh specific surface area. J. Colloid Interf. Sci. 157:318–327.
- Skipper, N.T. 1998a. Computer simulation of aqueous pore fluids in 2:1 clay minerals. Miner. Mag. 62:657–667.
- Skipper, N.T. 1998b. Monte Carlo and molecular dynamics computer simulation of aqueous interlayer fluids in clays. p. 90–126. *In J.D. Kubicki* and W.F. Bleam (ed.) Molecular modeling of clays and mineral surfaces. Clay Miner. Soc., Boulder, CO.
- Skipper, N.T., F.-R.C. Chang, and G. Sposito. 1995a. Monte Carlo simulation of interlayer molecular structure in swelling clay minerals. 1. Methodology. Clays Clay Miner. 43:285–293.
- Skipper, N.T., K. Refson, and J.D.C. McConnell. 1991. Computer simulation of interlayer water in 2:1 clays. J. Chem. Phys. 94:7434–7445.
- Skipper, N.T., G. Sposito, and F.-R.C. Chang. 1995b. Monte Carlo simulation of interlayer molecular structure in swelling clay minerals. 2. Monolayer hydrates. Clays Clay Miner. 43:294–303.
- Smith, D.E. 1998. Molecular computer simulations of the swelling properties and interlayer structure of cesium-montmorillonite. Langmuir 14:5959–5967.
- Sposito, G. 1984. The surface chemistry of soils. Oxford Univ. Press, New York.
- Straatsma, T. P., H.J.C. Berendsen, and J.P.M. Postma. 1986. Free-energy of hydrophobic hydration—a molecular-dynamics study of noble-gases in water. J. Chem. Phys. 85:6720–6727.
- Teppen, B.J. 1997. Theoretical calibration of the alkylammonium ion-exchange mechanism for layer-charge determination. p. A74. *In* The 11th Int. Clay Conf., Program with Abstracts, Ottawa, Can. 15–21 June. Clay Miner. Soc., Boulder, CO.
- Teppen, B.J., D.M. Miller, S.Q. Newton, and L. Schäfer. 1994. Choice of computational techniques and molecular models for ab initio calculations pertaining to solid silicates. J. Phys. Chem. 98:12545–12557.
- Teppen, B. J., K. Rasmussen, P.M. Bertsch, D.M. Miller, and L. Schäfer. 1997. Molecular dynamics modeling of clay minerals. 1. Gibbsite, kaolinite, pyrophyllite, and beidellite. J. Phys. Chem. 101:1579–1587.
- Teppen, B.J., R.R. Arands, and J. Farrell. 1998a. TCE interactions with mineral surfaces: Correlating molecular simulations with experimental data. p. 197. *In* Agronomy abstracts. ASA, Madison, WI.
- Teppen, B.J., C.-H. Yu, D.M. Miller, and L. Schäfer. 1998b. Molecular dynamics simulations of sorption of organic compounds at the clay mineral/aqueous solution interface. J. Comp. Chem. 19:144–153.
- Teppen, B.J., C.-H. Yu, D.M. Miller, and L. Schäfer. 1998c. Molecular modeling studies of TCE sorption/desorption on clays. p. 39. *In* Molecular modeling of clays and clay surface properties. Meet. Progr. Abstracts, 35th Annu. Meet., Cleveland, OH. 6–10 June. Clay Miner. Soc., Boulder, CO.
- West, C.C. 1992. Surfactant-enhanced solubilization of tetrachloroethylene and degradation products in pump and treat remediation. p. 149–158. *In* D.A. Sabatini and R.C. Knox (ed.) Transport and remediation of subsurface contaminants. Colloidal, interfacial, and surfactant phenomena. ACS, Washington, DC.